PACIFIC EARTHQUAKE ENGINEERING RESEARCH CENTER

Shaking Table Tests and Numerical Investigation of Self-Centering Reinforced Concrete Bridge Columns

Hyung IL Jeong
University of California, Berkeley

Junichi Sakai
Public Works Research Institute, Tsukuba, Japan

Stephen A. Mahin
University of California, Berkeley

PEER 2008/06
SEPT. 2008

Shaking Table Tests and Numerical Investigation of Self-Centering Reinforced Concrete Bridge Columns

Hyung IL Jeong

Postdoctoral Researcher
Department of Civil and Environmental Engineering
University of California, Berkeley

Junichi Sakai

Senior Researcher
Center for Advanced Engineering Structural Assessment and Research
Public Works Research Institute, Tsukuba, Japan

Stephen A. Mahin

Professor
Department of Civil and Environmental Engineering
University of California, Berkeley

PEER Report 2008/06
Pacific Earthquake Engineering Research Center
College of Engineering
University of California, Berkeley

September 2008

ABSTRACT

The research presented in this report is part of a larger analytical and experimental investigation to develop and validate design methods for self-centering concrete columns that inherently have relatively small residual displacements following severe earthquake shaking. The main objectives of this study are to investigate the seismic performance, identify the key design variables, and evaluate the effect of different ground motions and different column configurations for a self-centering reinforced concrete (RC) column with unbonded prestressing strand placed at the center of the cross section.

To achieve these objectives, a series of shaking table tests and analytical studies were performed. The research was conducted in three phases. First, to develop and validate new refined design methods for self-centering bridge columns, two series of shaking table tests were performed. In the first series of these tests, four cantilever-type partially prestressed reinforced concrete bridge columns with different details were subjected to bidirectional earthquake loading. In the second series of shaking table tests, one two-column bent specimen was evaluated. Second, analytical investigations were conducted to develop and validate analytical methods and models that can accurately capture key performance attributes of conventional concrete columns and unbonded post-tensioned concrete columns under earthquake excitation. . In the third phase, a series of parametric studies for self-centering columns was carried out to evaluate the effect of different ground motions and column configurations.

The experimental results demonstrated that the developed self-centering system generally has effective re-centering characteristics after a severe earthquake. This test program demonstrates the substantial benefits of partially prestressed reinforced concrete columns with locally unbonded mild reinforcement and surrounded by a steel jacket. Based on the findings of the analysis, recommendations are made regarding the modeling of RC and self-centering columns. A parametric study using the developed model confirmed the effectiveness of the self-centering system in different ground motions and with different column configurations.

ACKNOWLEDGMENTS

This work was sponsored by the Pacific Earthquake Engineering Research (PEER) Center's Transportation Program supported by the State of California. This work made use of the Earthquake Engineering Research Centers Shared Facilities supported by the National Science Foundation, under award number EEC-9701568 through PEER.

Any opinions, findings, and conclusions or recommendations expressed in this material are those of the authors and do not necessarily reflect those of the State of California or the National Science Foundation.

Special thanks are due to Don Clyde, Wesley Neighbour, Shakhzod Takhirov, David Patterson, David Maclam, Jose Robels, and Nathaniel Knight of the EERC laboratory staff for their advice and help in the shaking table tests. Gita Dombrowski, Michel Davieau, and Eric Okstard (student assistants) have the authors' gratitude for their hard work during the preparation of the tests.

CONTENTS

LIST OF FIGURES

LIST OF TABLES

1 Introduction

1.1 BACKGROUND

In recent years, bridges in regions of high seismicity have been designed and constructed using reinforced concrete bridge columns with high-ductility capacity so they can avoid collapse during strong ground shaking (California Department of Transportation 2001; Japan Road Association 2002). Such conventionally designed reinforced concrete bridge columns can achieve large inelastic deformations without significant loss of vertical or lateral load capacity, but may have significant post-earthquake residual displacements. Large residual displacements might result in substantial disruption of traffic or long-term closure of highways while the bridge undergoes expensive repairs, or even complete replacement. For instance, following the Hyogo-Ken Nanbu earthquake in 1995, more than 100 reinforced concrete bridge columns were demolished in Kobe, Japan, because of residual drift indices exceeding 1.75%.

In response, Japanese design criteria (Japan Road Association 2002) were modified to explicitly require designers to limit permanent drifts to less than 1%. In spite of such requirements, and increasing concern about this issue by highway departments and public officials worldwide, few effective and economical methods have been developed to control post-earthquake residual displacements of bridge columns. One mitigation strategy is to design the columns to be stronger, thereby limiting inelastic deformations. However, this approach may result in substantial increases in costs due to corresponding increases in costs of foundation systems and bridge superstructures. Another popular approach in many parts of the world is to seismically isolate the bridge superstructure from the columns and substructures using isolation devices with re-centering characteristics. Uncertainties about the long-term durability of isolators and their post-earthquake properties have limited the application of this approach in some areas. Recent research (Kawashima et al. 2005; Espinoza and Mahin 2006) has suggested that bridge systems that undergo controlled uplift of their foundations during strong earthquakes may also exhibit re-centering characteristics. However, these studies have not developed to the point where such ideas can be generally applied. Thus, greater attention has been placed recently on the use of structural systems that behave nonlinearly but have hysteretic characteristics that are origin oriented upon unloading, e.g., systems that undergo controlled rocking during seismic excitations or that contain partially prestressed columns with unbonded tendons. A review of past research on such systems is provided subsequently.

The research presented in this report is part of a larger analytical and experimental investigation to develop and validate design methods for bridge columns that inherently have relatively small residual displacements following severe earthquake shaking. A previously conducted theoretical and numerical study (Sakai and Mahin 2004) proposed a straightforward method to reduce residual displacements by incorporating an unbonded prestressing tendon at the center of a lightly reinforced concrete column. They focused their investigation on cast-in-place circular columns having shear resistance and confinement provided by spiral reinforcement. The study demonstrated that (1) incorporating unbonded prestressing strands at the center of a reinforced concrete cross section with a lowered ratio of mild longitudinal reinforcement can achieve restoring force and ductility characteristics similar to a conventionally designed column upon loading, but with substantially less residual displacement upon unloading; (2) such self-centering columns perform very well under unidirectional earthquake excitation; predicted residual displacements of the proposed columns are only about 10% of those of conventionally detailed columns, while the peak responses are virtually identical; and (3) unbonding of longitudinal mild reinforcing bars reduces strain demands on the mild reinforcement.

A preliminary experimental study (Sakai and Mahin 2006) to investigate the seismic behavior of the proposed self-centering columns validated the beneficial effects of providing unbonded prestressing strands at the center of the cross section. This study demonstrated through a series of bidirectional shaking table tests that such columns exhibit approximately the same stiffness and strength as conventional columns, with residual displacements following strong shaking reduced by 70–80%.

Although the study showed the effectiveness of the proposed design approach in reducing residual displacements, several concerns remained. For example, because the residual displacements of the partially prestressed concrete column were not as large as those of the companion reinforced column, a repetition of the test simulating a maximum credible earthquake was possible. However, during the second test, 6 of the 12 bonded longitudinal reinforcing bars fractured, resulting in a significant loss of restoring force and collapse of the specimen. This failure, in a column that did not exhibit significant signs of structural damage following the previous severe shaking, suggests the need for a more thorough understanding of self-centering columns and perhaps more robust design details. To apply this new system to the real structural system, validation of the complex system is also needed.

1.2 OBJECTIVE AND SCOPE OF RESEARCH

The objectives of this study are threefold. The first objective is to develop and validate new refined design methods for bridge columns that inherently have relatively small residual displacements following severe earthquake shaking. Based on the literature review and analytical study, it appears that improvements in behavior might be achieved by unbonding the mild reinforcement, increasing the amount of confinement, or providing a steel jacket. The latter option has the added benefit of preventing spalling of the concrete cover during inelastic response. Another practical concern is the amount of the prestressing force applied to the column. Greater post-tensioning would be expected to increase re-centering tendencies, but the increased compression forces in the confined concrete might trigger earlier failure. At the first stage of the experimental program in this research, four reinforced concrete bridge columns with unbonded prestressing tendons were tested by shaking table. To apply this new system to a real-world situation, a two-column bent system with unbonded prestressing tendons and steel jacketing at the plastic hinge length was tested as the second experimental phase of this research.

The second objective is to develop and validate analytical methods and models that can accurately capture key performance attributes of conventional concrete columns and unbonded post-tensioned concrete columns under earthquake excitation using the test data. Open Systems for Earthquake Engineering Simulation (OpenSees) is used as the analytical platform. The shaking table test results were used to calibrate various analytical models and evaluate their accuracy and reliability.

The third objective is to use the validated analytical models to evaluate the effect of different ground motions and different aspect ratios for the newly developed method that can reduce the residual displacements following severe earthquake shaking by parametric study.

1.3 ORGANIZATION

This report is divided into seven chapters. Chapter 2 provides a review of recent computational and experimental research on self-centering systems.

Chapter 3 presents a test program of four single-column specimens with varying detail under bidirectional seismic input. The test results for global and local behaviors of the four reinforced concrete bridge columns with unbonded prestressing tendons with different details are provided in this chapter. Also, a comparison between the specimens can be found. Chapter 4 presents the test program of a two-column bent specimen with unbonded prestressing tendons and steel jacketing at the plastic hinge region.

Chapter 5 develops the analytical model for conventional reinforced concrete columns and unbonded prestressing reinforced concrete columns that can capture the main aspects of the behavior under earthquake input and validates the model using the test results of Chapters 3 and 4. Chapter 6 presents the parametric study of the analytical model to evaluate the effect of different ground motions and different aspect ratios for a new system that can reduce residual displacements.

Finally, Chapter 7 summarizes the conclusions and recommendations for future research.

2 Literature Review

During the past ten years, a number of innovative earthquake-resistant systems that reduce residual displacements, called "self-centering" or "re-centering" systems, have been studied analytically and experimentally for various structural systems. This chapter provides background information on the previous research on self-centering systems, limited to concrete structural components (the focus of this research), and analytical studies of residual displacement.

2.1 SELF-CENTERING SYSTEMS IN CONCRETE STRUCTURES

Several investigators have examined reinforced concrete components and systems that exhibit origin-oriented or other hysteretic characteristics thought to reduce post-earthquake residual displacements. In some of these cases, the focus of the investigation was not on limiting residual displacements in systems that might yield during a severe earthquake. For example, several studies have examined the use of unbonded prestressing tendons to accelerate or facilitate the construction process in precast concrete. Since these types of details exhibit hysteretic characteristics that might contribute to reduced residual displacements, they are included in this literature review.

In this section, review of previous experimental and computational research is subdivided into categories related to precast concrete beam-column connections, precast concrete walls, precast concrete columns, and reinforced concrete columns. Figure 2.1 shows various self-centering hysteretic behaviors that have been observed in the previous research for cyclic loading tests.

2.1.1 Precast Concrete Beam-Column Connections

An early application of prestressing tendon in precast concrete beam-column connections was performed by Blakeley and Park (1971). They performed cyclic loading tests for four full-sized precast concrete beam-column connections joined by post-tensioning under cyclic loading. Each test assembly consisted of a pre-tensioned column with a post-tensioned beam framing on one side at mid-height.

A number of researchers studied precast concrete building systems using unbonded prestressing tendon. Many of these studies are associated with the NSF-funded PREcast Seismic Structural Systems (PRESSS) research project, which developed recommendations for the seismic design of buildings composed of precast concrete components. Priestley and Tao (1993) investigated the seismic performance of precast prestressed concrete frames by conducting dynamic inelastic analyses considering four types of hysteretic behavior. Priestley and MacRae (1996) tested two unbonded post-tensioned precast concrete beam-to-column joint subassemblages under cyclic reversals of inelastic displacement to assess seismic response. El-Sheikh et al. (1999) studied the behavior of two six-story unbonded post-tensioned frames using nonlinear pushover static analyses and time-history dynamic analyses. These studies found that the behavior of unbonded post-tensioned precast frames has a self-centering capability. Stone et al. (1995) tested 10 hybrid precast concrete beam-column connections consisting of mild steel and post-tensioned steel with cyclic loading.

Stanton and Nakaki (2001) developed several new types of seismic framing systems that use precast concrete. Some of them are based on the use of unbonded prestressing, which provides nonlinear elastic response to seismic loads; the prestressing can be supplemented with bonded mild steel in order to dissipate energy. Recently, cyclic loading tests were performed by Kim et al. (2004) for this precast hybrid frame connection as proof-of-concept needed to gain regulatory acceptance of the system for use in a 40-story building in San Francisco. Similar concepts have also been used in steel frames (Ricles et al. 2001, 2002; Christopoulos et al. 2002a,b).

2.1.2 Precast Concrete Walls

During the past decade, extensive research on precast concrete walls using unbonded prestressing tendon has been performed by Kurama et al. (1999a,b, 2002, 2006). Kurama et al. (1999b) conducted a large number of nonlinear dynamic time-history analyses of unbonded post-tensioned precast concrete walls by post-tensioning precast wall panels across horizontal joints using post-tensioning steel that was not bonded to the concrete. Kurama (2000) used supplemental viscous damping to reduce the lateral drift of unbonded post-tensioned precast concrete walls under earthquakes. Nonlinear dynamic time-history analyses of a series of walls with different fundamental periods of vibration showed that the proposed energy-dissipation system and the design approach are effective in reducing the maximum roof drift to prevent significant damage in the walls. Recently, Kurama et al. (2006) conducted 11 half-scale experiments to investigate the nonlinear reversed cyclic behavior of coupling beam subassemblages in a new type of hybrid coupled-wall system for seismic regions. The specimens were able to sustain large nonlinear displacements without significant damage in the beams and the wall regions. The residual deformations upon unloading of the specimens were negligible due to the restoring effect of the post-tensioning force.

Holden et al. (2003) tested half-scale precast concrete cantilever wall units under quasi-static reversed cyclic lateral loading and compared the precast partially prestressed wall system and the precast reinforced wall unit. The test results evidenced the self-centering characteristics of the post-tensioned system. Rahman and Sritharan (2006) presented a multiple-level performance-based seismic evaluation of two five-story unbonded post-tensioned jointed precast wall systems and investigated the feasibility of controlling the maximum transient inter-story drift in a jointed wall system by increasing the number of energy-dissipating shear connectors between the walls while not significantly affecting its re-centering capability.

2.1.3 Precast Concrete Columns

Recently, several researchers carried out analytical and experimental investigations of precast concrete columns. Hewes and Priestley (2002) conducted quasi-static loading tests and analytical research on the transverse seismic loading of prestressing segmental bridge columns in order to investigate the strength-deformation response and performance of a precast column. The test results showed minimal residual drift because of the unbonded tendon design.

Kwan and Billington (2003a,b) evaluated the seismic response characteristics of an unbonded post-tensioned precast concrete bridge pier system with extensive time-history analyses on single-degree-of-freedom (SDOF) models. Billington and Yoon (2004) conducted tests to study the hysteretic behavior of unbonded post-tensioned precast concrete bridge piers that were constructed using a ductile fiber-reinforced cement-based composite (DRFCC) material. The testing showed minimal residual displacements of unbonded post-tensioning columns by preventing localized yielding of the reinforcement. Lee et al. (2004) applied a performance-based framework developed by the Pacific Earthquake Engineering Research Center (PEER) to a precast segmental concrete bridge pier system that uses unbonded post-tensioning to join the precast segments and has the option of using a high-performance fiber-reinforced cement-based composite (HPRFCC) in the precast segments at potential plastic hinging regions.

Ou et al. (2006) examined the cyclic performance of an unbonded precast concrete segmental bridge column system. This system utilizes unbonded post-tensioning to enhance the self-centering capability and mild steel reinforcement extended across the segment joints to enhance the energy-dissipation capability. Chou and Chen (2006) conducted cyclic tests of ungrouted post-tensioned precast concrete-filled tube (CFT) segmental bridge columns under lateral cyclic loading to evaluate the seismic performance of the column details. Specimens were able to develop the maximum flexural strength at about the design drift and reach 6% drift with small strength degradation and residual displacement.

Yamashita and Sanders (2006) conducted shake table testing and analysis to investigate the seismic performance of unbonded prestressed precast segmental concrete columns. Shake table testing was conducted using the Kobe earthquake motion. The specimen performed very well with essentially no residual displacement and only limited spalling at the base.

Mander and Cheng (1997) investigated the rocking response of concrete-filled steel tube reinforced with unbonded prestressing. Cheng (2007) investigated this rocking precast bridge pier concept under a free-vibration test.

2.1.4 Reinforced Concrete Columns

Since the Kobe earthquake, intensive research programs have been instituted to develop new systems that can reduce residual displacement in reinforced concrete (RC) columns.

Some of these studies have focused on altering the envelop of the overall hysteretic loops, e.g., by increasing the post-yield tangential stiffness of the column. Iemura and Takahashi (2000) and Iemura et al. (2002) proposed using additional unbonded high-strength longitudinal bars in reinforced concrete bridge columns, together with conventional mild longitudinal reinforcement. The high-strength bars are intended to remain elastic, thereby increasing the column stiffness following yielding of the mild reinforcement. The effectiveness of the proposed design approach was investigated through hybrid earthquake loading tests for three specimens and nonlinear analyses.

Another approach has used post-tensioning to achieve inelastic response having origin-oriented hysteretic characteristics upon unloading. Ikeda (1998) performed tests for prestressed concrete (PRC) columns with cyclic loading to verify seismic performance. The test demonstrated the self-centering hysteretic characteristic of a prestressed concrete column. Zatar and Mutsuyoshi (2001) also investigated the effects of prestressing to reduce the residual displacement. Seven specimens were tested under cyclic loading or pseudo-dynamic loading to clarify the inelastic behavior of partially prestressed columns under cyclic and hybrid loading. The testing showed the restoration characteristics and small residual displacements of a PRC column.

While the cyclic or pseudo-dynamic experimental studies of Ikeda (1998) and Zatar and Mutsuyoshi (2001) evidenced the self-centering characteristic of partially prestressed reinforced concrete columns using unbonded tendons, the tests were limited to unidirectional loading using cyclic and pseudo-dynamic test protocols. As mentioned in Chapter 1, Sakai and Mahin (2004, 2006) extended these studies to include shaking table tests with two horizontal components of motion. By comparing the experimental results for otherwise comparable conventional and partially prestressed reinforced concrete column designs, and conducting extensive numerical simulations, they were able to demonstrate the effectiveness of this approach under more realistic earthquake loading conditions. Because of the small number of specimens tested, and the lack of warning of impending collapse, they recommended that additional tests be performed considering a wider range of design parameters.

Lee and Billington (2006) applied performance-based assessment to a self-centering system using the experimental test data from Billington and Yoon (2004) and Sakai and Mahin (2006). The self-centering bridge was found to behave well under all considered hazard levels with minimal damage and virtually no residual displacement.

2.2 ANALYTICAL STUDIES OF RESIDUAL DISPLACEMENT

In addition to the experimental and analytical assessments of self-centering earthquake-resistant systems described above, a number of analytical studies have been conducted to model and predict the degree of post-earthquake residual displacements in structures. The following is a survey of recent investigations of residual displacement in conventional reinforced concrete column systems.

Kawashima et al. (1998) performed analyses of many SDOF bilinear hysteresis models, with different natural periods, damping ratios, ductility factors, bilinear factors, and 63 input ground motions, to obtain a method of estimating the likely residual displacements of real SDOF structures. Residual displacements for different earthquake records were dominated by the slope of the post-yielding branch of the bilinear loop. Based partly on this study, an examination of residual displacement of bridge columns was included in the Japanese seismic design specification for highway bridges (Japan Road Association 1996). In the specifications, it is required that residual displacement (u_r) developed at the center of gravity of the superstructure after an earthquake be

$$u_r \le u_{ra} \tag{2.1}$$

where

$$u_r = S_{RDR}(\mu_r - 1)(1 - r)u_y \tag{2.2}$$

and where u_{ra} is the allowable residual displacement of a column; r is the bilinear factor defined as a ratio between the initial stiffness and the post-yield stiffness of the column (0 for reinforced concrete columns); S_{RDR} is a factor dependant on the bilinear factor r (0.6 for reinforced concrete columns); μ_r is the response displacement ductility factor of the column; and u_y is the yield displacement of the column. Here, 1% drift is used as the allowable residual displacement (u_{ra}) in the Japanese specification. For 6-ft (1.83-m) diameter columns with aspect ratios in the range of 4 to 10, designed in accordance with the California Department of Transportation (Caltrans) Seismic Design Criteria (SDC) (California Department of Transportation 2001), the residual displacements estimated using Equation (2.2) are larger than the allowable 1% drift (Sakai and Mahin 2004).

Mackie and Stojadinović (2004) applied a performance-based earthquake engineering framework to highway bridges to find post-earthquake capacity. They proposed four methods to derive damage fragility surfaces. The methods introduce post-earthquake displacement as a better proxy for capacity loss of bridges. Thus, predicting residual displacement is important for performance evaluation of bridge columns.

Ruiz-García and Miranda (2006) performed analytical studies using response time-history analyses of SDOF systems having six levels of relative lateral strength when subjected to an ensemble of 240 earthquake ground motions to evaluate residual displacement ratios ($C_r = \Delta_r / S_d$), which allows the estimation of residual displacement demands (Δ_r) from maximum elastic displacement demands (S_d). Three hysteretic models (modified Clough, Takeda, and a modified origin-oriented model) were used in this investigation. The study concluded that mean residual displacement ratios are more sensitive to changes in local site conditions, earthquake magnitude, distance to the source, and hysteretic behavior than are mean inelastic displacement ratios. This study proposed a simplified equation to estimate the central tendency of the residual displacement ratio (C_r) for elasto-plastic systems:

$$C_r = [\frac{1}{\theta_1} + \frac{1}{41T^{\theta_2}}]\beta \tag{2.3}$$

where T is the period, β is given by

$$\beta = \theta_3[1 - \exp(-\theta_4(R-1)^{\theta_5})] \tag{2.4}$$

and R is the lateral strength ratio; parameters θ_1, θ_2, θ_3, θ_4, and θ_5 depend on site conditions.

Sakai and Mahin (2006) have indicated that while many numerical models can predict peak inelastic deformations for reinforced concrete columns subjected to multiple components of motion, few of these models appear able to predict residual displacements accurately for either conventional or self-centering columns. Lee (2007) has developed an improved hysteretic model for concrete that they report improves prediction of residual displacement of conventional RC columns. Phan et al. (2007) tested two conventional RC columns under unidirectional near-fault ground motion on a shake table. The test results showed large residual displacements even under moderate motions. A new bilinear hysteresis model that accounts for stiffness degradation was developed to capture this effect and was incorporated into an analytical model.

While some studies have been performed regarding residual displacements of conventional RC columns, most of them are limited to using simple SDOF bilinear hysteresis models. Analytical models need to be developed and validated to predict seismic performance, especially residual displacement, of conventional and self-centering reinforced concrete systems.

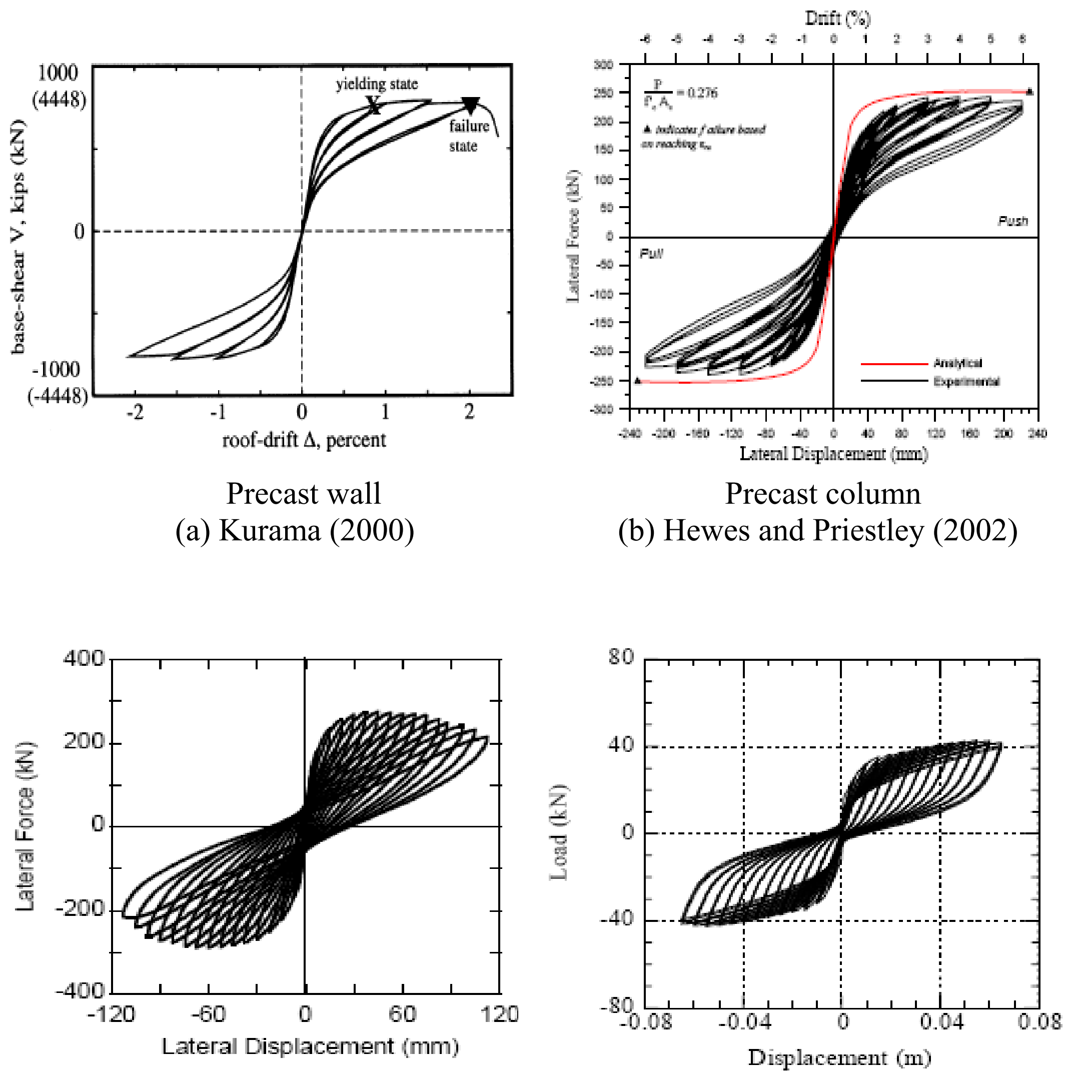

Precast wall
(a) Kurama (2000)

Precast column
(b) Hewes and Priestley (2002)

RC column
(c) Ikeda (1998)

RC column
(d) Iemura and Takahashi (2000)

Fig. 2.1 Examples of self-centering hysteretic relationships observed in previous experimental studies (cyclic loading tests)

3 Experiments on Single-Column Specimens

3.1 INTRODUCTION

The results of the previous studies by Sakai and Mahin (2004, 2006) demonstrated the basic viability and feasibility of self-centering columns for bridges. However, the study indicated that further research was needed to explore options for making the columns more robust, i.e., reducing vulnerability to concrete crushing and fracture of the longitudinal mild reinforcement. The numerical study by Sakai and Mahin (2004) showed that local unbonding of the mild reinforcement in the plastic hinge region increases fatigue life by reducing the peak strains developed. Greater resistance to crushing of the concrete core can be conveniently achieved by further increasing the amount of spiral reinforcement or providing steel jacketing. Sakai and Mahin also suggested that increasing the area of post-tensioning strand can help compensate for the small loss in stiffness associated with unbonding mild reinforcement in the plastic hinge region. Thus, it appears that improvements in behavior might be achieved via unbonding the mild reinforcement, increasing the amount of confinement, or providing a steel jacket. The latter option has the added benefit of preventing spalling of the concrete cover during inelastic response.

Another practical concern is the magnitude of the prestressing force applied to the column. Greater post-tensioning would be expected to increase re-centering tendencies, but the increased compression forces in the confined concrete might trigger earlier failure. As such, it was of interest to study the behavior of a self-centering column with a higher post-tensioning force.

The main objectives of the experiments reported in this chapter are to investigate

- The effect of the unbonding of the mild reinforcing bars in the vicinity of the expected plastic hinge to reduce the maximum strain induced in the bars;

- The effect of steel jacketing combined with local unbonding of the mild reinforcement; and
- The effect of the magnitude of the prestressing force.

The research presented herein investigates the seismic performance of partially prestressed reinforced concrete bridge columns with different details under near-field strong ground excitation through a series of earthquake simulator tests. Four reinforced concrete bridge columns with unbonded prestressing tendons were tested.

Section 3.2 describes the design of the reinforced concrete bridge column models tested, construction of the models, material properties, and selection of ground motions used. Test setup, instrumentation, and data acquisition are described in Section 3.3. Section 3.4 summarizes dynamic behaviors of the four test specimens under earthquake excitation. Conclusions are presented in Section 3.5.

3.2 SPECIMEN DESIGN AND CONSTRUCTION

3.2.1 Prototype Column

The simple, commonly used reinforced concrete bridge column analyzed in the previous study (Sakai and Mahin 2004) was selected as the prototype column for this investigation. The column is designed in accordance with the Caltrans SDC.

Figure 3.1 shows the cross section, dimensions, and reinforcement of the prototype column. The prototype column has a circular cross section with a diameter of 6 ft (1.83 m). To achieve a target aspect ratio of 6, the column was 36 ft (10.97 m) high, from the bottom of the column to the center of gravity of the superstructure. The axial load (P) in the prototype column was taken to be $0.05\,P/f'_{co}A_g$, based on the nominal strength of unconfined concrete (5 ksi or 34.5 MPa).

The prototype column was reinforced longitudinally with 48 No. 9 (29-mm diameter) deformed bars, providing a longitudinal reinforcement ratio (ρ_l) of 1.18%. To confine the concrete core, No. 5 (16-mm diameter) spirals were used, spaced at a 3-in. (76-mm) pitch, resulting in a volumetric ratio (ρ_s) of 0.61%. Nominal yield strength of 60 ksi (420 MPa) was considered for both the longitudinal and spiral reinforcement.

Figure 3.2 shows the results of the static pushover analysis recommended by the SDC. The ultimate lateral load capacity was 290 kip (1.29 MN), with a yield and ultimate displacement of 4.3 in. (0.11 m) and 22.8 in. (0.58 m), respectively. Thus, the column has a displacement ductility capacity of 5.2. The evaluated effective natural period of the prototype column is 1.26 s.

3.2.2 Design of Specimens

3.2.2.1 Dimensional Analysis

Because of the limitations of the size of the shaking table, test specimens are usually constructed at a reduced scale. The diameter of the model column was set at 16 in. (406 mm), which corresponds to a prototype model length scale factor of 4.5.

Dimensional analyses (e.g., see Krawinkler and Moncarz 1982) were applied to decide scaling factors of the other physical quantities and dimensions of the specimens. Dimensional similitude requirements for dynamic tests were determined considering (1) the above-length scale factor be used; (2) the acceleration of gravity be maintained; and (3) the modulus of elasticity of materials be identical. These conditions are expressed as follows:

$$L = 4.5 \tag{3.1}$$

$$LT^{-2} = 1 \tag{3.2}$$

$$ML^{-1}T^{-2} = 1 \tag{3.3}$$

Table 3.1 summarizes dimensions of physical quantities and target scaling factors. More details of the dimensional analytical results can be found in the previous research report (Sakai and Mahin 2006).

3.2.2.2 Design of Test Specimens

In the previous research (Sakai and Mahin 2006), two specimens were tested. One was conventionally designed and will be referred to as specimen RC. The second specimen was a partially prestressed reinforced concrete column and will be referred to as specimen PRC. The RC specimen was designed following the target scale factors from the dimensional analysis of the prototype column. Based on the findings from the analytical study (Sakai and Mahin 2004), the PRC specimen was designed as a lightly reinforced column with a central unbonded prestressing tendon.

Based on the design of the PRC specimen (Sakai and Mahin 2006), four new 16-in. (406-mm) diameter partially prestressed reinforced concrete column specimens were designed. The first column was essentially the same as the PRC specimen and will be referred to as specimen PRC-2. The second column contained unbonded mild reinforcing bars at the expected plastic hinge, and had a lower prestressing force than specimen PRC; this will be referred to as specimen PRC-U. The third column also contained the unbonded mild bar at the plastic hinge, but had a higher prestressing force, and will be referred to as specimen PRC-U2. The last column was provided with a steel jacket and wider spiral pitch at the expected plastic hinge in addition to the unbonded mild bar; this column will be referred to as specimen PRC-UJ.

Table 3.2 summarizes the differences among the specimens, and Figure 3.3 shows a flowchart of the design of all four specimens. The specimens are fairly similar, with the exception of a few parameters. All four new specimens had larger diameter post-tensioning tendons than specimen PRC. Specimens PRC-2, PRC-U, and PRC-UJ had a lower prestressing force than specimen PRC. Specimen PRC-U2 had a higher prestressing force than the other three new specimens, but this was lower than in specimen PRC.

As noted above, the general specimen design was nearly identical to the specimen design in the previous study except for the supports for the top mass block. To facilitate construction, reusable steel brackets were designed to support the mass blocks without the top slab used in the first set of specimens. Figure 3.4 shows the effective height of the specimen with mass blocks that represent the weight and inertial mass of the superstructure of the prototype bridge, and Figures 3.5 and 3.6 show the cross section and reinforcement details of specimens PRC-2 and PRC-U/U2, respectively. Figure 3.7 shows the difference between the plastic hinge regions of specimens PRC-2, PRC-U/U2, and PRC-UJ.

Previous analysis (Sakai and Mahin 2004) determined an unbonded length of mild bar equal to two times the column diameter to be adequate. To debond the longitudinal mild reinforcement from the concrete in specimens PRC-U, PRC-U2, and PRC-UJ, the bars were coated with wax and covered with a plastic sheath.

In the design of the specimen with the steel jacket, PRC-UJ, the spiral pitch and the thickness of the steel jacket were determined by analysis to maintain a similar computed confined concrete stress-strain relation for specimens PRC-U and PRC-UJ. Due to concerns related to sliding shear near the base of the column, no gap was provided between the base of the steel jacket and the top of the footing.

As mentioned above, the test columns were 16 in. (0.41 m) in diameter, and the height from the bottom of the column to the center of gravity of the assembly of the steel bracket and weight blocks was 8 ft 3 in. (2.51 m). The column was reinforced with 12 No. 3 (10-mm diameter) deformed bars longitudinally. As spiral reinforcement, W3.5 round wire (5.4-mm diameter) with a 1-1/4-in. (32-mm) pitch was used for specimens PRC-2, PRC-U, and PRC-U2. For specimen PRC-UJ, W3.5 round wire (5.4-mm diameter) with a 5-in. (127-mm) pitch was used. The longitudinal reinforcement ratio (ρ_l) was 0.66%; and the volumetric ratio of spiral reinforcement (ρ_s) was 0.76% for specimens PRC-2, PRC-U, and PRC-U2, and 0.25% for specimen PRC-UJ. Normal density of concrete was used, and the design strength of concrete (f'_{co}) was specified to be 5 ksi (34.5 MPa). Gr60 reinforcing bars were used for the longitudinal reinforcement, and Gr80 wires were used for the spirals. The nominal yield strengths of the steel were 60 ksi (420 MPa) and 80 ksi (550 MPa), respectively. Gr150 (1,035 MPa) bar from Williams Form Engineering Corp. was used as the post-tensioning tendon. The size and length of the tendons were 1-3/8 in. (36 mm) in diameter and 10 ft (3.05 m), respectively. The nominal ultimate strength of the tendon was computed to be 237 kip (1,055 kN).

The dead load due to the steel bracket and the three weight blocks was 54 kip (240 kN), resulting in an axial force ratio ($\alpha_{DL} = P / f'_{co} A_g$) of 5.7%.

For specimen RC, according to the static pushover analytical procedures recommended by the SDC, the yield and ultimate displacements, and the lateral strength were evaluated to be 1.02 in. (0.026 m), 8.26 in. (0.21 m), and 15 kip (67.6 kN), respectively. Expressed as a drift ratio (displacement divided by column height measured from column base to center of gravity of the mass blocks), the yield and ultimate displacements occur at drift ratios of 1.02% and 8.3%, respectively. Here, a plastic hinge length of 12.9 in. (0.328 m) was assumed based on an equation proposed by Priestley et al. (1996).

3.2.2.3 Footing and Steel Brackets

Designed to remain elastic during the tests, steel brackets and a footing were fixed to the column to support the weight blocks and to attach the column to the earthquake simulator platform.

Forces to the footing were evaluated based on the plastic moment capacity of the column when the plastic hinge was fully developed, while the steel bracket was checked for bending and shear due to the supported load of the weight blocks times a factor of safety.

The footing was 5 ft (1.52 m) sq and 18 in. (0.46 m) thick, and was reinforced longitudinally with No. 6 (19-mm diameter) deformed bars and transversally with No. 3 (10-mm diameter) stirrup ties, as shown in Figure 3.8. Figure 3.9 shows the steel brackets used at the four corners of the top of the column specimen.

The weights of the footing and the set of steel brackets were 5.6 kip (24.9 kN) and 1.84 kip (8.18 kN), respectively. The total weight of one specimen was 9.12 kip (40.6 kN), including the weight of the column, footing and the set of steel brackets, but not including the weight of the mass blocks.

3.2.2.4 Mass Blocks

Three 10 ft × 10 ft × 14 in. (3.05 × 3.05 × 0.66 m) concrete blocks were used to represent the weight and mass of the superstructure of a bridge. The weight of each block was 17.1 kip (76 kN), resulting in a total weight of 54 kip (240 kN) for the mass blocks and steel brackets. One block, which was placed directly on the steel brackets, had a square hole 15 × 15 in. (0.38 × 0.38 m) to allow for the anchorage of the post-tensioning tendon at the top of the column, and its weight was 1.5% smaller than the other blocks.

3.2.3 Construction of Specimens

The specimens were constructed as follows:

1. Construction of forms for the footings (Fig. 3.10);
2. Assembly of steel cages (Figs. 3.11 and 3.12);
3. Casting footing concrete (on 2005 April 27, shown in Figs. 3.13–3.15);
4. Construction of forms for the columns (Fig. 3.16);
5. Casting column concrete (on 2005 May 6, shown in Figs. 3.17 and 3.18); and
6. Removal of the forms (finished on 2005 June 5, shown in Fig. 3.19).

Before casting the column concrete, 1/2-in. (13-mm) diameter threaded rods were inserted transversely through the column forms in order to provide a means for measuring the curvature distribution along the height of the columns. The slump of concrete, which had been specified to be 5 in. (127 mm), was measured to be 3.5 in. (89 mm) for the footing concrete and 9.5 in. (241 mm) for the columns. The column concrete was cured for about 28 days before the forms were removed.

3.2.4 Measured Material Properties

3.2.4.1 Concrete

The concrete of the columns was specified as normal weight with a 28-day design strength of no less than 4 ksi (27.6 MPa) and no more than 5.5 ksi (38 MPa) to represent the actual properties of concrete used in reinforced concrete bridges. Detailed concrete mix design is presented in Table 3.3.

Twenty-seven 6 × 12 in. standard cylinders were cast at the casting of the column and were used to measure the concrete compressive strength and stress-strain relationship. Compressive strength tests were performed at 8 and 29 days after casting the footing concrete, and at 7, 14, 21, and 28 days after casting the column concrete. Additional cylinders were tested a day after the shaking table test of each specimen.

In each test, three cylinders were tested. Tables 3.4 and 3.5 summarize the test results, and Figure 3.20 shows stress-strain curves of the column concrete for each specimen. The column concrete had a 28-day strength of 3.9 ksi (27.3 MPa), while the footing concrete had a strength of 5.25 ksi (36.8 MPa). The average strength of column concrete for all four specimens on testing day was about 4.7 ksi (32.9 MPa). The average tangent and secant moduli of elasticity of concrete for all four specimens, which are defined below (McCormac 2004), were evaluated to be 2,753 ksi (19.2 GPa) and 2,453 ksi (17.2 GPa), respectively.

$$E_{c\cdot tan} = \frac{f_{c\cdot 50}}{\varepsilon_{c\cdot 50}} \tag{3.4}$$

$$E_{c\cdot sec} = \frac{f_{c\cdot 50} - f_{c\cdot 25}}{\varepsilon_{c\cdot 50} - \varepsilon_{c\cdot 25}} \tag{3.5}$$

3.2.4.2 Reinforcing Steel

The column longitudinal steel was specified as ASTM A706 Gr60 steel. To obtain the mechanical properties of the reinforcing bars, tensile tests for steel coupons were conducted. Two coupons were tested for No. 3 bars for the specimens. The test results are summarized in Table 3.6(a) and Figure 3.21. The yield strength, ultimate strength, and modulus of elasticity of the No. 3 bars were 69.1 ksi (476 MPa), 90.9 ksi (627 MPa), and 29,090 ksi (201 GPa), respectively.

The spiral reinforcement was specified as ASTM A82 Gr80. No tensile test was performed due to the absence of coupons for spirals, and no certified mill test report was available.

3.2.4.3 Prestressing Tendon

For the post-tensioning tendon, ASTM A722 Gr150 (1,035 MPa) bar from Williams Form Engineering Corp. was used. According to the numerical studies, the size of the tendon was determined to be 1-3/8 in. (35 mm) in diameter. To obtain the mechanical properties of the tendon, a tensile test for steel coupons was conducted. The middle portion of the coupon was machined down to 3/4 in. (19 mm) in diameter to ensure that the ultimate strength did not exceed the capacity of the testing equipment, and then a tensile test was conducted.

Figure 3.22 shows a stress-strain curve obtained from the test. Yield strength, ultimate strength, and modulus of elasticity of the tendon were 132 ksi (910 MPa), 161 ksi (1,110 MPa), and 29,700 ksi (205 GPa), respectively (see Table 3.6(b)). Thus, the yield and ultimate strengths of the tendon were estimated to be 208 kip (926 kN) and 254 kip (1,130 kN), respectively.

3.2.4.4 Steel Jacket

The steel plate for the jacket was specified as ASTM A36 steel plate. To obtain the mechanical properties, a tensile test for a steel plate coupon was conducted. The test results are summarized in Table 3.6(c). The yield strength, ultimate strength, and modulus of elasticity of the steel plate were 42.3 ksi (291 MPa), 51.7 ksi (356 MPa), and 27,200 ksi (187 GPa), respectively.

3.3 EXPERIMENTAL SETUP AND TEST PROGRAM

3.3.1 Test Setup

A series of shaking table tests was performed at the Richmond Field Station Earthquake Simulation Laboratory, University of California, Berkeley. Table 3.7 summarizes the characteristics of the shaking table. Figure 3.23 shows a specimen setup on the table. In order to simulate a fixed support at the base of the column, four 3-in.- (76-mm-) thick steel plates were fabricated, each with a threaded hole on the bottom to prestress the plate to the table, and four threaded holes on the top to attach a tri-axial load cell (see Fig. 3.26). Each of the four plates was fixed to the shaking table with a prestressing tendon, which was concentrically located below the attachment for the load cell on top of the plate. Hydrostone was placed between the plates and the shaking table, and between the tops of the plates and the load cells, to provide a solid bearing surface. Each load cell was bolted to a fixed plate; it was later attached to the footing of the test specimen by means of four 7/8-in. (22-mm) diameter high-strength bolts that extended through vertical conduits placed in the specimen's footing during casting.

To support the mass blocks, steel brackets were attached to the top of the column using prestressing rods, as shown in Figures 3.24 and 3.25. A layer of hydrostone was placed between the steel brackets and the specimen surface. The specimen with steel brackets attached was then carried by a 20-kip (89-kN) capacity bridge crane and placed onto the load cells (see Fig. 3.27). As noted above, the specimen was fixed to the load cells with a total of sixteen 7/8-in. (22-mm) or 3/4-in. (19-mm) diameter high-strength steel rods. To provide a uniform contact surface, a layer of hydrostone was placed between the load cells and the bottom of the footing. The specimen center was placed with an 18-in. (0.46-m) offset to the south and west sides of the shaking table center because of the difference in the layout of the table's prestressing holes and the layout of the specimen's holes. It might be supposed that the offset between the center of the shaking table and the specimen might cause some torsion response of the earthquake simulator, but a previous study determined that the torsion effects were negligible.

A 1-3/8-in. (36-mm) diameter post-tensioning tendon was installed in the specimen. Steel plates (9 × 9 × 1-5/8 in.) were used at both ends of the tendon to distribute the bearing stresses on the concrete. A layer of hydrostone was placed between the plates and the specimen surface. A 200-kip (890-kN) capacity load cell with a center hole was placed underneath the specimen to monitor the prestressing force induced in the column. The prestressing force was then applied to the tendon with a hydraulic jack, as shown in Figure 3.28.

The target prestressing force was determined during the previous study (Sakai and Mahin 2004, 2006). Based on an estimate of the loss of the prestressing force due to creep and axial load from the added mass blocks (determined in the previous study), the prestressing force of specimen PRC-U (the first of the specimens to be tested) was determined to be 58 kip (258 kN). After seven days, when all three mass blocks were placed on top of the steel brackets after the prestressing force had been induced, the force decreased to 47 kip (209 kN). This 12-kip (53-kN) loss of the prestressing force was four times more than was noted in the previous study. Based on this loss of specimen PRC-U's prestressing force and the results of PRC-U's next concrete strength test, the prestressing force selected for both the second specimen (PRC-UJ) and third specimen (PRC-2) was 49 kip (218 kN).

Based on the average concrete strength from cylinder tests (4.6 ksi) and defined in Eq. (3.6), the total axial force ratio (α_{total}) for specimens PRC-U, PRC-UJ, and PRC-2 was around 12%. For specimen PRC-U2, with an average concrete strength of 4.7 ksi, α_{total} was 14.9%.

$$\alpha_{total} = \frac{P + P_{ps}}{f'_{co} A_g} \tag{3.6}$$

where P_{ps} is the prestressing force; f'_{co} is the measured unconfined concrete strength; and A_g is the gross section area. Table 3.8 shows the prestressing force for each specimen on the testing day and the total axial force ratio for the concrete strength determined from the cylinder tests.

Following the prestressing of the tendon, the weight blocks were placed on the steel brackets of the specimen, as shown in Figure 3.29. The block with a center hole was placed directly onto the steel brackets to provide a space for the prestressing tendon. Hydrostone was also used between the steel brackets and the block, and between the block layers for the same reason described above. Four 1-in. (25-mm) diameter post-tensioning tendons were used to tie the steel bracket and three-weight-block assembly together.

To prevent collapse of the specimen during the tests, two steel chains were connected to each corner of the steel brackets, as shown in Figure 3.23. The length of the chain was adjusted to accommodate at least 10 in. (0.25 m) of lateral column displacement, which corresponds to the maximum displacement of the previous test.

3.3.2 Coordinate System

Figures 3.30(a–c) show the global coordinate system of a specimen on the shaking table and the system used to number the longitudinal bars to help identify the location of the damage. As noted above, the specimen's center was offset 18 in. (0.46 m) from the center of the shaking table. In this study, the north-south axis is designated the x direction, the east-west axis is the y direction, and the vertical axis is the z direction. The origin of the xy plane of the coordinate system is taken as the center of the column. The origin of the z-axis is assumed to be at the top of the footing of the specimen, as shown in Figure 3.30(c).

3.3.3 Instrumentation

3.3.3.1 Overview

A total of 128 channels was used for each of the shaking table tests. The 128 channels were distributed as follows:

- 16 channels for monitoring accelerations and displacements of the shaking table;
- 20 channels for tri-axial load cells monitoring the restoring force of the specimen;
- 17 channels for accelerometers;
- 32 channels for linear displacement potentiometers (LPs) monitoring global displacement;
- 28 channels for direct current displacement transducers (DCDTs) monitoring local column deformation;
- 12 channels for strain gauges monitoring longitudinal reinforcing bars;
- 1 channel for load cell monitoring of tendon behavior;
- 1 channel for a linear voltage displacement transducer (LVDT) monitoring the displacement at C.G. during the free-vibration test; and
- 1 channel for load cell monitoring of the pullback force during the pullback test.

The data were sampled at a rate of 0.005 s. More detailed information on the instrumentation is presented below.

3.3.3.2 Shaking Table Instrumentation

A total of 16 channels was used to capture the performance of the shaking table. Horizontal accelerations and displacements were monitored through four accelerometers placed at the beams of the table and four displacement transducers acting along the outer horizontal actuators. Vertical accelerations and displacements were monitored through four accelerometers and four displacement transducers placed near the four corners of the table, allowing for computation of acceleration and displacement components in all 6-degrees-of-freedom.

3.3.3.3 Load Cells

Figure 3.26 shows the setup of the four tri-axial load cells. These load cells supported the specimen at the four corners of the footing, monitoring the axial load, the shear forces in the x and y directions, and bending moments about the x- and y-axes. The recorded axial loads were used to compute bending moment capacity of the columns, and the shear forces were used to estimate shear force applied to the columns.

A 200-kip (890-kN) load cell with a center hole was placed underneath the specimen to monitor behavior of the tendon for specimen PRC.

3.3.3.4 Accelerometers

Accelerations were measured by 17 accelerometers mounted at seven locations on the specimen and the weight blocks, as shown in Figure 3.31. Groups of three accelerometers, which monitored accelerations in three directions (horizontal x and y and vertical z), were placed on the west and south faces of the footing and weight blocks, and on top of the weight blocks. Measurements from the footing were used as the input acceleration in subsequent dynamic analyses. An additional two accelerometers were placed on the middle of the column to measure column accelerations in the x and y directions.

3.3.3.5 Linear Potentiometers (LPs)

Specimen movements and deformations during the tests were captured by a total of 32 linear potentiometers (LPs), as shown in Figure 3.32. Because the stiff instrumentation frames were placed in the south and west sides of the shaking table, the displacements of the specimen were measured from the south and west sides.

The displacement of the footing in each direction was measured by three LPs at both the south and west faces. Five LPs for each direction were placed at the south and west faces of the weight blocks assembly: one of them was placed at the center of gravity of the weight block assembly, and two were placed near the top edge of the weight blocks; the other two were placed near the bottom edge of the weight blocks, and this pair of LPs was arranged to capture rotational movement of the specimen.

To capture local deformations of the column, six LPs on both the south and west faces were placed 6 in. (152 mm), 12 in. (305 mm), 18 in. (457 mm), 24 in. (610 mm), 38 in. (965 mm), and 50 in. (1,270 mm) from the bottom of the column. An additional four LPs were placed atop the four corners of the footing to monitor vertical displacements between the footing and top steel bracket.

3.3.3.6 Direct Current Displacement Transducers (DCDTs)

Twenty-eight direct current displacement transducers (DCDTs) were used to measure the relative vertical displacements between different sections along the height of the column. These data were used to estimate average curvatures of the columns. Figures 3.33(a–b) show the locations of the DCDTs.

For the DCDT instrumentation setup, 1/2-in. (13-mm) diameter threaded rods were installed at heights of 1 in. (25 mm), 6 in. (152 mm), 12 in. (305 mm), 18 in. (457 mm), 24 in. (610 mm), 38 in. (965 mm), and 50 in. (1,270 mm) during the construction. The DCDTs were placed approximately 3-1/2 in. (89 mm) from the column surface. Actual horizontal distance between the DCDTs and the column surface, and vertical distance between the rods and the surface of the footing or top slab, were measured prior to the tests. The readings from the pairs of DCDTs located at 1 in. (25 mm) and 6 in. (152 mm) were used to estimate the amount of rebar pullout from the footing (see Fig. 33(a)).

3.3.3.7 Strain Gauges

A total of 12 strain gauges was used to monitor strain of longitudinal reinforcement in each specimen. Figure 3.34 shows the location of the strain gauges.

Four reinforcing bars, located at the north, east, south, and west sides, were gauged and protected with coating materials from Vishay Micro-Measurements prior to construction. The gauges were placed at the rebar surface facing outside. The gauges were located 4 in. (102 mm) and 22 in. (558 mm) above the bottom of the column, and 3 in. (76 mm) below the bottom of the column (see Fig. 3.34). For the unbonded mild bar specimens (specimens PRC-U, PRC-U2, and PRC-UJ), the strain gauges were placed inside the unbonding plastic material. To allow the attached wiring to move with the strain gauges, it was enclosed in foam tubing to separate it from the encasing concrete.

Although the gauges were carefully attached and protected, some of the gauges failed and did not record.

3.3.4 Data Acquisition and Documentation of Damage

During the tests, the data were recorded by the shaking table's data acquisition system. All the instruments of each specimen were calibrated with cables installed prior to the tests. The data were read from the channels once every 0.005 s (200 Hz) and saved in a text file. Data recording was initiated a few seconds prior to the beginning of the earthquake signal.

In addition to the digital data recorded, digital videos were taken during the tests to document specimen behaviors and progress of localized damage. Four video cameras were used simultaneously: two cameras were focused on the bottom portion of the column—where the plastic hinge was expected to be developed at the east and north faces—and two cameras were used to capture the global response of the specimen from the east and north sides.

Digital photographs were taken prior to and after each test to document localized damage of the column. In the intervals between tests, concrete cracks that occurred during the tests were traced manually by colored markers for easy identification.

Crack pattern drawings, discussed in Section 3.4.2, present the entire column face as a flattened surface. The west, south, east, and north column faces were labeled as W, S, E, and N, respectively, from left to right. To help identify the locations of localized damage, the specimens were painted white and a grid pattern was drawn with black markers on each specimen prior to the tests. Horizontal grid lines were spaced at 4-in. (102-mm) intervals vertically along the column; vertical grid lines were spaced at 30-degree increments (about 4.2 in.) around the circumference. These orientations and designations are used to describe the type and location of physical damage in the test specimens, including cracking and spalling of concrete, buckling and fracture of longitudinal reinforcing bars, fracture of spiral reinforcement, etc.

3.3.5 Ground Motion

Input ground motions used the same earthquake input data of the previous test (Sakai and Mahin 2006). These data were selected based on the results from dynamic analyses for the RC specimen. Since these tests were aimed at investigating (1) how a conventionally designed column produces large residual displacement; (2) how the proposed design mitigates such a large residual displacement; and (3) how both the conventionally designed and proposed specimens behave when they experience a very large nonlinear response, a ground motion that produces large maximum and residual displacements for the RC specimen was selected.

Modified Los Gatos records from the 1989 Loma Prieta earthquake were selected as input signals for these earthquake simulation tests. The initial records were taken from the SAC ground motion library of near-fault ground motions (Somerville et al.1997). To simplify interpretation of the test results, only the two horizontal components of excitation were imposed during the shaking table tests. As noted in Table 3.1, the time scale selected for the records used in the earthquake simulator tests was reduced by a factor of 2.12 ($=\sqrt{4.5}$) to account for the scaling factor (4.5) of the specimen. Because the displacement capacity of the simulator is 5 in. (0.13 m), as shown in Table 3.7, pre-processing was performed on the records. Table 3.9 shows the peak acceleration, velocity, and displacement data of the original data and filtered data. Figures 3.35(a–d) show Fourier spectra and ground acceleration, velocity, and displacement time histories of the pre-processed records, taking account of the scaling factor of the specimens. The processed records are also shown in Figures 3.35(a–d) for comparison. Each record has 2,500 data points, for a duration of 11.8 s. The peak ground acceleration, velocity, and displacement of the stronger component of filtered record are 0.74*g* (7.3 m/s^2), 29.1 in./s (0.739 m/s), and 4.8 in. (0.12 m), respectively.

The ground motion of stronger intensity, which is the fault-normal component, was used for the x (N-S) direction; the motion with weaker intensity (the fault-parallel component) was used for the y (E-W) direction.

3.3.6 Test Sequence

3.3.6.1 Pullback (Free-Vibration) Test

Prior to the shaking table tests, each specimen was subjected to pullback tests to investigate the dynamic properties of the specimen in the y direction. A cable was connected from an anchor on the laboratory floor to the top mass block of the specimen. The cable had a come-along winch at the anchor end. A machined bolt was placed at the other end of the winch along with a load cell used to measure pullback force. A DCDT was temporally installed between the center of gravity of the mass blocks and the instrumentation frame. A 1-kip (4.5-kN) force was applied to the top mass block with the come-along winch, and then the machined bolt was cut with a bolt cutter to initiate free vibration. During the pullback test, wood blocks were temporarily wedged between the shaking table and the surrounding foundation to prevent unintended table movement.

3.3.6.2 Shaking Table Test

After the free-vibration test, a series of shaking table tests were conducted. Low-amplitude white-noise tests were performed separately in the x and y directions following each earthquake excitation to detect the change of natural period and damping ratio due to accumulated damage. In the shaking table tests, the ground motion intensity was increased in four steps; these test levels were named elastic, yield, design, and maximum.

The specimen was expected to remain elastic during the elastic-level test. This test is intended to check performance of the shaking table and instrumentation setup, as well as to establish the baseline dynamic characteristics of specimens under low-level excitations. Next, each specimen was subjected to a test during which the reinforcing steel was expected to reach, or only slightly exceed, the initial yield level. The yield-level test determines the initial dynamic stiffness of a specimen and identifies column behavior under relatively small amplitude shaking associated with a frequent earthquake. The excitation level was then increased to the design level. For the design-level test, the specimens were expected to experience a response ductility of about 4. Following the design-level, the maximum-level earthquake shaking was imposed. For the maximum-level run, the specimens were expected to endure a displacement ductility of 8, just slightly less than the computed ultimate ductility capacity of the column. The intensities of ground shaking were determined based on the results of inelastic dynamic analyses conducted in the previous research. However, specimens RC and PRC experienced much larger responses than predicted for the design and maximum-level tests. Thus, the intensities used for this research were reduced slightly to better achieve the targeted displacement ductility levels.

After finishing the maximum-level run, the intensity level was taken back to the yield level for all of the specimens. This test was intended to determine the effect of a significant aftershock on a bridge that has been previously subjected to a very strong motion; comparison of two yield-level tests would permit a direct assessment of the effect of cumulative damage on specimen response. Specimens PRC-2, PRC-U2, and PRC-UJ were subjected to other higher amplitude tests to assess the effects of cumulative damage.

3.4 EXPERIMENTAL RESULTS

3.4.1 Introduction

The results obtained from the shaking table tests of four partially prestressed columns are presented in this section. For each specimen, the damage observed during each test run is described in Section 3.4.2. Global response measurements, i.e., natural frequency, time histories of acceleration, base shear and displacement of center of gravity, and hysteresis loops, are discussed in Section 3.4.3. Local response measurements, i.e., curvature, bar pullout, shear deformation, column deformation, local strain, and tendon force, are discussed in Section 3.4.4.

As mentioned in Section 3.3.2, the longitudinal bars were numbered and each specimen was painted white and a grid pattern drawn with black markers on the column face prior to the tests to help describe the location of damage. This notation is used extensively in this chapter.

To determine the maximum relative displacement of a specimen, the difference between the measured horizontal displacement at the center of gravity of the mass block and the horizontal displacement at the footing level was computed for both the x and y directions. In addition to the instantaneous projections of the displacement of the specimen onto the x- and y-axes, the instantaneous vector of horizontal displacement of the center of mass relative to the center of the footing was computed to determine the overall maximum peak and residual lateral displacements of the column. The relative residual displacements are reported either as (1) relative values based on the position of a specimen at the start of a particular run or (2) cumulative values based on the position of the specimen at the beginning of the first run. This enables one to assess the overall deformed position of the structure, as well as the effect of a particular run. When mentioned in the text, the drift ratios are based on the displacement quantity under discussion divided by the vertical distance from the top of the footing to the center of mass. The displacement ductility values presented are computed as the displacement quantity of interest divided by the nominal yield displacement of the column, computed using the static pushover analysis described in Caltrans SDC.

Load cell data were used to calculate the lateral base shear and global overturning moments. After the maximum-level test of specimen PRC-2, some of the load cell data were not available because of a faulty cable connection. Thus, in this case, horizontal column shears are estimated using Newton's second law as the value of the mass of the top mass block times the peak measured horizontal acceleration at the center of gravity of the mass block. Time histories of this product were used to estimate the time history of column shear.

3.4.2 Damage Observation

This section describes the damage observed during all the tests of the four specimens. Table 3.10 presents a summary of each of the tests for each specimen, while Tables 3.11–3.14 describe the damage evolution for each specimen in detail, along with abstracted information regarding the peak motion of the shaking table and specimen during the run in question.

Overall, no cracks or visual signs of damage were observed in any of the specimens after the elastic-level test. Only minor cracking was observed after the yield-level test. A horizontal hairline crack was observed around the column perimeter at the interface of the column with the footing for unbonded mild bar specimens PRC-U, PRC-U2, and PRC-UJ after the yield-level test.

Figures 3.36(a–d) compare the local damage of the columns at the NW side after the design-level test for all four specimens. The design-level test resulted in some additional cracks and moderate spalling of the cover concrete near the base of all the columns except that of specimen PRC-UJ. Specimen PRC-UJ showed a very small buckle (<1/8 in. (2 mm)) at one location at the base of the steel jacket near the footing (Fig. 3.36(b)). Most cracks in the other columns were observed to be concentrated in the lower part of the column, and the spalling of the cover concrete mostly occurred below the 12-in. (300-mm) elevation mark. The main damage to the columns was observed at the bottom of the NW and SE quadrants. Damage at the design level consisted mainly of minor local spalling of the concrete cover. At this stage, the measured permanent residual deformations were all generally quite small, as can be seen in Tables 3.11–3.14.

The maximum-level earthquake caused an increase in the displacement demand and resulted in more spalling and lengthening of the spalled region of concrete (except for specimen PRC-UJ). This event was expected to bring the columns very close to their theoretical displacement capacities. Consistent with this expectation, some of the longitudinal bars buckled following the maximum-level test, as noted in Table 3.10 and illustrated in Figure 3.37. Buckling of the longitudinal bars appears to be very sensitive to the accuracy of the spacing of the spiral confining reinforcement; observed buckling and fracture in all of the specimens, except for specimen PRC-UJ, occurred where the pitch between spirals was locally increased to permit placement of the transverse instrumentation rods through the column.

Figures 3.37(a–d) compare the local damage of the columns at the NW side after the maximum-level test for all four specimens. A spiral on the NW side of specimen PRC-U2 fractured during the maximum-level test (Fig. 3.37(d)). Specimen PRC-UJ did not show any significant damage compared with other specimens. As shown in Figure 3.37(b), minor "elephant foot" buckling was observed intermittently in three locations along the bottom of the steel jacket. The difference in the extent of the spalled regions in the non-jacketed specimens can also be observed in Figure 3.37. The effect of incorporating the unbonded mild bar can be seen in the length of the spalled region for unbonded specimens PRC-U/U2, which is shorter than that of specimen PRC-2. In addition, the effect of the higher prestressing force in specimen PRC-U2 results in the length of the spalled and damaged regions being considerably shorter than that of specimen PRC-U.

Following the primary design and maximum-level tests described above, all specimens were subjected to extra tests, including a second yield-level, a second design-level (except for specimen PRC-U), and a maximum-level excitation (only specimen PRC-UJ). These tests were done to help assess the effects of cumulative damage and the column's ability to sustain significant aftershocks. The tests were stopped after the specimen had sustained significant damage.

The second yield level caused minor additional damage consisting of the spalling of small pieces of concrete and additional cracking. During the second design-level test, some of the longitudinal reinforcements fractured in specimen PRC-2. Because of the higher prestressing force and fracture of the spiral reinforcement during the maximum-level test, all 12 longitudinal bars buckled in specimen PRC-U2 during the second design-level test, and the local damage of the column spread to all sides of the column, resulting in larger residual displacement.

No significant additional damage was observed in specimen PRC-UJ after the second design-level test; therefore, another larger test was performed. After the second maximum-level test, no significant damage was observed, and the residual displacement still remained below 1 in. (25 mm). The performance of specimen PRC-UJ throughout all the level tests was deemed very satisfactory.

After the tests were completed, all instrumentation and broken pieces of the concrete were removed. Figures 3.38(a–d) compare the localized damage of the columns at the NW side for all specimens. The development of the damage can be seen by comparing Figures 3.36–3.38.

To determine if there was any damage on the inside of the steel jacket of specimen PRC-UJ, the jacket was removed after all the tests. Figure 3.39 shows evidence of buckling of part of the steel jacket. After removal of all loose concrete fragments at the bottom of specimen PRC-UJ, four buckled longitudinal bars and two fractured bars were found, as shown in Figure 3.40. It is unknown exactly when these failures occurred during the tests. The damage pattern in the bars and concrete are consistent with moderate sliding of the base of the column with respect to the footing.

3.4.3 Global Response

This section describes the global responses of the specimens. These include natural frequency and viscous damping properties, acceleration response at the center of gravity, displacement response at the center of gravity, and lateral force–lateral displacement hystereses. The above responses were obtained either directly from collected data or by simple calculations.

3.4.3.1 Natural Frequency and Viscous Damping Properties

As mentioned in Section 3.3.6.1, prior to each of the tests, a series of pullback tests was performed in the y direction to obtain the free-vibration characteristics of the specimen. The response of the free-vibration test was used to estimate the period of vibration and viscous damping properties at low deformation amplitudes. The pullback tests were not performed between the runs, however, due to time and practical constraints. Instead, a white-noise signal was applied in each direction after each test.

By obtaining the Fourier spectrum of the response to the white noise, it was possible to approximate the period of each specimen. In order to approximate the damping, it is common to use the half-power (band-width) method, using a power spectral density estimate. This method, however, did not yield consistent results from the white-noise test results. Thus, the free-vibration portion at the end of each run (after the end of the earthquake excitation) was used to estimate damping and first mode periods at the end of each run. The results obtained were fairly consistent, especially for the period of vibration.

Table 3.15 shows the obtained fundamental periods and damping ratios. The values were also plotted as they changed throughout the test for each of the specimens (see Figs. 3.41–3.42). After the end of the elastic-level test, as expected, little change was observed in the first mode frequency and damping ratio. In summary, after examining the period and damping at the end of each run, it was found that the results for all four columns are remarkably similar, with the column period gradually elongated, on average, from about 0.50 s at an undamaged state to about 1.0 s at the end of the design-level test in both the x and y directions. The viscous damping ratio also gradually increased with repeated loading, ranging between 2.0% and 10%, and showed more variation from one specimen to the other, especially following the maximum-level tests. The increase in the measured period and damping coefficients is likely associated with the increased inelastic action in the damaged column at lower levels of excitation. Differences in fundamental period and damping values appear consistent with the differences in the physical damage of each specimen. The trends of the x and y directions are very similar.

3.4.3.2 Acceleration

The acceleration responses were directly obtained from accelerometers attached to the specimen. The measured accelerations were low-pass filtered with cutoff frequency of 20 Hz to remove the high-frequency measurement noise. Figures 3.43–3.44 show acceleration response at the center of gravity of the mass blocks for all specimens at the design-level and the maximum-level tests, respectively, and Table 3.16 summarizes the maximum acceleration values.

All specimens had very close fundamental natural periods at the end of the yield-level test (0.66–0.69 s) and at the end of the maximum-level test (0.85–0.95 s); the acceleration response showed very similar response in the x and y directions. The response accelerations of the specimens had small offsets at the end of the response because the accelerometers recorded the acceleration of gravity associated with tilting of the specimens.

The maximum acceleration values are plotted for each run for all the specimens (see Fig. 3.45). In general, after the design-level test specimen PRC-UJ exhibited the largest maximum acceleration in both the x and y directions.

3.4.3.3 Displacement

The displacement histories of each specimen were tracked over each test run. The complete relative displacement history of each specimen is plotted in Figures 3.46–3.49. These plots provide a global view of all shaking table tests performed on each specimen, including the offset of the displacement baseline due to cumulating residual displacements. Note that the vertical lines in each plot correspond to the end of a run, after which the testing was stopped for observation.

The peak relative displacement is the peak relative displacement for each run, assuming the specimen started with an initial displacement of zero at the beginning of the test. The cumulative peak relative displacement measures the actual peak deformation during a given run, including the residual deformation at the end of the previous test. Figure 3.50 illustrates the different terminology for the peak (or max) and residual relative displacements.

Table 3.17 lists values of peak relative and residual displacements. The distances from the origin were calculated to determine the maximum distance and residual distance of each test. Figures 3.51–3.53 show the relative displacement responses at the center of gravity for all four specimens at the design, maximum, and second design-level tests, respectively. The orbits of the design and maximum-level tests are shown in Figure 3.54. The cumulative maximum and residual distances calculated from the origin are shown in Figures 3.55 and 3.56, respectively. Figures 3.57 and 3.58 show the cumulative residual displacements of the maximum, second design, and second maximum-level tests captured from the video files.

Elastic and Yield-level Tests

As shown in Figure 3.55, all four specimens have virtually identical maximum displacements at the elastic-level and yield-level tests. In general, there are no residual displacements following the elastic and yield-level tests, as expected (see Fig. 3.56).

Design-Level Test

As shown in Figure 3.51, all four specimens exhibited similar directional response during the first design-level excitation. For example, the cumulative peak displacements (drift ratios) were larger in the *x* direction for all specimens, equaling 3.6 in. (91.4 mm) (3.6%), 3.8 in. (96.5 mm) (3.8%), 3.6 in. (91.4 mm) (3.6%), and 3.7 in. (94.0 mm) (3.7%) for specimens PRC-U, PRC-UJ, PRC-2, and PRC-U2, respectively. These values correspond to a nominal displacement ductility factor of about 4 in the *x*-direction. Considering the instantaneous SRSS displacement of the center of gravity, lateral displacement ductilities of about 5 were developed in all of the specimens. All the specimens demonstrated an impressive ability to re-center. The residual drift ratios for all these specimens were smaller than 0.1%, which corresponds to about 10% of the yield displacement.

Figure 3.54(a) shows an orbit of response displacements at the center of gravity of the top blocks. The specimens mostly responded in the NW-SE direction. Their responses show a generally symmetric shape at the origin, with residual displacements all in the same (negative) direction.

Maximum-Level Test

By increasing ground motion intensity to the maximum level, some differences in behavior among the specimens became evident. All the specimens reached the maximum response during the first main pulse in both directions. When evaluated as distances from the origin, the response of specimen PRC-U was the largest, while that of specimen PRC-UJ was the smallest. The cumulative maximum response displacements from the origin exceeded 10 in. (254 mm), corresponding to a nominal displacement ductility of about 10. The cumulative residual displacements from the origin increased during the maximum-level test and showed much more variability from specimen to specimen, but all were less than 2.5 in. (63 mm) (< 2.5% drift). The cumulative residual displacements from the origin were 2.30 in. (58 mm) (2.3% drift), 0.61 in. (15 mm) (0.6% drift), 2.05 in. (52 mm) (2.1% drift), and 0.93 in. (24 mm) (0.9% drift) for specimens PRC-U, PRC-UJ, PRC-2, and PRC-U2, respectively, demonstrating that incorporating the steel jacket and higher prestressing force effectively reduces the residual displacement after strong ground excitation. The small value of residual drift for specimens PRC-UJ and PRC-U2 at this stage is remarkable.

Figure 3.54(b) shows an orbit of response displacements at the center of gravity of the top blocks. The specimens mostly responded in the NW-SE direction, as they did during the design-level test, but the response is no longer symmetric about the origin.

Aftershock Tests

Following the tests described above, the specimens were subjected to a second yield-level, design-level, and maximum-level excitation to assess the effects of cumulative damage and the ability of the column to sustain significant aftershocks. A comparison with the first yield-level test shows that the maximum distance from the origin (SRSS value) during a repeat of this excitation increased from 2 in. (51 mm) to 3 in. (76 mm) because of damage sustained in the maximum-level test. Nonetheless, the residual displacement did not change much from the previous test.

As shown in Figure 3.53, the three specimens subjected to a second design-level excitation responded somewhat differently. The cumulative maximum responses of specimens PRC-U2 and PRC-2 were similar, while the response of specimen PRC-UJ was the smallest. The second design-level events induced larger peak responses compared to the first design-level tests. The residual displacements during the second design-level excitation increased significantly for specimens PRC-2 and PRC-U2, while specimen PRC-UJ showed no increase. As will be discussed in Section 3.4.2, during the second design-level test, all longitudinal bars buckled in specimen PRC-U2 and it experienced larger residual displacement in both the x and y directions as shown in Figure 3.53.

Only specimen PRC-UJ was subjected to the second maximum-level test, since the other specimens suffered substantial damage and residual deformation after the second design-level tests. During the second maximum-level test, specimen PRC-UJ developed about the same peak displacement as measured during the first excursion to this level, but the residual displacement increased. Nonetheless, the residual displacement at this level was still smaller than that of the other self-centering columns during the first maximum excursion, except for the case of specimen PRC-U2.

3.4.3.4 Lateral Force–Lateral Displacement Hystereses

Figures 3.59–3.62 show lateral force versus lateral displacement hystereses based on the column shear and the displacement at the center of gravity of the top blocks for all the specimens. As shown in Figures 3.59 and 3.60, no significant nonlinear response was observed for all four specimens during the elastic and yield-level tests. The basic origin-oriented hysteretic shape can be detected in Figure 3.60 for some of the larger loops that occurred during the yield-level test. As shown in Figure 3.61, during the design-level test, all specimens showed similar skeleton curves as they moved away from the origin in the x and y directions. Higher frequency oscillations in the shears developed in the specimens are noticeable in the hysteresis loops. As noted by Hachem et al. (2003), these are due to high mode vibrations of the specimen involving rotation about a horizontal axis of the top mass blocks. Interestingly, the hysteretic loops projected onto the x- and y-axes do not exhibit the classic origin-oriented shape upon unloading. This behavior is due to the bidirectional nature of the response, as noted previously by Sakai and Mahin (2006).

Figure 3.62 compares the displacement response and the lateral force versus lateral displacement hystereses at the center of gravity of the top mass of all specimens subjected to the maximum-level input. specimens PRC-U and PRC-U2 show negative post-yield stiffness (with the unbonding mild bar); however, the addition of the steel jacket for specimen PRC-UJ shows a little positive post-yield stiffness.

3.4.4 Local Response

This section describes the local responses of the specimens. These include the curvature of the column, the bar pullout, the shear deformation, deformation of the column, strain, and tendon force. The above responses were obtained either directly from collected data or by simple calculations.

3.4.4.1 Curvature of Column

Curvatures were estimated over regions of the column extending between the locations of DCDT instruments attached to the face of the column.

Figure 3.63 shows curvature distributions along the column at the positive and negative peaks during the maximum and design-level testing for all the specimens. Because some DCDT measurements of specimen PRC-U showed inconsistent responses, the curvature of specimen PRC-U is excluded in Figures 3.63 and 3.64. The measurements that might possibly include the effect of pullout of reinforcement from the footing are not shown in the figures and will be discussed later. Nonlinear deformation mainly occurred at the bottom portion of the column for all specimens, which matches the location where the visible damage, e.g., concrete cracks and spalling of cover concrete, occurred. As shown in Figure 3.63, the curvatures in the bottom section [below the 3-in. (76-mm) height] of the column were largest in specimen PRC-UJ in the x and y directions for both the design and maximum-level tests. In the same instances, the nonlinear deformation range was highest in specimen PRC-2, as is evident visually.

Figure 3.64 shows the curvature distribution along the column for each specimen. The curvature distributions of specimen PRC-UJ have a unique shape, with large curvature at the bottom region (from 0 to 6 in. [152 mm]), then negligible curvature up to the steel jacket height; the small curvatures are consistent with the damage observed in specimen PRC-UJ, which shows damage only at the bottom of the specimen. The curvature distribution of specimen PRC-2 shows that the plastic hinge region increased as the test level increased.

Figure 3.65 shows the average residual curvature distribution along the column for the design and maximum-level tests for all specimens in the x and y directions. For the design-level test, the residual curvatures for all four specimens were small and corresponded with the residual displacement results. For the maximum-level test, the residual curvatures were the smallest for specimen PRC-UJ in both directions. In the *y* direction, the curvatures of specimen PRC-2 were the largest among the specimens. In specimen PRC-2, the residual curvatures of the second height section [6–12 in. (152–305 mm)] were the highest, while the other specimens had their largest values at the bottom section of the specimen, [0–6 in. (0–152 mm)], corresponding to the observed damage.

3.4.4.2 Bar Pullout

The pullout of the longitudinal reinforcement from the footing can be approximately calculated from the measurement data from the DCDT instruments mounted on rods located at 1 in. (25 mm) and 6 in. (152 mm) from the footing surface. The difference between the two measurements could be considered for practical purposes as the pullout of the longitudinal reinforcement from the footing. The maximum bar pullout values were plotted as they changed throughout the testing for each of the specimens (see Fig. 3.66). As mentioned above, due to a measurement problem of the DCDTs for specimen PRC-U, the PRC-U data are excluded.

As shown in Figure 3.66, at all test levels specimen PRC-UJ shows the largest maximum bar pullout value, and specimen PRC-2 shows the smallest maximum bar pullout value; the value for specimen PRC-U2 was between the two of them. Based on this observation, unbonding of the reinforcement increases the potential for bar pullout. The large pullout of specimen PRC-UJ can be seen in Figure 3.67, captured from the video file.

3.4.4.3 Shear Deformation

The shear deformation of the section can be approximately calculated from the vertical displacement measurement (DCDTs) and the horizontal displacement measurement (LP) at the 6-in. (152-mm) height. The difference between calculated horizontal displacement, from the DCDT measurement, and measured horizontal displacement at the same height can be assumed to be the displacement contributed by shear over the bottom 6 in. (152 mm) of height. This measurement is an indirect indication of the amount of sliding that may have occurred at the interface between the column and the footing.

Figure 3.69 shows the shear deformation response at 6 in. (152 mm) for the design and maximum-level tests for all specimens in the *x* and *y* directions. Comparison of the peak shear deformation of the different levels is plotted for all specimens. In general, shear deformations of the *x* (N-S) direction for all the specimens were larger than those of the *y* (E-W) direction. The second yield-level and design-level events for steel jacket specimen PRC-UJ resulted in larger peak deformation compared to the first excursions. Largest shear deformations were observed in specimen PRC-UJ for both directions, as shown in Figure 3.69. In the second maximum-level test, the maximum shear deformation of specimen PRC-UJ was 0.83 in. (21 mm) in the *x* direction, and 0.32 in. (8 mm) in the *y* direction. It should be noted that the shear reinforcement crossing over the interface between the bottom of the steel jacket and the footing is considerably smaller than for the other specimens (see Fig. 3.7). In most instances, deformation of specimen PRC-U2 was smaller than for the other two unbonded specimens (PRC-U, PRC-UJ). There were not many differences in the shear deformation between specimens PRC-U and PRC-U2. The graph shapes show very similar trends for maximum bar pullout (see Fig. 3.66) and shear deformation in the *x* direction (see Fig. 3.70).

3.4.4.4 Deformation of Column

Figures 3.71(1 and 2) show lateral deformation distributions along the column at the positive and negative peaks during the maximum and design-level testing for all specimens. As expected, response increases as the location of measurement moves up the column. The deformation distribution diagrams in the *x* and *y* directions are very similar for the design-level test and maximum-level test. At the design level, the deformations of the negative peak and positive peak show a symmetric shape, but the deformation diagram tends to a negative peak in the maximum-level test.

3.4.4.5 Strain

Figure 3.68 shows the maximum strain distribution along the column of the longitudinal reinforcing bars for the elastic, yield, and design-level tests. As mentioned in Section 3.3.3.7, due to malfunction of the strain gauge for specimen PRC-2, an investigation of the effects of the unbonding bar is somewhat difficult. During the main pulses of the yield-level test, most of the longitudinal reinforcement around the bottom of the column yielded, and during the design-level test maximum, the longitudinal reinforcement around the bottom of the column was damaged and not able to capture the strain of the reinforcement after the main pulses.

In summary, after examining the maximum strain of each test, it was found that the strain at the 4-in. (102-mm) height of specimen PRC-2 generally showed the maximum value, and the strain at 3 in. (76 mm) below the footing of specimen PRC-2 generally showed the minimum value.

3.4.4.6 Tendon Force

Figure 3.72 shows the prestressing force of the tendon installed in the specimen during the design and maximum-level tests. The tendon force increased when the deformation of the specimen increased, and it decreased when the specimen went back to near the origin.

Table 3.18 shows the initial, maximum, and change of tendon force throughout the testing for all specimens. The maximum of the peak tendon force was 150 kip (668 kN) during the maximum-level test of specimen PRC-U2; this is less than the nominal yield value, 208 kip (926 kN), of the tendon.

Figure 3.73 shows the change of the initial tendon force throughout each level of testing for all specimens. After each test, the tendon forces decreased, as seen in the figure. For example, the decrements of the tendon force during the maximum-level test were 3.56 kip (15.8 kN), 5.18 kip (23.1 kN), 4.53 kip (20.2 kN), and 12.27 kip (54.6 kN) for specimens PRC-U, PRC-UJ, PRC-2, and PRC-U2, respectively. Those values were about 15% of the initial tendon force.

Figure 3.74 shows the peak relative tendon force that is defined by the peak tendon force occurring for each test assuming that the specimen started with an initial tendon force of zero at the beginning of the test. As shown in Figure 3.74, the peak relative tendon forces of all the specimens at each level of testing were very similar, except for specimen PRC-UJ, which had the largest value at each test level.

3.5 CONCLUSION

A series of shaking table tests were conducted to assess the ability of partially prestressed reinforced concrete columns with unbonded post-tensioning tendons to reduce residual displacements resulting from strong earthquake ground motions. The specific objectives of this test were to study the effect of debonding the mild reinforcing bars in the area of the expected plastic hinge; to study the effect of incorporating steel jacketing, combined with local unbonding of the mild reinforcement; and to investigate the effect of magnitude on the prestressing force.

Four reinforced concrete bridge columns with unbonded prestressing tendons were designed and constructed: the first one represents a standard lightly reinforced concrete column with an unbonded prestressing tendon (nearly identical to the PRC specimen used in the previous research study); the second column incorporated unbonded mild reinforcing bars at the expected area of the plastic hinge (specimen PRC-U); the third column also incorporated the unbonded mild bar at the area of expected plastic hinge, but used a higher prestressing force (specimen PRC-U2); and the last column incorporated the unbonded mild bars in conjunction with a steel jacket and wider spiral pitch at the expected plastic hinge (specimen PRC-UJ). All four specimens were 16 in. (406 mm) in diameter, with an aspect ratio of 6.

The specimens were tested under two components of horizontal ground excitation. Modified Los Gatos records from the 1989 Loma Prieta earthquake were used as input ground motions. The columns were subjected to four levels of ground motion intensity. They are referred to as the elastic level (10% as a scaling factor), the yield level (25%), the design level (50%), and the maximum (75%) level.

Below are the conclusions determined from the shaking table tests:

- All four specimens exhibited similar maximum cumulative response displacement (SRSS) of about 4.8 in. (122 mm) during the first design-level excitation, for a ductility of about 5. During the maximum-level test, the maximum cumulative response displacements (SRSS) increased up to about 10 in. (254 mm) for all four specimens. The higher prestressing force specimen PRC-U2 and steel jacket specimen PRC-UJ exhibited slightly lower responses, but the difference was modest.
- After the design-level test, all specimens demonstrated an impressive ability to re-center. The cumulative residual displacements (SRSS) for all these specimens were smaller than a drift of 0.1%, corresponding to about 10% of the yield displacement. The cumulative residual displacements (SRSS) increased during the maximum-level test and showed much more variability from specimen to specimen, but all were less than 2.5 in. (63 mm) (< 2.5% drift). The cumulative residual displacements from the origin were 2.30 in. (58 mm) (2.3% drift), 0.61 in. (15 mm) (0.6% drift), 2.05 in. (52 mm) (2.1% drift), and 0.93

in. (24 mm) (0.9% drift) for specimens PRC-U, PRC-UJ, PRC-2, and PRC-U2, respectively, demonstrating that incorporating the steel jacket and higher prestressing force effectively reduces the residual displacement even after strong ground excitation.

- All four specimens showed similar lateral force versus lateral displacement hystereses until the design-level test. As noted previously [Sakai and Mahin (2006)], upon unloading the force-displacement relations projected onto the *x*- and *y*-axes did not show a characteristic origin-oriented hysteresis shape. During the maximum-level test, specimens PRC-U and PRC-U2 (with the mild unbonding bars) exhibited slightly negative post-yield tangential lateral stiffness, corroborating the results of previous analysis. Incorporating the steel jacket in specimen PRC-UJ resulted in a modestly positive post-yield tangential lateral stiffness.
- Observed local damage in all specimens (except specimen PRC-UJ) after the design-level tests was very similar. After experiencing a response ductility of 5, no core concrete crushing, no buckling of the longitudinal reinforcement, and no fracture of the longitudinal and spiral reinforcement were observed. After the maximum-level tests, however, some of the longitudinal rebar of specimens PRC-U and PRC-U2 were buckled and one spiral bar of specimen PRC-2 was fractured. Specimen PRC-UJ showed moderate "elephant foot" buckling at the bottom of the steel jacket; in order to prevent this type of damage, Caltrans requirements stipulate that a gap be provided between the bottom of the jacket and the top of the footing.
- During a second design-level test, all of the longitudinal rebar of specimen PRC-U2 buckled and two bars fractured; two of the longitudinal rebar of specimen PRC-2 fractured as well.
- For all four specimens, the tendon remained elastic during the tests.
- Comparing the responses of specimens PRC-U and PRC-2 showed that unbonding of the mild bar resulted in a shorter plastic hinge region and a slightly larger maximum displacement and residual displacement, most likely due to the lower flexibility and negative post-yield stiffness in the *x* and *y* directions.
- As might be expected, the use of a higher prestressing force decreased the maximum displacements and residual displacements when subjected to the design and maximum-level tests, but the damage to specimen PRC-U2 was more severe than to specimen PRC-U, due to the higher compression force.

- A confining steel jacket sheathing a partially prestressed reinforced concrete column with locally unbonded mild reinforcement prevented any significant observable damage throughout the entire test program. For the design-level excitation, the residual drift index of specimen PRC-UJ was less than 0.1%, and remained less than 0.6% even for the maximum-level test. This test program demonstrates the substantial benefits of partially prestressed reinforced concrete columns with locally unbonded mild reinforcement and surrounded by a steel jacket.

Table 3.1 Dimensions of physical quantities and target scaling factors

Physical quantity	Dimension	Target scale factor
Length	L	4.5
Acceleration	LT^{-2}	1
Modulus of elasticity	$ML^{-1}T^{-2}$	1
Time	T	2.12
Frequency	T^{-1}	0.471
Velocity	LT^{-1}	2.12
Displacement	L	4.5
Area	L^2	20.25
Mass	M	20.25
Rotational mass	ML^2	410.06
Force	MLT^{-2}	20.25
Stiffness	MT^{-2}	4.5
Moment	ML^2T^{-2}	91.13
Energy	ML^2T^{-2}	91.13
Weight density	$ML^{-2}T^{-2}$	0.222
Strain	1	1
Stress	$ML^{-1}T^{-2}$	1

Table 3.2 Differences among specimens

Specimen	Description	Characteristic	Main parameter
RC	Reinforced concrete column	Based on the dimensional study of prototype column	12 No. 4 longitudinal bars
PRC	Partially prestressed reinforced concrete column	Modified from RC specimen	12 No. 3 longitudinal bars 1-1/4″ tendon
PRC-2	Partially prestressed reinforced concrete column	Same as PRC except top slab portion: uses steel bracket instead of top slab	12 No. 3 longitudinal bars 1-3/8″ tendon
PRC-U	PRC-2 with unbonded mild reinforcing bars	Similar to PRC-2 except contains unbonded mild bar	12 No. 3 longitudinal bars 1-3/8″ tendon Unbonded mild bar at plastic hinge
PRC-U2	PRC-U with larger prestressing force	Same as PRC-U except higher prestressing force	12 No. 3 longitudinal bars 1-3/8″ tendon Unbonded mild bar at plastic hinge
PRC-UJ	PRC-U with steel jacketing	Sheathed with a steel jacket at plastic hinge; Wider spiral pitch (5″)	12 No. 3 longitudinal bars 1-3/8″ tendon Unbonded mild bar at plastic hinge Steel jacket at the plastic hinge

Table 3.3 Concrete mix design

(a) Mix Specifications

Cement	ASTM C-150 TYPE II
Fly ash	ASTM C-618 CLASS F, 15%
Admixture (water reducer)	ASTM C-494 TYPE A
Minimum 28-day strength	3,850 psi (26.6 MPa)
Maximum 28-day strength	4,350 psi (30.0 MPa)
Cementitious sacks/yd^3	5.60
Maximum size aggregate	3/8″ (9.5 mm)
Slump	5″
Water/cement ratio	0.603

(b) Mix Design and Quantities

Material	Specific gravity	Absolute volume	SSD weight
3/8″ × #8 gravel	2.68	5.98 ft^3 (0.167 m^3)	1,000 lb (453 kg)
Regular top sand	2.67	9.02 ft^3 (0.253 m^3)	1,503 lb (681 kg)
SR blend sand	2.60	3.69 ft^3 (0.103 m^3)	599 lb (271 kg)
Cement Type II	*3.15*	2.27 ft^3 (0.064 m^3)	447 lb (202 kg)
Fly ash	*0.00*	0.55 ft^3 (0.015 m^3)	79 lb (36 kg)
Water	1.00	5.08 ft^3 (0.142 m^3)	317 lb (144 kg)
Water reducer	-----	0.41 ft^3 (0.011 m^3)	26.3 fl oz (778 ml)
Total	-----	27 ft^3 (0.756 m^3)	3,945 lb (1,787 kg)

Table 3.4 Compressive strength of concrete

(a) Concrete for Footings

Day	No. 1 (ksi)	No. 2 (ksi)	No. 3 (ksi)	Average (ksi)
8	3.31	3.54	3.27	3.38
29	5.44	5.15	5.16	5.25

(b) Concrete for Columns

Day	No. 1 (ksi)	No. 2 (ksi)	No. 3 (ksi)	Average (ksi)
7	2.20	2.52	2.18	2.30
14	2.93	2.88	2.97	2.93
21	3.53	3.60	4.49	3.54
28*	3.86	3.88	3.97	3.90
70 (PRC-U)	4.76	4.37	4.87	4.66
81 (PRC-UJ)	4.84	4.77	4.62	4.65
84 (PRC-2)	4.98	4.62	4.55	4.72
90 (PRC-U2)	4.94	4.58	-	4.76

*After 28 days curing, the form was removed.

Table 3.5 Concrete properties from cylinder tests

Specimen	No.	Strength (MPa)	Modulus of elasticity (GPa)	
			Tangent modulus $E_{c \cdot tan}$	Secant modulus $E_{c \cdot sec}$
PRC-U	No. 1	32.81	19.22	17.33
	No. 2	30.13	19.19	17.26
	No. 3	33.60	20.03	18.07
	Average	32.18 (4.66 ksi)	19.5 (2,823 ksi)	17.55 (2,544 ksi)
PRC-UJ	No. 1	33.38	18.75	16.54
	No. 2	32.19	18.07	16.05
	No. 3	29.88	17.72	15.46
	Average	32.06 (4.65 ksi)	18.18 (2,635 ksi)	16.02 (2,321 ksi)
PRC-2	No. 1	34.06	19.52	17.44
	No. 2	31.60	19.55	17.30
	No. 3	-	-	-
	Average	32.83 (4.71 ksi)	19.53 (2,830 ksi)	17.37 (2,517 ksi)
PRC-U2	No. 1	31.42	18.90	16.71
	No. 2	31.88	18.82	16.97
	No. 3	34.35	18.74	16.70
	Average	32.55 (4.76 ksi)	18.82 (2,727 ksi)	16.79 (2,433 ksi)

Table 3.6 .Mechanical properties of steel from tensile test

(a) No. 3 (10-mm Diameter) Reinforcing Bar

	Yield strength (MPa)	Ultimate strength (MPa)	Modulus of elasticity (GPa)
No. 1	476 (69.1 ksi)	627 (90.9 ksi)	201 (29,090 ksi)

(b) 1-3/8-in. (35-mm) Diameter Tendon

	Yield strength (MPa)	Ultimate strength (MPa)	Modulus of elasticity (GPa)
No. 1	910 (132 ksi)	1,110 (161 ksi)	205 (29,700 ksi)

(c) Steel Jacket

	Yield strength (MPa)	Ultimate strength (MPa)	Modulus of elasticity (GPa)
No. 1	291 (42.3 ksi)	356 (51.7 ksi)	187 (27,200 ksi)

Table 3.7 Shaking table characteristics

Table dimensions	20×20 ft, 100 kip
Maximum specimen height	40 ft to ceiling, 32 ft to crane hook
Component of motion	6-degrees-of-freedom: x, y, and z, plus rotational components - pitch, roll, and yaw
Displacement limits	x and y limits are $\pm 5''$, z limit is $\pm 2''$
Velocity limits	30 in./s in all axes with an unloaded table
Acceleration limits	Approximately 3g in all axes with an unloaded table
Data acquisition system	192 channels at 200 Hz

Table 3.8 Total axial force ratio

Specimen	Concrete strength (f'_{c0}) (ksi)	Area of section (A_g) (in^2)	Axial force (P) (kip)	Prestress force (P_{ps}) (kip)	Total force (P_{total}) (kip)	Total axial force ratio (α_{total}) (%)
PRC-U	4.66	188.49	53.98	46.62	100.60	11.45
PRC-UJ	4.65	188.49	53.98	48.70	102.68	11.72
PRC-2	4.72	188.49	53.98	49.44	103.42	11.62
PRC-U2	4.71	188.49	53.98	77.88	131.86	14.85

Table 3.9 Input signals

	Original NF03 (Fault-normal)	Filtered Signal in x (N-S) component	Original NF04 (Fault-parallel)	Filtered Signal in y (E-W) component
Acceleration	7.04 m/s^2 (0.72g)	7.30 m/s^2 (0.74g)	4.49 m/s^2 (0.46g)	4.46 m/s^2 (0.45g)
Velocity	0.815 m/s (32.1 ips)	0.739 m/s (29.1 ips)	0.429 m/s (16.9 ips)	0.422 m/s (16.6 ips)
Displacement	0.144 m (5.7 in.)	0.122 m (4.8 in.)	0.082 m (3.2 in.)	0.067 m (2.6 in.)

Table 3.10 Test summary for each specimen

	PRC-U	PRC-UJ	PRC-2	PRC-U2
Aftershock test sequence	Yield 2	Yield 2, Design2, Max 2	Yield 2, Design 2	Yield 2, Design 2
Bonded/unbonded mild bar	Unbonded	Unbonded	Bonded	Unbonded
Initial prestressing force (kip)	46.62	48.70	49.74	77.88
Elastic level	No crack or visual damage			
Yield level	Perimeter crack (bottom , 12-in. height)	Perimeter crack (top and bottom of steel jacket)	No perimeter crack	Perimeter crack (bottom)
Design level	Some spalling Cracks developed	Steel jacket buckled (1 place)	Some spalling Cracks developed	Some spalling Cracks developed
Maximum level	2 bars buckled	Steel jacket buckled (3 places)	3 bars buckled	6 bars buckled 1 spiral fracture
Yield 2 level	Minor additional spalling and crack		Minor damage	
Design 2 level	N/A	No new damage	2 bars fractured	All 12 bars buckled
Maximum 2 level	N/A	Little more crushing	N/A	N/A
Main damage region	Below 13-in. height	Below 2-in. height	Below 19-in. height	Below 10-in. height

Table 3.11 Summary of response for specimen PRC-U

Run #	Performance level	Table displacement and acceleration		Relative displacement		Observation
		PGA (g)	PGD (in.)	Peak[a] (in.)	Residual[b] (in.)	
		x	x	x	x	
1	Elastic level 10%	0.092	0.481	0.262	0.026	No cracks or visual signs of damage.
2	Yield level 1 25%	0.201	1.273	1.875	0.003	A perimeter crack formed at the interface with the footing and 12-in. (300-mm) height.
3	Design-level 1 50%	0.432	2.549	3.627	-0.047	Some spalling appeared at the bottom of NW and SE sides. Cracks developed between bottom and 12-in. (300-mm) height.
4	Maximum level 1 75%	0.654	3.861	8.577	-1.864	On the NW side, significant spalling occurred between the bottom and 12-in. (300-mm) height. One bar bucked at the 5-in. (130-mm) height of NW side (bar # 11). Additional concrete spalled on the SE side with two bars buckling (bars #4, 5). A perimeter crack formed at the 21-in. (530-mm) and 28-in. (710-mm) heights.
5	Yield level 2 25%	0.210	1.249	2.305	-1.636	Minor additional spalling and cracks were observed.

[a]Peak relative displacement assuming zero displacement at the beginning of each test.

[b]Cumulative residual relative displacement at the end of the test.

Table 3.12 Summary of response for specimen PRC-UJ

Run #	Performance level	Table displacement and acceleration		Relative displacement		Observation
		PGA (g)	PGD (in.)	Peak[a] (in.)	Residual[b] (in.)	
		x	x	x	x	
1	Elastic level 10%	0.112	0.479	0.232	-0.019	No cracks or visual signs of damage.
2	Yield level 1 25%	0.204	1.265	2.056	-0.054	A perimeter crack formed at the interface with top and bottom of the steel jacket.
3	Design-level 1 50%	0.421	2.565	3.795	-0.027	Steel jacket buckled at the bottom on SE side. From the sound comparison, concrete and steel jacket apparently separated at the buckled side.
4	Maximum level 1 75%	0.650	3.865	7.609	-0.433	Two more incidents of buckling of the steel jacket occurred at the bottom of the NW and SE sides. A large crack was observed at the bottom. The column and footing evidenced separation with a large crack opening and crushing of all sides.
5	Yield level 2 25%	0.201	1.267	1.899	-0.385	No new damage was observed.
6	Design-level 2 50%	0.416	2.573	4.762	-0.436	No visual signs of new damage. From the comparisons of hammering sounds, the separation between steel jacket and concrete increased at the buckled portion. Some sliding deformations observed between base of jacket and foundation.
7	Maximum level 2 70%	0.633	3.603	7.580	-0.986	A little more crushing at the bottom of the NW and SE sides. Sliding deformations visually observed to increase, though they appeared to remain small compared to the flexural deformations.

[a]Peak relative displacement assuming zero displacement at the beginning of each test.

[b]Cumulative residual relative displacement at the end of the test.

Table 3.13 Summary of response for specimen PRC-2

Run #	Performance level	Table displacement and acceleration		Relative displacement		Observation
		PGA (g)	PGD (in.)	Peak[a] (in.)	Residual[b] (in.)	
		x	x	x	x	
1	Elastic level 10%	0.102	0.498	0.247	-0.009	No cracks or visual signs of damage.
2	Yield level 1 25%	0.201	1.247	1.947	-0.026	Some horizontal cracks appeared below the 12-in. (300-mm) height.
3	Design-level 1 50%	0.419	2.577	3.587	-0.023	Some spalling appeared between 4-in. (100-mm) and 16-in. (400-mm) heights on NW and SE sides with some spirals. Cracks developed between 4-in. (100-mm) and 12-in. (300-mm) heights.
4	Maximum level 1 75%	0.641	3.877	8.279	-1.282	On the NW side, significant spalling occurred between 4-in. (100-mm) and 16-in. (400-mm) heights with no bar bucking. Additional concrete spalled on the SE side with three bars buckling between 5-in. (130-mm) and 8-in. (200-mm) heights (bars #4, 5, 6). Many cracks developed between bottom and 20-in. (500-mm) height.
5	Yield level 2 25%	0.210	1.272	1.988	-1.186	Minor additional spalling and cracks were observed.
6	Design-level 2 50%	0.400	2.559	4.921	-1.729	More spalling occurred around bars. Bars #4 and 5 on the SE side fractured in tension at the end of the run.

[a]Peak relative displacement assuming zero displacement at the beginning of each test.

[b]Cumulative residual relative displacement at the end of the test.

Table 3.14 Summary of response for specimen PRC-U2

Run #	Performance level	Table displacement and acceleration		Relative displacement		Observation
		PGA (g)	PGD (in.)	Peak[a] (in.)	Residual[b] (in.)	
		x	x	x	x	
1	Elastic level 10%	0.098	0.482	0.245	-0.007	No cracks or visual signs of damage.
2	Yield level 1 25%	0.199	1.247	2.121	-0.034	A perimeter crack formed at the interface with the footing. A few horizontal cracks occurred at the 16-in. (400-mm) height.
3	Design-level 1 50%	0.402	2.588	3.704	-0.006	Some spalling appeared at the bottom of NW and SE sides between 0-in. and 8-in. (200-mm) heights. Cracks developed between column bottom and 8-in. (200-mm) height.
4	Maximum level 1 75%	0.618	3.875	7.844	-0.807	On most sides, significant spalling occurred between bottom and 10-in. (250-mm) height. The third spiral on the NW side (bar #10) fractured during the maximum-level run. The distance between the fractured spirals was 1.8 in. (45 mm). Six bars buckled between 3-in. (75-mm) and 6-in. (150-mm) heights of NW and SE sides (bars # 2, 3, 4, 5, 9, 10). Crushing of the bottom 3 in. (75 mm) of concrete occurred at N side. The maximum crack opening was 1/4 in. (6 mm) on the E side. Minor damage occurred at the defection part of the SW side.

[a]Peak relative displacement assuming zero displacement at the beginning of each test.

[b]Cumulative residual relative displacement at the end of the test.

Table 3.14—*Continued*

Run #	Performance level	Table displacement and acceleration		Relative displacement		Observation
		PGA (g)	PGD (in.)	Peak[a] (in.)	Residual[b] (in.)	
		x	*x*	*x*	*x*	
5	Yield level 2 25%	0.197	1.261	2.351	-0.856	Minor additional spalling and cracks were observed.
6	Design-level 2 50%	0.388	2.552	5.704	-3.789	The distance of the previously fractured spirals widened to 6 in. (150 mm), causing more buckling and large residual displacement. Almost all area below the 10-in. (250-mm) height was spalled with significant crushing. All 12 bars buckled causing more crushing. (The maximum depth from the cover was 1-1/4 in. (32 mm) at the NW side.) The neighboring two bars also buckled between the 3-in. (75-mm) and 7-in. (175-mm) heights (bars # 6, 11). Two bars buckled at the bottom (bars # 7, 12). Bars #1 and 8 buckled slightly.

[a]Peak relative displacement assuming zero displacement at the beginning of each test.

[b]Cumulative residual relative displacement at the end of the test.

Table 3.15 Change of natural period and damping ratio

EQ level	Specimen	Natural period (s)		Damping ratio (%)	
		x	*y*	*x*	*y*
Free vibration	PRC-U	-	0.49	-	1.83
	PRC-UJ	-	0.45	-	1.59
	PRC-2	-	0.48	-	1.63
	PRC-U2	-	0.49	-	1.36
Elastic level 10%	PRC-U	0.51	0.51	2.17	1.69
	PRC-UJ	0.48	0.48	2.98	2.25
	PRC-2	0.51	0.50	1.93	2.50
	PRC-U2	0.50	0.50	2.26	1.76
Yield level 25%	PRC-U	0.69	0.70	7.31	7.25
	PRC-UJ	0.66	0.65	7.06	6.63
	PRC-2	0.67	0.67	6.54	7.13
	PRC-U2	0.65	0.64	6.36	6.99
Design level 50%	PRC-U	0.91	0.93	7.58	8.89
	PRC-UJ	0.95	0.95	10.07	10.06
	PRC-2	0.85	0.85	7.32	7.74
	PRC-U2	0.87	0.87	8.22	8.91
Max. level 75%	PRC-U	0.93	0.95	7.76	10.72
	PRC-UJ	0.78	0.97	8.58	9.85
	PRC-2	0.85	1.11	7.73	6.89
	PRC-U2	0.79	1.05	7.69	9.38

Table 3.16 Maximum acceleration response at C.G.

EQ level	Specimen	Max acceleration (g)	
		x direction	y direction
Elastic level 10%	Unbonded 1	0.102	0.073
	Steel jacket	0.112	0.085
	Bonded	0.101	0.081
	Unbonded 2	0.127	0.077
Yield level 25%	Unbonded 1	0.208	0.131
	Steel jacket	0.222	0.147
	Bonded	0.234	0.155
	Unbonded 2	0.249	0.151
Design level 50%	Unbonded 1	0.273	0.223
	Steel jacket	0.285	0.232
	Bonded	0.269	0.226
	Unbonded 2	0.280	0.227
Max. level 75%	Unbonded 1	0.233	0.206
	Steel jacket	0.260	0.235
	Bonded	0.226	0.210
	Unbonded 2	0.226	0.202

Table 3.16—*Continued*

EQ level	Specimen	Max acceleration (g)	
		x direction	*y* direction
After maximum: yield level 2 25%	Unbonded 1	0.084	0.125
	Steel jacket	0.135	0.156
	Bonded	0.117	0.153
	Unbonded 2	-	-
After maximum: design-level 2 50%	Unbonded 1	-	-
	Steel jacket	0.170	0.219
	Bonded	0.157	0.166
	Unbonded 2	0.155	0.164
After maximum: max. level 2 70%	Unbonded 1	-	-
	Steel jacket	0.208	0.230
	Bonded	-	-
	Unbonded 2	-	--

Table 3.17 Maximum and residual displacement response at C.G.

EQ level	Specimen	Max dis. (in.) (Residual dis.) (in.)			Cumulative max dis. (in.) (Cumulative residual) (in.)		
		x direction	*y* direction	SRSS	*x* direction	*y* direction	SRSS
Elastic level 10%	PRC-U	0.262 (0.025)	0.207 (0.004)	0.301 (0.026)	0.262 (0.025)	0.207 (0.004)	0.301 (0.026)
	PRC-UJ	0.232 (0.019)	0.219 (0.015)	0.282 (0.024)	0.232 (0.019)	0.219 (0.015)	0.282 (0.024)
	PRC-2	0.247 (0.009)	0.210 (0.006)	0.287 (0.011)	0.247 (0.009)	0.210 (0.006)	0.287 (0.011)
	PRC-U2	0.245 (0.007)	0.196 (0.007)	0.279 (0.011)	0.245 (0.007)	0.196 (0.007)	0.279 (0.011)
Yield level 25%	PRC-U	1.875 (0.014)	0.983 (0.032)	1.984 (0.035)	1.858 (0.003)	0.976 (0.025)	1.972 (0.025)
	PRC-UJ	2.056 (0.062)	0.738 (0.016)	2.123 (0.064)	2.048 (0.057)	0.745 (0.009)	2.118 (0.055)
	PRC-2	1.947 (0.036)	0.800 (0.010)	2.018 (0.037)	1.936 (0.026)	0.811 (0.001)	2.011 (0.026)
	PRC-U2	2.121 (0.055)	0.764 (0.004)	2.162 (0.071)	2.100 (0.034)	0.741 (0.018)	2.148 (0.039)
Design level 50%	PRC-U	3.627 (0.081)	3.379 (0.043)	4.912 (0.092)	3.592 (0.047)	3.380 (0.042)	4.888 (0.063)
	PRC-UJ	3.795 (0.013)	3.206 (0.022)	4.790 (0.025)	3.856 (0.027)	3.191 (0.037)	4.832 (0.046)
	PRC-2	3.587 (0.035)	2.927 (0.067)	4.579 (0.075)	3.575 (0.023)	2.956 (0.096)	4.587 (0.098)
	PRC-U2	3.704 (0.025)	3.627 (0.048)	4.641 (0.055)	3.736 (0.006)	3.598 (0.006)	4.684 (0.021)
Max. level 75%	PRC-U	8.577 (1.863)	7.205 (1.372)	10.979 (2.314)	8.578 (1.864)	7.176 (1.343)	10.961 (2.297)
	PRC-UJ	7.609 (0.434)	6.052 (0.364)	9.628 (0.566)	7.609 (0.433)	6.113 (0.425)	9.665 (0.607)
	PRC-2	8.279 (1.300)	6.741 (1.505)	10.540 (1.988)	8.261 (1.282)	6.838 (1.601)	10.586 (2.051)
	PRC-U2	7.844 (0.803)	6.164 (0.486)	9.891 (0.939)	7.848 (0.807)	6.129 (0.451)	9.873 (0.925)

Table 3.17—*Continued*

EQ level	Specimen	Max dis. (in.) (Residual dis.) (in.)			Cumulative max dis. (in.) (Cumulative residual) (in.)		
		x direction	y direction	SRSS	x direction	y direction	SRSS
Yield level 2 25%	PRC-U	2.3054 (0.215)	2.193 (0.217)	3.129 (0.305)	4.156 (1.636)	3.583 (1.153)	5.423 (2.002)
	PRC-UJ	1.898 (0.049)	2.995 (0.051)	3.288 (0.071)	2.332 (0.385)	3.425 (0.379)	3.868 (0.541)
	PRC-2	1.988 (0.072)	2.169 (0.171)	2.758 (0.186)	3.245 (1.186)	3.796 (1.455)	4.802 (1.877)
	PRC-U2	2.351 (0.052)	3.221 (0.035)	3.387 (0.063)	3.154 (0.856)	3.714 (0.528)	4.155 (1.006)
Design-level 2 50%	PRC-U	- -	- -	- -	- -	- -	- -
	PRC-UJ	4.762 (0.065)	5.053 (0.043)	6.725 (0.078)	5.132 (0.435)	5.460 (0.449)	7.275 (0.626)
	PRC-2	4.921 (0.572)	4.993 (0.751)	6.793 (0.944)	6.078 (1.729)	6.458 (2.217)	8.649 (2.811)
	PRC-U2	5.704 (2.938)	5.860 (2.400)	7.486 (3.793)	6.556 (3.789)	6.403 (2.934)	8.483 (4.798)
Max. level 2 70%	PRC-U	- -	- -	- -	- -	- -	- -
	PRC-UJ	7.580 0.552	8.109 0.493	10.103 (0.740)	8.014 (0.986)	8.581 (0.965)	10.743 (1.380)
	PRC-2	- -	- -	- -	- -	- -	- -
	PRC-U2	- -	- -	- -	- -	- -	- -

Table 3.18 Change of tendon force

EQ level	Specimen	Tendon force (kip)			
		Initial	Maximum	Change	Cumulative change
Elastic level 10%	PRC-U	46.62	48.33	-0.14	-0.14
	PRC-UJ	48.70	49.57	-0.70	-0.70
	PRC-2	49.44	50.70	-0.29	-0.29
	PRC-U2	77.88	79.06	-0.23	-0.23
Yield level 25%	PRC-U	46.45	75.63	-1.84	-1.98
	PRC-UJ	47.97	74.40	-1.41	-2.11
	PRC-2	49.16	77.50	-0.003	-0.29
	PRC-U2	77.61	105.83	-0.862	-1.09
Design level 50%	PRC-U	44.57	97.36	-1.60	-3.58
	PRC-UJ	46.53	108.29	-1.18	-3.29
	PRC-2	49.13	97.47	-1.03	-1.32
	PRC-U2	76.71	129.16	-2.67	-3.76
Max. level 75%	PRC-U	42.85	124.53	-3.56	-7.14
	PRC-UJ	45.31	147.94	-5.18	-8.47
	PRC-2	48.09	128.96	-4.53	-5.85
	PRC-U2	73.89	152.84	-12.27	-16.03
Yield level 2 25%	PRC-U	38.89	58.79	-2.93	-10.07
	PRC-UJ	40.08	68.01	-1.16	-9.63
	PRC-2	43.27	61.19	-1.78	-7.63
	PRC-U2	61.33	97.53	-2.23	-18.26
Design-level 2 50%	PRC-U	-	-	-	-
	PRC-UJ	38.86	105.35	-0.62	-10.25
	PRC-2	41.39	94.38	0.41 (lean)	-7.22
	PRC-U2	58.98	104.60	1.91(lean)	-16.35

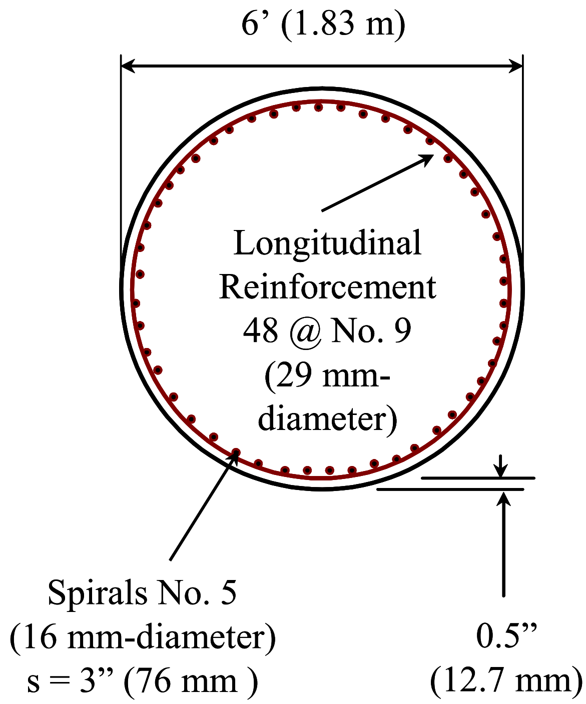

(a) Cross section

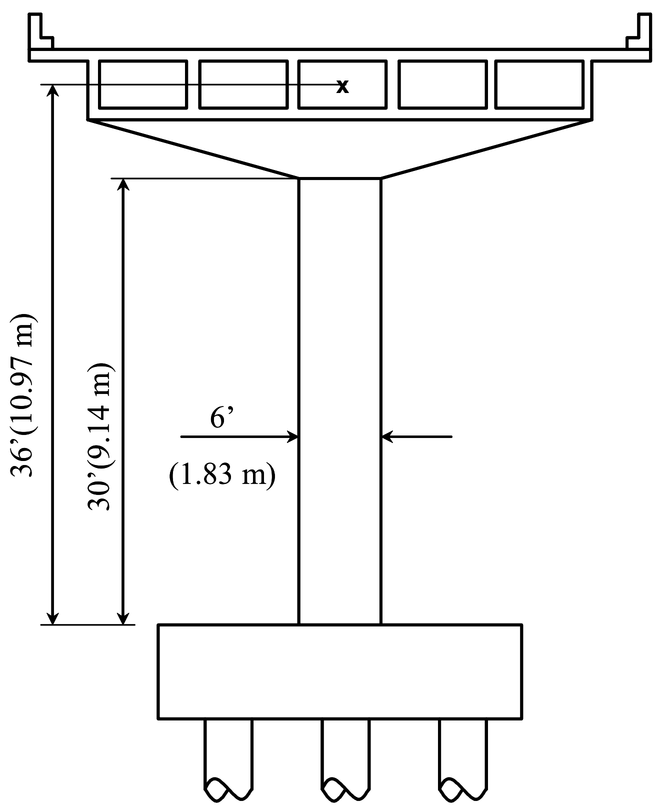

(b) Bridge column

Fig. 3.1 Prototype column

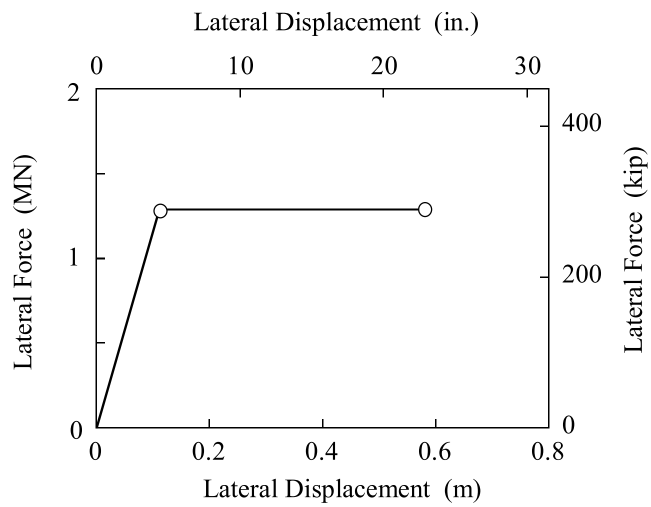

Fig. 3.2 Ductility and flexural capacity of prototype column

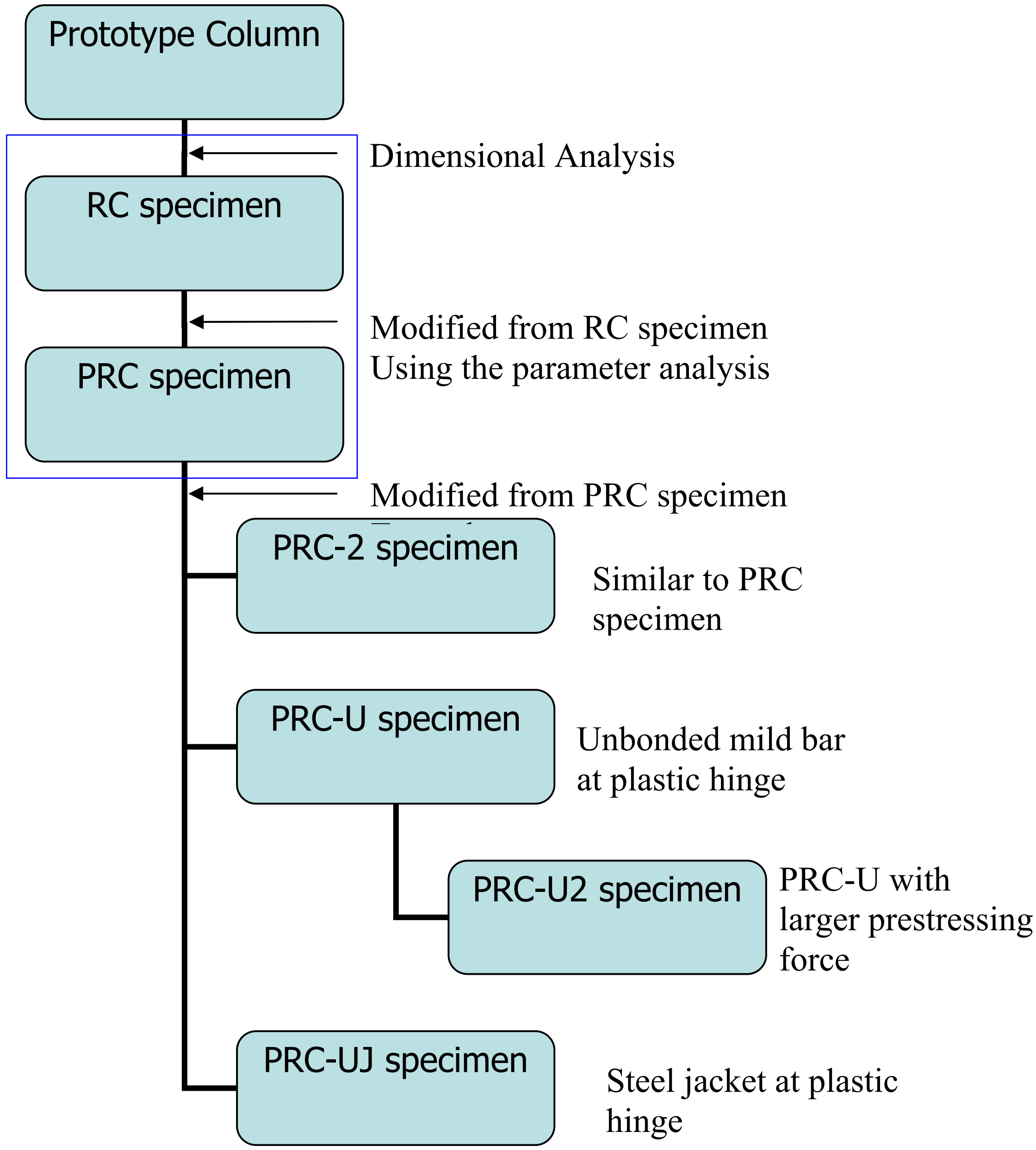

Fig. 3.3 Flowchart of specimen design

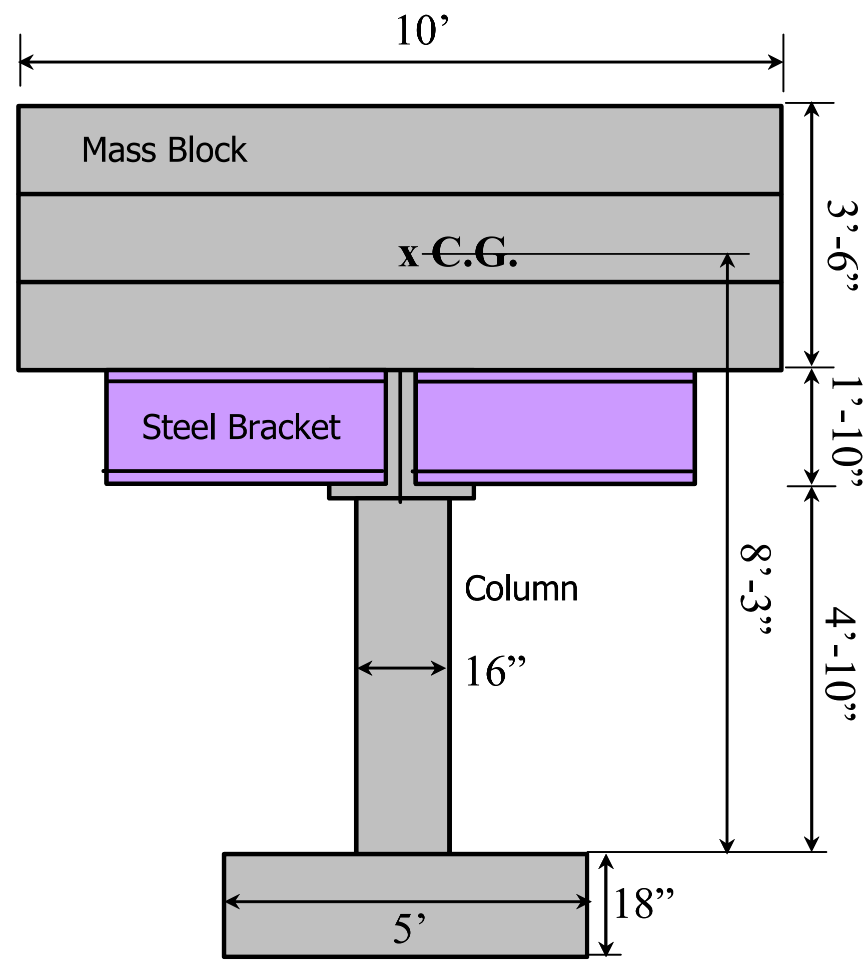

Fig. 3.4 Specimen with mass blocks

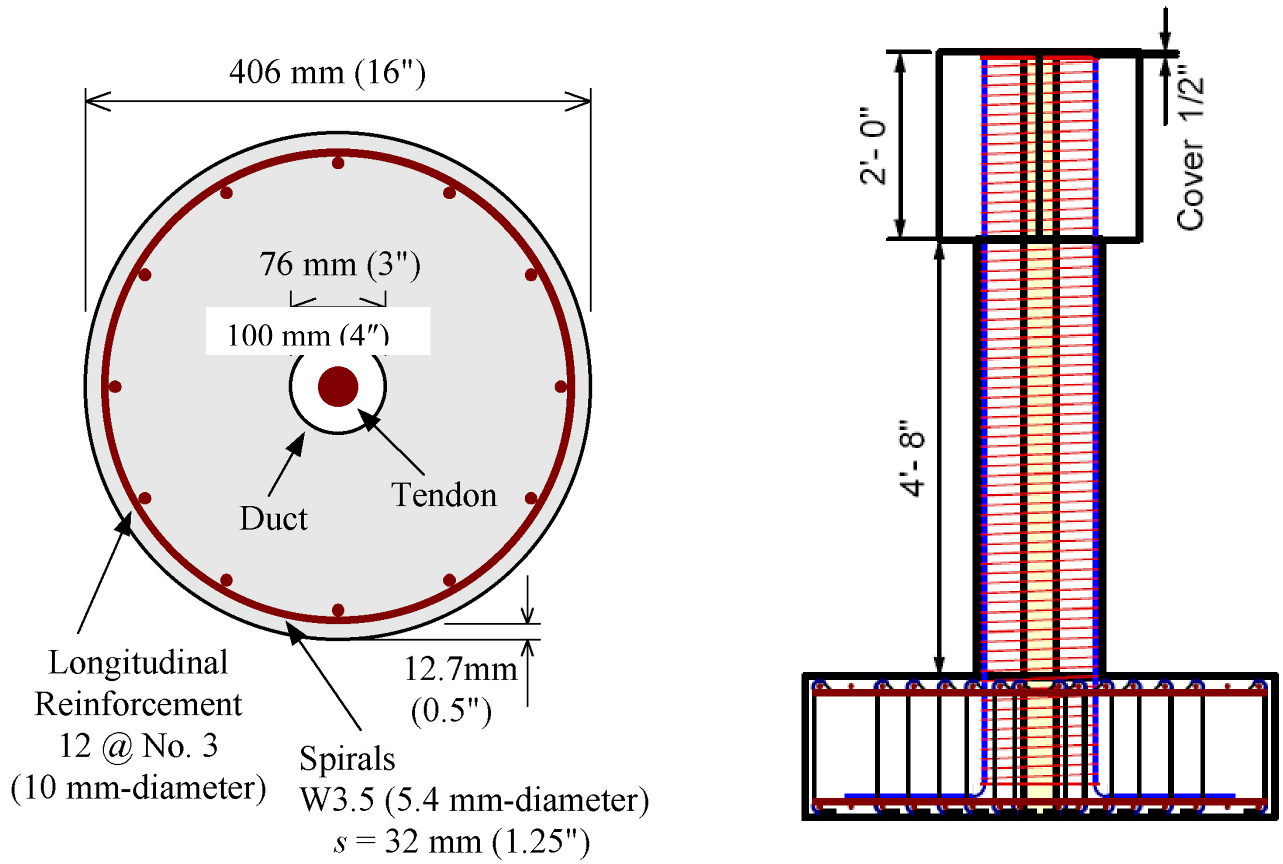

(a) Cross section (b) Specimen

Fig. 3.5 Reinforcement details of specimen PRC-2

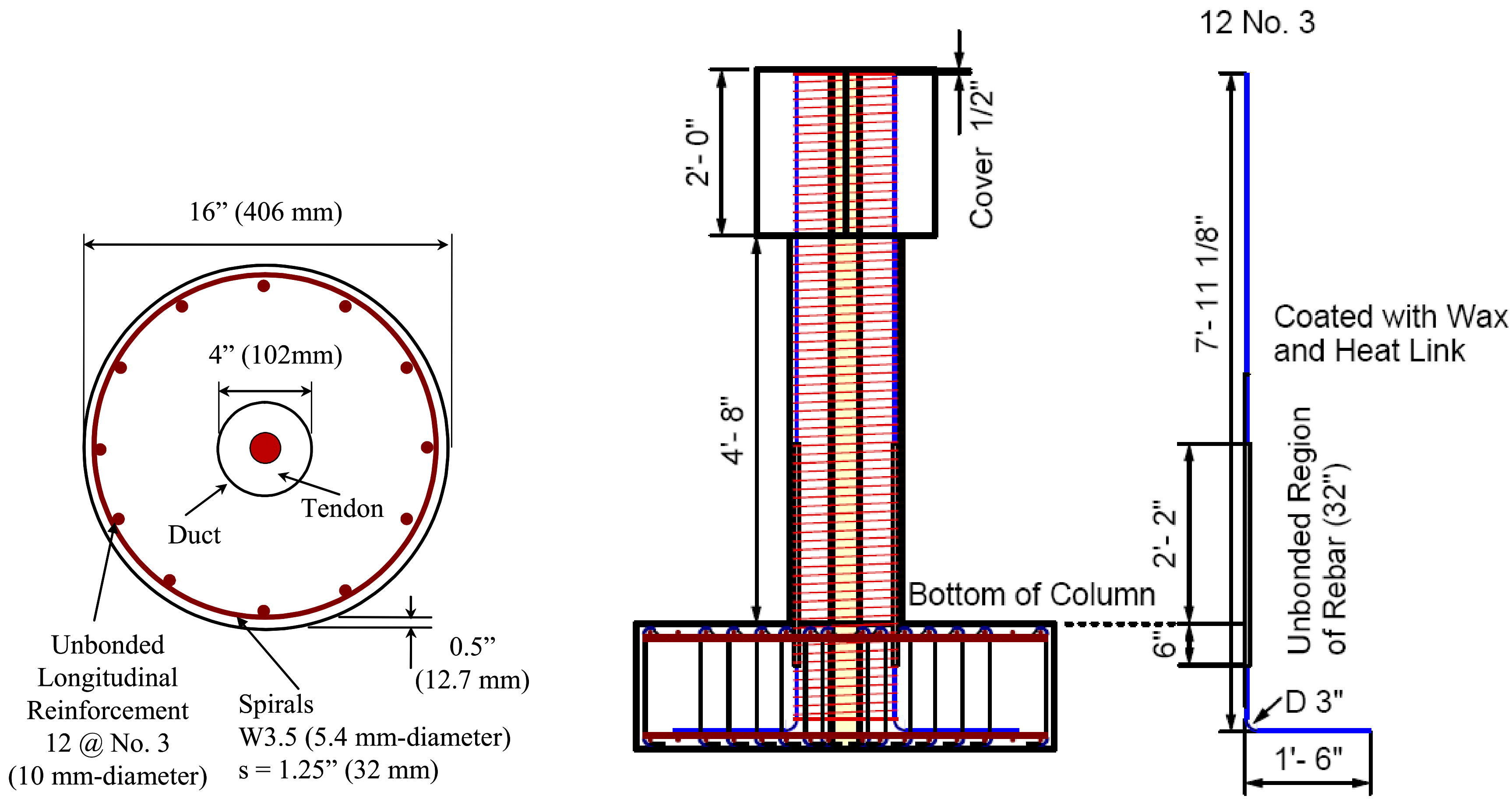

(a) Cross section (b) Specimen (c) Unbonded bar detail

Fig. 3.6 Reinforcement details of specimens PRC-U and PRC-U2

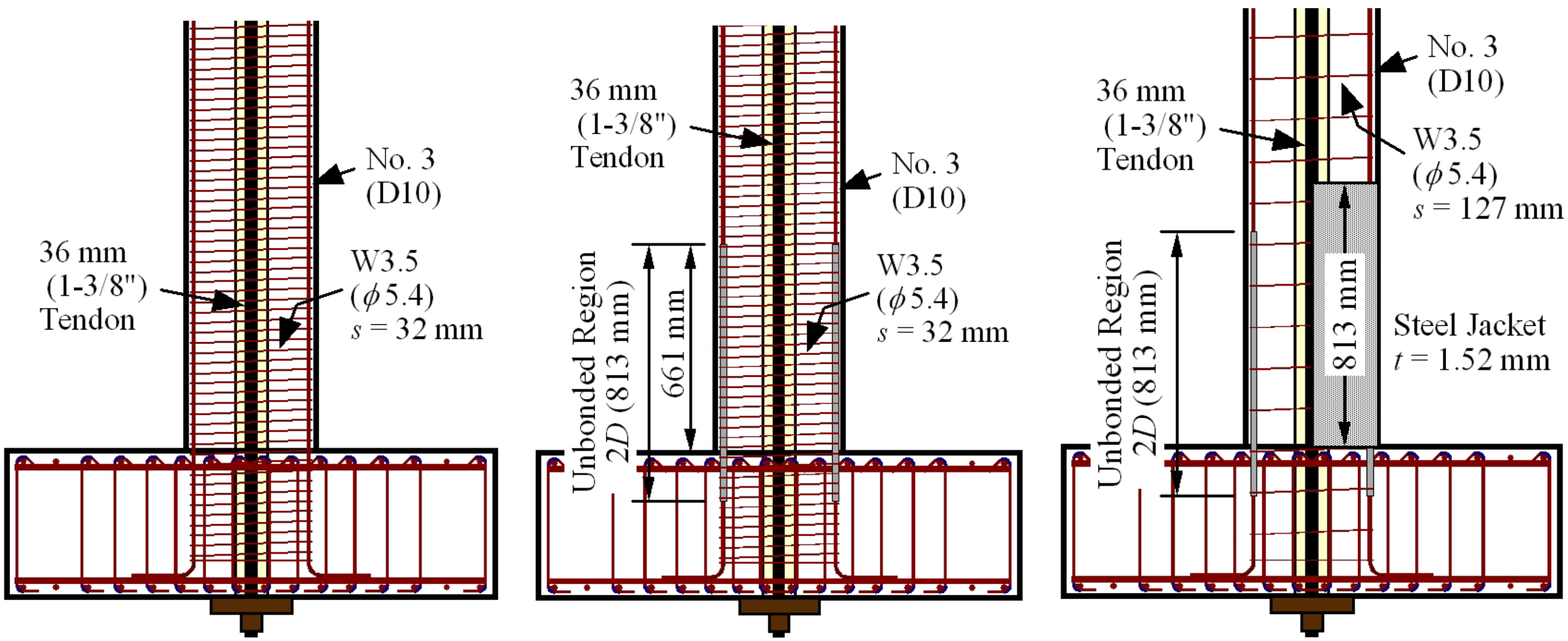

(a) Specimen PRC-2 (b) Specimens PRC-U/U2 (c) Specimen PRC-UJ

Fig. 3.7 Reinforcement details of specimens at plastic hinge regions

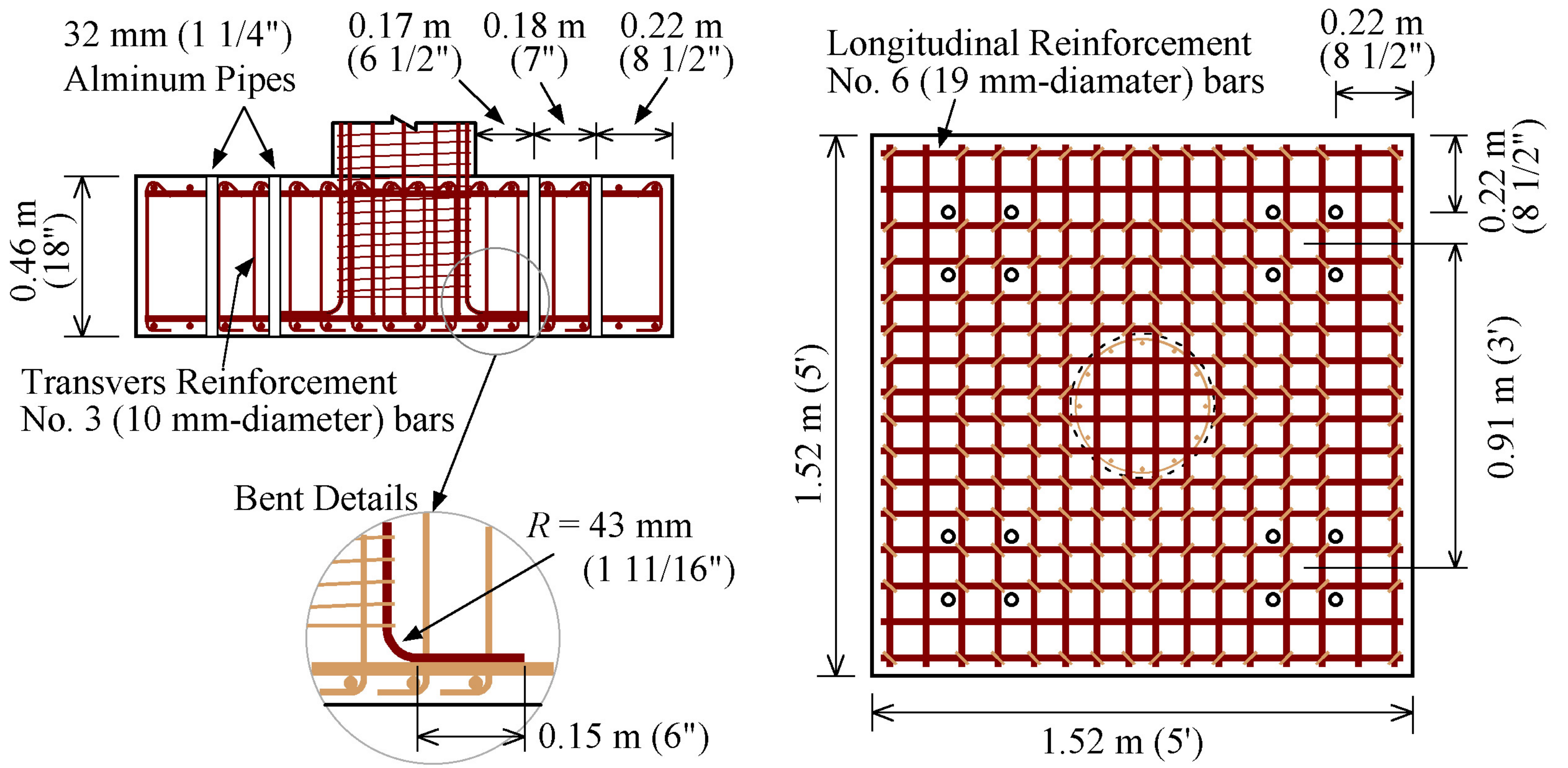

(a) Elevation and reinforcement details

(b) Plan view

Fig. 3.8 Reinforcement details of footing

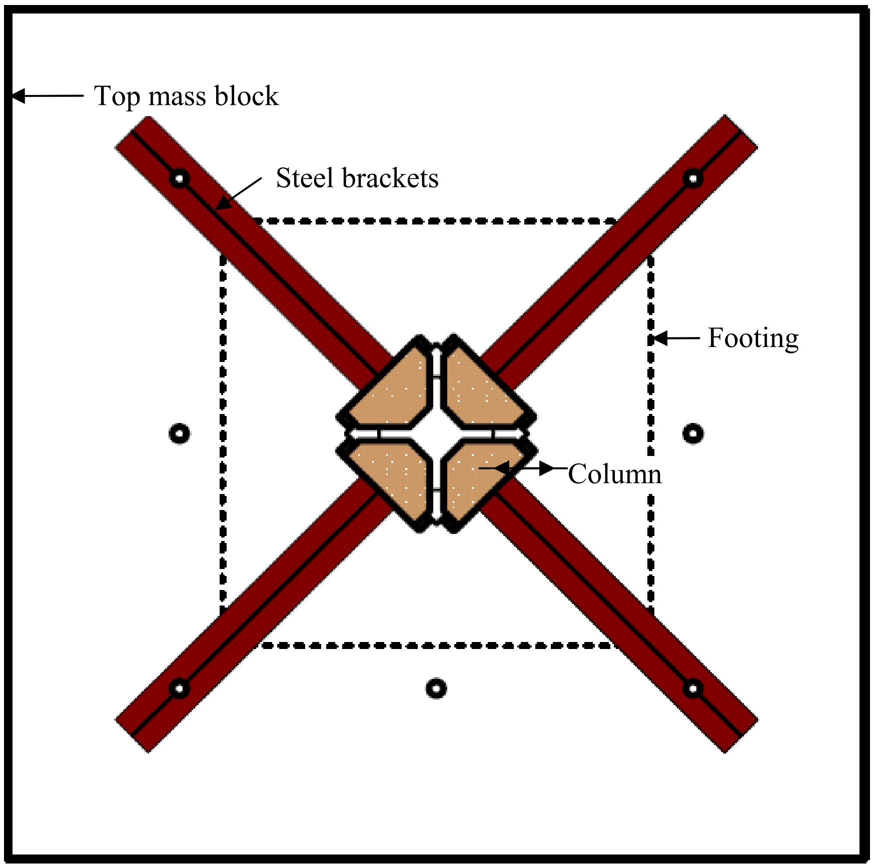

(a) Top view of steel bracket setting

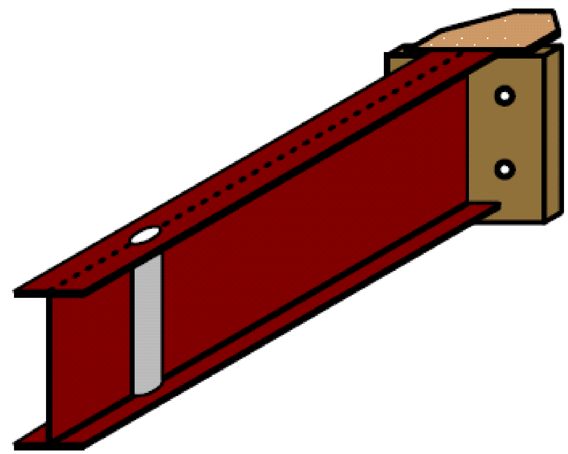

(b) Perspective view of one steel bracket

Fig. 3.9 Steel bracket.

Fig. 3.10 Construction of forms

Fig. 3.11 Assembly of steel cages

Fig. 3.12 Assembly of footing reinforcement

Fig. 3.13 Specimen and concrete truck

Fig. 3.14 Pouring concrete footing

Fig. 3.15 Finishing footing concrete

Fig. 3.16 Column formwork

Fig. 3.17 Casting concrete column

Fig. 3.18 After casting column concrete

Fig. 3.19 Completion of construction of specimen

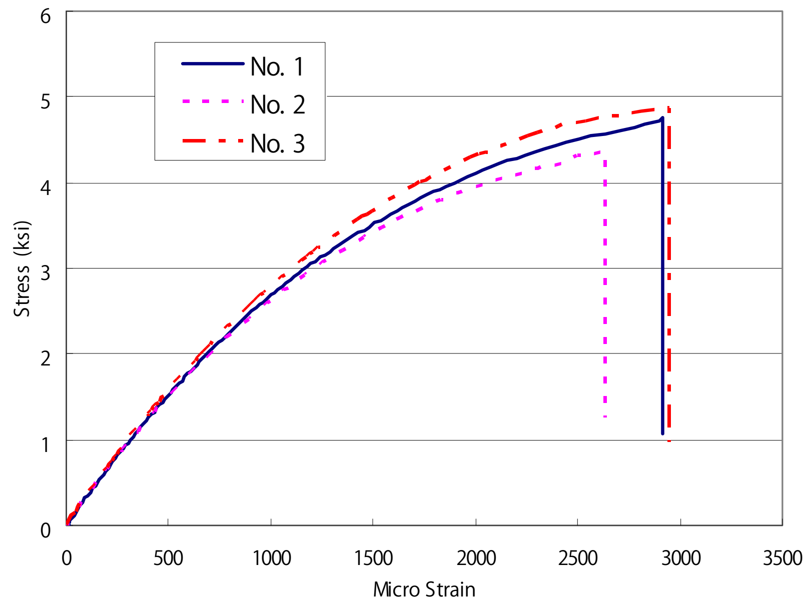

(a) Specimen PRC-U

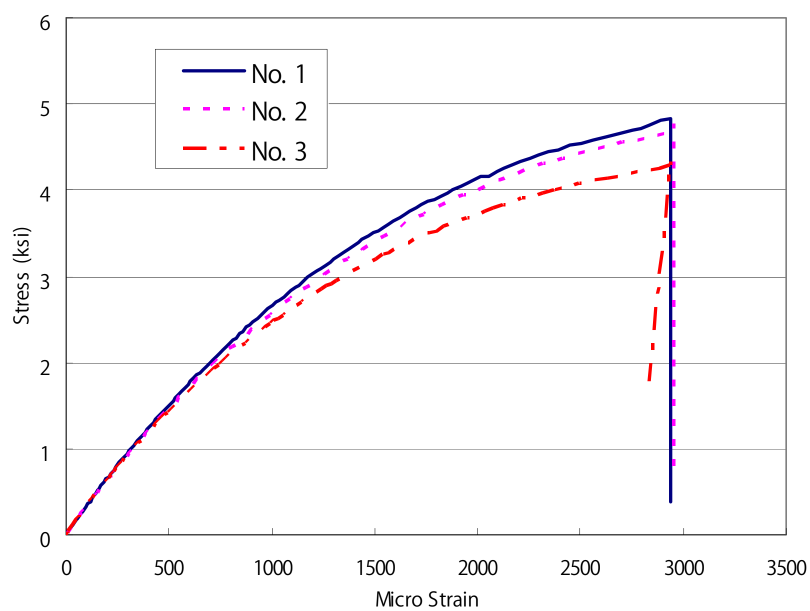

(b) Specimen PRC-UJ

Fig. 3.20 Stress-strain curves of concrete cylinders

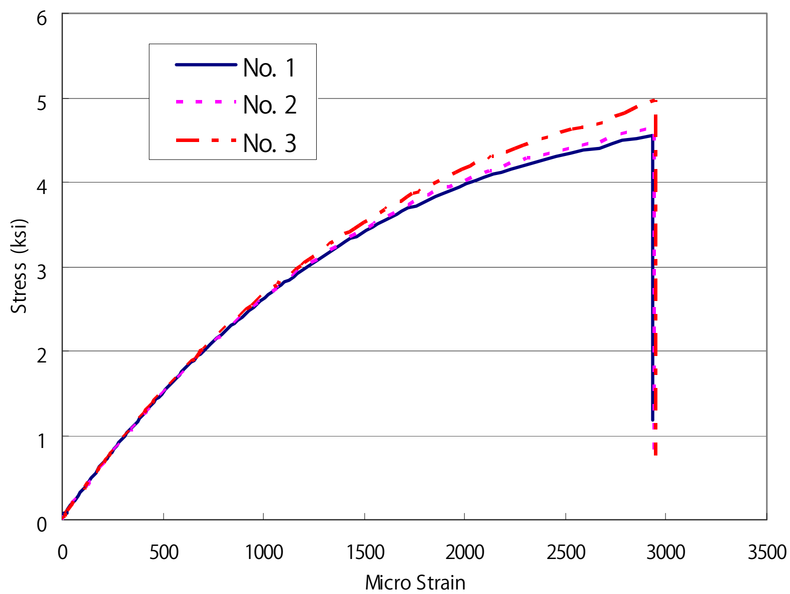

(c) Specimen PRC-2

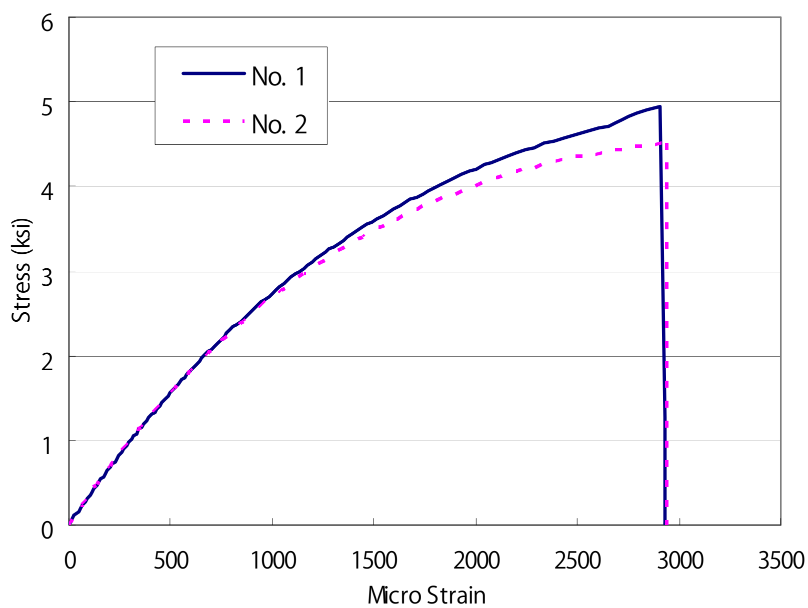

(d) Specimen PRC-U2

Fig. 3.20—*Continued*

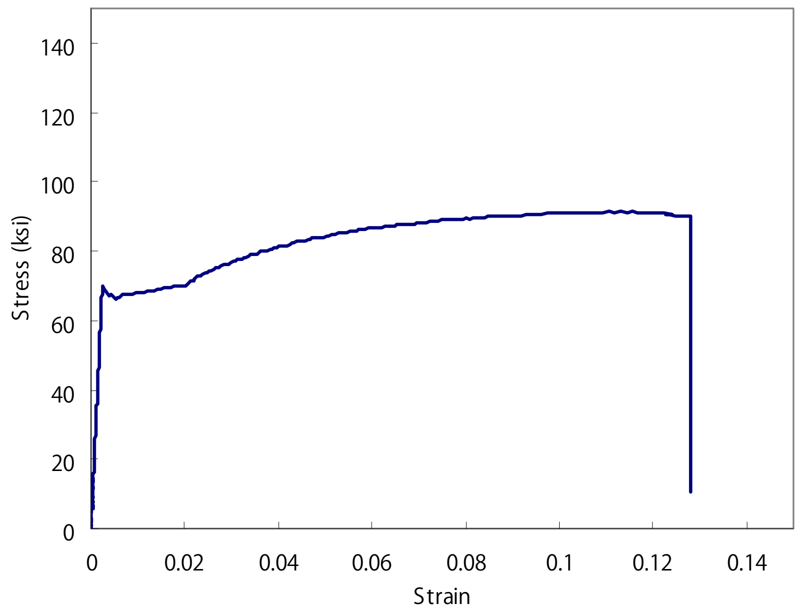

Fig. 3.21 Stress-strain curve of No 3 reinforcing bars

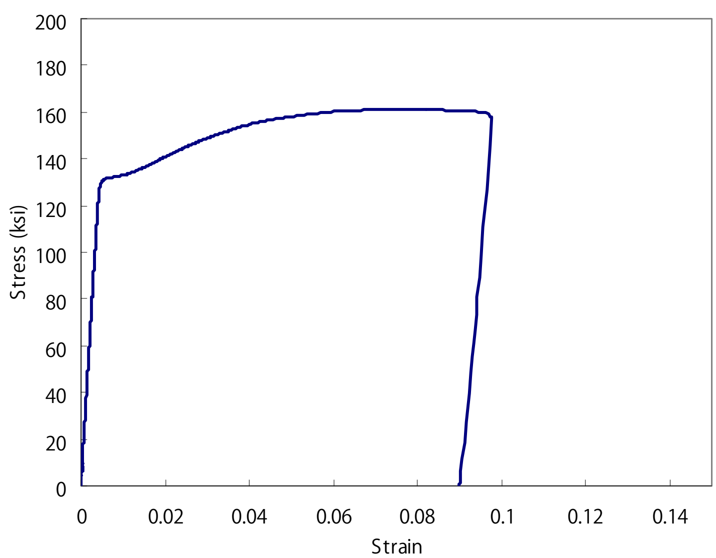

Fig. 3.22 Stress-strain curve of tendon

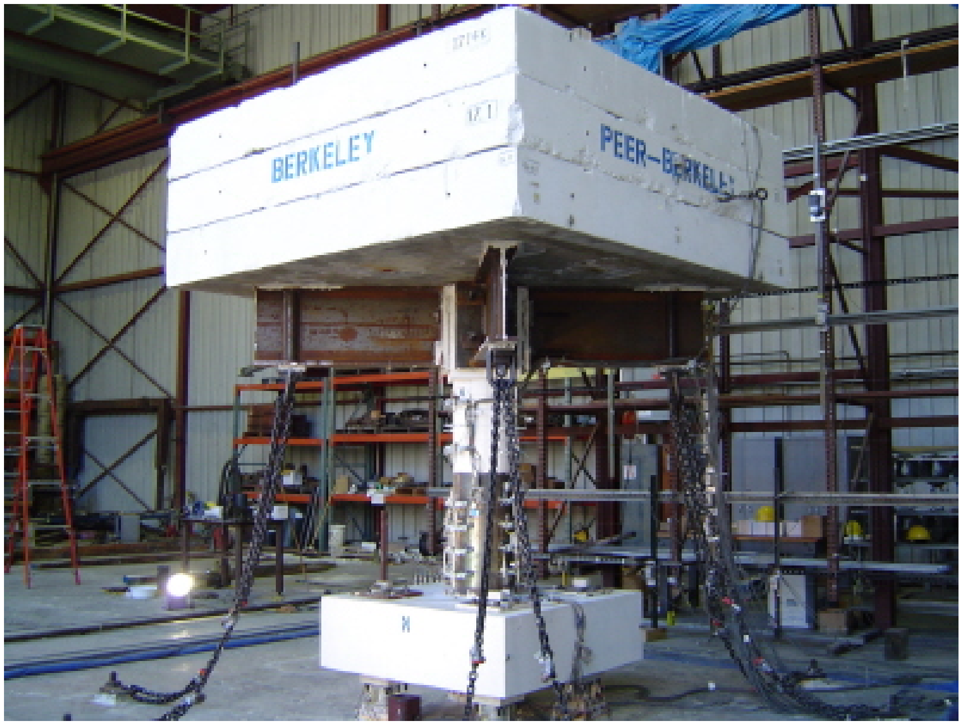

(a) Specimen on table

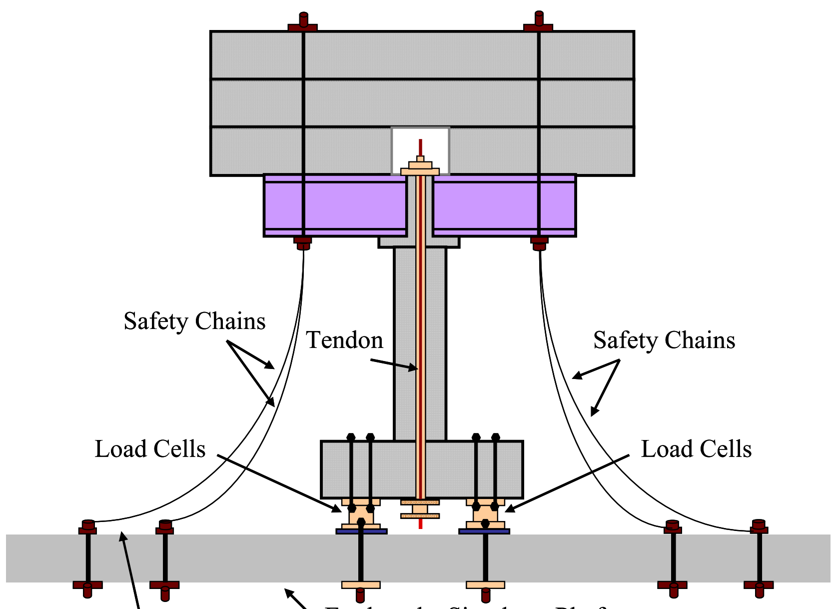

(b) Test setup

Fig. 3.23 Setup of specimen PRC-UJ

Fig. 3.24 Setup of steel bracket

Fig. 3.25 Setup of steel bracket

Fig. 3.26 Setup of load cell on table

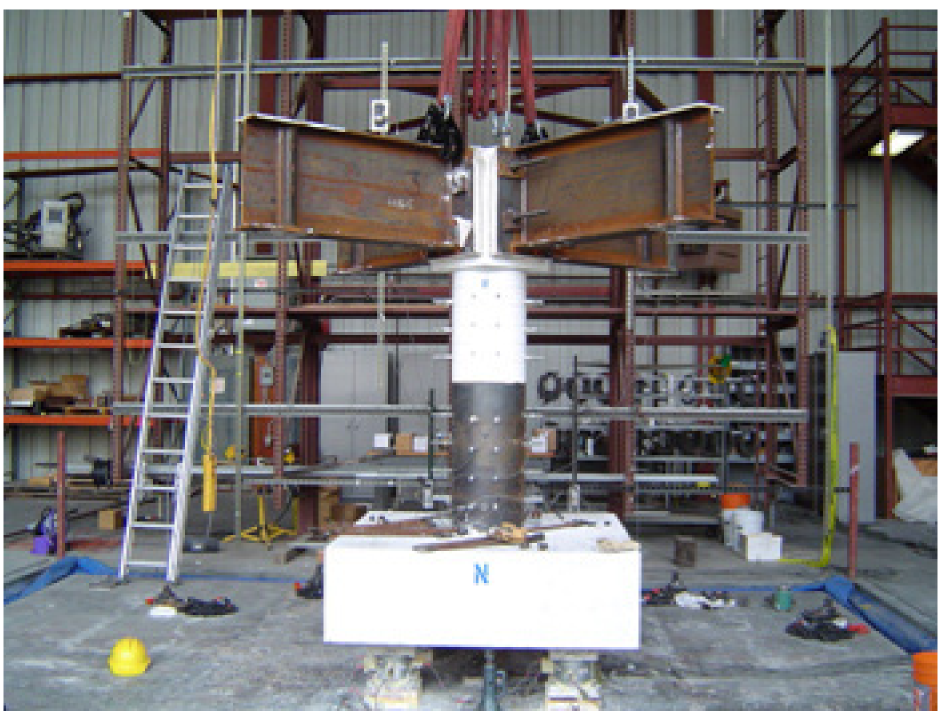

Fig. 3.27 Moving specimen onto load cell

Fig. 3.28 Installation of prestressing tendon

Fig. 3.29 Moving mass block onto steel bracket

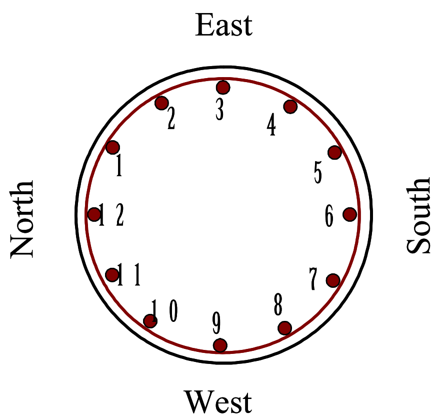

(a) Bar numbering

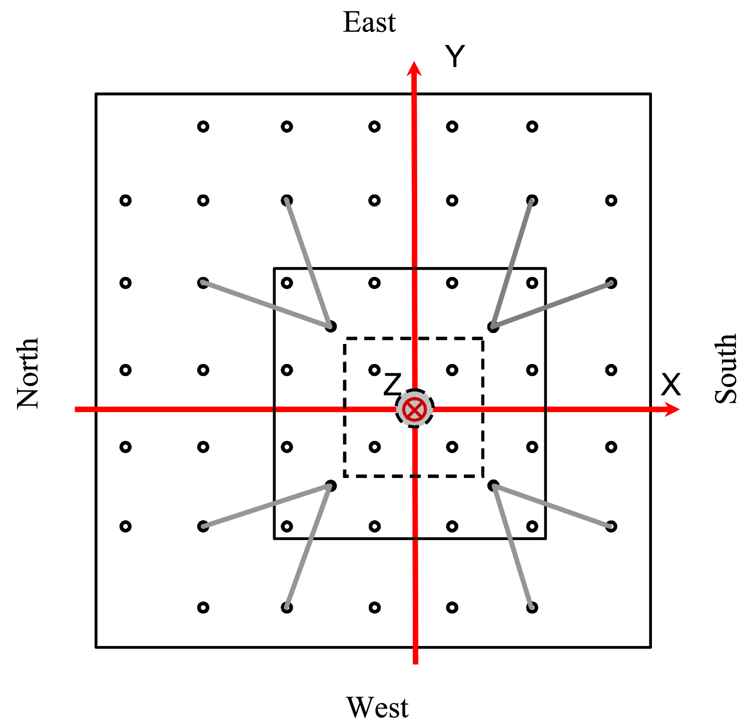

(b) *XY* plane .

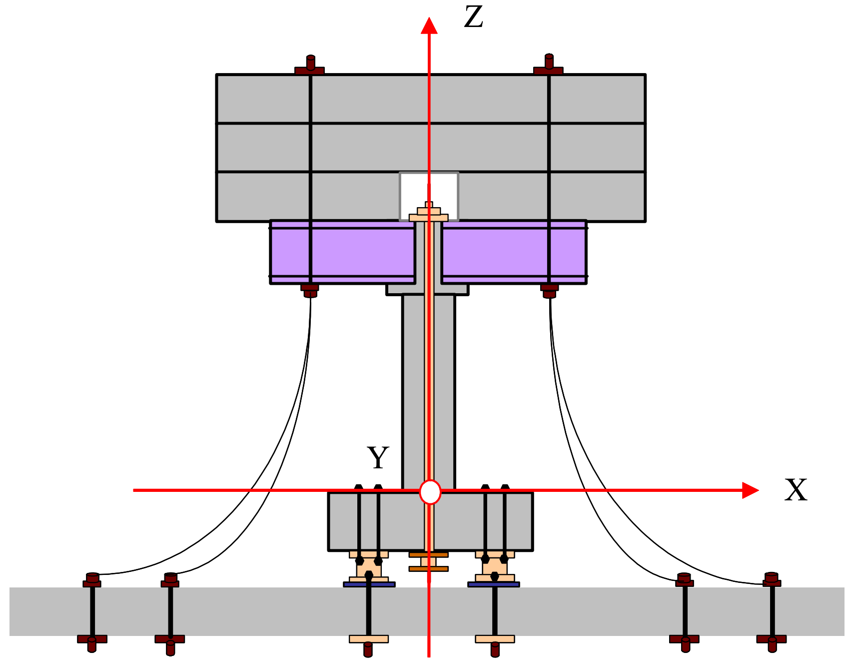

(c) *XZ* plane

Fig. 3.30 Coordinate system

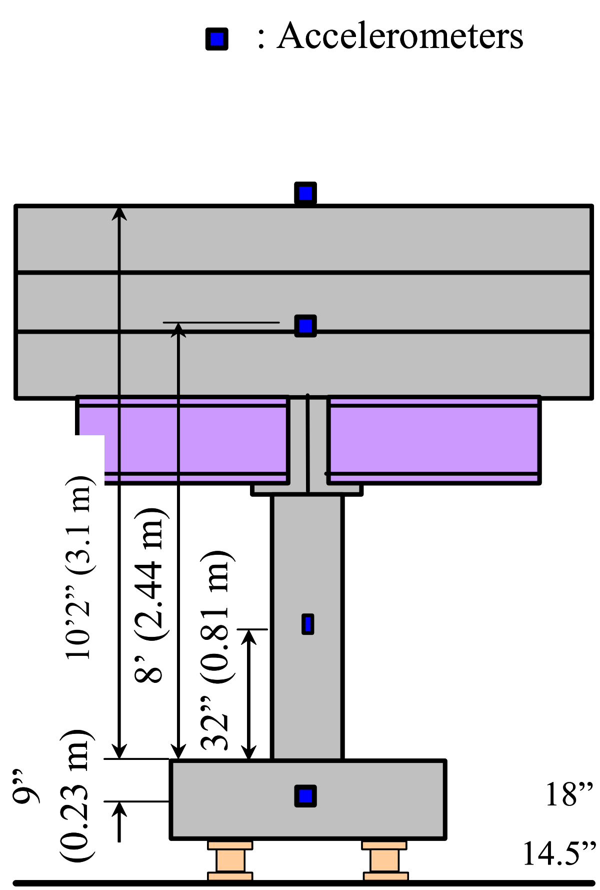

Fig. 3.31 Locations of accelerometers

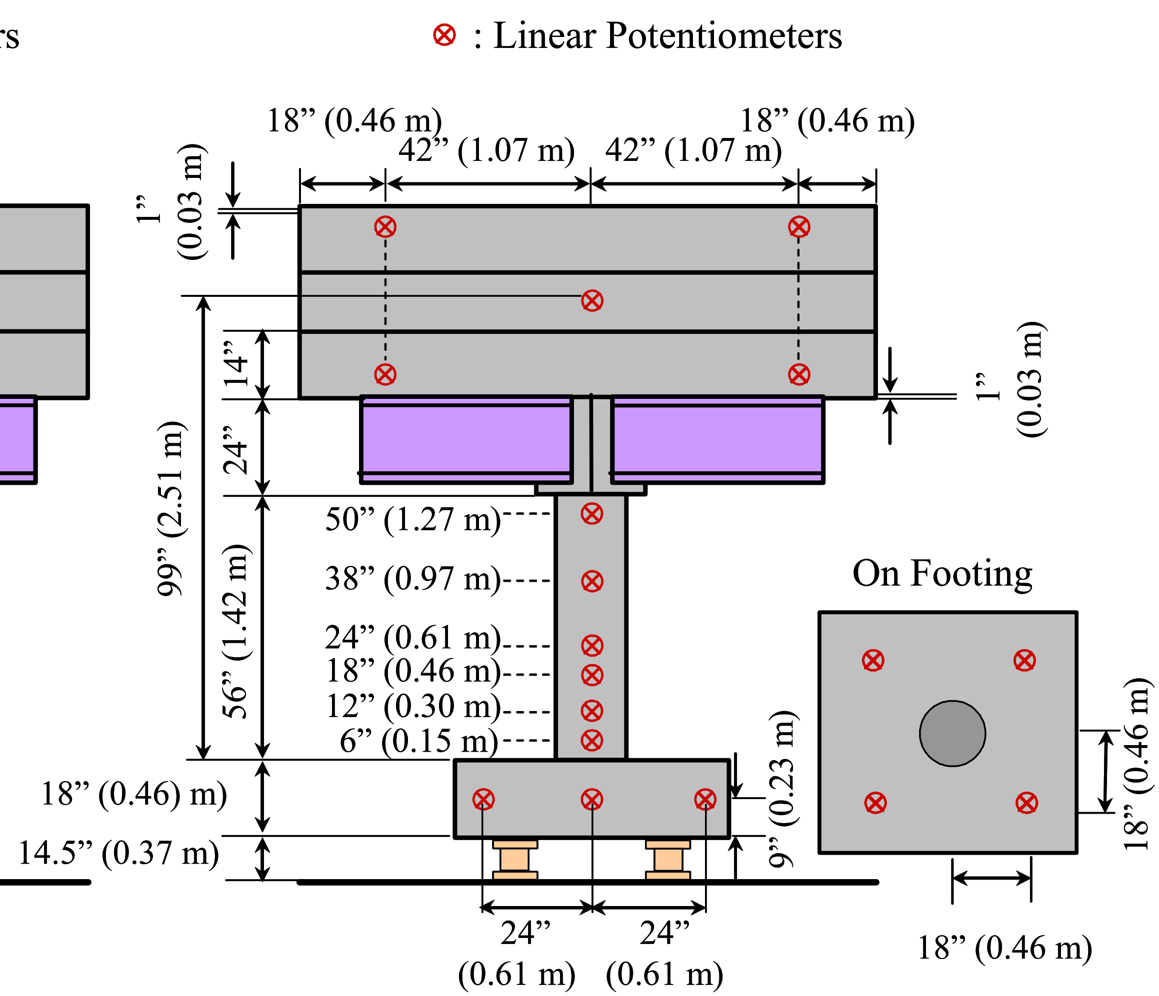

Fig. 3.32 Locations of linear potentiometers

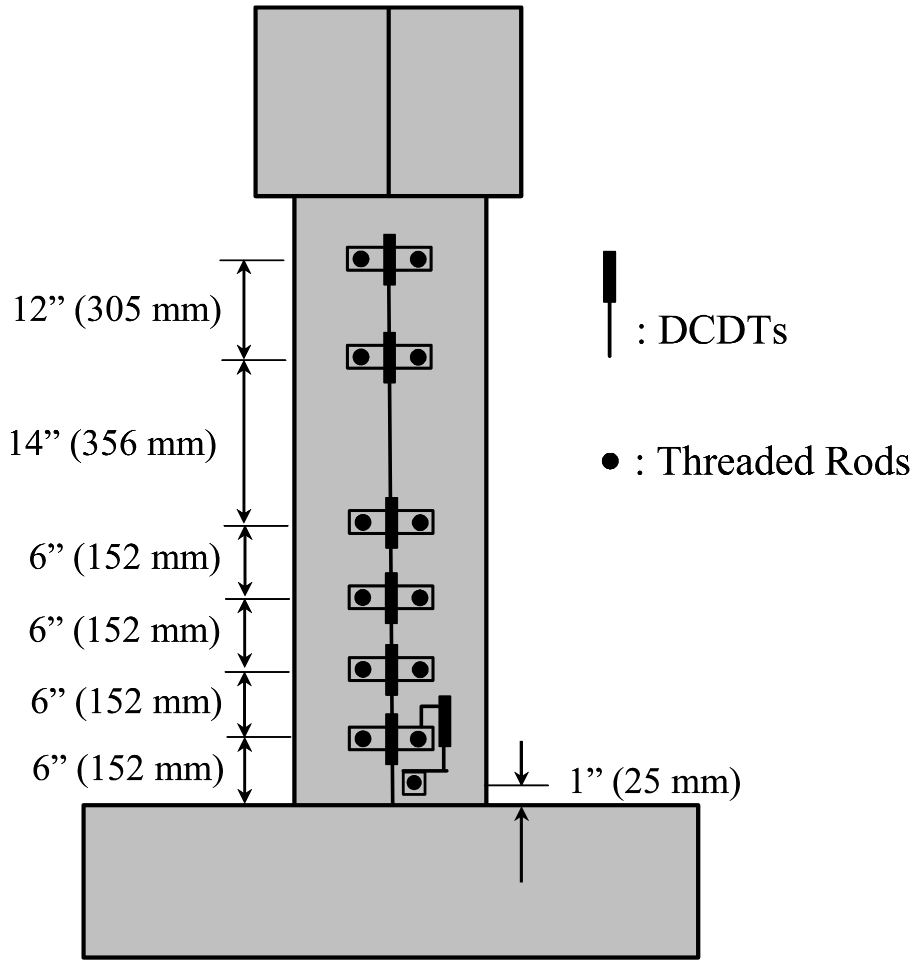

(a) Locations of DCDTs

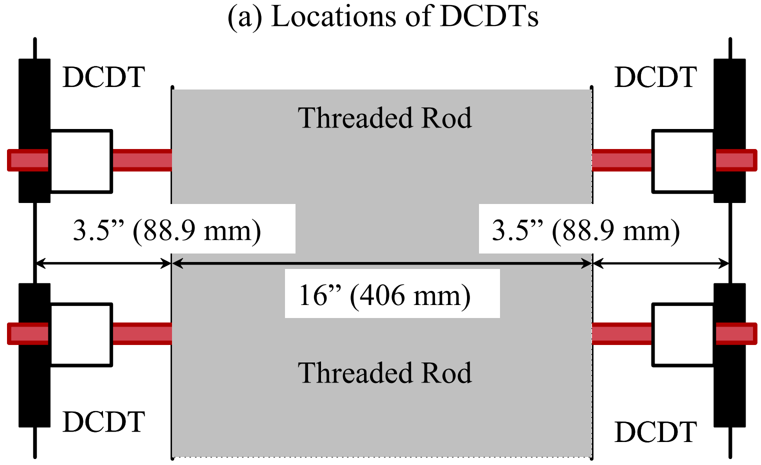

(b) Side view

Fig. 3.33 Setup of DCDTs

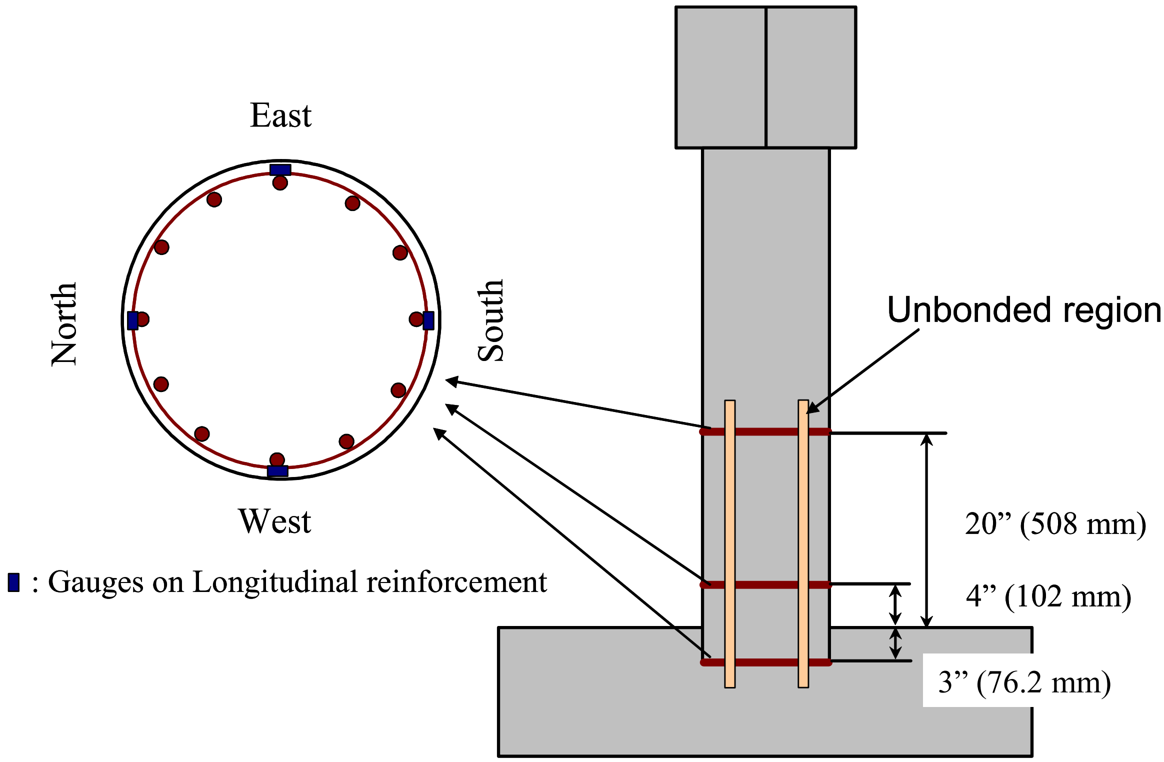

Fig. 3.34 Locations of strain gauges

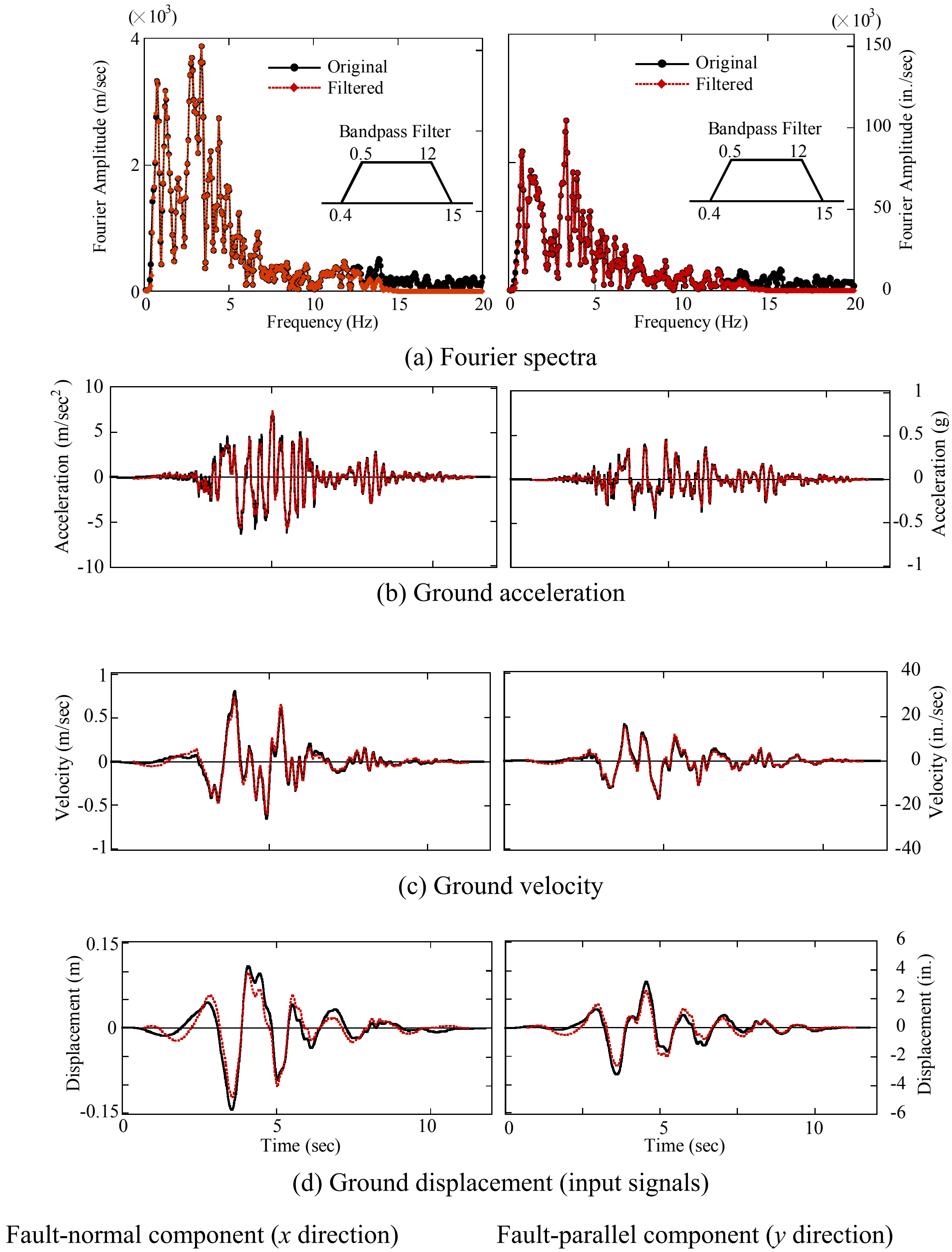

Fig. 3.35 Filtered ground motion

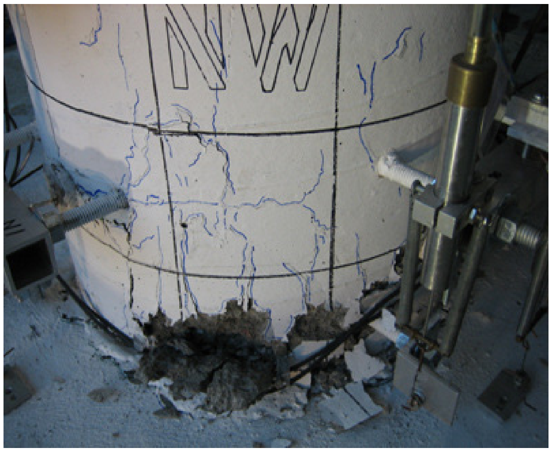

(a) PRC-U specimen

(b) PRC-UJ specimen

(c) PRC-2 specimen

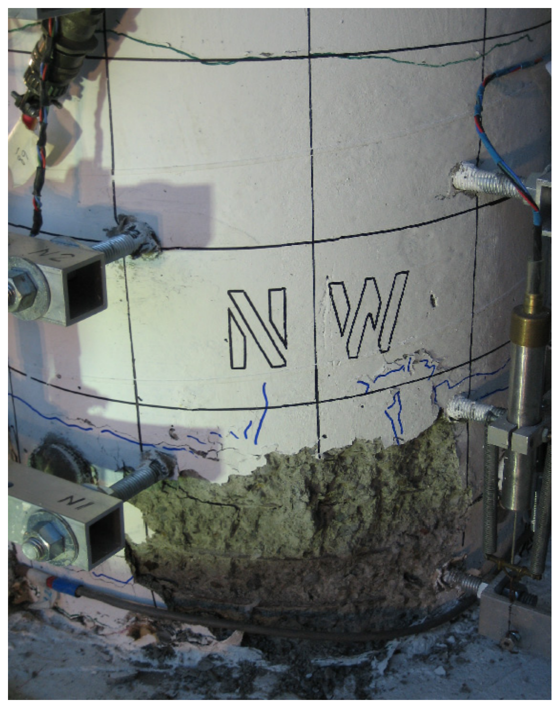

(d) PRC-U2 specimen

Fig. 3.36 Damage after design-level run (NW side)

(a) PRC-U specimen

(b) PRC-UJ specimen

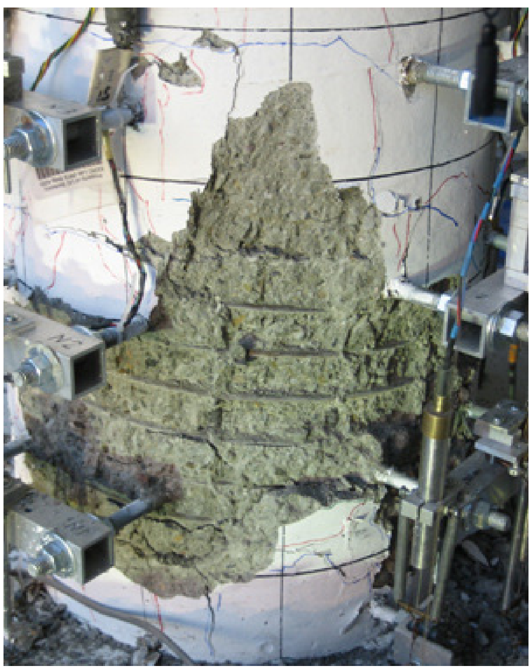

(c) PRC-2 specimen

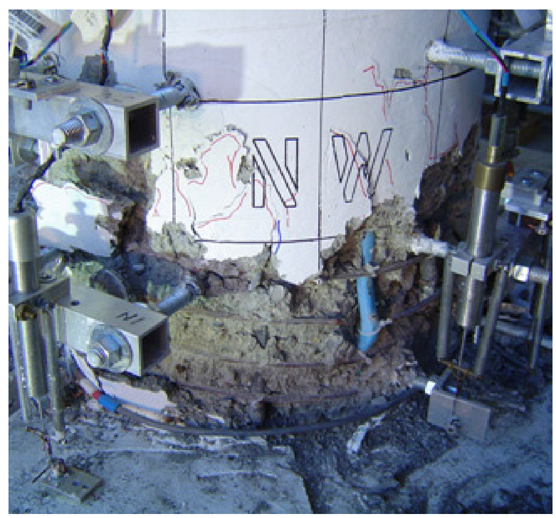

(d) PRC-U2 specimen

Fig. 3.37 Damage after maximum-level run (NW side)

(a) PRC-U specimen (after yield 2)

(b) PRC-UJ specimen (after max 2)

(c) PRC-2 specimen (after design 2)

(d) PRC-U2 specimen (after design 2)

Fig. 3.38 Damage after all tests (NW side)

Fig. 3.39 Steel jacket after removal from specimen

Fig. 3.40 Bar fracture of specimen PRC-UJ

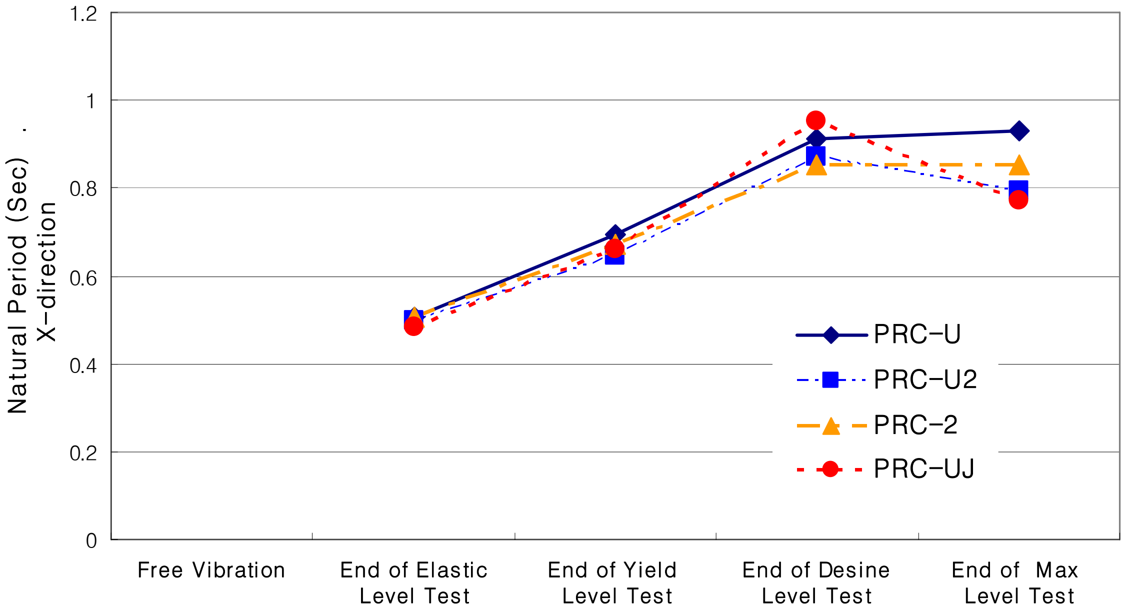

(a) *X* (N-S) direction

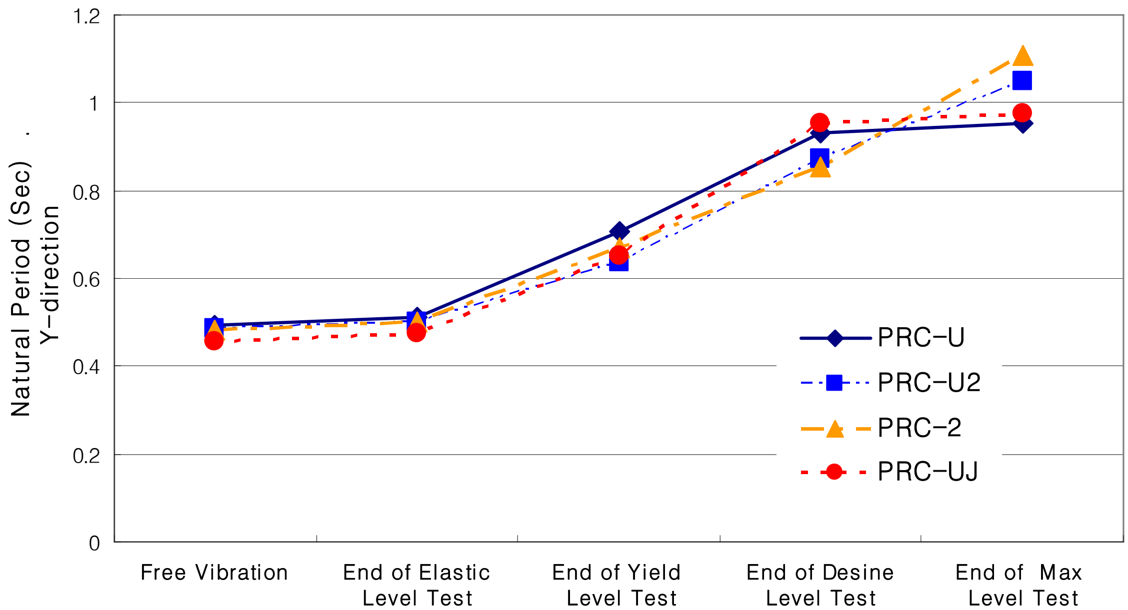

(b) *Y* (E-W) direction

Fig. 3.41 Change of natural period of specimens

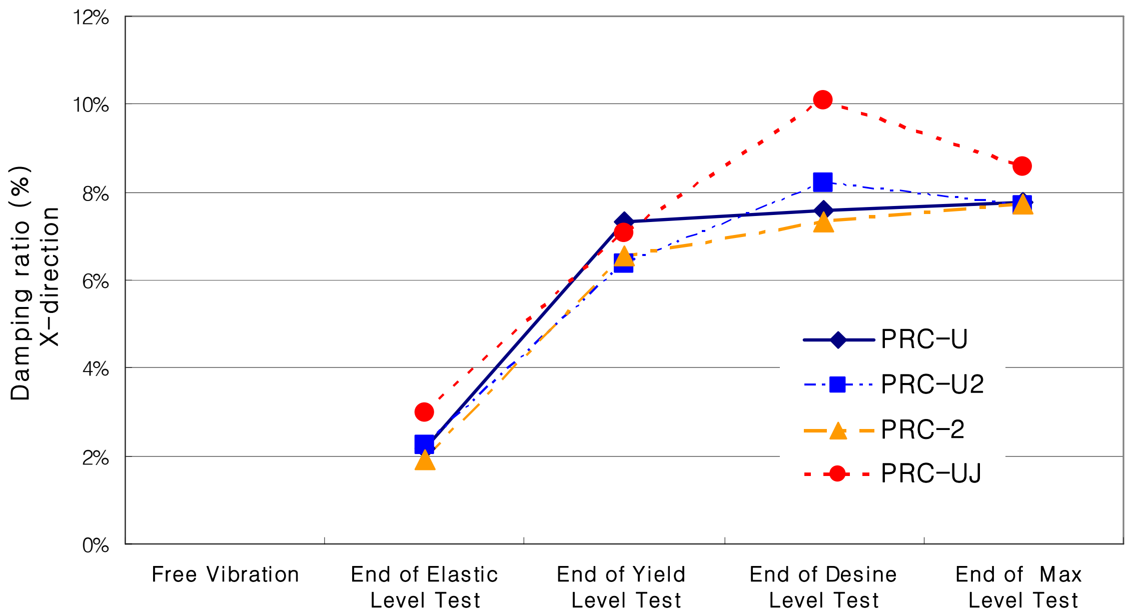

(a) *X* (N-S) direction

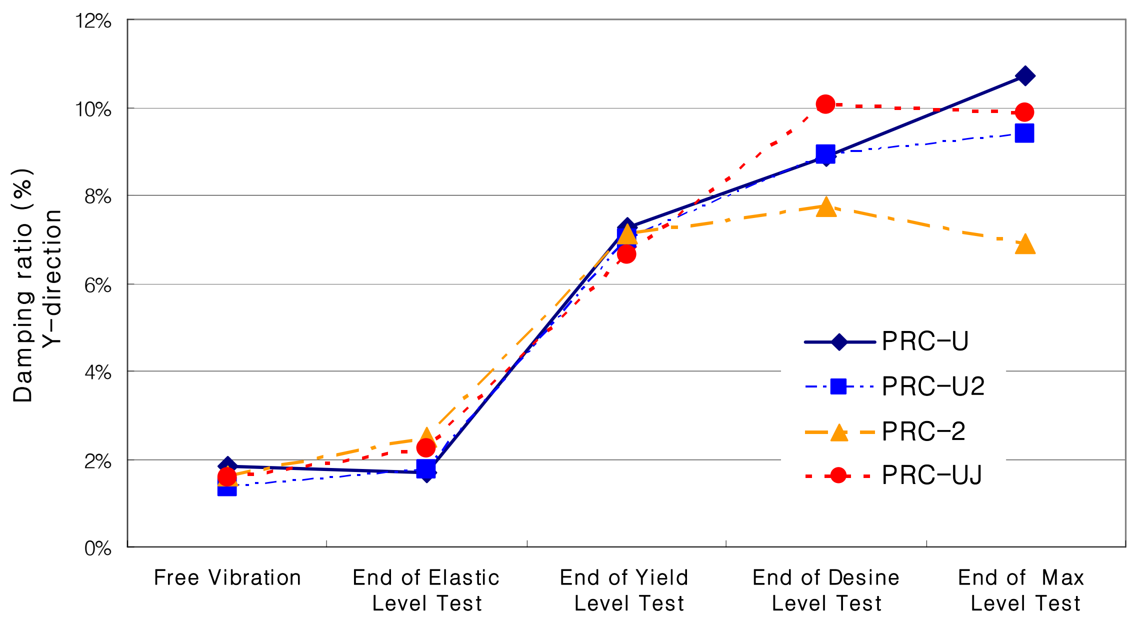

(b) *Y* (E-W) direction

Fig. 3.42 Change of damping ratio of specimens

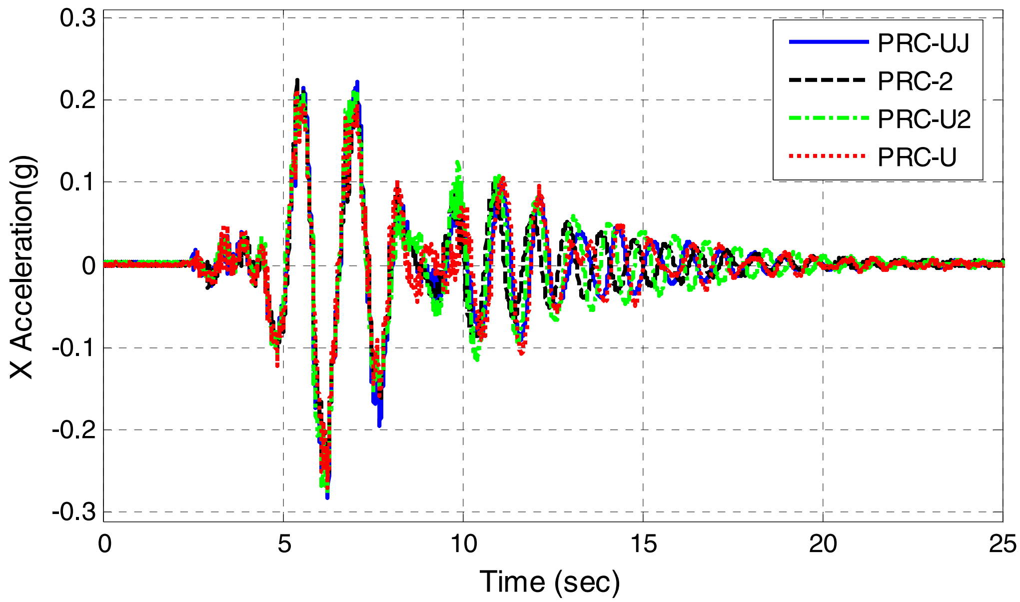

(a) X (N-S) direction

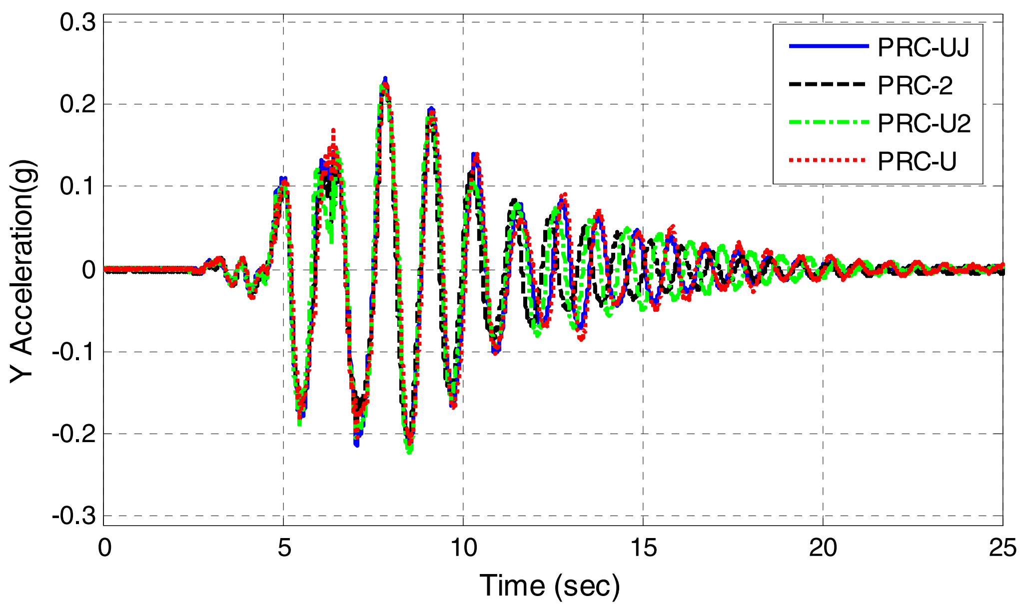

(b) Y (E-W) direction

Fig. 3.43 Acceleration responses at C.G. (design-level test)

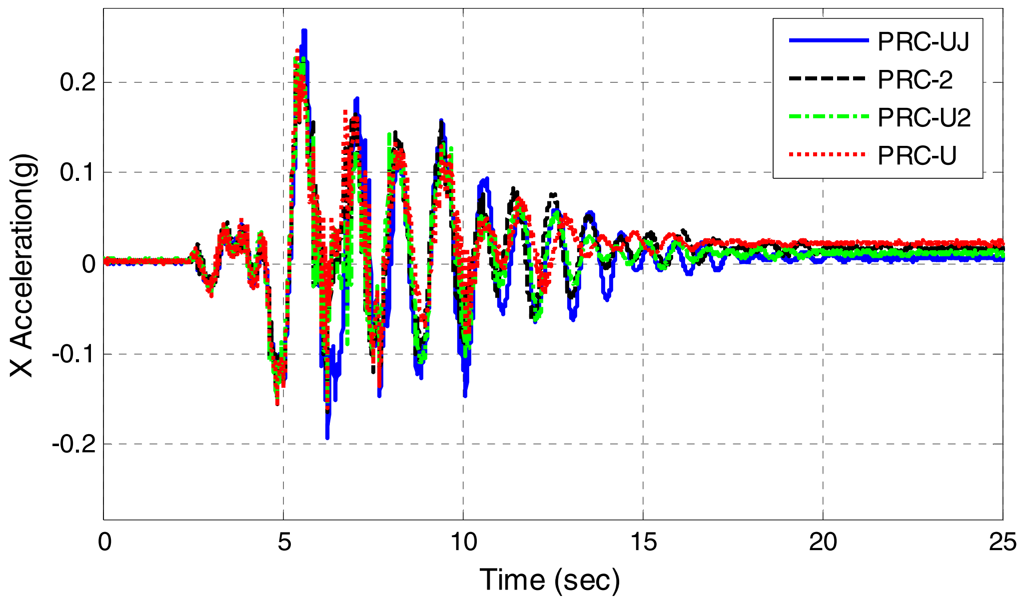

(a) *X* (N-S) direction

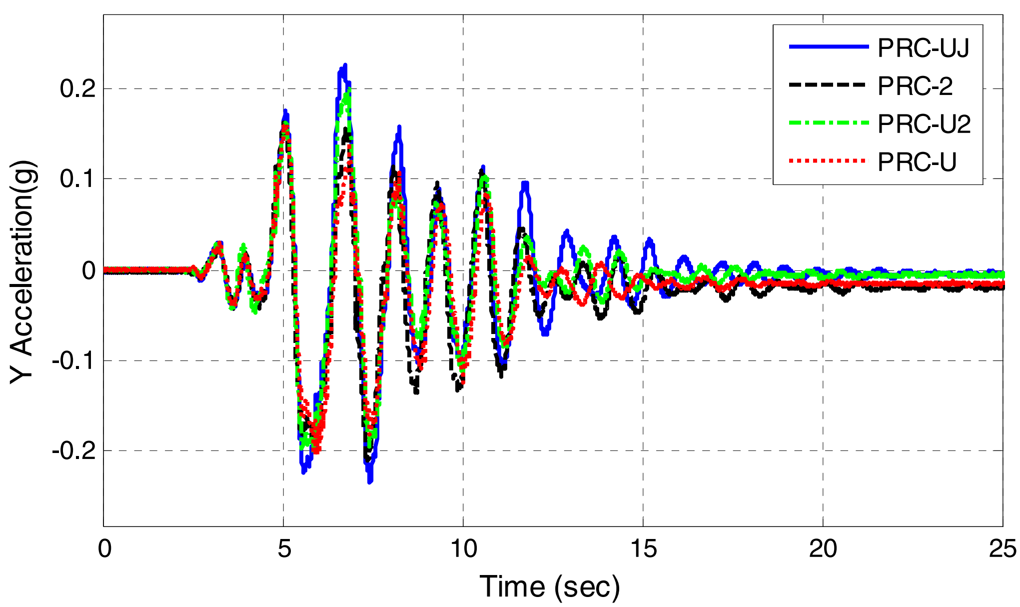

(b) *Y* (E-W) direction

Fig. 3.44 Acceleration responses at C.G. (maximum-level test)

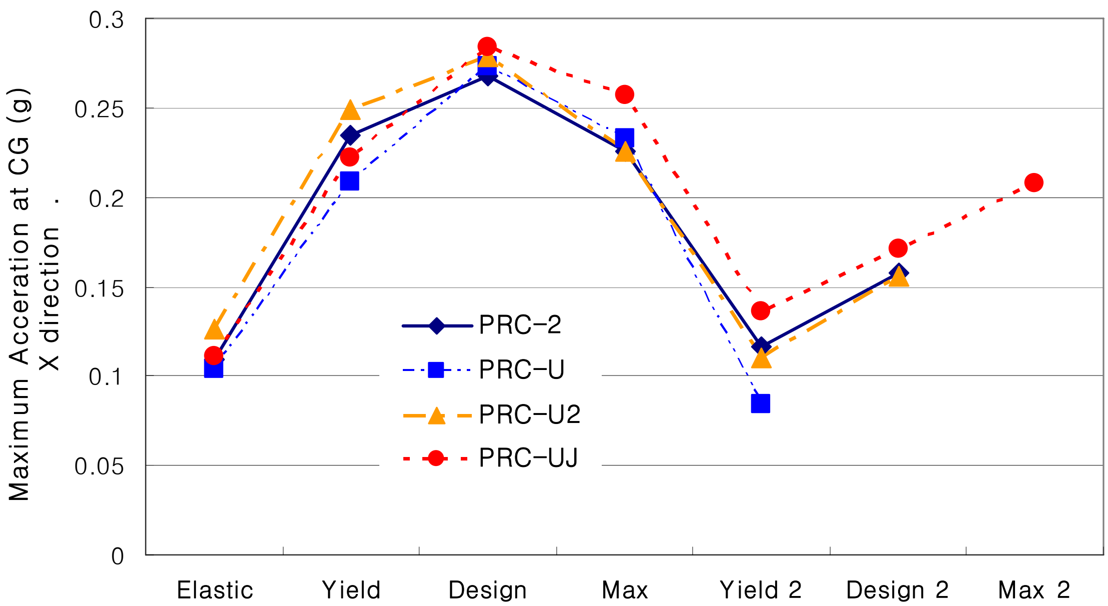

(a) *X* (N-S) direction

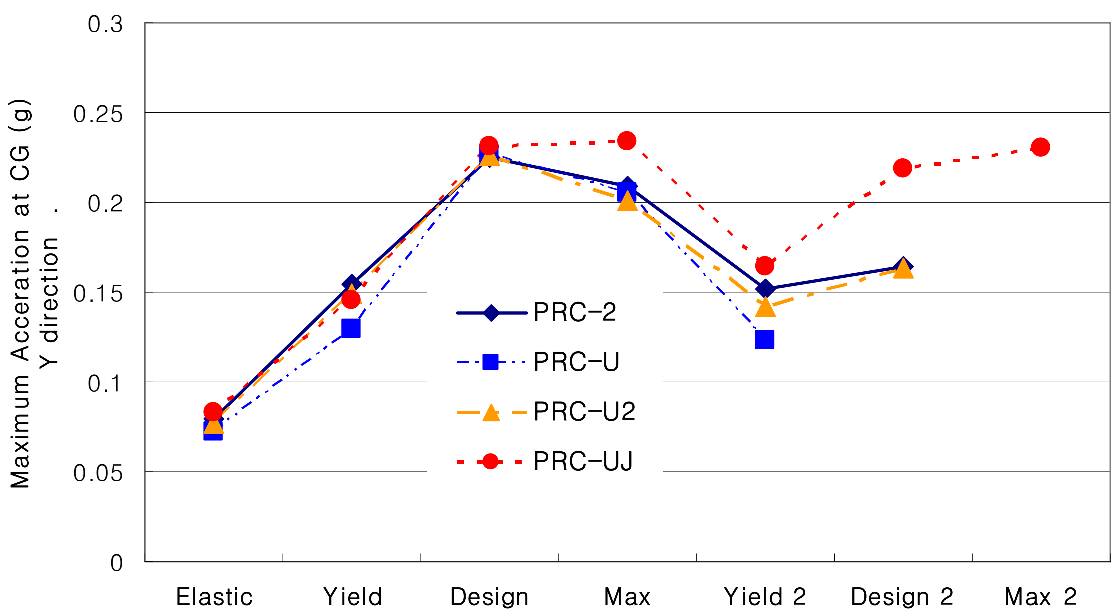

(b) *Y* (E-W) direction

Fig. 3.45 Maximum acceleration responses at C.G.

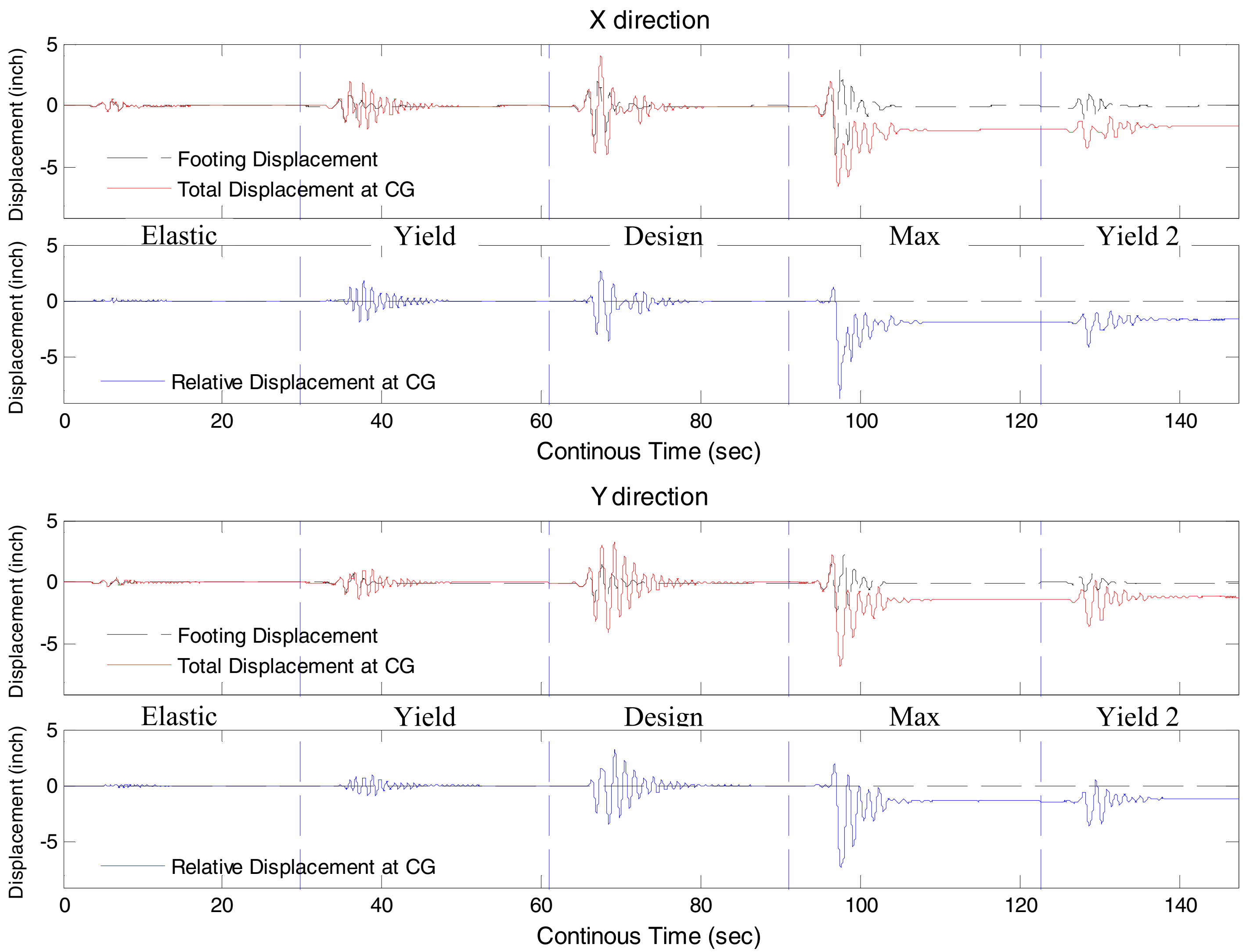

Fig. 3.46 Displacement response for all tests (specimen PRC-U)

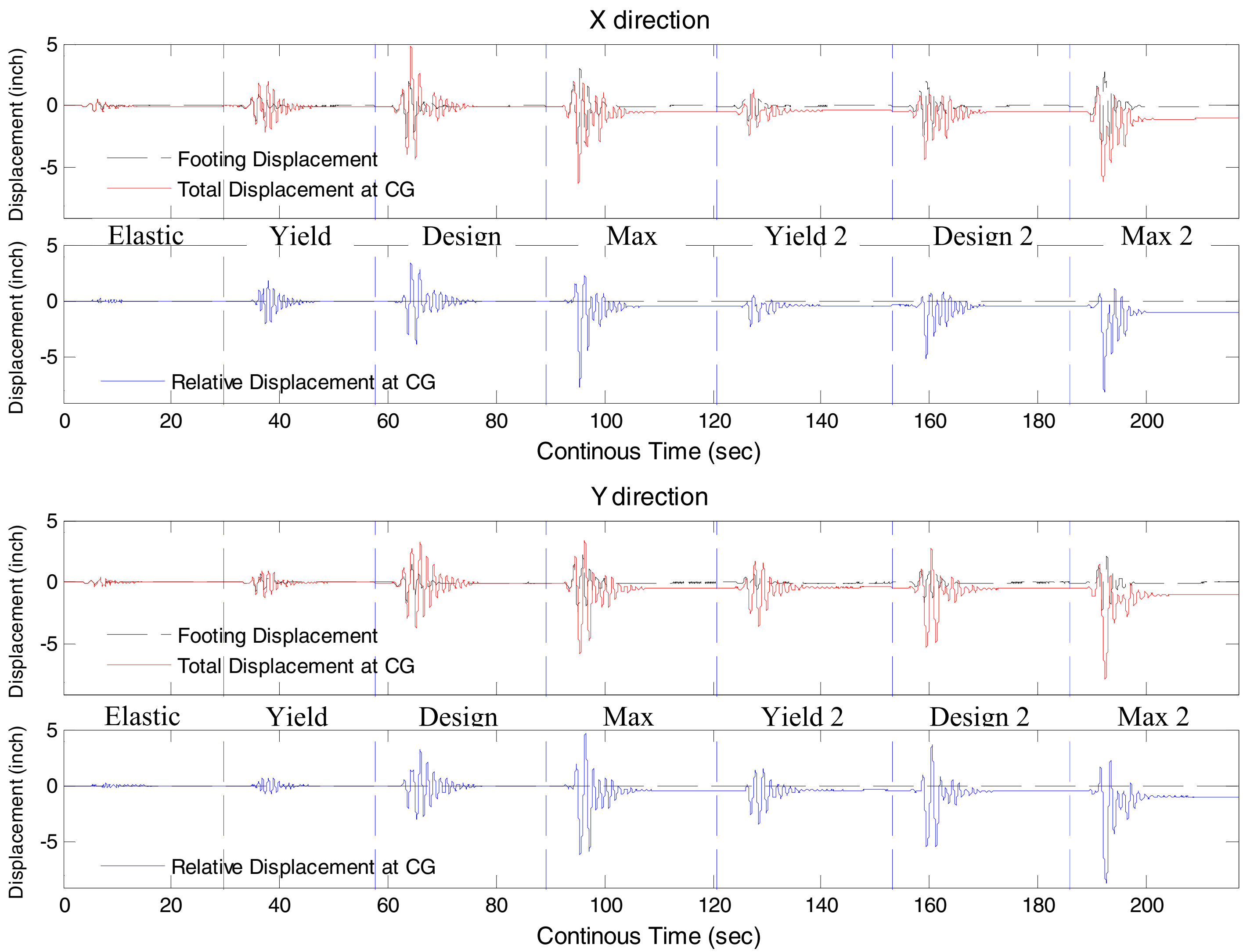

Fig. 3.47 Displacement response for all tests (specimen PRC-UJ)

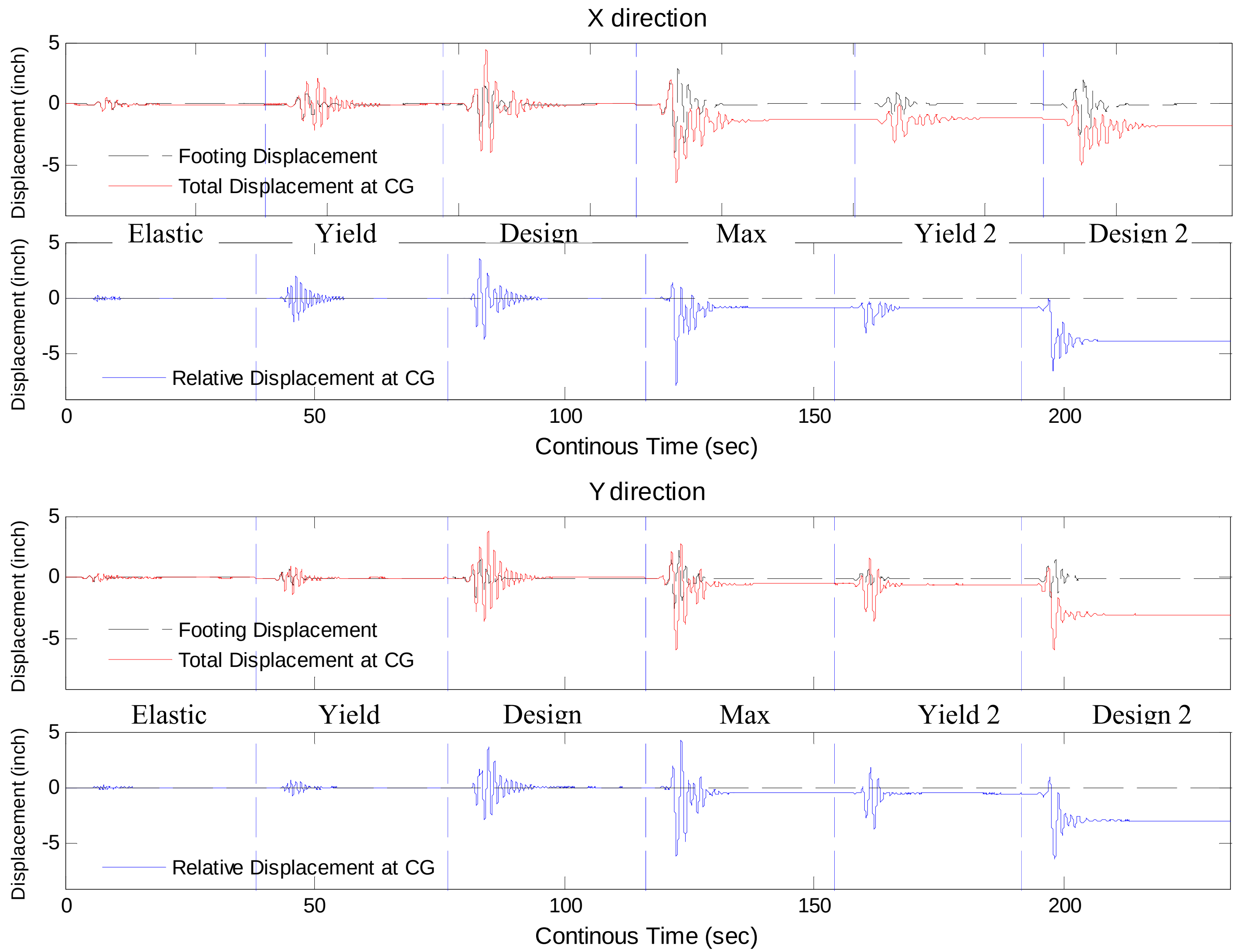

Fig. 3.48 Displacement response for all tests (Specimen PRC-2)

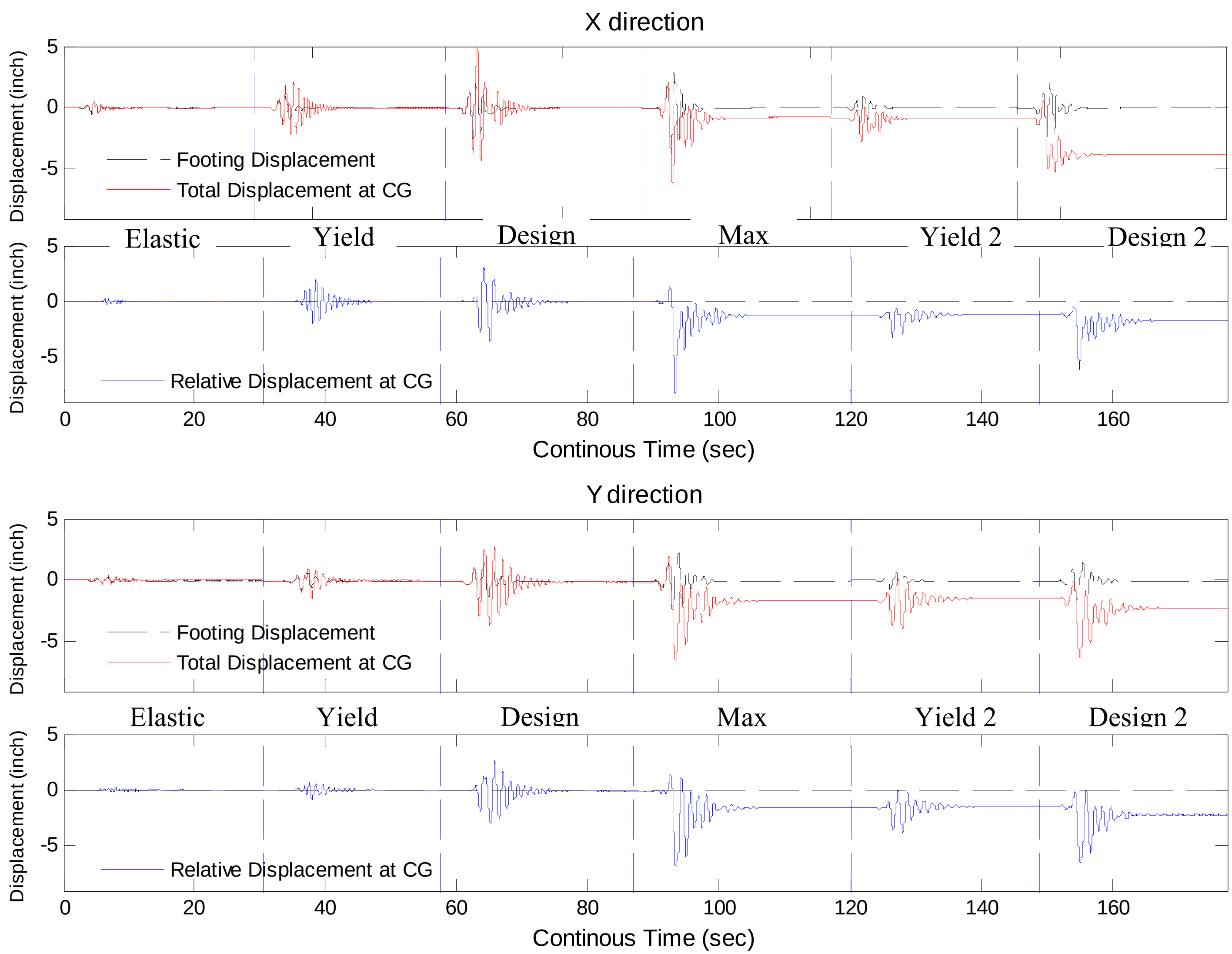

Fig. 3.49 Displacement response for all tests (Specimen PRC-U2)

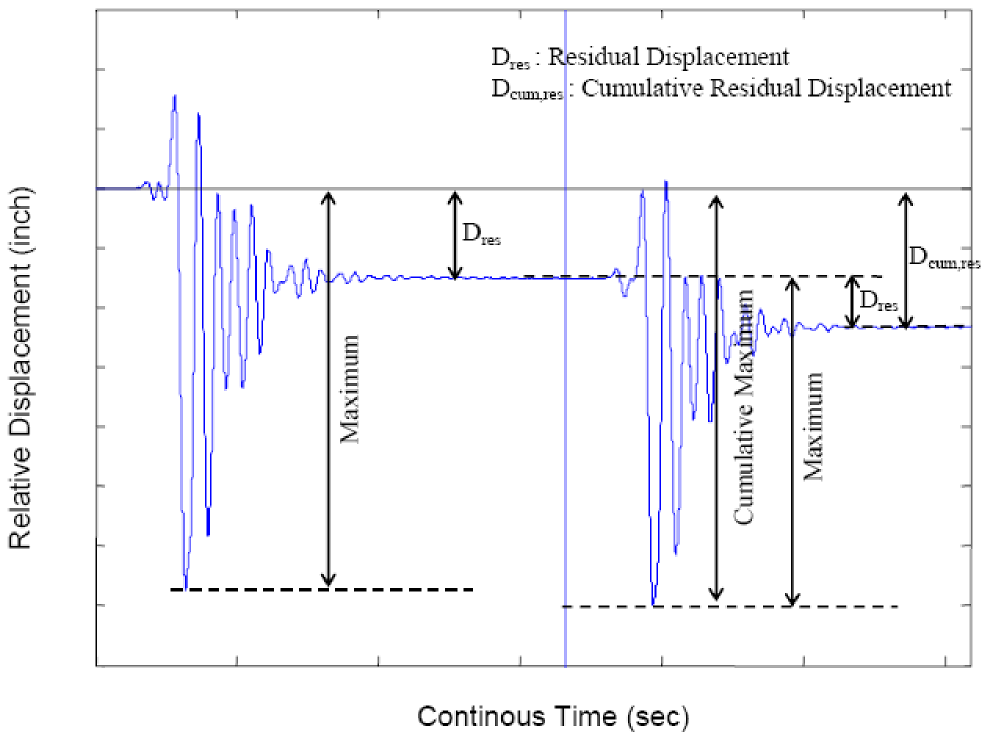

Fig. 3.50 Illustration of terminology used for maximum and residual displacement

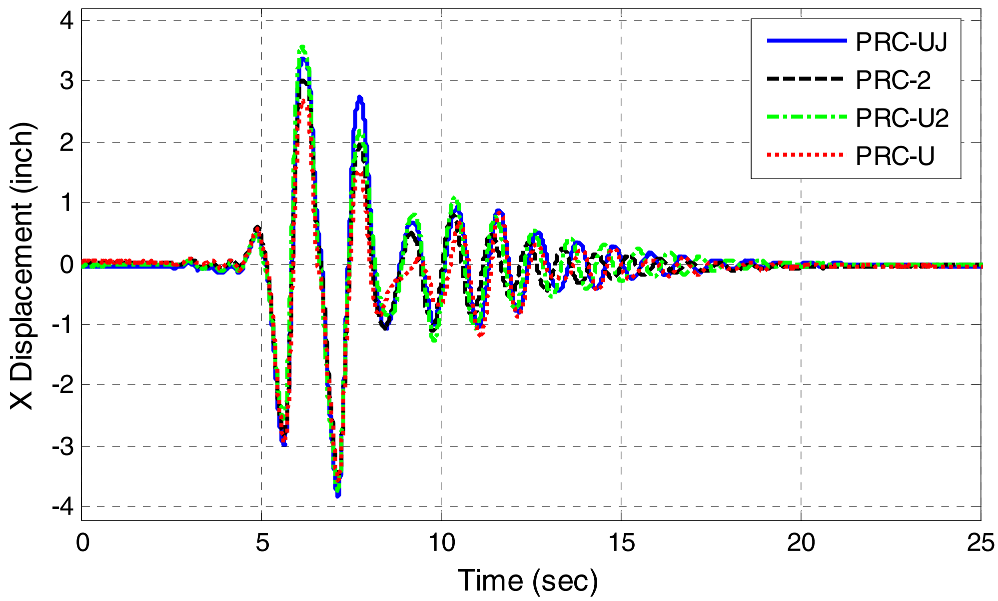

(a) *X* (N-S) direction

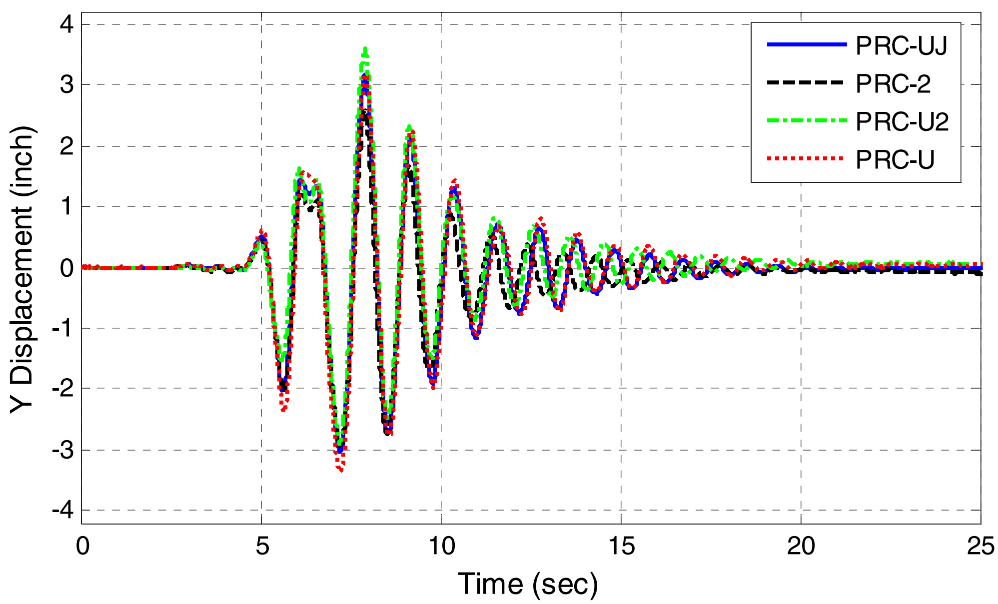

(b) *Y* (E-W) direction

Fig. 3.51 Cumulative displacement responses at C.G. (design-level test)

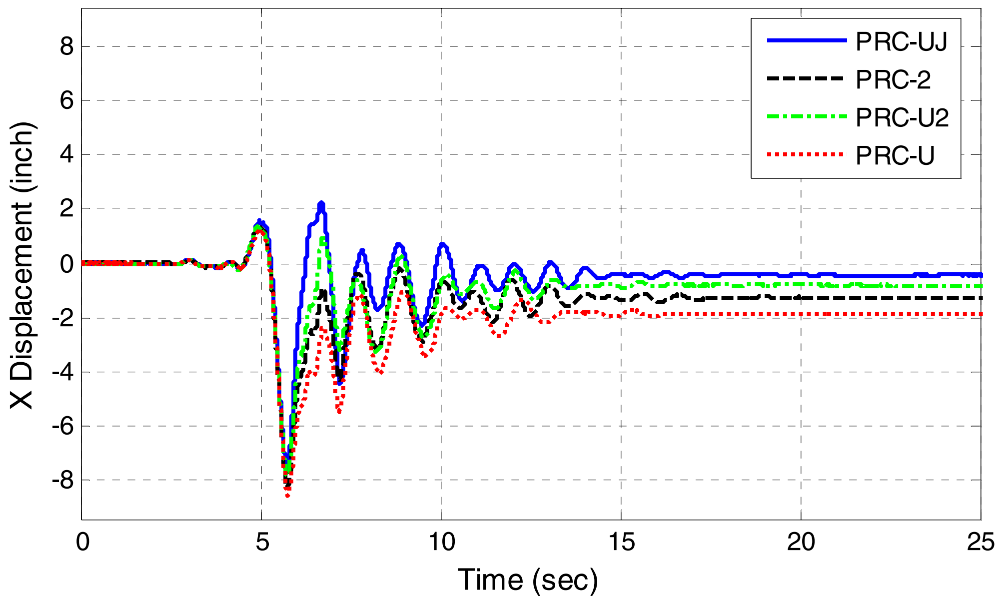

(a) X (N-S) direction

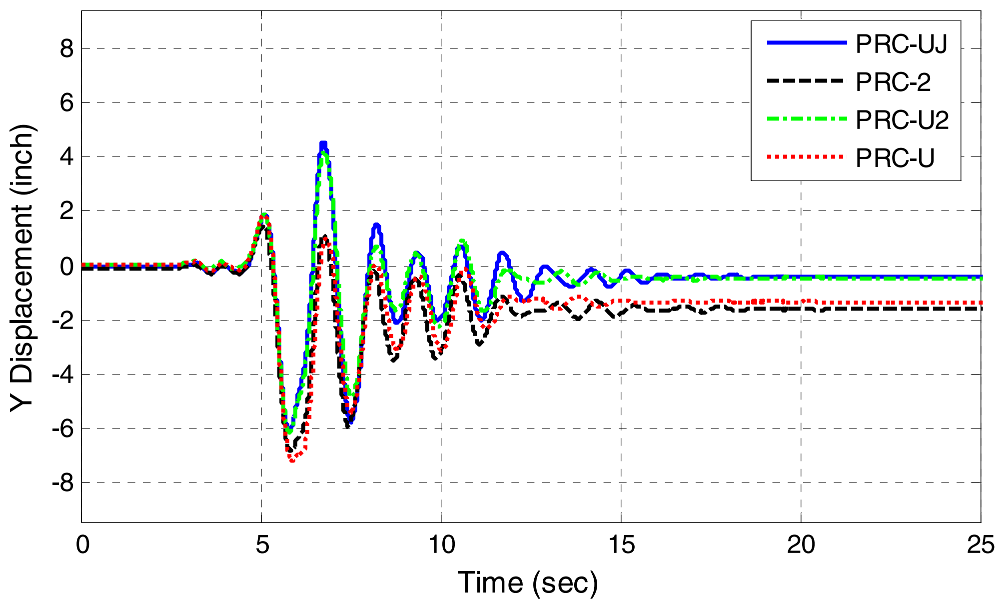

(b) Y (E-W) direction

Fig. 3.52 Cumulative displacement responses at C.G. (maximum-level test)

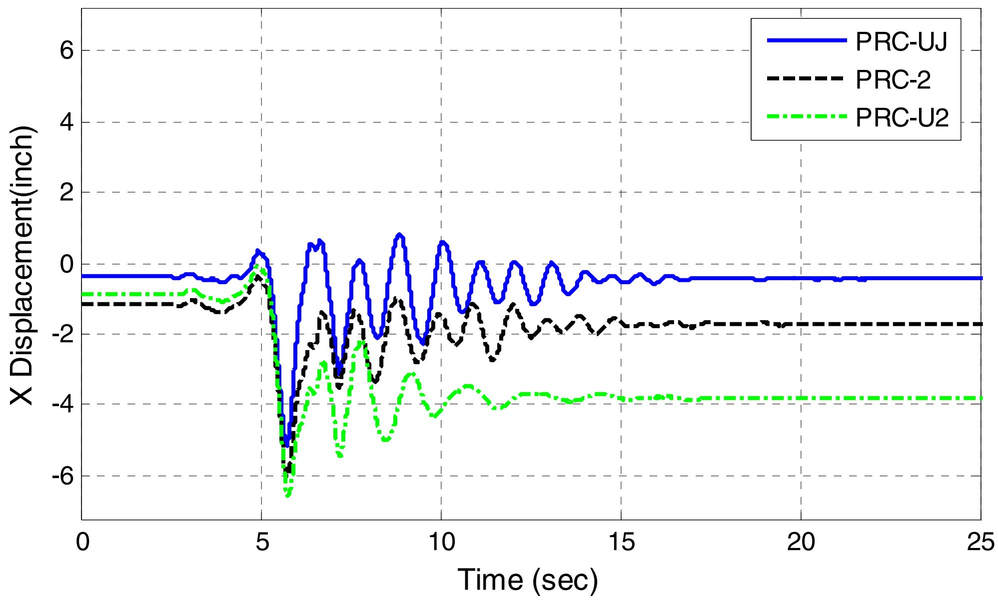

(a) *X* (N-S) direction

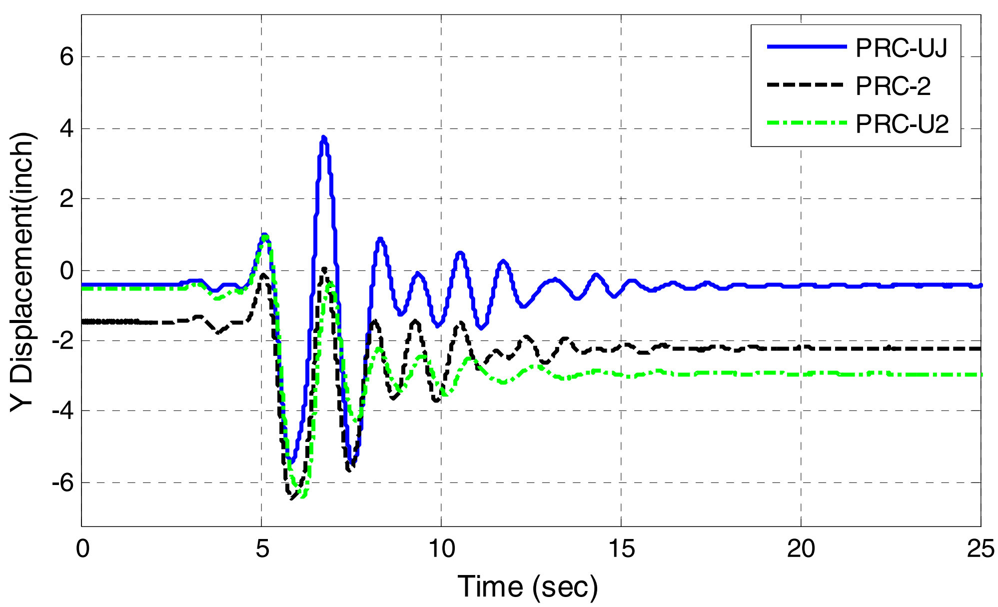

(b) *Y* (E-W) direction

Fig. 3.53 Cumulative displacement responses at C.G. (second design-level test)

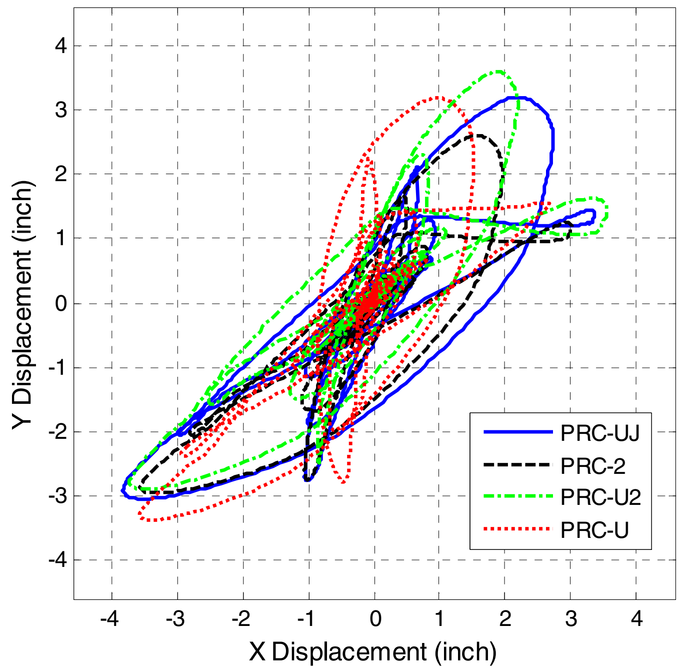

(a) Design-level run

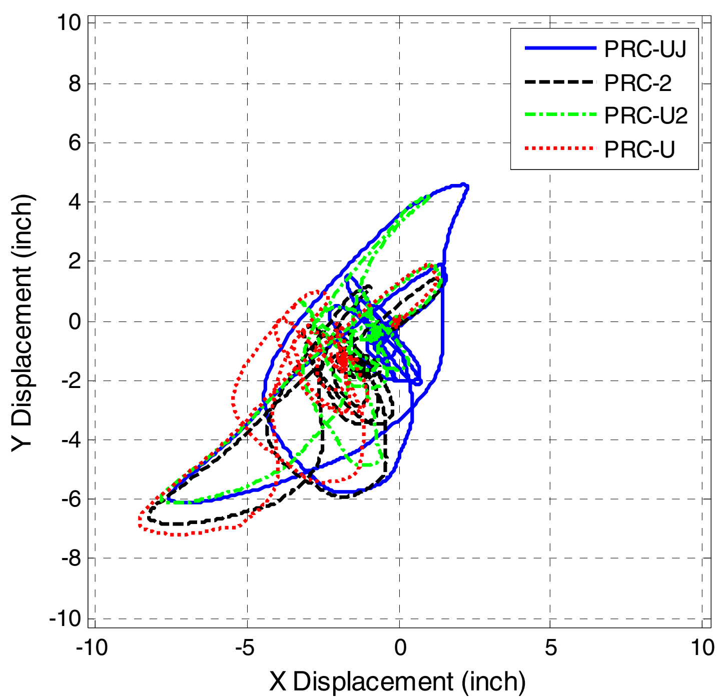

(b) Maximum-level run

Fig. 3.54 Orbits

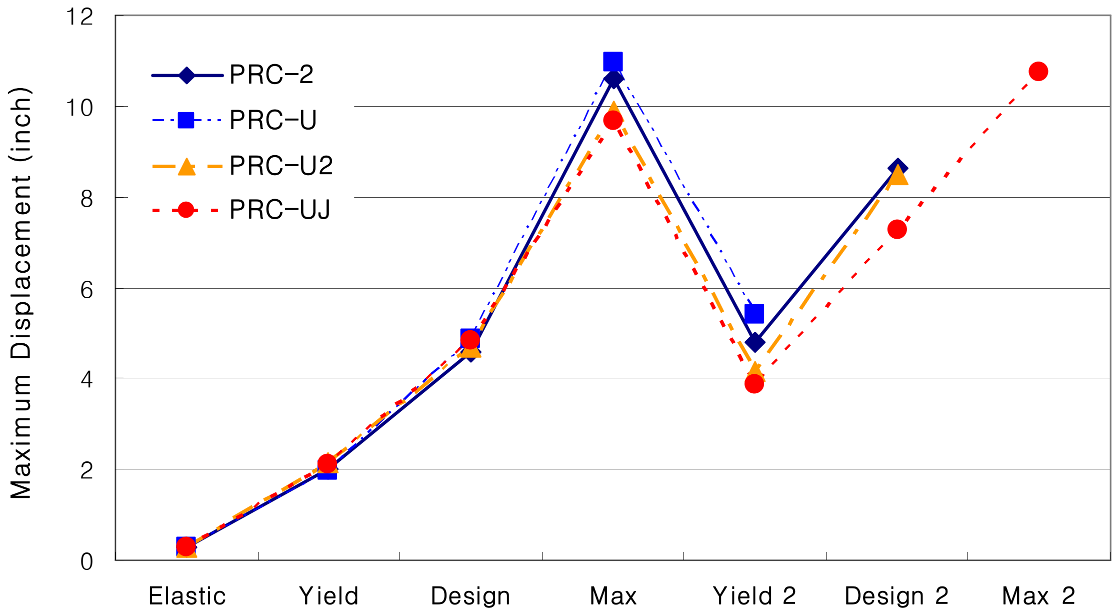

Fig. 3.55 Cumulative maximum displacement at C.G.

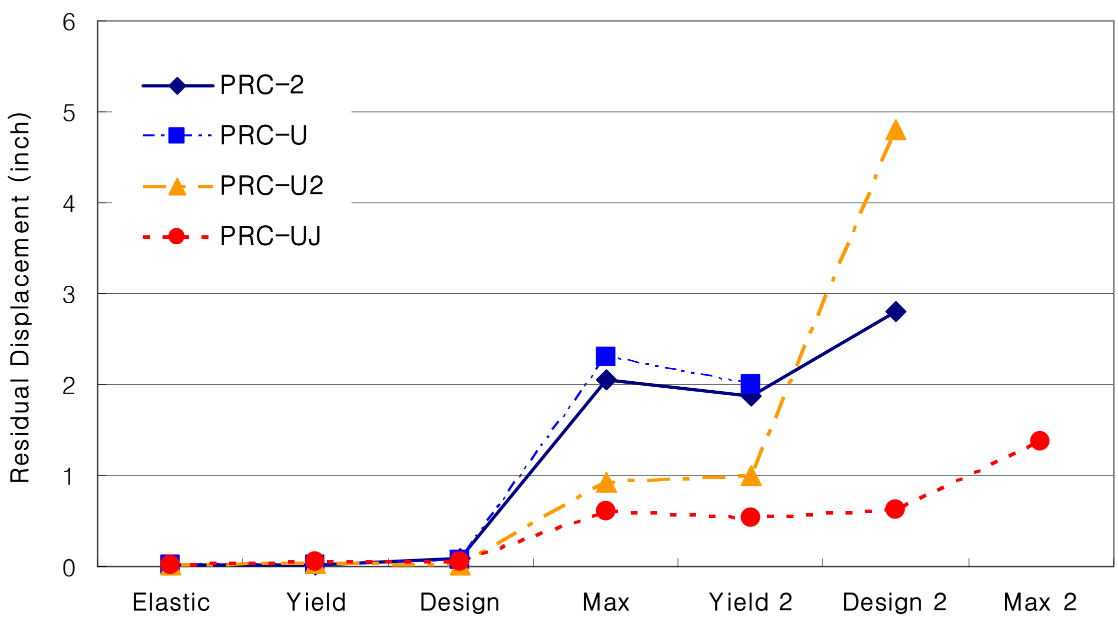

Fig. 3.56 Cumulative residual displacement at C.G.

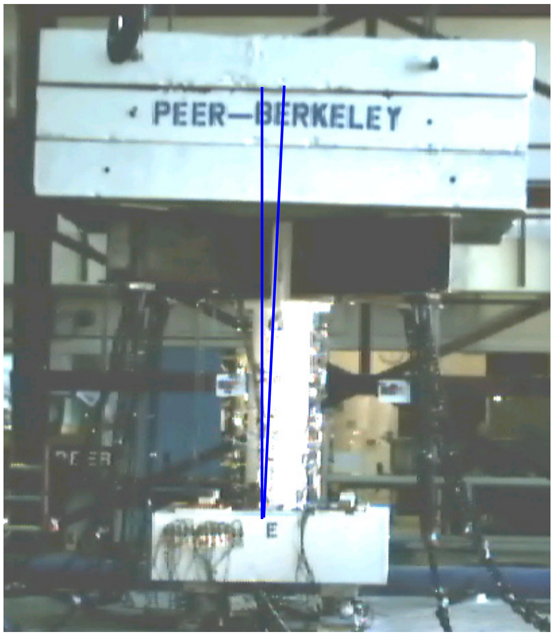

(a) PRC-U specimen, after maximum run

Residual displacement = 1.86 in. (472 mm)

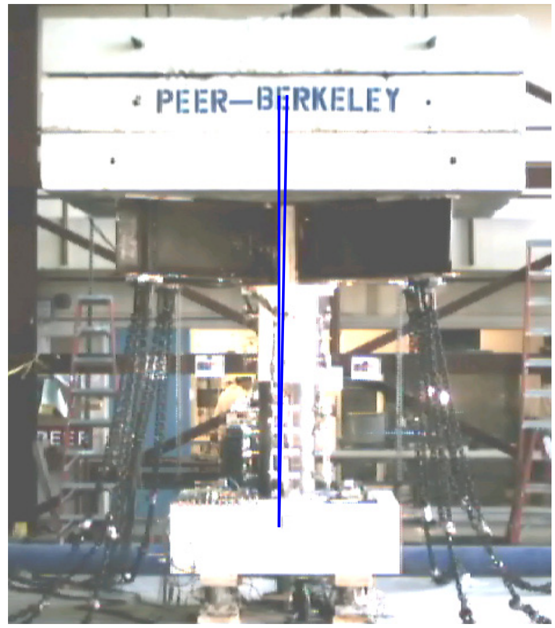

(b) PRC-UJ specimen, after maximum run

Residual displacement = 0.43 in. (109 mm)

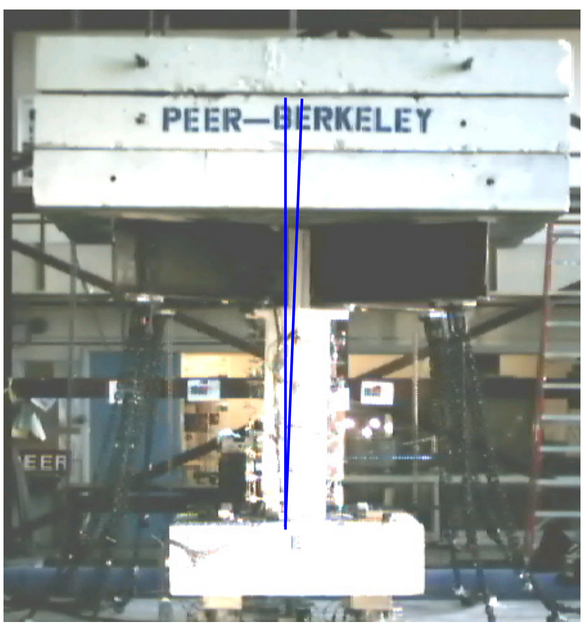

(c) PRC-2 specimen, after maximum run

Residual displacement = 1.28 in. (325 mm)

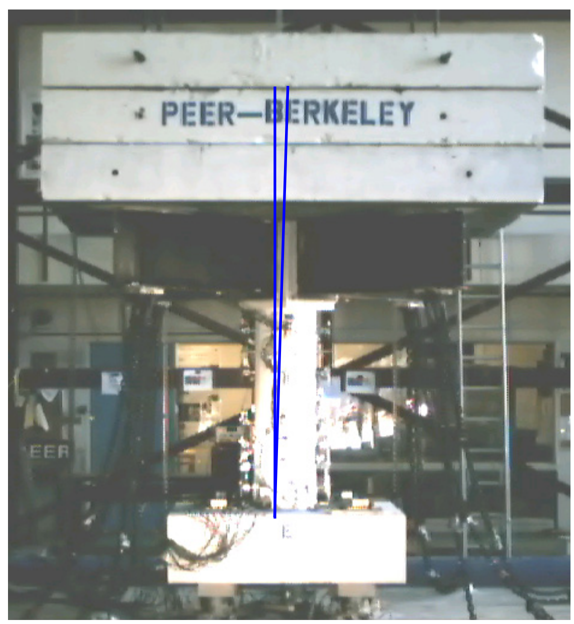

(d) PRC-U2 specimen, after maximum run

Residual displacement = 0.87 in. (221 mm)

Fig. 3.57 After end of maximum-level run

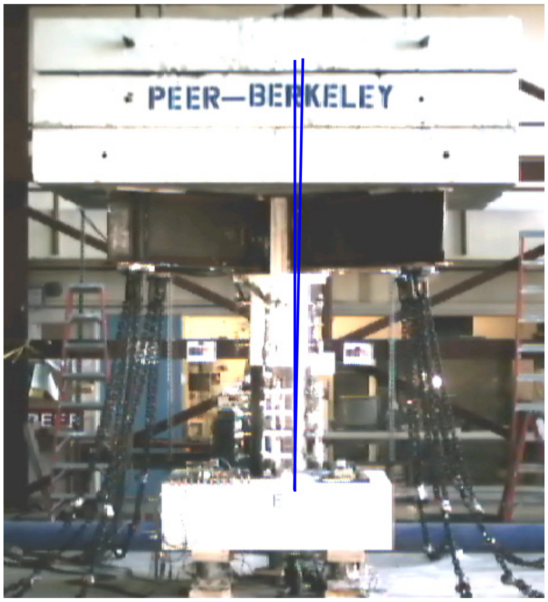

(a) PRC-UJ specimen, after design 2 run

Residual displacement = 0.44 in. (112 mm)

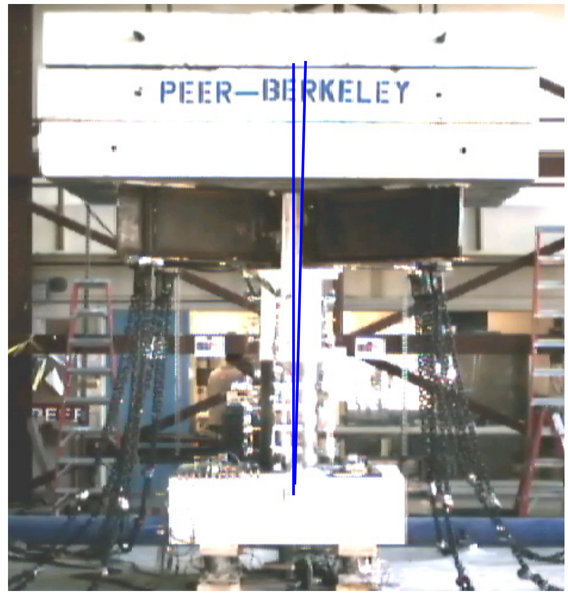

(b) PRC-UJ specimen, after maximum 2 run

Residual displacement = 0.99 in. (252 mm)

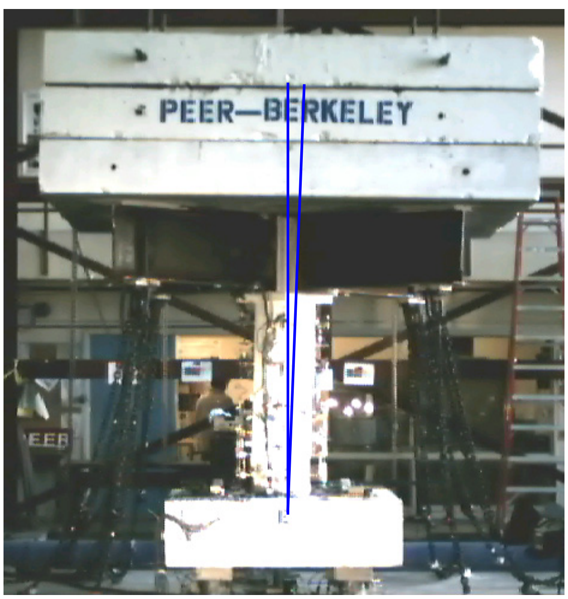

(c) PRC-2 specimen, after design 2 run

Residual displacement = 1.73 in. (439 mm)

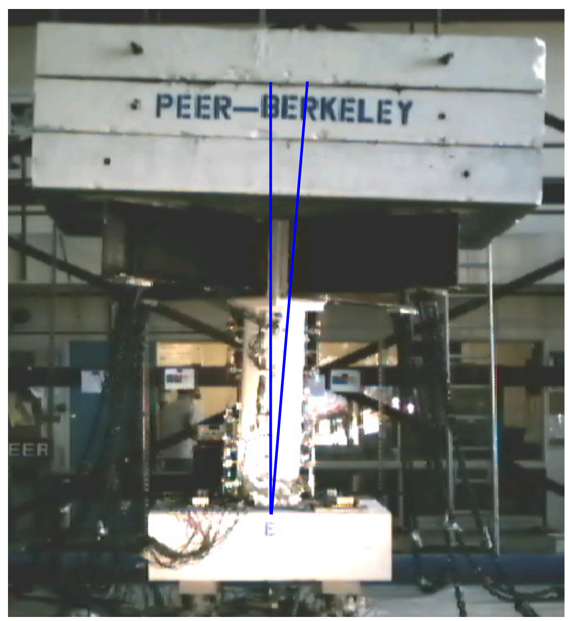

(d) PRC-U2 specimen, after design 2 run

Residual displacement = 3.80 in. (965 mm)

Fig. 3.58 After end of design 2- and maximum 2-level runs

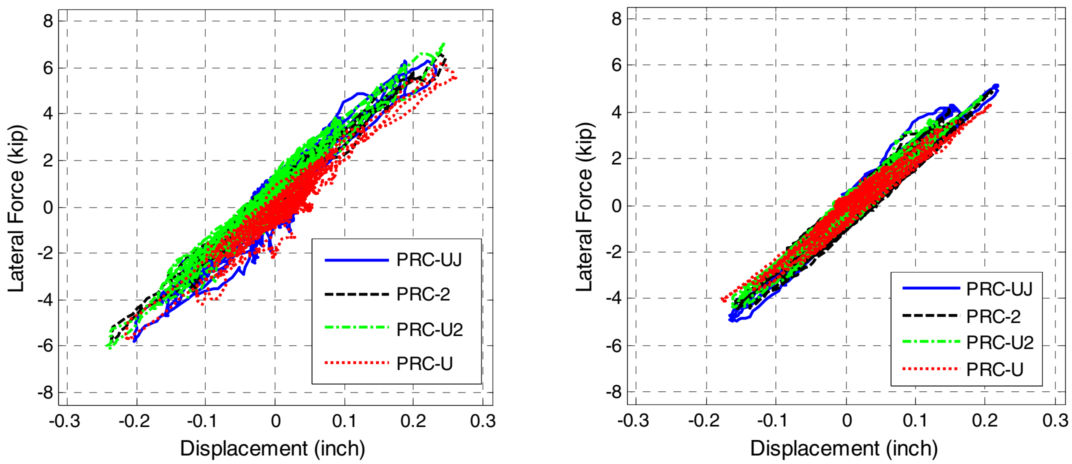

(a) X (N-S) direction(b) Y (E-W) direction

Fig. 3.59 Lateral force–lateral displacement hystereses (elastic-level test)

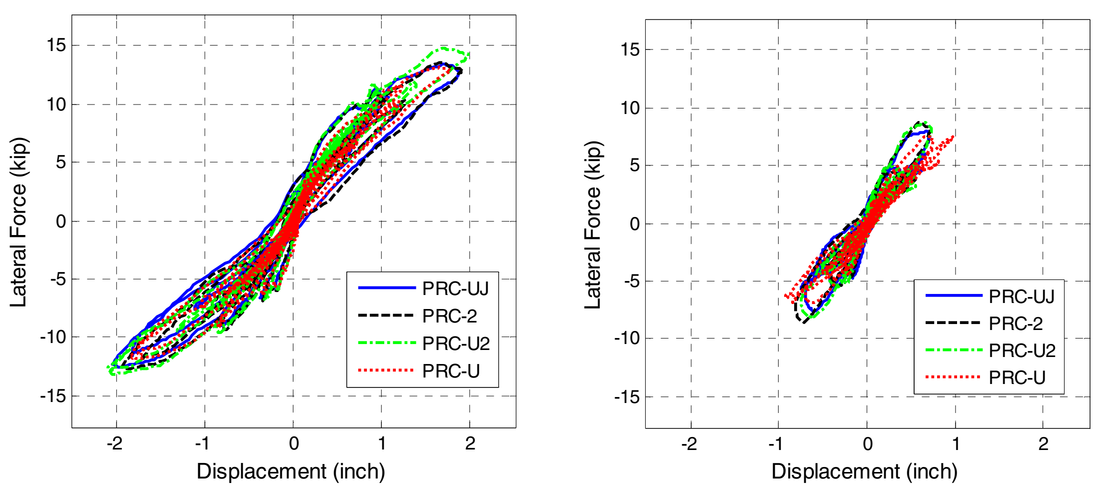

(a) X (N-S) direction

(b) Y (E-W) direction

Fig. 3.60 Lateral force–lateral displacement hystereses (yield-level test)

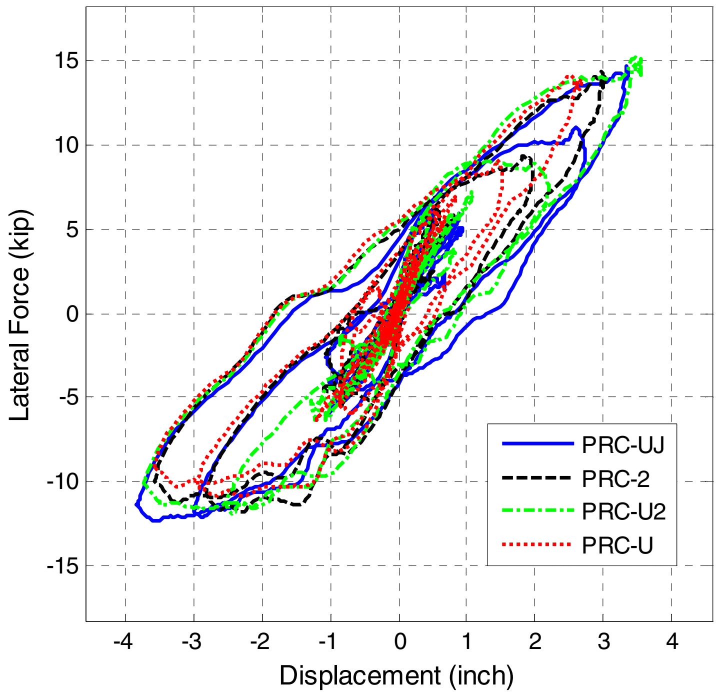

(a) *X* (N-S) direction

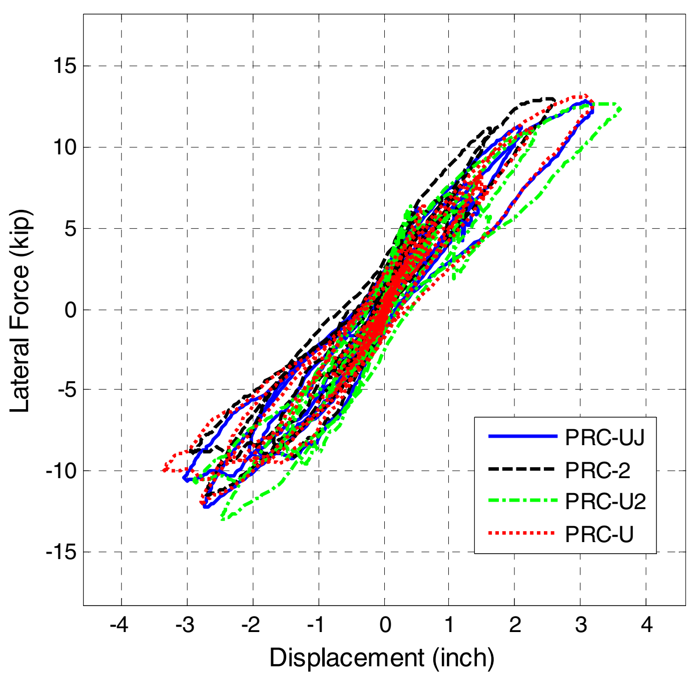

(b) *Y* (E-W) direction

Fig. 3.61 Lateral force–lateral displacement hystereses (design-level test)

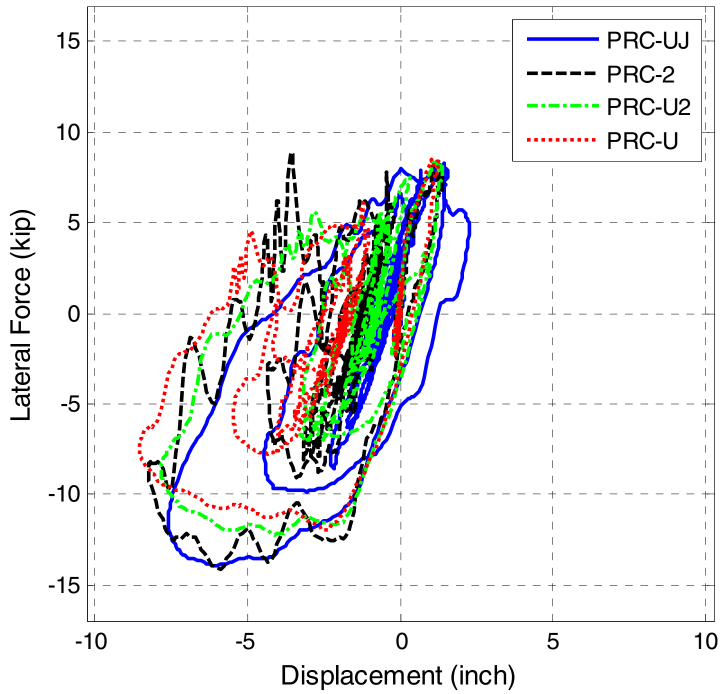

(a) *X* (N-S) direction

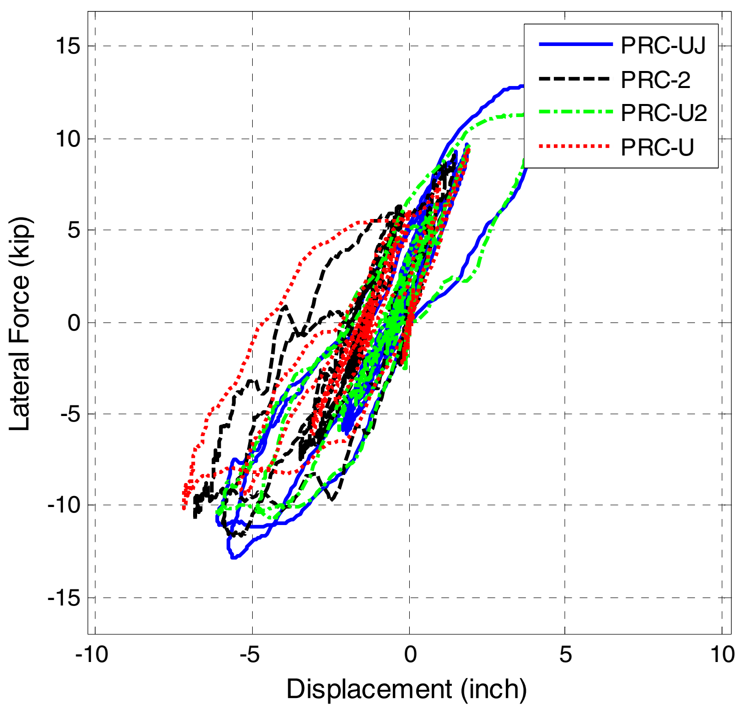

(b) *Y* (E-W) direction

Fig. 3.62 Lateral force–lateral displacement hystereses (maximum-level test)

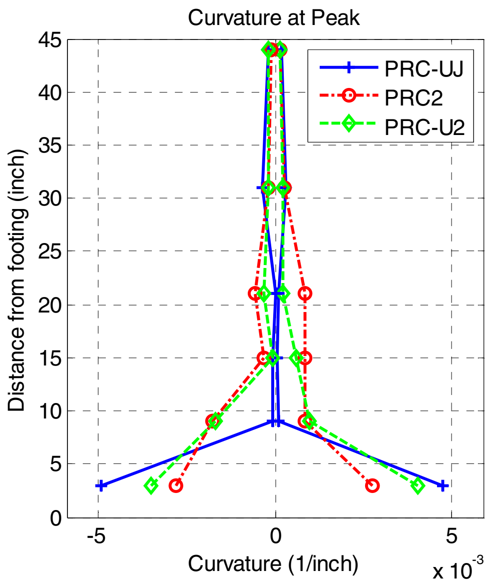

(a) X (N-S) direction

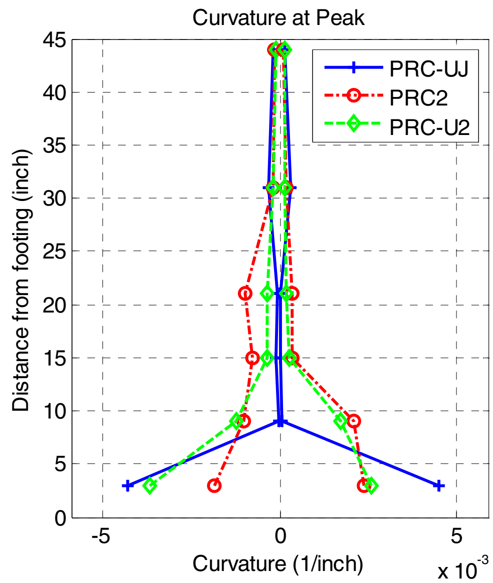

(b) Y (E-W) direction

Design level

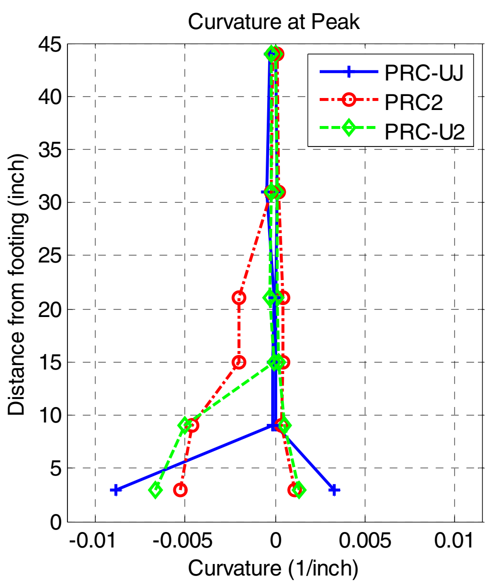

(a) X (N-S) direction

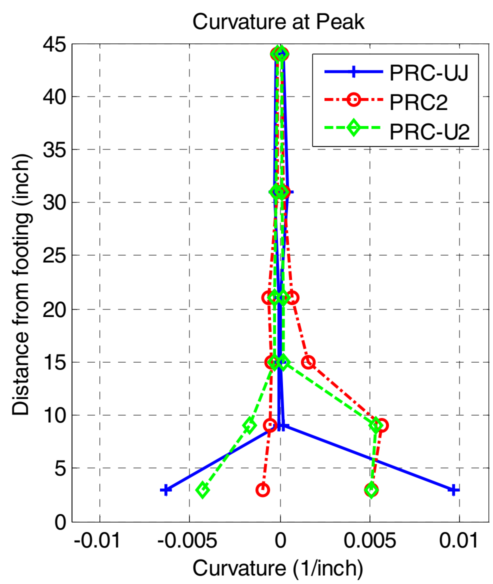

(b) Y (E-W) direction

Maximum level

Fig. 3.63 Curvature distribution along columns (design and maximum levels)

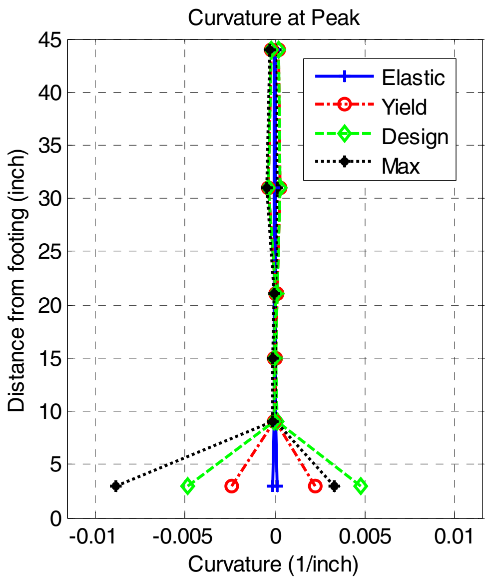

(a) *X* (N-S) direction

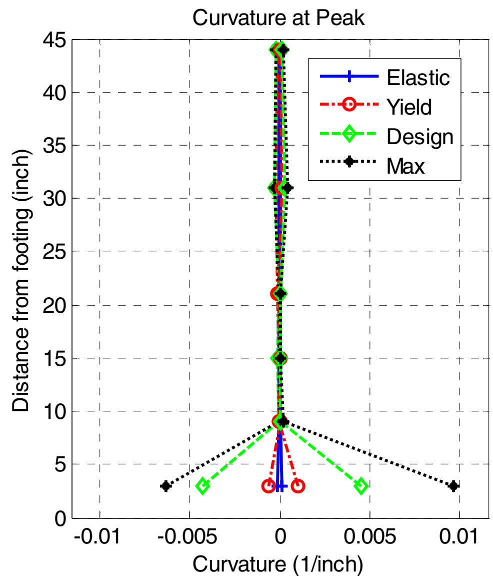

(b) *Y* (E-W) direction

Specimen PRC-UJ

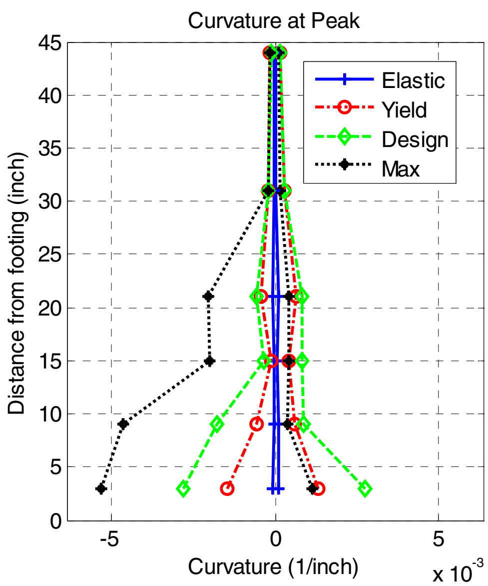

(a) *X* (N-S) direction

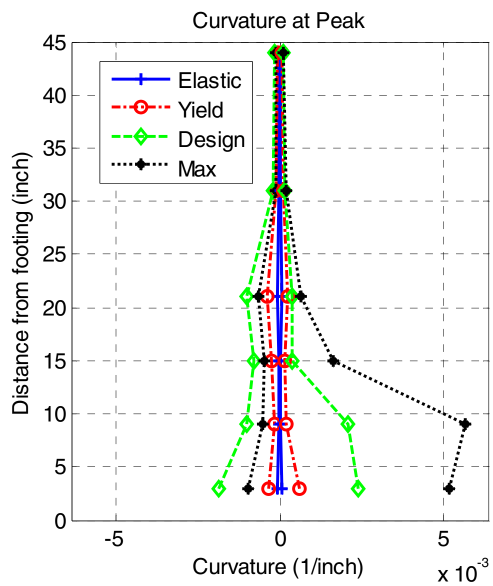

(b) *Y* (E-W) direction

Specimen PRC-2

Fig. 3.64 Curvature distribution along columns for each specimen

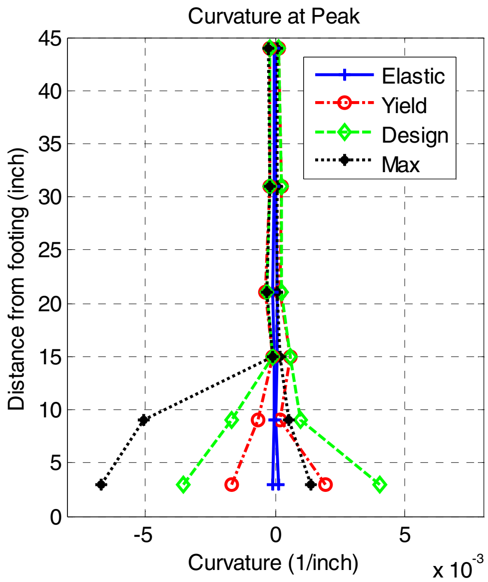

(a) X (N-S) direction

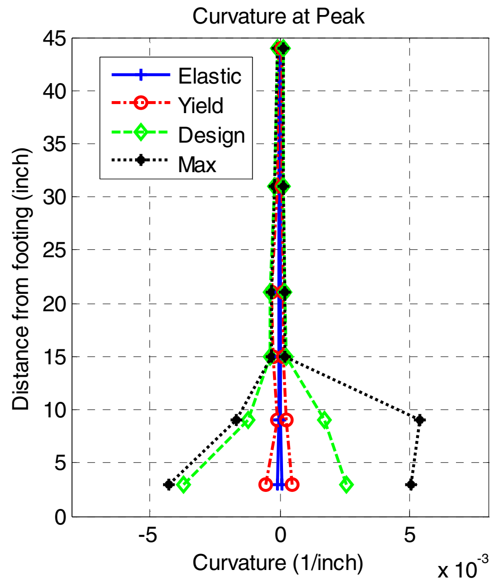

(b) Y (E-W) direction

Specimen PRC-U2

Fig. 3.64—*Continued*

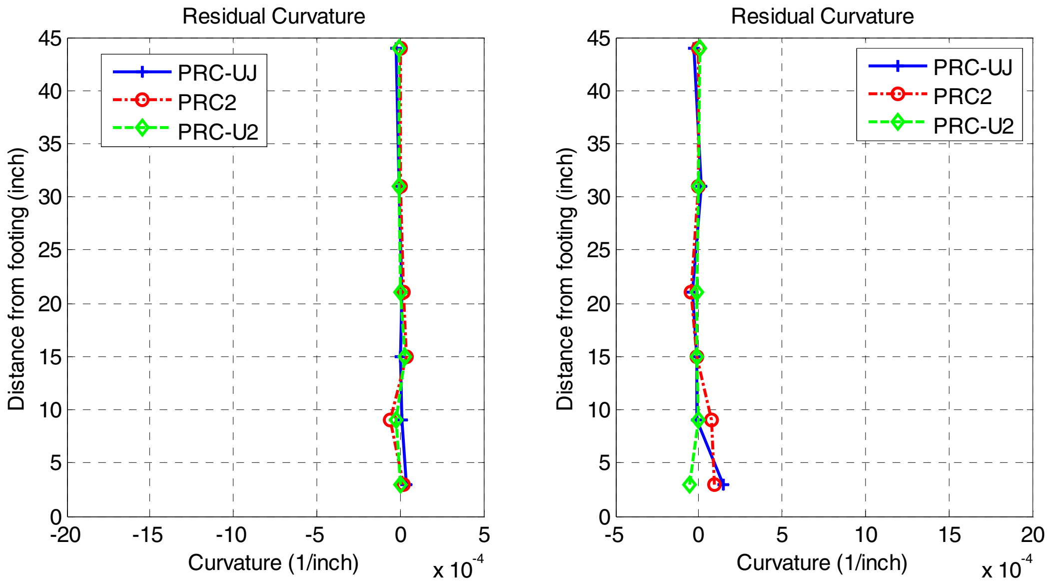

(a) X (N-S) direction (b) Y (E-W) direction

Design level

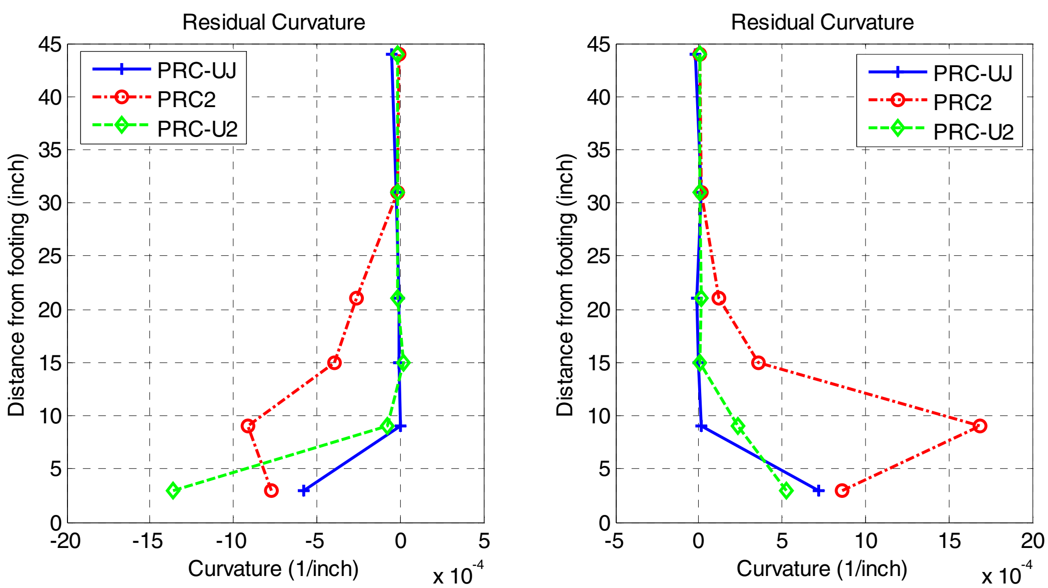

(a) X (N-S) direction (b) Y (E-W) direction

Maximum level

Fig. 3.65 Residual curvature distribution along columns

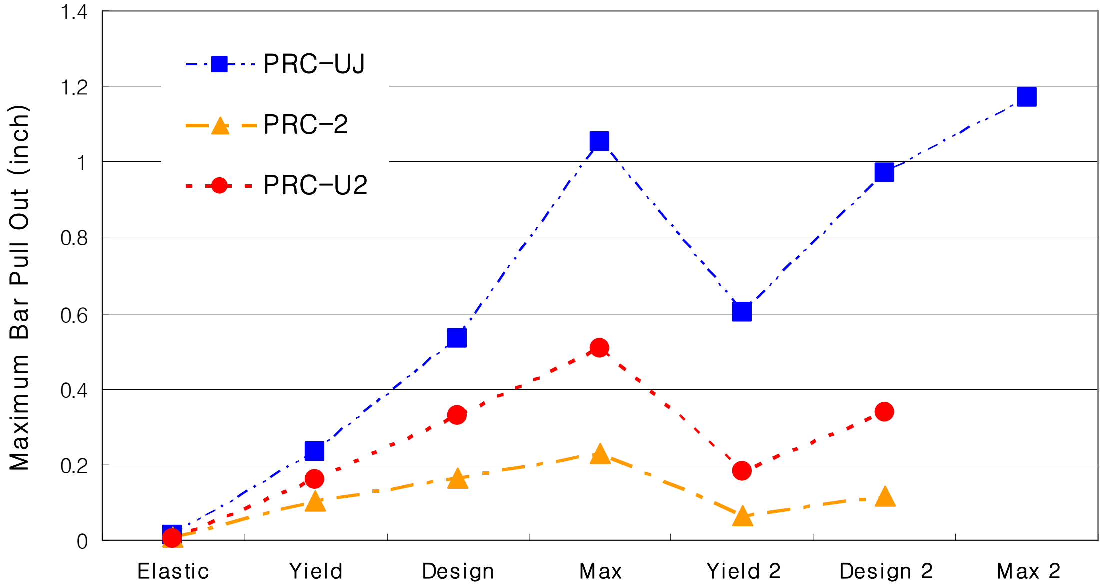

Fig. 3.66 Maximum bar pullout

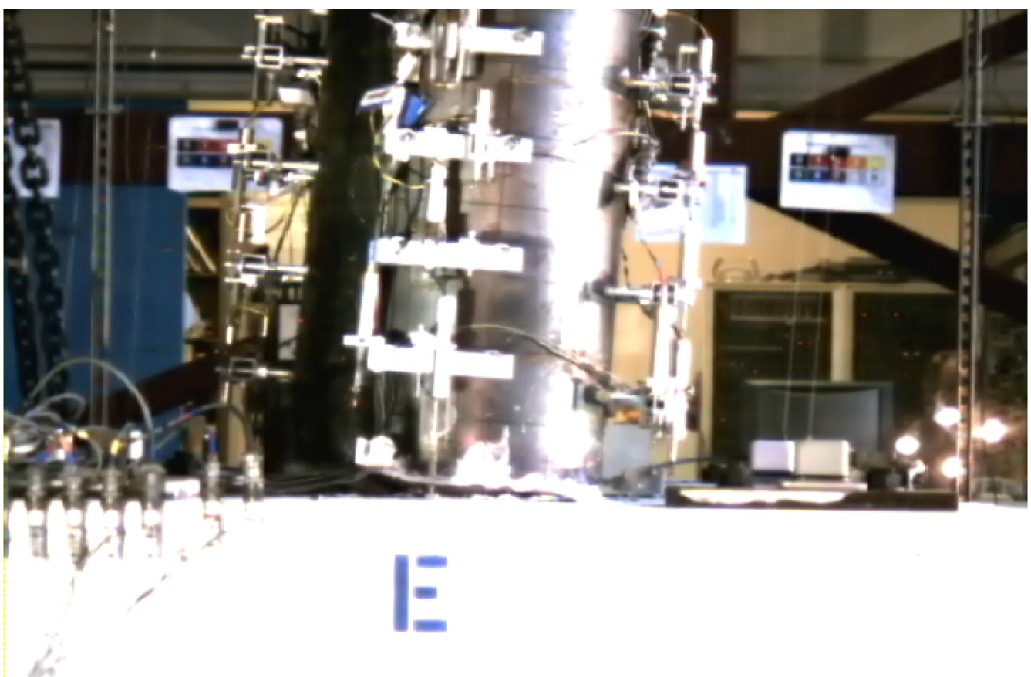

Fig. 3.67 Bar pullout of specimen PRC-UJ (maximum-level test).

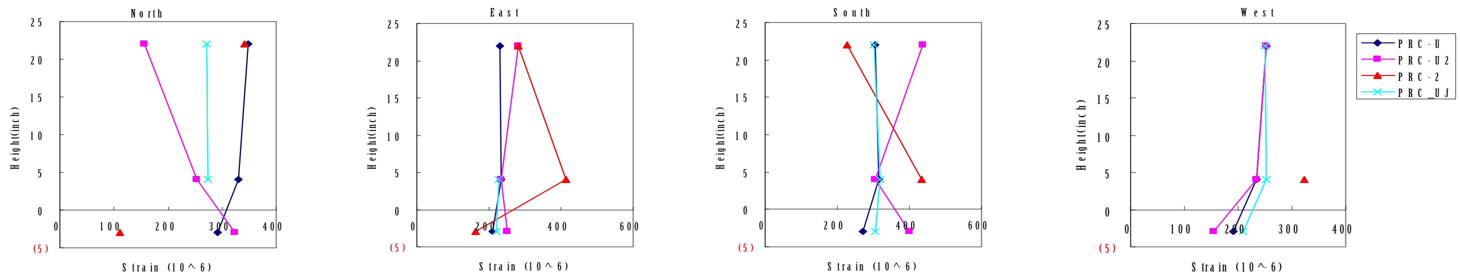

Elastic level

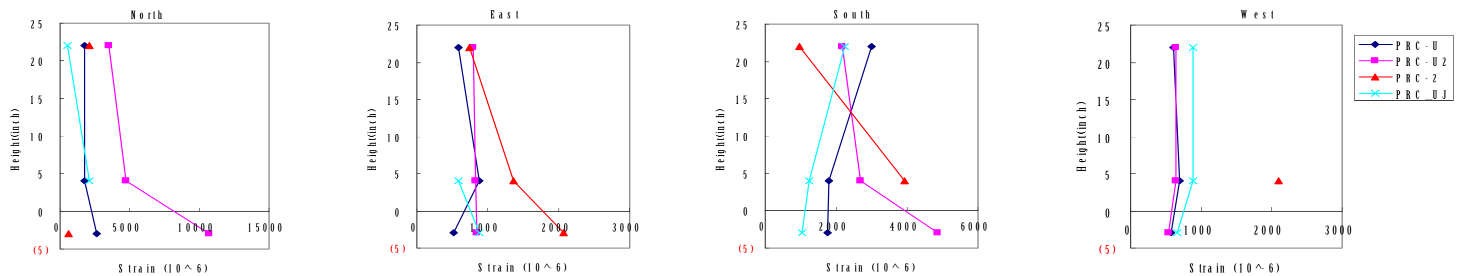

Yield level

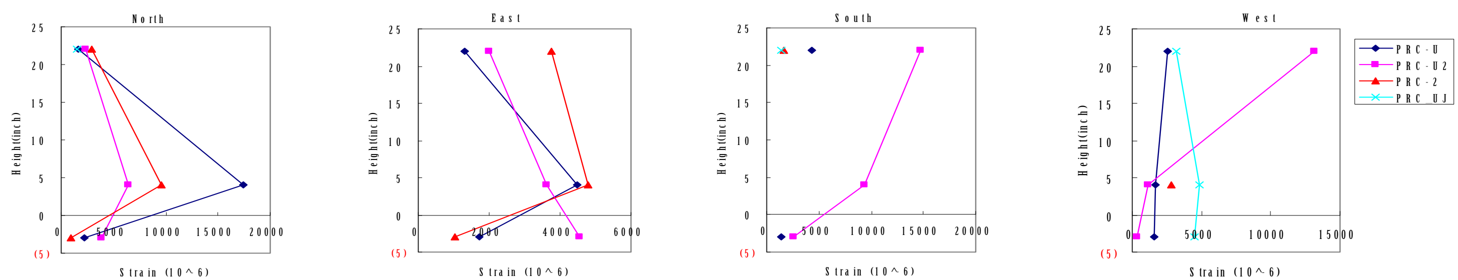

Design level

Fig. 3.68 Maximum strain distribution

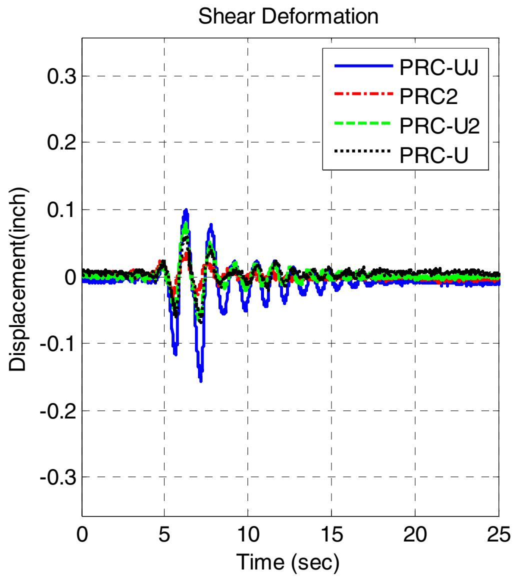

(a) X (N-S) direction

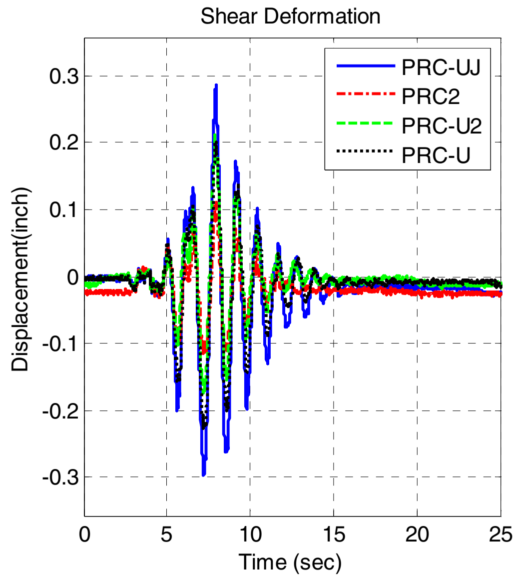

(b) Y (E-W) direction

Design level

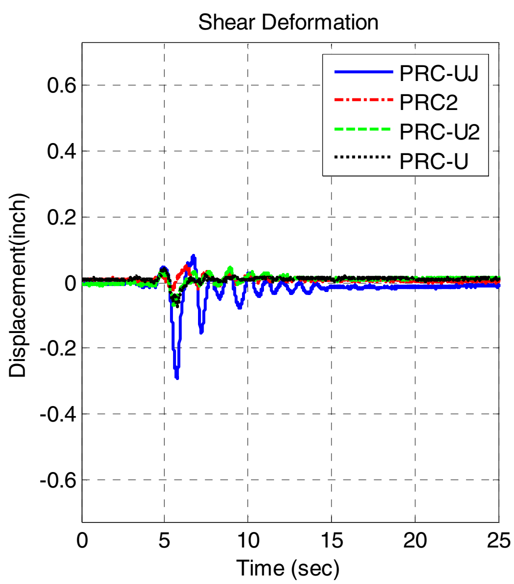

(a) X (N-S) direction

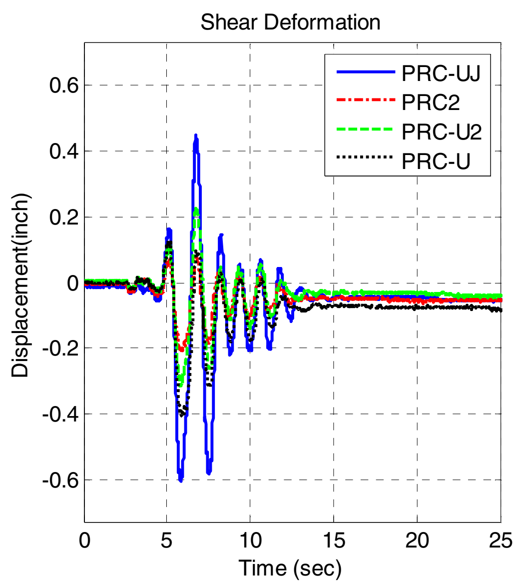

(b) Y (E-W) direction

Maximum level

Fig. 3.69 Shear deformation at 6-in. (152-mm) height section

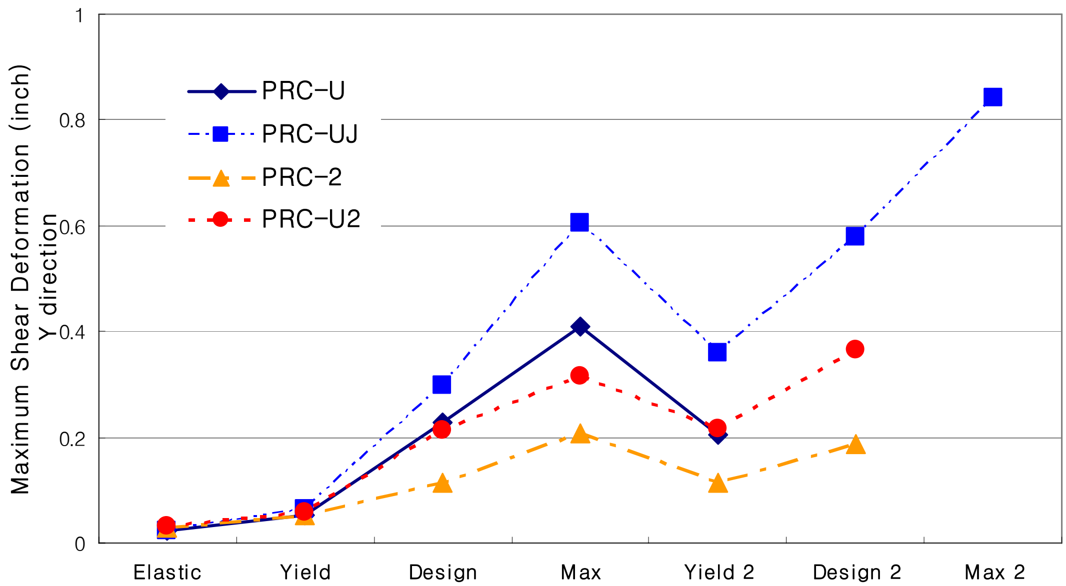

(1) *X* (N-S) direction

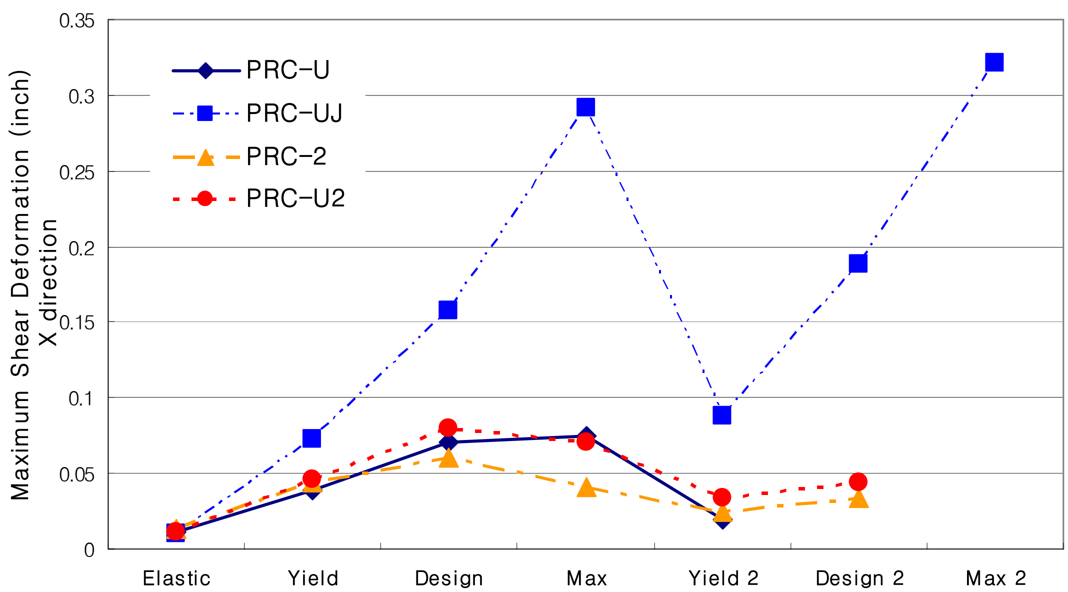

(2) *Y* (E-W) direction

Fig. 3.70 Maximum shear deformations at 6-in (152-mm) height section

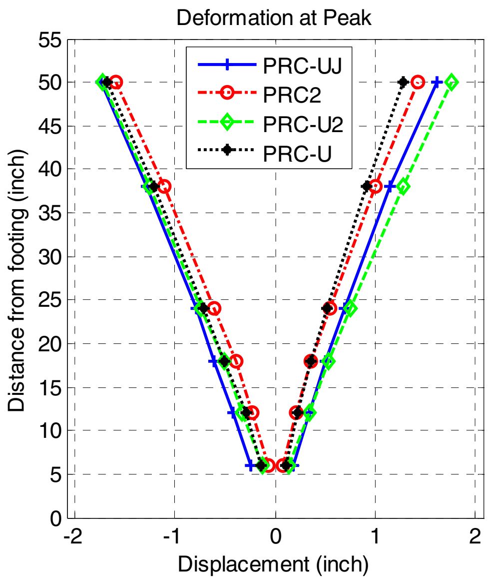

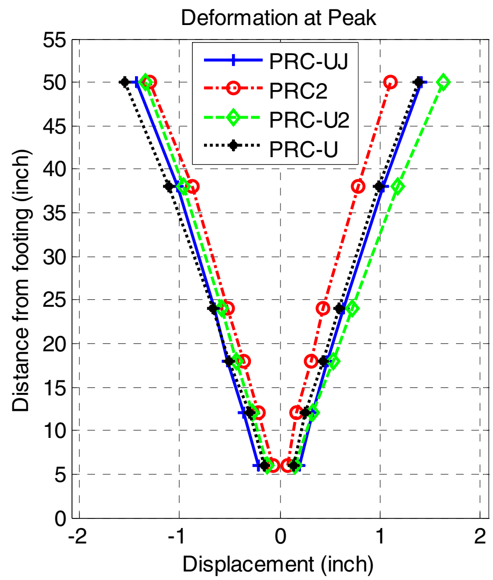

(a) *X* (N-S) direction (b) *Y* (E-W) direction

Design level

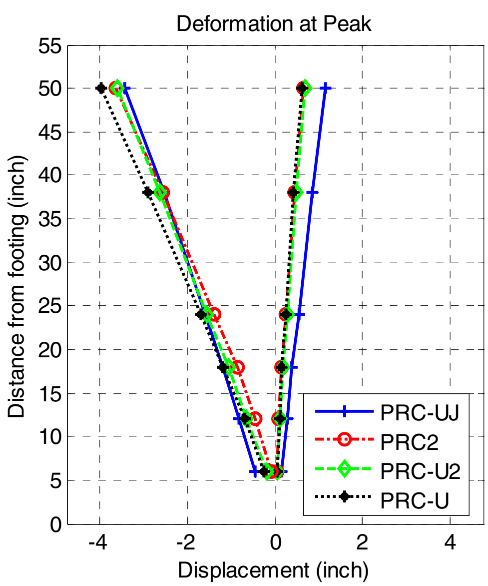

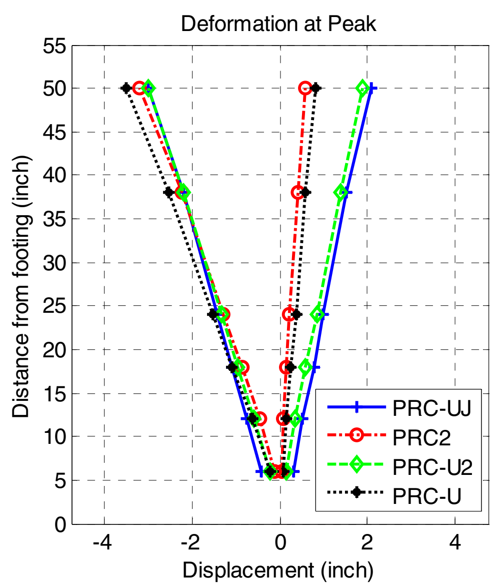

(a) *X* (N-S) direction (b) *Y* (E-W) direction

Maximum level

Fig. 3.71 Peak displacement response along columns

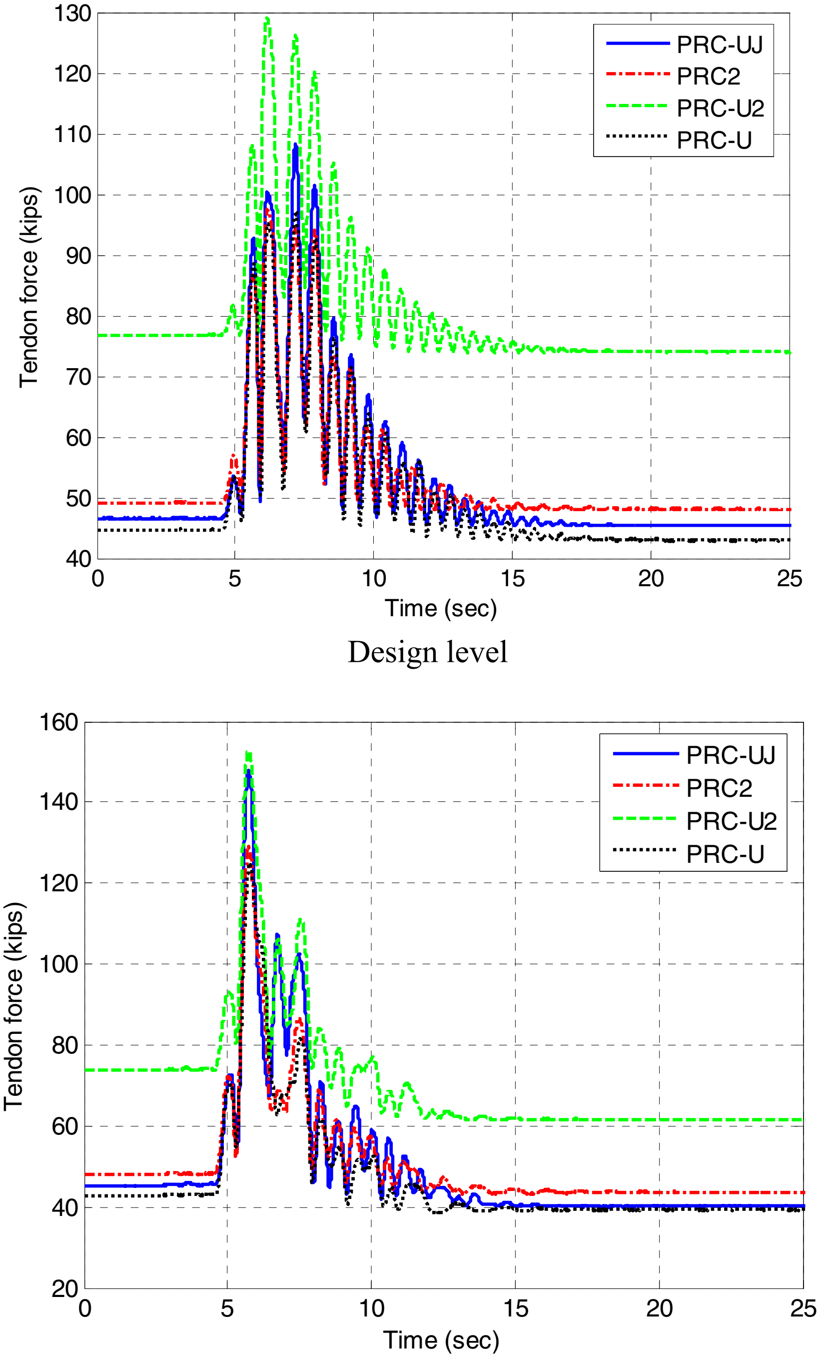

Design level

Maximum level

Fig. 3.72 Tendon force

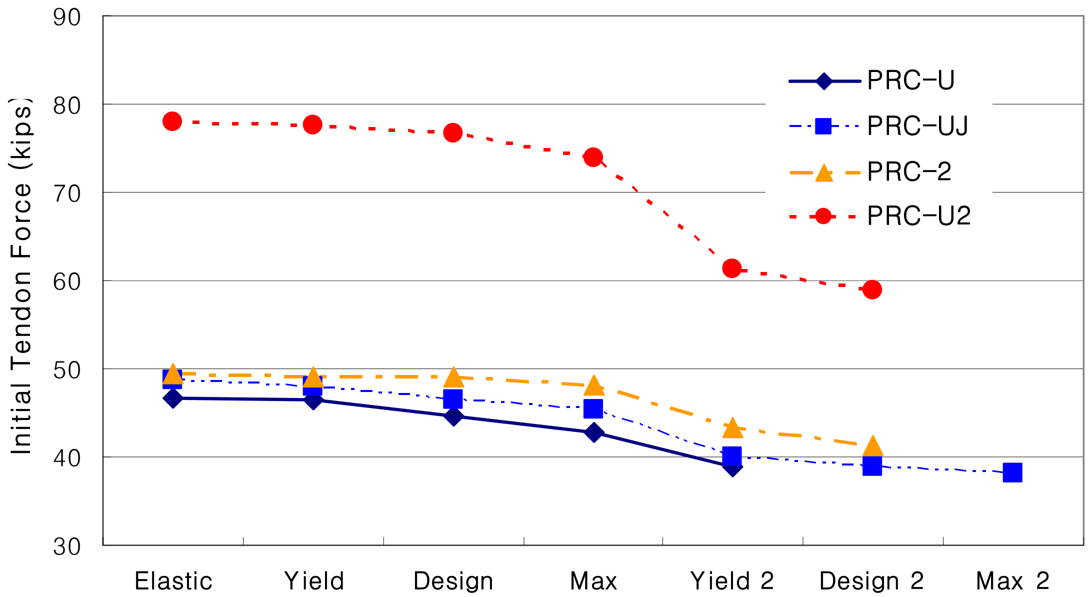

Fig. 3.73 Change of initial tendon force

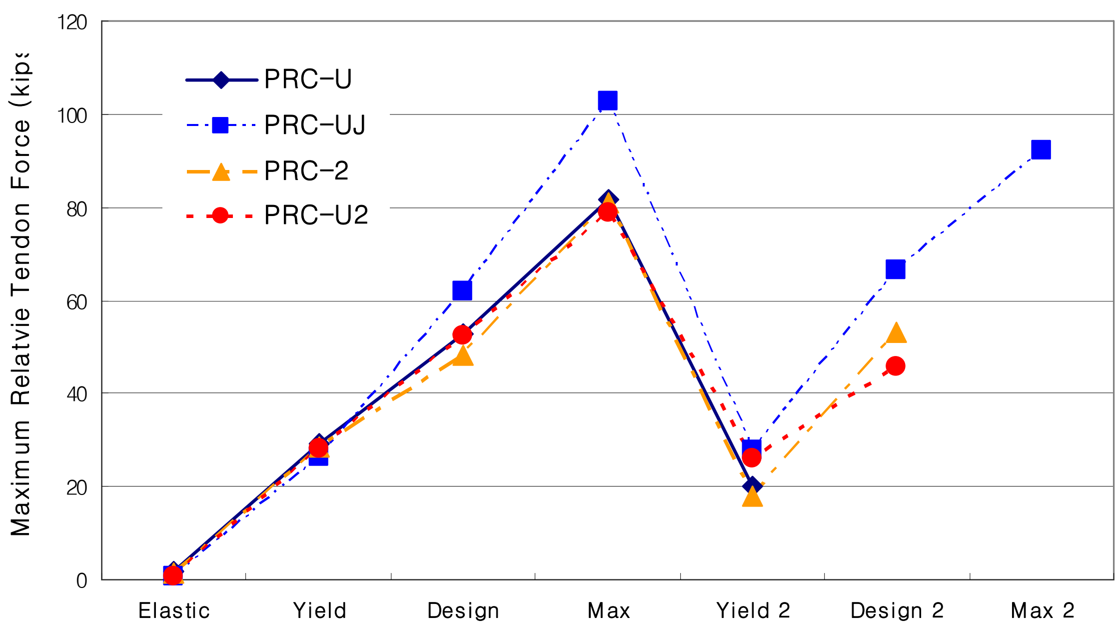

Fig. 3.74 Maximum relative tendon force

4 Experiment on Two-Column Bent Specimen

4.1 INTRODUCTION

From the test program in Chapter 3, it was found that the use of a steel jacket and unbonded mild bar at the plastic hinge region provides substantial benefit to reduce residual displacements. However, the previous test programs mostly focused on individual cantilever columns, not a bridge system. Thus, to assess the applicability of this self-centering system to real-world situations, tests involving more complex bridge systems are needed.

The test described in this chapter attempts to investigate the effectiveness of the new method in reducing the residual displacement of a more complex system. In this case, a simplified two-column frame from a single-column viaduct is considered with differing column heights. Based on the results of Chapter 3, the column plastic hinge regions are sheathed with steel jackets and the mild reinforcing bars in these regions are unbonded. In the longitudinal direction of the frame, the columns are expected to respond primarily in double curvature due to frame action, while in the transverse direction they will be responding primarily as cantilevers. The different height columns will introduce some torsion about a vertical axis and result in an asymmetric distribution of yielding in the columns. This experiment is intended to be a test of the ability of the self-centering bridge column concept being investigated herein to limit peak and residual displacements in bridge systems exhibiting more complex behavior.

Section 4.2 presents the design of the two-column bent reinforced concrete bridge system tested, construction of the model, material properties, and selection of ground motions used. The test setup, instrumentation, and data acquisition are described in Section 4.3. Section 4.4 summarizes the test results of the two-column bent reinforced concrete bridge under earthquake excitation. Conclusions are presented in Section 4.5.

4.2 SPECIMEN DESIGN AND CONSTRUCTION

4.2.1 Prototype Column

A two-column frame from a single column viaduct having different column heights was selected as the prototype column for this research, as shown in Figure 4.1.

The prototype of each column is the same as the prototype of the previous test program (Chapter 3). The details of the prototype of the single column (e.g., section, column design, dimensions, reinforcement, and capacity) can be found in Section 3.2.1.

4.2.2 Design of Specimen

The basic design of the test specimen for a two-column bent bridge in this section was very similar to that employed in the previous chapter. The model length scale factor was 4.5, the same as for the previous test (Chapter 3), due to the size limitation of the shaking table. The detail of the dimensional analysis can be found in Section 3.2.2.1.

4.2.2.1 Design of Test Specimen

The test specimen was designed based on the findings from the previous test results (Chapter 3). Among the four previous test specimens, specimen PRC-UJ, which incorporated the unbonded mild bar and the steel jacket at the expected plastic hinge, showed substantial benefits for reducing the residual displacement and robust response during main earthquake input and also aftershock input. Therefore, most of the details of the new specimen followed those of specimen PRC-UJ. The test specimen was designed as one bay with two partially prestressed reinforced concrete columns that incorporated the unbonded mild bar and the steel jacket at the expected plastic hinge, and will be referred to as the specimen PRC-system.

The specimen PRC-UJ and specimen PRC-system are fairly similar with the exception of a few parameters. Specimen PRC-UJ is a cantilever-type specimen with one column, while PRC-system consists of two columns with different height. The aspect ratio of the PRC-UJ specimen was 6. The aspect ratio in the transverse direction of the PRC-system specimen was selected as 6 for the short column and 6.5 for the long column. Because of the double curvature of the two-column system in the longitudinal direction, specimen PRC-system had a steel jacket and an unbonded region for the mild reinforcement at both the top and bottom of each column. Based on the test results of the curvature distribution along the column of the previous PRC-UJ specimen, the heights of the steel jacket and unbonded region were reduced from 2*D* (two times the column diameter) to 1*D*. To avoid the "elephant foot" buckling at the base of the steel jacket, a 1/2-in. (13-mm) gap was provided at the top and bottom of each column. At full scale this gap corresponds to the 2-in. (50-mm) space recommended by the SDC. The unbonding method for the longitudinal reinforcement of the PRC-UJ specimen was the use of wax and plastic wrap, but that of specimen PRC-system was the use of thin Teflon tubing just slightly larger than the diameter of the longitudinal bars. This debonding technique was much easier to implement than that previously used for PRC-UJ. Table 4.1 shows the differences between specimen PRC-UJ and the specimen PRC-system.

To facilitate construction and transportation, reusable steel beams were designed to support the mass blocks and connect the two columns without a top deck slab. Figure 4.2 shows the two-column bent specimen with mass blocks that represent the weight and inertial mass of the superstructure of the prototype bridge, and Figure 4.3 shows the reinforcement details of the specimen. Figure 4.4 shows the elevation and plan view of each column.

The test columns were 16 in. (0.41 m) in diameter; the height from the bottom of the short column to the center of gravity of the assembly of the steel bracket and weight blocks was 8 ft (2.44 m) (aspect ratio 6), and that of the long column was 8 ft 8 in. (2.64 m) (aspect ratio 6.5). The distance between columns was 9 ft (2.74 m). No attempt was made to represent the flexural and torsional stiffness of an actual bridge bent. It was expected that the steel beam–mass block assembly would result in an essentially rigid support connecting the top of each column.

Each column was reinforced with 12 No. 3 (10-mm diameter) deformed bars longitudinally. As spiral reinforcement, W3.5 round wire (5.4-mm diameter) with a 1-1/4-in. (32-mm) pitch was used for each column. The longitudinal reinforcement ratio (ρ_l) was 1.19%, and the volumetric ratio of spiral reinforcement (ρ_s) was 0.76%. Normal density of concrete was used, and the design strength of concrete (f'_{co}) was specified to be 5 ksi (34.5 MPa). Gr60 reinforcing bars were used for the longitudinal reinforcement, and Gr80 wires were used for the spirals. The nominal yield strengths of the longitudinal reinforcement and spiral were 60 ksi (420 MPa) and 80 ksi (550 MPa), respectively. Gr150 (1,035 MPa) bar from Williams Form Engineering Corp. was used as a post-tensioning tendon. The size and length of the tendons were

1-3/8 in. (36 mm) in diameter and 11 ft (3.35 m), respectively. The ultimate strength of the tendon was computed to be 237 kip (1,055 kN).

The dead load tributary to each column due to the steel beams and the weight blocks was 54 kip (240 kN), resulting in an axial force ratio of 5.7% (based on the design concrete strength).

4.2.2.2 Footing and Steel Beams

The design of the 5-ft- (1.52-m-) sq footing followed the previous footing design in Section 3.2.2.3. The difference between the long-column footing and the short-column footing was the thickness: the footing was 18 in. (0.46 m) thick for the long column, and was reinforced longitudinally with No. 6 (19-mm diameter) deformed bars and transversally with No. 3 (10-mm diameter) stirrup ties; the thickness of the short column was 26 in. (0.66 m), with like reinforcement. The weights of the footing for the long column and short column were 5.6 kip (24.9 kN) and 8.1 kip (36.0 kN), respectively.

Figure 4.6 shows the set of two steel beams used at both sides of the column top block. Each steel beam was made with two wide sections (W12 × 66). The length of each beam was about 22 ft (6.6 m); the weight was 3.3 kip (14.7 kN).

The total weight of the long-column and short-column specimen was 7.8 kip (34.7 kN) and 10.2 kip (45.4 kN), respectively, including the weight of the columns and footing, but not including the weight of the mass blocks and steel beams.

4.2.2.3 Mass Blocks and Steel Plate

Six 10 ft × 10 ft × 14 in. (3.05 × 3.05 × 0.36 m) concrete blocks were used to represent the weight and mass of the superstructure of a bridge. A large steel plate, 11 ft × 4 ft × 1 in. (3.35 m × 1.22 m × 25 mm), was used on the top of the mass block assemblage to insure the rigid motion of all six weight blocks. The weight of each block was about 17 kip (76 kN), resulting in a total weight of 55.4 kip (246 kN) for each column, which included the weight of the steel beams and the top steel plate. Two blocks, which were placed directly on the steel beams, each had a square hole 15 × 15 in. (0.38 × 0.38 m) to allow for the anchorage of the post-tensioning tendon.

4.2.3 Construction of Specimen

The specimen was constructed as follows:

1. Construction of forms for the footings (Fig. 4.7);
2. Assembly of steel cages (Fig. 4.8);
3. Casting footing concrete (on 2006 May 26, shown in Figs. 4.11 and 4.12);
4. Construction of forms for the columns (Figs. 4.13 and 4.14);
5. Casting column concrete (on 2006 June 15, in Fig. 4.15); and
6. Removal of the forms (finished on 2006 June 23, in Fig. 4.16).

Figures 4.9 and 4.10 show unbonded mild bars and steel jackets used for the construction of the specimen. Before casting of the column concrete, 1/2-in. (13-mm) diameter threaded rods were inserted transversely through the column forms in order to provide a means for measuring the curvature distribution along the height of the columns. A gap of about 1/4 in. (6 mm) was provided between these rods and the steel jacket to prevent impact of these rods on the steel jacketing. The slump of concrete, which had been specified to be 5 in. (127 mm), was measured to be 3-1/2 in. (89 mm) for the footing concrete and 5 in. (127 mm) for the columns.

4.2.4 Measured Material Properties

4.2.4.1 Concrete

The concrete of the columns was specified as normal weight with a 28-day design strength of no less than 4 ksi (27.6 MPa) and no more than 5.5 ksi (38 MPa) to represent the actual properties of concrete used in reinforced concrete bridges. The detailed concrete mix design is the same as that of the previous test program (see Table 3.3).

Eighteen 6 × 12 in. standard cylinders were cast at the casting of the column and were used to measure the concrete compressive strength and stress-strain relationship. Compressive strength tests were performed at 7 and 28 days after casting the footing concrete, and at 7, 14, 21, and 28 days after casting the column concrete. Additional cylinders were tested a day after the shaking table test of the specimen.

In each test, three cylinders were tested. Tables 4.2 and 4.3 summarize the test results, and Figure 4.17 shows the stress-strain curves of the column concrete for the specimen. The column concrete had a 28-day strength of 3.82 ksi (27.3 MPa), while the footing concrete had

4.64 ksi (36.8 MPa). The average strength of the column concrete for the specimen on testing day was about 4.1 ksi (32.9 MPa). The average tangential and secant moduli of elasticity of the concrete were evaluated to be 2,873 ksi (19.2 GPa) and 2,574 ksi (17.2 GPa), respectively.

4.2.4.2 Steel

The column longitudinal steel was specified as ASTM A706 Gr60 steel. To obtain the mechanical properties of the reinforcing bars, tensile tests for steel coupons were conducted. Two coupons were tested for No. 3 bars for the specimen. The test results are summarized in Table 4.4(a). Figure 4.18 shows the stress-strain relationship of a No. 3 bar from the test. The yield strength, ultimate strength, and modulus of elasticity of the No. 3 bars were 68.4 ksi (476 MPa), 91.8 ksi (627 MPa), and 29,350 ksi (201 GPa), respectively.

The spiral reinforcement was specified as ASTM A82 Gr80. Two coupons were tested for spiral reinforcement for the specimen. The test results are summarized in Table 4.4(b). The stress-strain relationship of a spiral wire can be seen in Figure 4.19**.**

For the post-tensioning tendon, ASTM A722 Gr150 (1,035 MPa) bar from Williams Form Engineering Corp. was used. The size of the tendon was 1-3/8 in. (35 mm) in diameter. To obtain the mechanical properties of the tendon, a tensile test for steel coupons was conducted. Figure 4.20 shows a stress-strain curve obtained from the test. The yield strength, ultimate strength, and modulus of elasticity of the tendon were 137 ksi, 160 ksi, and 28,120 ksi, respectively (Table 4.4(c)). Thus, the yield and ultimate strengths of the tendon were estimated to be 203 kip (926 kN) and 238 ksi (1,130 kN), respectively.

The steel plate for the jacket was specified as ASTM A36 steel plate. To obtain the mechanical properties of the steel plate, a tensile test for steel plate coupon was conducted. The test results are summarized in Table 4.4(d). The yield strength, ultimate strength, and modulus of elasticity of the steel plate were 41.3 ksi (284 MPa), 50.5 ksi (348 MPa), and 26,100 ksi (180 GPa), respectively.

4.3 EXPERIMENTAL SETUP AND TEST PROGRAM

4.3.1 Test Setup

Figure 4.21(a) shows a specimen setup on the table. In order to simulate fixed supports at the base of each column and to match the hole positions of the supports and the shaking table, four steel beams (two for each column) were constructed, each with three holes drilled vertically through the web and sheathed with steel tube to permit prestressing of the steel beam to the shaking table; and each with a series of holes on the top flange to attach two tri-axial load cells (four for each column) (see Fig. 4.21(b)). Vertical stiffeners were attached at the position of each load cell to give more strength. The steel beams were fixed to the shaking table with three prestressing tendons for each beam. Hydrostone was placed between the steel beams and the shaking table, and between the top of the flange and the load cells, to provide a solid bearing surface. The load cells, fastened to the beams on top of the shaking table, were each attached to the footing of the test specimen by means of four 7/8-in. (22-mm) diameter high-strength bolts that extended through vertical conduits placed in the specimen's footing. Figure 4.22 shows the setup of the steel beams and load cells on the table.

Each column was carried by a truck crane and placed onto the load cell sets as shown in Figures 4.23 and 4.24**.** Next, each column was fixed to the four load cells with sixteen 7/8-in. (22-mm) or 3/4-in. (19-mm) diameter high-strength steel rods. To provide a uniform contact surface, a layer of hydrostone was placed between the load cells and the bottom of the footing.

To support the mass blocks, two steel beams were attached to the sides of the columns' top blocks using prestressing rods, as shown in Figures 4.25 and 4.26. A layer of hydrostone was placed between the beam web and the specimen surface.

A 1-3/8-in. (36-mm) post-tensioning tendon was installed in the middle of each column. Steel plates, 9 × 9 × 1-5/8 in. (229 × 229 × 41 mm), were used at both ends of the tendon to distribute the bearing stresses on the concrete. A layer of hydrostone was placed between the plates and the specimen surface. A 200-kip- (890-kN-) capacity load cell with a center hole was placed underneath each column to monitor the prestressing force induced in the column. The prestressing force was applied to the tendons with a hydraulic jack, as shown in Figure 4.27.

The target prestressing force was determined from the previous test and analytical results. Based on the previous experience of the loss of prestressing force due to creep and axial load from the added mass blocks, the prestressing force of specimen PRC-system was determined to be 57 kip (254 kN). After seven days, when all three mass blocks were placed on top of the steel beams after the force was induced, the prestressing force decreased to about 49 kip (218 kN); the loss of the prestressing force was 8 kip (36 kN). This initial prestressing force was similar to that previously used for specimen PRC-UJ.

Based on the average concrete strength from cylinder tests, 4.1 ksi (28.6 MPa), the actual total axial force ratio (α_{total}) for the specimen PRC-system was around 13.4%, which is somewhat higher than for specimen PRC-UJ. Table 4.5 shows the prestressing force for each column on the testing day and the total axial force ratio for the concrete strength determined from the cylinder test of the testing day.

The weight blocks were then placed on the steel beams of the specimen, as shown in Figures 4.28 and 4.29. The blocks with a center hole were placed directly onto the steel beams of the specimen to provide space for the prestressing tendon. Hydrostone was also used between the steel beam and the block, and between the blocks for the same reason described above. To insure the rigid motion of all six weight blocks, a large steel plate, 11 ft × 4 ft × 1 in. (3.35 m × 1.22 m × 25 mm) was placed across the gap between to two topmost weight blocks. Three 1-1/4-in. (32-mm) diameter post-tensioning tendons were used to tie the steel beams to the six-weight-block assembly and six 1-in. (25-mm) diameter post-tensioning tendons were used to tie the six-weight-block assembly together.

To prevent collapse of the specimen during the tests due to excessive lateral displacement, eight steel chains were connected to six corners of the weight blocks, as shown in Figure 4.21(b). The length of the chain was adjusted to accommodate a displacement of at least 10 in. (0.25 m) of lateral column displacement, which corresponds to the maximum displacement of the previous test.

4.3.2 Coordinate System

Figures 4.30(a–c) show the global coordinate system of a specimen on the shaking table and the system used to number the longitudinal bars to help identify the location of the damage. The north-south axis is assigned to the x direction (transverse direction); the east-west axis is the y direction (longitudinal direction); and the vertical direction is the z direction in this study. The origin of the xy plane of the coordinate system is taken as the center of two columns. The origin of the z-axis is assumed to be at the top of the footing of the long column, as shown in Figure 4.30(c).

4.3.3 Instrumentation

4.3.3.1 Overview

A total of 185 channels were used on each of the shaking table tests. The channels were distributed as follows:

- 16 channels for monitoring accelerations and displacements of the shaking table;
- 24 channels for tri-axial load cells monitoring the restoring force of the specimen (12 channels for each column);
- 18 channels for accelerometers;
- 32 channels for linear displacement potentiometers (LPs) monitoring global displacement;
- 48 channels for direct current displacement transducers (DCDTs) monitoring local column deformation;
- 40 channels for strain gauges monitoring longitudinal reinforcing bars; and
- 2 channels for load cell monitoring of tendon behavior.

The data were sampled at a rate of 0.005 s. More detailed information on the instrumentation is presented below.

4.3.3.2 Shaking Table Instrumentation

A total of 16 channels were used to capture the performance of the shaking table. The details of the instrumentation of the shaking table can be found in Section 3.3.3.2.

4.3.3.3 Load Cells

Figure 4.22 shows the setup of the four tri-axial load cells for each column. These load cells supported the column at its four corners, monitoring the axial load and the shear forces in the x and y directions. The recorded axial loads were used to the compute bending moment capacity of the columns, and the shear forces were used to estimate the shear force applied to the columns.

A 200-kip (890-kN) load cell with a center hole was placed underneath each column to monitor behavior of the prestressing tendons.

4.3.3.4 Accelerometers

Accelerations were measured by accelerometers mounted at seven locations on the specimens and the weight blocks, as shown in Figures 4.31(a–b). Groups of three accelerometers, which monitored accelerations in three directions (horizontal *x* and *y* and vertical *z*), were placed on the center of gravity of the specimen and the top of the weight blocks. Groups of two accelerometers, which monitored accelerations in two horizontal directions, were placed on the footings. Measurements from the footings were used as the input acceleration of the subsequent analyses.

4.3.3.5 Linear Potentiometers (LPs)

Specimen movements and deformations during the tests were captured by a total of 32 linear potentiometers (LPs) as shown in Figures 4.32(a–b). Because the stiff instrumentation frames were placed in the south and west sides of the shaking table, the displacements of the specimen were measured from the south and west sides.

The displacement of the footings was measured by three LPs at the south and west faces. A total of eleven LPs were placed at the south and west faces of the weight block assembly. Three of them were placed at the center of gravity of the assembly, and four were placed near the top edge of the weight blocks. The other four were placed at the bottom edge of the weight blocks, and these pairs of LPs were arranged to capture rotational movement of the specimen.

To capture local deformations of the long column, six LPs for both the south and west directions were placed at 2 in. (51 mm), 6 in. (152 mm), 12 in. (305 mm), 18 in. (457 mm), 46 in. (1,168 mm), and 58 in. (1,473 mm) from the bottom of the long column. Another six LPs for the south direction were placed to capture local deformation of the short column at 2 in. (51 mm), 6 in. (152 mm), 12 in. (305 mm), 18 in. (457 mm), 38 in. (965 mm), and 50 in. (1,270 mm) from the bottom of the short column.

4.3.3.6 Direct Current Displacement Transducers (DCDTs)

A total of 48 direct current displacement transducers (DCDTs) were used to measure the relative vertical displacements between different sections along the height of the column. These data were used to estimate average curvatures of the columns. Figure 4.33 shows the locations of the DCDTs.

For the DCDT instrumentation setup, 1/2-in. (13-mm) diameter threaded rods were placed at heights of 2 in. (51 mm), 6 in. (152 mm), 12 in. (305 mm), 18 in. (457 mm), 46 in. (1,168 mm), and 58 in. (1,473 mm) during the construction for the long column and at heights of 2 in. (51 mm), 6 in. (152 mm), 12 in. (305 mm), 18 in. (457 mm), 38 in. (965 mm), and 50 in. (1,270 mm) for the short column. The DCDTs were placed approximately 3-1/2 in. (89 mm) from the column surface. Actual horizontal distance between the DCDTs and the column surface, and vertical distance between the rods and the surface of the footing or top slab, were measured prior to the tests. The readings from the pairs of DCDTs located at 2 in. (51 mm) and 6 in. (152 mm) were used to estimate the amount of rebar pullout from the footing.

4.3.3.7 Strain Gauges

A total of 20 strain gauges was used to monitor strain of longitudinal reinforcement in each column. Three strain gauges were used at the bottom of the column and two at the top of the column for the north, east, south, and west sides. Figure 4.34 shows the locations of the strain gauges. Placement of the gauges on the unbonded bar required removal of a small section of the unbonding material (Teflon tubing) to permit attachment of the electrical wiring at each strain gauge position. After coating each mounted gauge to protect it from moisture, plastic shrinkage tube was used to encase that region in lieu of the Teflon tubing segment that had been removed. To allow the attached wiring to move with the strain gauge, it was enclosed in foam pipe insulation to separate it from the encasing concrete.

Four reinforcing bars, located at the north, east, south, and west sides, were gauged and protected with coating materials from Vishay Micro-Measurements prior to construction. The gauges were placed at the rebar surface facing outward.

4.3.4 Data Acquisition and Documentation of Damage

The data were recorded during the tests by the shaking table's data acquisition system. All the instruments of each specimen were calibrated with cables prior to the tests. The sampling rate of the data were 200 Hz.

Data recording was initiated a few seconds prior to the beginning of the earthquake signal and finished after checking for negligible movement of the specimen.

In addition to these digital data recorded, digital videos were taken during the tests to document global behaviors and progress of localized damage. Seven video cameras were used simultaneously: four cameras recorded the local deformation of the top and bottom regions—where the plastic hinge was expected to be developed at the east and the north faces—and three cameras were used to capture a global response of the specimen from the east, north, and northeast sides.

Digital photographs were also taken prior to and after each test to document localized damage of the columns. In the intervals between tests, concrete cracks that occurred during the tests were traced manually by colored markers for easy identification.

Crack patterns, discussed in Section 4.4.2, were drawn as a flattened surface. The west, south, east, and north column faces were marked as W, S, E, and N, respectively, from left to right. To help identify the locations of localized damage, the specimens were painted white and a grid pattern was drawn with black markers on the specimen prior to the tests. Horizontal grid lines were spaced at 4-in. (102-mm) intervals vertically along each column; vertical grid lines were spaced at 30-degree increments (about 4.2 in.) around the perimeter. Because the top and bottom parts of each column were covered with steel jackets, the damage inside the steel jackets could not be evaluated during the tests.

4.3.5 Ground Motion

The same modified Los Gatos records used in the previous testing were used as input signals for specimen PRC-system. The details of the input signals can be found in Section 3.3.5.

The fault-normal component was used for the x (N-S, transverse) direction; the fault-parallel component was used for the y (E-W, longitudinal) direction.

4.3.6 Test Sequence

A series of shaking table tests were performed. All tests performed for the specimen are shown in Table 4.6. In the shaking table tests, the ground motion intensity was increased in four steps; these test levels were named elastic, yield, design, and maximum levels.

The specimen was expected to remain elastic during the elastic-level test. This test is intended to check the shaking table performance and instrumentation setup, as well as to establish the baseline dynamic characteristics of the specimen under low-level excitations. Next, the specimen was subjected to a test during which the reinforcing steel was expected to reach, or only slightly exceed, the initial yield level. The yield-level test determines the initial dynamic stiffness of the specimen and identifies the column behavior under relatively small amplitude shaking associated with a frequent earthquake. The level was then increased to the design level. For the design-level test, the specimen was expected to experience a response ductility of about 4 in the transverse direction. Following the design-level, maximum-level earthquake shaking was imposed. For the maximum-level run, the specimen was expected to endure a displacement ductility of 8 in the transverse direction, just slightly less than the computed ultimate ductility capacity of the column. To achieve the targeted displacement ductility levels, the intensities of ground shaking were determined based on the results of previous tests and nonlinear dynamic analysis (not shown in this report).

4.4 EXPERIMENTAL RESULTS

4.4.1 Introduction

The results obtained from the shaking table tests of the PRC-system specimen are presented in this section. The damage of each column observed during each test run is described in Section 4.4.2. Global response measurements, i.e., natural frequency, time histories of acceleration, base shear and displacement of center of gravity, and hysteresis loops, are discussed in Section 4.4.3. Local response measurements, i.e., curvature, bar pullout, shear deformation, column deformation, local strain, and tendon force, are discussed in Section 4.4.4.

To compute the maximum relative displacement of the specimen, the difference between the measured horizontal displacement at the center of gravity of the mass block assembly and the horizontal displacement at the footing level was computed for the x and y directions for each column.

In addition to the instantaneous projections of the displacement of the specimen onto the *x*- and *y*-axes, the instantaneous vector of horizontal displacement of the center of mass relative to the center of the footing was computed to determine the overall maximum peak and residual lateral displacements of each column. Relative residual displacements are reported either as (1) relative values based on the position of the specimen at the start of a particular run or (2) cumulative values based on the position of the specimen at the beginning of the first run. This enables assessment of the overall deformed position of the structure, as well as the effect of a particular run. When mentioned in the text, the drift ratios are based on the displacement quantity under discussion divided by the vertical distance from the top of the footing to the center of mass. Displacement ductility values presented are computed as the displacement quantity of interest divided by the nominal yield displacement of the column computed using the static pushover analysis described in the Caltrans SDC.

Load cell data were used to calculate the lateral base shear and global overturning moments.

4.4.2 Damage Observation

This section describes the damage observed in the long and short columns throughout the testing. Table 4.7 presents a summary of the tests for each of the columns and describes the damage evolution for each column in detail, along with abstracted information regarding the peak motions of the shaking table and specimen during the run.

Overall, no cracks or visual signs of damage were observed in either column after the elastic-level test, as expected. Only minor cracking was observed after the yield-level test; a horizontal hairline crack was observed around the column perimeter at the interface of the column with the footing.

The design-level test resulted in some additional cracks in the middle of the columns, but no spalling of the cover concrete was observed. In each column a large crack was found at the joint of the column and footing, and a small crack was found at the joint of the column and top block. No damage was observed at the steel jackets. Most cracks in the middle of each column were observed to be concentrated on the south side. At this stage, the measured permanent residual deformations were all generally quite small, as can be seen in Table 4.7.

The maximum-level earthquake caused an increase in displacement demand, and resulted in crushing and a large crack opening at the bottom of each column. The crack enlarged in the middle of the column, but still no spalling of the cover concrete was observed. Also, no damage of the steel jackets was observed.

Figures 4.35 and 4.36 show the local damage of the long and short columns at the bottom and middle part after the design-level and maximum-level tests. As shown in Figures 4.35(a–b), a perimeter crack was observed for each column after the design run. A large crack opening and concrete crushing due to the displacement of the columns during the maximum run are shown in Figures 4.36(a–b). The cracks primarily occurred at the north side of each column because the main displacement of the column was in the south direction (i.e., the main tension region of the column was the north side). Because there was no spalling of the concrete in the middle part of each column and no damage at the top or bottom of the steel jacketing, the columns appeared to have no damage, but the residual displacements were slightly large as seen in Table 4.7.

4.4.3 Global Response

4.4.3.1 Natural Frequency and Viscous Damping Properties

The pullback tests were not performed before and after each run due to time and practical constraints. Based on the previous test results, however, the natural frequency can be obtained with good accuracy without a pullback test. To determine the natural frequency and viscose damping properties, the free-vibration data of the end of each test result were used.

By obtaining the Fourier spectrum of the response to the free-vibration portion of each run, it was possible to approximate the period of the columns. In order to approximate the damping, it is common to use the half-power (band-width) method, using a power spectral density estimate. The results obtained were fairly consistent, especially for the period of vibration, but it was very difficult to get a consistent damping ratio result in the y direction.

Table 4.8 shows the obtained fundamental period and damping ratio (at the end of each run). The values were also plotted as they changed throughout the test (see Figs. 4.37 and 4.38). The results for the short and long columns were very similar in most cases, except for the damping ratio after the maximum-level test. The column period gradually elongated from about 0.57 s at an undamaged state to about 1.2 s at the end of the maximum-level test in the x direction. In the y direction, the fundamental period showed little change during all test levels.

The viscous damping ratio also gradually increased with repeated loading, ranging between 2.0%–20% in the *x* direction. In the *y* direction, it was very difficult to get a consistent damping ratio as each column had a different lateral displacement history. The increase in the measured period and damping coefficients is likely associated with the increased inelastic action in the damaged column at lower levels of excitation. Differences in fundamental period and damping values appear consistent with the differences in the physical damage of each specimen. The trends of the *x* vs. *y* directions are quite different, as expected.

4.4.3.2 Acceleration

The acceleration responses were directly obtained from accelerometers attached to the specimen. The measured accelerations were low-pass filtered with cutoff frequency of 20 Hz to remove the high-frequency measurement noise. Figures 4.39 and 4.40 show acceleration response at the center of gravity of the mass blocks for each column in the *x* direction and for the long column in the *y* direction. Table 4.9 summarizes the maximum acceleration values.

The results of the short and long column were very similar in the *x* direction. In the *y* direction, the results show the high-frequency components, as expected. The response accelerations of both columns in the maximum-level test have small offsets at the end of the response because the accelerometers recorded the acceleration of gravity due to tilting of the specimen.

The maximum acceleration values of each run are plotted for each column in Figure 4.41. In general, the maximum acceleration of the specimen gradually increased in both directions with repeated loading.

4.4.3.3 Displacement

The displacement histories were tracked over each test run. Peak relative displacement and cumulative peak relative displacement are defined in Section 3.4.3.3 and illustrated in Figure 3.50.

Table 4.10 lists values of peak relative and residual displacements in the *x* and *y* directions, and distances from the origin. The distances from the origin were calculated to find the maximum and residual distances of each test. Figures 4.42 and 4.43 show the relative displacement responses at the center of gravity for the design and maximum-level tests, respectively. The orbits of the design and maximum-level tests are shown in Figure 4.44. The cumulative maximum and cumulative residual distances calculated from the origin for each test level are shown in Figures 4.45 and 4.46, respectively.

Elastic- and Yield-Level Tests

In general, there were no residual displacements following the elastic and yield-level tests, as expected.

Design-Level Test

As shown in Figure 4.42, the long and short columns exhibited similar directional responses during the first design-level excitation. For example, the cumulative peak displacements were larger in the x direction, equaling 4.23 in. (107.4 mm) and 4.44 in. (112.8 mm) for the long column and short column, respectively. These values correspond to a nominal displacement ductility factor of about 4. The cumulative peak displacement for the y direction was 0.467 in. (11.9 mm). The specimen demonstrated an ability to re-center (see Fig. 4.47). The residual drift ratios for each column in the transverse direction were smaller than 0.4%, which corresponds to about 40% of the yield displacement. There was almost no residual displacement in the longitudinal(y) direction.

Figure 4.44(a) shows an orbit of response displacements at the center of gravity of the top blocks. The specimen mostly responded in the north-south direction, which corresponds to the transverse direction of a two-column bent. The orbit shows a generally symmetric shape at the origin in the design-level test.

Maximum-Level Test

In both columns the specimen reached maximum response in the x direction during the second main pulse. During this pulse, the columns did not return to the opposite side, resulting in large residual displacements. In general, the short column showed slightly larger maximum and residual displacements for all the tests. The cumulative maximum response displacements from the origin were 7.7 in. (196 mm) and 8.7 in. (221 mm) for the long column and short column, respectively, corresponding to a nominal displacement ductility of about 8. The cumulative residual displacements from the origin largely increased during the maximum-level test. These displacements were 3.78 in. (96 mm) and 4.18 in. (106 mm) for the long column and short column, respectively. The residual displacement was mostly induced by the *x*-direction response. As evident in Figure 4.48, the tilting of the specimen in the *x* direction was visible to the eye at the end of the maximum-level test.

Figure 4.44(b) shows an orbit of response displacements at the center of gravity of the top blocks. The specimen mostly responded in the north-south direction, as it did during the design-level test, but the response was no longer symmetric about the origin; the response was inclined toward the south direction (positive *x*).

4.4.3.4 Lateral Force–Lateral Displacement Hystereses

Figures 4.49–4.52 show lateral force versus lateral displacement hystereses, based on the column shear and the displacement at the center of gravity of the top blocks, for the long column and short column in each direction. As shown in Figures 4.49(b)–4.52(b), no significant nonlinear response was observed for the *y* direction during the elastic through maximum-level tests. In the *x* direction, the results show more complicated shapes. The basic origin-oriented hysteretic shape can be detected in Figure 4.50(a) for some of the larger loops that occurred during the yield-level test in the *x* direction. As seen in Figure 4.51, during the design-level test, both columns produced similar skeleton curves as they moved away from the origin in the *x* and *y* directions.

Figures 4.52(a–b) show the displacement response and the lateral force versus lateral displacement hystereses at the maximum-level input. The result does not show negative post-yield stiffness; however, the residual displacement was larger than that of the design-level test.

4.4.4 Local Response

4.4.4.1 Curvature of Column

Curvatures were estimated over regions of the column, extending between the locations of DCDT instruments attached to the face of the column.

Figures 4.53(1 and 2) show curvature distributions along the long and short columns at positive and negative peaks during the elastic, yield, design, and maximum-level tests. The measurements that might possibly include the effect of pullout of reinforcement from the footing are not shown in the figure and will be discussed later. The curvature distributions show the typical distribution shape of a specimen using a steel jacket, with large curvature at the bottom region (i.e., at the joint of the column and footing) and at the top region (i.e., at the joint of the column and top block). The curvatures of the bottom region are generally larger than those of the top region.

Figures 4.54(1 and 2) show the average residual curvature distribution along the column in the x and y directions for all tests. At the design-level test, the residual curvatures for both columns in both directions were small and corresponded to the residual displacement results. For the maximum-level test, the residual curvatures were larger in the x direction, resulting in larger residual displacement.

4.4.4.2 Bar Pullout

The pullout of longitudinal reinforcement from the footing and the concrete crushing at the joint between the column and footing can be approximately calculated using the measurement data from the DCDT instruments mounted on rods located at 2 in. (51 mm) and 6 in. (152 mm) from the footing surface. The positive and negative differences between the two measurements can be considered, for practical purposes, as the pullout of the longitudinal reinforcement from the footing and as the concrete crushing at the joint of the column and footing, respectively. Figures 4.55 and 4.56 show the bar pull response (positive: pullout; negative: concrete crushing) of the north and south sides of both columns in the design and maximum-level tests, respectively. The maximum bar pullout values were plotted as they changed throughout the test for both columns (see Fig. 4.57).

Figures 4.55 and 4.56 show that the bar pullout and concrete crushing of the short column are greater than those of the long column. At the end of the maximum response, we can see the permanent bar pullout and concrete crushing, corresponding to the permanent residual displacement. The maximum concrete crushing (maximum negative north-side value in Figures 4.55 and 4.56) is almost half of the maximum bar pullout (maximum positive south-side value in Figures 4.55 and 4.56).

As shown in Figure 4.57, the maximum bar pullout value increased with increasing test levels. The large pullout of the short column can be seen in Figure 4.58, captured from the video file during the maximum-level test.

4.4.4.3 Shear Deformation

The shear deformation of the section can be approximately calculated from the horizontal displacement measurement (LP) at 2 in. (51 mm) above the long-column footing. The difference of this horizontal displacement measurement and the horizontal displacement measurement of the footing can be assumed to be the displacement contributed by shear over the bottom two inches of height. This measurement is an indirect indication of the amount of sliding that may have occurred at the interface between the column and the footing.

Figures 4.59(a–b) show the long column's shear deformation response at 2 in. (51 mm) in both directions for the design and maximum-level tests. The maximum shear values for the x and y directions were plotted as they changed throughout the testing; as shown in Figure 4.60**,** the maximum bar pullout value increased with increasing test levels. The shear response was larger in the x direction than in the y direction, as expected.

4.4.4.4 Deformation of Column

Figures 4.61 show deformation distributions along the long and short columns at positive and negative peaks during the design and maximum-level tests. As expected, response increases as the location of measurement moves toward the top of the column. The deformation distribution diagrams for the long and short columns are very similar for all test levels, as shown in the figure**.** At the design level, the deformations of the negative peak and positive peak of both columns show a symmetric shape in the x direction, but the deformation diagrams tend to a positive peak in the maximum-level test.

4.4.4.5 Strain

Figures 4.62–4.65 show the longitudinal reinforcing bars' maximum compression and tension strain distribution along the columns for the elastic, yield, and design-level tests. During the main pulses of the yield-level test, most of the longitudinal reinforcement near the bottom and top of the columns yielded, and during the design-level test maximum, the longitudinal reinforcement at the bottom and top of the columns was damaged and not able capture the strain of the reinforcement after the main pulses.

In summary, after examining the maximum strain of each test, it was found that the strains at the 2-in. (51-mm) or 11-in. (279-mm) height generally showed the maximum value, and the strain at 2 in. (51 mm) below the footing generally showed the minimum value.

4.4.4.6 Tendon Force

Figures 4.66(a–b) show prestressing force response of the tendons installed in the specimen during the design and maximum-level tests. The tendon force increased when the deformation of the specimen increased, and it decreased when the specimen returned to near the origin, as expected.

Table 4.11 shows the initial, maximum, and change of the tendon force throughout the testing for both columns. The maximum of the peak tendon force was 130 kip (579 kN) for the long column during the maximum-level test; this is less than the nominal yield value, 208 kip (926 kN), of the tendon.

Figure 4.67 shows the change of the initial tendon force at each level of testing for both columns. After each test, the tendon forces decreased. For example, the decrement of the tendon force in the short column during the maximum-level test was 1.69 kip (7.5 kN). Figure 4.68 shows maximum tendon force. The peak relative tendon forces of the long and short columns at each test level were very similar.

4.5 CONCLUSION

To evaluate the practical application, i.e., to a real bridge system, of a newly developed self-centering system, a series of shaking table tests was conducted. The specific objective of this testing was to investigate the effect of sheathing with a steel jacket and unbonding the mild reinforcing bars in the vicinity of the expected plastic hinge for a two-column bent system.

A two-column bent reinforced concrete bridge system with columns of different height, each containing an unbonded prestressing tendon, was designed and constructed. The specimen contained the unbonded mild bar and steel jacket at the expected plastic hinge. The diameter of each column was 16 in. (0.41 m). The aspect ratio for the short column was 6 and that of the long column was 6.5.

The specimen was tested under two components of horizontal ground excitation. Modified Los Gatos records from the 1989 Loma Prieta earthquake were used as input ground motions. The specimen was subjected to four levels of ground motion intensity; they are referred to as the elastic level (10% as a scaling factor), the yield level (20%), the design level (45%), and the maximum level (70%).

Below are the conclusions determined from the shaking table tests:

- The cumulative peak displacements were larger in the *x* direction, equaling 4.23 in. (107.4 mm) and 4.44 in. (112.8 mm) for the long column and short column, respectively. During the maximum-level test, the cumulative maximum response displacements from the origin were 7.7 in. (196 mm) and 8.7 in. (221 mm) for the long column and short column, respectively, corresponding to a nominal displacement ductility of about 8.
- The cumulative peak displacements in the *y* direction were 0.47 in. (11.9 mm) and 0.7 in. (17.8 mm) for design and maximum level, respectively.
- After the design-level test, the specimen demonstrated an ability to re-center. The cumulative residual displacements for the two columns were smaller than a drift of 0.4%, corresponding to about 40% of the yield displacement. But the cumulative residual displacements greatly increased during the maximum-level test; the cumulative residual displacements from the origin were 3.78 in. (96 mm) and 4.18 in. (106 mm) for the long column and the short column, respectively. There was almost no residual displacement for the *y* direction after the design and maximum-level tests.
- During the design-level test, both columns showed similar lateral force versus lateral displacement hystereses as they moved away from the origin in the *x* and *y* directions. The result does not show negative post-yield stiffness; however, the residual displacement was larger in the maximum-level test.
- The design-level test resulted in some additional cracks in the middle of the columns, but no spalling of the cover concrete was observed. For each column a large crack was found at the joint of the column and footing; a small crack was found at the joint of the column and top block. A small crack was also detected in this area at the joint of the column and top block for each column. The maximum-level earthquake caused an increase in displacement demand and resulted in the opening of a large crack and crushing at the

bottom of the column between the steel jacket and the footing. The cracks enlarged in the middle of the column away from the jackets, but still no spalling of the cover concrete was observed. Until the maximum-level test, no damage was observed at the steel jacket.

- For both columns, the tendon remained elastic during the tests.

Table 4.1 Differences of specimens PRC-UJ and PRC-system

Specimen	PRC-UJ	PRC- System
Number of columns	1 column	2-column system
Aspect ratio	6	6 for short column 6.5 for long column
Reinforcement	12- No. 3 bar	12- No. 3 bar for each column
Spiral	W3.5 wire with 1.5-in. spiral pitch	W3.5 wire with 1.5-in. spiral pitch
Steel jacket	Steel jacket (h = 2*D*) at the bottom of the column	Steel jacket (1*D*) at the top and bottom of each column
Unbonded mild bar	Unbonded mild bar (2*D*) at the bottom of the column	Unbonded mild bar (1*D*) at the top and bottom of each column
Gap between jacket and footing	No gap	0.5-in. gap at the top and bottom of each column
Prestressing tendon	1-3/8-in. diameter	1-3/8-in. diameter

Table 4.2 Compressive strength of concrete

(a) Concrete for footings

Day	No. 1 (ksi)	No. 2 (ksi)	No. 3 (ksi)	Average (ksi)
7	3.23	3.34	3.15	3.24
28	4.69	4.33	4.60	4.55
73 (testing day)	5.93	6.23	5.77	5.98

(b) Concrete for columns

Day	No. 1 (ksi)	No. 2 (ksi)	No. 3 (ksi)	Average (ksi)
7	2.20	2.52	2.18	2.30
14	3.21	2.77	2.92	2.97
21	3.01	3.40	3.37	3.26
28	3.94	3.95	3.56	3.82
53 (testing day)	4.26	4.09	4.02	4.14

Note: After 7 days of curing, the form was removed.

Table 4.3 Concrete properties from cylinder tests

No.	Strength (MPa)	Modulus of elasticity (GPa)	
		Tangent modulus $E_{c \cdot tan}$	Secant modulus $E_{c \cdot sec}$
No. 1	29.39	20.21	18.04
No. 2	28.22	19.71	17.68
No. 3	28.08	19.54	17.57
Average	28.56 (4.14 ksi)	19.82 (2,873 ksi)	17.76 (2,574 ksi)

Table 4.4 Mechanical properties of steel from tensile test

(a) No. 3 (10-mm diameter) Reinforcing Bar

	Yield strength (MPa)	Ultimate strength (MPa)	Modulus of elasticity (GPa)
No. 1	476.4 (69.1 ksi)	629.5 (91.3 ksi)	202 (29,300 ksi)
No. 2	470.2 (68.2 ksi)	634.3 (92.0 ksi)	193 (28,040 ksi)
Average	473.3 (68.7 ksi)	631.9 (91.7 ksi)	198 (28,700 ksi)

(b) W3.5 Wire

	Yield strength (MPa)	Ultimate strength (MPa)	Modulus of elasticity (GPa)
No. 1	-	731 (106 ksi)	198 (28,700 ksi)
No. 2	-	738 (107 ksi)	185 (26,800 ksi)
Average	-	734 (107 ksi)	191 (27,800 ksi)

(c) 1-3/8-in. (35-mm) Diameter Tendon

	Yield strength (MPa)	Ultimate strength (MPa)	Modulus of elasticity (GPa)
No. 1	945 (137 ksi)	1110 (161 ksi)	190 (27,600 ksi)
No. 2	958 (139 ksi)	1103 (160 ksi)	194 (28,100 ksi)
Average	952 (138 ksi)	1106 (161 ksi)	192 (27,900 ksi)

(d) Gage 16 (1.5 2mm) Thickness Steel Jacket

	Yield strength (MPa)	Ultimate strength (MPa)	Modulus of elasticity (GPa)
No. 1	284 (41.3 ksi)	348 (50.5 ksi)	180 (26,100 ksi)

Table 4.5 Total axial force ratio

Specimen	Concrete strength (f'_{c0}) ksi	Area of section (A_g) in^2	Axial force (P) kip	Prestress force (P_{ps}) kip	Total force (P_{total}) kip	Total axial force ratio (α_{total}) %
Long column	4.14	188.49	54.4	49.10	103.5	13.26
Short column	4.14	188.49	54.4	48.98	103.4	13.25

Table 4.6 Test sequence

No.	Test	Signal (% of signal)	Date	File name
H-1	Free vibration *x*	-	8/3/2006	20060803 104755
H-2	Free vibration *y*	-	8/3/2006	20060803 104816
H-3	Elastic-level run	10	8/3/2006	20060803 115218
H-4	Yield-level run	25	8/3/2006	20060803 130623
H-5	Design-level run	45	8/3/2006	20060803 144707
H-6	Maximum-level run	70	8/3/2006	20060803 153939

Table 4.7 Summary of response for specimen PRC-system (long column)

Run #	Performance Level	Table Displacement and Acceleration		Relative Displacement		Observation
		PGA (g)	PGD (in.)	Peak[a] (in.)	Residual[b] (in.)	
		x	x	x	x	
1	Elastic level 10%	0.176	0.434	0.414	0.015	No cracks or visual signs of damage.
2	Yield-level 1 25%	0.296	0.918	1.607	0.039	A perimeter crack formed at the interface with top and bottom of the steel jacket.
3	Design-level 1 50%	0.436	2.088	4.183	0.411	Several cracks appeared at the middle of the column on north side.
4	Maximum level 1 75%	0.688	3.227	7.316	3.781	Cracks that appeared during the design-level test enlarged during maximum level. A large crack was observed at the bottom. The column and footing evidenced separation, with the large crack opening and crushing. No spalling in concrete and no damage in steel jacket observed.

[a] Peak relative displacement assuming zero displacement at the beginning of each test.

[b] Cumulative residual relative displacement at the end of the test.

Table 4.8 Change of natural period and damping ratio

EQ level	Natural period (s)			Damping ratio (%)		
	x-Long	*x*-Short	*y*	*x*-Long	*x*-Short	*y*
Elastic	0.55	0.55	0.25	2.99	3.11	1.80
Yield	0.67	0.67	0.28	6.24	6.26	0.47
Design	0.93	0.95	0.28	11.46	11.48	0.95
Maximum	1.24	1.20	0.29	19.89	15.12	3.59

Table 4.9 Maximum acceleration response at C.G.

EQ level	Maximum acceleration (*g*)		
	x-Long	*x*-Short	*y*
Elastic	0.170	0.147	0.151
Yield	0.204	0.195	0.305
Design	0.285	0.286	0.466
Maximum	0.264	0.318	0.522

Table 4.10 Maximum and residual displacement response at C.G.

EQ level	Maximum displacement (in.) (Residual displacement) (in.)				Cumulative max displacement (in.) (Cumulative residual) (in.)			
	x-Long	x-Short	y	SRSS	x-Long	x-Short	y	SRSS
Elastic	0.414	0.437	0.079	0.415	0.414	0.437	0.079	0.414
	(0.015)	(0.027)	(0.003)	(0.015)	(0.015)	(0.027)	(0.003)	(0.015)
Yield	1.607	1.636	0.188	1.607	1.570	1.693	0.185	1.570
	(0.075)	(0.050)	(0.008)	(0.076)	(0.039)	(0.107)	(0.005)	(0.039)
Design	4.183	4.330	0.467	4.194	4.225	4.435	0.462	4.235
	(0.370)	(0.371)	(0.001)	(0.370)	(0.411)	(0.477)	(0.006)	(0.411)
Maximum	7.316	8.127	0.701	7.328	7.659	8.652	0.694	7.671
	(3.437)	(3.659)	(0.020)	(3.438)	(3.781)	(4.184)	(0.026)	(3.780)

Table 4.11 Change of tendon force

EQ level	Specimen	Tendon force (kip)		
		Initial	Maximum	Change
Elastic	Long column	49.10	51.38	-0.11
	Short column	48.98	51.00	-0.18
Yield	Long column	48.99	67.49	-0.31
	Short column	48.80	63.49	-0.67
Design	Long column	48.68	102.99	0.59
	Short column	48.13	90.42	-1.69
Maximum	Long column	49.27	129.34	24.58
	Short column	46.44	121.37	11.79

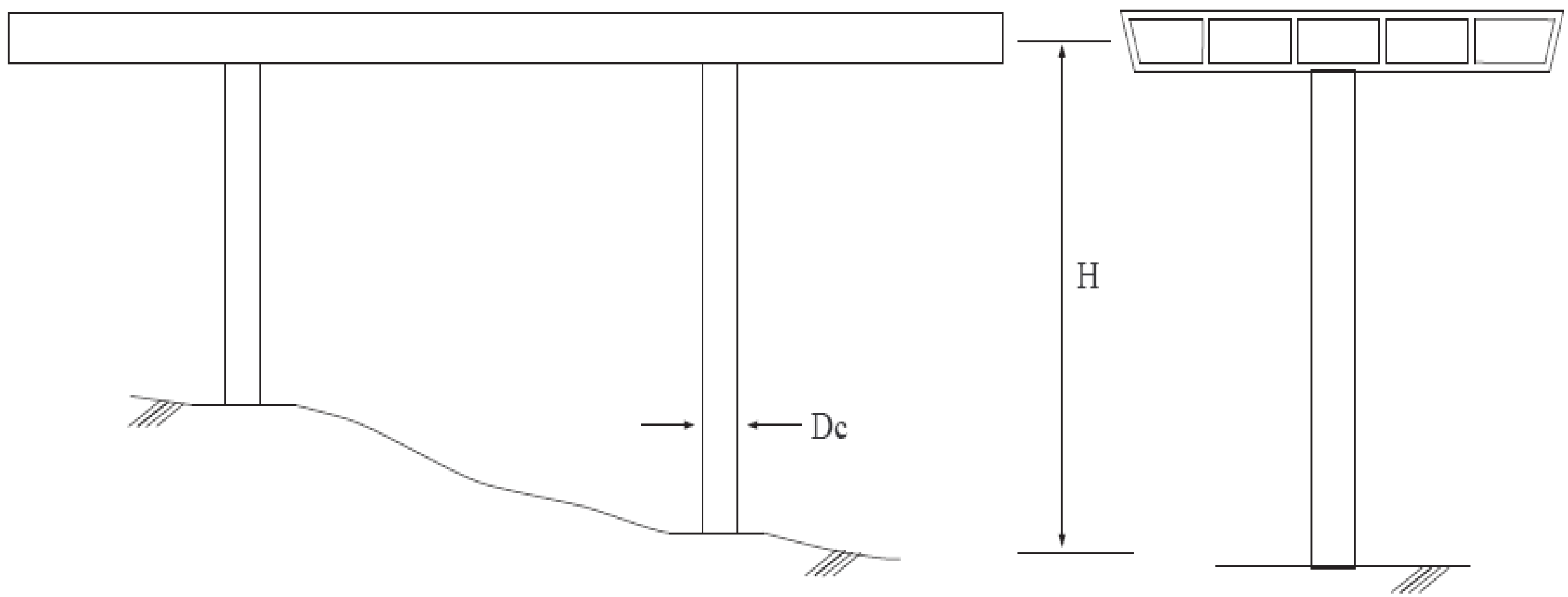

(a) Cross section

(b) Bridge column

Fig. 4.1 Prototype two-column bent bridge

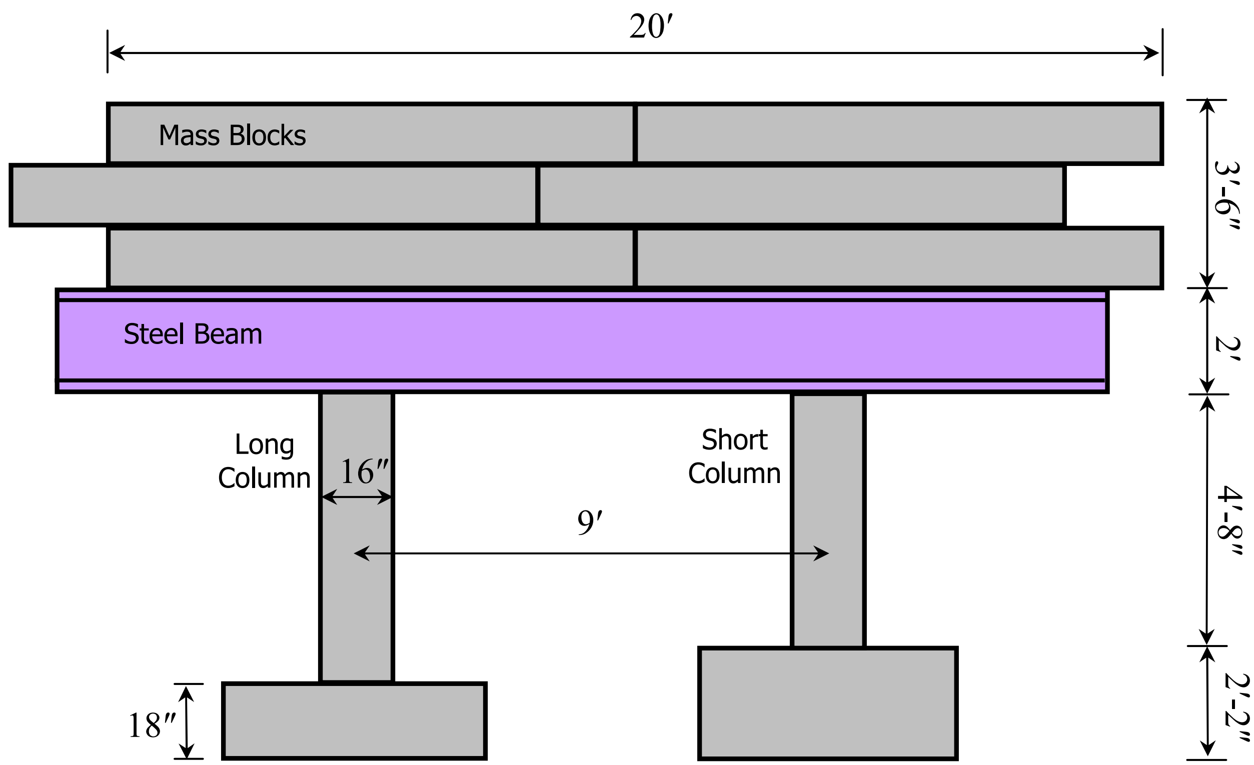

Fig. 4.2 PRC-system specimen with mass blocks

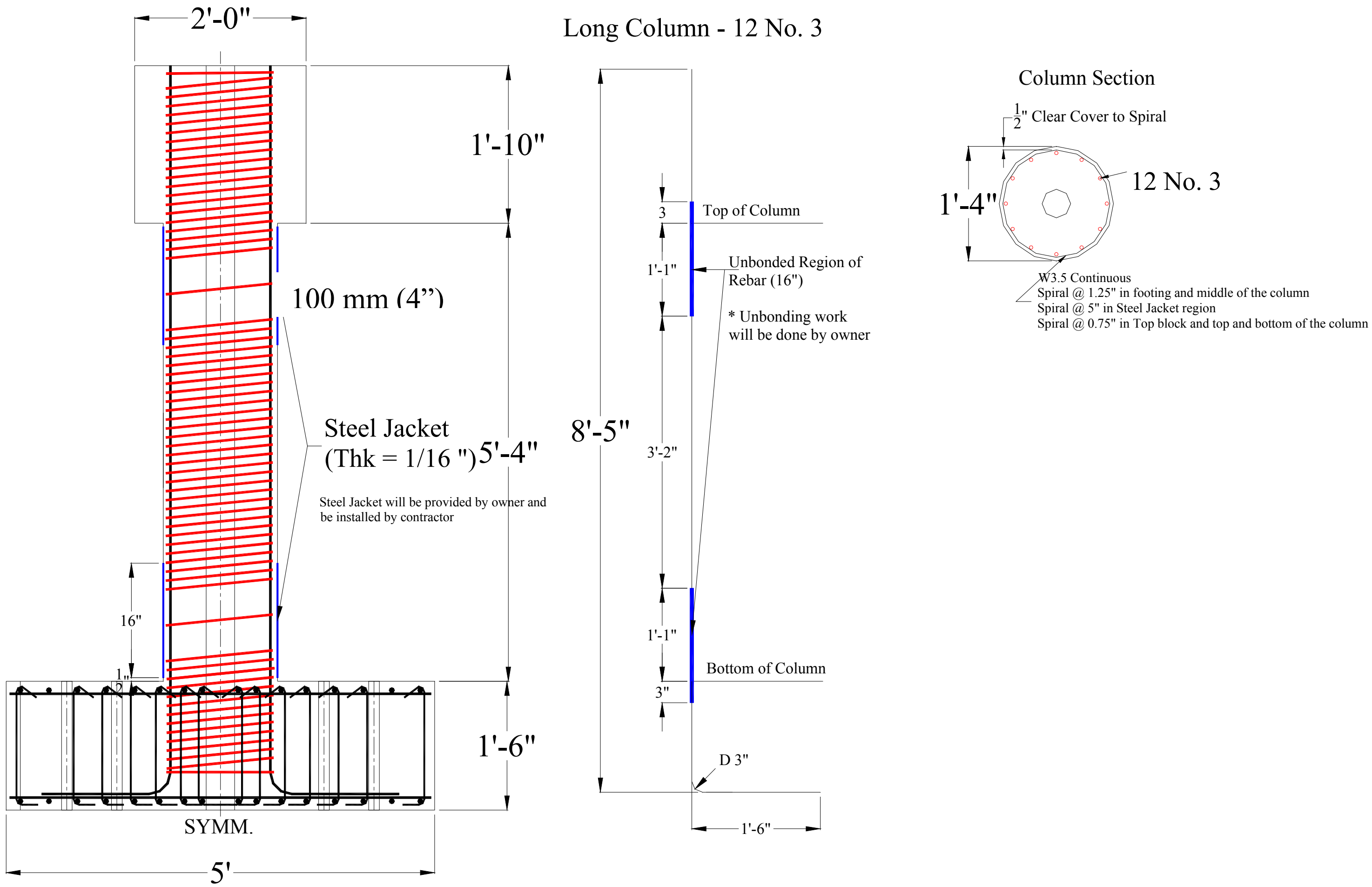

Fig. 4.3 Reinforcement details of specimen PRC-system

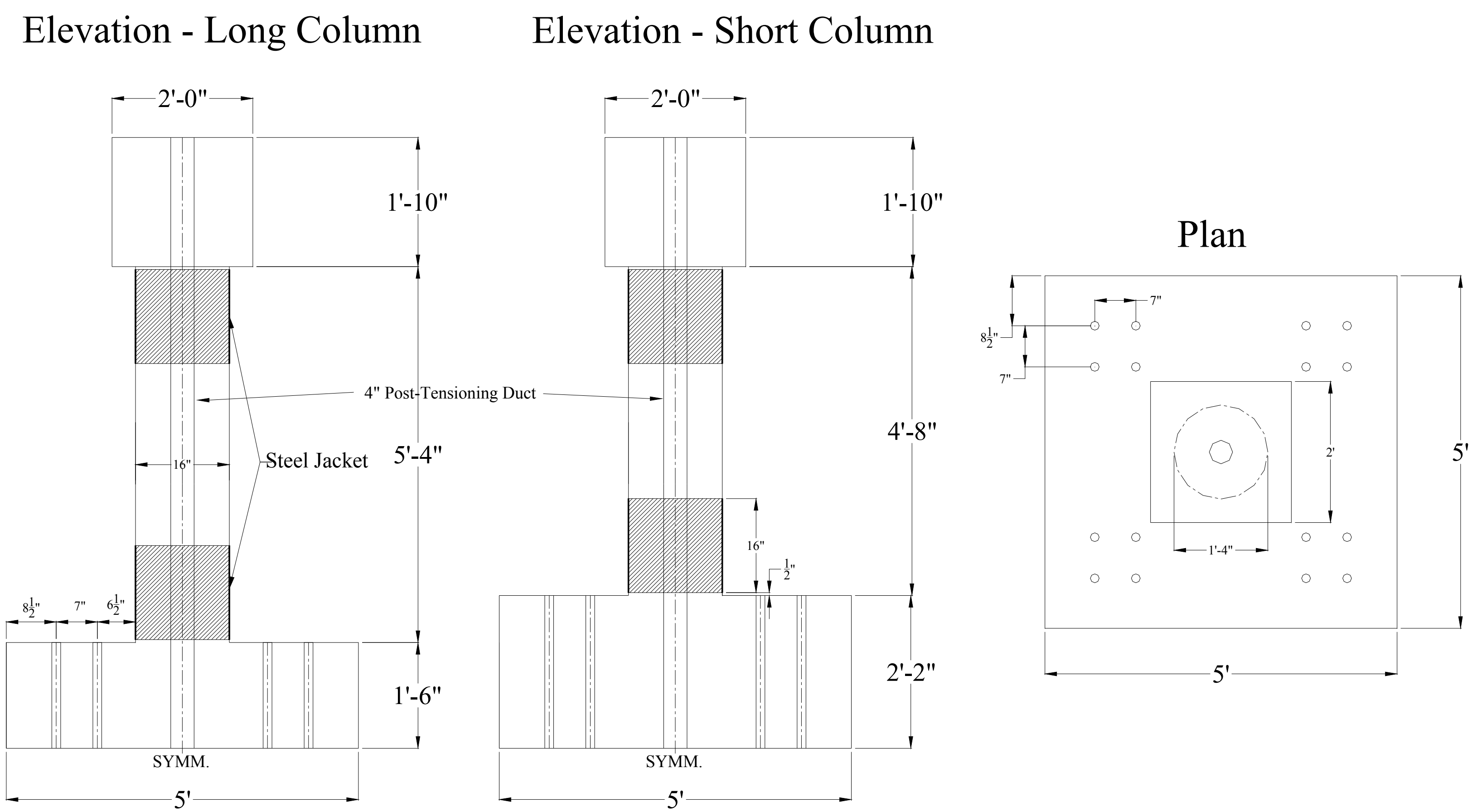

Fig. 4.4 Elevation and plan view of each column

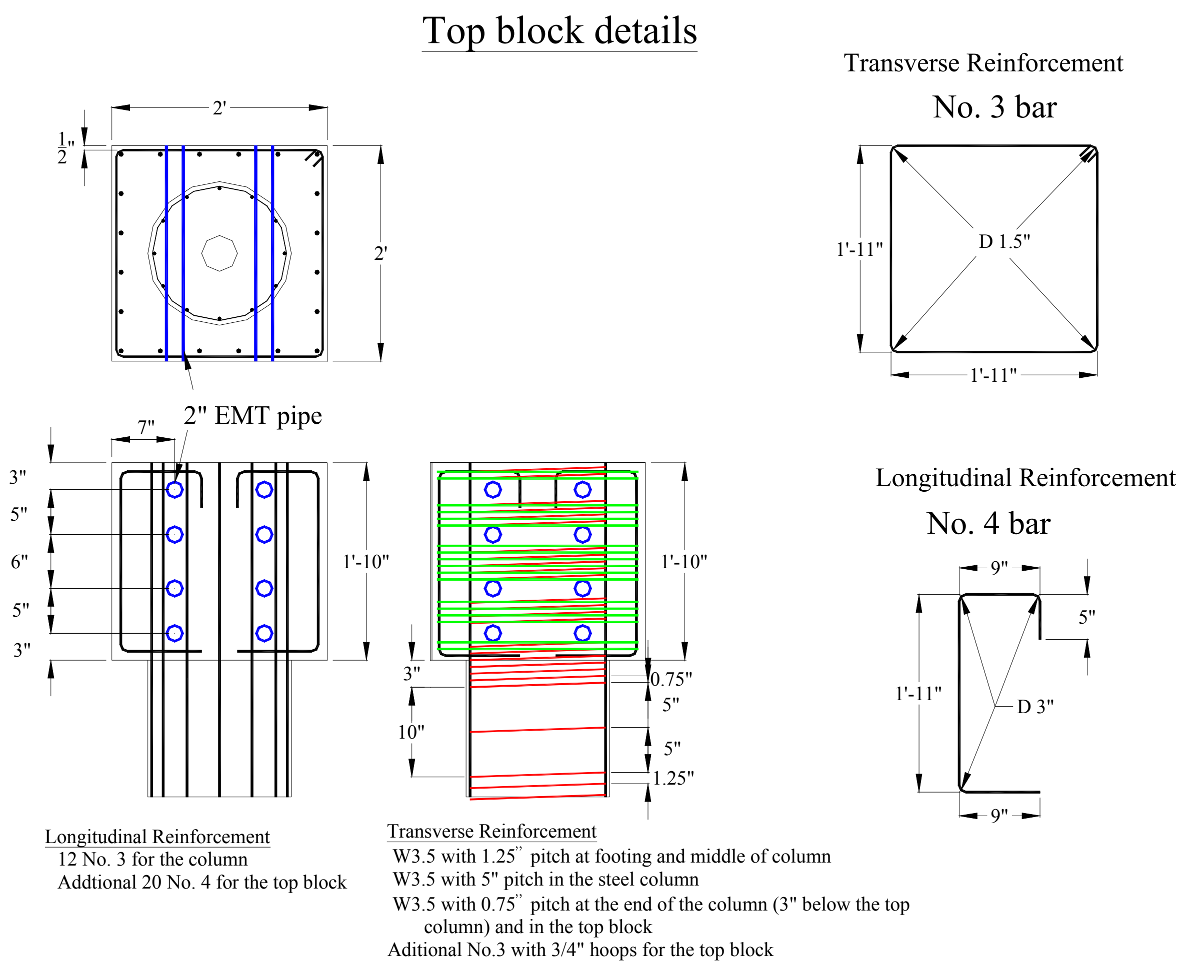

Fig. 4.5 Reinforcement details of top block

(a) One set of steel beams

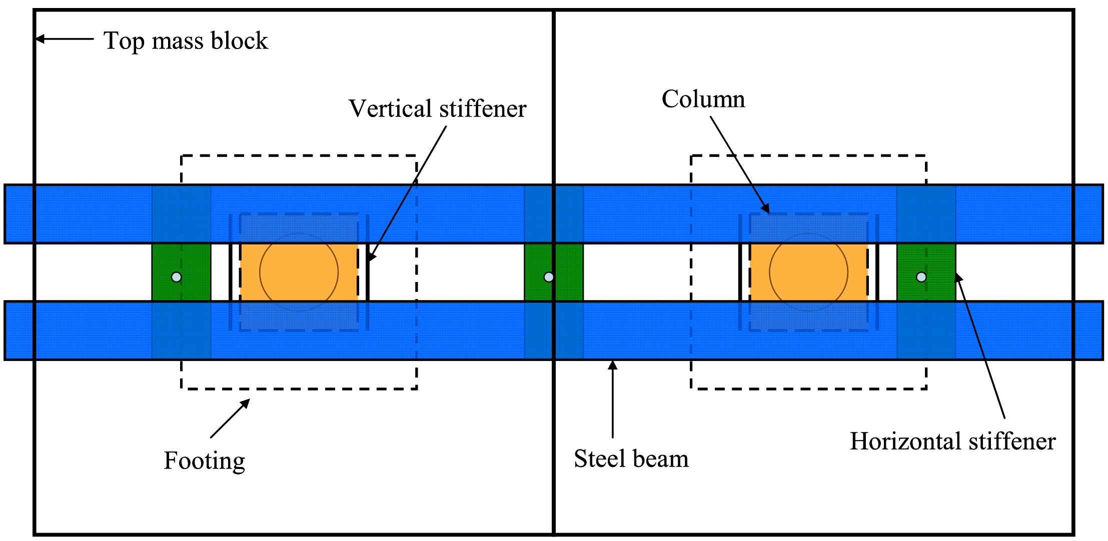

(b) Top view of steel beams setting

Fig. 4.6 Steel beams

Fig. 4.7 Construction of forms

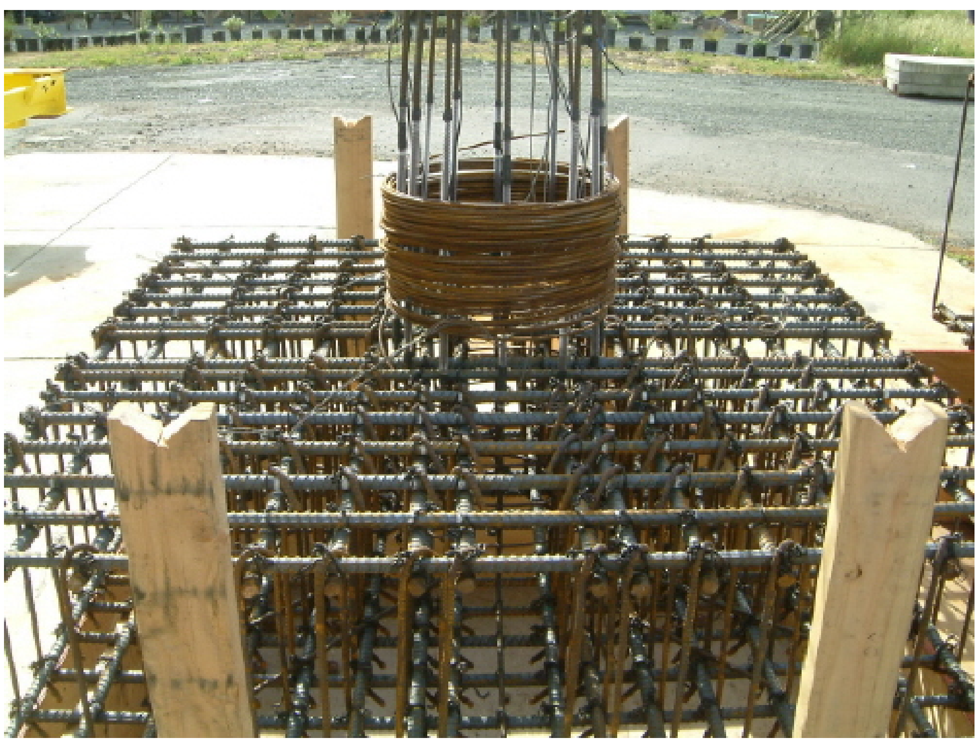

Fig. 4.8 Assembly of steel cages

Fig. 4.9 Unbonded mild bar

Fig. 4.10 Steel jackets

Fig. 4.11 Specimen and concrete truck

Fig. 4.12 Pouring concrete footing

Fig. 4.13 Column formwork (steel jacket)

Fig. 4.14 Column formwork

Fig. 4.15 Casting concrete column

Fig. 4.16 Completion of construction of specimen

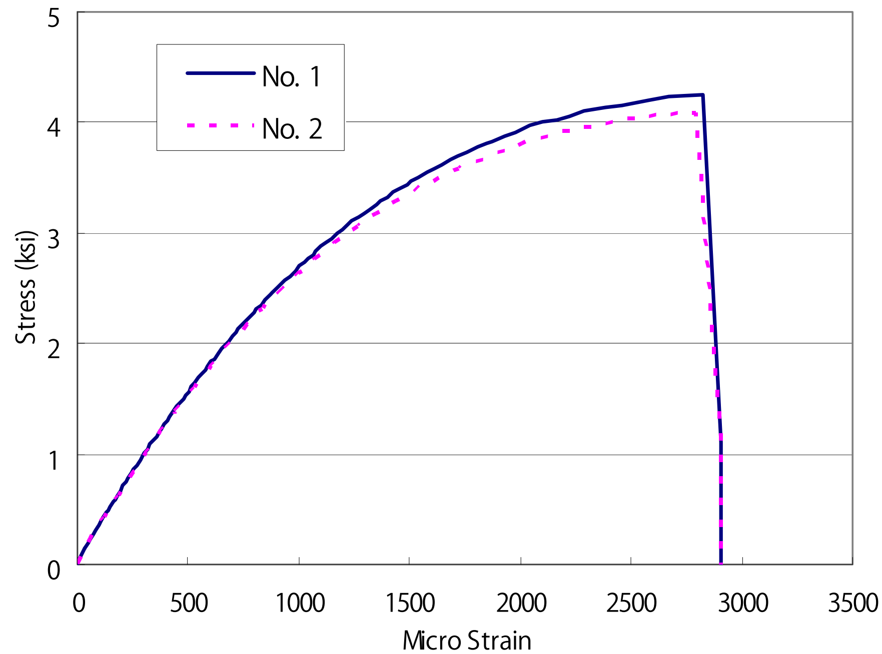

Fig. 4.17 Stress-strain curves of concrete cylinders

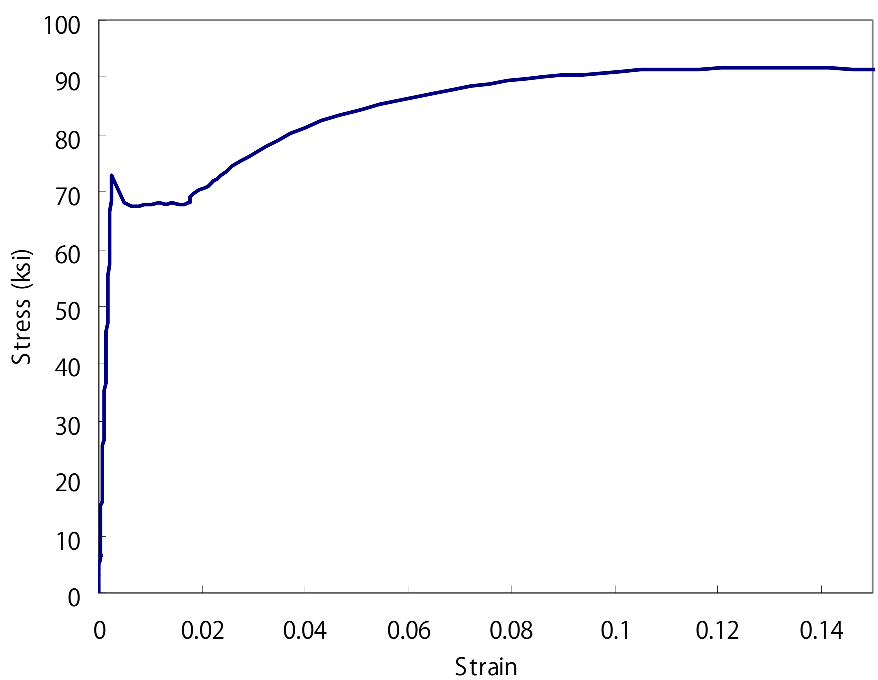

Fig. 4.18 Stress-strain curve of No 3 reinforcing bars

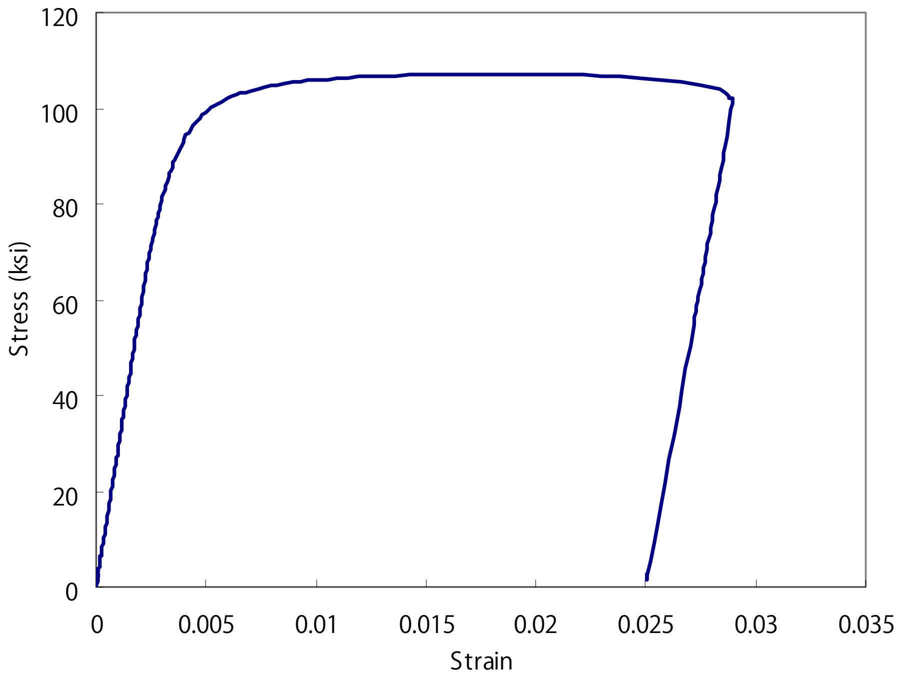

Fig. 4.19 Stress-strain curve of spiral wire

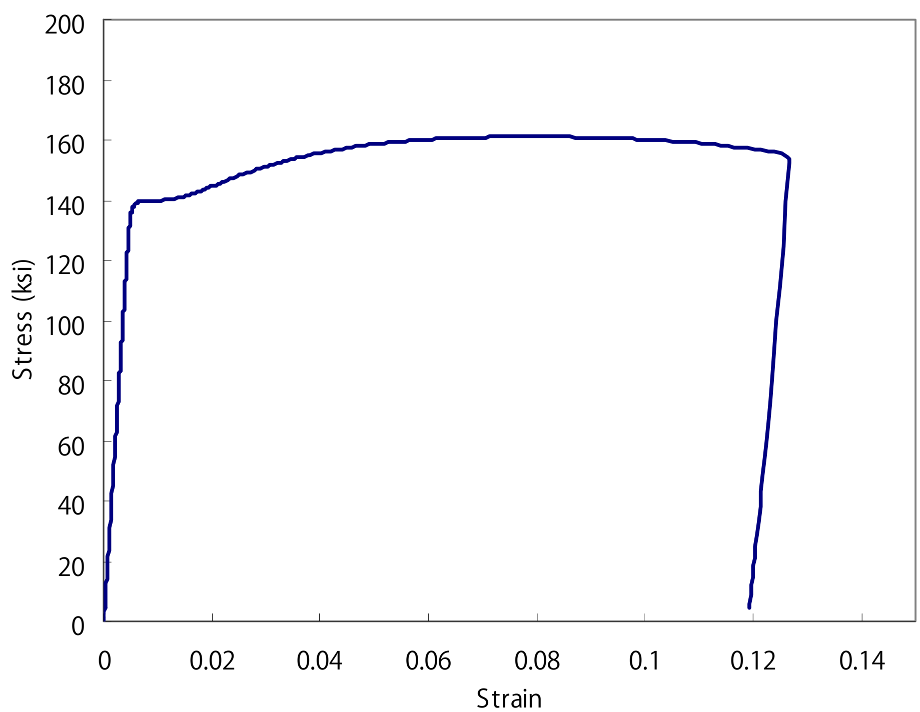

Fig. 4.20 Stress-strain curve of tendon

(a) Specimen on table

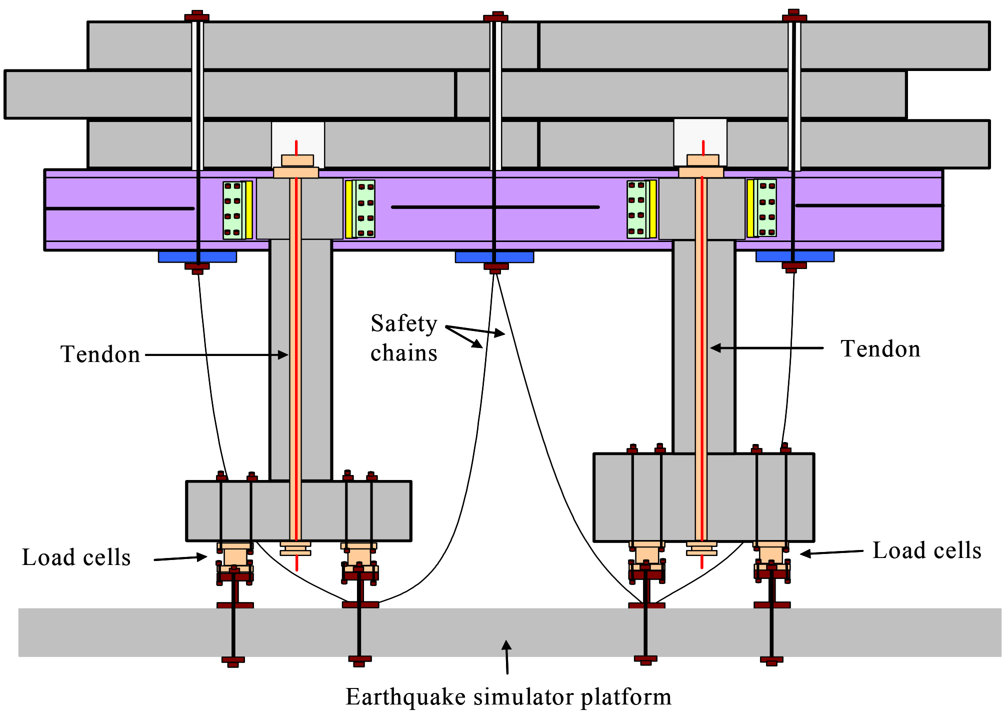

(b) Test setup

Fig. 4.21 Setup of specimen PRC-system

Fig. 4.22 Setup of steel beam and load cells

Fig. 4.23 Setup of first column on load cells

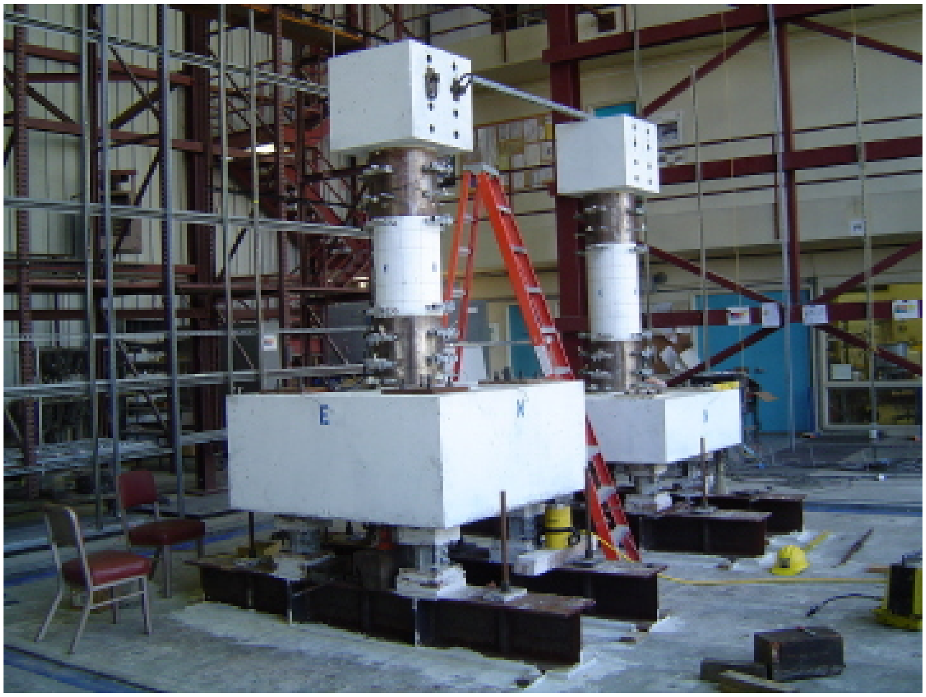

Fig. 4.24 Second column moved onto load cells

Fig. 4.25 Preparing top beams

Fig. 4.26 Moving first beam of top beam set

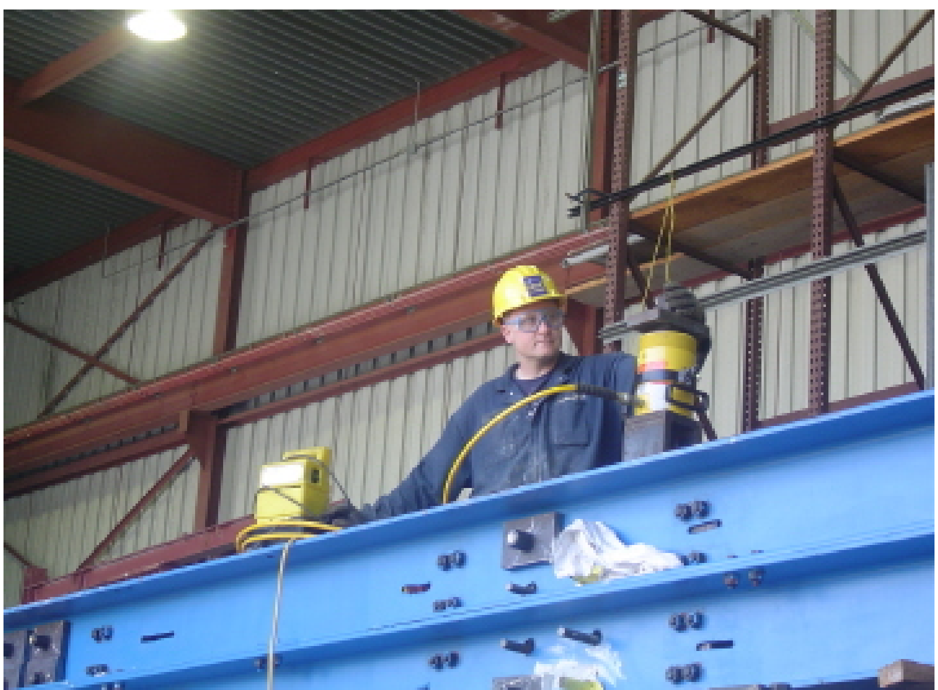

Fig. 4.27 Installation of prestressing tendon

Fig. 4.28 Moving mass block onto steel beam set

Fig. 4.29 Moving last mass block

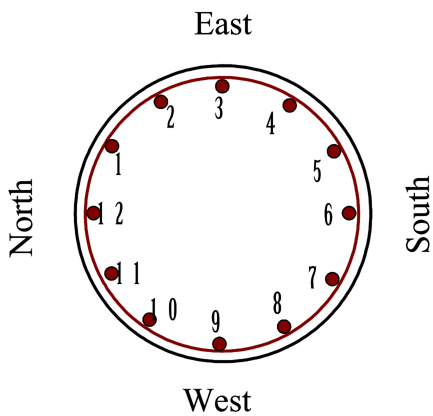

(a) Bar numbering

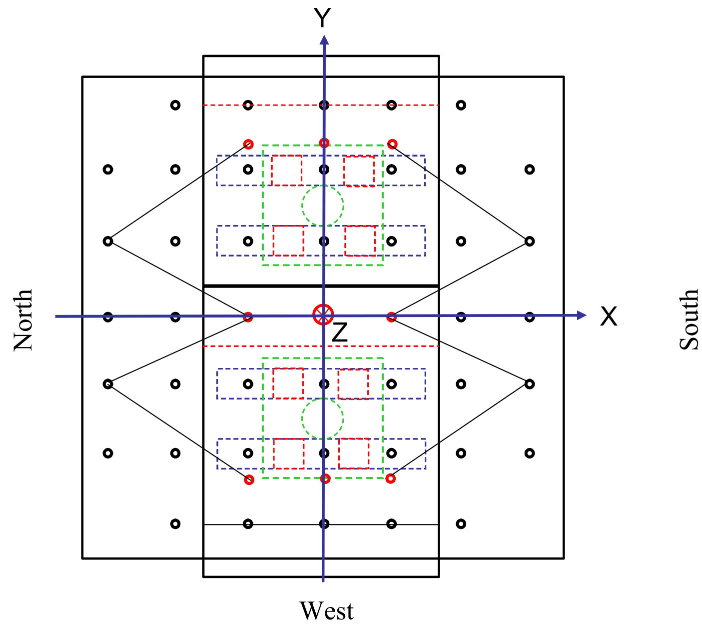

(b) *XY* plane .

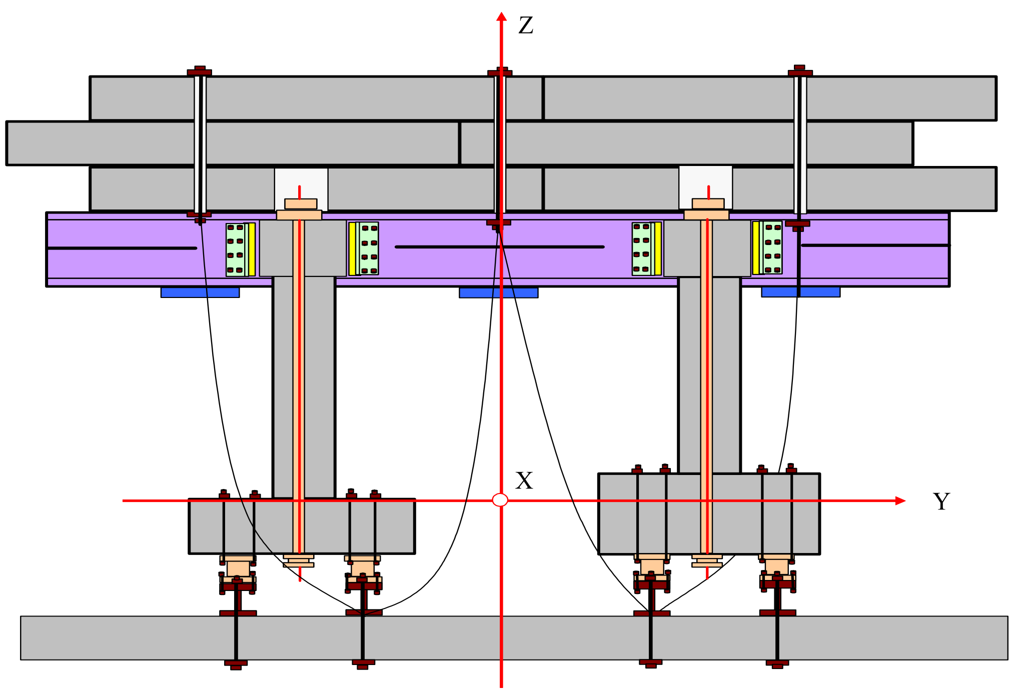

(c) *YZ* plane

Fig. 4.30 Coordinate system

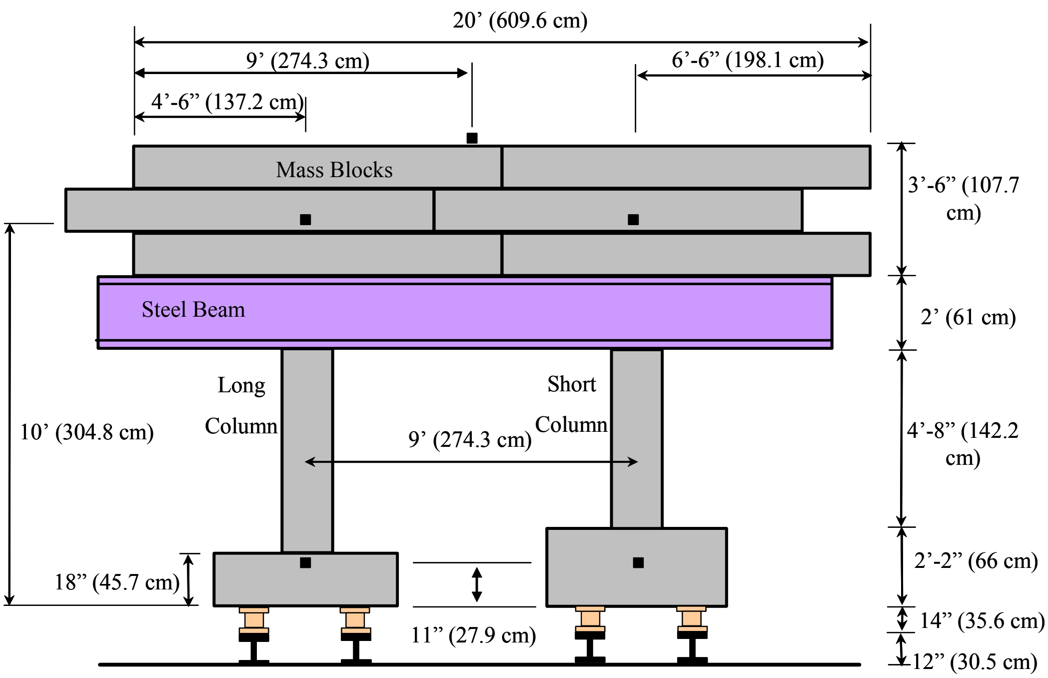

(a) Front (south) view

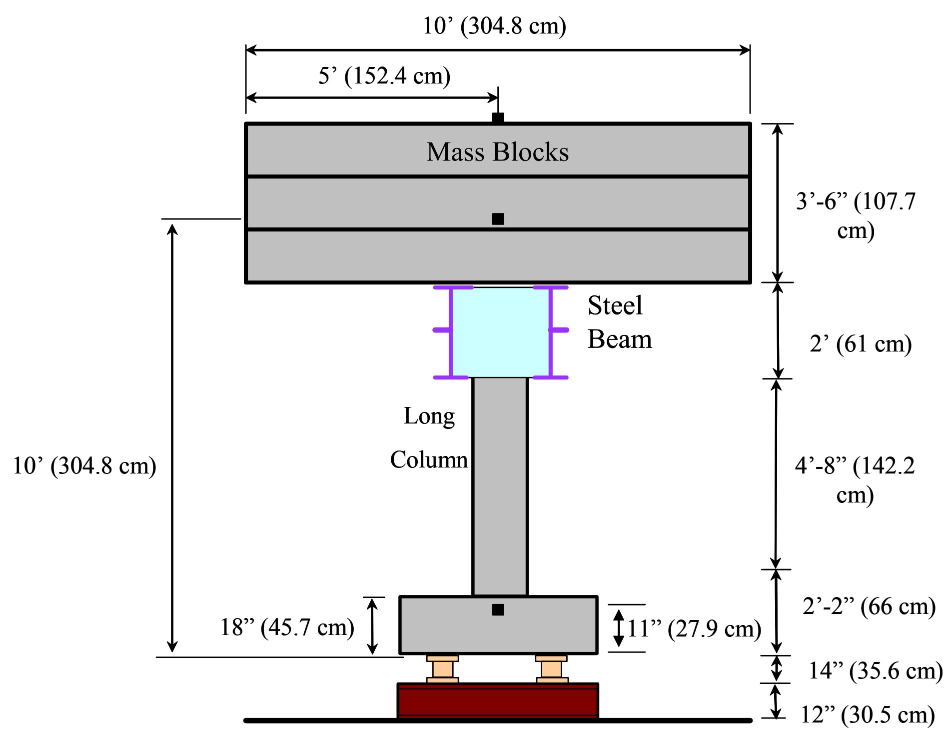

(b) Side (west) view

Fig. 4.31 Locations of accelerometers

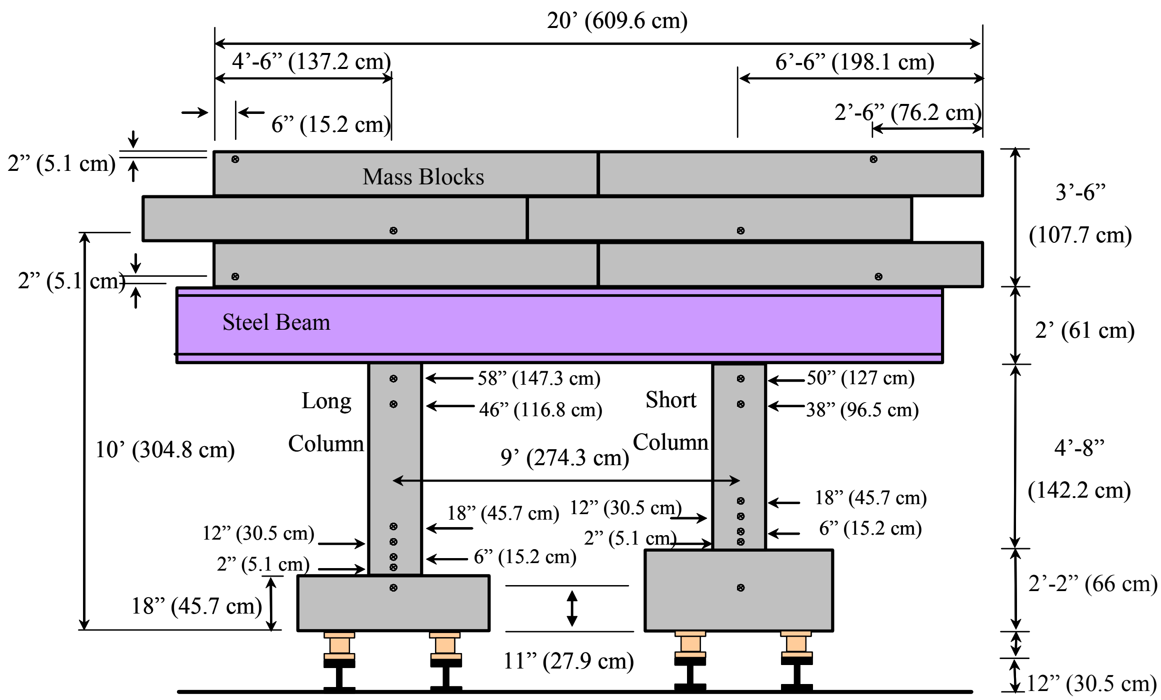

(a) Front (south) view

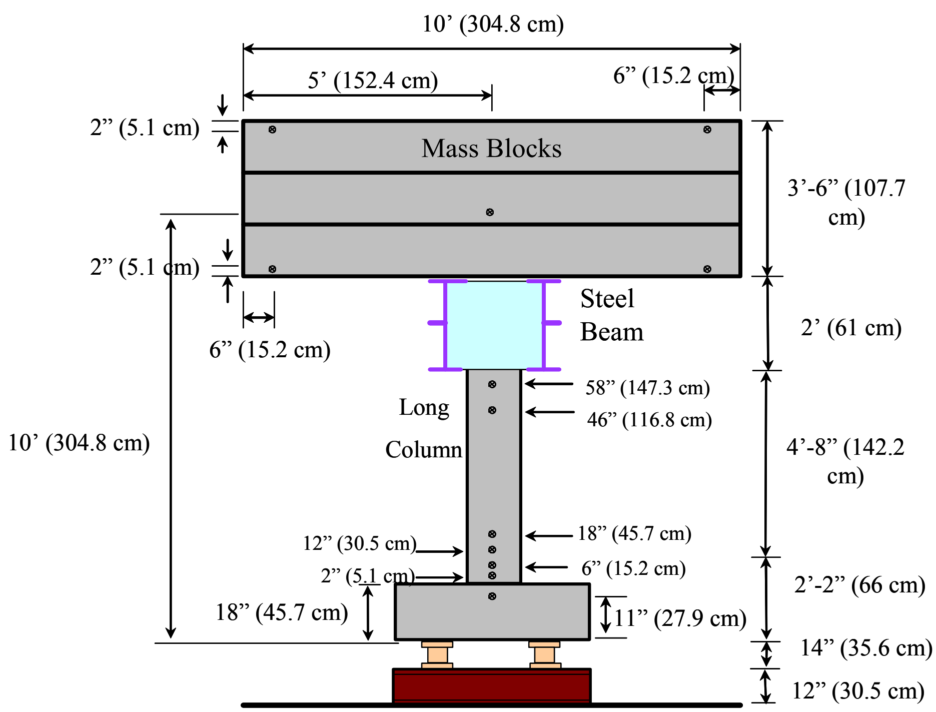

(b) Side (west) view

Fig. 4.32 Locations of linear potentiometers (LPs)

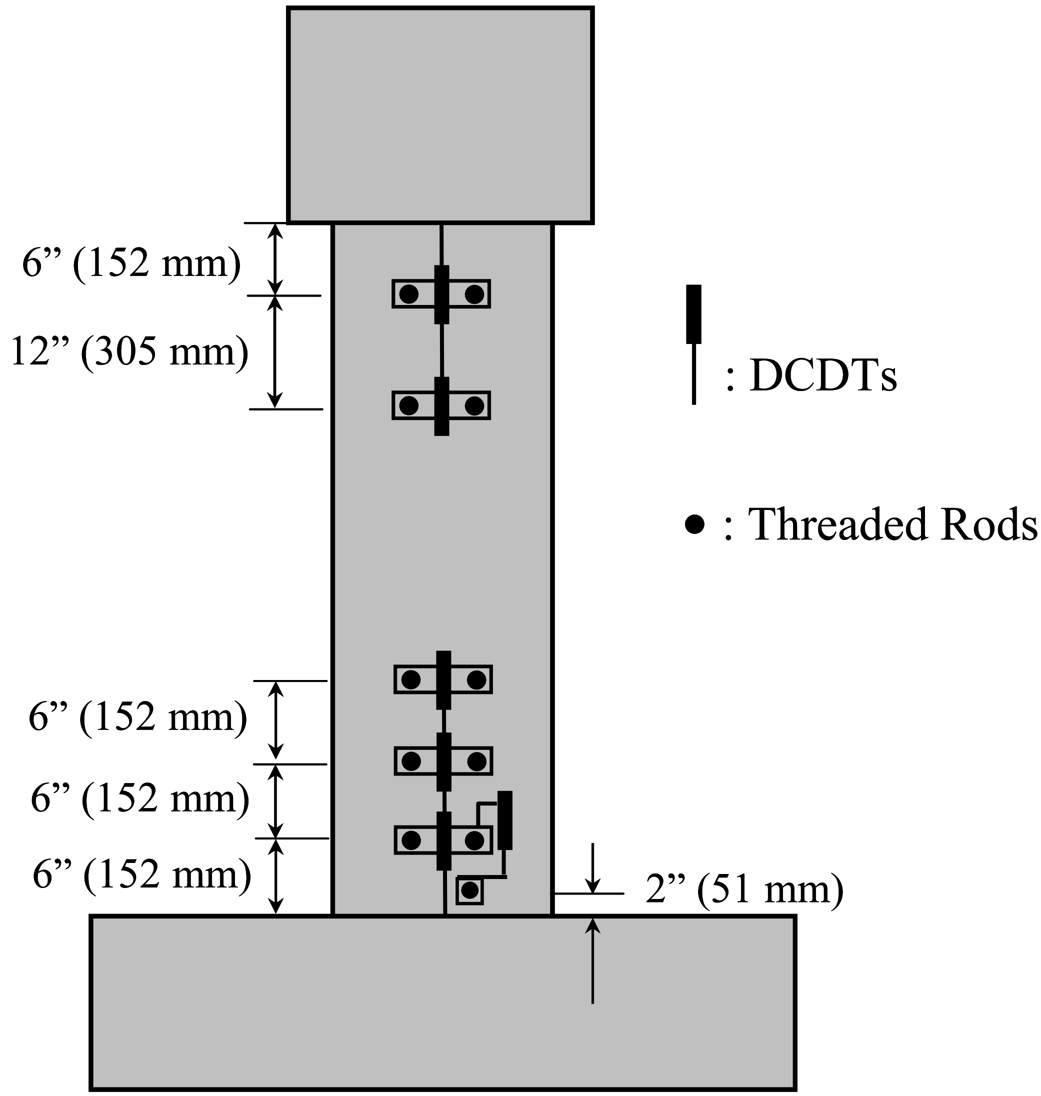

Fig. 4.33 Setup of DCDTs

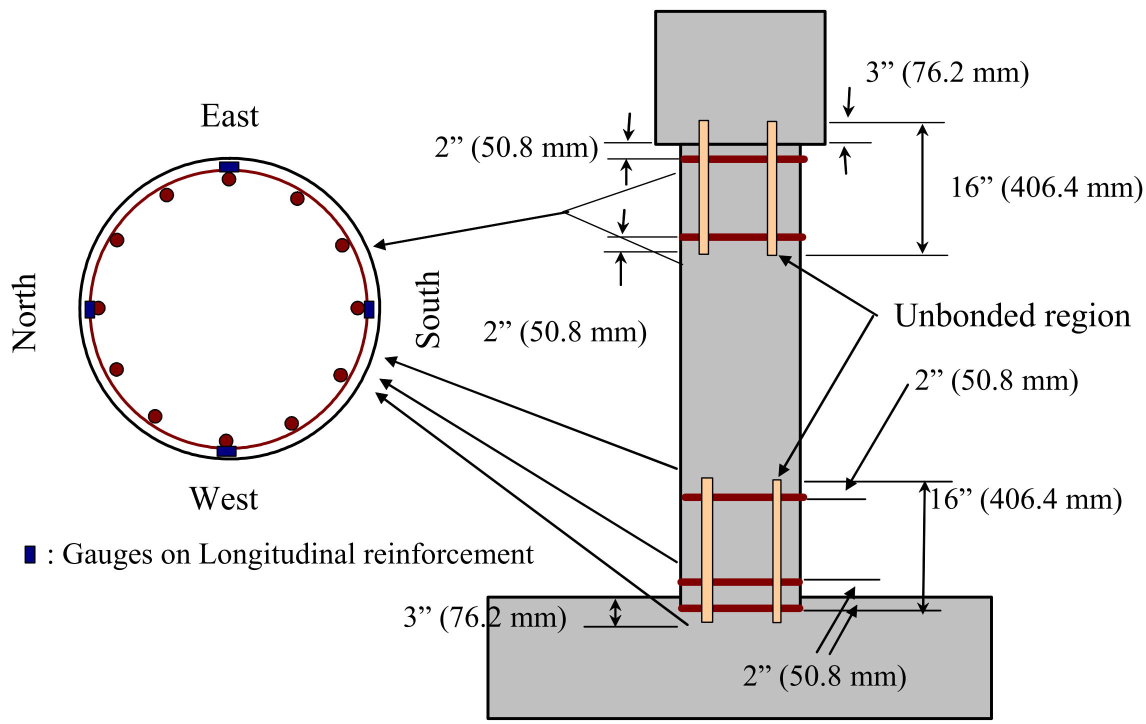

Fig. 4.34 Locations of strain gauges

(a) Bottom of short column

(b) Bottom of long column

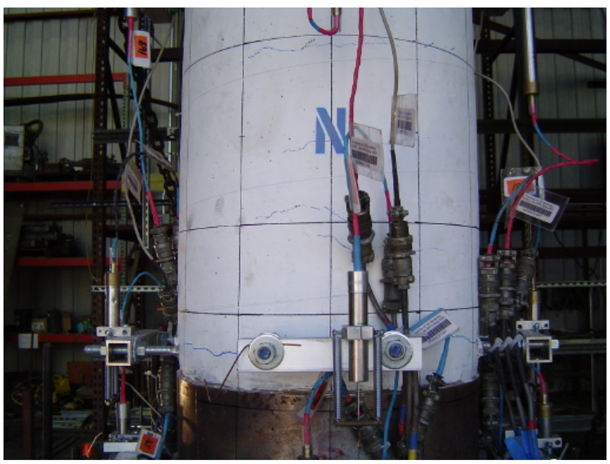

(c) Middle of short column

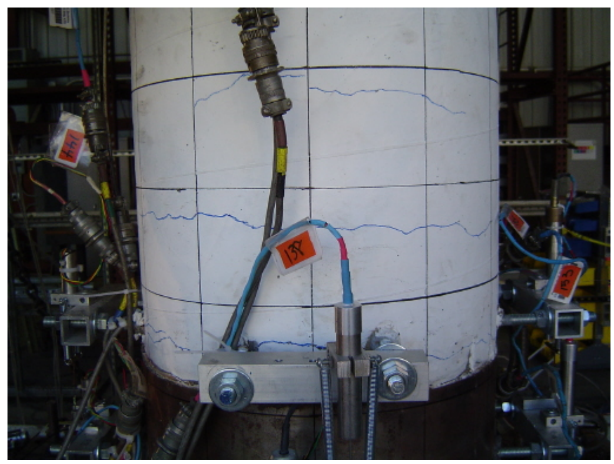

(d) Middle of long column

Fig. 4.35 Damage after design-level run (south view)

(a) Short column (crack opening of concrete)

(b) Short column (crushing of concrete)

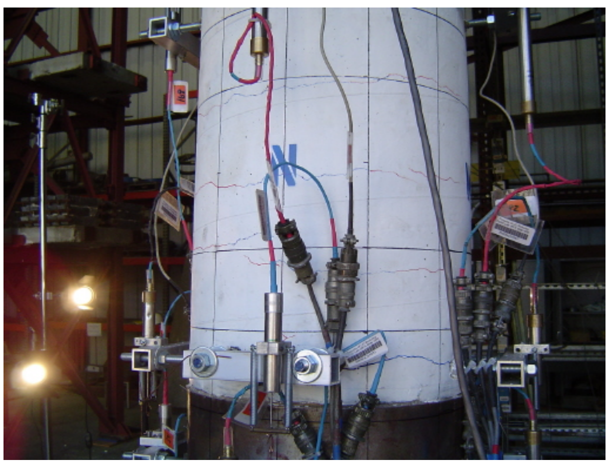

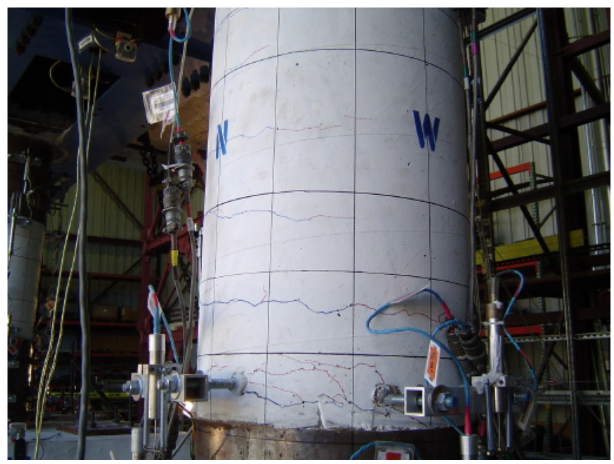

(c) Middle of short column

(d) Middle of long column

Fig. 4.36 Damage after maximum-level test (northwest view)

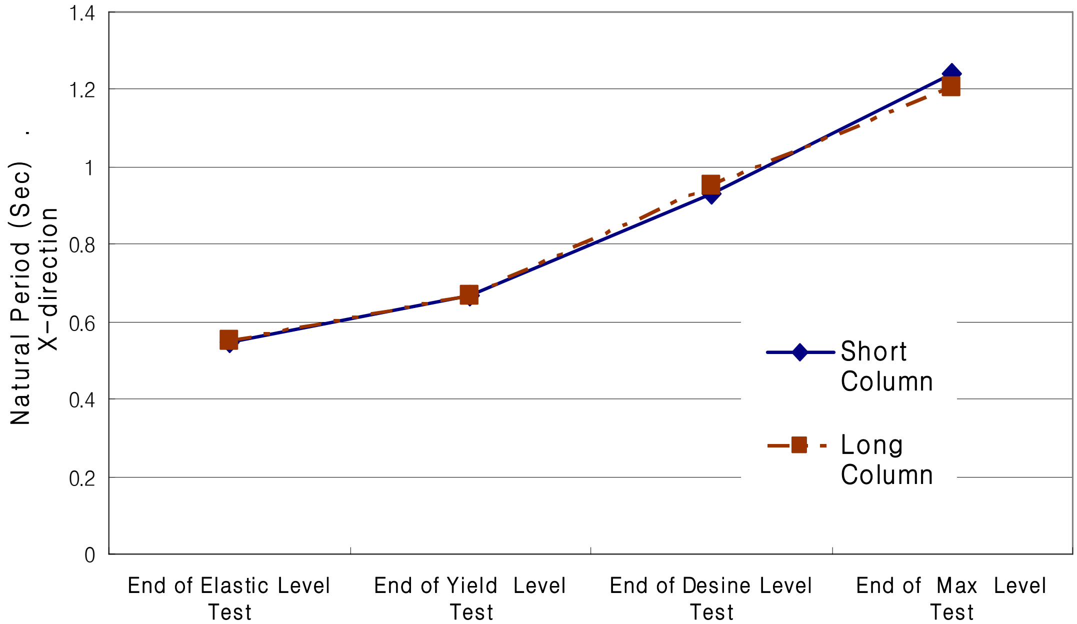

(a) *X* (N-S) direction

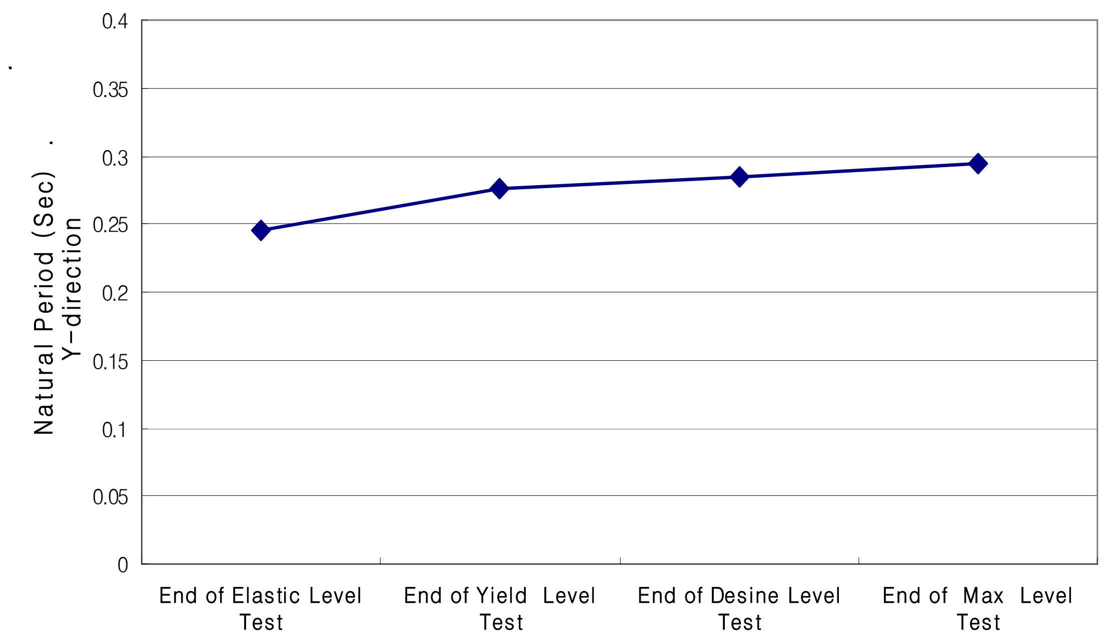

(b) *Y* (E-W) direction

Fig. 4.37 Change of natural period of specimen

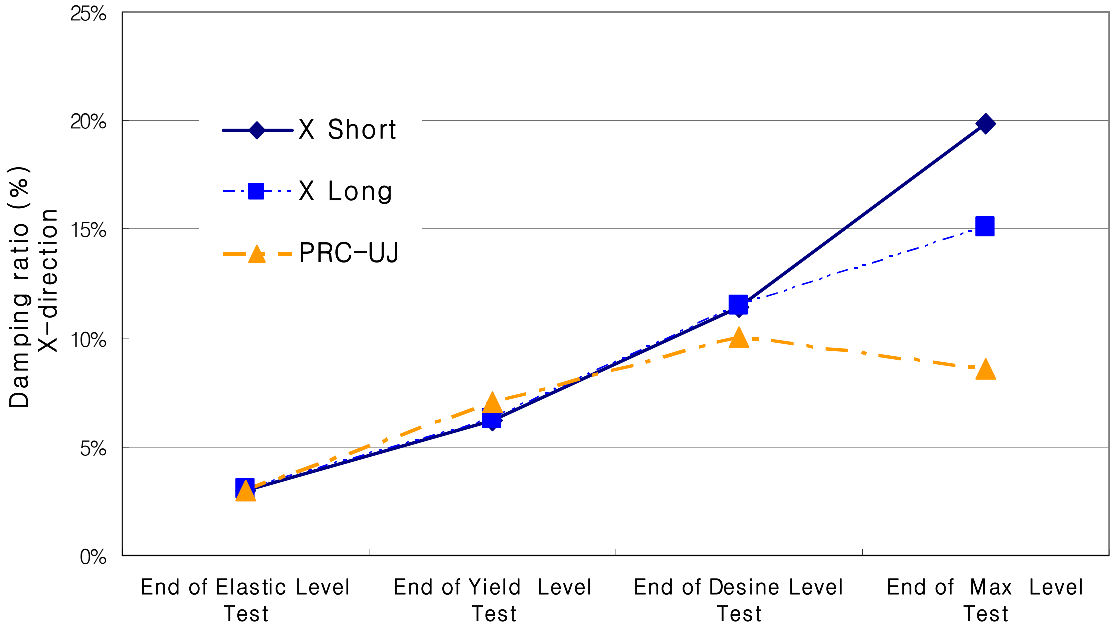

Fig. 4.38 Change of damping ratio of specimens, *x* (N-S) direction

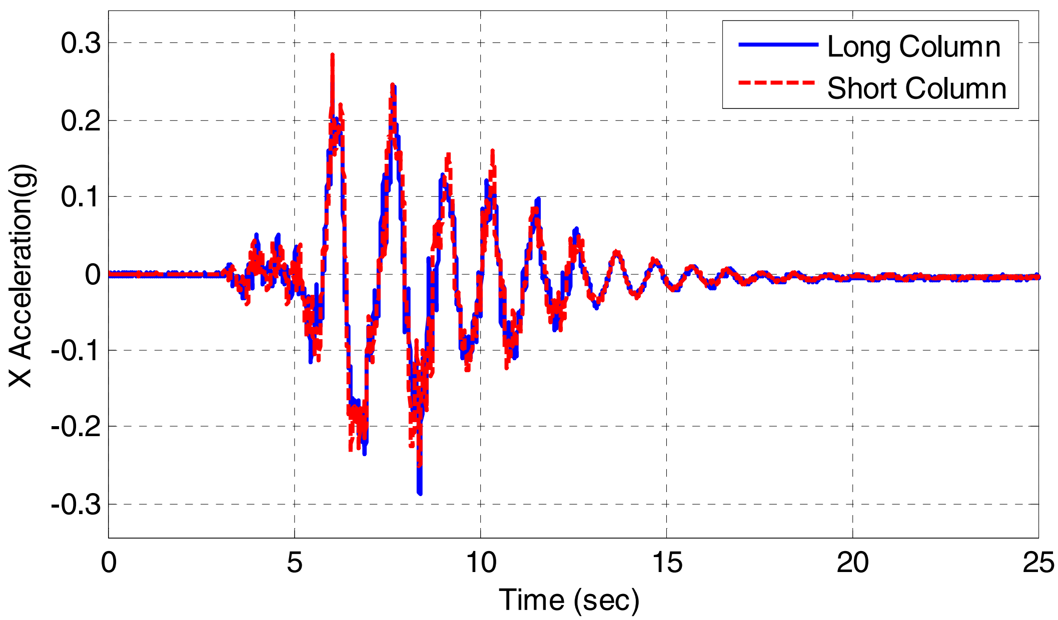

(a) *X* (N-S) direction

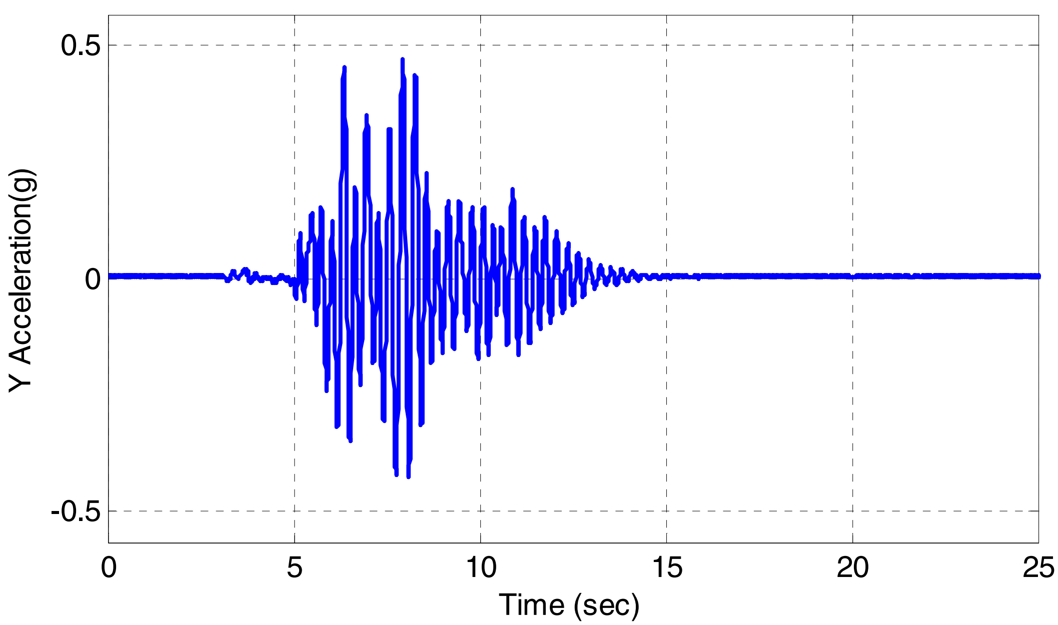

(b) *Y* (E-W) direction

Fig. 4.39 Acceleration responses at C.G. (design-level test)

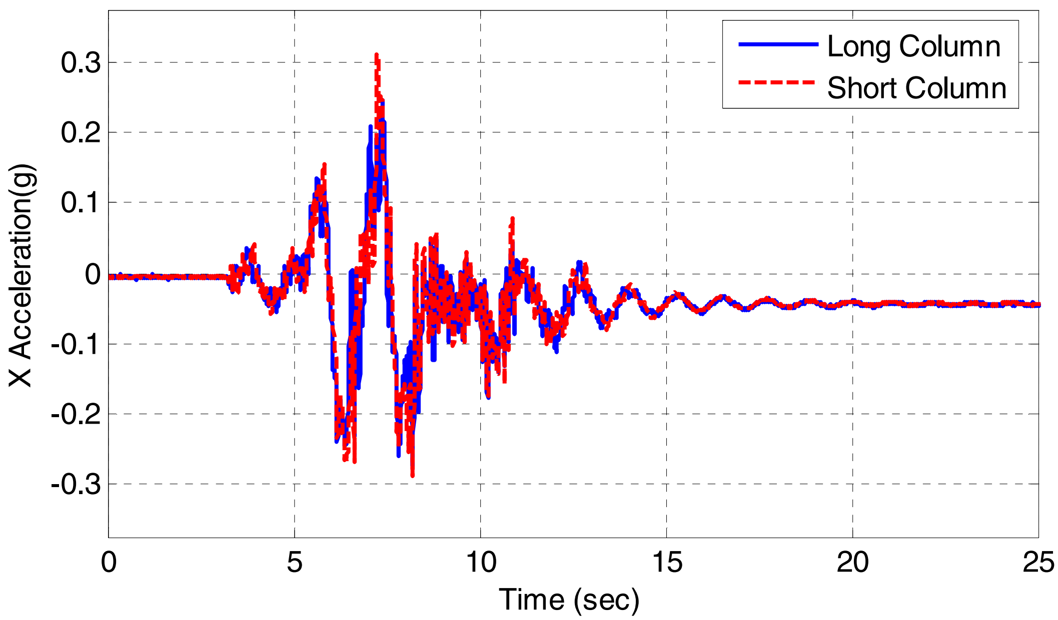

(a) *X* (N-S) direction

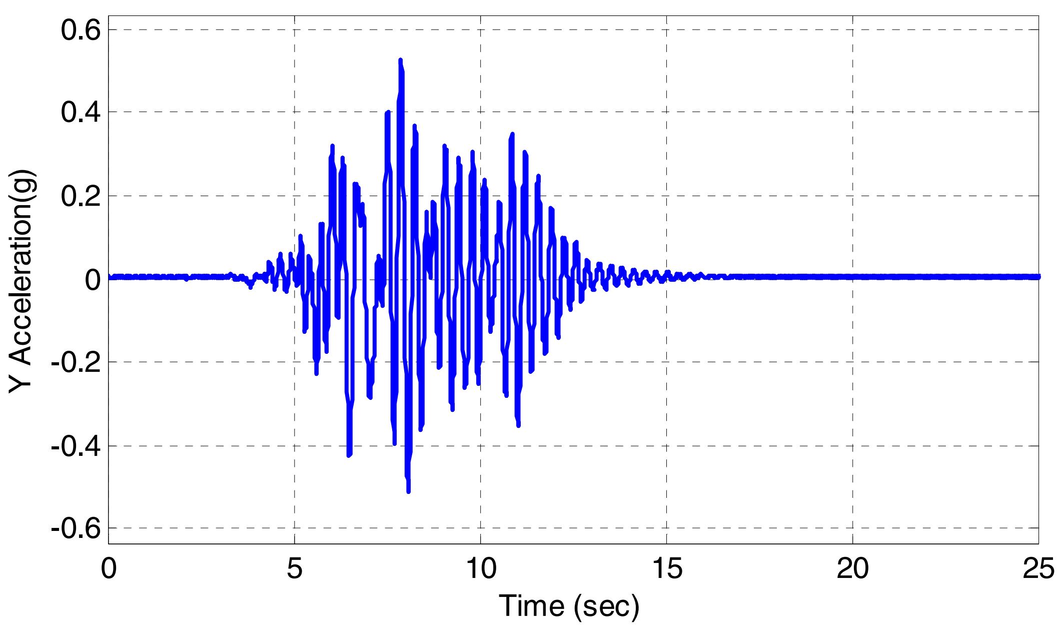

(b) *Y* (E-W) direction

Fig. 4.40 Acceleration responses at C.G. (maximum-level test)

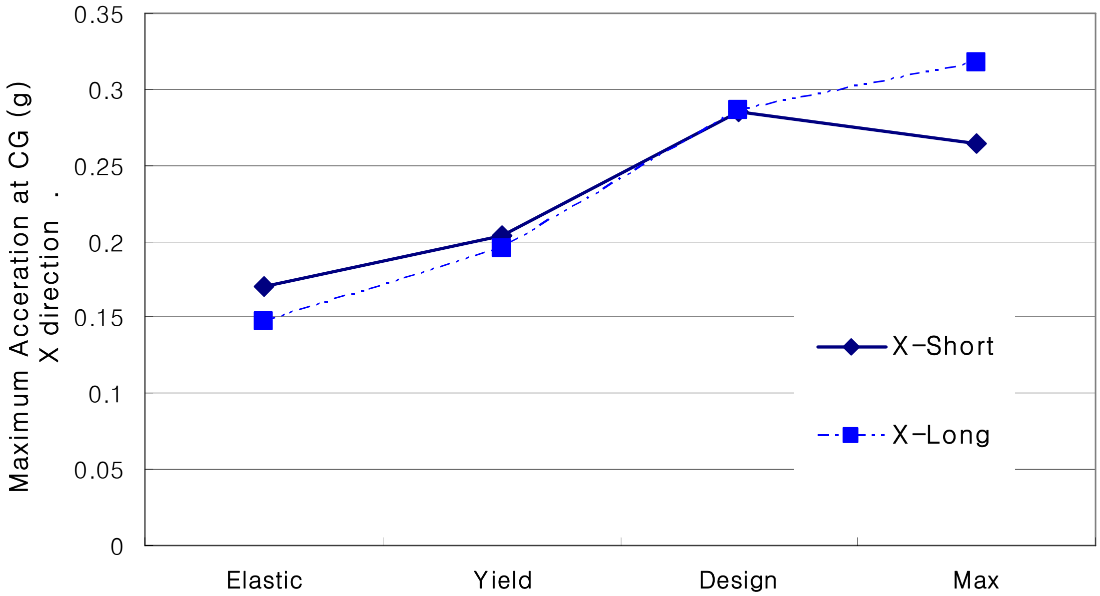

(a) *X* (N-S) direction

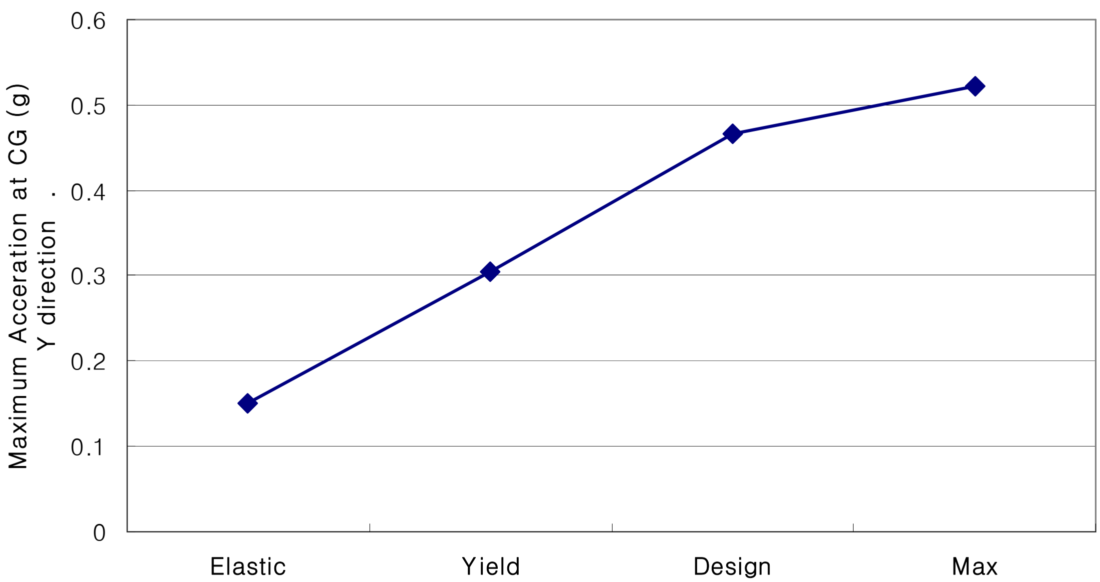

(b) *Y* (E-W) direction

Fig. 4.41 Maximum acceleration responses at C.G.

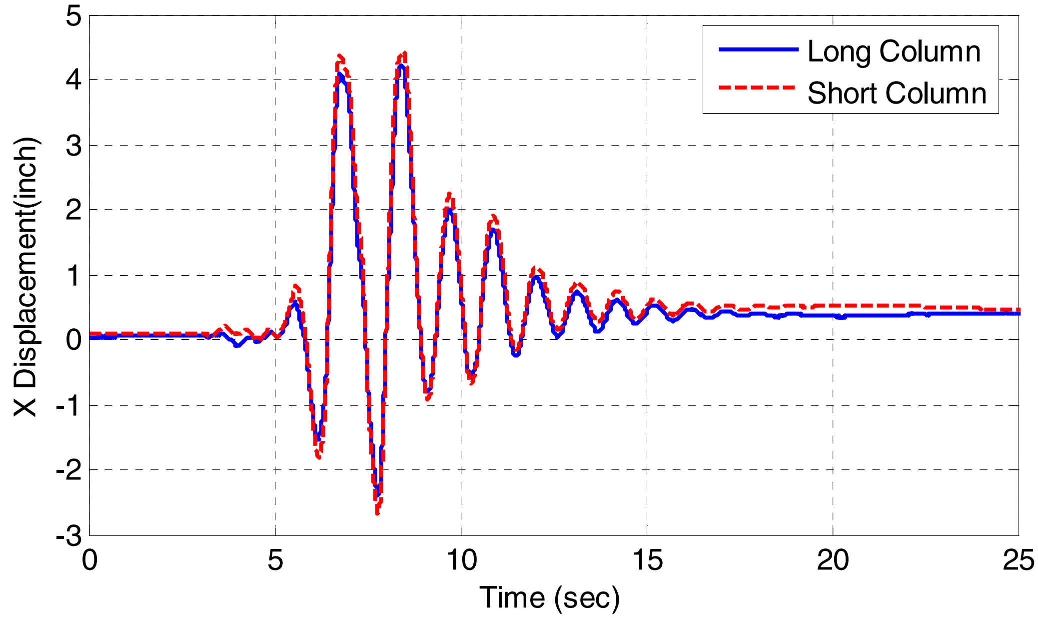

(a) X (N-S) direction

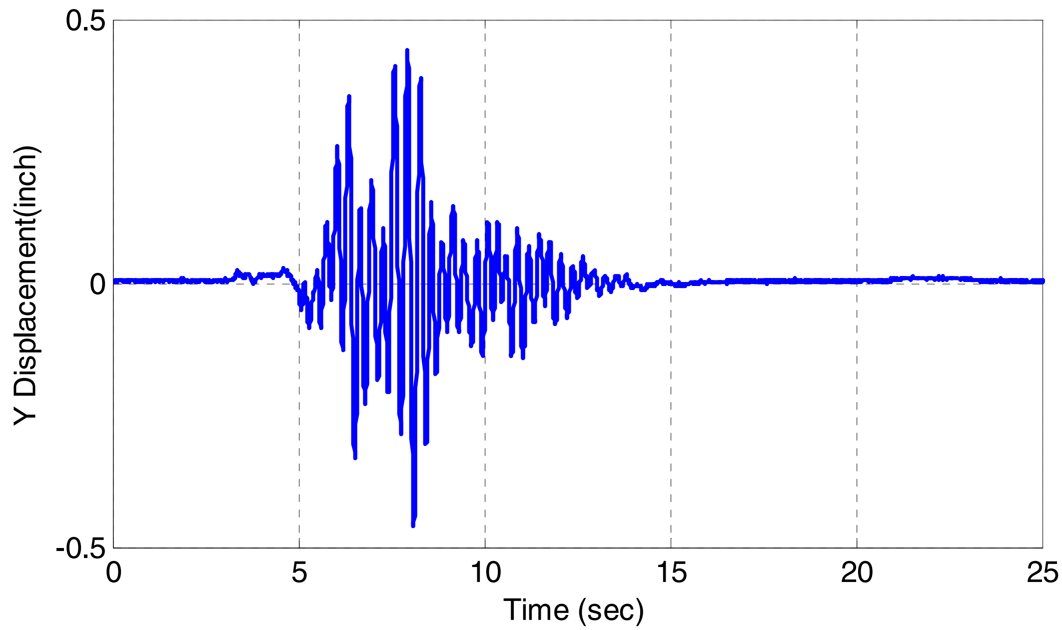

(b) Y (E-W) direction

Fig. 4.42 Displacement responses at C.G. (design-level test)

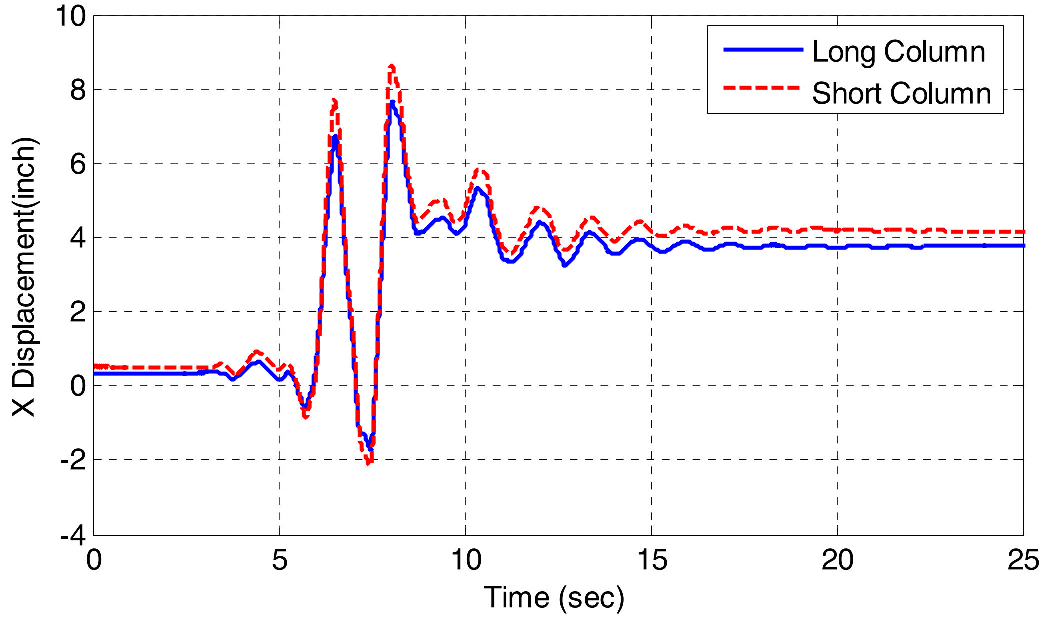

(a) *X* (N-S) direction

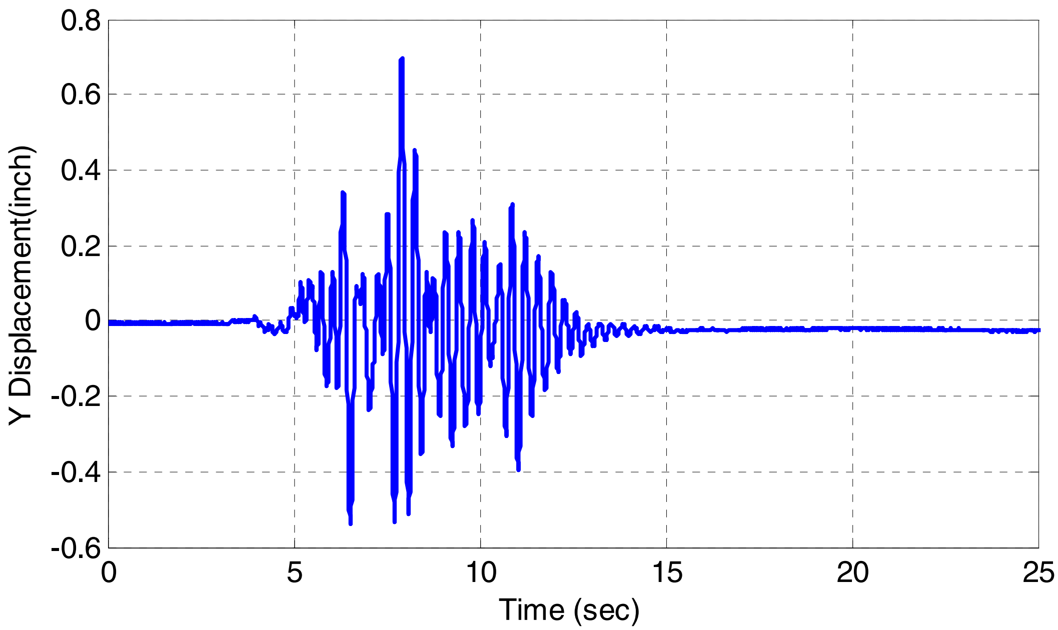

(b) *Y* (E-W) direction

Fig. 4.43 Displacement responses at C.G. (maximum-level test)

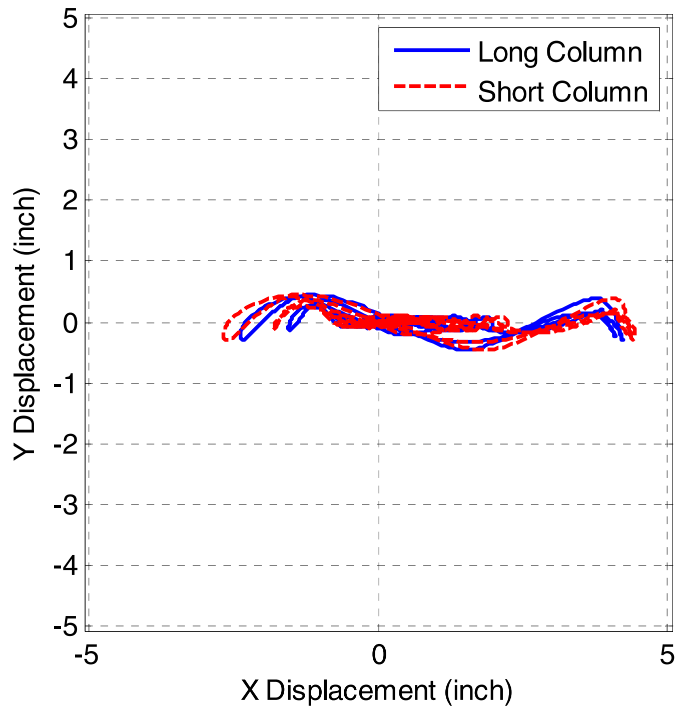

(a) Design-level run

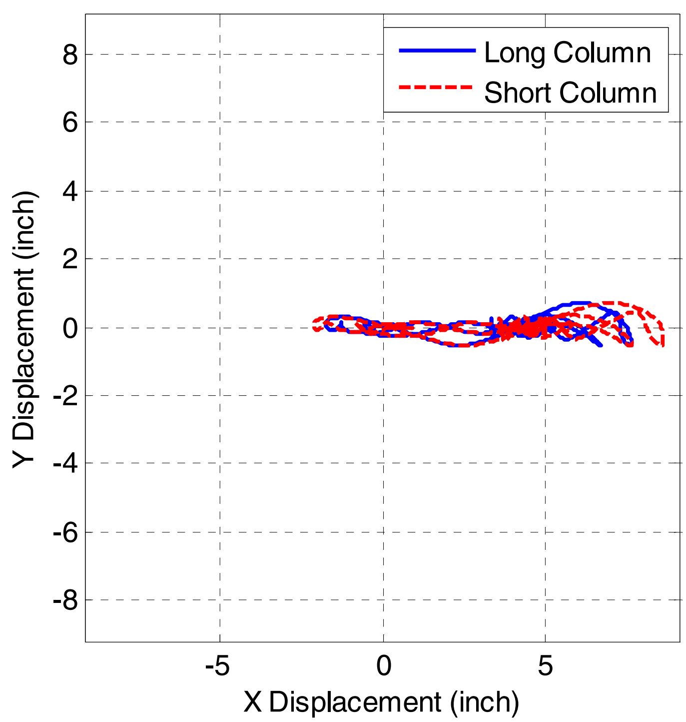

(b) Maximum-level run

Fig. 4.44 Orbits

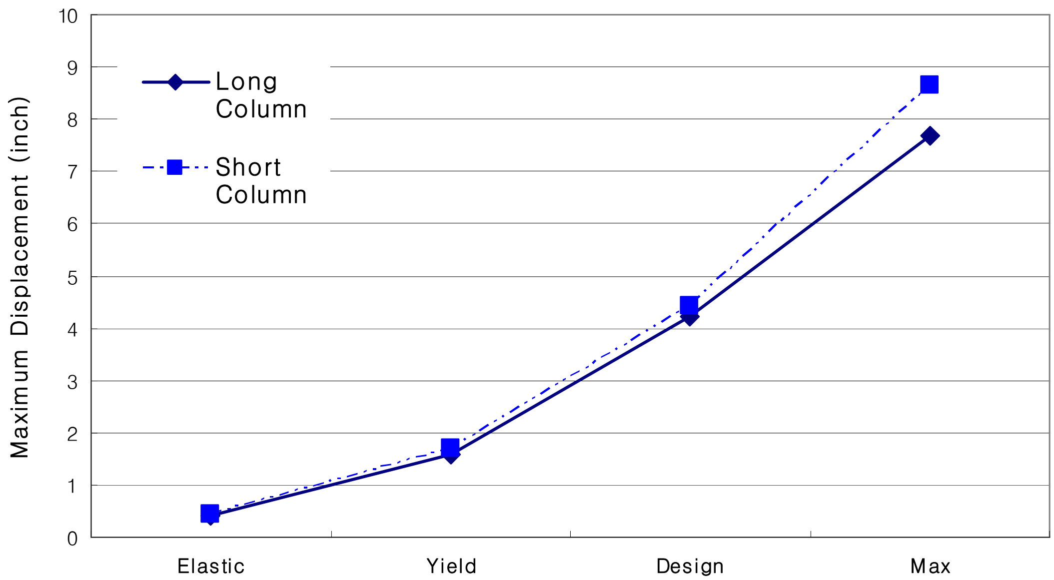

Fig. 4.45 Cumulative maximum displacement at C.G. (*x* direction)

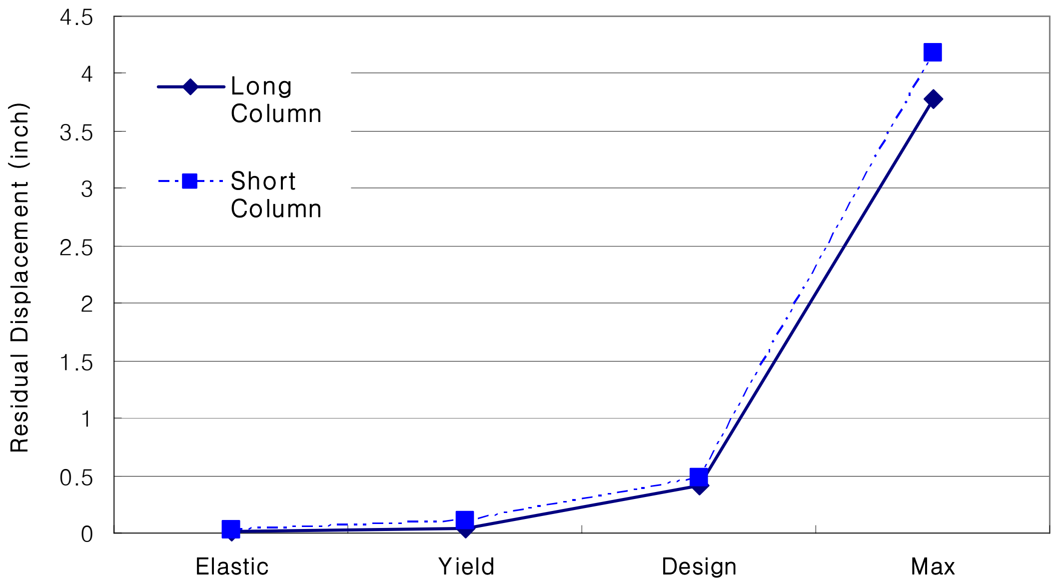

Fig. 4.46 Cumulative residual displacement at C.G. (*x* direction)

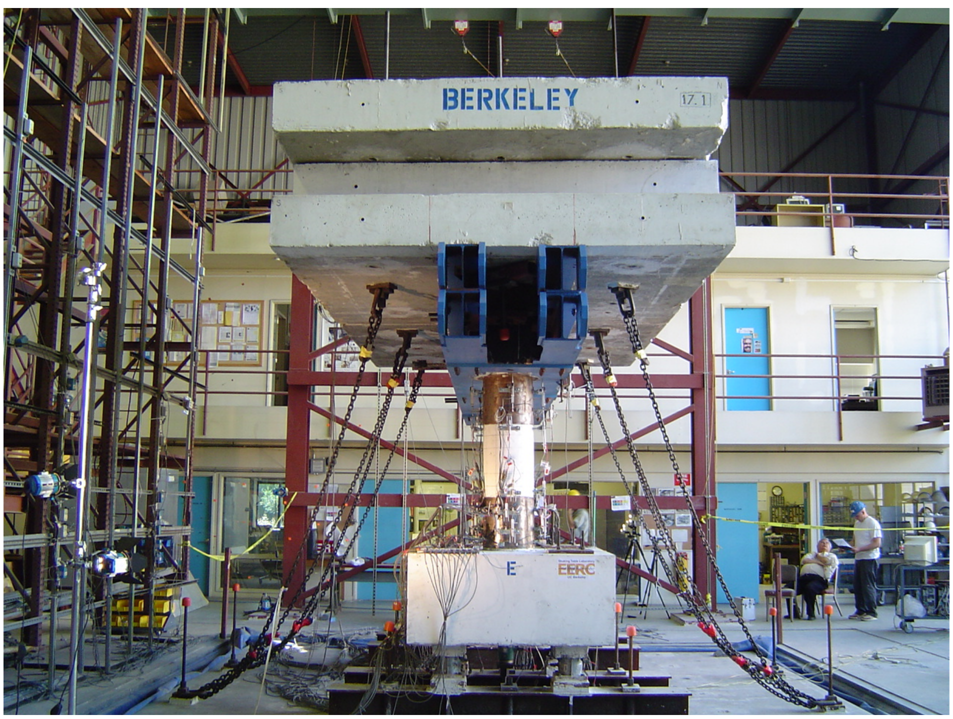

After design-level run
Residual displacement = 0.411 in. (10 mm)

Fig. 4.47 End of design-level run

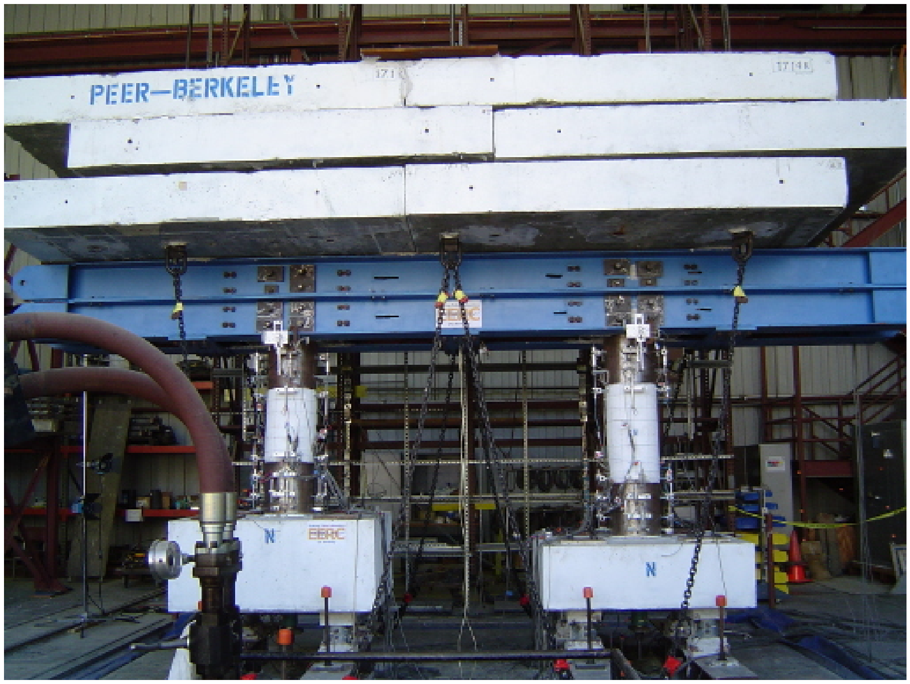

After maximum-level run
Residual displacement = 3.78 in. (96 mm)

Fig. 4.48 End of maximum-level run

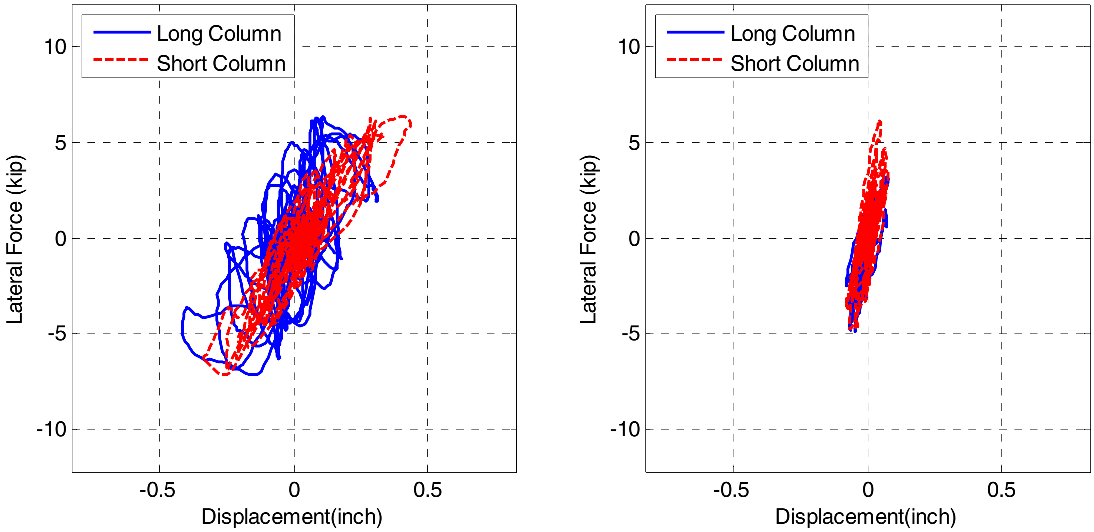

(a) X (N-S) direction (b) Y (E-W) direction

Fig. 4.49 Lateral force–lateral displacement hystereses (elastic-level test)

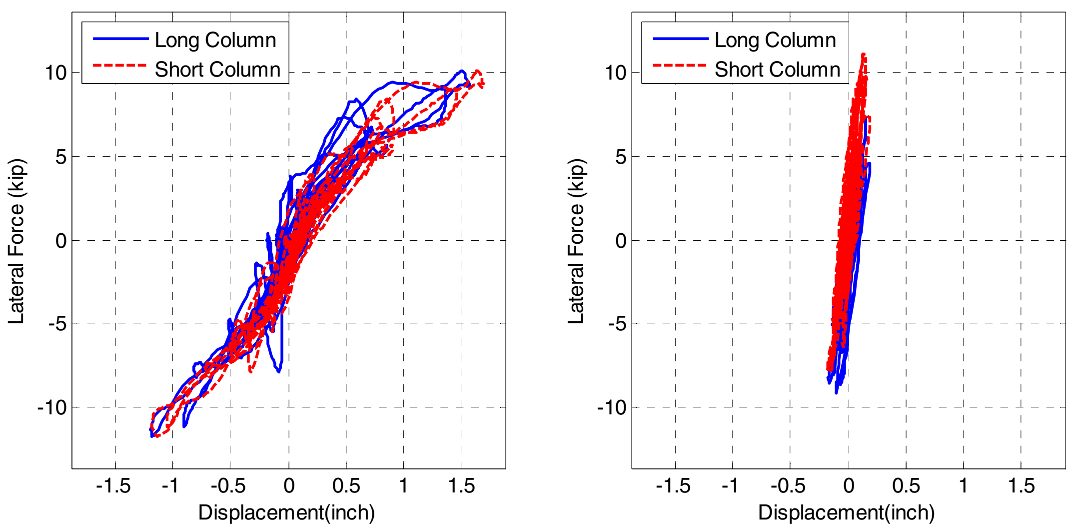

(a) X (N-S) direction (b) Y(E-W) direction

Fig. 4.50 Lateral force–lateral displacement hystereses (yield-level test)

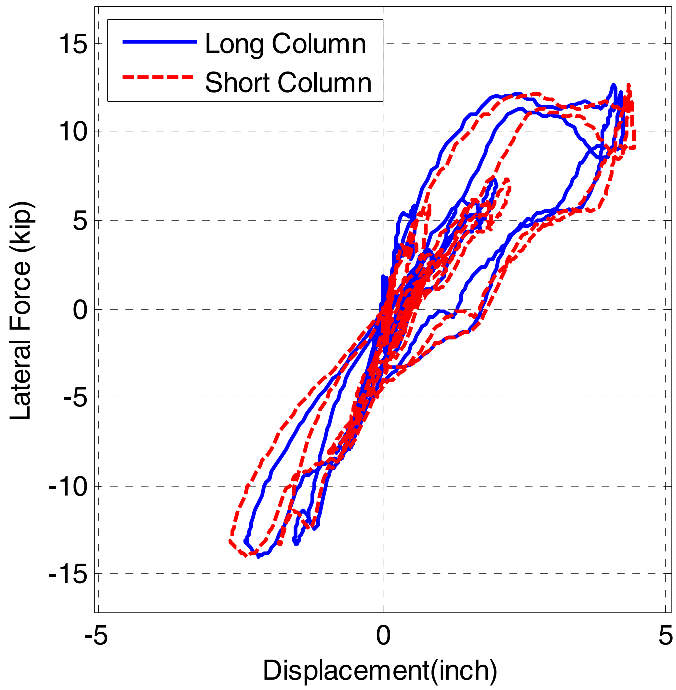

(a) X (N-S) direction

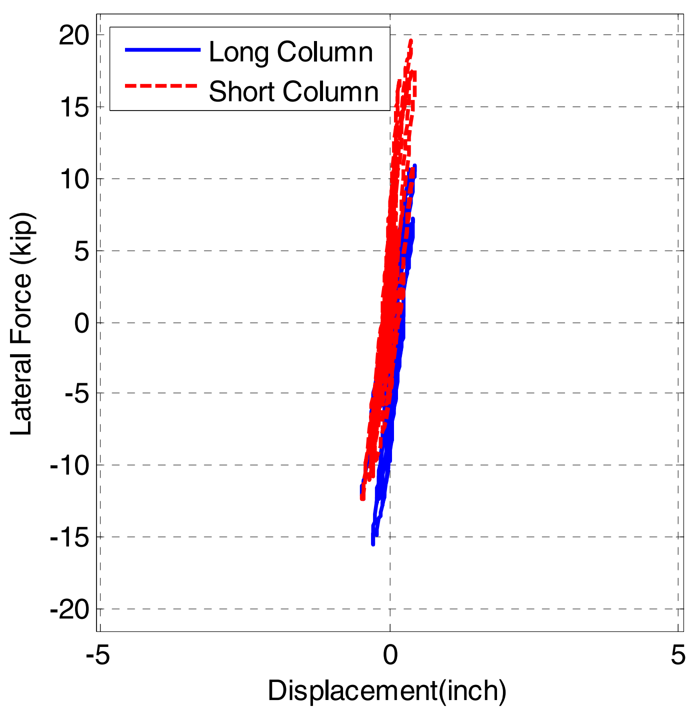

(b) Y (E-W) direction

Fig. 4.51 Lateral force–lateral displacement hystereses (design-level test)

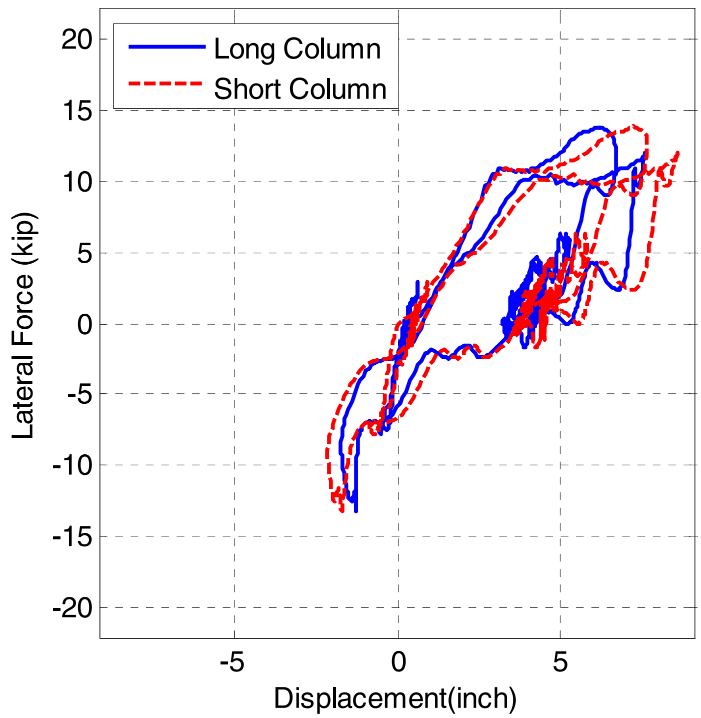

(a) *X* (N-S) direction

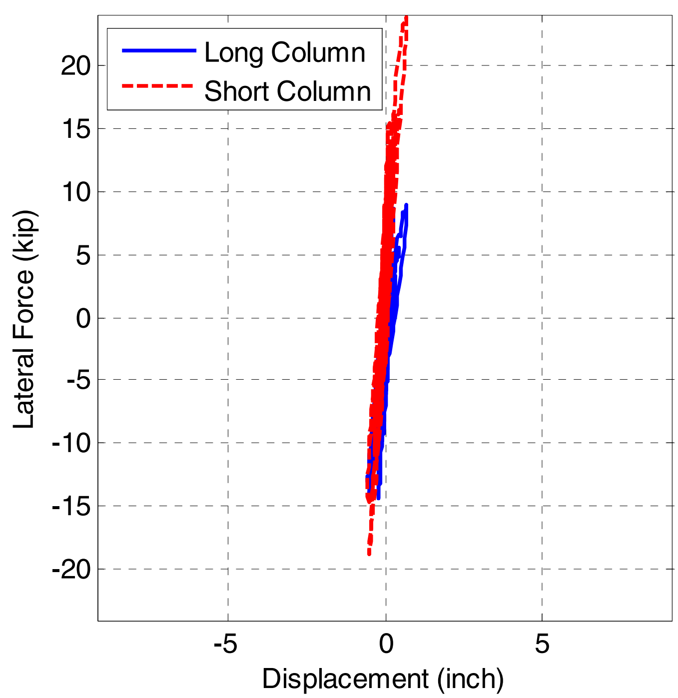

(b) *Y* (E-W) direction

Fig. 4.52 Lateral force–lateral displacement hystereses (maximum-level test)

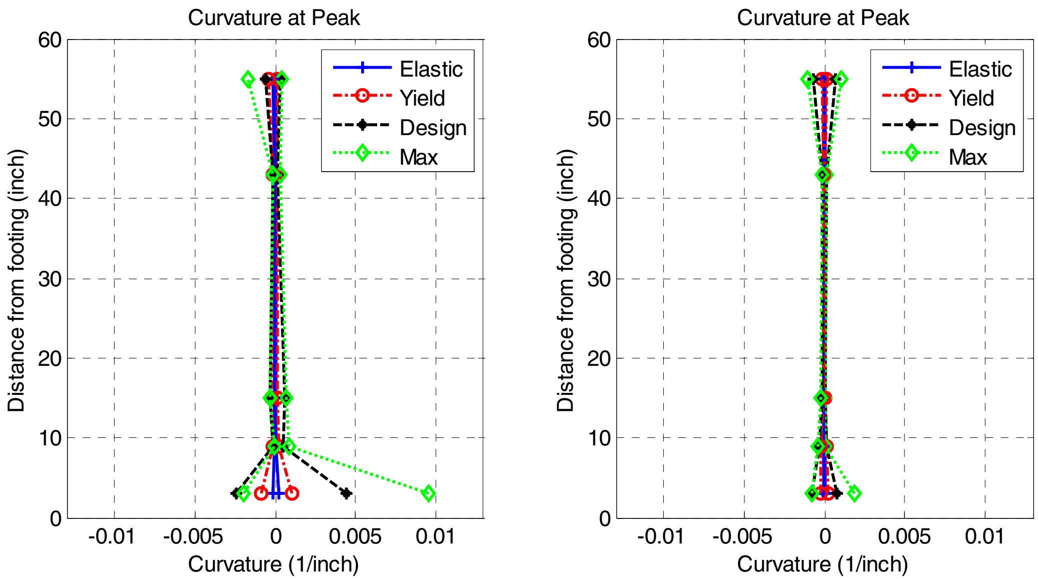

(a) X (N-S) direction (b) Y (E-W) direction

Long column

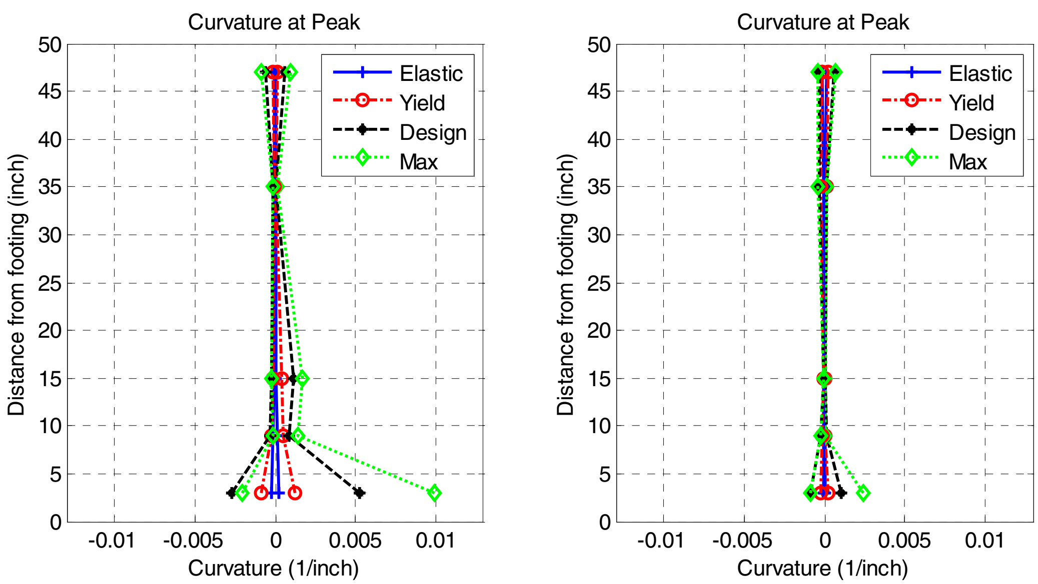

(a) X (N-S) direction (b) Y (E-W) direction

Short column

Fig. 4.53 Curvature distributions along columns

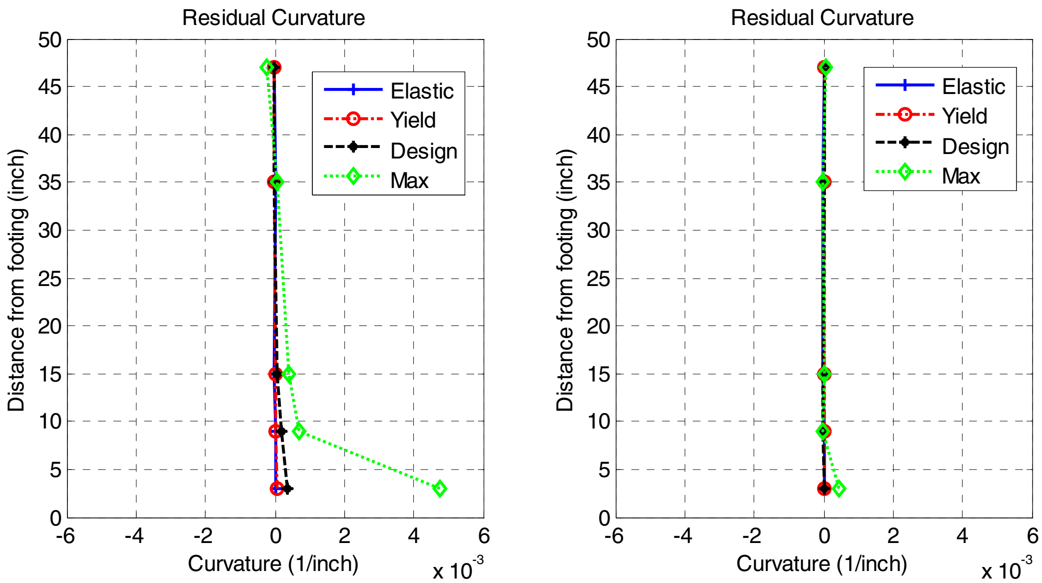

(a) X (N-S) direction (b) Y (E-W) direction

Long column

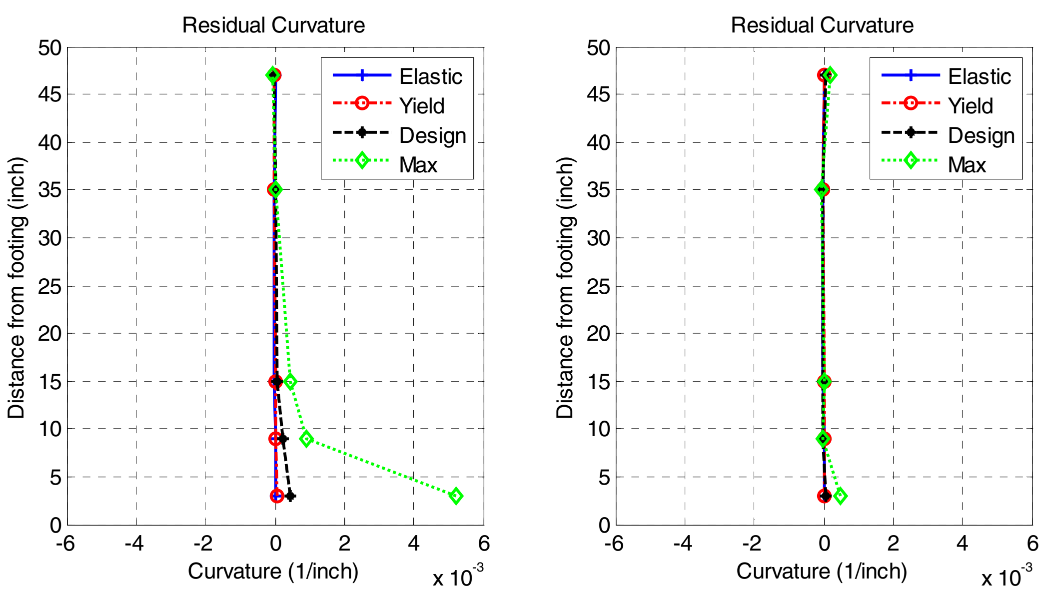

(a) X (N-S) direction (b) Y (E-W) direction

Short column

Fig. 4.54 Residual curvature distributions along columns

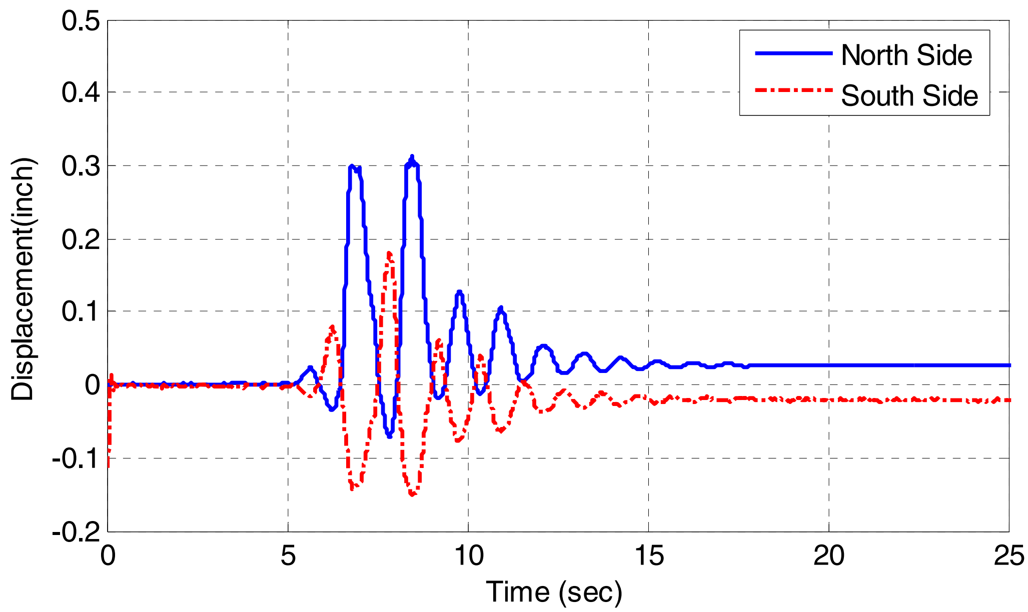

(a) Long column

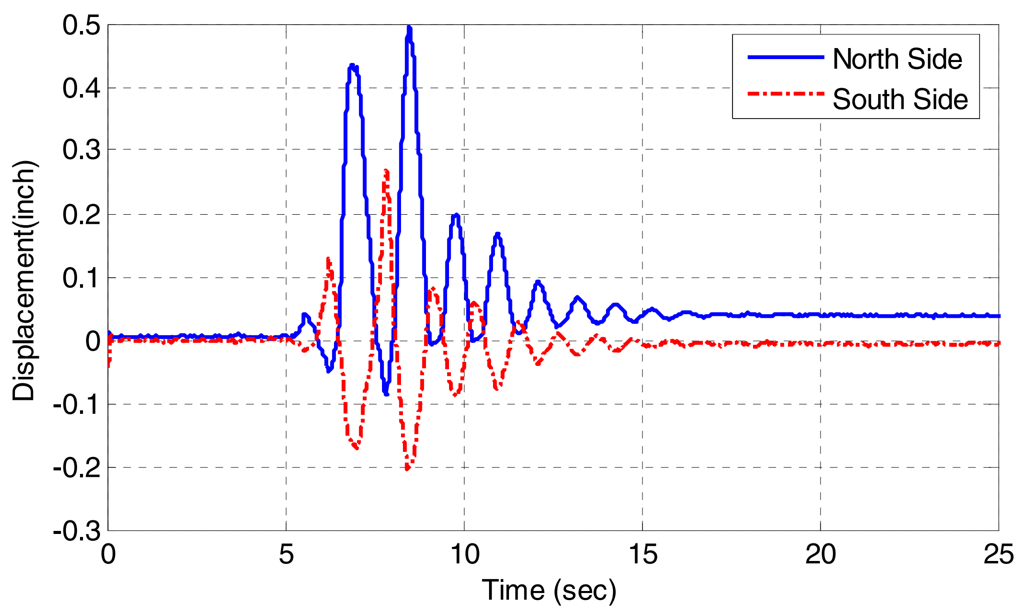

(b) Short column

Fig. 4.55 Bar pullout and concrete crushing at bottom (design-level test)

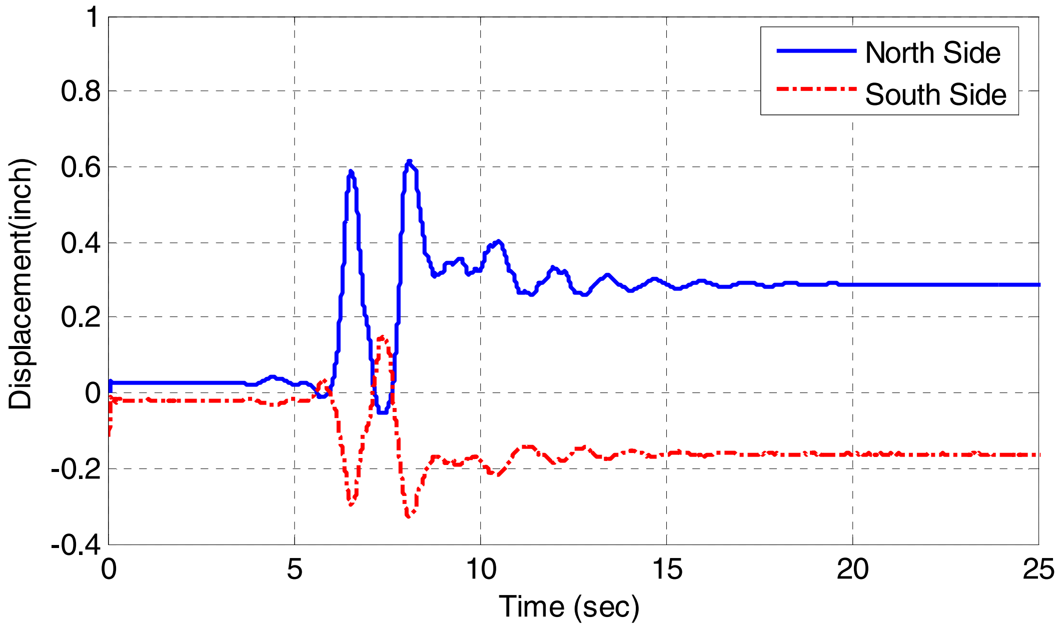

(a) Long column

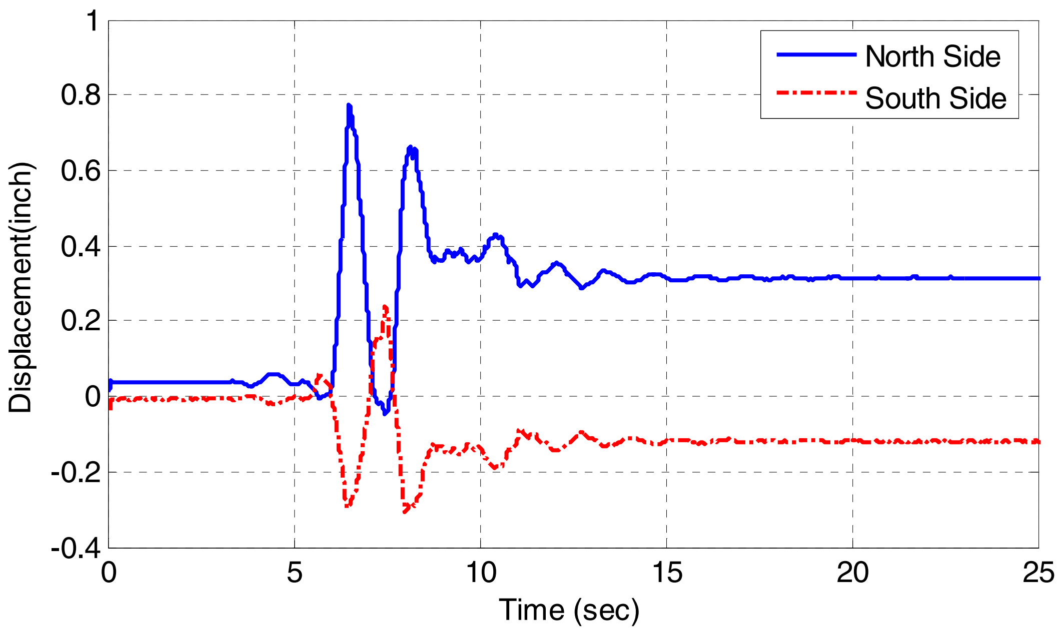

(b) Short column

Fig. 4.56 Bar pullout and concrete crushing at bottom (maximum-level test)

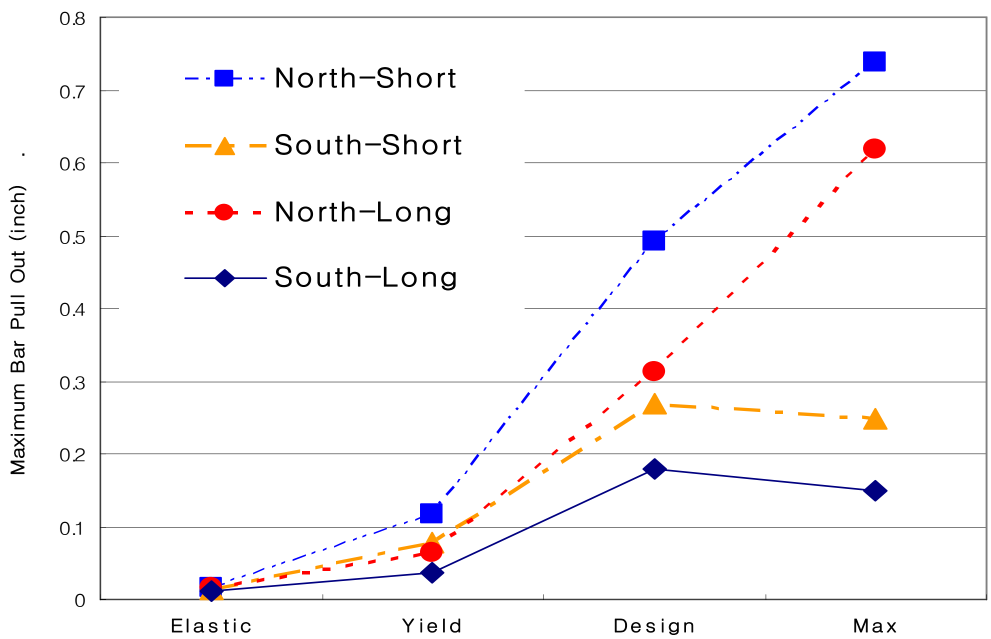

Fig. 4.57 Maximum bar pullout

Fig. 4.58 Bar pullout of Specimen PRC-System (maximum level test)

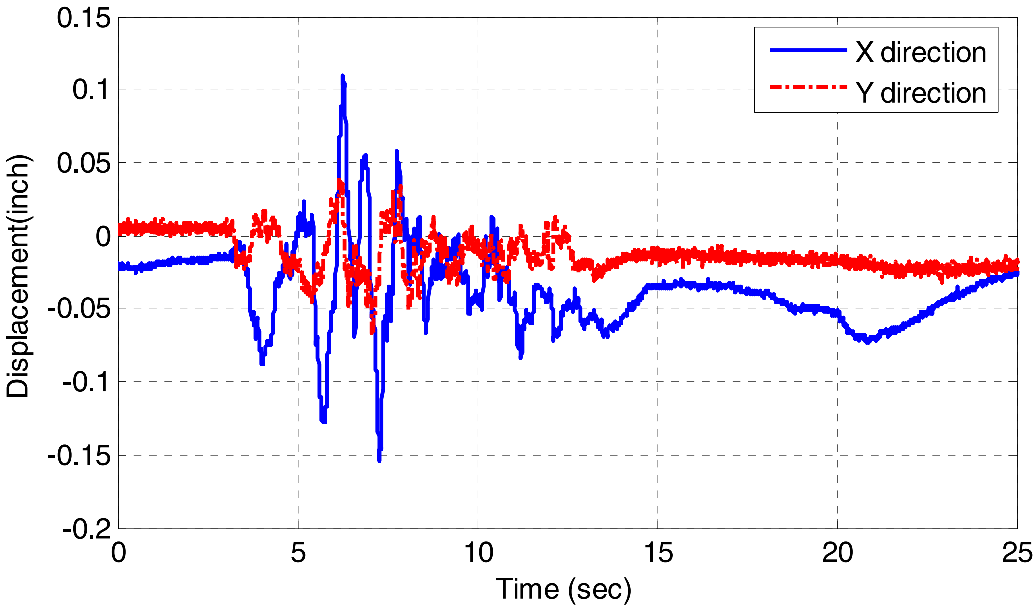

(a) Design level

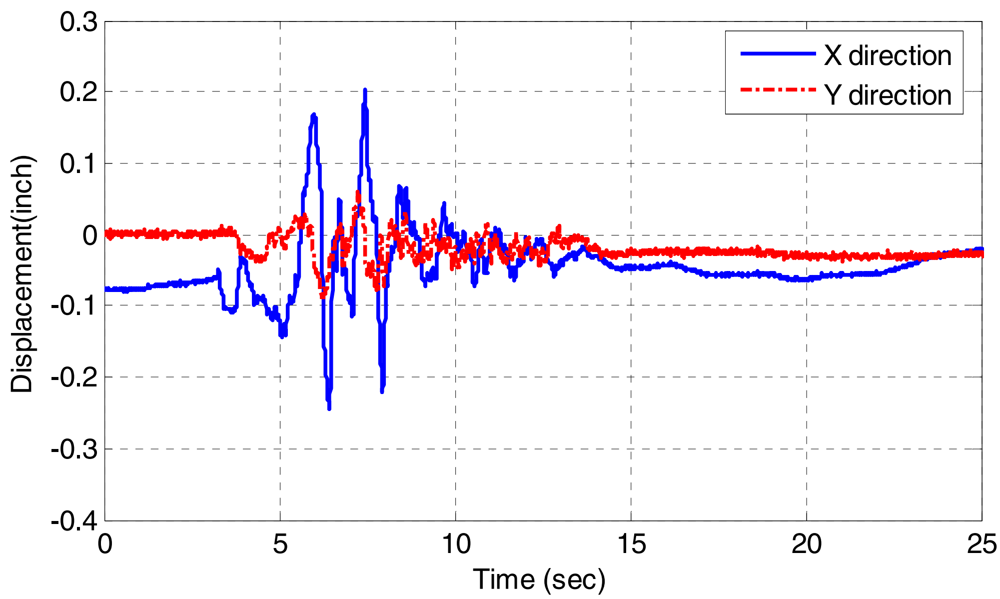

(b) Maximum level

Fig. 4.59 Shear deformation at 2-in.-height section (long column)

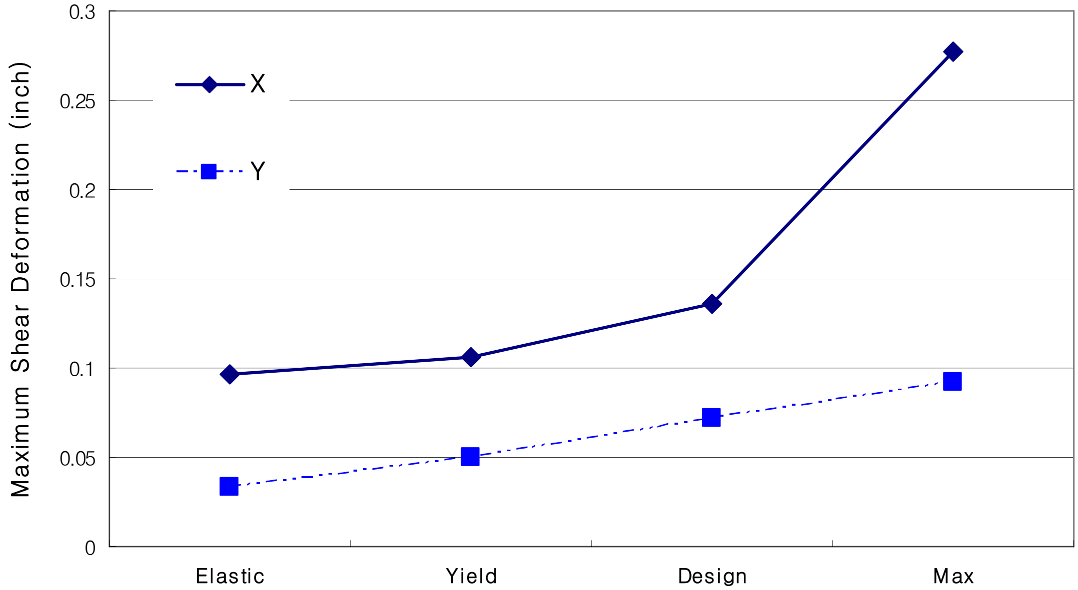

Fig. 4.60 Maximum shear deformation at 2-in-height section (long column)

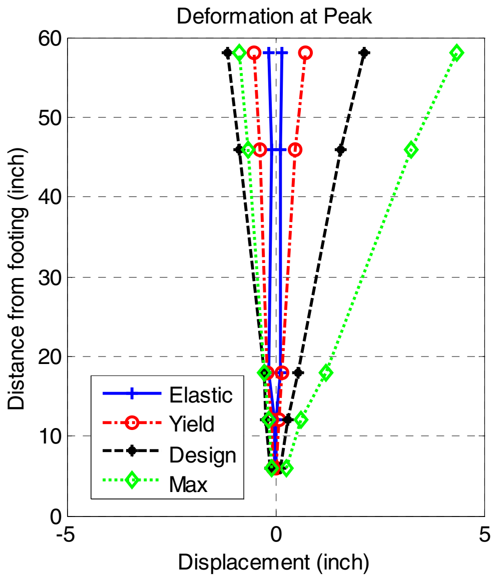

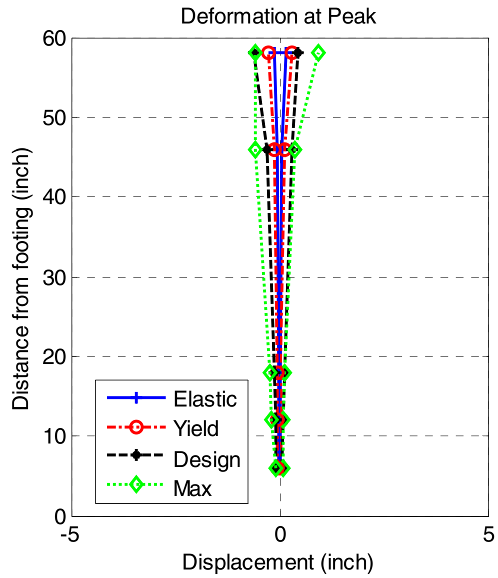

(a) *X* (N-S) direction (b) *Y* (E-W) direction

Long column

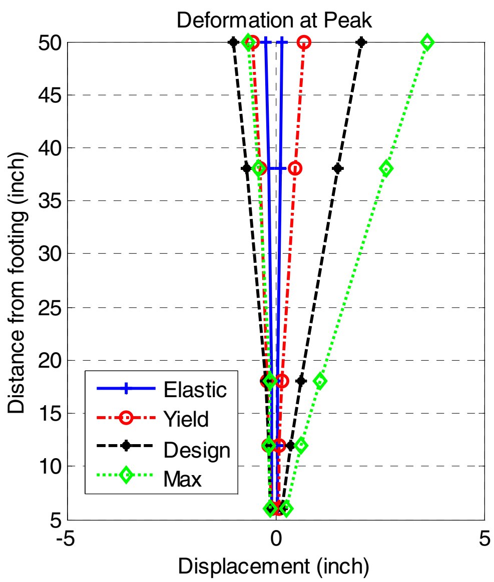

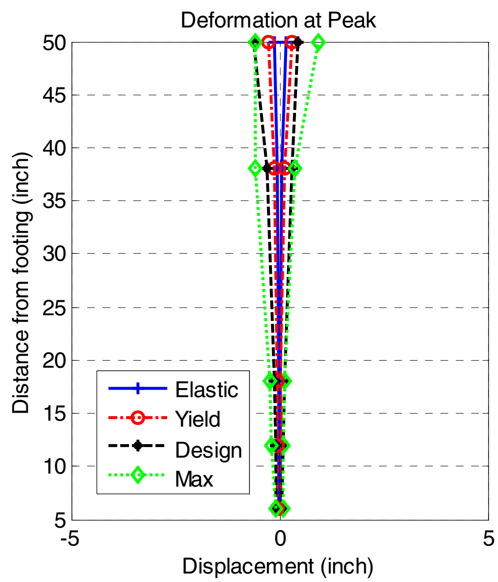

(a) *X* (N-S) direction (b) *Y* (E-W) direction

Short column

Fig. 4.61 Peak displacement responses along columns

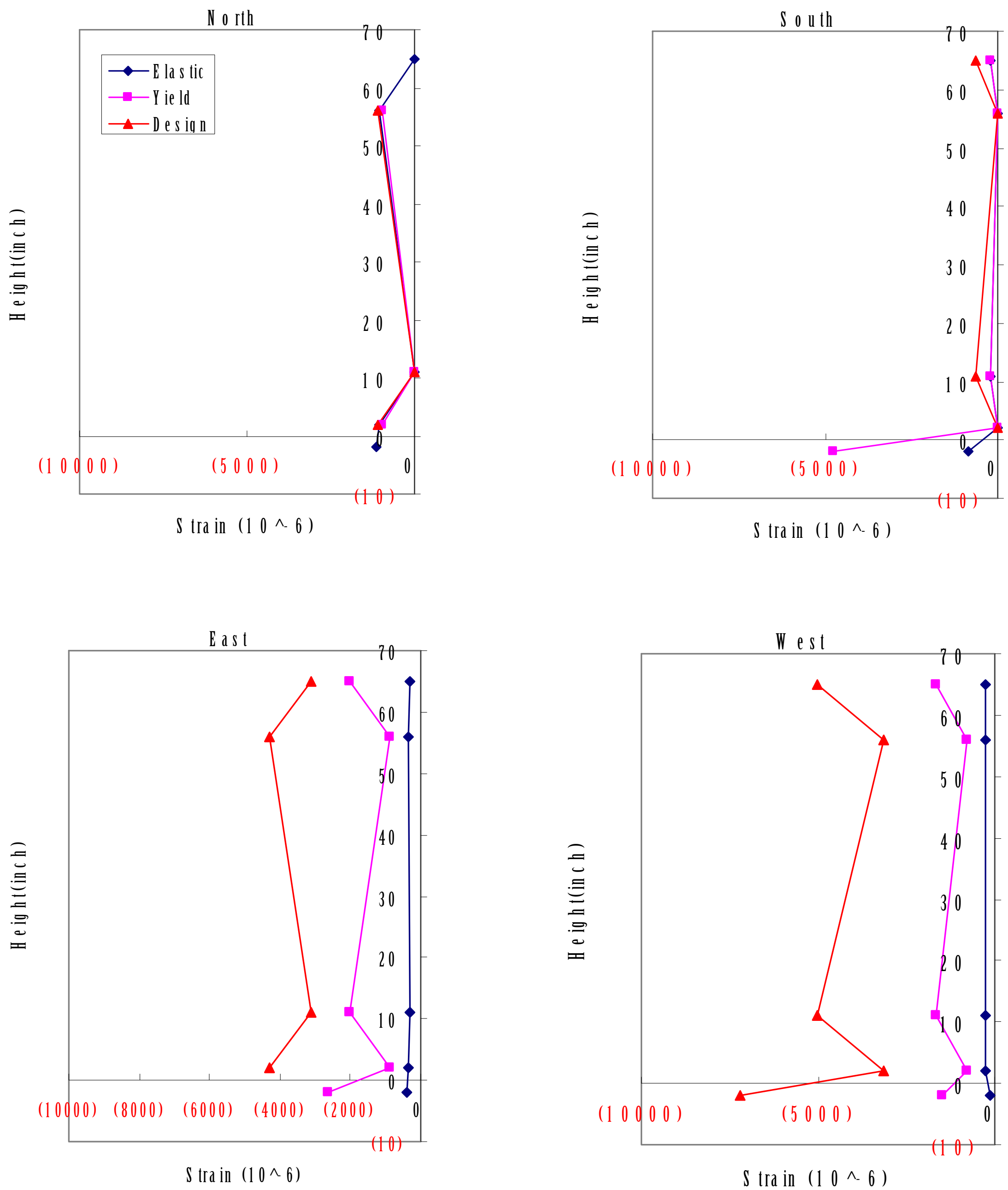

Fig. 4.62 Maximum compression strain distribution (long column)

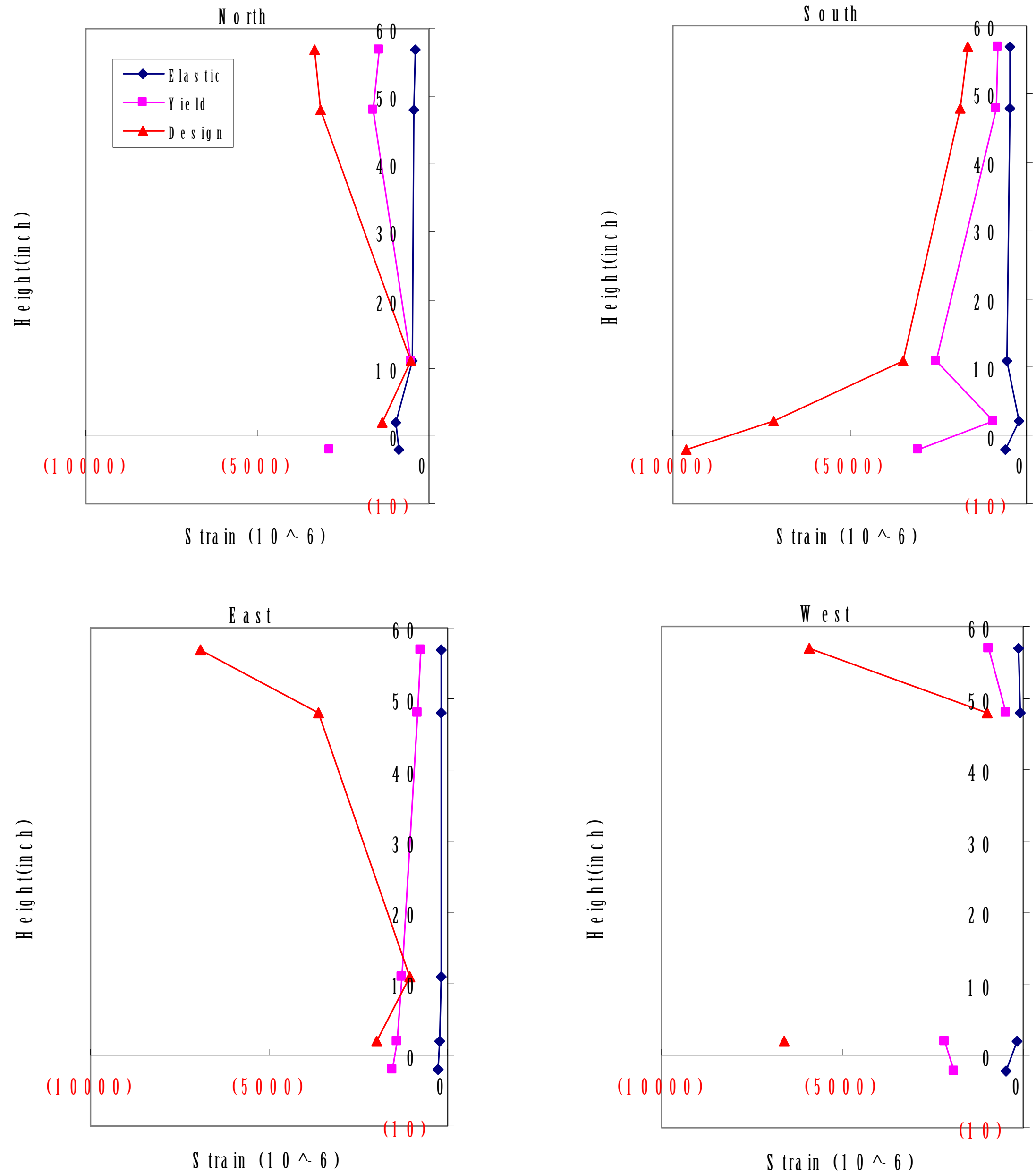

Fig. 4.63 Maximum compression strain distribution (short column)

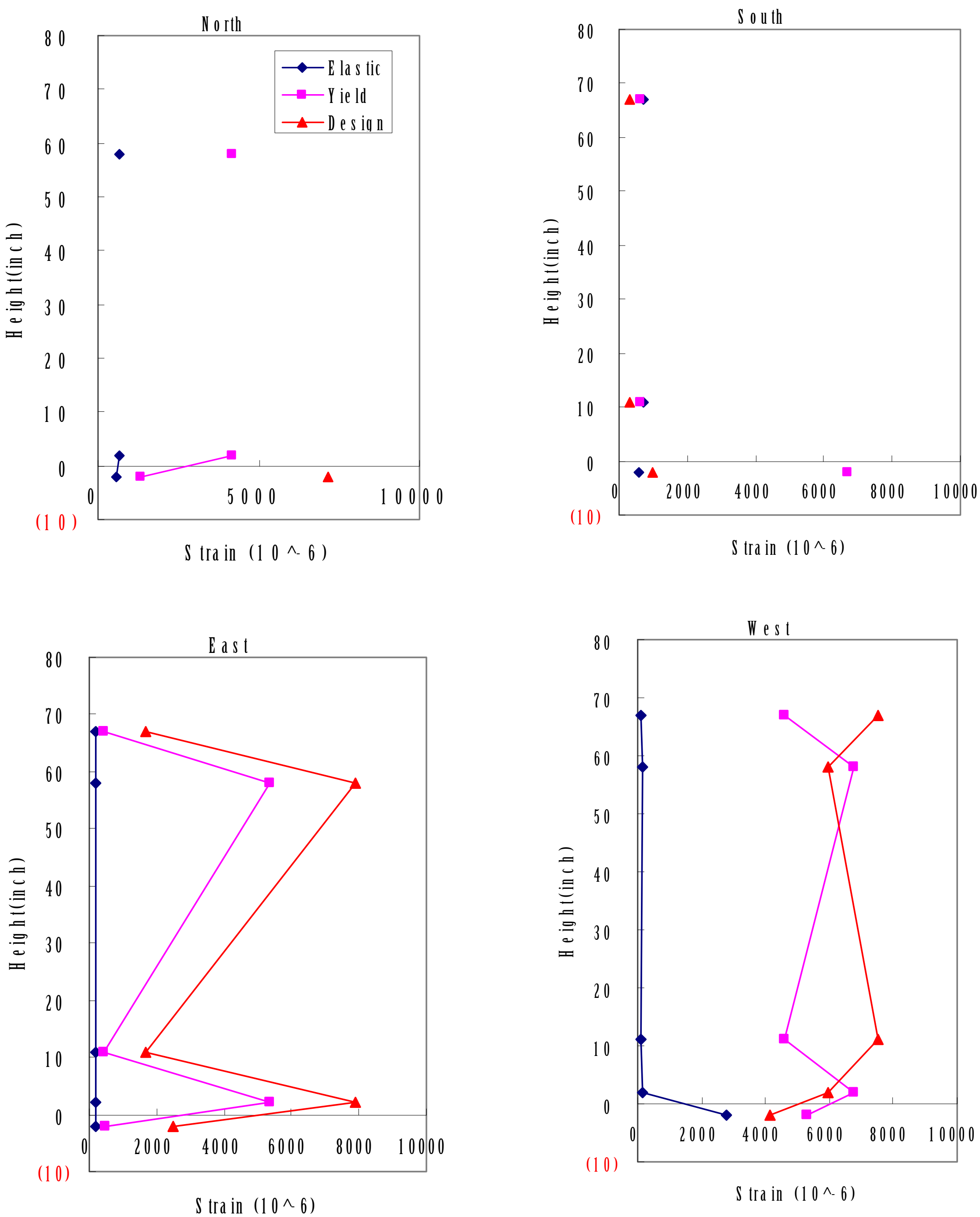

Fig. 4.64 Maximum tension strain distribution (long column)

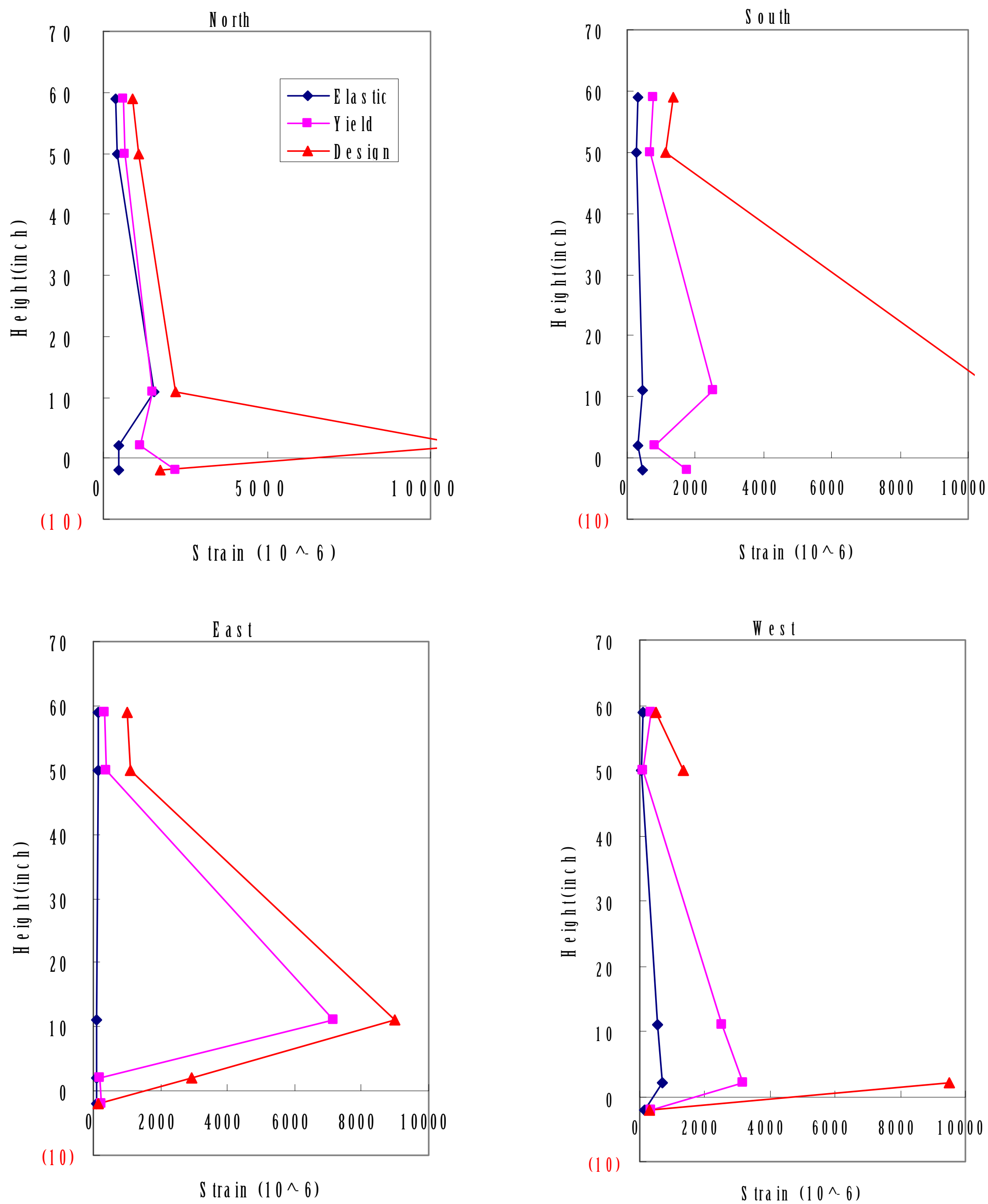

Fig. 4.65 Maximum tension strain distribution (short column)

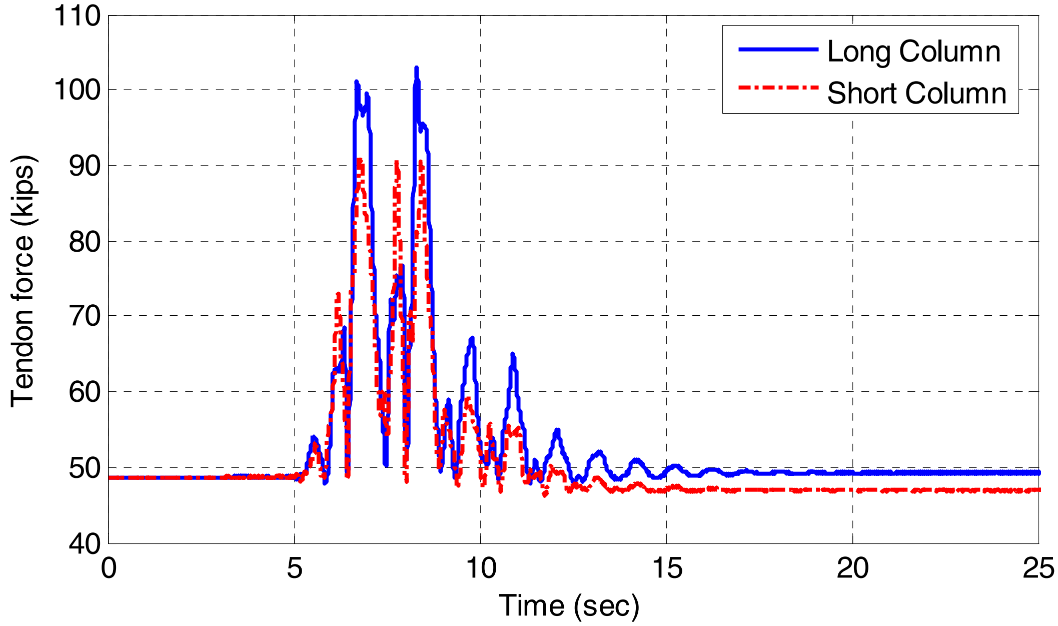

(a) Design level

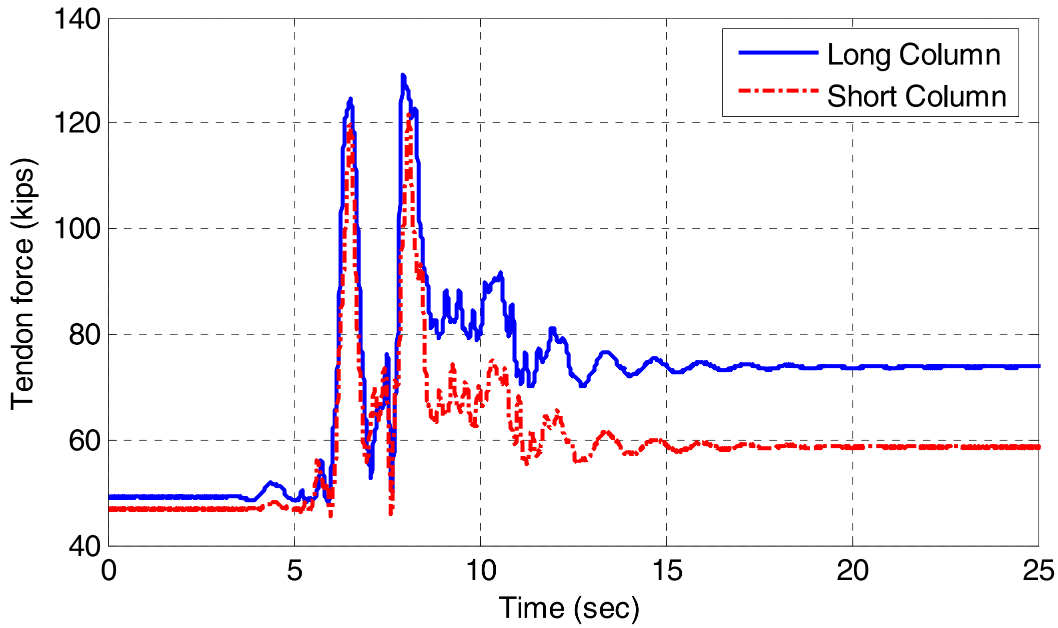

(b) Maximum level

Fig. 4.66 Tendon force

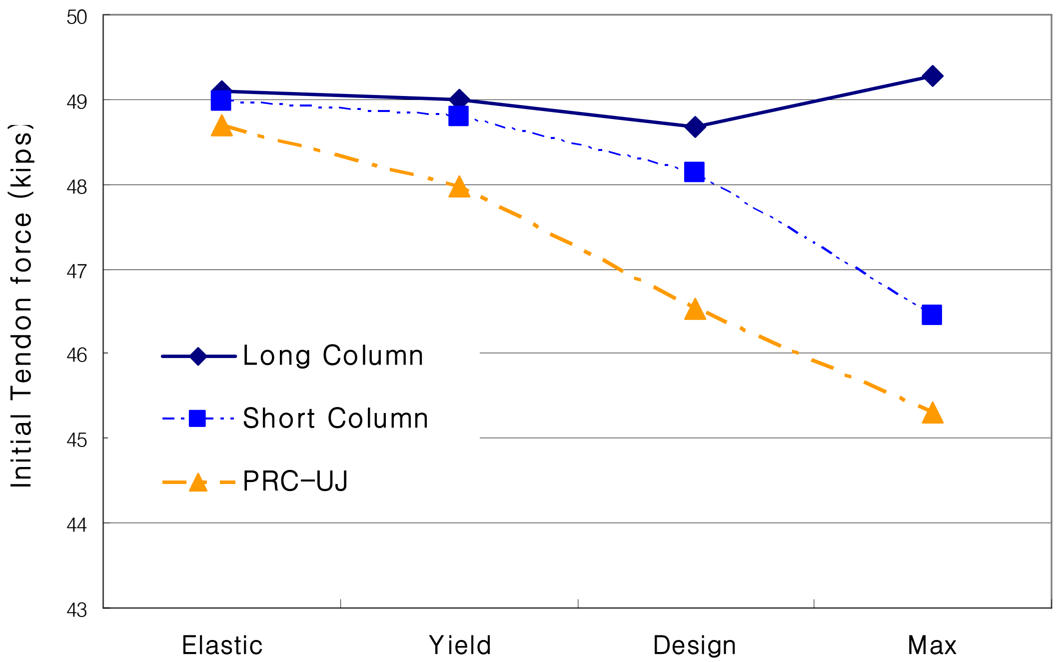

Fig. 4.67 Change of initial tendon force

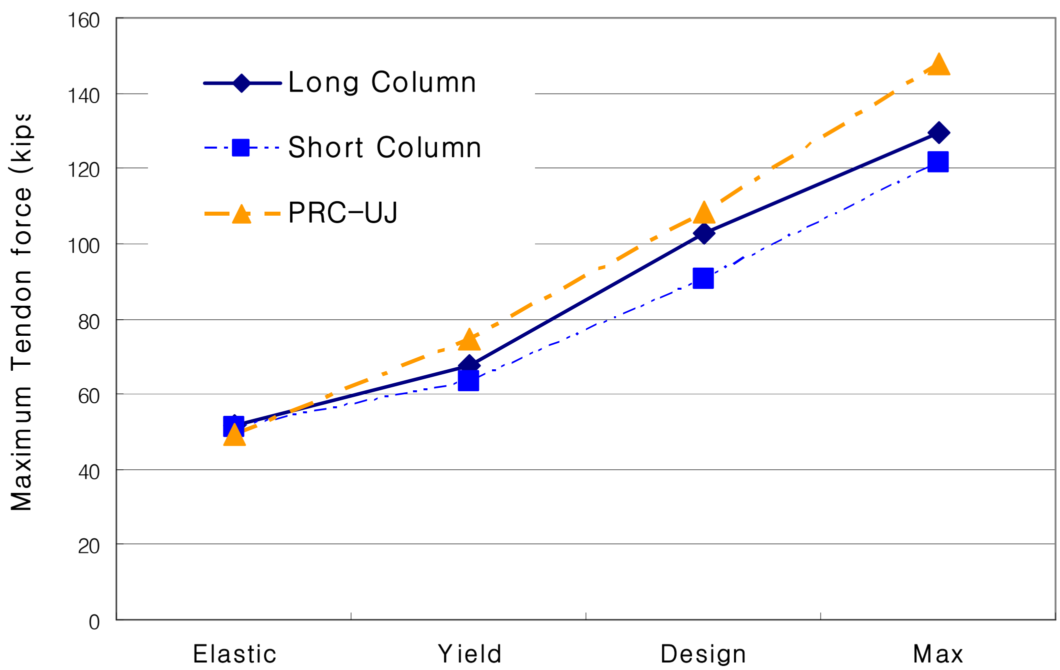

Fig. 4.68 Maximum tendon force

5 Development and Validation of Analytical Models Using Experimental Data

5.1 INTRODUCTION

One of the main objectives of this research is to develop analytical models for predicting with confidence the seismic performance, especially residual displacement, of reinforced concrete bridge columns. Design and evaluation of bridge systems and development of design guidelines related to residual displacements depend on analytical tools and models capable of accurately predicting details of the response time history. To this end, some of the experimental results presented in the previous two chapters and a previous report (Sakai and Mahin 2006) are compared in this chapter with the results predicted using several analytical methods and modeling approaches. Prior modeling guidelines for reinforced concrete bridge columns (Berry and Eberhard 2006) are used as a starting point. The comparisons in this chapter are made to refine such analyses and modeling guidelines and to extend them to partially prestressed reinforced concrete columns of the type investigated herein.

An object-oriented framework, Open Systems for Earthquake Engineering Simulation (OpenSees), was used to create the analytical models and perform nonlinear dynamic analyses described in this chapter. OpenSees is an open-source software framework for earthquake analysis of structures developed by PEER researchers (http://opensees.berkeley.edu). The open-source nature of the framework enables researchers and engineers to easily add and share enhancements to the material and element models.

To develop the appropriate analytical model for each specimen, the analytical model for the RC specimen from the previous research is examined first. This specimen sustained significant residual displacement, and the ability to predict this displacement is a necessary first step. Then the development of the PRC specimen model follows. A roadmap for the development of the analytical models is shown in Figure 5.1. The test results for the initial RC and PRC specimens can be found in the previous report (Sakai and Mahin 2006).

Section 5.2 describes the approaches considered in this study for modeling reinforced concrete materials and members. The results of dynamic analysis performed using these models for the different specimens are compared with the shaking table test results in Section 5.3. Global response parameters, i.e., peak lateral displacement, residual lateral displacements, base shear, overturning moment, and lateral accelerations are considered. Various other issues related to modeling are also described in this section, e.g., the effect of different concrete models, steel models, and damping. Conclusions are presented in Section 5.4 regarding modeling and analytical practices. Using these experimentally validated models, a broad range of structural and ground motion parameters are considered in the analyses presented in Chapter 6. These parametric analyses are used to identify robust recommendations for proportioning partially prestressed reinforced concrete self-centering columns.

5.2 ANALYTICAL MODELING

Because of the highly nonlinear bidirectional response of the systems of interest, elastic analytical methods are not applicable, and inelastic methods based on simplified phenomenological models are unlikely to be sufficiently accurate for the purpose of these studies. As a result, the basic modeling approach followed in this chapter uses force-based fiber elements capable of modeling the behavior of columns under varying axial load and bidirectional end moment. In these models, cross sections at discrete locations along the length of the member are represented by assemblages of longitudinally oriented, unidirectional steel and concrete fibers. For these analyses, member torsional and shearing contributions to response are assumed to be negligible. In addition, the effects of bar pullout from the column support regions are not explicitly modeled, but rather incorporated into the selection of plastic hinge and material properties.

This section discusses the types of hysteretic models used to represent material properties, the approach used to discretize the cross section into fibers, numerical formulations used to simulate overall member behavior, and techniques used to characterize viscous damping.

5.2.1 Material Modeling

In fiber models, accurate modeling of material stress-strain responses is required to predict member behavior. Under seismic loading, adequate modeling of unloading and reloading behavior of the material may be critical. A brief description of the material models used in this study is presented below. More details about the foundations of the numerical models discussed can be found in documentation available at the OpenSees website (http://opensees.berkeley.edu).

5.2.1.1 Reinforcing Steel

For the modeling of the longitudinal reinforcing steel in the specimen, two different uniaxial material models in the OpenSees program were considered: the Steel02 and the ReinforcingSteel material models.

Steel02 Material Model in OpenSees

The Steel02 model is based on a Giuffre-Menegotto-Pinto constitutive model (Taucer et al. 1991). The model has a bilinear backbone curve with a post-yield stiffness expressed as a proportion of the initial modulus of elasticity of the steel. The model accounts for the Bauschinger effect, which contributes to the gradual stiffness degradation of reinforced concrete members under cyclic response. This model has an isotropic hardening option for tension and compression portions of the hysteresis. Despite its simplicity, this bilinear model predicts the basic material response accurately over most of the strain range, but it does not account for the initial yield plateau of the reinforcing steel or the degradation of the steel strength due to bar buckling or rupture. The yield point of the model was selected to match the measured stress-strain response from coupon tests. Figure 5.2 shows the stress-strain responses of Steel02 (with a post-yield slope of 0.01) and a coupon test. In this case, the input parameters were selected to mimic a traditional bilinear backbone curve.

ReinforcingSteel Material Model in OpenSees

The ReinforcingSteel model uses a nonlinear backbone curve shifted as described by Chang and Mander (1994) to account for isotropic hardening. To account for change in area as the bar is stressed, the backbone curve is transformed from engineering stress space to natural stress space. This allows the single backbone to represent both tensile and compressive stress-strain relations. The tension and compression backbone curves are thus not the same in engineering stress space for this model. This transformation assumes small strain relations described by Dodd and Restrepo-Posada (1995). In this model, several buckling options can be used to simulate the buckling of the reinforcing bar, but these options were not used for the analysis in this chapter. Several parameters of the model, i.e., yield stress, ultimate stress, initial elastic tangent, tangent at initial strain hardening, and strain at peak stress, were selected to match the measured stress-strain response from coupon tests. Figure 5.3 shows the stress-strain responses of ReinforcingSteel and a coupon test. The nonlinear backbone curve of the model can be closely matched with the coupon test results, as seen in the figure.

5.2.1.2 Concrete

For the modeling of the confined concrete (core concrete) and unconfined concrete (cover concrete) in the specimen, a uniaxial material model in the OpenSees program was considered to evaluate the effect of the concrete modeling.

The relations described by Mander et al. (1988) were used to compute enhanced strength and strain capacity of confined concrete.

Concrete02 Material Model in OpenSees

The Concrete02 model is a modification of Concrete01 with tensile strength added. Concrete02 uses the Kent-Park model to represent the concrete compressive stress-strain curve and straight lines for the rising and falling segments of the tension region. The unloading stress-strain characteristics are based on Karsan and Jirsa (1969). Concrete02 provides tension strength that can therefore model the initial cracking of the cover concrete. Concrete02 has some parameters that can control the descending slope and residual strength. Figure 5.4 shows the stress-strain response of the unconfined and confined concrete model. A peak point of the unconfined concrete model was chosen to match the results of the cylinder tests of the concrete.

5.2.2 Fiber Section Modeling

A fiber section was constructed by using reinforcing steel fibers and fibers with different properties for the unconfined and confined concrete. A total of 252 fibers were used for modeling the RC section (200 for confined concrete fibers, 40 for unconfined concrete fibers, and 12 for reinforcing steel fibers). Figure 5.5 shows the details of the section modeling in the RC and PRC specimens. The discretization for the PRC specimens was similar to that for the RC specimen except for deleting some concrete fibers to form a void at the center of the section.

5.2.3 Modeling of Reinforced Concrete Column

Two column modeling strategies are mainly used herein for modeling a cantilever concrete bridge column. One method utilizes distributed-plasticity theory with a force-based beam-column element. The other method utilizes concentrated- (lumped-) plasticity theory in which nonlinear deformations are concentrated within a defined plastic hinge region. The following describes the key aspects of the distributed-plasticity modeling strategy and the concentrated- (lumped-) plasticity modeling strategy.

The specimens are idealized as a three-dimensional discrete model as shown in Figures 5.6–5.9. A lumped transverse mass with rotational mass of inertia is applied at the top node positioned at the center of gravity of the weight block assemblage. The top mass block and footing regions are assumed to be rigid, and are modeled in OpenSees by an element rigid end offset option. One element, with two rigid end offsets, is thus used for modeling each column.

5.2.3.1 Nonlinear Force-Based Beam-Column Element (Distributed-Plasticity Modeling)

A distributed-plasticity beam-column [OpenSees nonlinearBeamColumn] element was used to model a flexural component of the column. This element is a line element in which the moment-curvature (and axial load–axial deformation) response at each integration point is determined from the section assigned to that integration point. Figure 5.6(a) shows the schematic drawing for a nonlinear beam column element with 5 integration points along its length.

A flexibility-based formulation imposes a moment and axial force distribution along the length of the column in equilibrium with the loads imposed at the end nodes of the member, and the curvatures (and axial deformations) at each integration point are subsequently estimated by iteration given the moment (and axial load) at that section. The column response is then obtained through weighted integration of the section deformations (Taucer et al. 1991) along the length of the member. Because most inelastic behavior occurs near the ends of a column, this element utilizes the Gauss-Lobatto integration scheme, in which integration points are placed at the ends of the element, as well as along the column length, at locations that increase the efficiency of the integration (i.e., they are not set by the user). The main parameter of this element is the number of integration points.

5.2.3.2 Beam with Hinges Element (Concentrated-Plasticity Modeling)

This element is not a lumped-plasticity element in the conventional sense, wherein the nonlinear behavior is lumped into moment-rotation springs at the ends of an element. Rather, the element is still a fiber-based element but with nonlinear constitutive behavior limited to user-specified plastic hinge regions at the ends of the element. The remainder of the element behaves elastically linear. Figure 5.6(b) shows the schematic drawing for a beam with hinges [OpenSees beamWithHinges] element with a plastic hinge localized at one end.

While the integration of distributed-plasticity force-based elements distributes the Gauss points along the entire element length, the beamWithHinges element localizes the integration points in the hinge regions. Two integration points per hinge are used to be able to represent the curvature distribution accurately. The full details of the element formulation can be found in Scott and Fenves (2006). This recently developed element makes use of a modified Gauss-Radau quadrature rule for integrating element stiffness to eliminate objectivity in the nonlinear response while maintaining the exact response under linear conditions. Main parameters of this element are plastic hinge lengths and effective stiffness of the elastic part of the column.

5.2.4 Damping Modeling

Damping properties of the analytical models are usually idealized using Rayleigh damping. The Rayleigh damping matrix is computed as a linear combination of the mass and stiffness matrices. The damping matrix can be selected three different ways: mass-only proportional, stiffness-only proportional, and mass-and-stiffness proportional. To evaluate the effects of the damping modeling on the analytical results, all three approaches were used. Damping ratio values typically used for the design of reinforced concrete structures range from 3% to 7%. The value most widely used by building codes is 5%. Based on the damping observed in the shaking table tests (Section 3.4.3), the Rayleigh coefficients α and β were selected. The damping matrix was formed at each analytical step using the current tangent stiffness matrix and/or mass matrix.

5.2.5 Input Acceleration

The recorded accelerations at the footing of the specimens are used as the input earthquake data for the analysis. The accelerations recorded at the west surface are used for the *x* direction, while those recorded at the south surface are used for the *y* direction. The recorded accelerations are low-pass filtered with a cutoff frequency of 20 Hz. The recorded signals of the different levels of the earthquake input (elastic, yield, design, and maximum-level tests) are combined in series into a single long record. A sufficient interval of no excitation was inserted between the periods of table motion so that the specimen response damped out prior to the start of the next period of shaking. By inspecting the resulting numerical response following the analysis, maximum displacements, cumulative displacements, residual displacement, cumulative residual displacements, and local curvatures and strains could be determined.

5.2.6 Prestressing Tendon

There are several ways to model an unbonded prestressing tendon in the middle of a concrete column. Initially, a truss element was used to model the prestressing tendon with an initial strain representing the prestressing force. The initial strain of a simple truss model showed a secondary geometric effect, i.e., the P-Δ effect, whereas the tendon force does not have secondary effect in the real system. Therefore, instead of a simple truss element, a co-rotational truss (OpenSees corotTruss element] was used to remove the secondary effect of using the initial strain as the means of generating the prestressing force.

5.2.7 Unbonded Mild Rebar

Unbonded mild rebar was used in several of the specimens to avoid strain concentration within the plastic hinge region of the column. It is not easy to model the unbonded mild rebar in the fiber element because of the model's basic assumption that the cross section of the member remains plane during the response. To model the effect of unbonding of the mild reinforcement with the fiber-based elements, it was assumed that the strain of each bar is constant throughout the plastic hinge length. To achieve a constant strain in the rebar, only one integration point was used for modeling all rebar in the plastic hinge length. The location for the integration point was calibrated using the experimental data.

Figure 5.9 shows a schematic drawing of the analytical model for the PRC specimens (PRC-U, PRC-U2, and PRC-UJ) using unbonded mild bar at the plastic hinge region. In this region, two separate nonlinearBeamColumn elements with two integration points are applied with different fiber sections; one element consists of only concrete fibers, and the other element has only steel fibers. An elastic beam-column [OpenSees elasticBeamColumn] element with an effective stiffness is assigned to the middle of the column.

5.2.8 Steel Jacket

The steel jacket used in specimen PRC-UJ was assumed to be a continuous spiral in order to use the relations described by Mander et al. (1988) to compute the enhanced strength and strain capacity of the concrete confined by the steel jacket. The possible composite action of the steel jacket was ignored.

5.3 COMPARISON OF ANALYTICAL AND TEST RESULTS

In developing a robust analytical model for all the test specimens, initial efforts focused on the RC specimen. Then other models with a prestressing tendon, unbonded mild bar, and steel jacketing were developed. Section 5.3.1 describes the process of developing the analytical model for the RC specimen and provides a comparison of the analytical and test results. Subsequent sections are mainly parallel comparisons of the analytical and test results for the other specimen models; as such, some portions of the content are repeated. The results shown below are only a small fraction of those used to identify optimal modeling parameters. From these studies, it is clear that due to the large number of modeling parameters involved, there is not a unique set of parameters that will produce reasonable results.

5.3.1 RC Specimen

For the RC specimen analysis, the recommended model by Berry and Eberhard (2006) was used as the basic model. The parameters of this base model are as follows:

- Column modeling: nonlinear beam-column (NLBC) model (nonlinearBeamColumn element];
- Concrete modeling: Concrete02 with Mander equation;
- Steel modeling: Steel02 with hardening ratio of 0.01; and
- Number of integration points: 5

Table 5.1 shows the detailed values for a base model of the RC specimen and Figure 5.11(a) shows the comparisons of the analytical and real results of the design and maximum-level tests. As can be seen from the results, the NLBC analytical model displaces less than the test specimen in both directions; appears to initially have a slightly shorter period; and shows almost no residual displacement in analysis at either the design or maximum levels.

Discussion with the researcher who did the previous test for the RC specimen revealed that during the setup on the shaking table, the table was discovered to be out of order, necessitating repair of the table with the RC specimen in place. Consequently, during the repair time the specimen experienced repeated small shaking in the *elastic* range. Due to this shaking, the RC specimen was already cracked before the main test. The NLBC element model was not able to incorporate these prior conditions.

To improve the suitability of the NLBC model represented by the damaged RC specimen, the beam with hinge (BWH) model with appropriate effective stiffness was selected as the new base model. The length of the plastic hinge was 13.01 in. (330.4 mm), derived using the Priestley plastic hinge model (Priestley et al. 1996); and the effective stiffness of the central portion of the column was chosen as 0.2 EI_g (gross stiffness), selected to match the natural period of the test results. The other parameters remained the same as in the previous model. Figure 5.11(b) shows the results of the design and maximum-level tests. In this new base model, the analytical and real maximum displacements of both the design and maximum levels and the apparent periods are quite well matched. In contrast, the residual displacements do not match for either level in either direction; the analysis does not show residual displacement, while the test shows relatively large residual displacement in the maximum-level test.

As the next step in refining the model of the RC specimen, the effects of the steel modeling were investigated. Instead of the Steel02 bilinear model, the ReinforcingSteel model was used. Other parameters were the same as in the previous model. As seen in Figure 5.11(c), the ReinforcingSteel model results in some residual displacements. Especially at the design-level the analytical results match the test results quite well, but there is still some difference at the maximum level of the testing. The analytical results for the maximum displacements are quite similar between the different steel models.

To further refine the analytical model of the RC specimen, some descending parameters of the concrete modeling were investigated. After some parametric study, a combination of several descending parameters providing good agreement with the test results was identified.

Sakai and Unjoh (2006) tried to match the results of the shaking table test with the analytical results; they found that lower damping can give good results for the residual displacements. In this study, the effects of the damping were also considered. Investigation of different damping ratios and different damping methods revealed that stiffness-only damping with 2% or 3% gives good agreement. Figure 5.11(d) shows the results from a calibrated BWH model for the RC specimen using the improved descending branch parameters for concrete and a stiffness-only viscous damping value of 2%. The close match of analysis and test are evident in the figure.

From the parametric study of the analytical model, the following model is suggested for the analysis of the RC specimen:

- Column modeling: beam with hinge (BWH) model [beamWithHinges element];
- Concrete modeling: Concrete02 with the following suggested descending parameters for confined concrete:
    - Suggested residual stress (f_{cu}) is 50–70% of peak compressive stress (f'_c);
    - Suggested strain at ultimate stress(ε_{cu}) is 2.5–3.0 times strain at peak compressive stress (ε_{co});
- Steel modeling: ReinforcingSteel; and
- Damping: stiffness-only damping (2–3%).

Table 5.2 shows the detailed values for the suggested model of the RC specimen. Based on this recommended model, Figures 5.12–5.15 show global response comparisons between the test and analytical results of the RC specimen for all four test levels. Table 5.3 displays global responses of the test and analysis, and ratios of the two, for both directions at the design and maximum test levels.

Figures 5.12(a–d) show relative displacement response at the center of gravity for all four test levels (elastic, yield, design, and maximum) for the *x* and *y* directions using the recommended numerical model. The analytical results are significantly well matched with the test results for all test levels in both directions. At the lower levels, the first few cycles are quite well matched; but after that, the analytical results show greater stiffness than the test results. The residual displacement of the maximum level in the *x* direction in analysis is a little smaller than test results, about 10% less. The differences between test and analysis for the maximum and residual displacements are within 15% as shown in Table 5.3.

In addition to the relative displacement at the center of gravity, other global response values of the analytical results based on the recommended model were compared with the test results. Figures 5.13(a–d) show acceleration response at the center of gravity for all four tests. Again, the test and analytical results are relatively close through all test levels. At the maximum level, the test shows some residual due to the inclination of the specimen introducing an acceleration reading in the accelerometer, but the analysis does not show the residual, as expected. The difference between test and analysis for the maximum acceleration are within 30% as shown in Table 5.3.

Lateral force responses at the bottom of the footing in the *x* and *y* directions for each test are shown in Figures 5.14(a–d). There are good agreements between measured and calculated lateral force responses through all test levels in general. The difference between test and analysis for the maximum shear force at the design and maximum levels are within 6% as shown in Table 5.3.

Figures 5.15(a–d) compare moment-displacement responses for all four test levels in both directions. The elastic and yield-level tests show good agreement of stiffness between test and analysis.

As shown in Figures 5.12–5.15, the recommended analytical model matches quite well with the test results for several global responses at different test levels. As seen in Table 5.3, most of the differences between test and analysis are within 15%.

Based on the study to develop the analytical model of the RC specimen, findings include the following:

- Proper steel modeling is important to predict residual displacement;
- The descending branch of the concrete modeling can be affected to predict residual displacement; and
- When hysteretic damping is playing an important role in the total damping, the Rayleigh damping ratio should be reduced to model appropriate damping of the system.

5.3.2 PRC Specimen

Based on the analytical modeling of the RC specimen developed in the previous section, the analytical model for the PRC specimen was created. Since the mild longitudinal reinforcement was bonded for this specimen, the only differences between the PRC specimen and the RC specimen are the changes needed to account for the unbonded prestressing tendon at the middle of the column. As mentioned in Section 5.2.6, a co-rotational truss element with initial strain was used for the modeling of an unbonded prestressing tendon. Other modeling parameters for the PRC specimen followed the suggested RC specimen model. Because the PRC specimen did not sustain damage before the testing, analysis for two effective stiffness values was performed to check the effect of the initial stiffness for the elastic region of the beamWithHinges element. One was chosen from Caltrans SDC that considers the total axial force ratio ($EI_{eff} = 0.36\ EI_g$), and the other was chosen to match the natural frequency of the test specimen ($EI_{eff} = 0.6\ EI_g$). Figure 5.16(a) compares the analytical results (for different EI_{eff} values) and actual results of the yield and design-level tests. The analytical results for 0.36 EI_g are a little higher than test results at the lower levels (elastic and yield), but the analytical results with 0.6 EI_g are in very good agreement with the test results. As seen in Figure 5.16(a), one of the important factors in matching the results at the lower levels is the appropriate natural frequency; when effective stiffness for the elastic region of the beamWithHinges is properly selected, the lower levels can be easily matched. Figure 5.16(b) shows the design and maximum-level test comparisons of the analytical and actual results. The analytical results for 0.36 EI_g and 0.6 EI_g are both in very good agreement with the test results; the results from higher level input are not as sensitive to the selection of the effective stiffness of the elastic part of the beamWithHinges element.

Table 5.4 shows the values of the suggested model for the PRC specimen. The main difference with the RC specimen model is effective stiffness and residual stress. For the PRC specimen, higher residual stress (70% of peak compressive stress) gives good agreement for residual displacement.

Figures 5.17–5.21 show global response comparisons between the test and analytical results of the PRC specimen for all four test levels. Table 5.5 displays global responses of the test and analysis, and ratios of the two, in both directions for the design and maximum levels.

Figures 5.17(a–d) show relative displacement response at the center of gravity for all four test levels (elastic, yield, design, and maximum) in both the *x* and *y* directions. The analytical results are in very good agreement with the test results for all four test levels in both directions. The differences between test and analysis for the maximum and residual displacements at the maximum level are within 15% as shown in Table 5.5. The ratio for the residual displacement at the design level in the *y* direction is 32%, but the difference in actual displacement terms is only 0.2 in. For a small residual displacement, the ratio between analysis and test might be large while the actual difference is small; the difference as well as ratio should be checked when making a residual displacement comparison.

As with the RC specimen, in addition to the relative displacement at the center of gravity, other analytical values are also compared with the test results. Figures 5.18(a–d) show acceleration response at the center of gravity for all four test levels in both directions. The analytical results are in very good agreement with the test results for all levels in both directions.

Lateral force responses for all test levels in both directions are shown in Figures 5.19(a–d). The same trends in the acceleration results can be observed in the lateral force results. The difference between test and analysis for the maximum shear force at the design and maximum levels are within 20% as shown in Table 5.5.

Figures 5.20(a–d) compare moment-displacement responses for all four test levels. The test results show quite similar stiffness with the analytical results, as expected from the displacement results in the elastic and yield-level tests. At the higher levels, the response shows good agreement between test and analysis.

Figures 5.21(a–b) compare prestressing tendon force responses for the design and maximum levels. The results are quite well matched. The difference between test and analysis for the maximum tendon force at the design and maximum levels are within 7% as shown in Table 5.5.

As can be seen in Figures 5.17–5.21, the analytical results for the PRC specimen are quite well matched with the test results for all other global responses. The analysis of the PRC specimen verifies that using a co-rotational truss element with initial strain is appropriate as a modeling of the prestressing tendon.

5.3.3 PRC-2 Specimen

As mentioned in Section 3.2.2.2, the PRC-2 specimen followed the design of the PRC specimen; most of the design details of PRC-2 are the same as those of specimen PRC. The main difference is material properties: concrete strength and steel strength, and the intensity of the ground motion record.

The analytical model of the PRC specimen was chosen for the PRC-2 specimen with suitable modifications for the concrete and steel strengths. The effective stiffness for the elastic region of the beamWithHinges element was chosen to match the natural frequency of the test specimen. Table 5.6 shows the values that were used for analytical modeling of the PRC-2 specimen.

Figures 5.22–5.26 show global response comparisons between the test and analytical results of the PRC-2 specimen for all four test levels. Table 5.7 displays global responses of the test and analysis, and ratios of the two, in both directions for the design and maximum levels.

The comparison between the analytical and experimental results of relative displacement response at the center of gravity are shown in Figures 5.22(a–d). At all levels, the analytical results are remarkably well matched with the test results. Especially in the PRC-2 analysis, because the natural frequency was calibrated by the effective stiffness of the elastic region in the beamWithHinges element, the lower-level test results are quite similar. The difference between test and analysis for the maximum and residual displacements at the maximum level are within 15% as shown in Table 5.7. The ratio for the residual displacement at the design level in the x direction is 22%, but the difference is only 0.05 in.; thus, the calculated residual displacements are also very close to the measured values.

Figures 5.23(a–d) show relative acceleration response at the center of gravity for all four test levels in both directions. At each level, the first few cycles are quite well matched, but after that the analytical results show greater stiffness than the test results. Overall, the calculated and measured results are very similar. The differences between test and analysis for the maximum acceleration at the design and maximum levels are within 20% as shown in Table 5.7.

Lateral force responses are shown in Figures 5.24(a–d). The same trends in the acceleration results can be observed in the lateral force results. The difference between test and analysis for the maximum shear force at the maximum level are within 25% as shown in Table 5.7. The calculated results are smaller than the measured results in general.

Figures 5.25(a–d) compare moment-displacement responses for all four test levels. The test results match quite well with the analytical results at the elastic level, as expected. The response shows overall good agreement between test and analysis.

Figures 5.26(a–b) compare prestressing tendon force responses for the design and maximum levels. The results are very close. The differences between test and analysis for the maximum tendon force at the design and maximum levels are within 10% as shown in Table 5.7.

As evident in Figures 5.22–5.26, the analytical results for the PRC-2 specimen closely match the test results for several global responses. The analysis of the PRC-2 specimen confirms that the analytical model for specimen PRC is appropriate.

5.3.4 PRC-U Specimen

As mentioned in Section 5.2.7, for the modeling of the unbonded mild rebar, it is assumed that the strain of each unbonded rebar along the plastic hinge length is constant. To apply that assumption to the analytical model, one integration point was assigned to rebar fibers in the plastic hinge region. The position of the integration was chosen by calibration to the test results. The height of the integration point from the footing was 30% of the plastic hinge length. The details of the analytical model for specimen PRC-U can be found in Section 5.2.7. Most of the other parameters of the analytical model for PRC-U are the same as for the PRC column model. Table 5.8 shows the values that used for analytical model of the PRC-U specimen.

Figures 5.27–5.31 show global response comparisons between the test and analytical results of the PRC-U specimen for all test levels. Table 5.9 displays global responses of the test and analysis, and ratios of the two, in both directions for design and maximum levels.

Comparisons between the analytical and experimental results in both directions of relative displacement response at the center of gravity are shown in Figures 5.27(a–d). For the four test levels, the first few cycles are quite well matched, but after that the analytical results indicate greater stiffness than the test results. In general, the calculated and measured results closely match at the design level. At the maximum level, the analytical response of the *x* direction is a little smaller than that of the test result after peak response, but the analytical response of the *y* direction is a little larger than the test result. The differences between test and analysis for the maximum displacement at the design and maximum levels are within 15% as shown in Table 5.9. The ratios between measured and calculated residual displacements at the design level in the *x* and *y* directions are 62% and 185%, but the differences are less than 0.04 in. However, at the maximum level the difference between the measured and calculated residual displacements is 0.73 in. This might reflect the difficulty in modeling the unbonded mild rebar, but the analytical results are well matched with the test results in general.

Figures 5.28(a–d) show the acceleration response at the center of gravity for all tests in both directions. For the four levels, the first few cycles are quite well matched, but after that the analytical results reflect greater stiffness than the test results. Overall, the calculated and measured results are close. The differences between test and analysis for maximum acceleration at the design and maximum levels are within 20% as shown in Table 5.9.

Lateral force responses are shown in Figures 5.29(a–d). The same trends in the acceleration results can be observed in the lateral force results. The calculated results are larger than the measured results in general. The difference between test and analysis for the maximum shear force at the maximum level are within 25% as shown in Table 5.9.

Figures 5.30(a–d) compare moment-displacement responses for all four test levels. The test result matches quite well the analytical result at the elastic level, as expected. The responses show good agreement between test and analysis overall.

Figures 5.31(a–b) compare prestressing tendon force responses for the design and maximum levels. The analytical results are a little smaller than the measured values at the design level but are quite well matched at the maximum level. The differences between test and analysis for the maximum tendon force at the design and maximum levels are within 5% as shown in Table 5.9.

Figures 5.27–5.31 indicate that the analytical results for the PRC-U specimen provide a very good match with the test results for global responses at the design level. There are slightly greater differences at the maximum level, especially in residual displacement.

5.3.5 PRC-U2 Specimen

The main difference between specimens PRC-U and PRC-U2 is the prestressing tendon force; different initial strain values for the truss element were used as the respective prestressing force. Most of the other parameters are the same as for the PRC-U specimen except for concrete strength.

Figures 5.32–5.36 show global response comparisons between the test and analytical results of the PRC-U2 specimen for all four test levels. Table 5.10 displays global responses of the test and analysis, and ratios of the two, for both directions at the design and maximum levels.

The comparisons between the analytical and experimental results for the four test levels in both directions of relative displacement response at the center of gravity are shown in Figures 5.32(a–d). At all levels, the first few cycles are quite well matched, but after that the analytical results show greater stiffness than the test results. In general, the calculated and measured results are well matched through all the test levels except the residual part of the maximum level in the *y* direction; the analytical response of the *y* direction is a little larger than that of the test result after peak response as seen in Figure 5.32(d). The differences between test and analysis for the maximum displacement at the design and maximum levels are within 25% as shown in Table 5.10. The ratios between the measured and calculated residual displacements at the design level in the *x* and *y* directions are 314% and 65%, respectively, but the difference is less than 0.1 in. The ratios between measured and calculated residual displacements at the maximum level in the *x* and *y* directions are 120% and 387%, and the difference in the *x* and *y* directions are 0.16 and 1.2 in., respectively These larger differences between the predicted and actual displacements might reflect the difficulty in modeling the unbonded mild rebar. In general, the analytical results well match the test results.

Figures 5.33(a–d) show acceleration responses at the center of gravity. As with displacement responses, at each level the first few cycles are quite well matched, but thereafter the analytical results show greater stiffness than the test results. Overall, the calculated and measured results are close. The differences between test and analysis for the maximum acceleration at the design and maximum levels are within 20% as shown in Table 5.10.

The lateral force responses for all test levels in both directions are shown in Figures 5.34(a–d). The same trends in the acceleration results can be observed in the lateral force results. The differences between test and analysis for the maximum shear force at the maximum level are within 25% as shown in Table 5.10. The calculated results are larger than the measured results in general.

Figures 5.35(a–d) compare moment-displacement responses for all four test levels. The responses show good agreement between test and analysis in general.

Figures 5.36(a–b) compare prestressing tendon force responses for the design and maximum levels. The analytical results are a little smaller than the measured values at the design level, but the analytical results are well matched at the maximum level. The differences between test and analysis for the maximum tendon force at the design and maximum levels are within 15% as shown in Table 5.10.

As seen in Figures 5.32–5.36, the analytical results for the PRC-U2 specimen match well with the test results for global responses. There are some differences at the maximum level in the *y* direction, especially in residual displacement.

5.3.6 PRC-UJ Specimen

A steel jacket is used at the plastic hinge region in the PRC-UJ specimen. For the appropriate modeling of the steel jacket component, the stress-strain relation for concrete confined by a steel jacket is needed. But there exist relatively few reliable constitutive models of confinement by steel jacketing, although constitutive models of concrete confined by traditional hoop reinforcement have been developed for reinforced concrete. Thus, the frequently cited constitutive model by Mander et al. (1988) is used for modeling the steel jacket by treating it as a continuous spiral. Most of the other parameters are the same as those of the analytical model for the PRC-U specimen. No attempt was made to model composite action between the concrete column and the steel jacket.

Figures 5.37–5.41 show the global response comparisons between the test and analytical results of the PRC-UJ specimen for all four test levels. Table 5.11 displays the global responses of the test and analysis, and ratios of the two, for both directions at the design and maximum levels.

Comparisons between the analytical and experimental results for the relative displacement response at the center of gravity are shown in Figures 5.37(a–d). For each level, the first few cycles are quite well matched; thereafter there is greater stiffness evident in the analytical results than in the test results. In general, the calculated and measured results are well matched through all test levels, except residual displacements at the maximum level. The differences between test and analysis for maximum displacement at the design and maximum levels are within 10% as shown in Table 5.11. The ratios between the measured and calculated residual displacements at the design level in the x and y directions are 45% and 153%, respectively, but the difference is less than 0.02 in. The respective ratios between the measured and calculated residual displacements at the maximum level in the x and y directions are 206% and 260%, and the differences in the x and y directions are 0.48 and 0.66 in., respectively.

Figures 5.38(a–d) show acceleration responses at the center of gravity. The calculated and measured results are well matched in general. The differences between test and analysis for the maximum acceleration at the design and maximum levels are within 22% as shown in Table 5.11.

The lateral force responses for all test levels for both directions are shown in Figures 5.39(a–d). The same trends in the acceleration results can be observed in the lateral force results. The difference between test and analysis for the maximum shear force at the maximum level is within 25% as shown in Table 5.11.

Figures 5.40(a–d) compare moment-displacement responses for all four test levels. The analytical responses of moment in both directions are a little smaller than those of the test results in general as can be seen in the figure. The test results match quite well the analytical results at the elastic level. The responses show good agreement between test and analysis overall.

Figures 5.41(a–b) compare prestressing tendon force responses at the design and maximum levels. The analytical results are a little smaller than the measured values at both levels. The differences between test and analysis for the maximum tendon force at the design and maximum levels are within 15% as shown in Table 5.11.

As evident in Figures 5.37–5.41, the analytical results for specimen PRC-UJ match well with the test results for global responses.

5.3.7 PRC-System Specimen

Based on the analytical model of the PRC-UJ specimen, a model for the two-column bent PRC-system was developed. Figure 5.10 shows a schematic drawing of the analytical model for specimen PRC-system. Each column's modeling closely follows the modeling of the PRC-UJ column. To model the steel beam between the columns, one elastic beam-column [OpenSees elasticBeamColumn] element is used for the steel beam. Table 5.12 shows the values chosen for the analytical model of the PRC-U specimen.

Figures 5.42–5.51 show global response comparisons between the test and analytical results of the short and long columns of the PRC-system specimen for all four test levels. Tables 5.13 and 5.14 show global responses of the test and analysis, and ratios of the two, for both the short and long columns in the PRC-system specimen.

The analytical and experimental relative displacement responses at the center of gravity in the *x* direction for all four test levels are shown in Figures 5.42 and 5.43 for the long and short column, respectively. The long- and short-column responses show very similar trends in the *x* direction. In general, the calculated and measured results for the maximum displacements are well matched through all the test levels. For the maximum displacement the differences between test and analysis at the design and maximum levels are within 20% as shown in Table 5.13; but the residual displacement responses reveal quite a difference between the analysis and test results at both levels. At the design level in the *x* direction, the ratios between measured and calculated residual displacements in the long and short columns are 15% and 12%, respectively, and the corresponding differences are 0.35 and 0.41 in. At the maximum level, the respective ratios between the measured and calculated residual displacements in the long and short columns are 5% and 4%, and the differences are 3.61 and 3.96 in. The analysis shows almost no residual displacement, but the test results show some residual displacement at both the design and maximum levels. The actual columns have a short gap between the bottom of the jacket and the top of the footing. Considerable damage was noted in the test specimen in this region. This region was not included in the numerical model.

Figure 5.44 follows Figures 5.42 and 5.43 with a comparison of relative displacement responses in the *y* direction for the long column. The cycles display some differences through the test levels but the maximum and residual displacements have good agreement with calculated and measured values. The differences between test and analysis for the maximum displacement at the design and maximum levels are within 20% as shown in Table 5.13. The differences between test and analysis for the residual displacements at both levels in the *y* direction are within 0.01 in. as shown in Table 5.13.

Figures 5.45–5.47 show the acceleration responses at the center of gravity for all four test levels in both columns. There are some cyclic differences at the elastic level, but the other levels show good agreement in cycle and maximum values in the *x* direction. There is a small residual acceleration in the measured values at the maximum level due to inclination of the column. For the long column at both the design and maximum levels, the differences between test and analysis for the maximum acceleration in the x direction are within 30%, but for the y direction are about 6% as shown in Table 5.13.

For each column the lateral force responses for all tests in both directions are shown in Figures 5.48–5.51. In the x direction the analytical results for the long column are smaller than those of the measured values, especially at the design and maximum levels, while the analytical and test results for the short column are quite similar (see Figs. 5.48 and 5.49). Table**s** 5.14 and 5.15 indicate that at the design and maximum levels, the differences between test and analysis for the maximum shear force of the long column are within 40%, but those for the short column are about 20%.

Figures 5.52 and 5.53 compare prestressing tendon force responses for the design and maximum levels of the long and short columns. At the design level the analytical results are a little smaller than the measured values for the short column, while very similar for the long column. The maximum-level response in the prestressing force strongly reflects the displacement response; due to the residual displacement in the test results, the prestressing force increases at the end of the maximum test. In contrast, there is almost no residual displacement in the analytical values, resulting in little change in the calculated prestressing force. The differences between test and analysis for the maximum tendon force at the design and maximum levels are within 25% as shown in Table**s** 5.13 and 5.14.

5.4 SUMMARY AND CONCLUSIONS

Based on the comparison of measured global responses and nonlinear analysis for different specimens, analytical models for predicting the seismic performance, especially residual displacement, of reinforced concrete bridge columns were developed. An object-oriented framework, OpenSees, was used to create analytical models and perform nonlinear dynamic analyses.

Section 5.4.1 summarizes the general findings from observation of different analytical models. The summary of the comparison of the dynamic analytical and test results for each specimen is presented in Section 5.4.2. Recommendations for modeling a reinforced concrete column are suggested in Section 5.4.3.

5.4.1 Summary of Analytical Modeling

The following are the general findings from the analysis of different analytical models:

- The analytical response is sensitive to the natural frequency in the elastic system. When the elastic response governs at lower-level excitations, it is important to match the natural frequency of the system in order to achieve good agreement between the measured and calculated results. It is difficult to control the natural frequency of the analytical model by using a nonlinear beam-column element; the natural frequency can easily be controlled by changing the effective flexural stiffness with a beam with a hinge element.
- In contrast, at the higher levels (design and maximum) the maximum responses are controlled by nonlinearity of the system. The analytical results are not very sensitive to the natural frequency.
- The maximum responses (displacement, shear, acceleration) at higher levels are not sensitive to different material models; regardless of the different steel and concrete models considered in this chapter, the maximum responses are similar.
- Residual displacements are sensitive to modeling of materials and damping. The following are parameters that affect residual displacement in column modeling:
    - Concrete descending region (a large descending slope gives some residual displacement);
    - Steel hardening ratio (a lower value gives some residual displacement);
    - Isotropic hardening in steel (using a small value for the isotropic hardening option in the compression region gives some residual displacement); and
    - Damping ratio (lower damping in higher level analysis gives more residual displacement).

5.4.2 Summary of Analytical Observations of Each Specimen

The comparison of the dynamic analysis and test results for each specimen suggests the following important observations:

- After studying different modeling parameters of the RC specimen, an analytical model that gives good agreement with the measured results is suggested for modeling a reinforced cantilever concrete bridge column (see Section 5.4.3). Standard models can result in significant errors, especially with respect to residual displacements.

- The analytical results using a co-rotational truss element with initial strain to represent the unbonded prestressing tendon for specimen PRC (which is otherwise identical to the RC specimen model) give good agreement with the measured results.
- The analysis results for the PRC-2 specimen closely match the test results for several global response quantities. The analysis of the PRC-2 specimen confirms that the analytical model for specimen PRC is appropriate with different material parameters.
- The analytical results for the PRC-U specimen provide a very good match with the test results for global responses at the design level. There are slightly greater differences at the maximum level, especially in residual displacement. The differences might reflect the difficulty of modeling unbonded rebar at the plastic hinge region.
- The analytical results for the PRC-U2 specimen using different initial strain of a co-rotational truss element match well with the test results for global responses. There are some differences at the maximum level in the *y* direction, especially in residual displacement.
- The analytical results for specimen PRC-UJ using the constitutive model by Mander et al. (1988) for modeling the steel jacket by treating the steel jacket as a continuous spiral match well with the test results for global responses except in residual displacement at the maximum level.
- The analytical results for maximum response of the PRC-system model (based on the analytical model of the PRC-UJ specimen) are well matched with the measured response through all the test levels, but the residual displacement responses reveal quite a difference between the analytical and test results at both the design and maximum levels. The analysis shows almost no residual displacement, as expected, but the test results show some residual displacement. Additional research is needed to improve modeling of the steel-jacketed plastic hinge regions.

5.4.3 Recommendations for Modeling of RC and PRC Columns

Based on the findings of the analysis, the following recommendations are made regarding the modeling of RC and PRC columns [indicates OpenSees object]:

- Column modeling:
  - Beam with hinge (BWH) model [beamWithHinges element];

- Priestley plastic hinge length; and
- Effective stiffness for the elastic region of the BWH model: 0.2–0.3 EI for RC column with a lower axial force, 0.4–0.6 EI for PRC column with a higher axial force;

- Concrete modeling:
  - [Concrete02] with the following suggested descending parameters for confined concrete:
    - Suggested residual stress (f_{cu}) is 50–70% of peak compressive stress (f'_c);
    - Suggested strain at ultimate stress(ε_{cu}) is 2.5–3.0 times the strain at peak compressive stress (ε_{co});
- Steel modeling: [ReinforcingSteel];
- Damping: stiffness-only damping (2–3%); and
- Prestressing tendon: co-rotational truss element [CorotTruss] with initial strain.

Table**s** 5.15 and 5.16 show the average and coefficient of variation (C.V.) of the ratios of the analytical to the experimental results for the RC specimen, all the PRC specimens combined (PRC, PRC-2, PRC-U, PRC-U2, PRC-UJ, and PRC-system), and all specimens combined for various response quantities at the design and maximum level, respectively.

Using the recommended numerical model for RC and PRC columns, maximum displacement can be predicted within 10% error with 10% C.V.; residual displacement can be predicted within 40% error with 110% C.V.; maximum acceleration can be predicted within 15% error with 15% C.V.; shear force can be predicted within 15% error with 15% C.V.; moment can be predicted within 15% error with 10% C.V.; and prestressing tendon force can be predicted within 10% with 10% C.V. at both the design and maximum levels as seen in Table**s** 5.15 and 5.16.

Most of the response quantities considered in this chapter can be predicted using the recommended models within 15% error with less than 15% C.V. at both the design and maximum levels, except residual displacement. The residual displacement responses have some error (within 40%) with large C.V. (110%). But, as mentioned in section 5.3.2, when comparing residual displacements, the difference as well as the ratio should be checked. Higher errors can be expected for most response quantities if standard modeling approaches are used.

Figures 5.54(a–b) show measured and calculated residual displacement (SRSS value) at the design and maximum levels. As shown in Figure 5.54(a), the design-level differences are quite small, except for the PRC-system specimen: the average differences of residual displacements for all the specimens combined are 0.14 in. (3.6 mm) for the *x* direction and 0.05 in. (1.3 mm) for the *y* direction; but the respective differences change to 0.04 in. (1.1 mm) and 0.06 in. (1.5 mm) when the PRC-system specimen is excluded, reflecting PRC-system's large impact on the *x* direction average. Thus, overall, the calculated residual displacements can be considered to be very close to the measured values at the design level. For the maximum level, the average differences of residual displacements for all the specimens are 1.31 in. (33.3 mm) and 0.28 in. (7.1 mm) for the *x* and *y* direction, respectively; the corresponding differences change to 0.48 in. (12.2 mm) and 0.38 in. (9.7 mm) when the PRC-system specimen is excluded.

Based on these comparisons, the recommended analytical models for the RC and PRC columns have sufficient accuracy to predict global responses at the design and maximum levels. However, additional research is needed to improve modeling of steel-jacketed plastic hinge regions and unbonded mild bar.

Table 5.1 Parametric values of base model for RC specimen

Parameter	Value		*Definition*
Column model	nonlinearBeamColumn in OpenSees		
Integration points	5		
Concrete model	Concrete02 in OpenSees		
f'_c (ksi)	6.0*	Cover	*Peak compressive stress*
	7.81**	Confined core	
ε_{co}	0.0028*	Cover	*Strain at peak compressive stress*
	0.007**	Confined core	
f_{cu} (ksi)	0	Cover	*Residual stress*
	6.9**	Confined core	
ε_{cu}	0.006	Cover	*Strain at ultimate stress*
	0.0183**	Confined core	
Steel model	Steel02 in OpenSees		
F_y (ksi)	69*		*Yield strength*
b	0.01		*Hardening ratio*
Damping model	Stiffness-and-mass proportional		
Damping ratio	*2% for 1st and 2nd natural frequency*		

* From material test results

** Equation from Mander et al. (1988)

Table 5.2 Parametric values of suggested model for RC specimen

Parameter	Value		*Definition*
Column model	beamWithHinges in OpenSees		
L_p	13.01 (from Priestley Eq.)		*Plastic hinge length*
EI_{eff}	0.2 EI_g		*Effective stiffness*
Concrete model	Concrete02 in OpenSees		
f'_c (ksi)	6.0*	Cover	*Peak compressive stress*
	7.81**	Confined core	
ε_{co}	0.0028*	Cover	*Strain at peak compressive stress*
	0.007**	Confined core	
f_{cu} (ksi)	0	Cover	*Residual stress*
	0.5 f'_c***	Confined core	
ε_{cu}	0.006	Cover	*Strain at ultimate stress*
	2.5 ε_{co}***	Confined core	
Steel model	ReinforcingSteel in OpenSees		
F_y (ksi)	71.1*		*Yield stress*
F_u (ksi)	105.5*		*Ultimate stress*
ε_{sh}	0.005*		*Strain corresponding to initial strain hardening*
ε_{ult}	0.12*		*Strain at peak stress*
Damping model	Stiffness-only proportional		
Damping ratio	*2% for 1st natural frequency*		

* From material test results

** Equation from Mander et al. (1988)

*** Suggested descending parameters in Concrete02

Table 5.3 Test vs. analytical results of RC specimen based on recommended model

	Design level			Maximum level		
	Test	Analysis	Ratio (%)	Test	Analysis	Ratio (%)
D*x*_max (in.)	6.11	5.08	83	12.71	11.97	94
D*y*_max (in.)	4.38	4.63	106	6.93	7.26	105
D*srss*_max (in.)	7.36	6.28	85	13.73	13.30	97
D*x*_res (in.)	0.97	0.94	97	10.01	8.87	89
D*y*_res (in.)	0.78	0.85	109	5.27	5.12	97
D*srss*_res (in.)	1.24	1.27	102	11.31	10.24	91
A*x*_max (*g*)	0.32	0.25	78	0.29	0.25	88
A*y*_max (*g*)	0.21	0.17	79	0.23	0.16	70
S*x*_max (kip)	14.57	14.83	102	12.16	12.07	99
S*y*_max (kip)	9.36	9.94	106	8.46	7.93	94
M*x*_max (kip-in.)	1700	1579	93	1746	1584.70	91
M*y*_max (kip-in.)	1287	1188	92	1187	1139.50	96

D*x* max, D*y*_max: maximum displacement in *x* and *y* directions

D*srss*_max, D*srss*_res: maximum and residual distance from origin

A*x*_max, A*y*_max: maximum acceleration in *x* and *y* directions

S*x*_max, S*y*_max: maximum shear force in *x* and *y* directions

M*x*_max, M*y*_max: maximum top moment in *x* and *y* directions

Table 5.4 Parametric values of suggested model for PRC specimen

Parameter	Value		***Definition***
Column model	beamWithHinges in OpenSees		
L_p	11.80 (from Priestley Eq.)		*Plastic hinge length*
EI_{eff}	0.60 EI_g (matched to natural frequency)		*Effective stiffness*
Concrete model	Concrete02 in OpenSees		
f'_c (ksi)	6.0*	Cover	*Peak compressive stress*
	7.81**	Confined core	
ε_{co}	0.0028*	Cover	*Strain at peak compressive stress*
	0.007**	Confined core	
f_{cu} (ksi)	0	Cover	*Residual stress*
	0.7 f'_c***	Confined core	
ε_{cu}	0.006	Cover	*Strain at ultimate stress*
	2.5 ε_{co}***	Confined core	
Steel model	ReinforcingSteel in OpenSees		
F_y (ksi)	70.7*		*Yield stress*
F_u (ksi)	114.8*		*Ultimate stress*
Prestressing tendon model	corotTruss in OpenSees		
F_y (ksi)	148*		*Yield stress*
Damping model	Stiffness-only proportional		
Damping ratio	*2% for 1st natural frequency*		

* From material test results

** Equation from Mander et al. (1988)

*** Suggested descending parameters in Concrete02

Table 5.5 Test vs. analytical results of PRC specimen based on recommended model

	Design level			Maximum level		
	Test	Analysis	Ratio (%)	Test	Analysis	Ratio (%)
D*x*_max (in.)	5.80	4.93	85	10.08	8.80	87
D*y*_max (in.)	5.16	4.81	93	8.75	8.06	92
D*srss*_max (in.)	7.43	6.51	88	12.72	11.66	92
D*x*_res (in.)	0.10	0.07	78	2.09	1.86	89
D*y*_res (in.)	0.30	0.10	32	2.66	2.57	97
D*srss*_res (in.)	0.31	0.15	48	3.38	3.17	94
A*x*_max (*g*)	0.32	0.39	121	0.28	0.27	98
A*y*_max (*g*)	0.25	0.19	76	0.29	0.18	62
S*x*_max (kip)	15.20	18.21	120	13.13	12.94	99
S*y*_max (kip)	13.81	12.47	90	9.94	9.06	91
M*x*_max (kip-in.)	1849	1746	94	1678.10	1529.20	91
M*y*_max (kip-in.)	1668	1669	100	1483.70	1202.80	81
T_max (kip)	137.08	145.50	106	150.96	162.07	107

D*x* max, D*y*_max: maximum displacement in *x* and *y* directions
D*srss*_max, D*srss*_res: maximum and residual distance from origin
A*x*_max, A*y*_max: maximum acceleration in *x* and *y* directions
S*x*_max, S*y*_max: maximum shear force in *x* and *y* directions
M*x*_max, M*y*_max: maximum top moment in *x* and *y* directions
T_max: maximum prestressing tendon force

Table 5.6 Parametric values of suggested model for PRC-2 specimen

Parameter	Value		*Definition*
Column model	beamWithHinges in OpenSees		
L_p	11.65 (from Priestley Eq.)		*Plastic hinge length*
EI_{eff}	0.60 EI_g (matched to natural frequency)		*Effective stiffness*
Concrete model	Concrete02 in OpenSees		
f'_c (ksi)	4.72*	Cover	*Peak compressive stress*
	6.46**	Confined core	
ε_{co}	0.0028*	Cover	*Strain at peak compressive stress*
	0.0080**	Confined core	
f_{cu} (ksi)	0	Cover	*Residual stress*
	0.7 f'_c***	Confined core	
ε_{cu}	0.006	Cover	*Strain at ultimate stress*
	2.5 ε_{co}***	Confined core	
Steel model	ReinforcingSteel in OpenSees		
F_y (ksi)	69.1*		*Yield stress*
F_u (ksi)	90.9*		*Ultimate stress*
Prestressing tendon model	corotTruss in OpenSees		
F_y (ksi)	132*		*Yield stress*
Damping model	Stiffness-only proportional		
Damping ratio	*2% for 1st natural frequency*		

* From material test results

** Equation from Mander et al. (1988)

*** Suggested descending parameters in Concrete02

Table 5.7 Test vs. analytical results of PRC-2 specimen based on recommended model

	Design level			Maximum level		
	Test	Analysis	Ratio (%)	Test	Analysis	Ratio (%)
D*x*_max (in.)	3.59	3.47	97	8.27	7.07	85
D*y*_max (in.)	2.95	2.93	99	6.83	6.54	96
D*srss*_max (in.)	4.59	4.52	98	10.59	9.53	90
D*x*_res (in.)	0.04	0.01	22	1.29	1.20	94
D*y*_res (in.)	0.08	0.04	44	1.57	1.55	99
D*srss*_res (in.)	0.09	0.04	48	2.03	1.97	97
A*x*_max (*g*)	0.27	0.25	93	0.23	0.20	89
A*y*_max (*g*)	0.23	0.19	84	0.21	0.17	82
S*x*_max (kip)	14.06	11.32	80	13.16	10.16	77
S*y*_max (kip)	11.37	8.96	79	9.51	8.58	90
M*x*_max (kip-in.)	1549.50	1376.60	89	1357.80	1246.30	92
M*y*_max (kip-in.)	1403.80	1278.50	91	1263.00	1298.30	103
T_max (kip)	97.467	91.507	94	128.96	118.77	92

D*x* max, D*y*_max: maximum displacement in *x* and *y* directions

D*srss*_max, D*srss*_res: maximum and residual distance from origin

A*x*_max, A*y*_max: maximum acceleration in *x* and *y* directions

S*x*_max, S*y*_max: maximum shear force in *x* and *y* directions

M*x*_max, M*y*_max: maximum top moment in *x* and *y* directions

T_max: maximum prestressing tendon force

Table 5.8 Parametric values of suggested model for PRC-U specimen

Parameter	Value		Definition
Middle of column model	elasticBeamColumn in OpenSees		
EI_{eff}	0.60 EI_g (matched to natural frequency)		Effective stiffness
Plastic hinge region model	nonLinearBeamColumn in OpenSees for concrete with two integration point		
	nonLinearBeamColumn in OpenSees for unbonded reinforcing steel with one integration point		
L_p	11.65 (from Priestley Eq.)		Plastic hinge length
H_{ip}	0.3 L_p***		Height of one integration point from bottom of column
Concrete model	Concrete02 in OpenSees		
f'_c (ksi)	4.66*	Cover	Peak compressive stress
	6.41**	Confined core	
ε_{co}	0.0028*	Cover	Strain at peak compressive stress
	0.0080**	Confined core	
f_{cu} (ksi)	0	Cover	Residual stress
	0.7 f'_c***	Confined core	
ε_{cu}	0.006	Cover	Strain at ultimate stress
	2.5 ε_{co}***	Confined core	
Steel model	ReinforcingSteel in OpenSees		
F_y (ksi)	69.1*		Yield stress
F_u (ksi)	90.9*		Ultimate stress
Prestressing tendon model	corotTruss in OpenSees		
F_y (ksi)	132*		Yield stress
Damping model	Stiffness-only proportional		
Damping ratio	2% for 1st natural frequency		

* From material test results

** Equation from Mander et al. (1988)

*** Suggested descending parameters in Concrete02

Table 5.9 Test vs. analytical results of PRC-U specimen based on recommended model

	Design level			Maximum level		
	Test	Analysis	Ratio (%)	Test	Analysis	Ratio (%)
D*x*_max (in.)	3.61	3.76	104	8.60	7.46	87
D*y*_max (in.)	3.37	3.42	102	7.17	6.85	96
D*srss*_max (in.)	4.90	5.05	103	10.97	9.99	91
D*x*_res (in.)	0.06	0.04	62	1.89	1.12	59
D*y*_res (in.)	0.04	0.08	185	1.35	1.48	109
D*srss*_res (in.)	0.08	0.09	118	2.32	1.85	80
A*x*_max (*g*)	0.27	0.23	83	0.24	0.22	93
A*y*_max (*g*)	0.23	0.19	83	0.21	0.17	80
S*x*_max (kip)	13.84	11.18	81	13.23	9.88	75
S*y*_max (kip)	10.95	8.75	80	8.48	7.99	94
M*x*_max (kip-in.)	1525.70	1337.50	88	1292.20	1195.10	92
M*y*_may (kip-in.)	1418.00	1276.10	90	1094.10	1176.70	108
T_max (kip)	97.365	94.256	97	124.53	120.13	96

D*x* max, D*y*_max: maximum displacement in *x* and *y* directions
D*srss*_max, D*srss*_res: maximum and residual distance from origin
A*x*_max, A*y*_max: maximum acceleration in *x* and *y* directions
S*x*_max, S*y*_max: maximum shear force in *x* and *y* directions
M*x*_max, M*y*_max: maximum top moment in *x* and *y* directions
T_max: maximum prestressing tendon force

Table 5.10 Test vs. analytical results of PRC-U2 specimen based on recommended model

	Design level			Maximum level		
	Test	Analysis	Ratio (%)	Test	Analysis	Ratio (%)
D*x*_max (in.)	3.76	3.58	95	7.87	6.60	84
D*y*_max (in.)	3.63	2.79	77	6.10	6.19	102
D*srss*_max (in.)	4.68	3.91	84	9.87	8.98	91
D*x*_res (in.)	0.04	0.14	314	0.84	1.00	120
D*y*_res (in.)	0.08	0.05	65	0.43	1.65	387
D*srss*_res (in.)	0.09	0.15	164	0.94	1.93	205
A*x*_max (*g*)	0.43	0.36	85	0.64	0.57	89
A*y*_max (*g*)	0.31	0.25	81	0.37	0.34	90
S*x*_max (kip)	14.20	10.72	75	12.74	11.42	90
S*y*_max (kip)	10.95	9.85	90	9.33	9.62	103
M*x*_max (kip-in.)	1642.30	1402.40	85	1319.30	1302.80	99
M*y*_max (kip-in.)	1407.80	1356.00	96	1232.20	1412.90	115
T_max (kip)	129.16	113.54	88	152.84	140.35	92

D*x* max, D*y*_max: maximum displacement in *x* and *y* directions
D*srss*_max, D*srss*_res: maximum and residual distance from origin
A*x*_max, A*y*_max: maximum acceleration in *x* and *y* directions
S*x*_max, S*y*_max: maximum shear force in *x* and *y* directions
M*x*_max, M*y*_max: maximum top moment in *x* and *y* directions
T_max: maximum prestressing tendon force

Table 5.11 Test vs. analytical results of PRC-UJ specimen based on recommended model

	Design level			Maximum level		
	Test	Analysis	Ratio (%)	Test	Analysis	Ratio (%)
D*x*_max (in.)	3.84	3.60	94	7.62	7.40	97
D*y*_max (in.)	3.20	3.08	96	6.11	6.62	108
D*srss*_max (in.)	4.83	4.70	97	9.67	9.81	102
D*x*_res (in.)	0.04	0.02	45	0.45	0.93	206
D*y*_res (in.)	0.016	0.024	153	0.42	1.08	260
D*srss*_res (in.)	0.04	0.05	108	0.61	1.42	232
A*x*_max (*g*)	0.43	0.38	89	0.65	0.60	91
A*y*_max (*g*)	0.33	0.26	78	0.41	0.34	82
S*x*_max (kip)	14.55	11.15	77	12.41	10.47	84
S*y*_max (kip)	10.76	8.90	83	10.55	8.49	80
M*x*_max (kip-in.)	1581.10	1318.30	83	1506.70	1207.20	80
M*y*_max (kip-in.)	1385.70	1251.70	90	1401.20	1282.90	92
T_max (kip)	108.29	95.589	88	147.95	130.36	88

D*x* max, D*y*_max: maximum displacement in *x* and *y* directions

D*srss*_max, D*srss*_res: maximum and residual distance from origin

A*x*_max, A*y*_max: maximum acceleration in *x* and *y* directions

S*x*_max, S*y*_max: maximum shear force in *x* and *y* directions

M*x*_max, M*y*_max: maximum top moment in *x* and *y* directions

T_max: maximum prestressing tendon force

Table 5.12 Parametric values of suggested model for PRC-system specimen

Parameter	Value		Definition
Beam	elasticBeamColumn in OpenSees		
Middle of column model	elasticBeamColumn in OpenSees		
EI_{eff}	0.40 EI_g (matched to natural frequency)		Effective stiffness
Plastic hinge region model	nonLinearBeamColumn in OpenSees for concrete with two integration point		
	nonLinearBeamColumn in OpenSees for unbonded reinforcing steel with one integration point		
L_p	12.97 (from Priestley Eq.)		Plastic hinge length
H_{ip}	0.3 L_p***		Height of one integration point from bottom of column
Concrete Model	Concrete02 in OpenSees		
f'_c (ksi)	4.14*	Cover	Peak compressive stress
	5.86**	Confined core	
ε_{co}	0.0028*	Cover	Strain at peak compressive stress
	0.0086**	Confined core	
f_{cu} (ksi)	0	Cover	Residual stress
	5.32**	Confined core	
ε_{cu}	0.006	Cover	Strain at ultimate stress
	0.0248**	Confined core	
Steel model	ReinforcingSteel in OpenSees		
F_y (ksi)	69.1*		Yield stress
F_u (ksi)	90.9*		Ultimate stress
Prestressing tendon model	corotTruss in OpenSees		
F_y (ksi)	132*		Yield stress
Damping model	Stiffness-only proportional		
Damping ratio	2% for 1st natural frequency		

* From material test results

** Equation from Mander et al. (1988)

Table 5.13 Test vs. analytical results of PRC-system (long-column) specimen based on recommended model.

	Design level			Maximum level		
	Test	Analysis	Ratio (%)	Test	Analysis	Ratio (%)
D*x*_max (in.)	4.22	3.48	82	7.66	7.03	92
D*y*_max (in.)	0.46	0.41	89	0.69	0.57	82
D*srss*_max (in.)	4.24	3.48	82	7.67	7.04	92
D*x*_res (in.)	0.41	0.06	15	3.80	0.19	5
D*y*_res (in.)	0.00	0.01	472	0.03	0.02	91
D*srss*_res (in.)	0.41	0.06	15	3.80	0.19	5
A*x*_max (*g*)	0.29	0.22	77	0.27	0.35	129
A*y*_max (*g*)	0.47	0.49	105	0.53	0.50	94
S*x*_max (kip)	14.04	10.99	78	13.69	8.32	61
S*y*_max (kip)	23.98	20.72	86	27.94	21.28	76
M*x*_max (kip-in.)	1570.00	1359.00	87	1552.10	1315.10	85
M*y*_max (kip-in.)	1586.60	1075.70	68	1763.50	978.25	55
T_max (kip)	100.51	82.371	82	126.73	142.24	112

D*x* max, D*y*_max: maximum displacement in *x* and *y* directions

D*srss*_max, D*srss*_res: maximum and residual distance from origin

A*x*_max, A*y*_max: maximum acceleration in *x* and *y* directions

S*x*_max, S*y*_max: maximum shear force in *x* and *y* directions

M*x*_max, M*y*_max: maximum top moment in *x* and *y* directions

T_max: maximum prestressing tendon force

Table 5.14 Test vs. analytical results of PRC-system (short-column) specimen based on recommended model

	Design level			**Maximum level**		
	Test	Analysis	Ratio (%)	Test	Analysis	Ratio (%)
D*x*_max (in.)	4.43	3.40	77	8.65	6.91	80
D*y*_max (in.)	0.46	0.41	89	0.69	0.57	82
D*srss*_max (in.)	4.44	3.40	77	8.66	6.91	80
D*x*_res (in.)	0.47	0.06	12	4.16	0.19	4
D*y*_res (in.)	0.00	0.01	472	0.03	0.02	91
D*srss*_res (in.)	0.47	0.06	13	4.16	0.19	4
A*x*_max (*g*)	0.27	0.22	80	0.31	0.26	85
A*y*_max (*g*)	0.47	0.49	105	0.53	0.50	94
S*x*_max (kip)	15.75	12.52	80	17.22	16.62	97
S*y*_max (kip)	23.99	21.91	91	28.54	24.45	86
M*x*_max (kip-in.)	1705.50	1269.70	74	1728.60	1506.80	87
M*y*_max (kip-in.)	1399.90	1158.80	83	1738.80	1225.70	70
T_max (kip)	88.069	90.939	103	118.84	148.07	125

Note: Short-column test results for the *y* direction are assumed to be the same as long-column responses for the *y* direction.

D*x* max, D*y*_max: maximum displacement in *x* and *y* directions

D*srss*_max, D*srss*_res: maximum and residual distance from origin

A*x*_max, A*y*_max: maximum acceleration in *x* and *y* directions

S*x*_max, S*y*_max: maximum shear force in *x* and *y* directions

M*x*_max, M*y*_max: maximum top moment in *x* and *y* directions

T_max: maximum prestressing tendon force

Table 5.15 Ratio of analytical to experimental results for RC, PRCs, and all specimens (mean and C.V.) at design level

Response quantity	Ratio of analytical to experimental results				
	RC	All PRCs		All specimens	
	-	Mean	C.V. (%)	Mean	C.V. (%)
D*x*_max	0.83	0.91	10.5	0.90	10.3
D*y*_max	1.06	0.92	8.9	0.94	9.5
D*srss*_max	0.85	0.90	11.0	0.89	10.4
Avg. of *x* and *y* directions	0.94	0.91	9.7	0.92	9.9
D*x*_res	0.97	0.78	136.8	0.80	123.2
D*y*_res	1.09	2.03	94.3	1.92	94.3
D*srss*_res	1.02	0.73	78.2	0.77	70.3
Avg. of residual displacement	1.03	1.41	115.6	1.36	108.7
A*x*_max	0.78	0.89	17.2	0.88	16.7
A*y*_max	0.79	0.88	13.4	0.87	13.0
Avg. of maximum acceleration	0.79	0.89	15.3	0.87	14.9
S*x*_max	1.02	0.84	18.6	0.87	18.3
S*y*_max	1.06	0.86	6.1	0.88	9.9
Avg. of maximum shear force	1.04	0.85	12.4	0.87	14.1
M*x*_max	0.93	0.86	7.1	0.87	7.1
M*y*_max	0.92	0.88	11.9	0.89	11.1
Avg. of maximum moment	0.93	0.87	9.5	0.88	9.1
T_max		0.94	9.2	0.94	9.2

D*x* max, D*y*_max, D_max: maximum displacement in *x* and *y* directions

D*srss*_max, D*srss*_res: maximum and residual distance from origin

A*x*_max, A*y*_max: maximum acceleration in *x* and *y* directions

S*x*_max, S*y*_max: maximum shear force in *x* and *y* directions

M*x*_max, M*y*_max: maximum top moment in *x* and *y* directions

T_max: maximum prestressing tendon force

Table 5.16 Ratio of analytical to experimental results for RC, PRCs, and all specimens (mean and C.V.) at maximum level

Response quantity	Ratio of analytical to experimental results				
	RC	All PRCs		All specimens	
	-	Mean	C.V. (%)	Mean	C.V. (%)
D*x*_max	0.83	0.91	10.5	0.90	10.3
D*y*_max	1.06	0.92	8.9	0.94	9.5
D*srss*_max	0.85	0.90	11.0	0.89	10.4
Avg. of *x* and *y* directions	0.94	0.91	9.7	0.92	9.9
D*x*_res	0.97	0.78	136.8	0.80	123.2
D*y*_res	1.09	2.03	94.3	1.92	94.3
D*srss*_res	1.02	0.73	78.2	0.77	70.3
Avg. of residual displacement	1.03	1.41	115.6	1.36	108.7
A*x*_max	0.78	0.89	17.2	0.88	16.7
A*y*_max	0.79	0.88	13.4	0.87	13.0
Avg. of maximum acceleration	0.79	0.89	15.3	0.87	14.9
S*x*_max	1.02	0.84	18.6	0.87	18.3
S*y*_max	1.06	0.86	6.1	0.88	9.9
Avg. of maximum shear force	1.04	0.85	12.4	0.87	14.1
M*x*_max	0.93	0.86	7.1	0.87	7.1
M*y*_max	0.92	0.88	11.9	0.89	11.1
Avg. of maximum moment	0.93	0.87	9.5	0.88	9.1
T_max		0.94	9.2	0.94	9.2

D*x* max, D*y*_max, D_max: maximum displacement in *x* and *y* directions

D*srss*_max, D*srss*_res: maximum and residual distance from origin

A*x*_max, A*y*_max: maximum acceleration in *x* and *y* directions

S*x*_max, S*y*_max: maximum shear force in *x* and *y* directions

M*x*_max, M*y*_max: maximum top moment in *x* and *y* directions

T_max: maximum prestressing tendon force

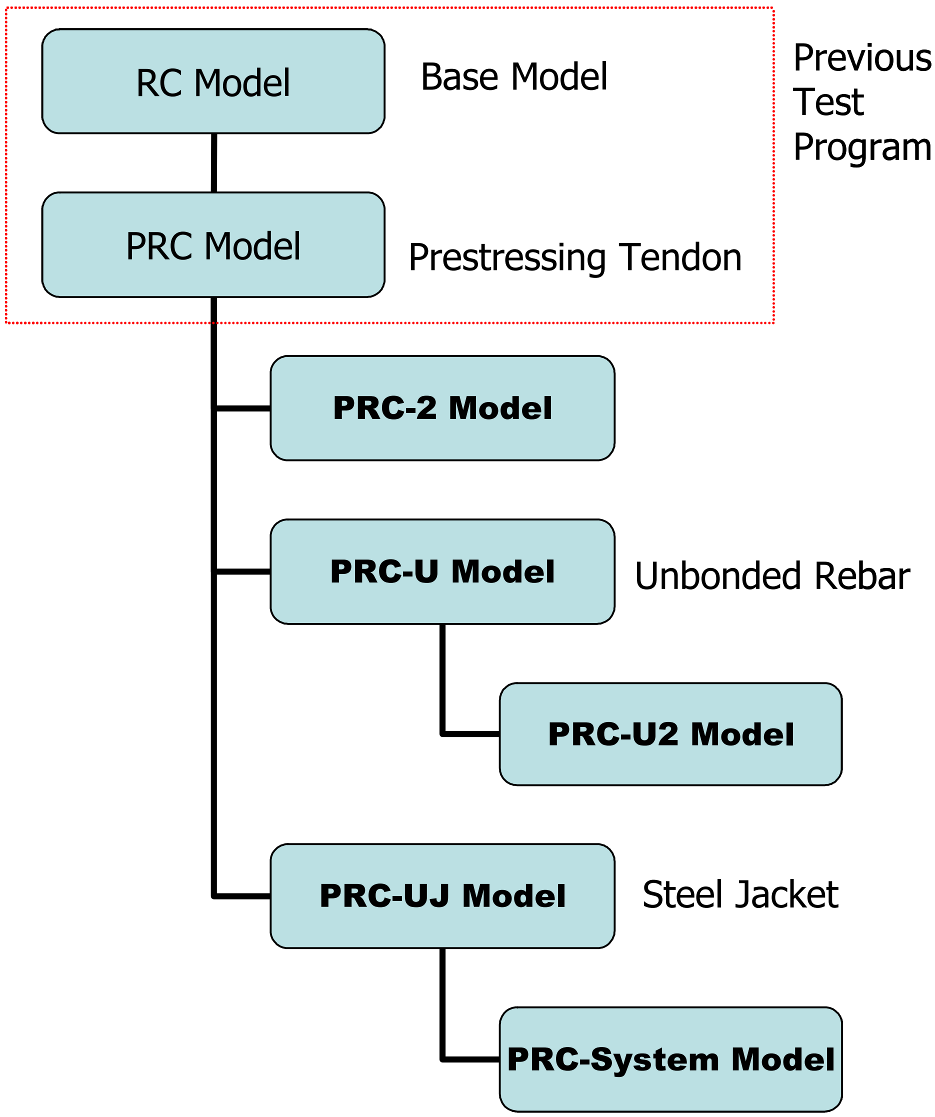

Fig. 5.1 Development of analytical model

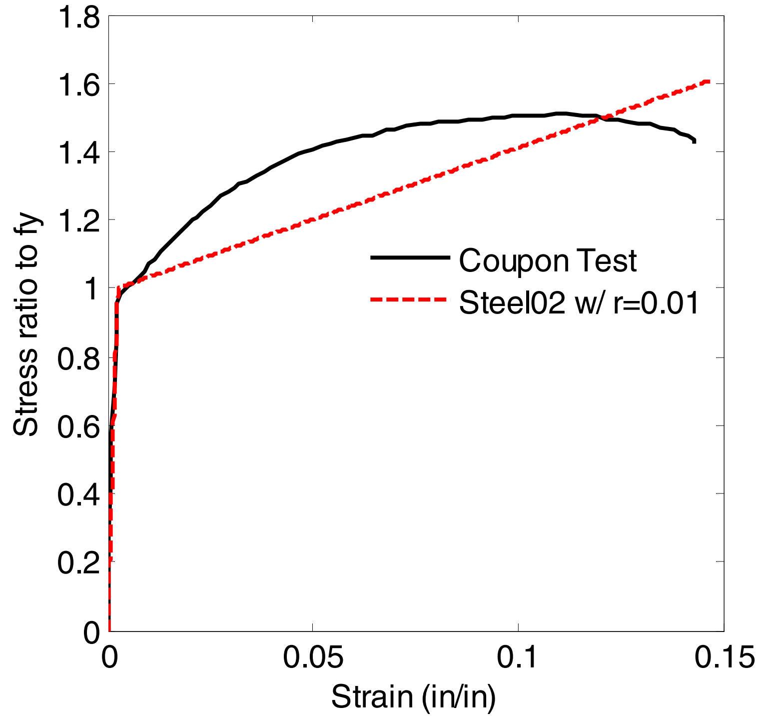

Fig. 5.2 Steel02 material model

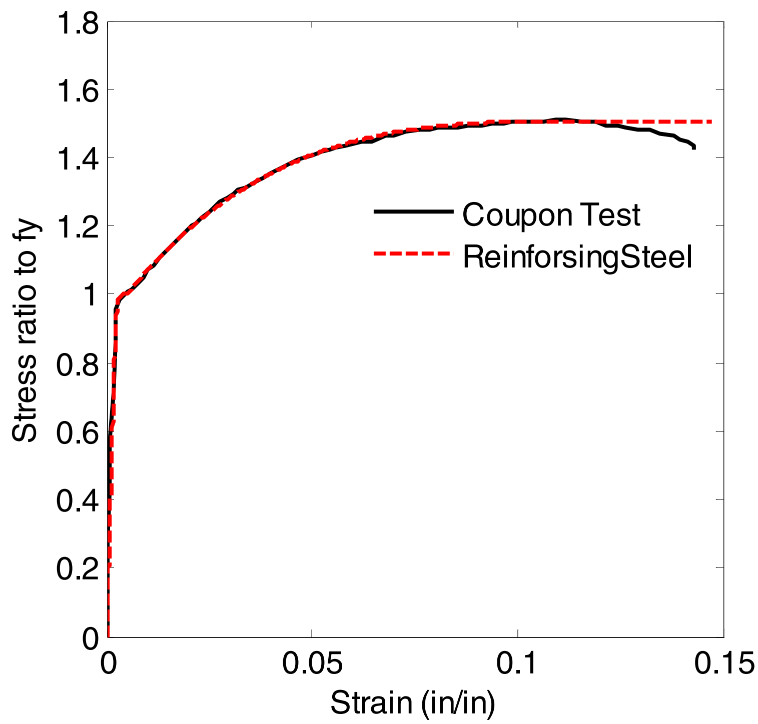

Fig. 5.3 ReinforcingSteel material model

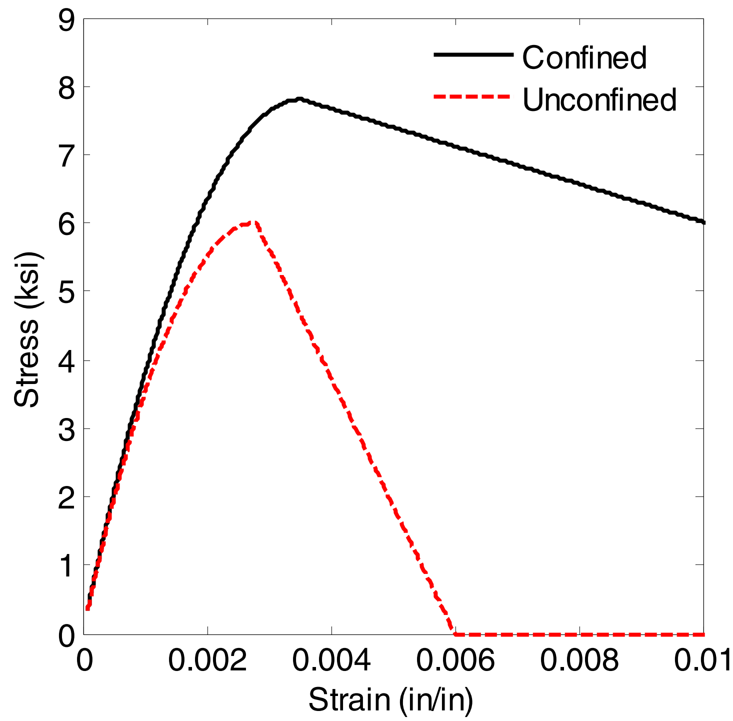

Fig. 5.4 Confined and unconfined concrete models

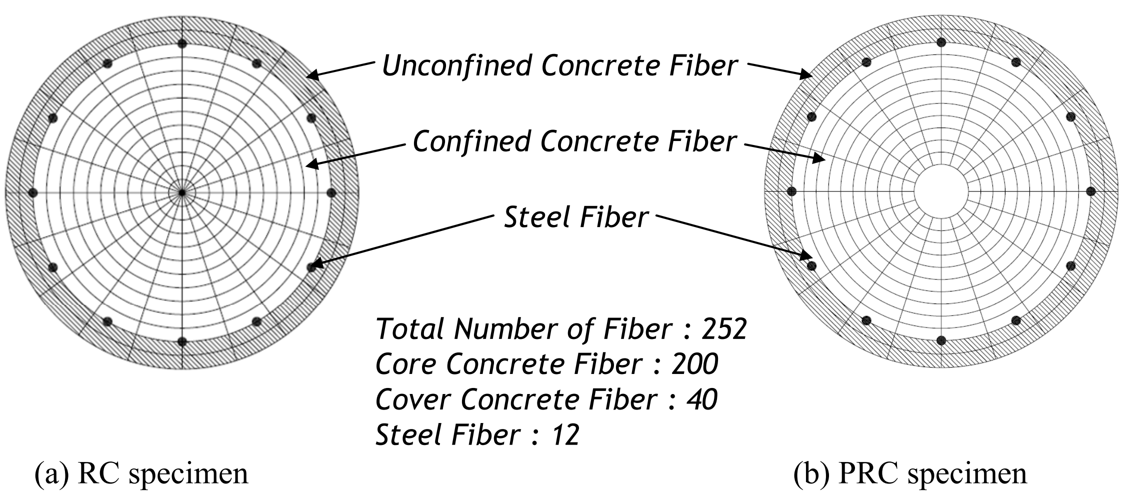

Fig. 5.5 Fiber section

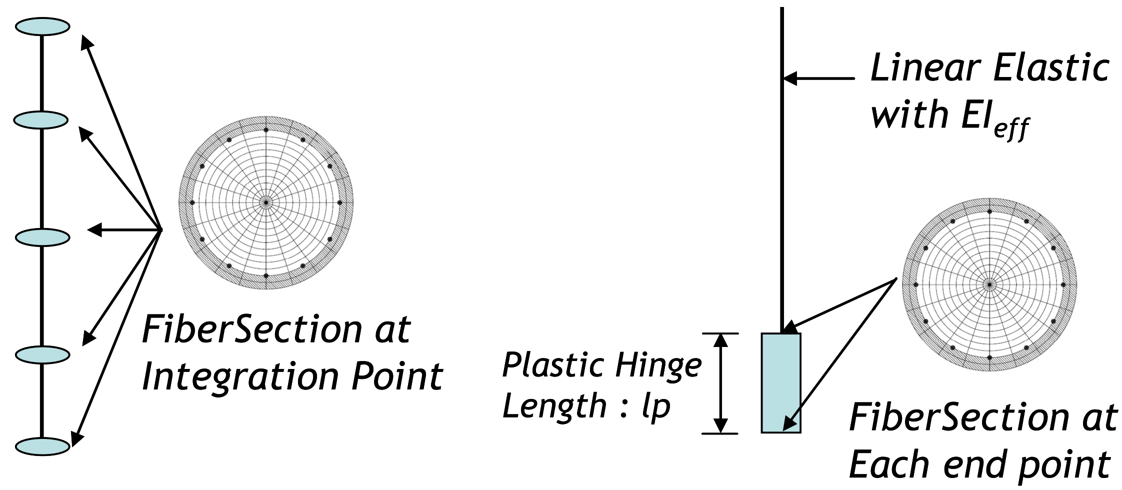

(a) NonlinearBeamColumn element
with 5 integration points

(b) BeamWithHinges element
with plastic hinge at one end

Fig. 5.6 Element models

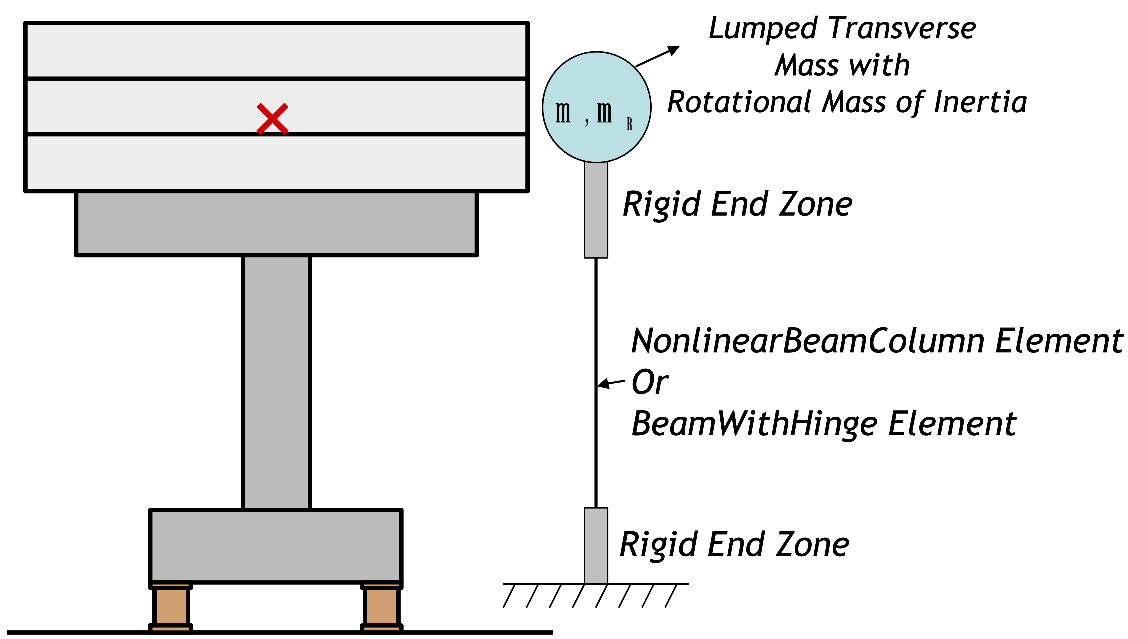

Fig. 5.7 Analytical model of RC specimen

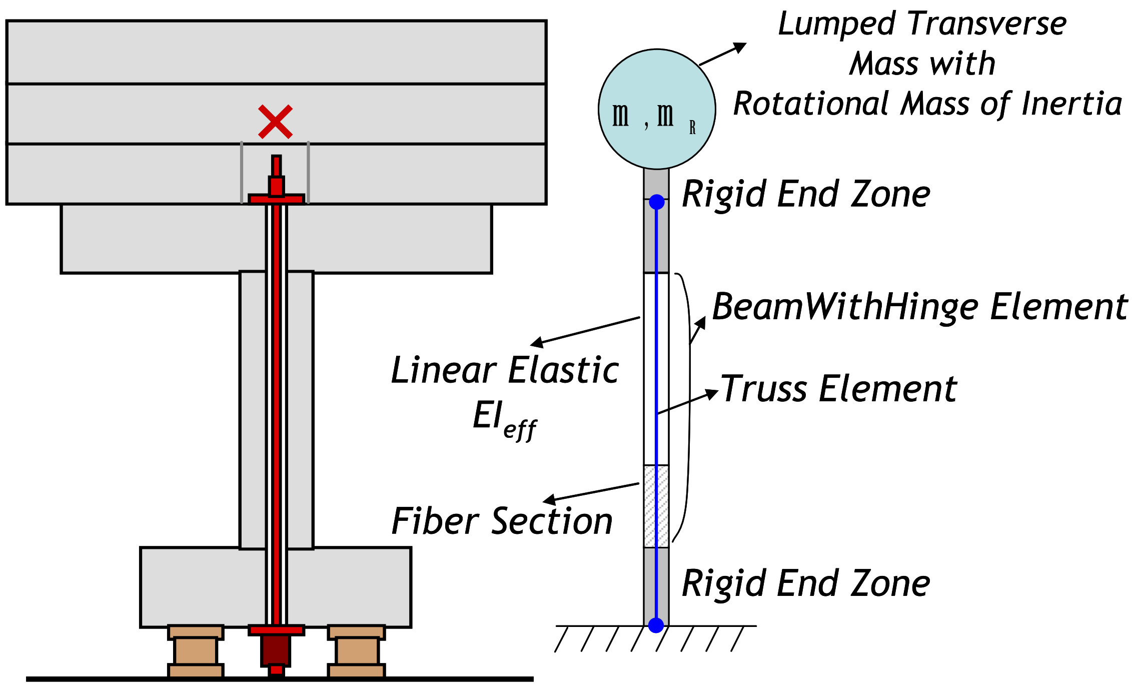

Fig. 5.8 Analytical model of PRC, PRC2 specimens

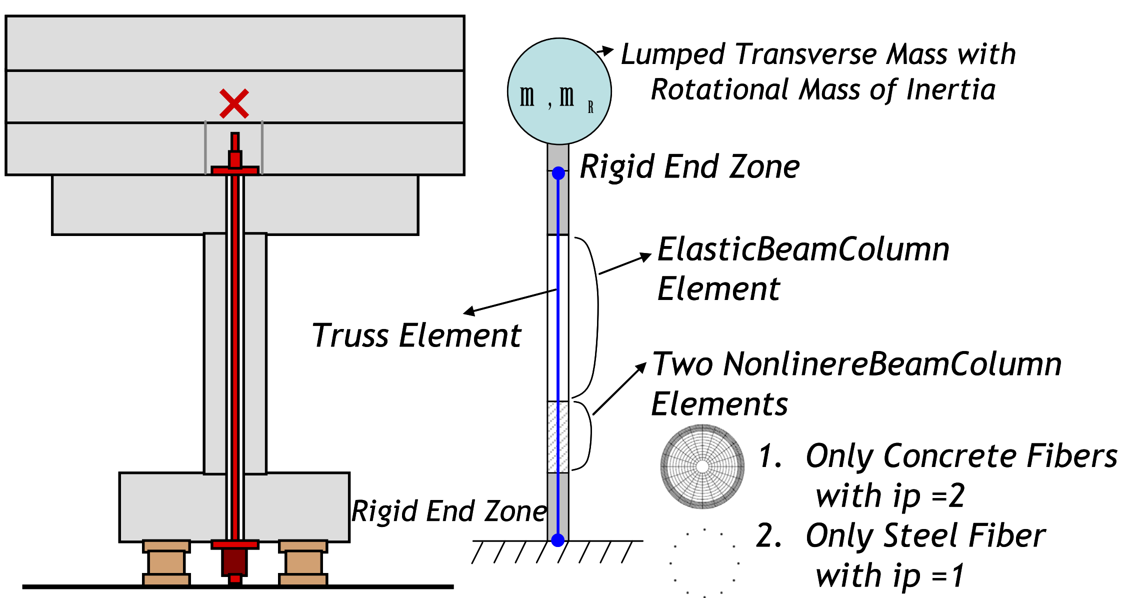

Fig. 5.9 Analytical model of PRC-U, PRC-U2, PRC-UJ specimens

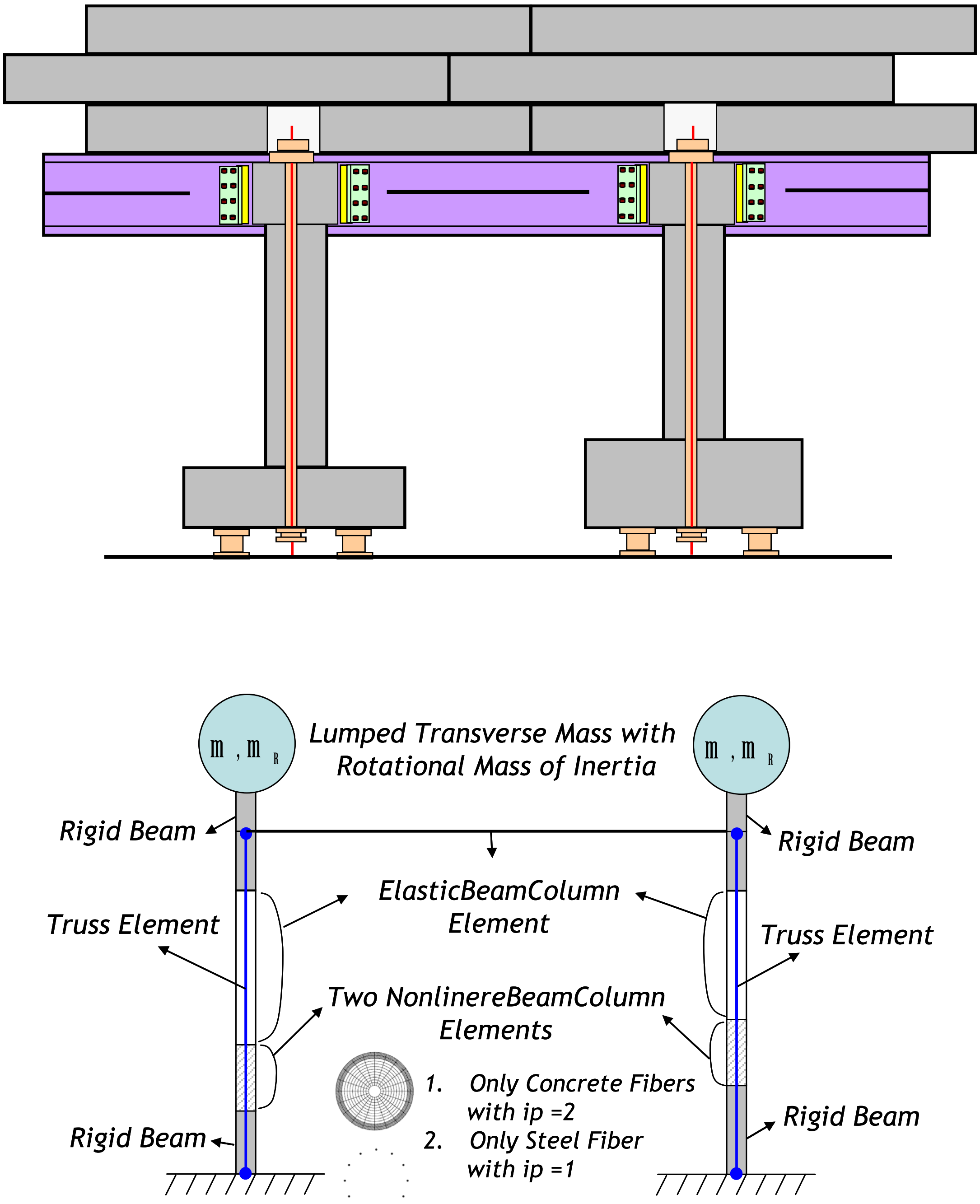

Fig. 5.10 Analytical model of PRC-system specimen

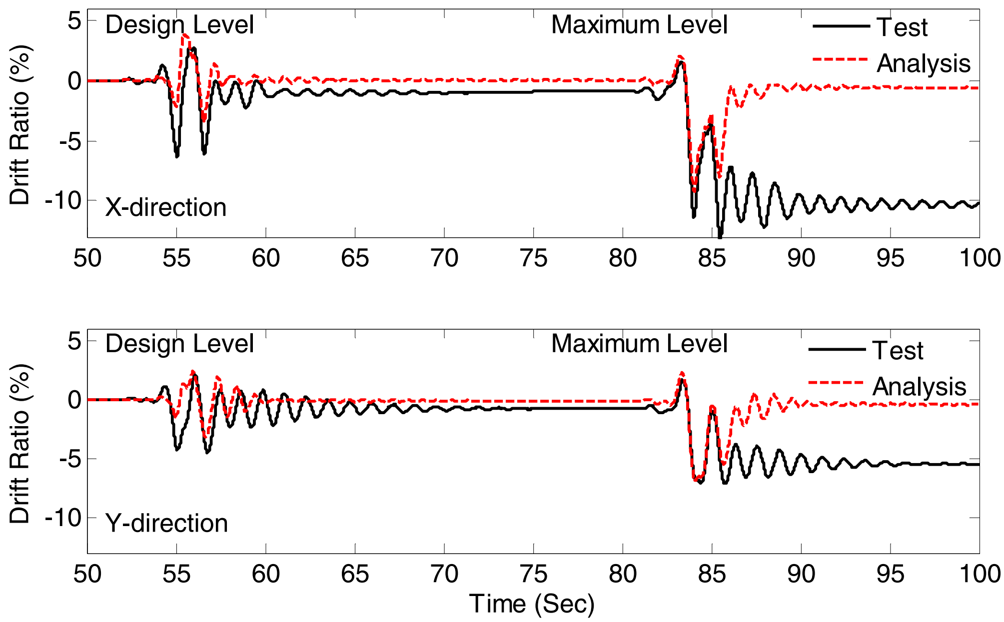

(a) NLBC base model

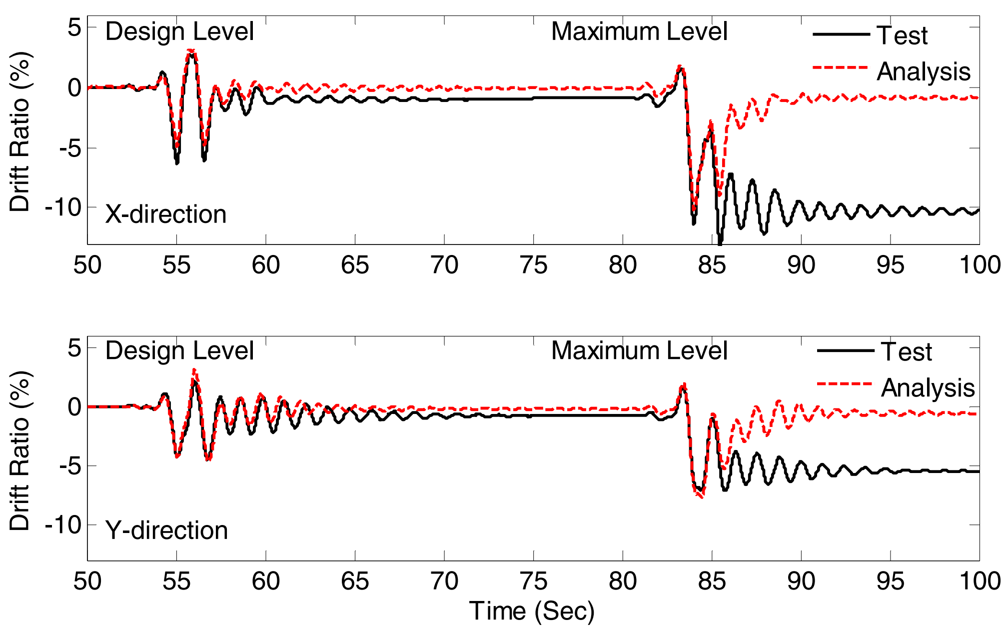

(b) BWH base model

Fig. 5.11 Analytical responses of different models of RC specimen

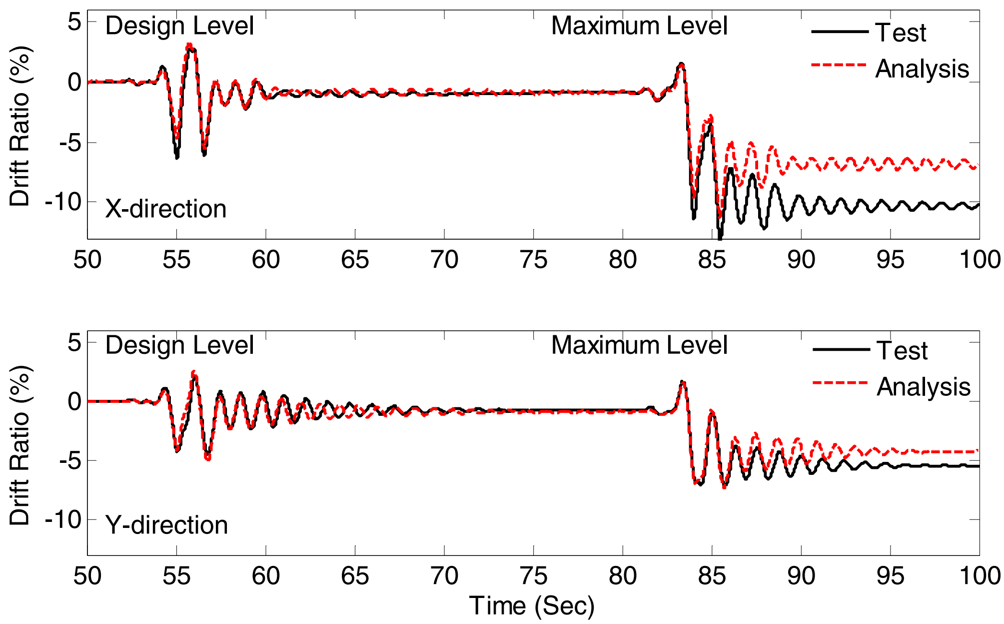

(c) BWH + ReinforcingSteel

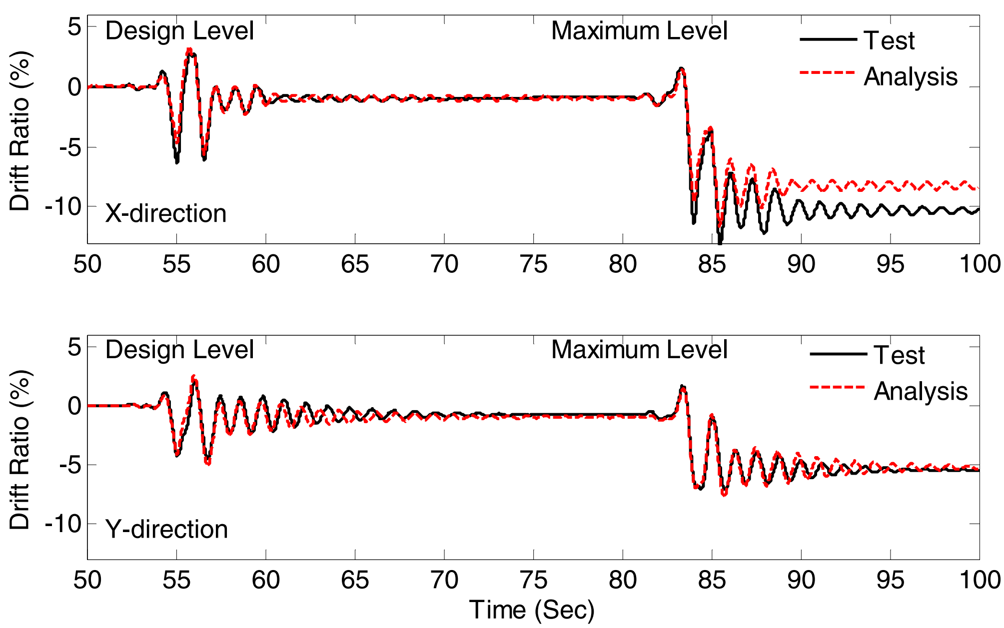

(d) BWH best model

Fig. 5.11—*Continued*

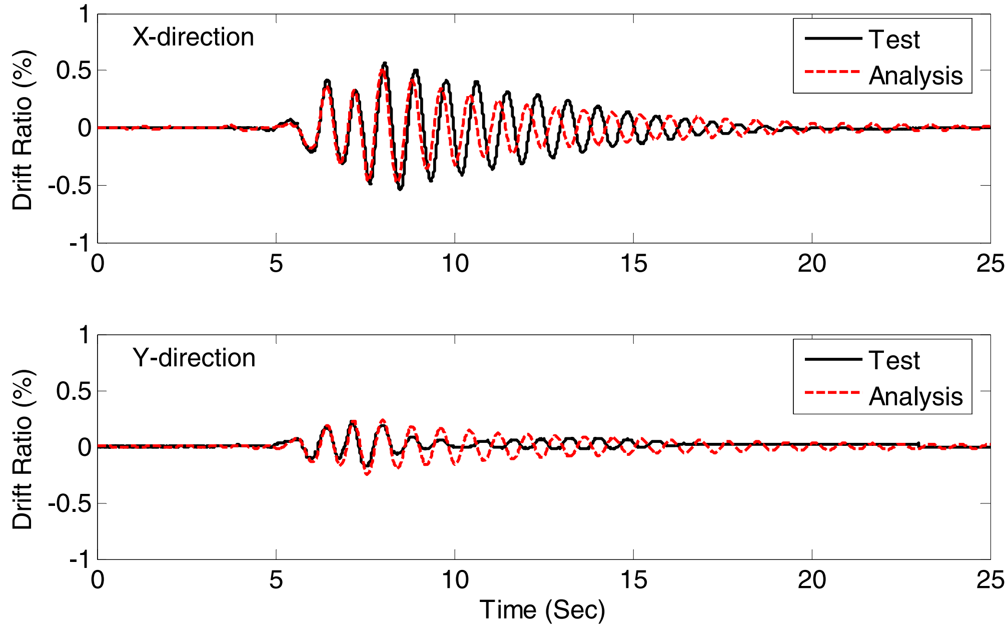

(a) Elastic level

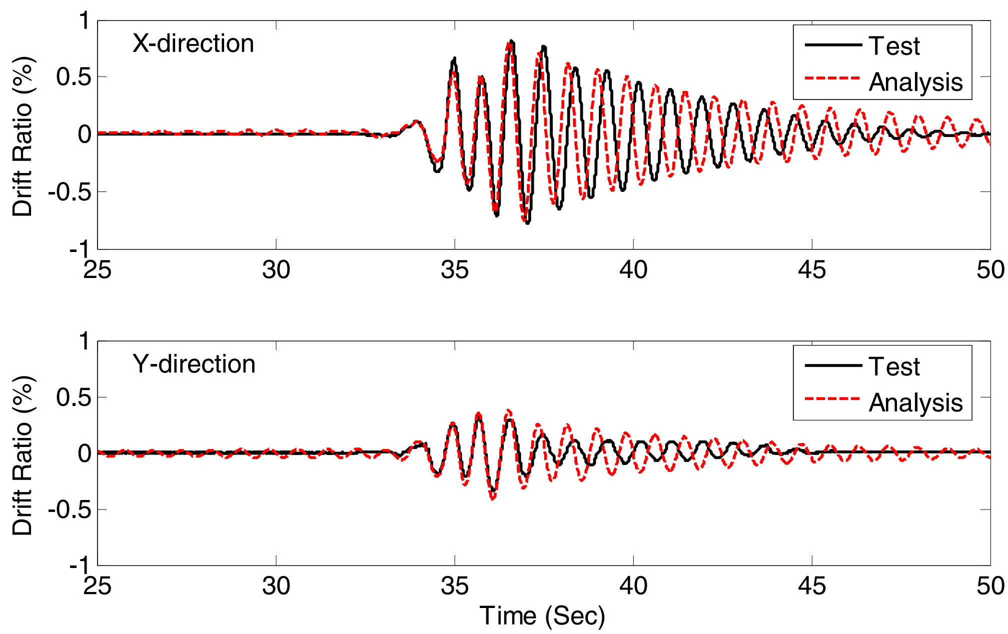

(b) Yield level

Fig. 5.12 Displacement of RC specimen based on recommended model

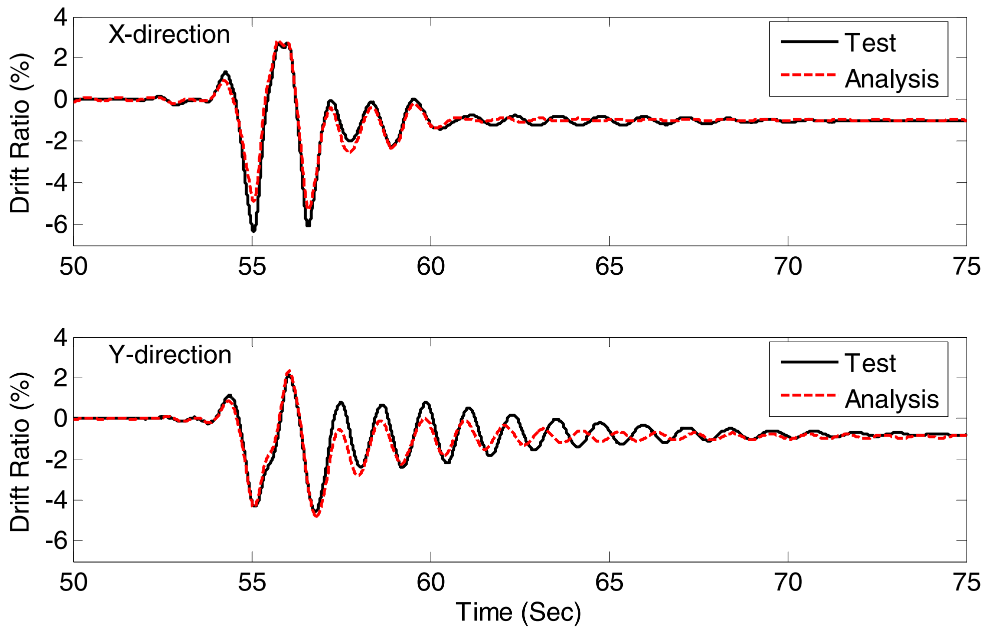

(c) Design level

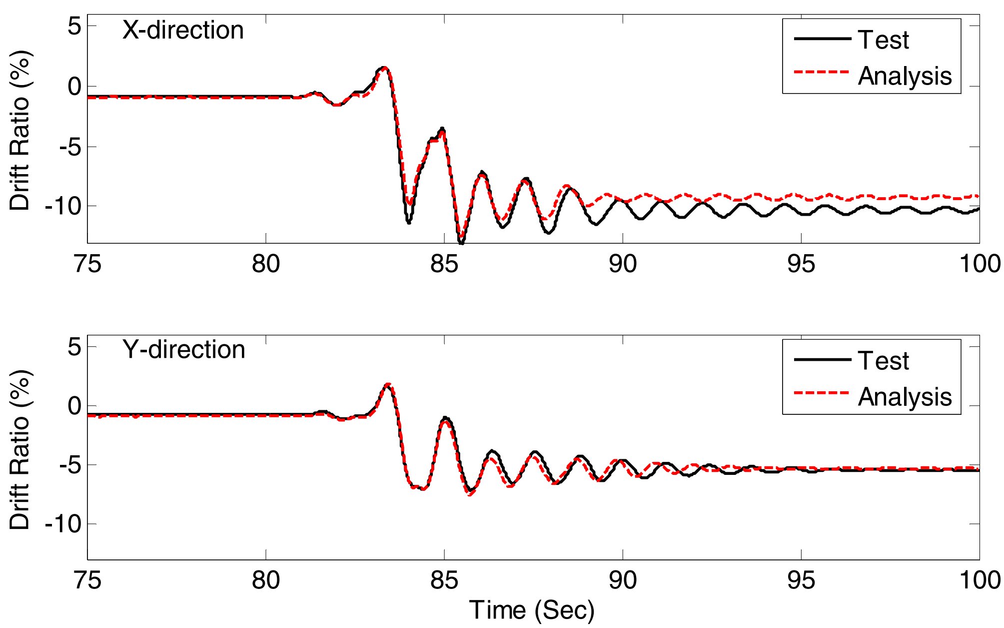

(d) Maximum level

Fig. 5.12—*Continued*

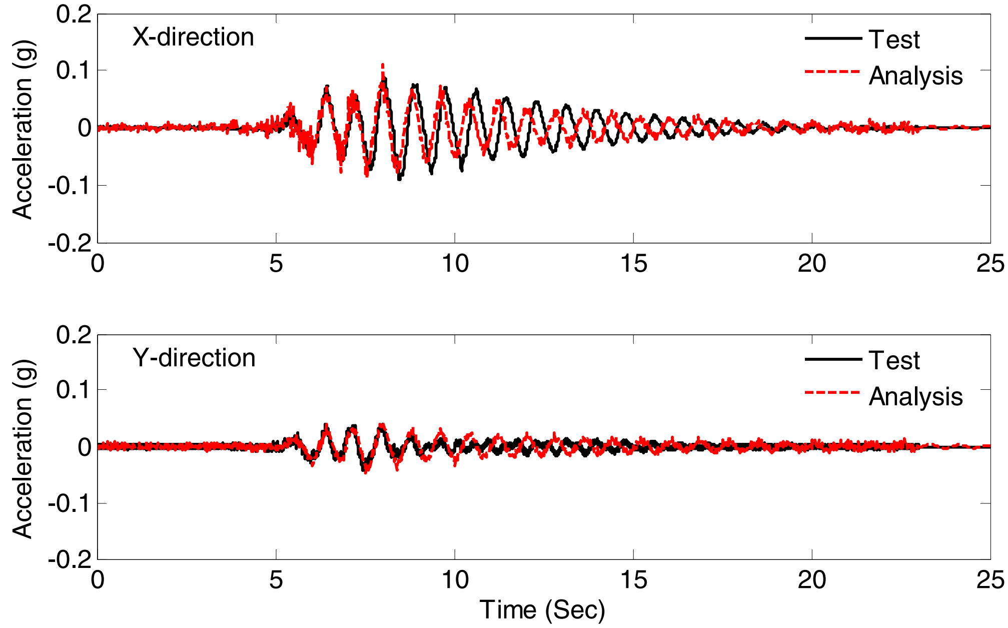

(a) Elastic level

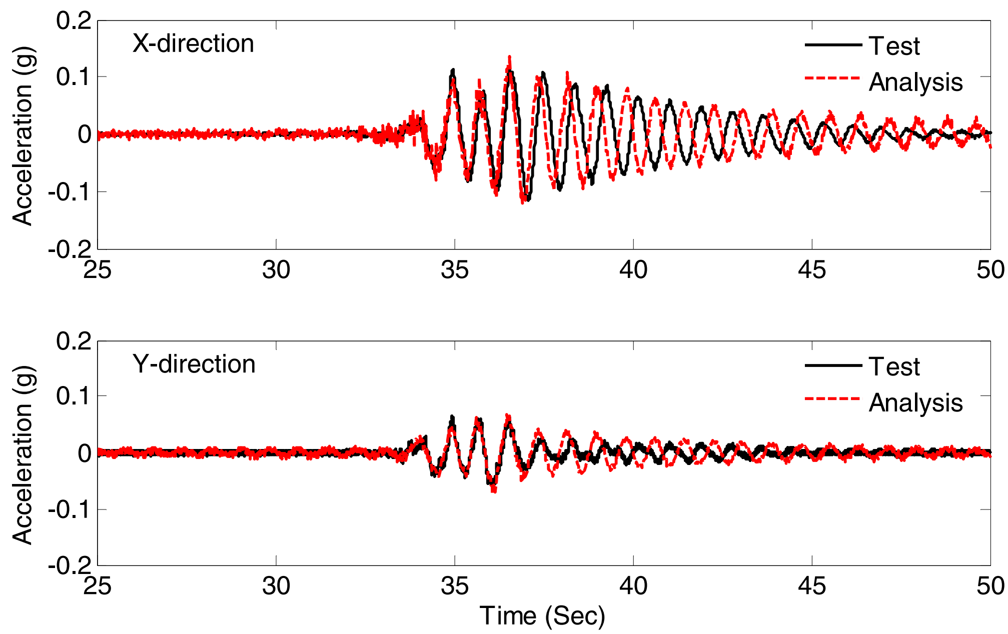

(b) Yield level

Fig. 5.13 Acceleration of RC specimen based on recommended model

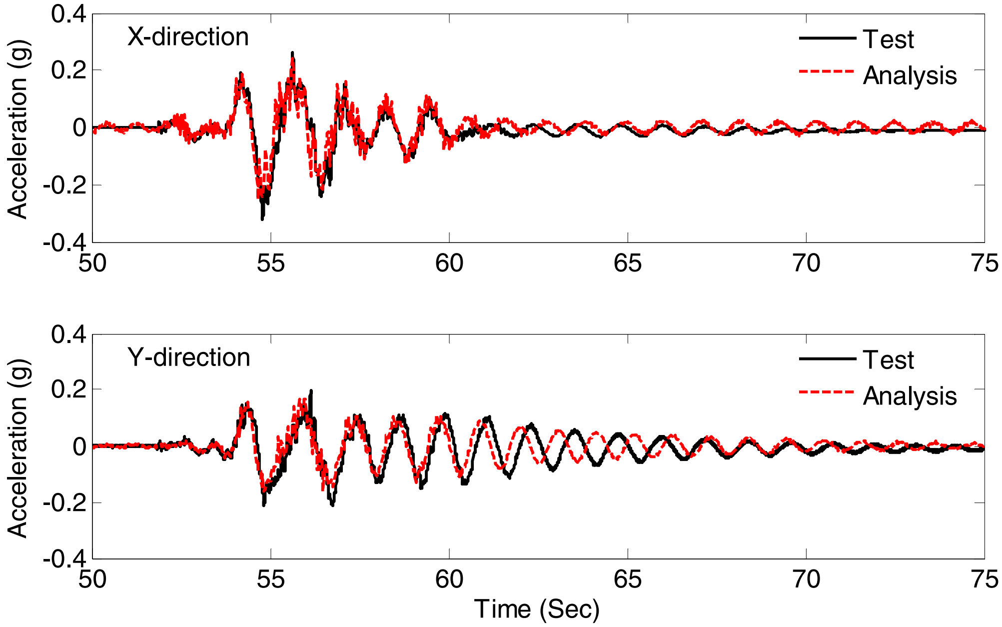

(c) Design level

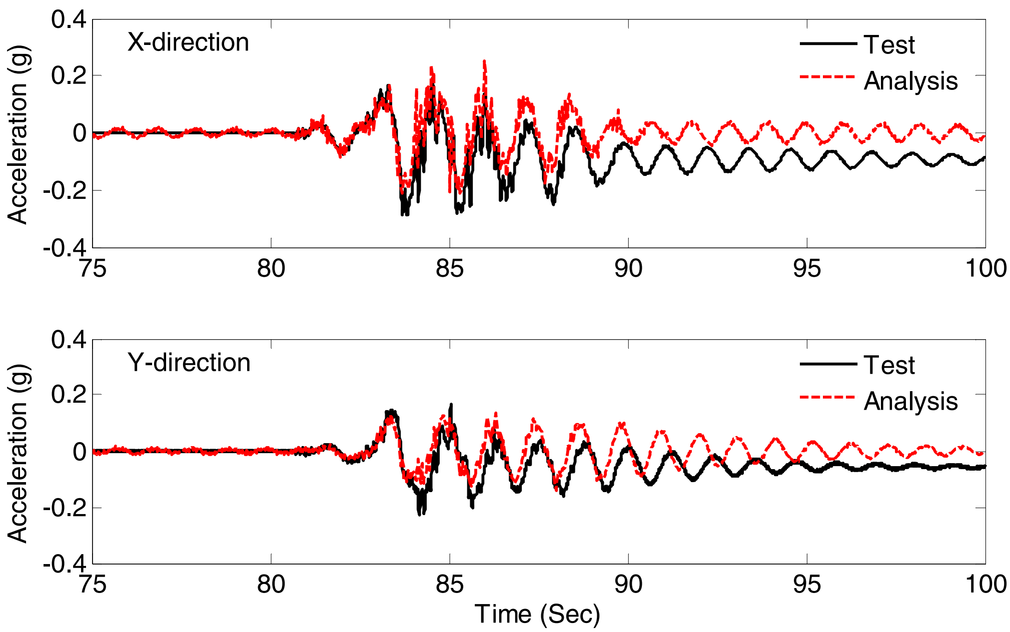

(d) Maximum level

Fig. 5.13—*Continued*

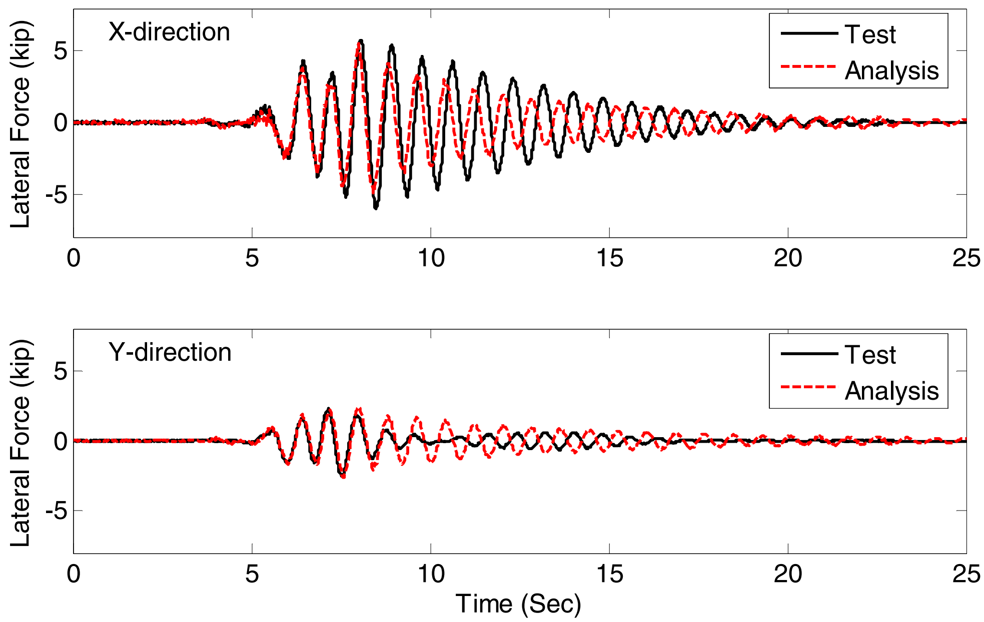

(a) Elastic level

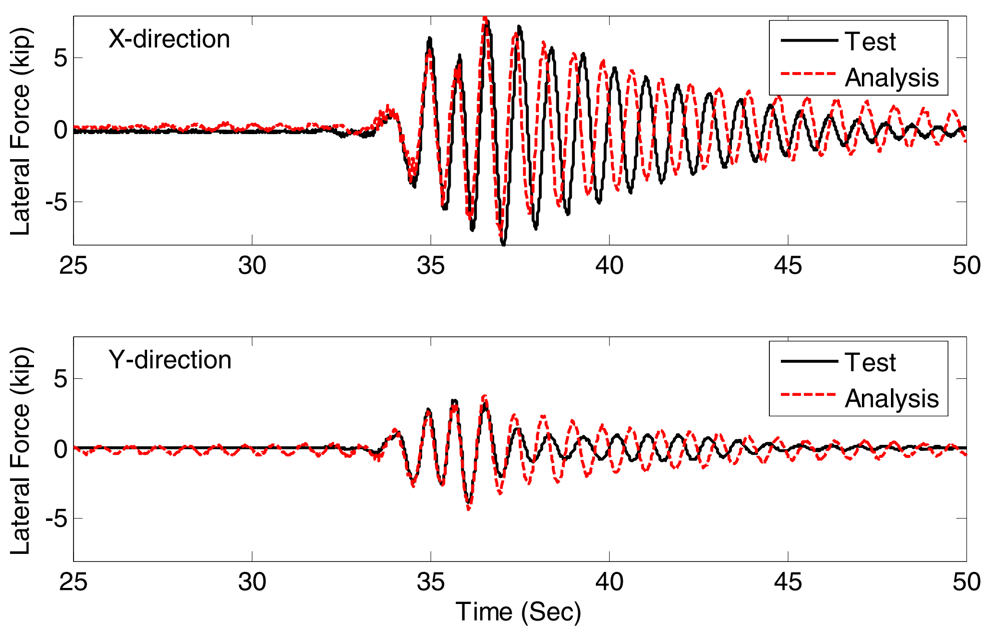

(b) Yield level

Fig. 5.14 Lateral force of RC specimen based on recommended model

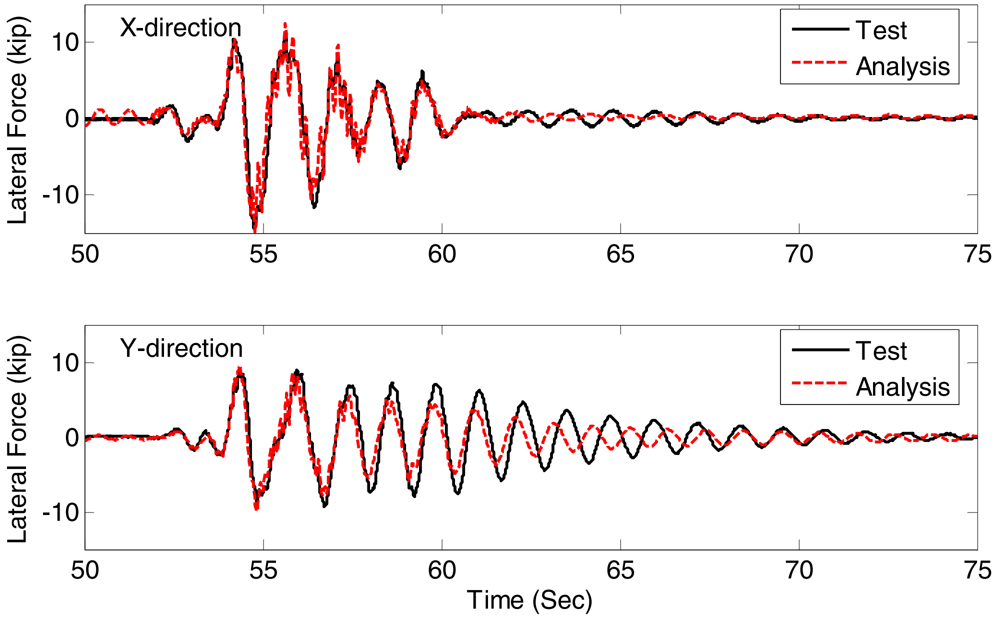

(c) Design level

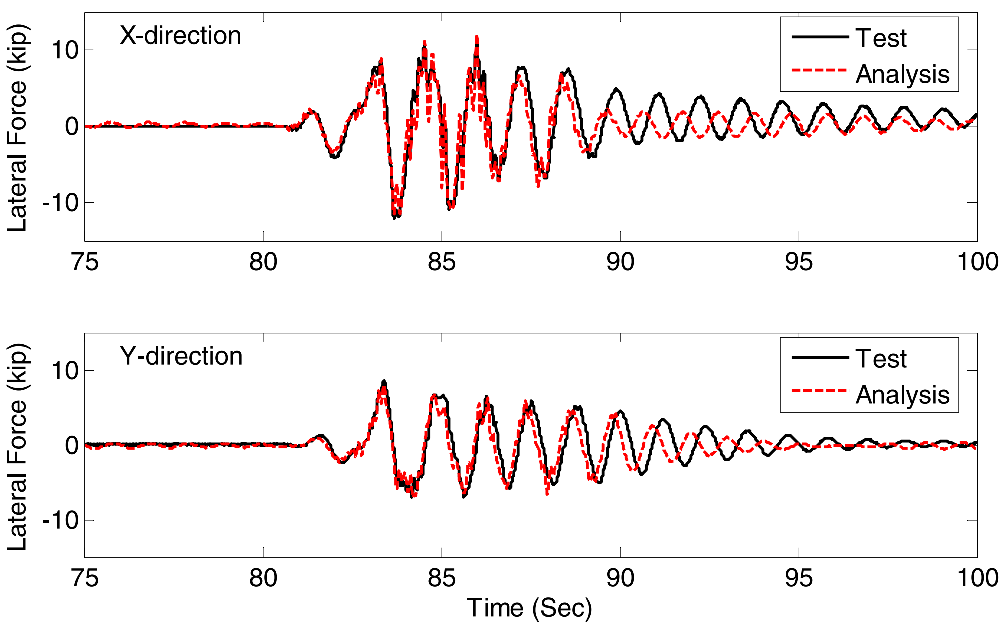

(d) Maximum level

Fig. 5.14—*Continued*

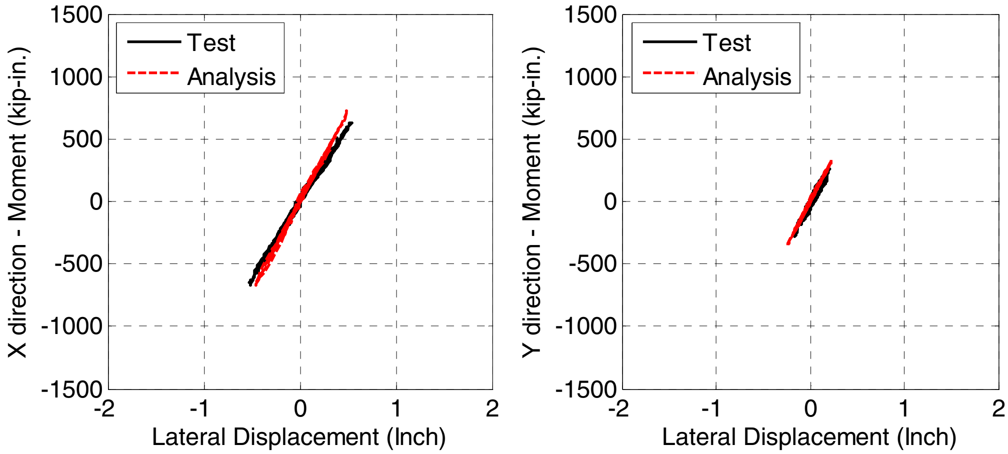

(a) Elastic level

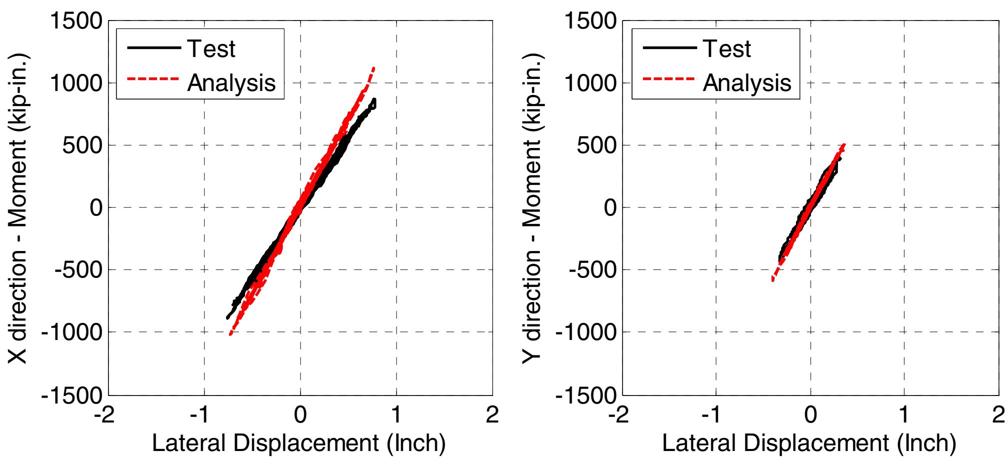

(b) Yield level

Fig. 5.15 Moment-displacement hysteresis of RC specimen based on recommended model

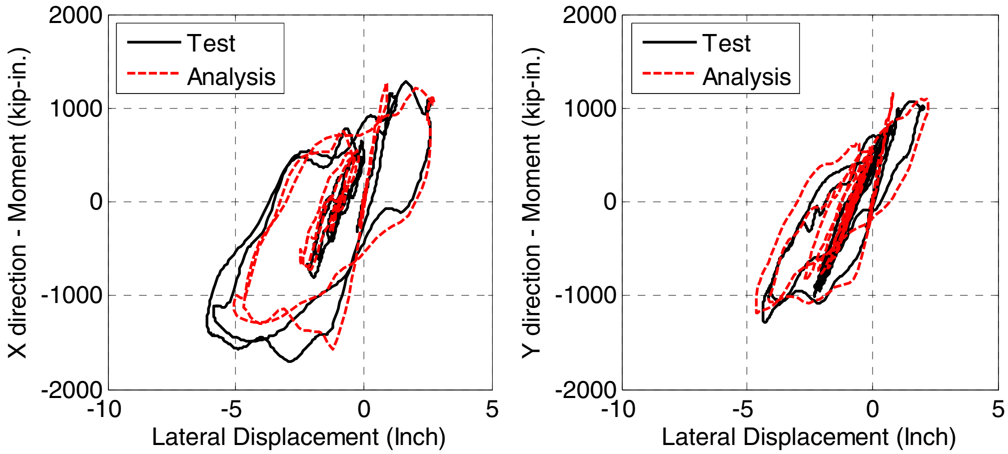

(c) Design level

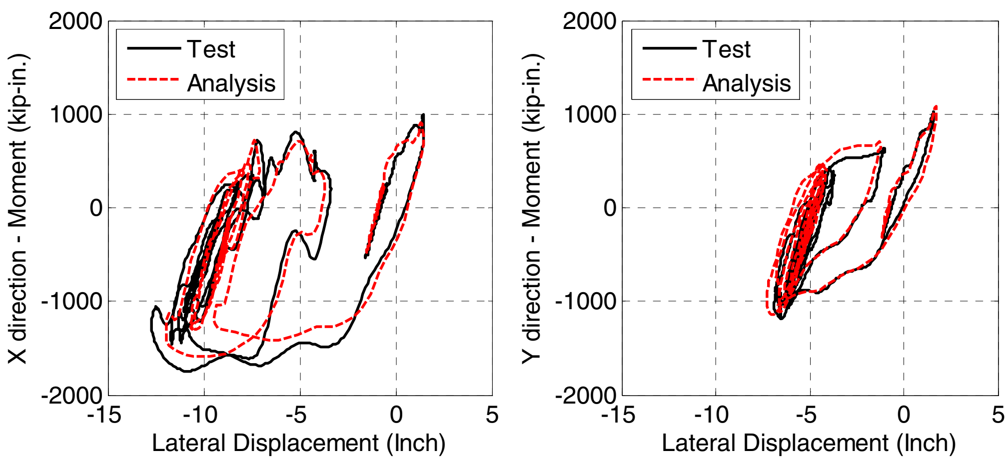

(d) Maximum level

Fig. 5.15—*Continued*

7

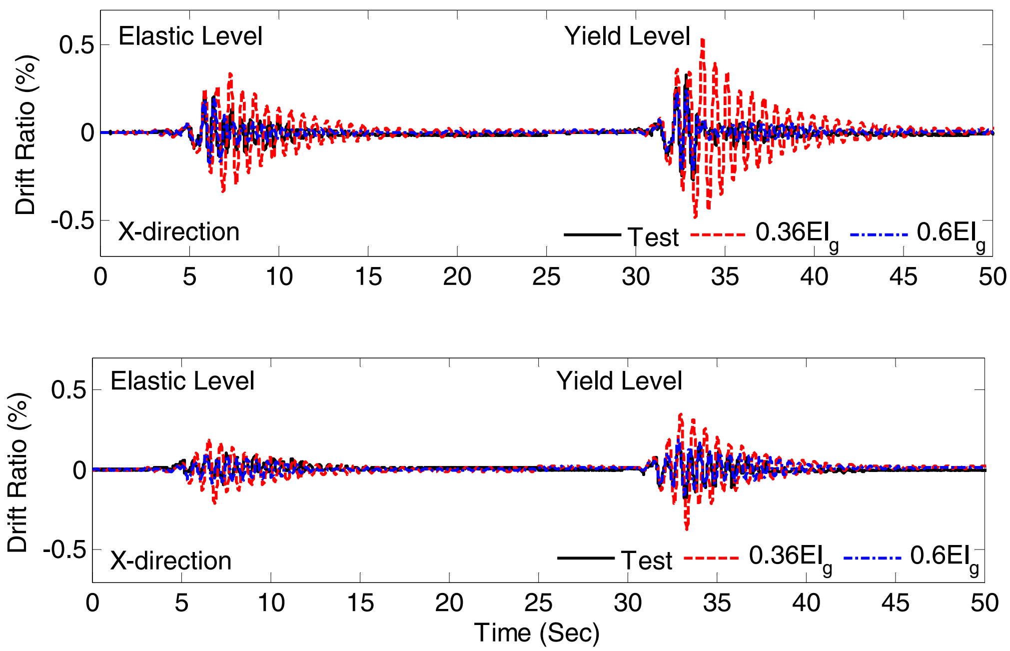

(a) Elastic and yield level

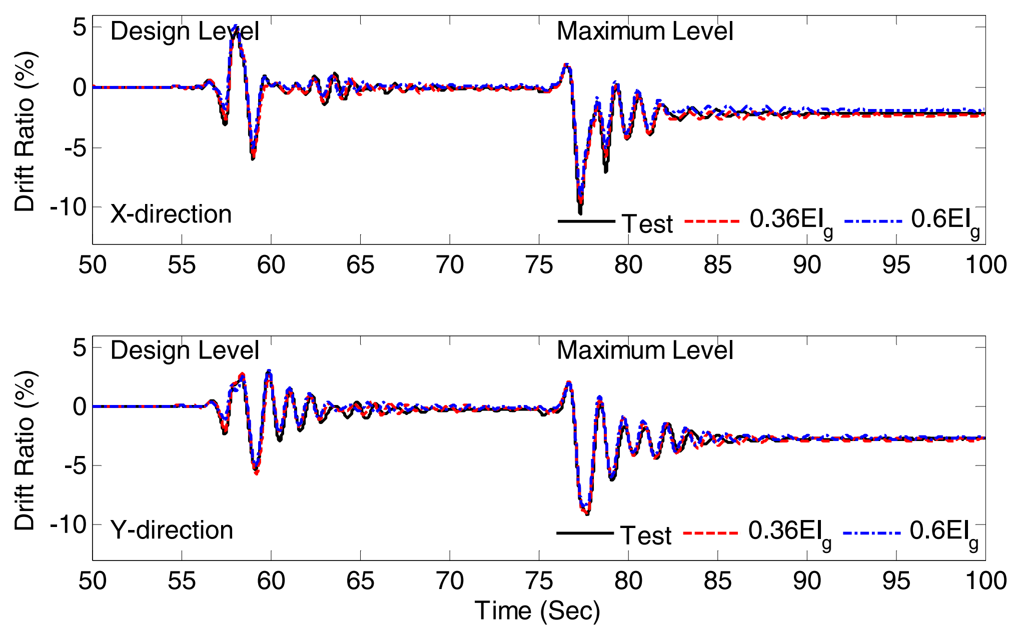

(b) Design and maximum level

Fig. 5.16 Analytical responses of varying effective stiffness of PRC specimen (0.36 EI_g—Caltrans SDC; 0.6 EI_g—matched to natural frequency)

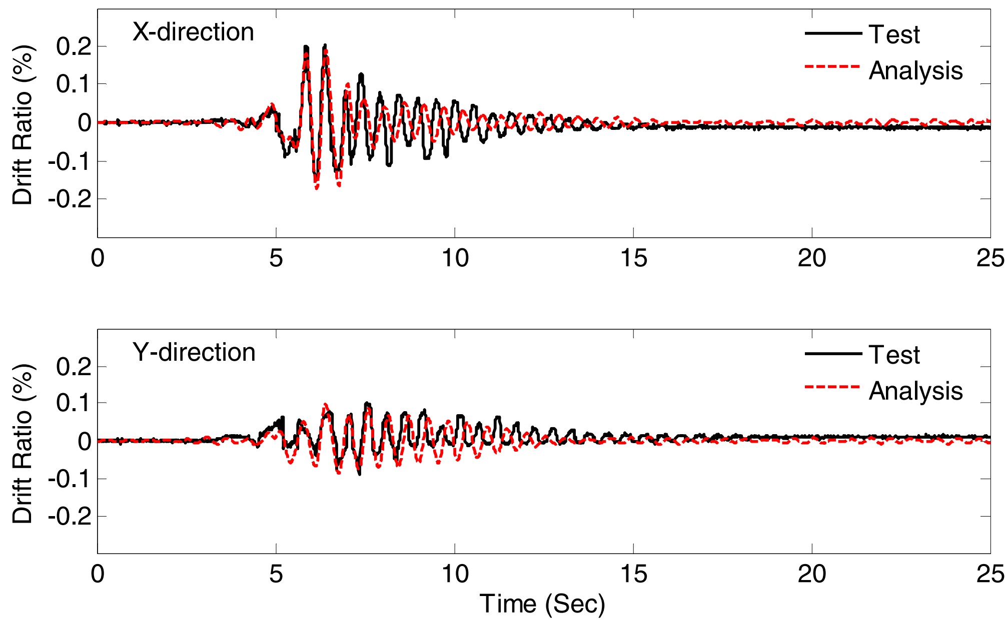

(a) Elastic level

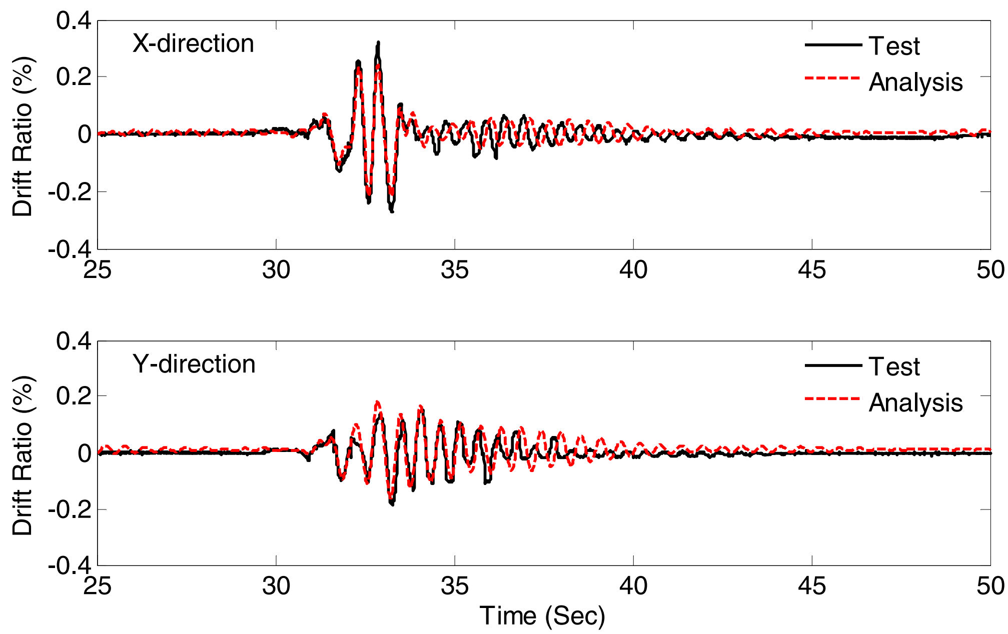

(b) Yield level

Fig. 5.17 Displacement of PRC specimen based on recommended model

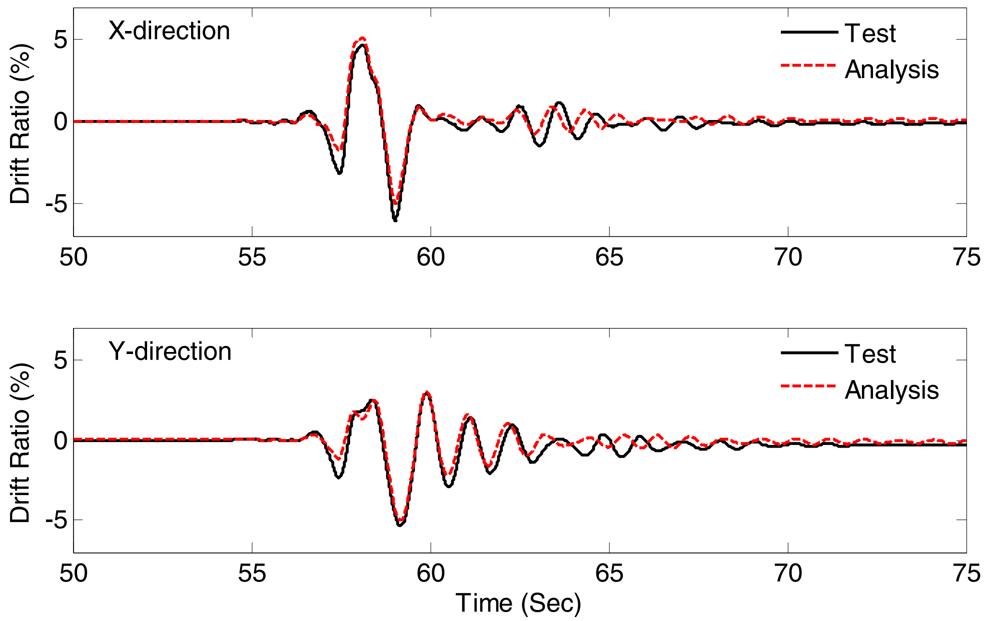

(c) Design level

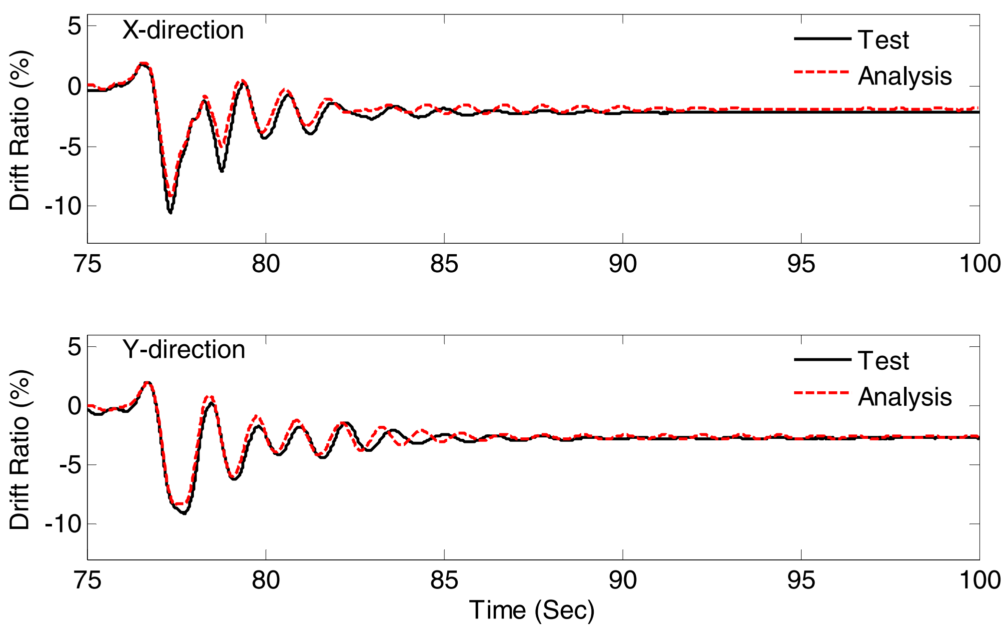

(d) Maximum level

Fig. 5.17—*Continued*

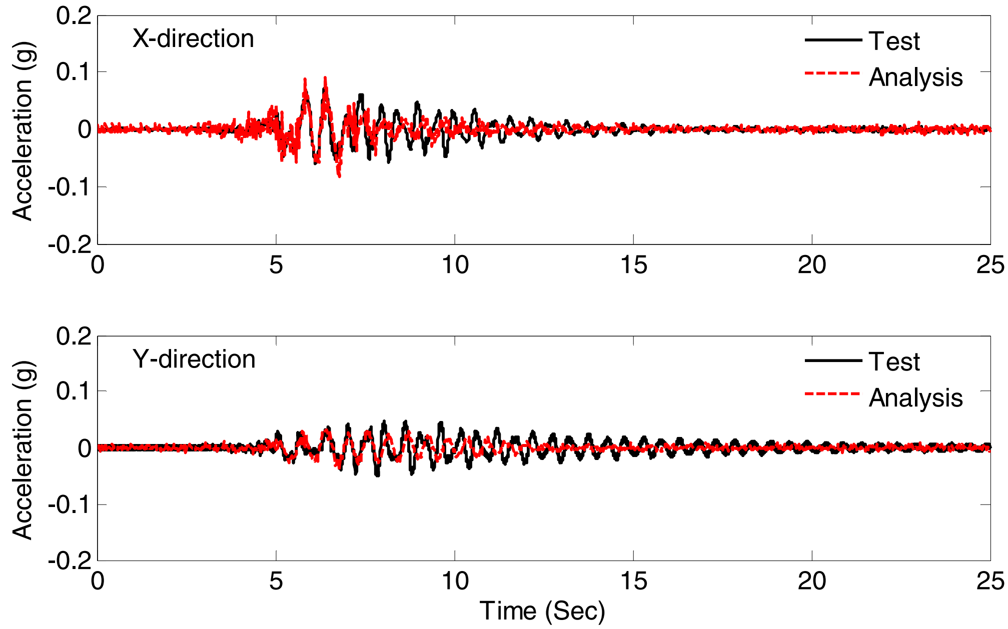

(a) Elastic level

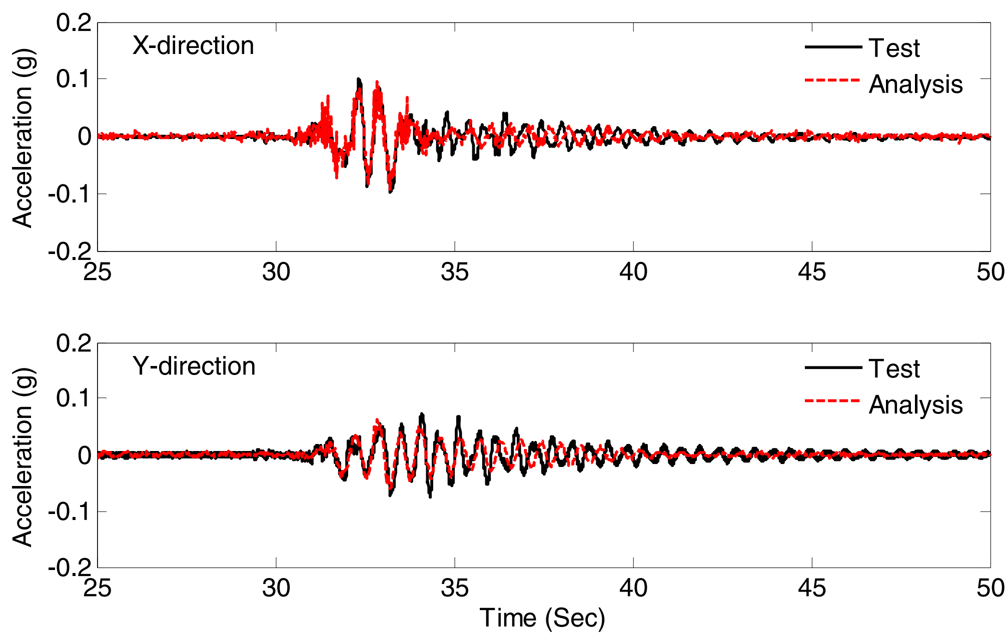

(b) Yield level

Fig. 5.18 Acceleration of PRC specimen based on recommended model

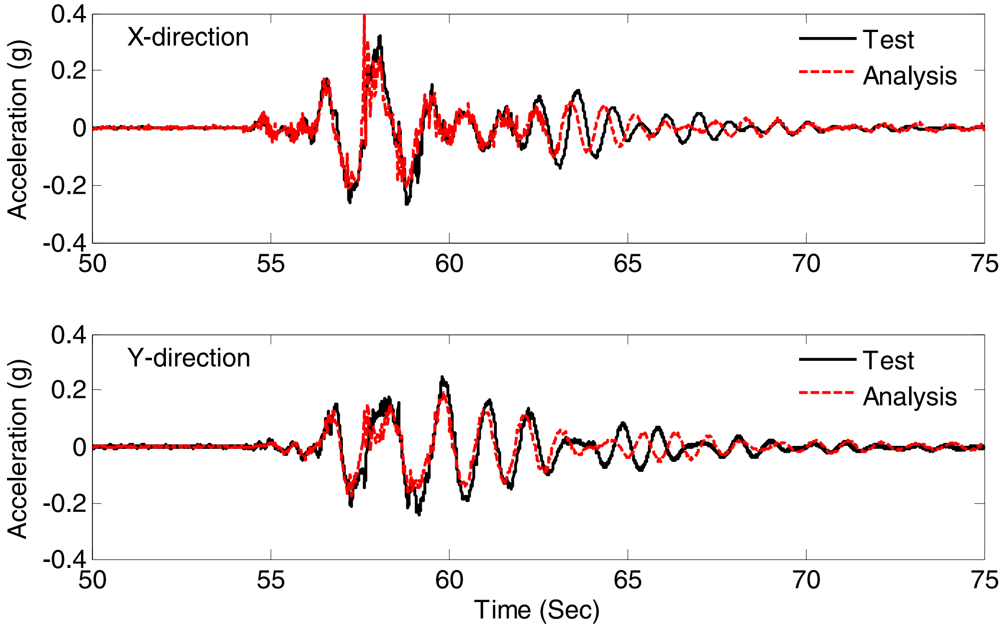

(c) Design level

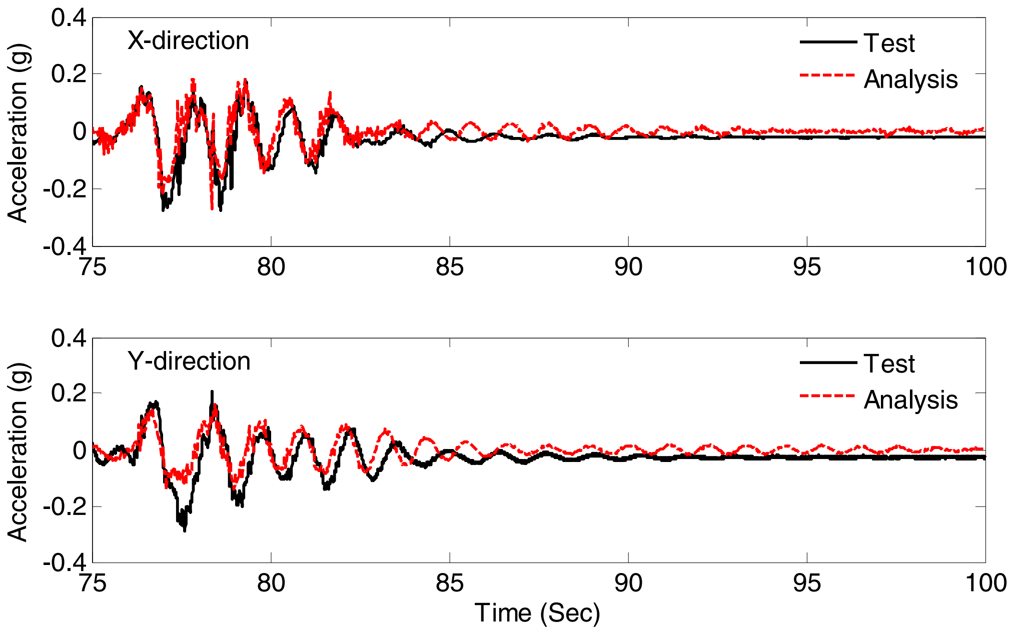

(d) Maximum level

Fig. 5.18—*Continued*

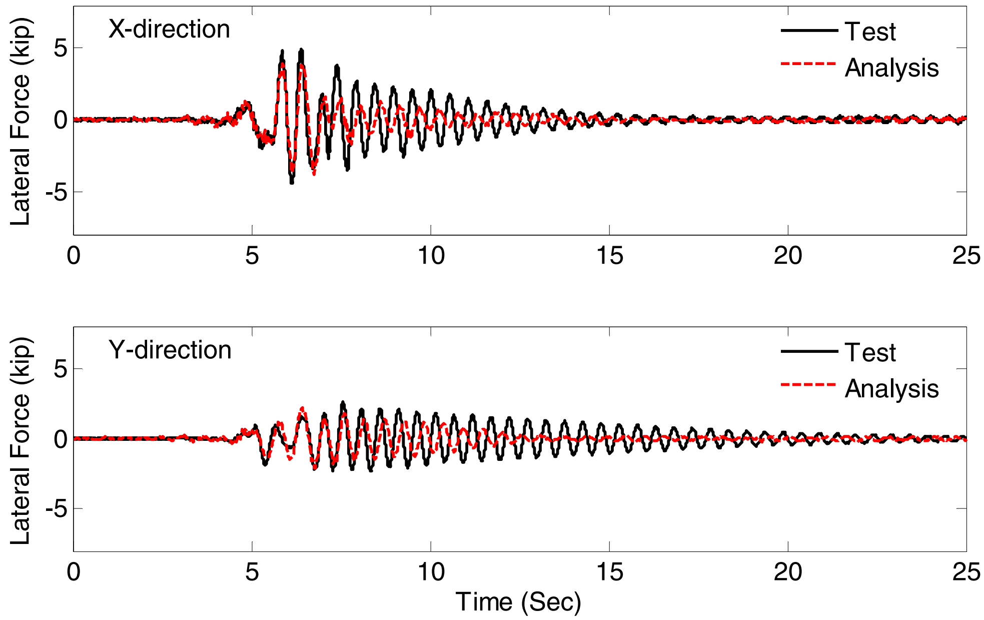

(a) Elastic level

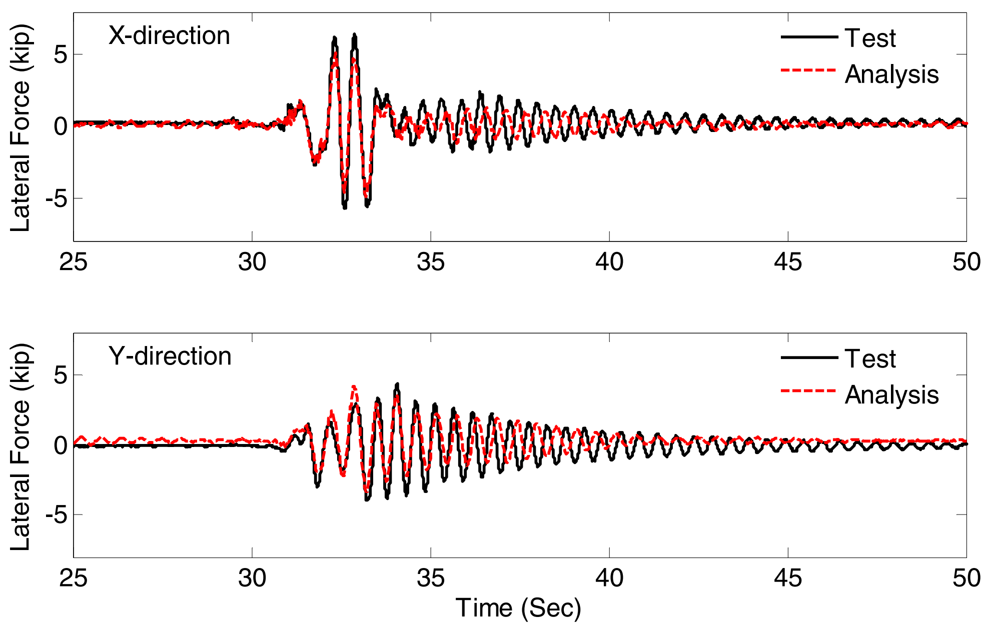

(b) Yield level

Fig. 5.19 Lateral force of PRC specimen based on recommended model

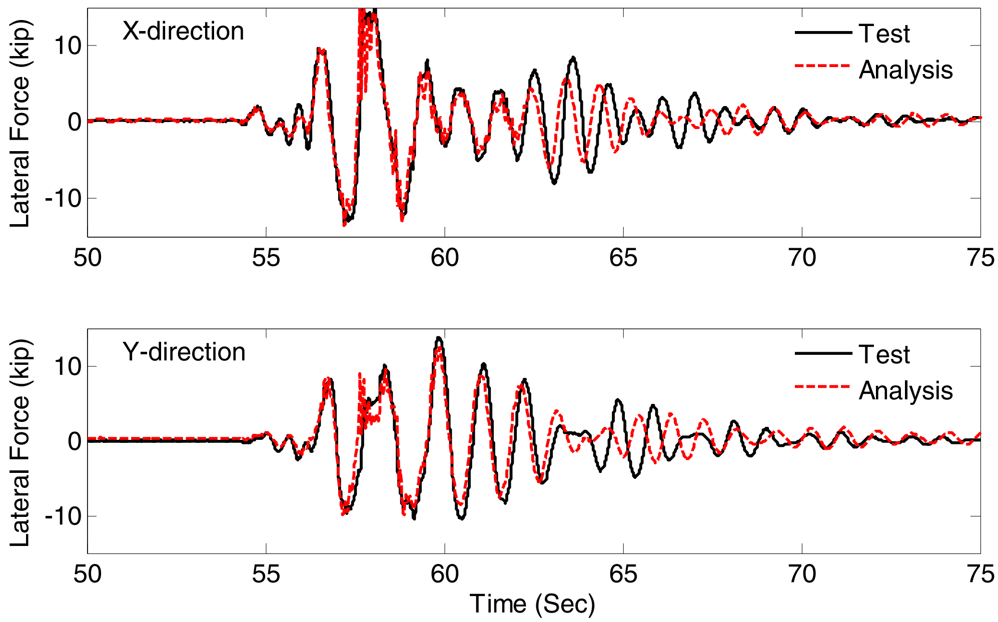

(c) Design level

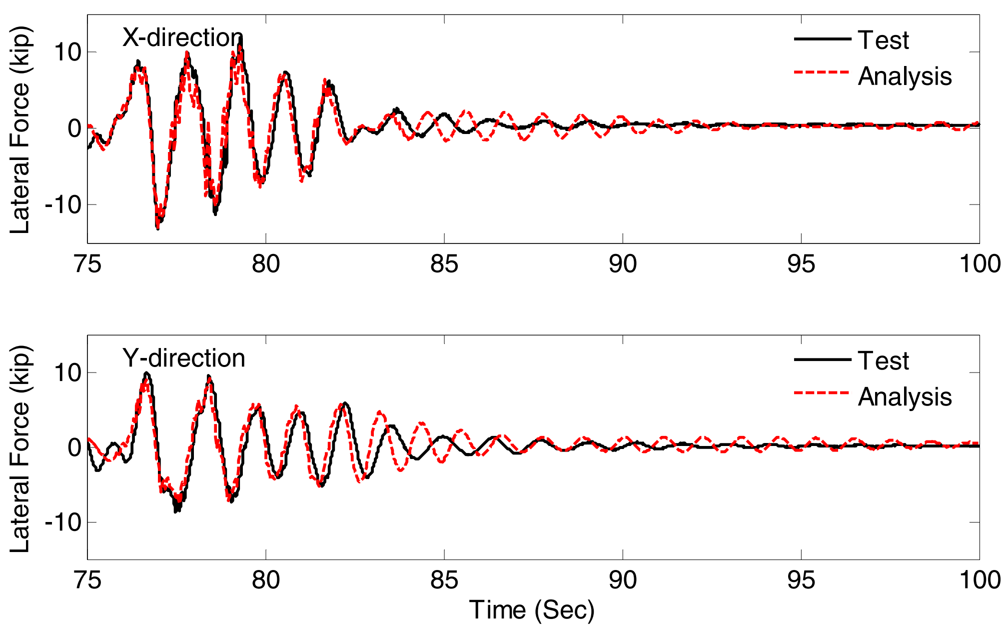

(d) Maximum level

Fig. 5.19—*Continued*

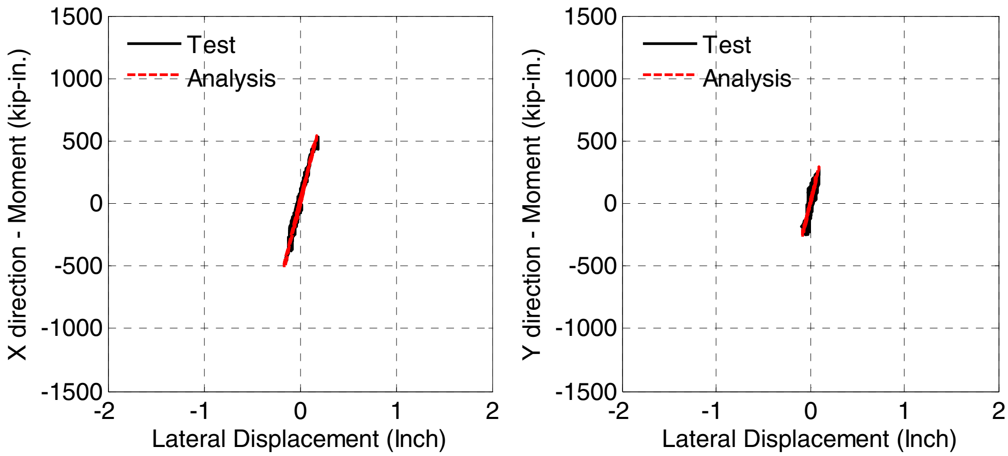

(a) Elastic level

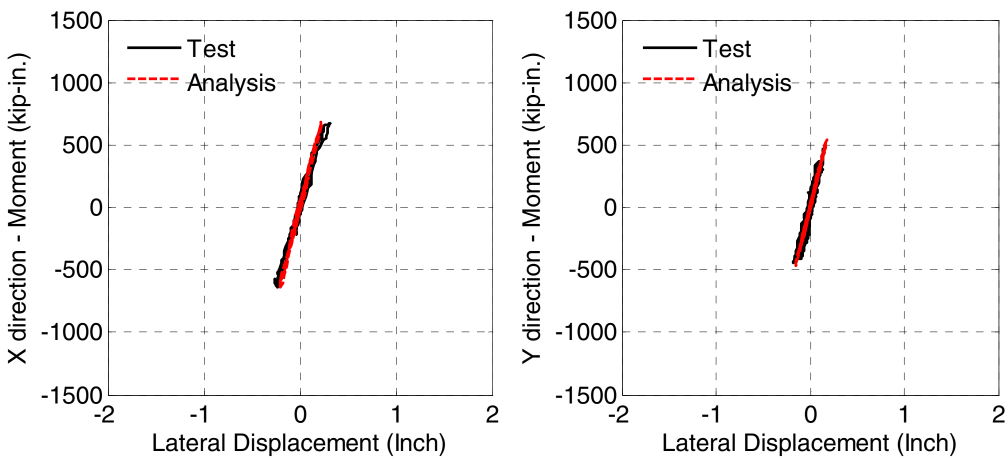

(b) Yield level

Fig. 5.20 Moment-displacement hysteresis of PRC specimen based on recommended model

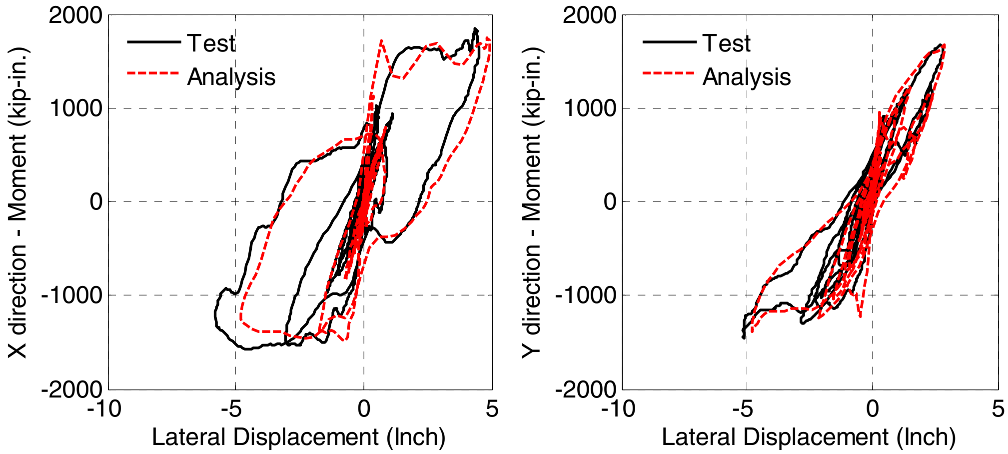

(c) Design level

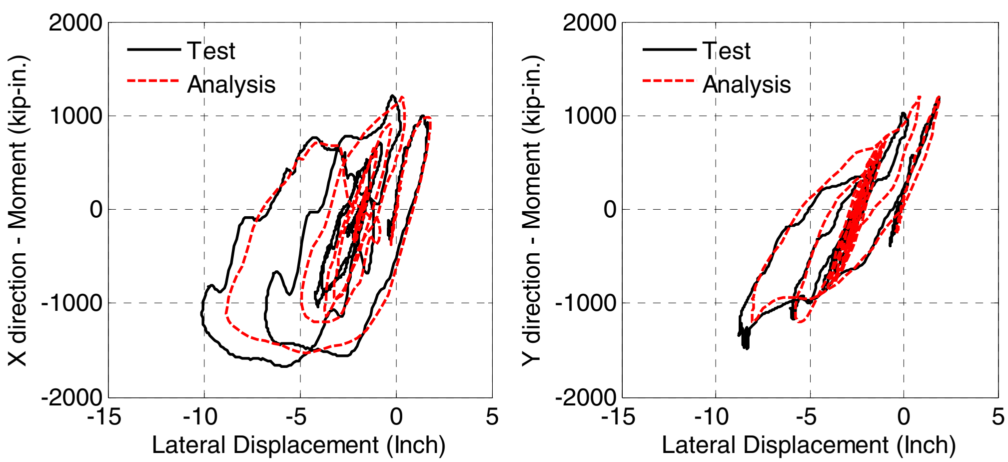

(d) Maximum level

Fig. 5.20—*Continued*

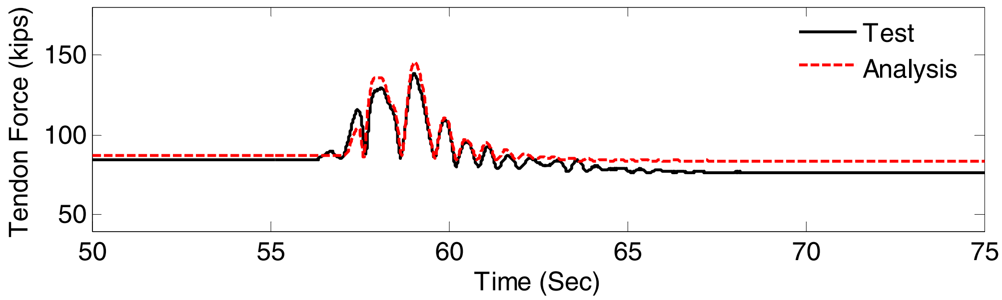

(a) Design level

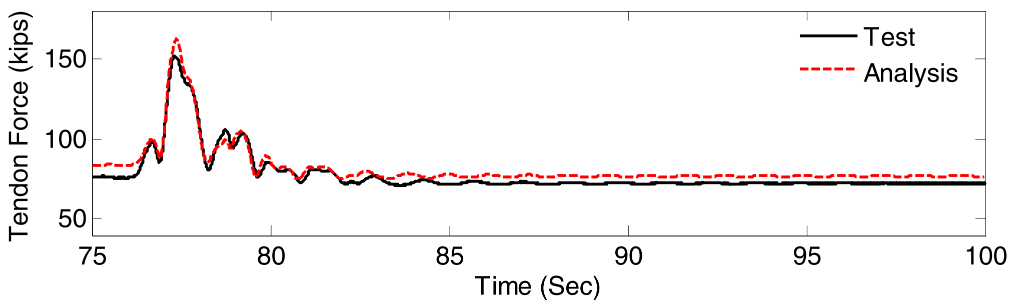

(b) Maximum level

Fig. 5.21 Prestressing force of PRC specimen based on recommended model

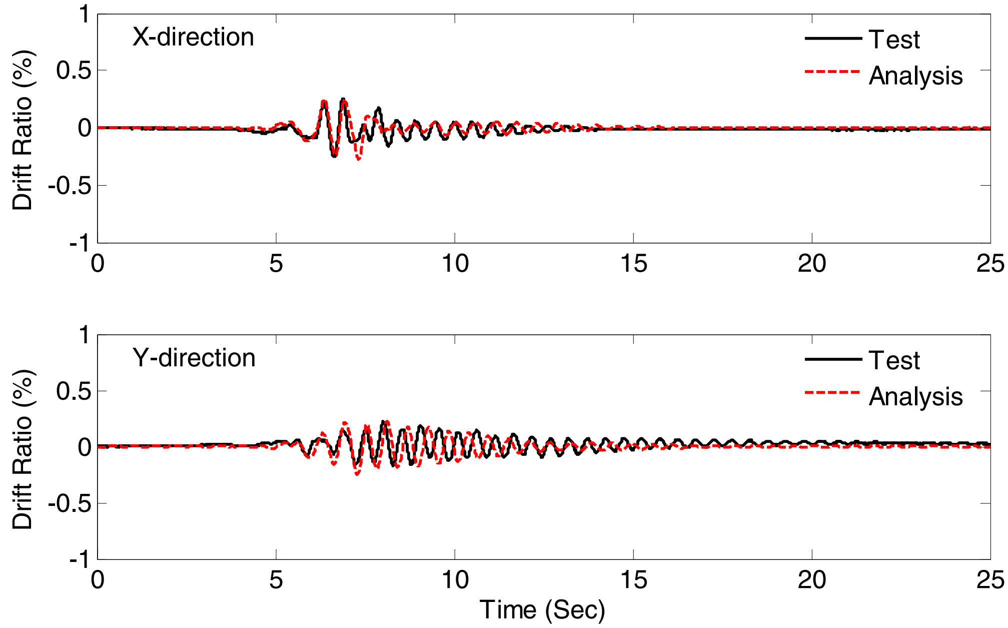

(a) Elastic level

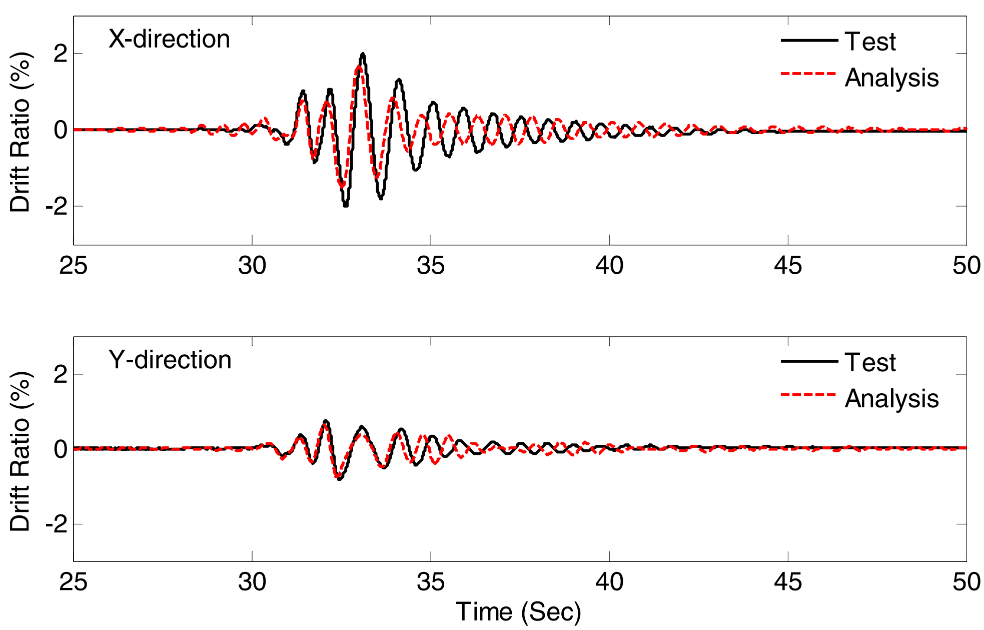

(b) Yield level

Fig. 5.22 Displacement of PRC-2 specimen based on recommended model

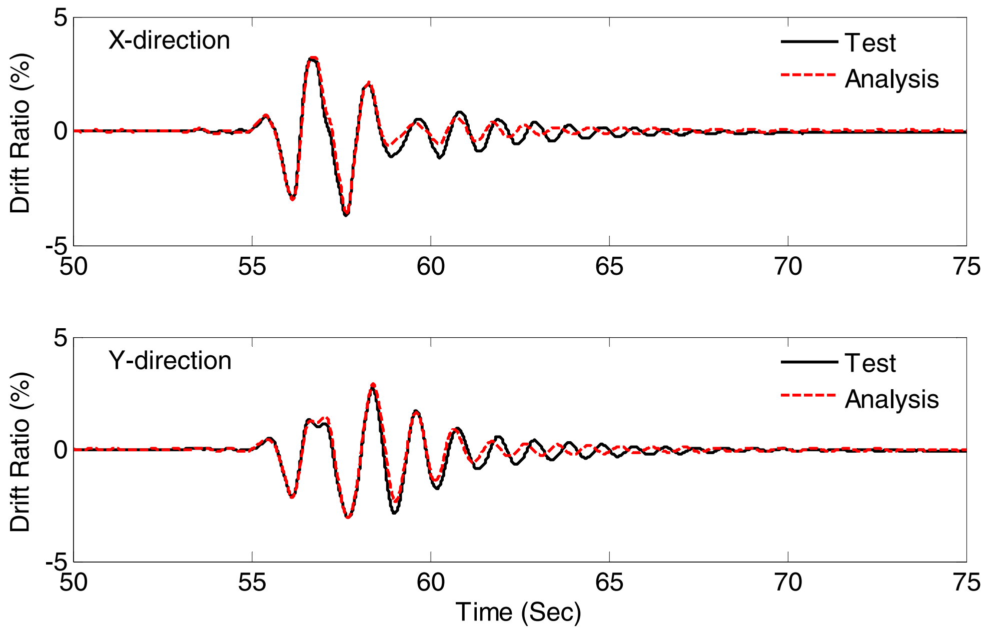

(c) Design level

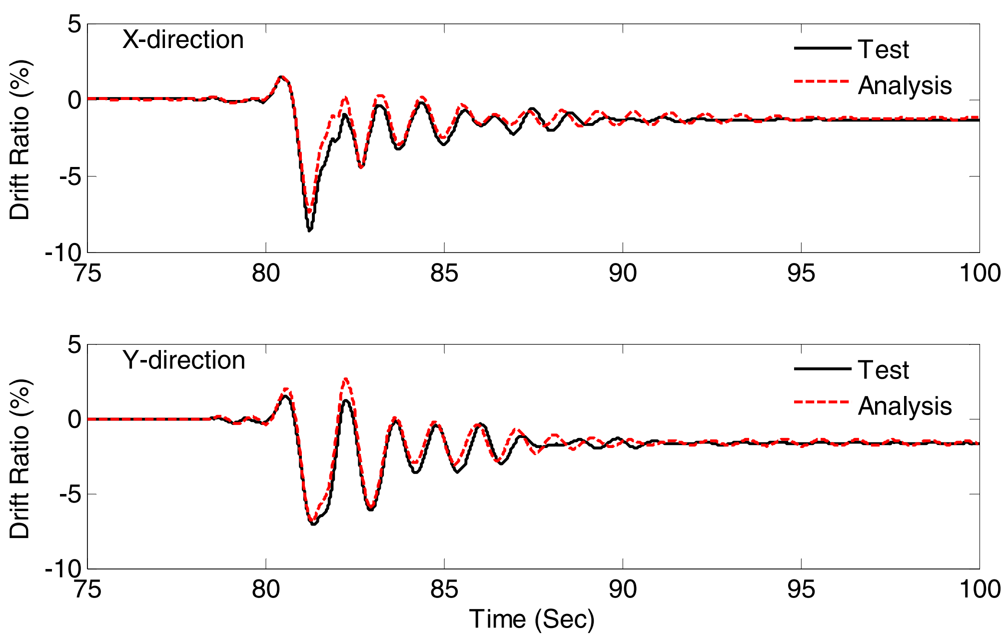

(d) Maximum level

Fig. 5.22—*Continued.*

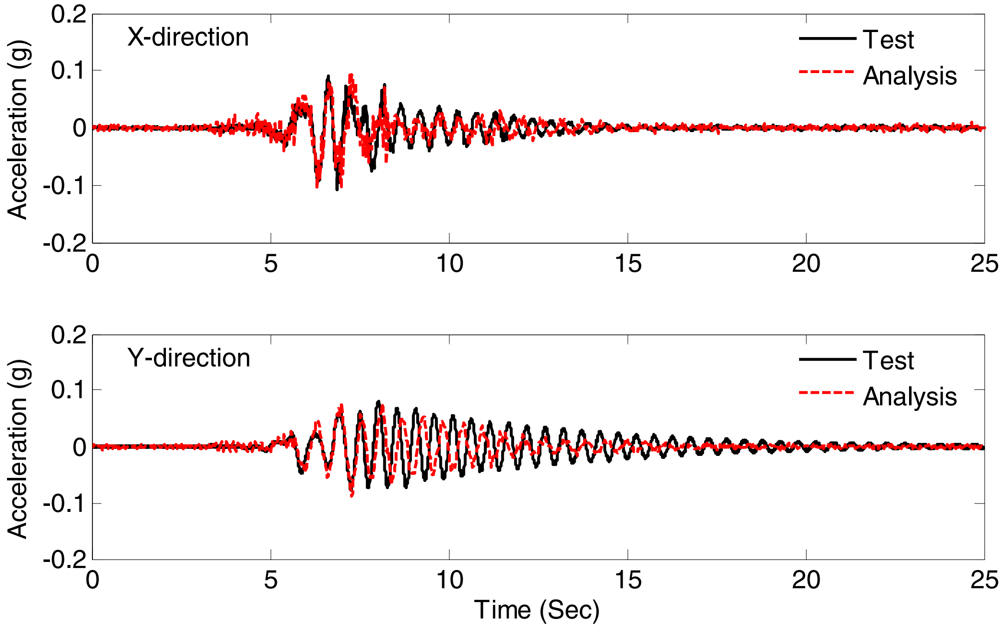

(a) Elastic level

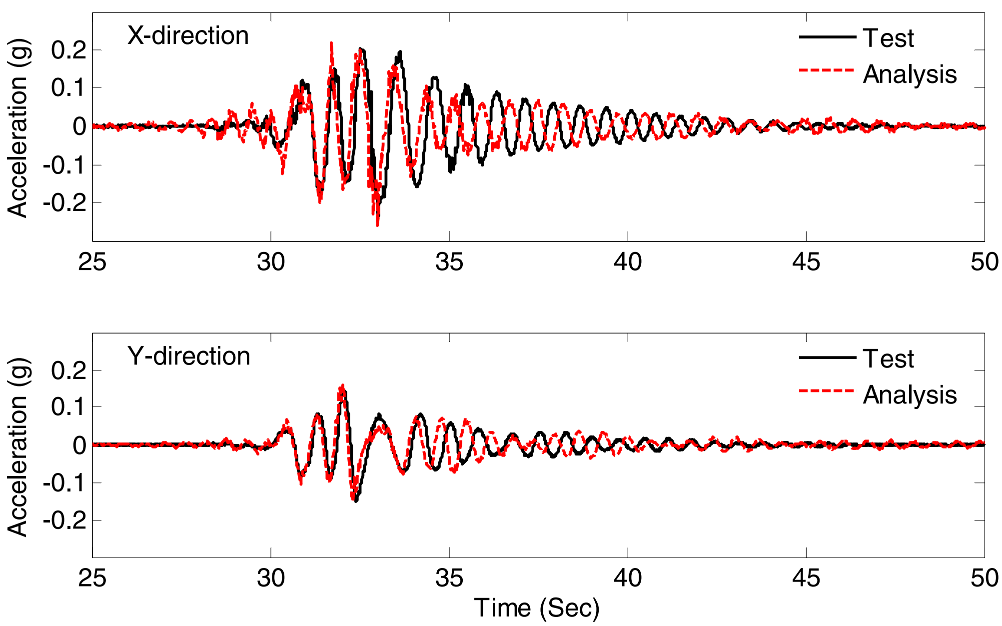

(b) Yield level

Fig. 5.23 Acceleration of PRC-2 specimen based on recommended model

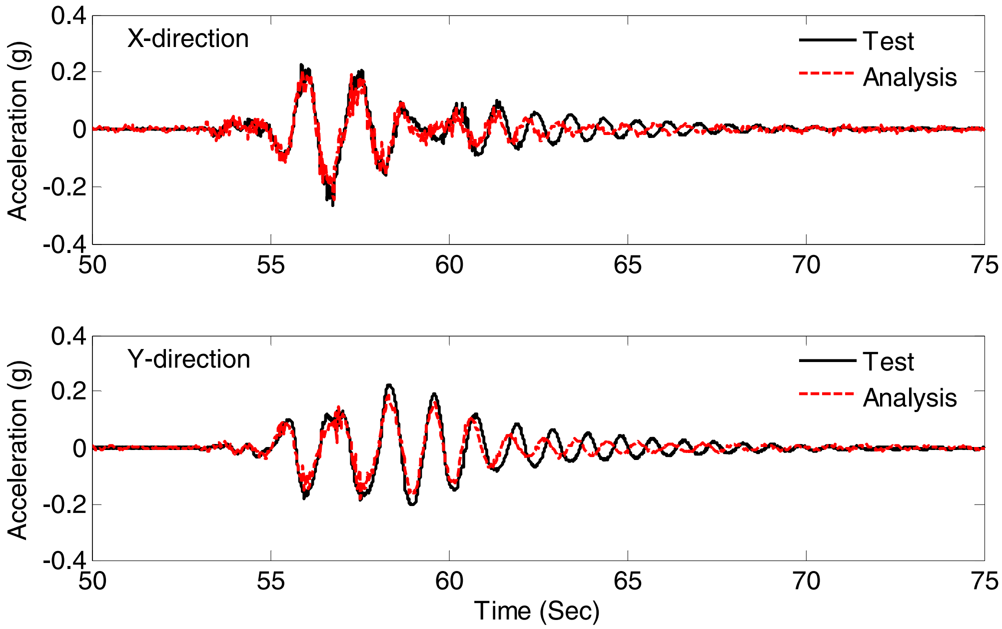

(c) Design level

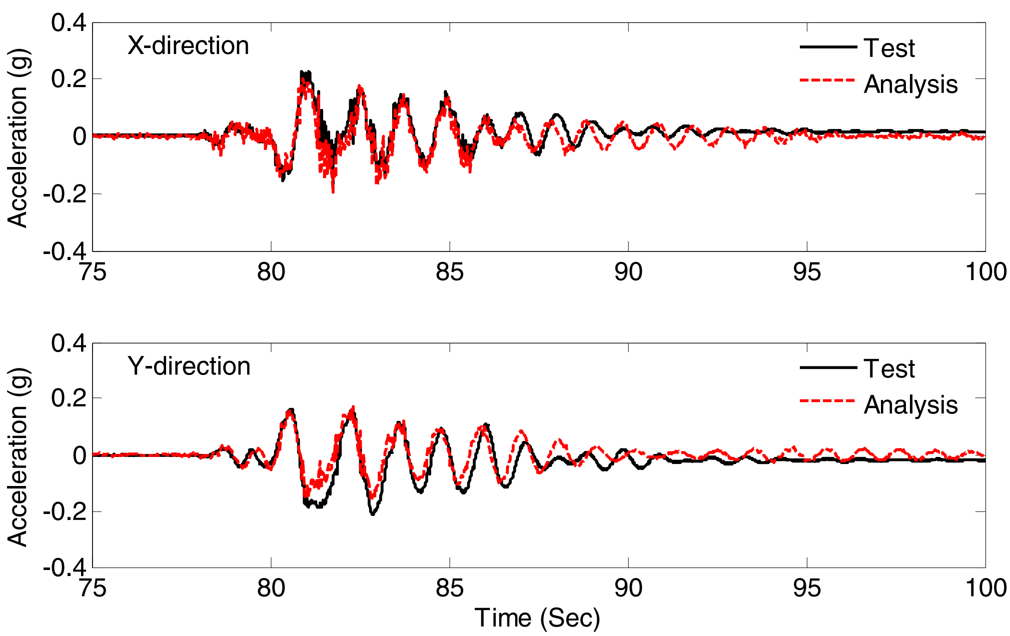

(d) Maximum level

Fig. 5.23—*Continued*

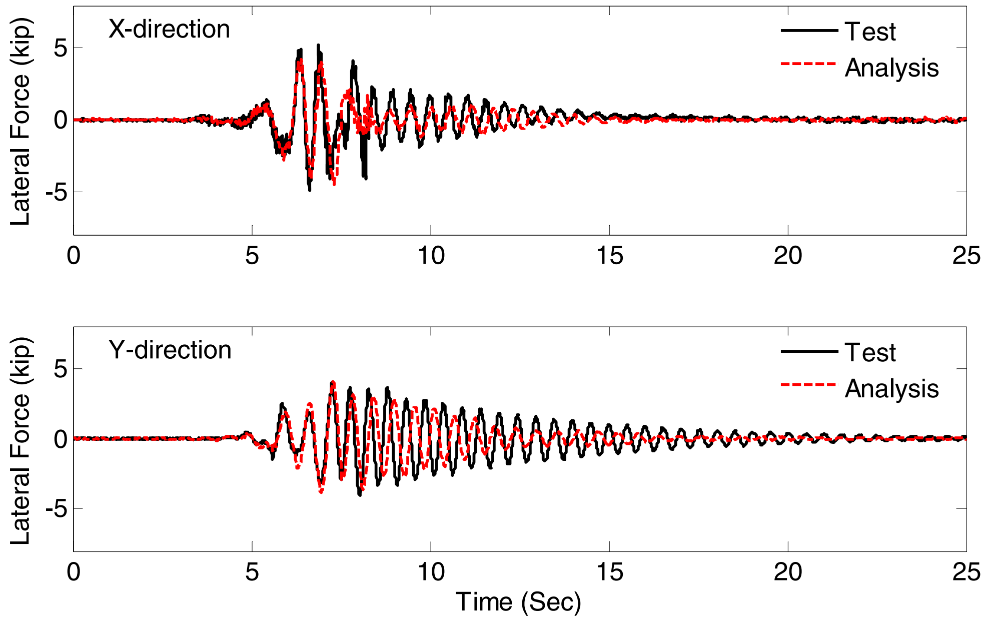

(a) Elastic level

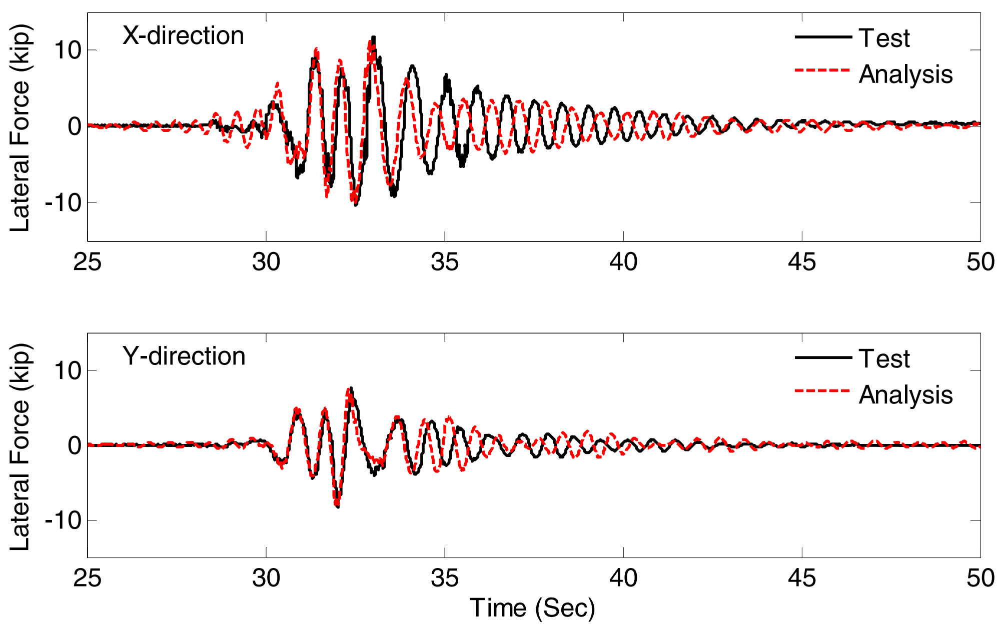

(b) Yield level

Fig. 5.24 Lateral force of PRC-2 specimen based on recommended model

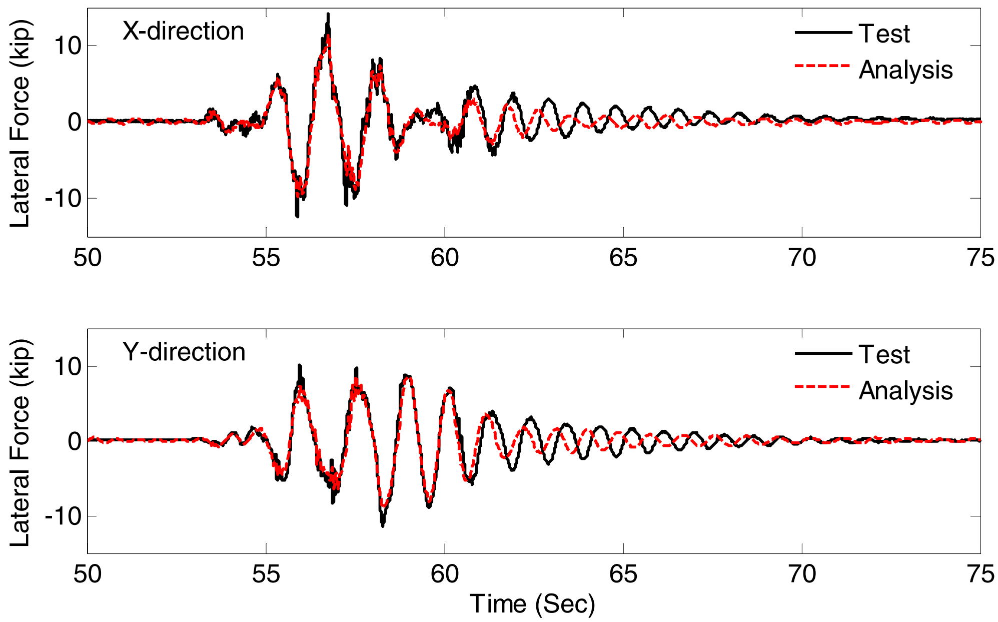

(c) Design level

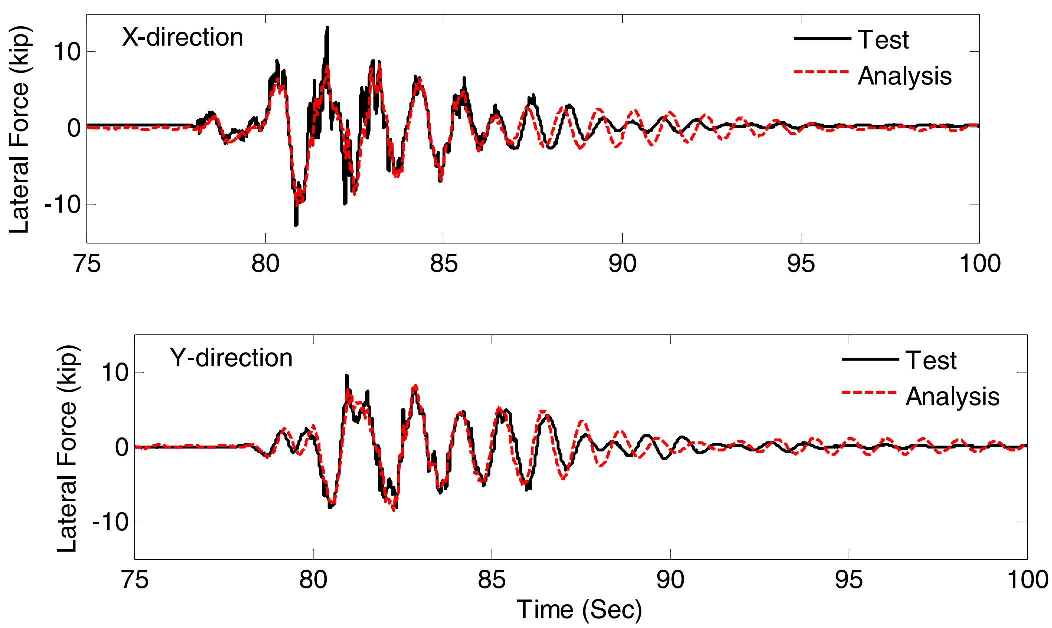

(d) Maximum level

Fig. 5.24—*Continued*

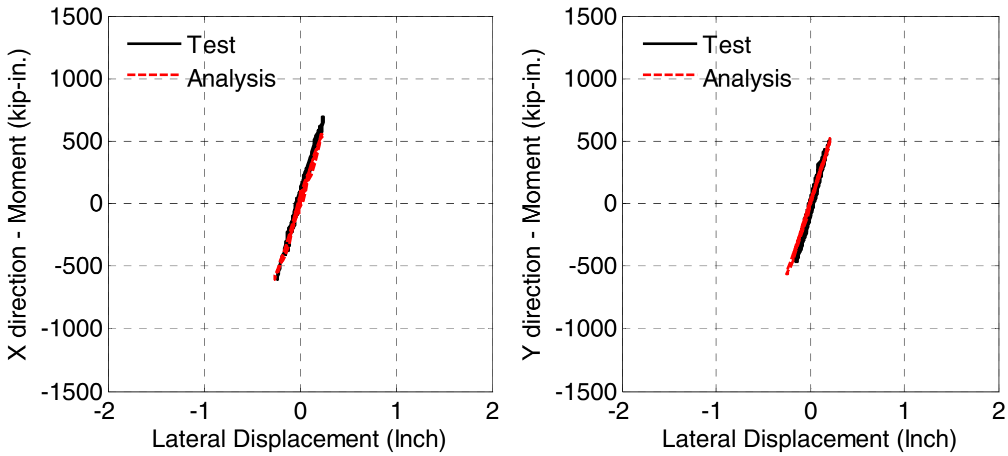

(a) Elastic level

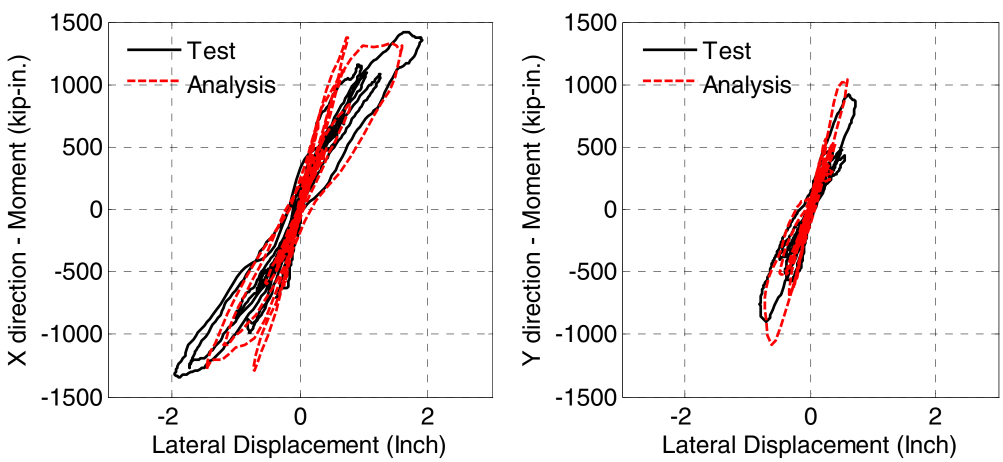

(b) Yield level

Fig. 5.25 Moment-displacement hysteresis of PRC2 specimen based on recommended model

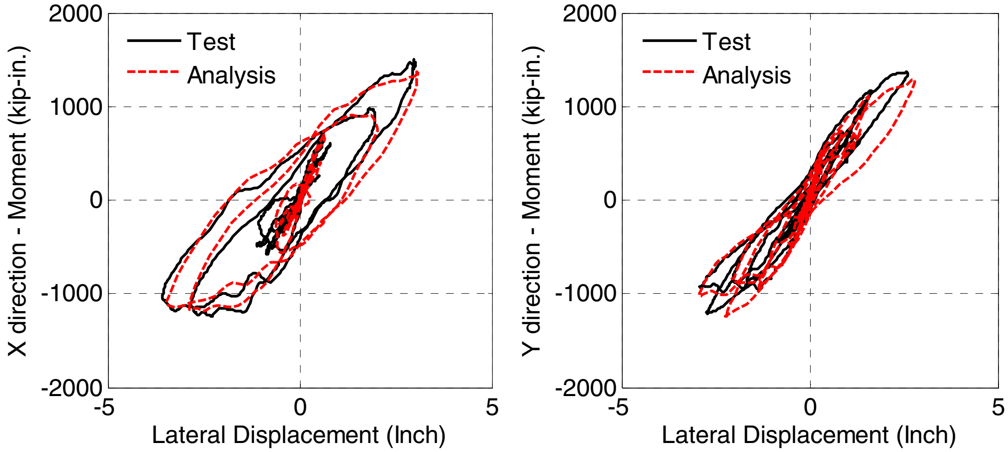

(c) Design level

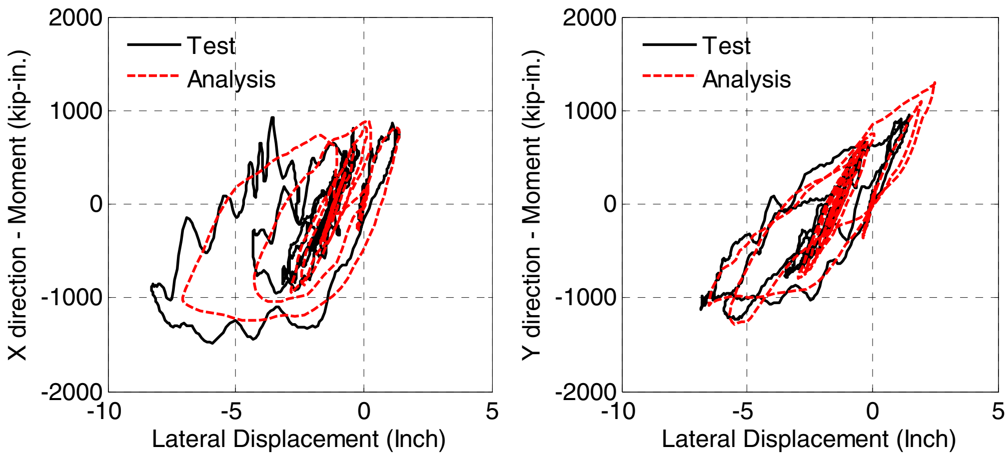

(d) Maximum level

Fig. 5.25—*Continued*

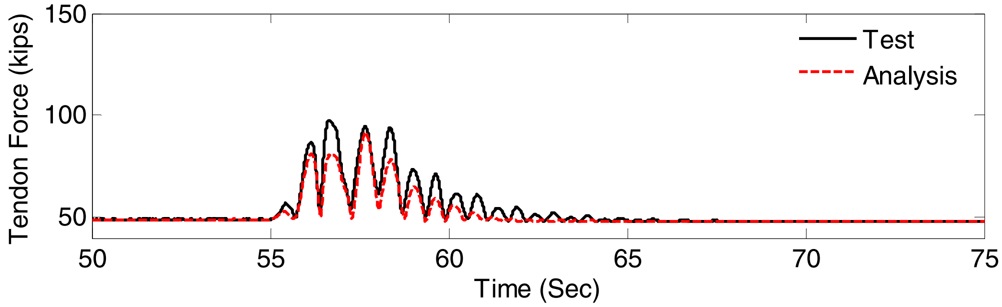

(a) Design level

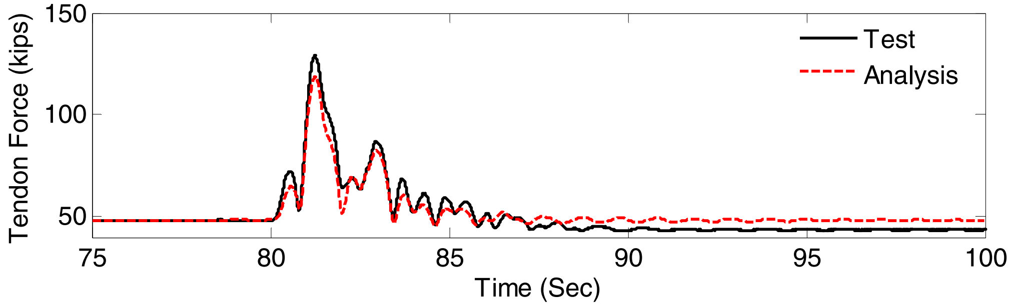

(b) Maximum level

Fig. 5.26 Prestressing force of PRC-2 specimen based on recommended model

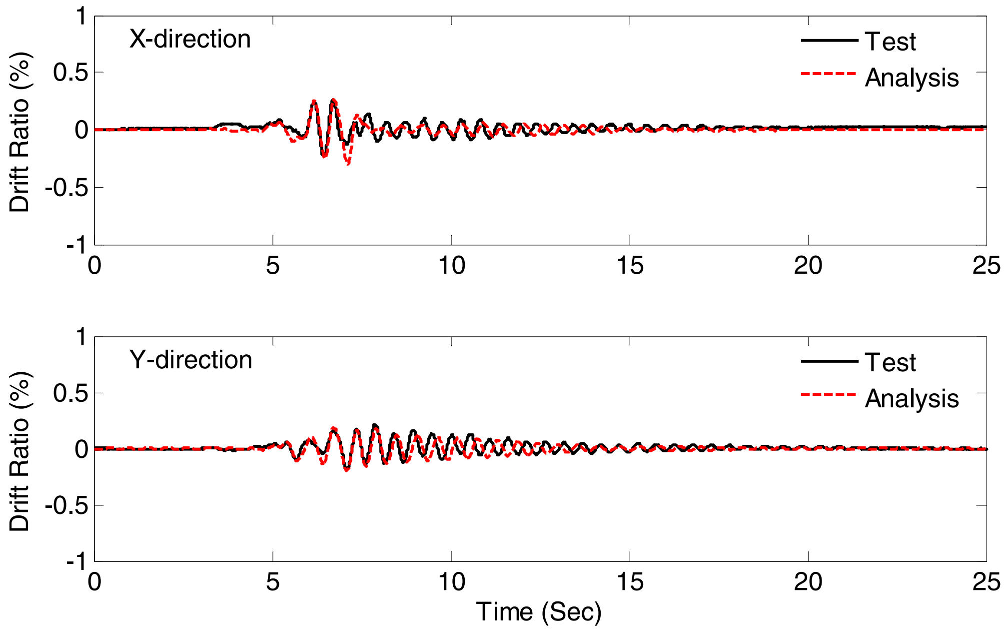

(a) Elastic level

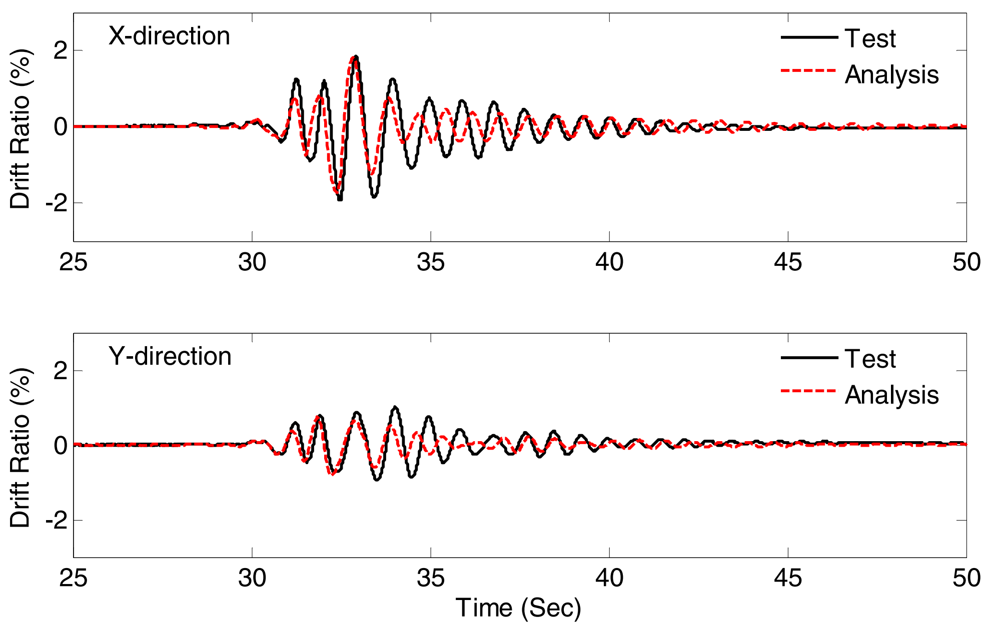

(b) Yield level

Fig. 5.27 Displacement of PRC-U specimen based on recommended model

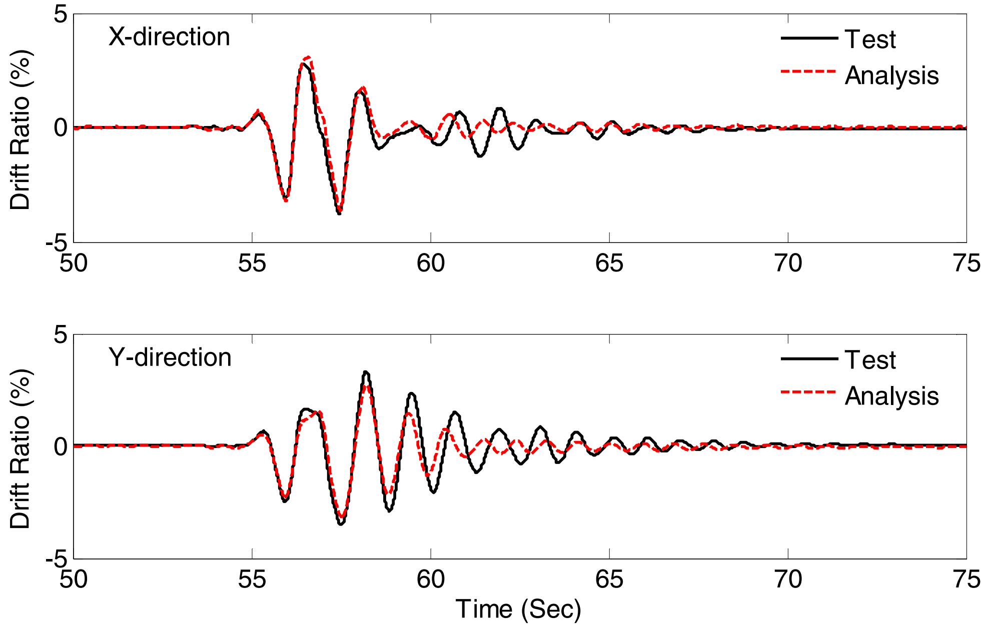

(c) Design level

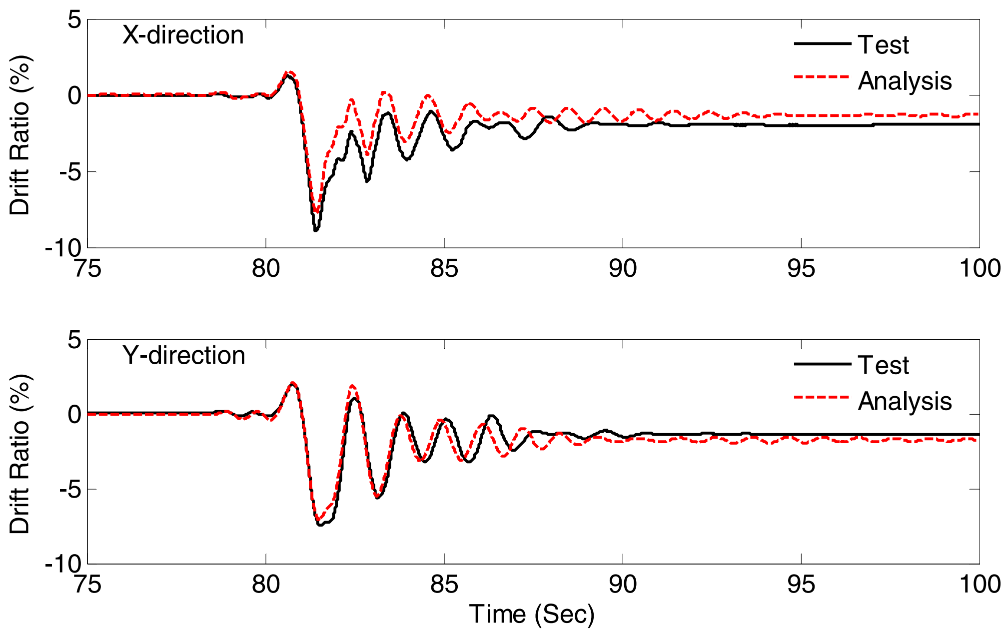

(d) Maximum level

Fig. 5.27—*Continued.*

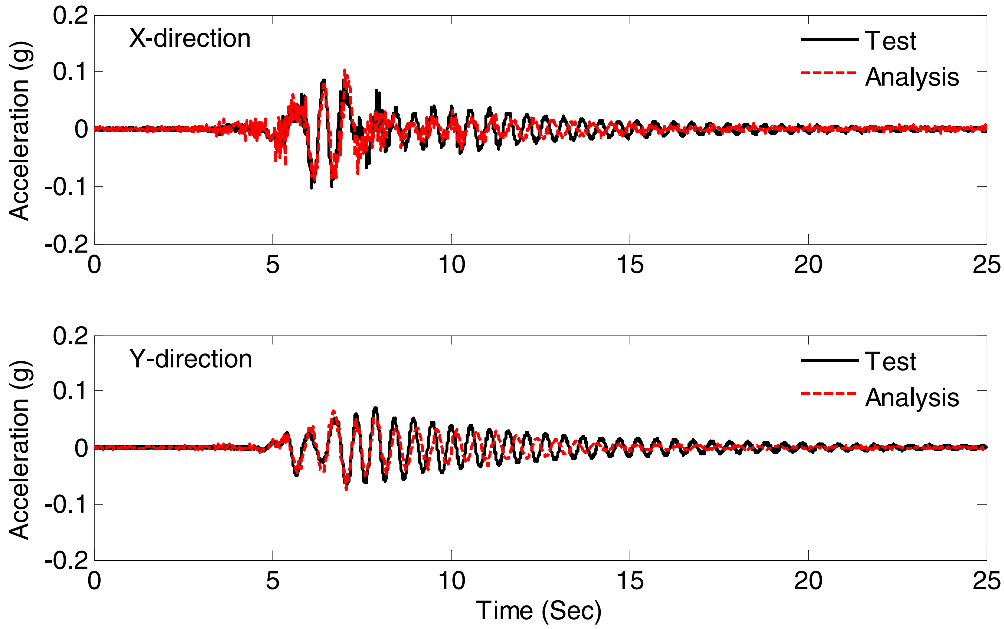

(a) Elastic level

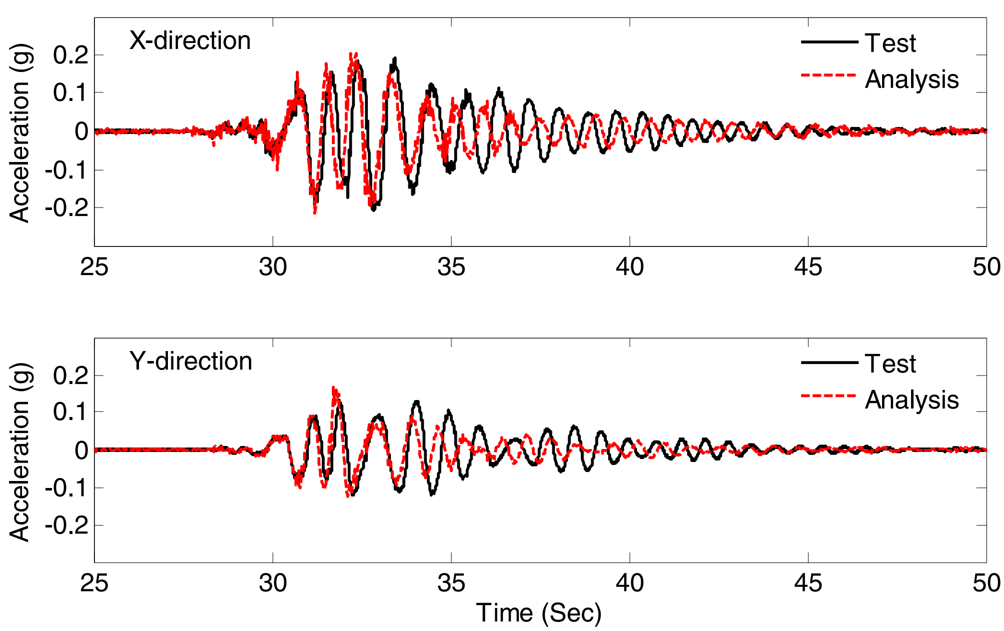

(b) Yield level

Fig. 5.28 Acceleration of PRC-U specimen based on recommended model

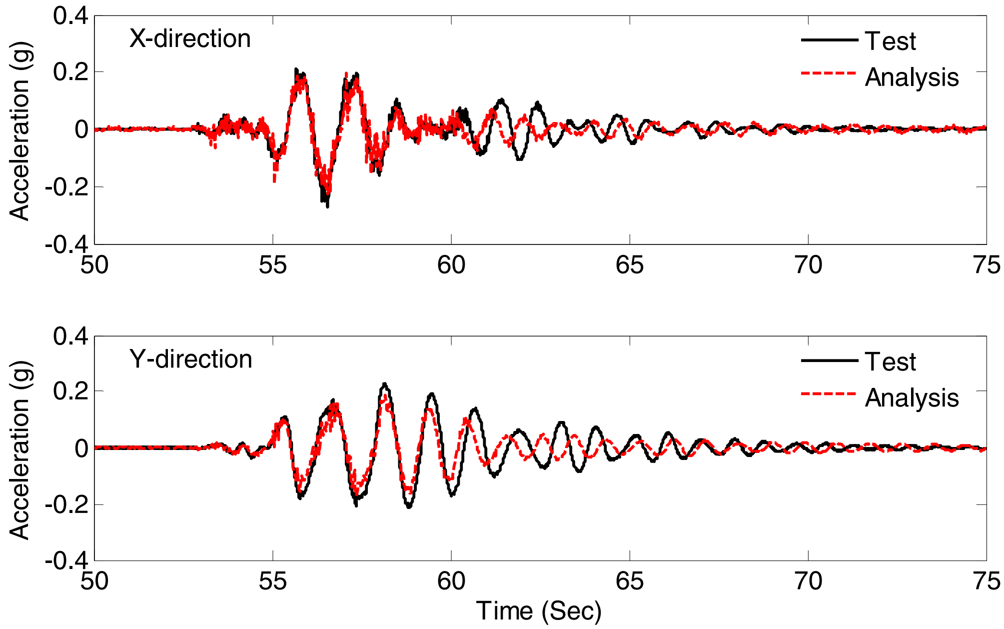

(c) Design level

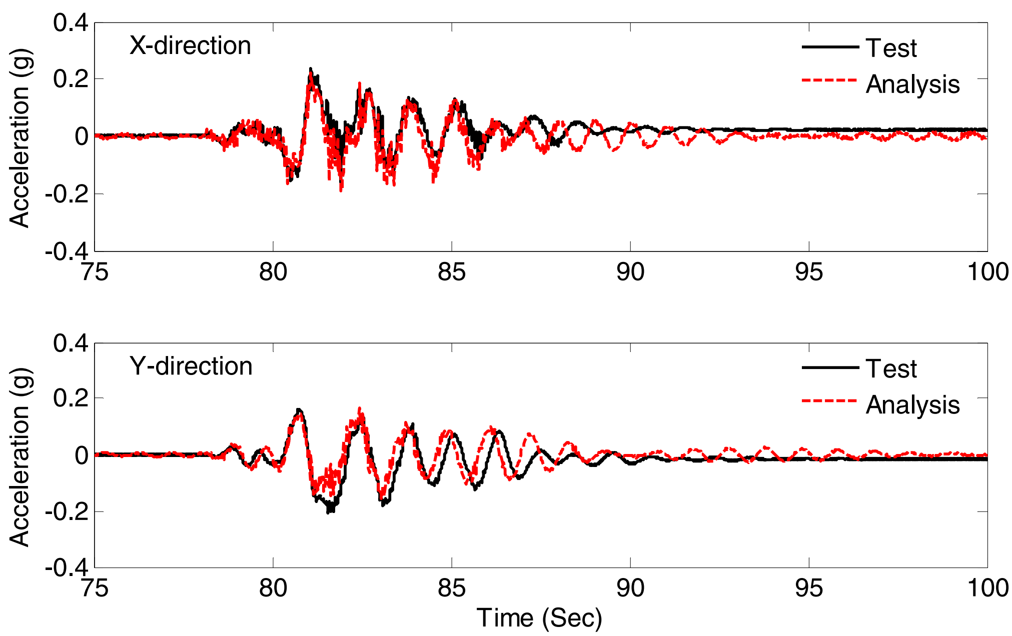

(d) Maximum level

Fig. 5.28—*Continued*

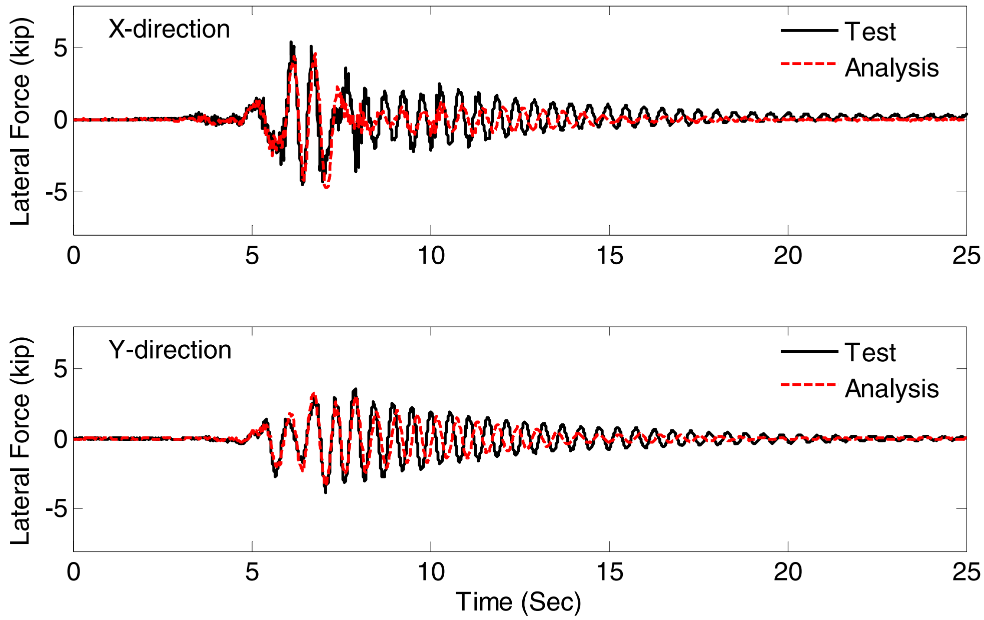

(a) Elastic level

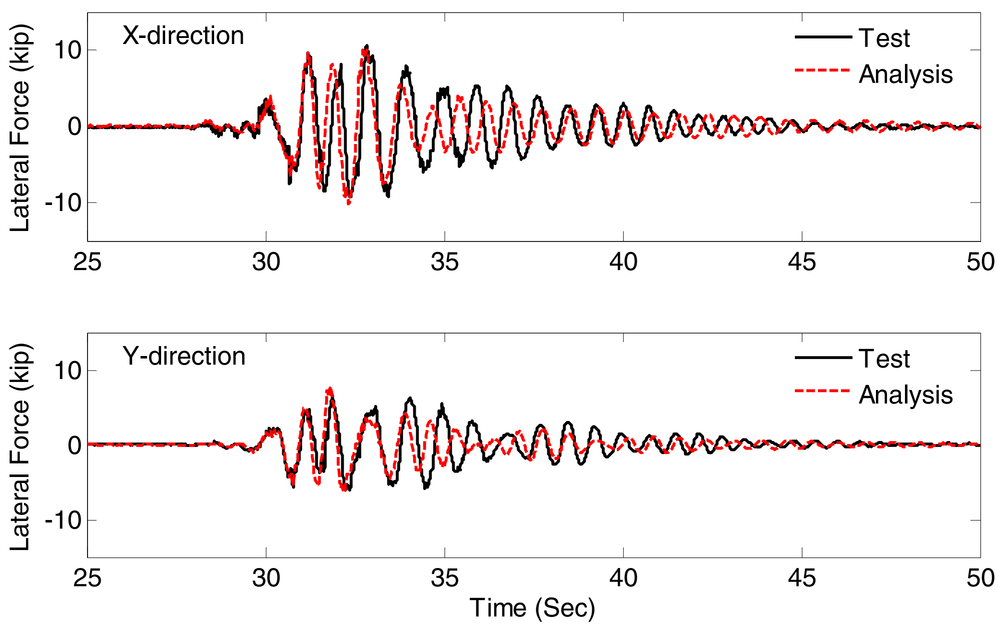

(b) Yield level

Fig. 5.29 Lateral force of PRC-U specimen based on recommended model

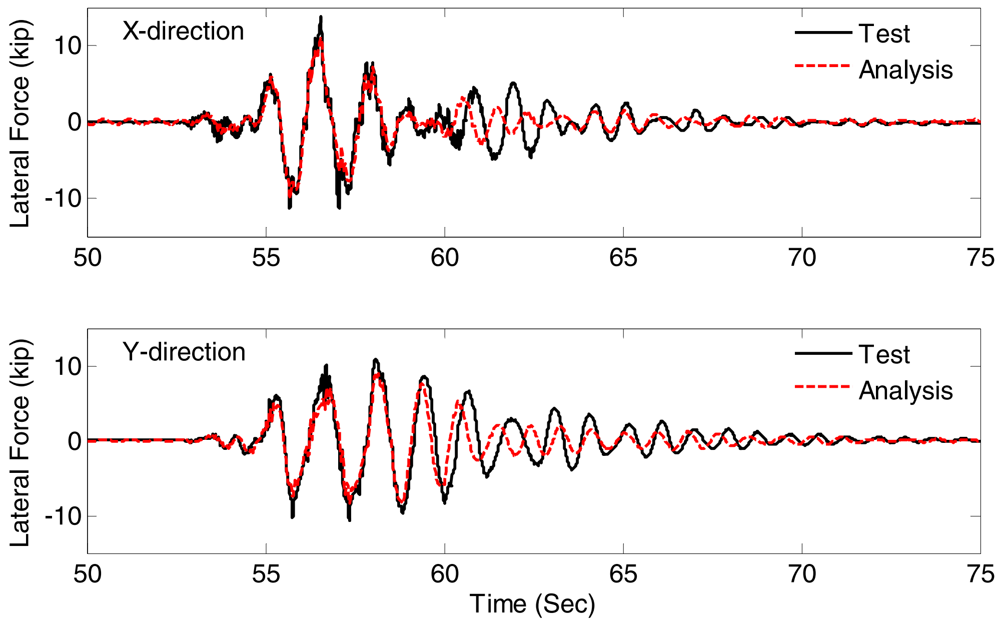

(c) Design level

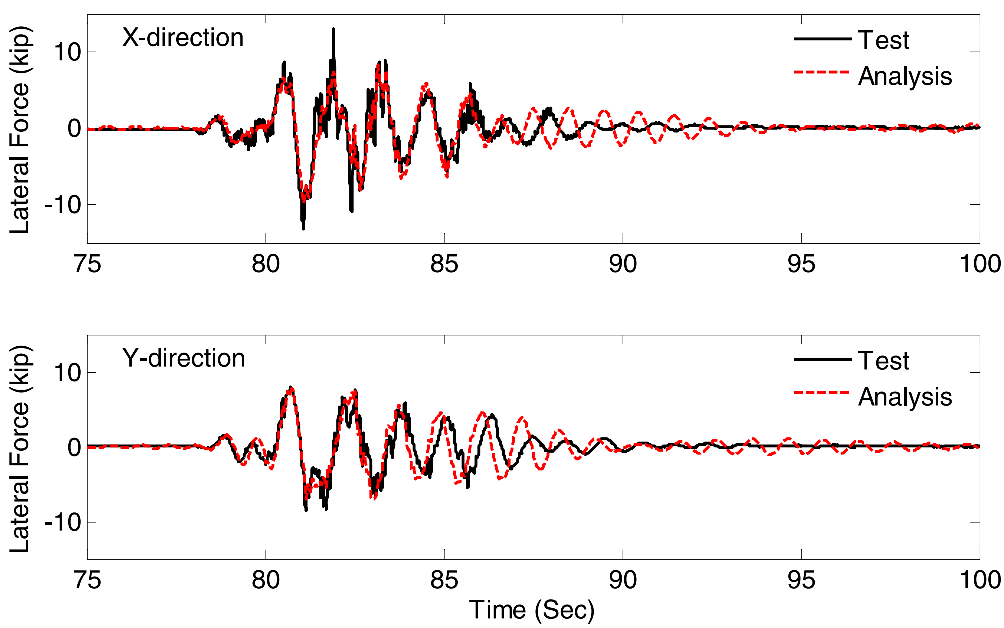

(d) Maximum level

Fig. 5.29—*Continued*

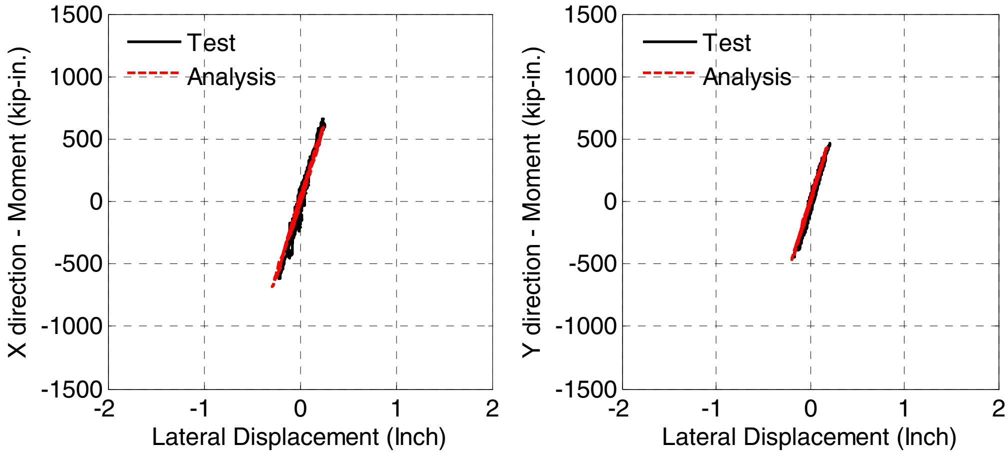

(a) Elastic level

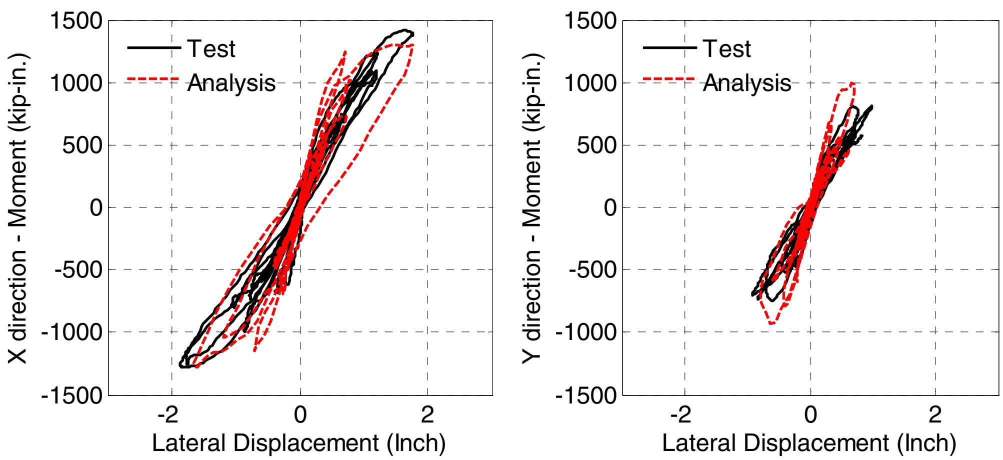

(b) Yield level

Fig. 5.30 Moment-displacement hysteresis of PRC-U specimen based on recommended model

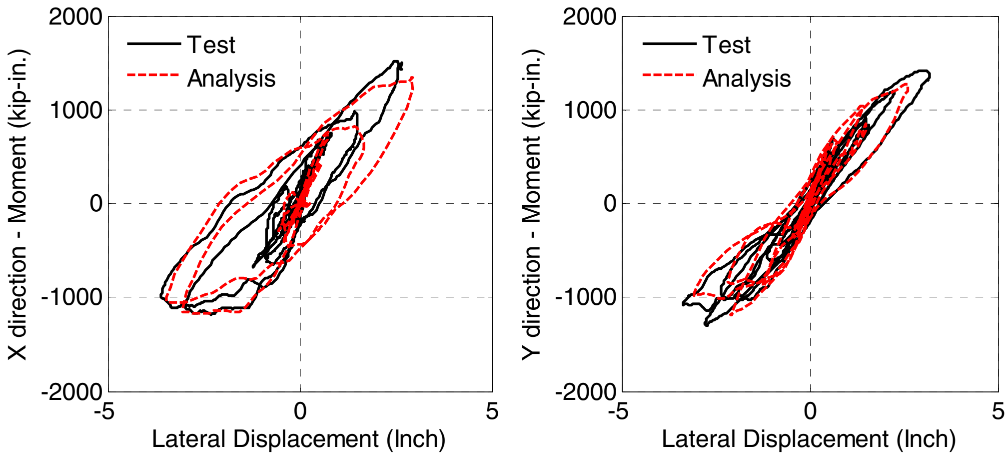

(c) Design level

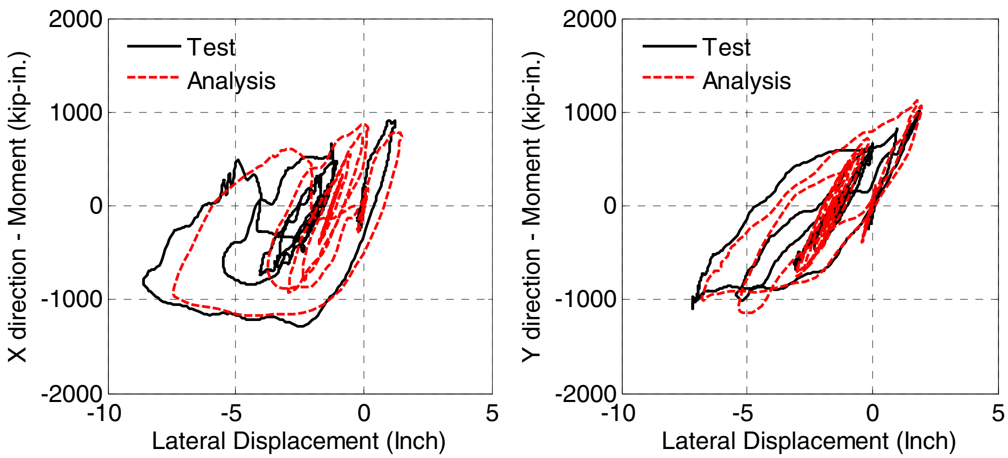

(d) Maximum level

Fig. 5.30—*Continued*

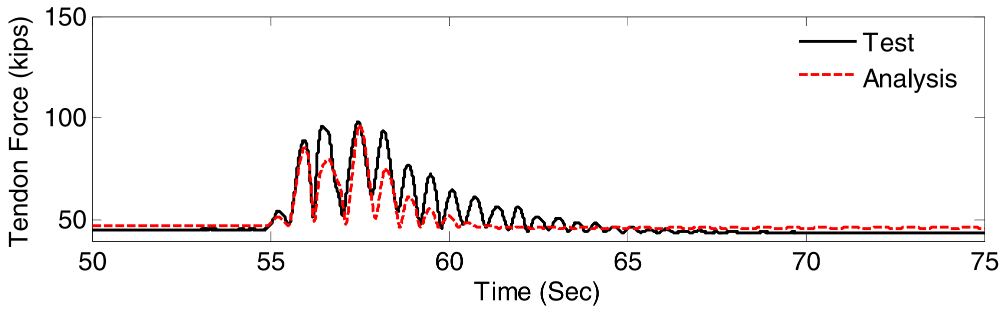

(a) Design level

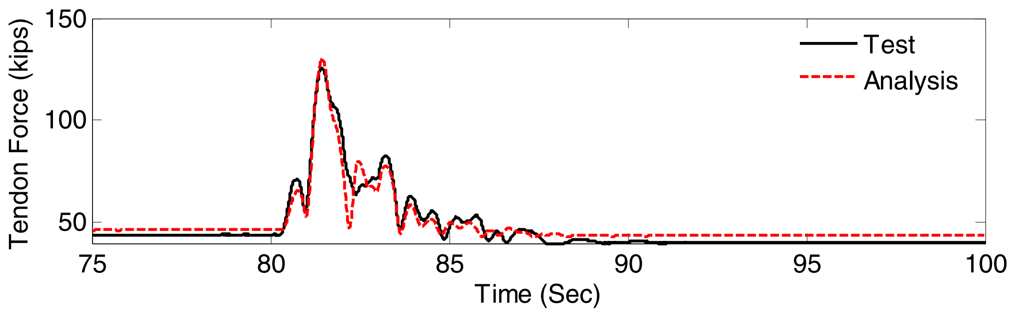

(b) Maximum level

Fig. 5.31 Prestressing force of PRC-U specimen based on recommended model

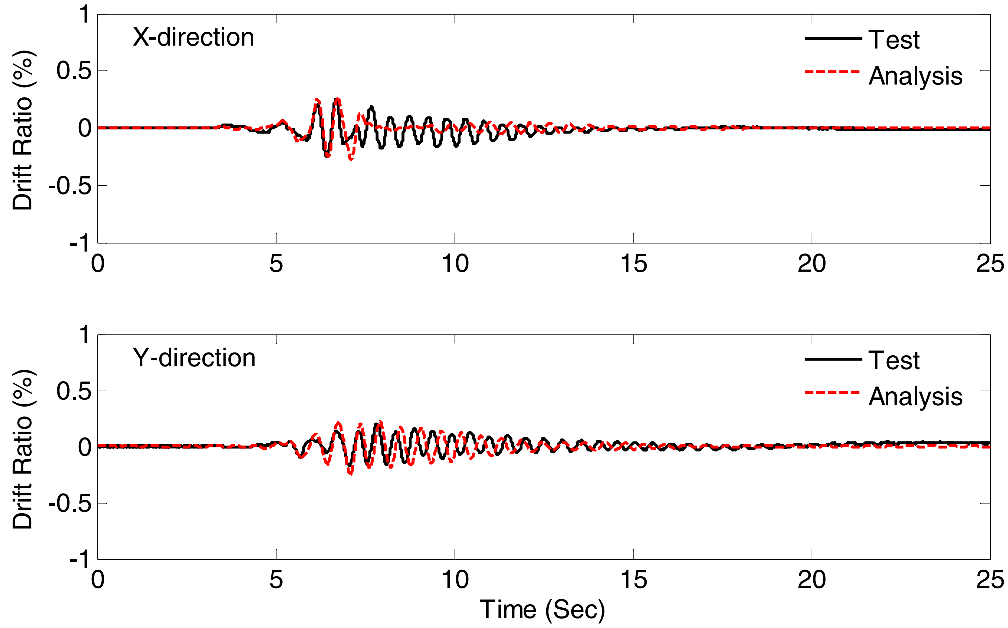

(a) Elastic level

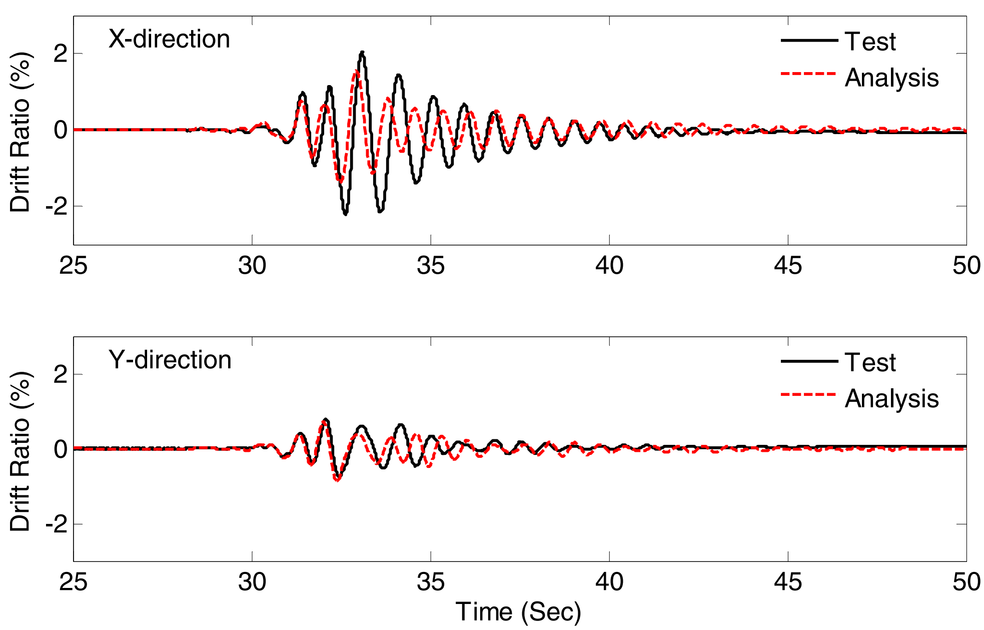

(b) Yield level

Fig. 5.32 Displacement of PRC-U2 specimen based on recommended model

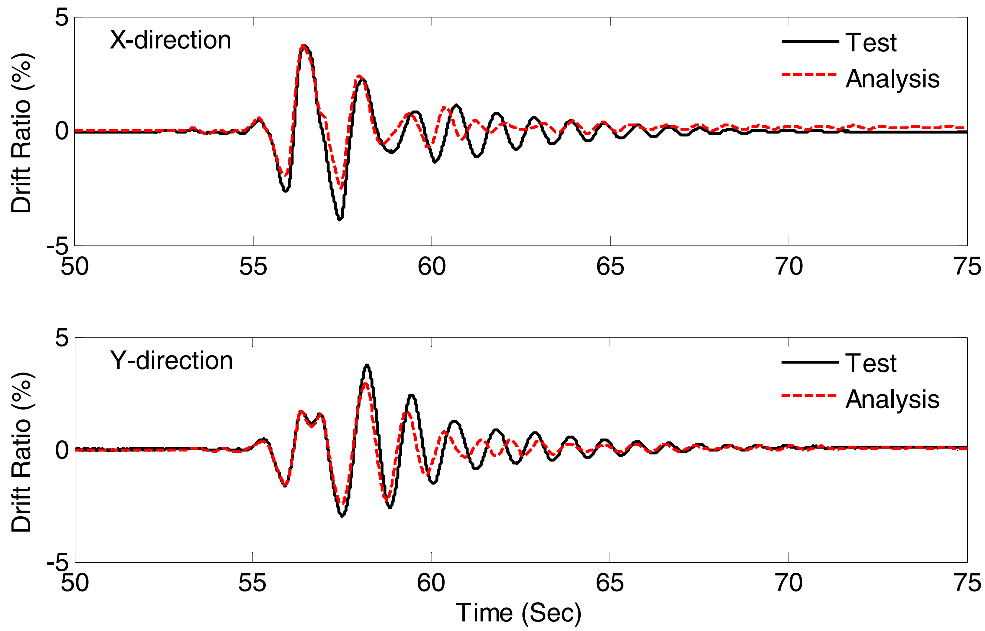

(c) Design level

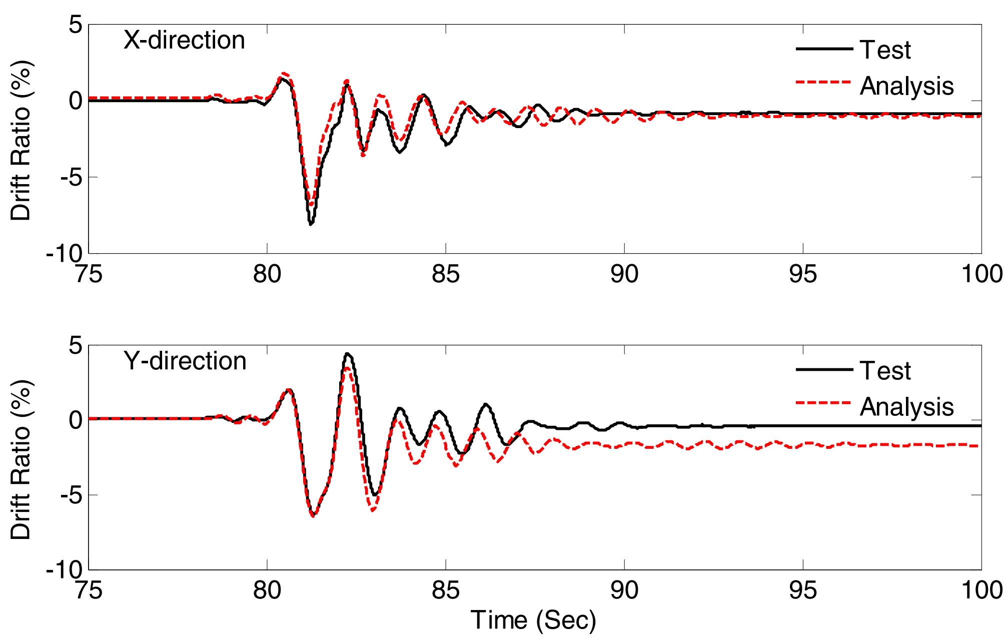

(d) Maximum level

Fig. 5.32—*Continued*

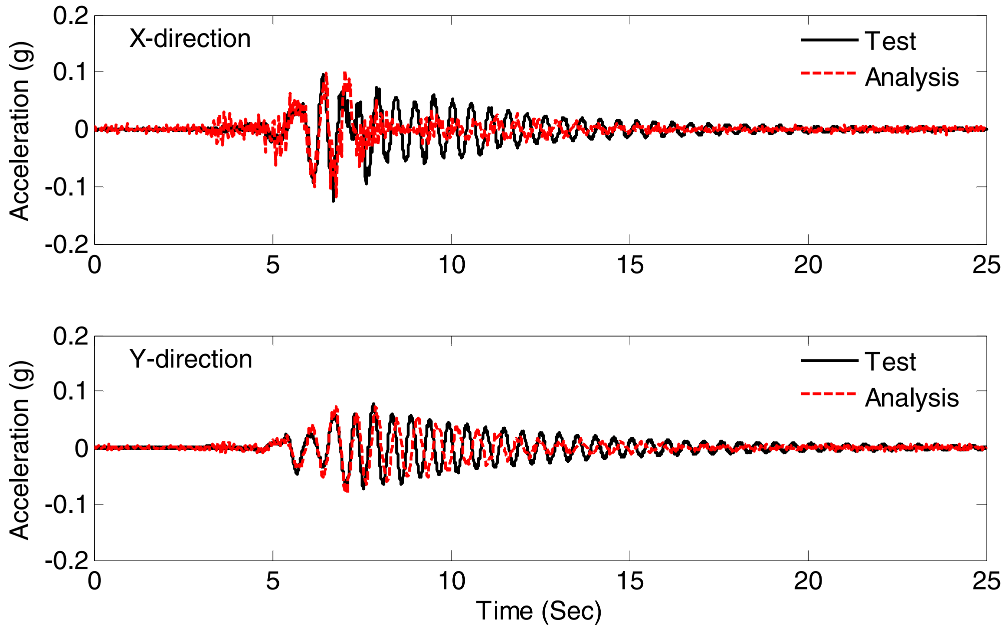

(a) Elastic level

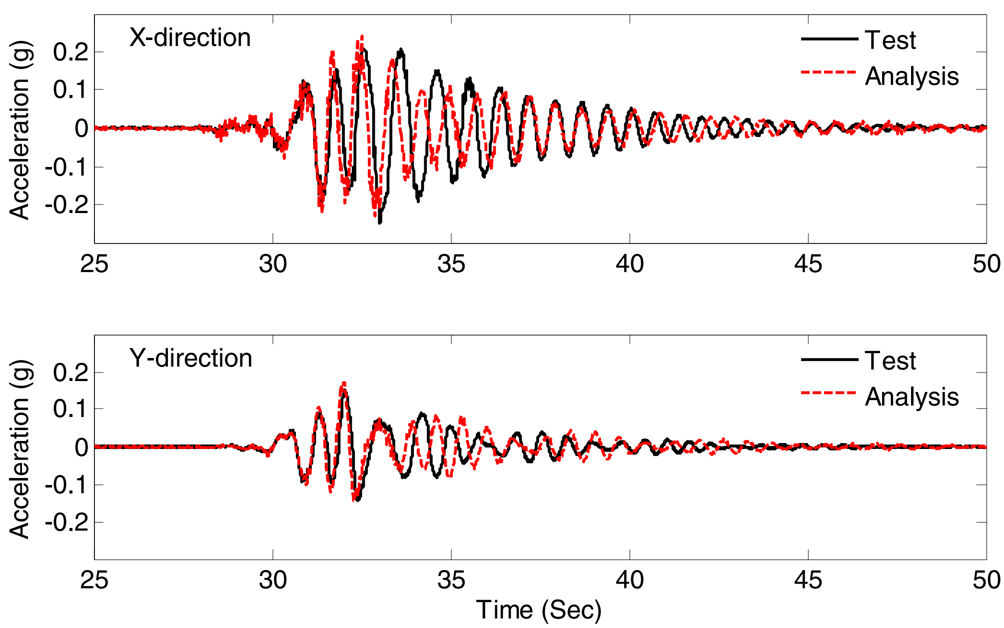

(b) Yield level

Fig. 5.33 Acceleration of PRC-U2 specimen based on recommended model

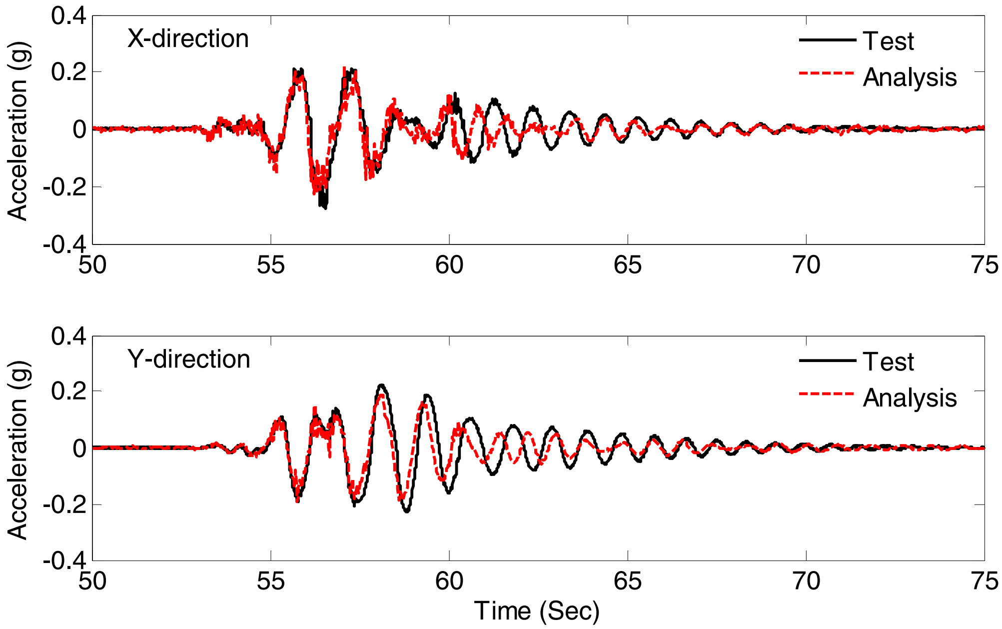

(c) Design level

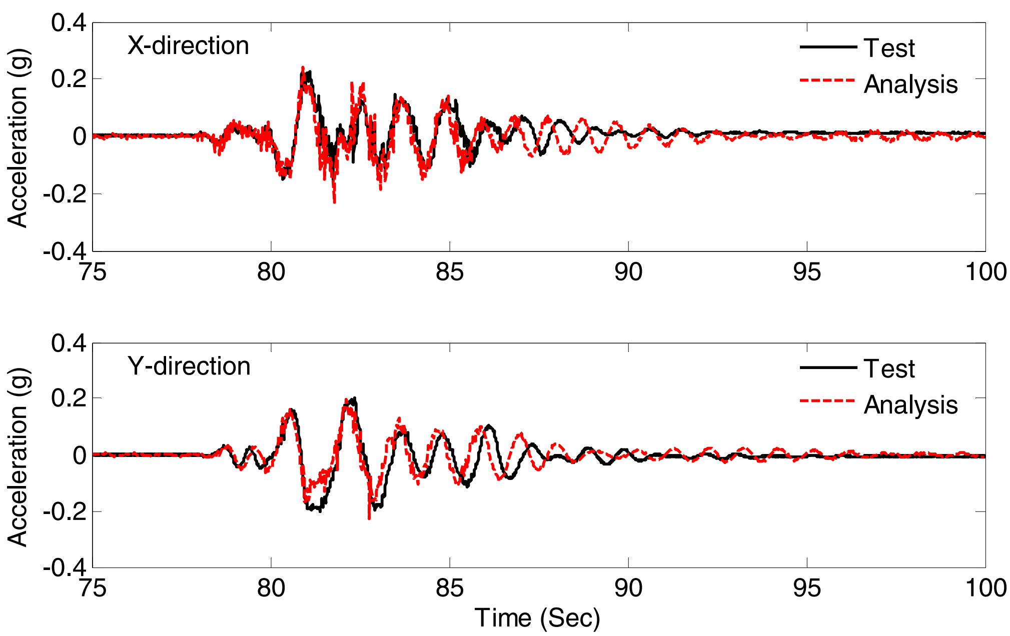

(d) Maximum level

Fig. 5.33—*Continued*

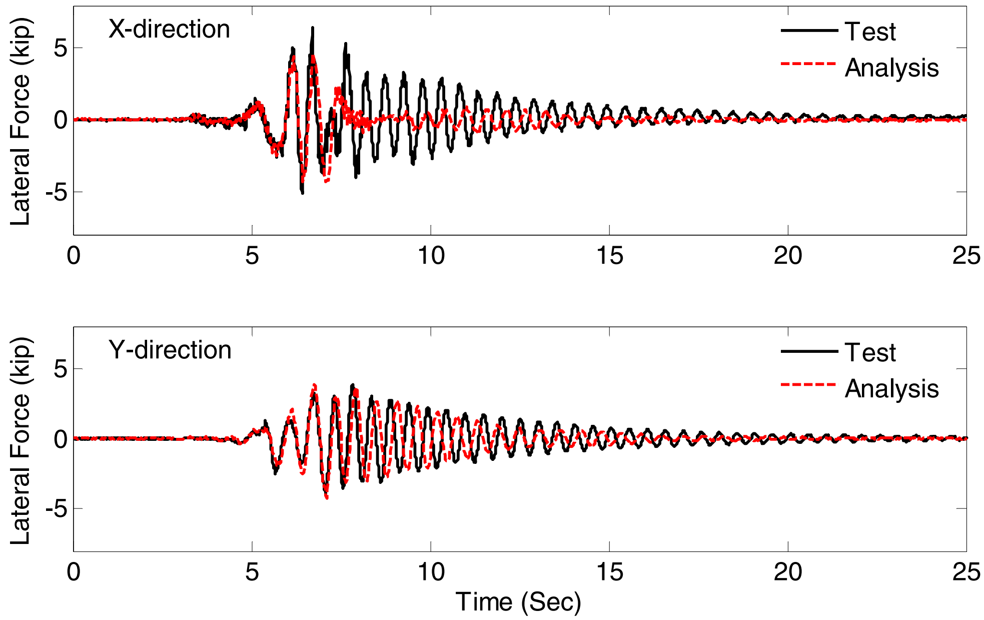

(a) Elastic level

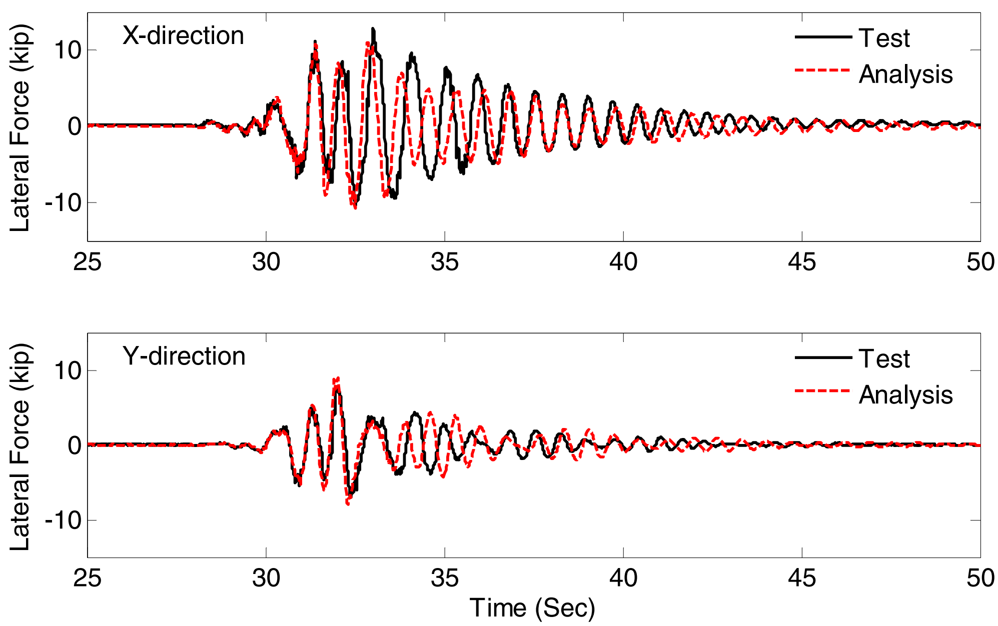

(b) Yield level

Fig. 5.34 Lateral force of PRC-U2 specimen based on recommended model

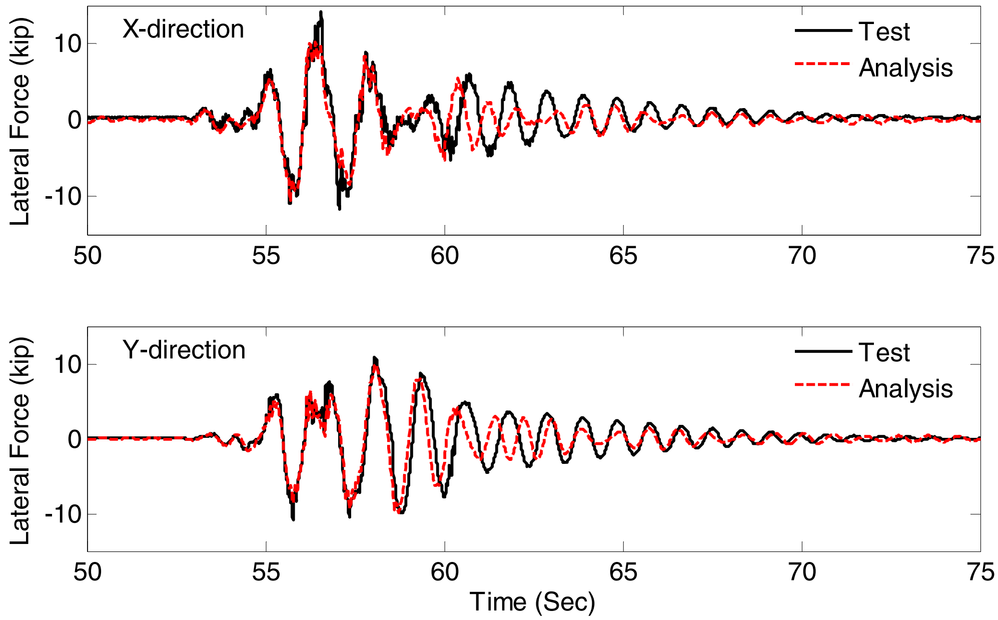

(c) Design level

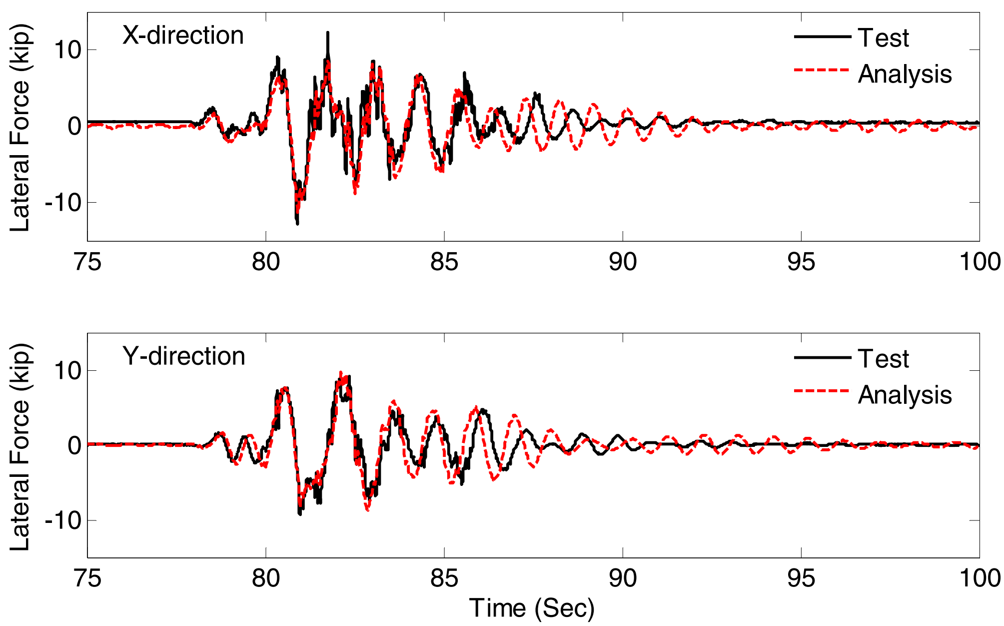

(d) Maximum level

Fig. 5.34—*Continued.*

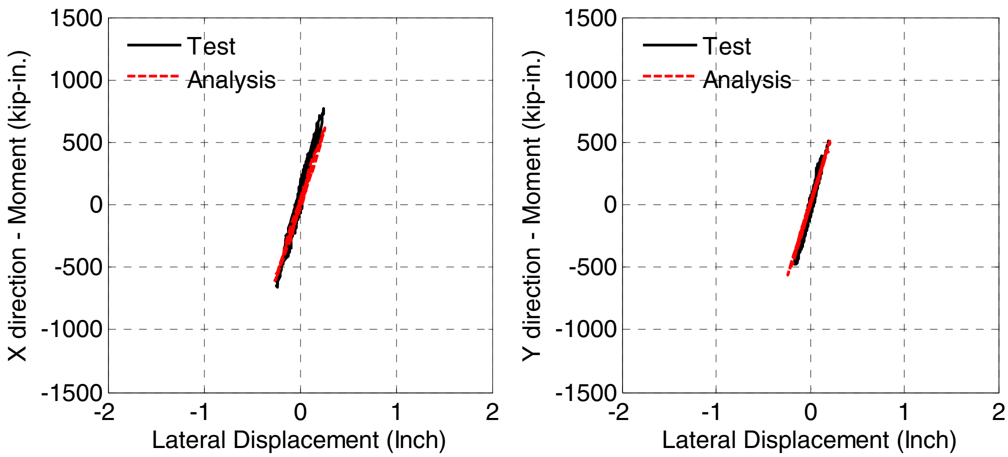

(a) Elastic level

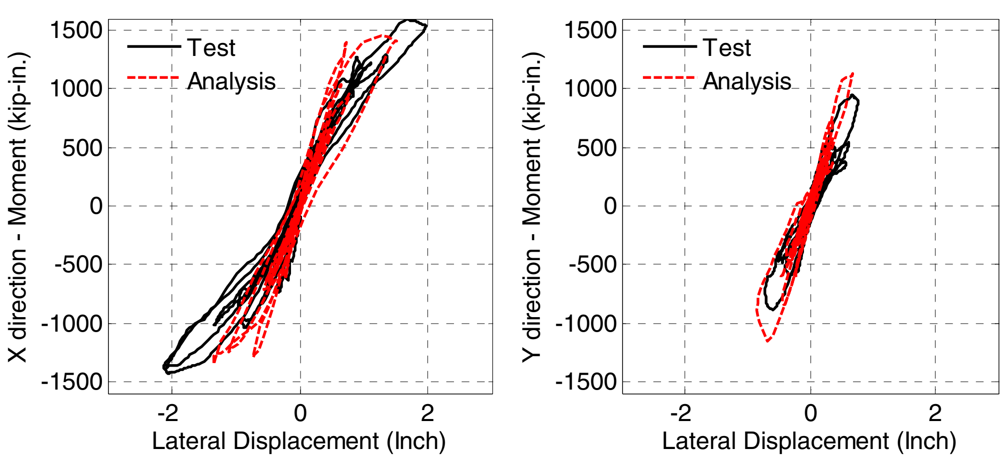

(b) Yield level

Fig. 5.35 Moment-displacement hysteresis of PRC-U2 specimen based on recommended model

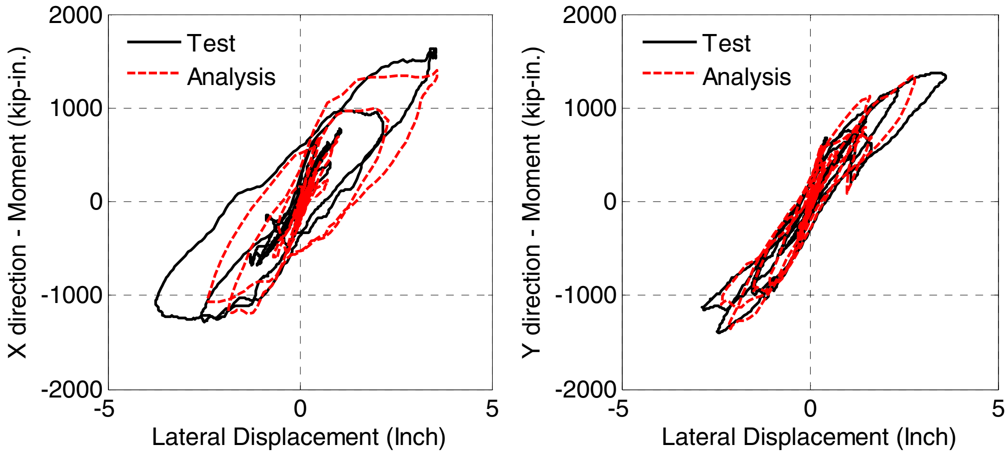

(c) Design level

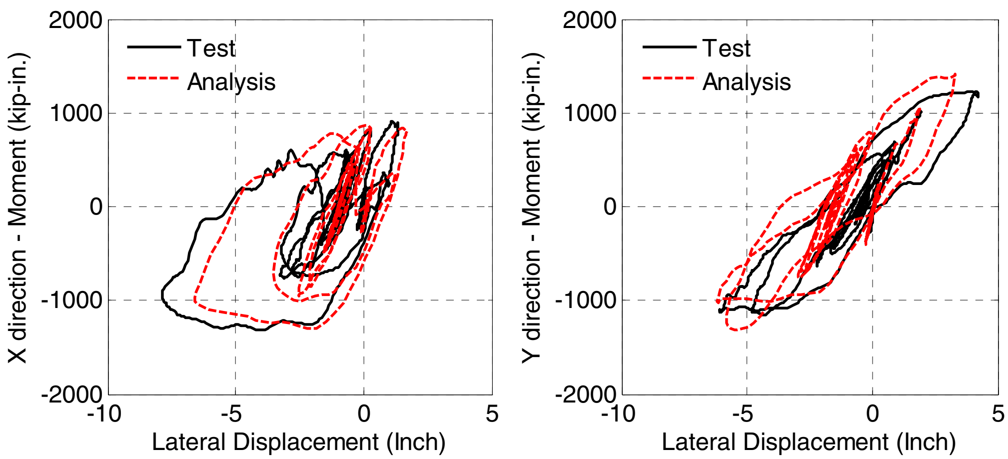

(d) Maximum level

Fig. 5.35—*Continued.*

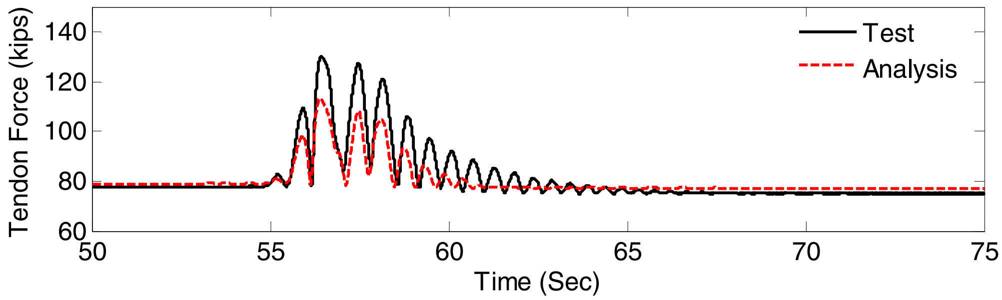

(a) Design level

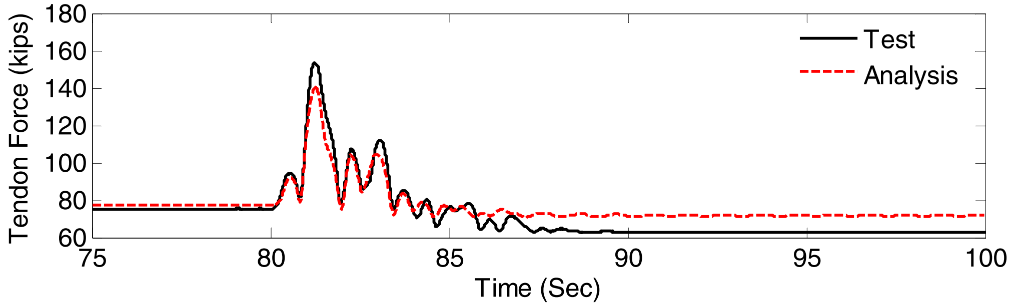

(b) Maximum level

Fig. 5.36 Prestressing force of PRC-U2 specimen based on recommended model

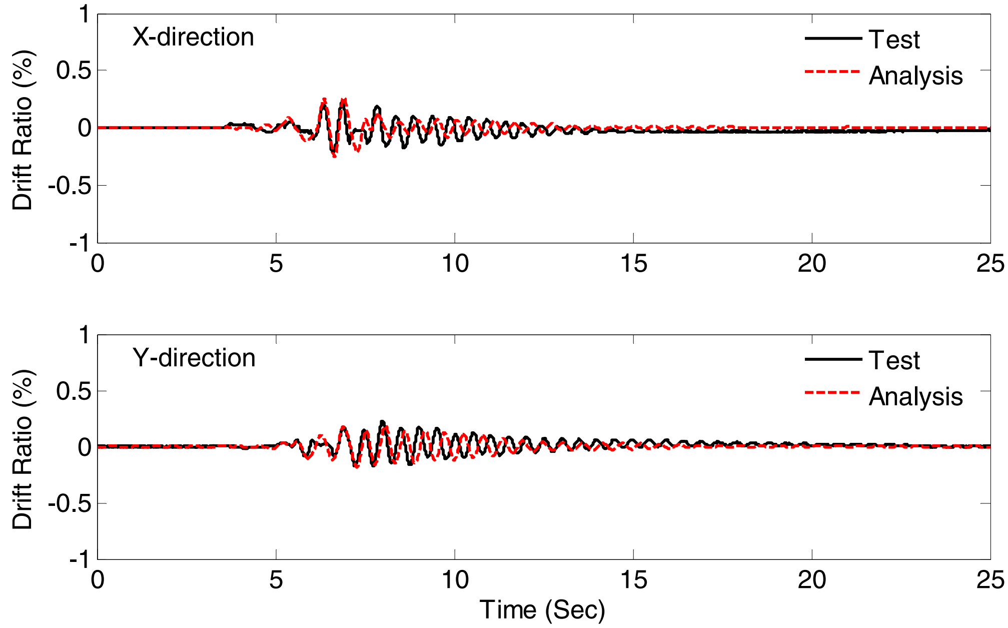

(a) Elastic level

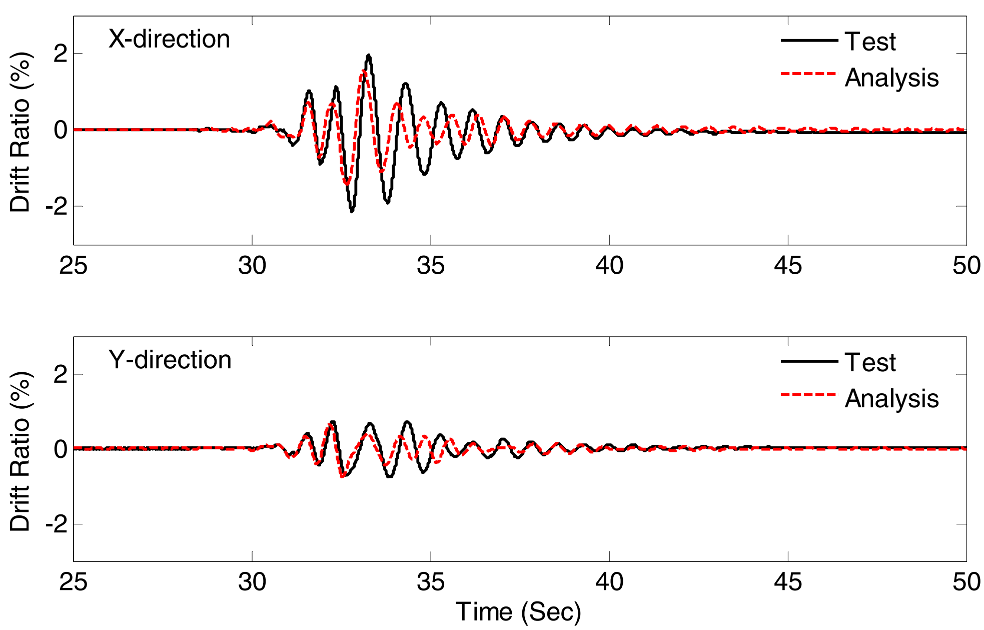

(b) Yield level

Fig. 5.37 Displacement of PRC-UJ specimen based on recommended model

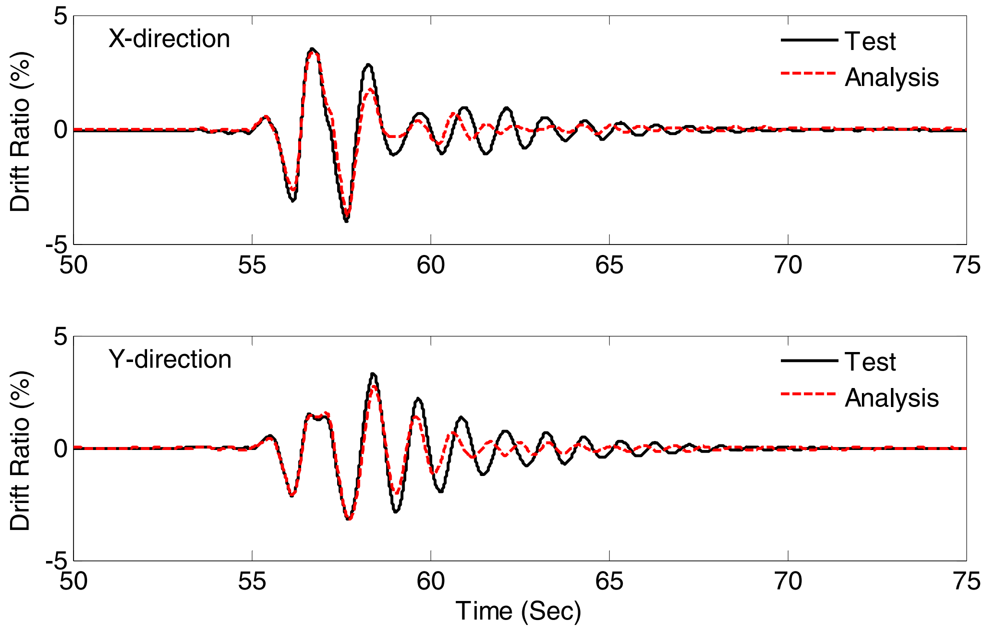

(c) Design level

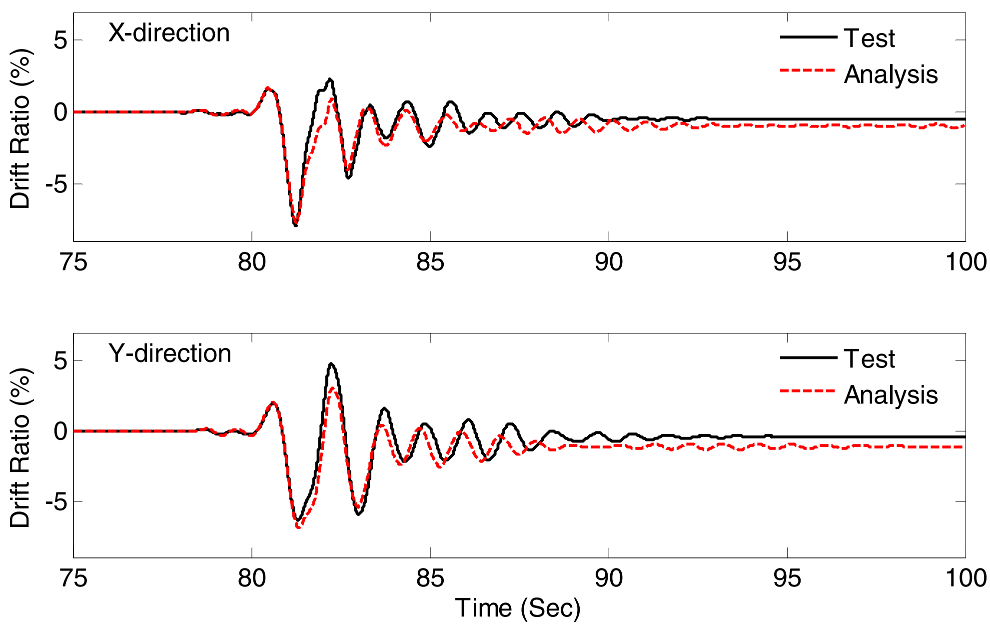

(d) Maximum level

Fig. 5.37—*Continued.*

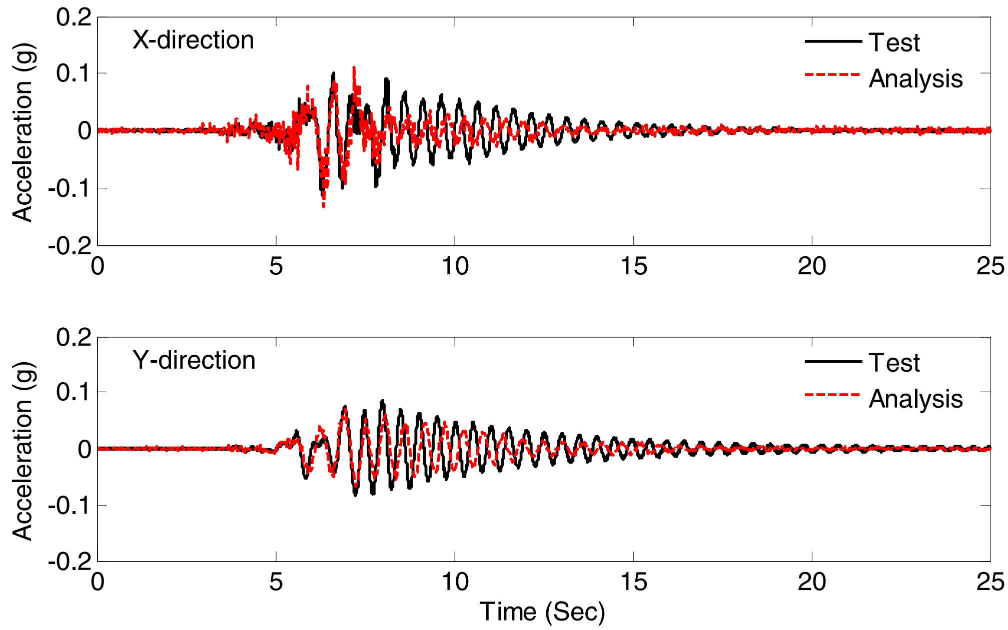

(a) Elastic level

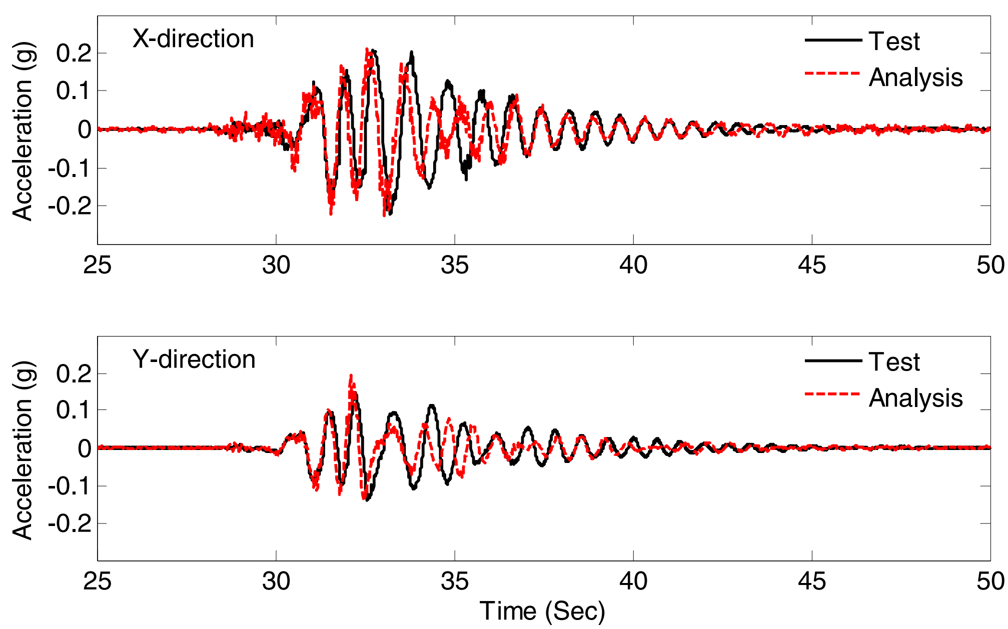

(b) Yield level

Fig. 5.38 Acceleration of PRC-UJ specimen based on recommended model

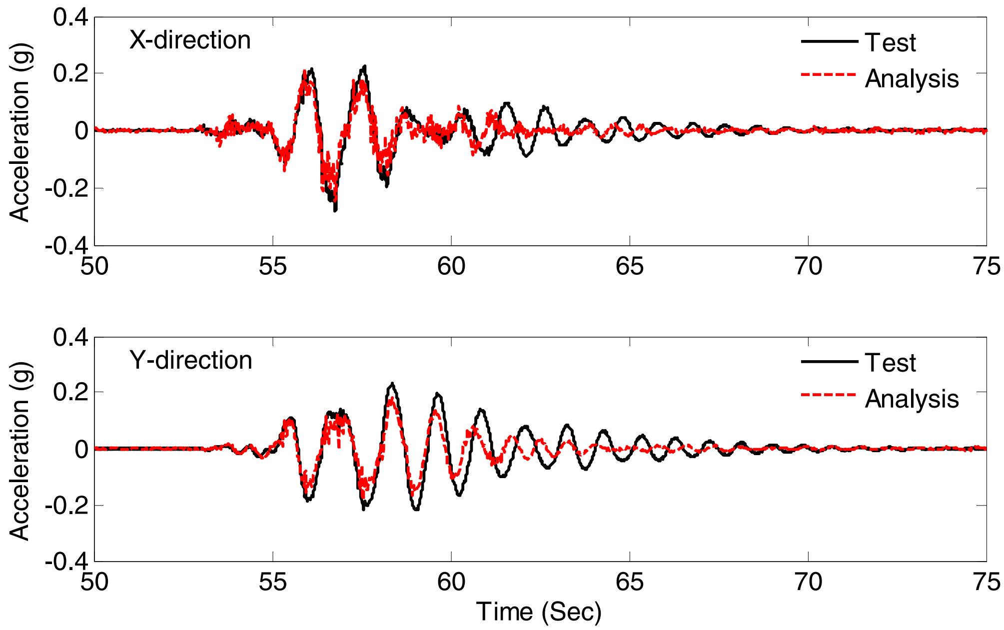

(c) Design level

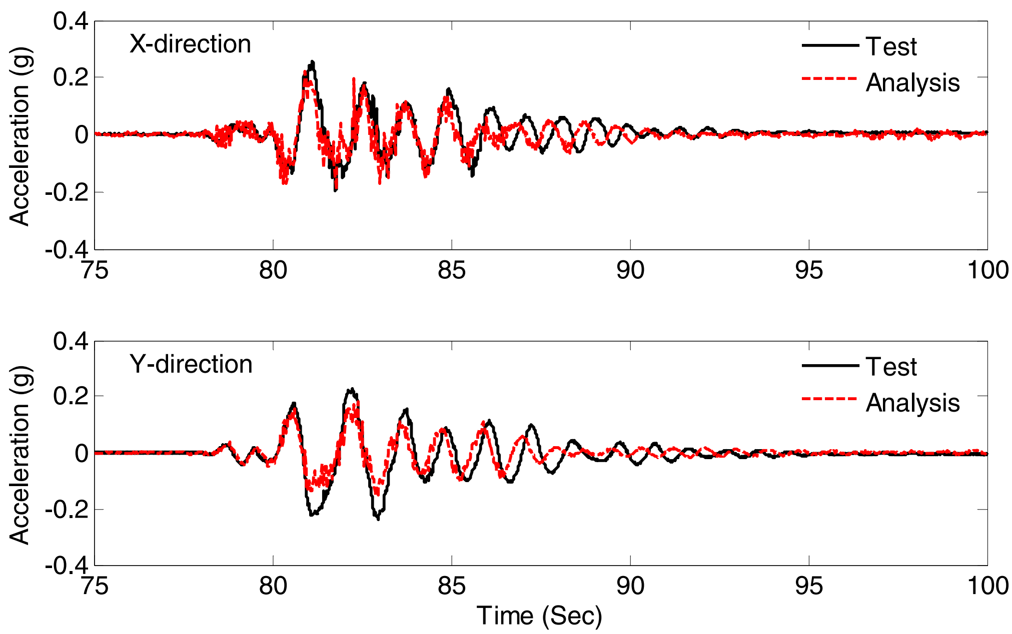

(d) Maximum level

Fig. 5.38—*Continued.*

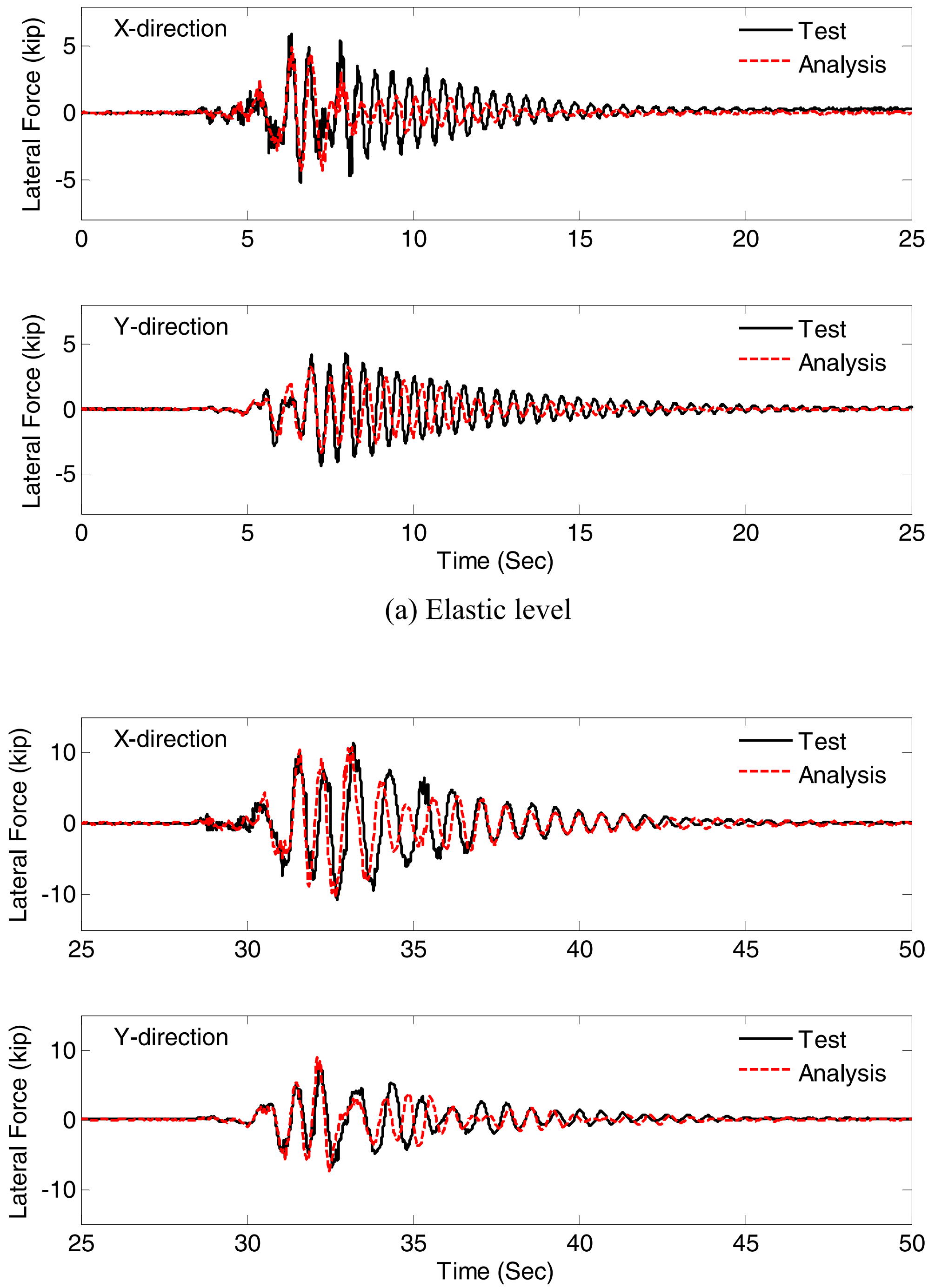

(a) Elastic level

(b) Yield level

Fig. 5.39 Lateral force of PRC-UJ specimen based on recommended model

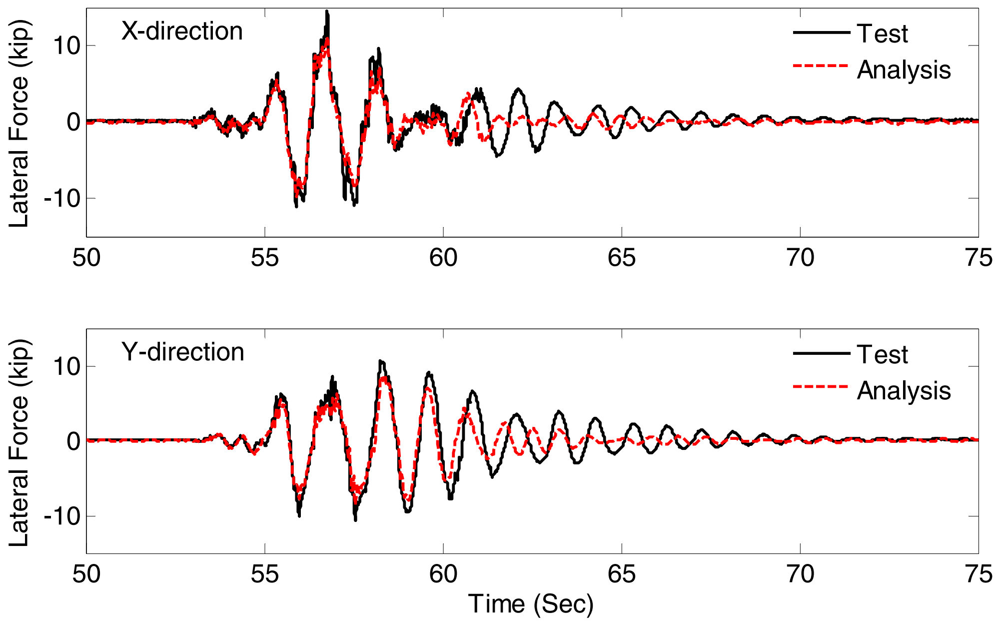

(c) Design level

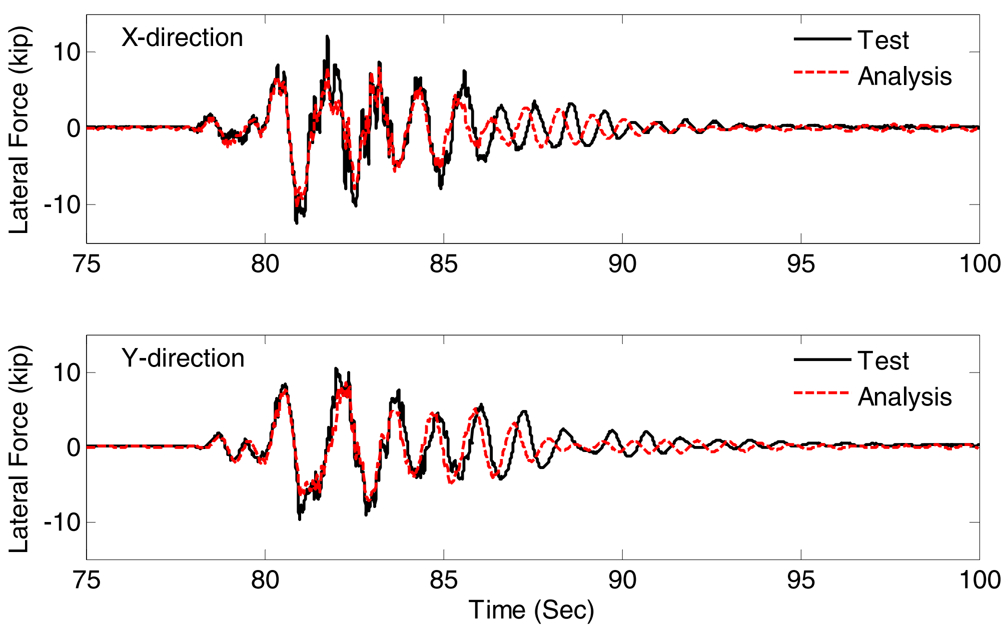

(d) Maximum level

Fig. 5.39—*Continued*

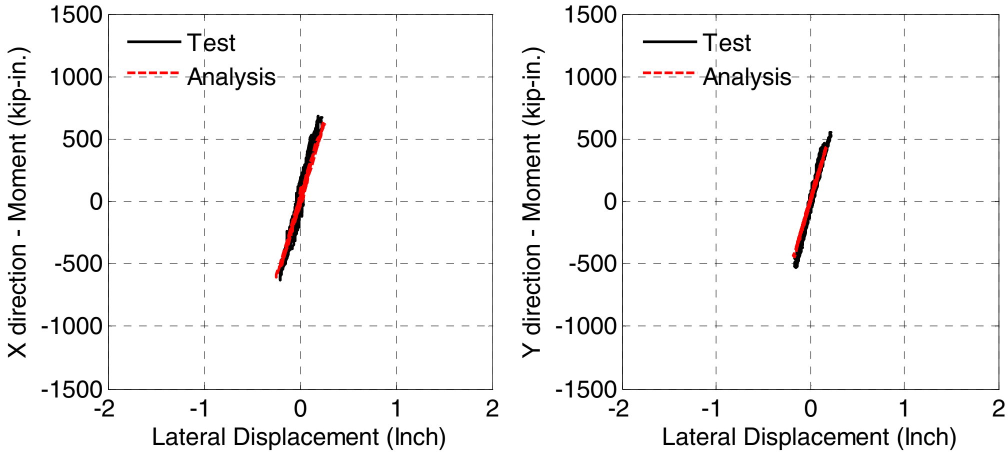

(a) Elastic level

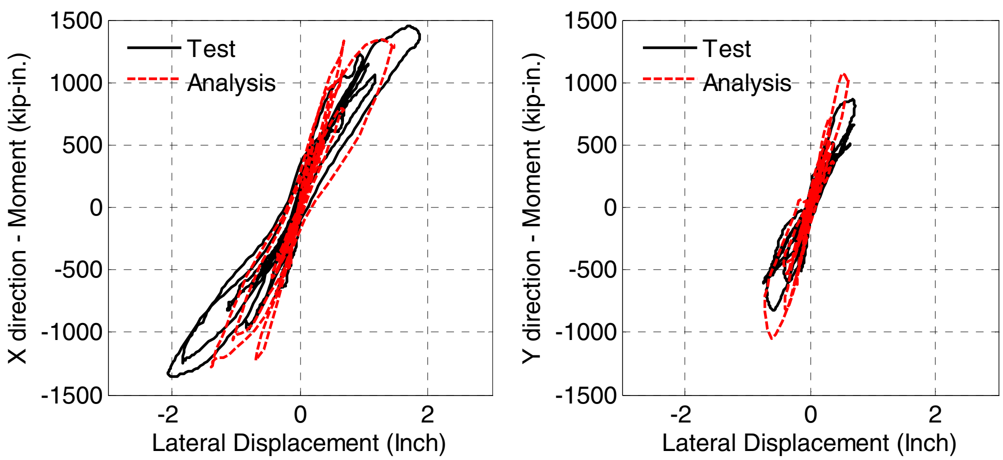

(b) Yield level

Fig. 5.40 Moment-displacement hysteresis of PRC-UJ specimen based on recommended model

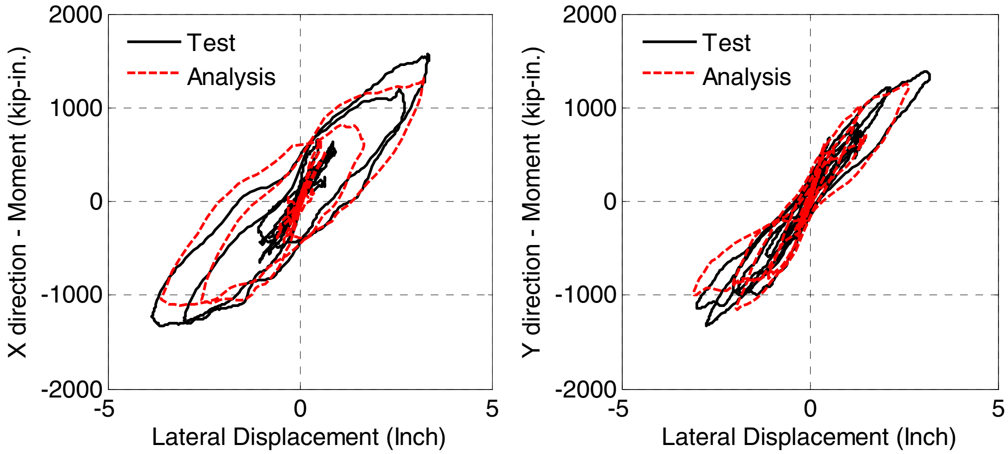

(c) Design level

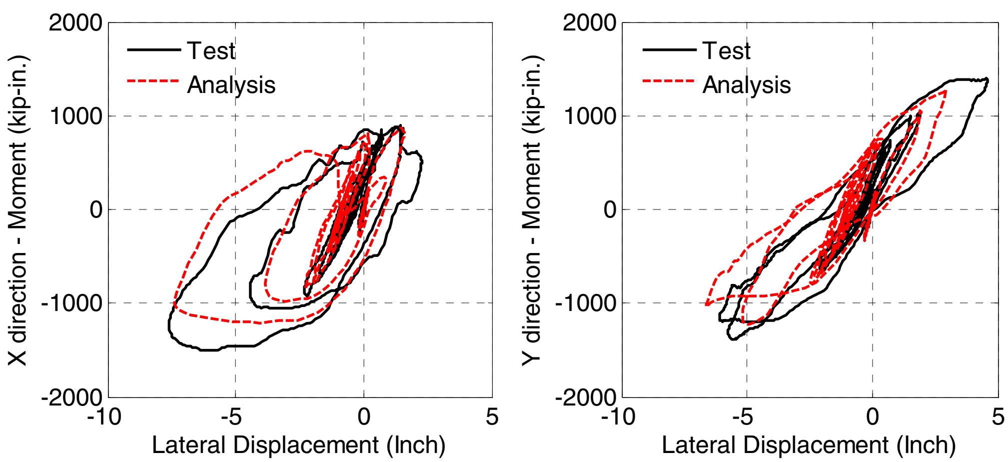

(d) Maximum level

Fig. 5.40—*Continued*

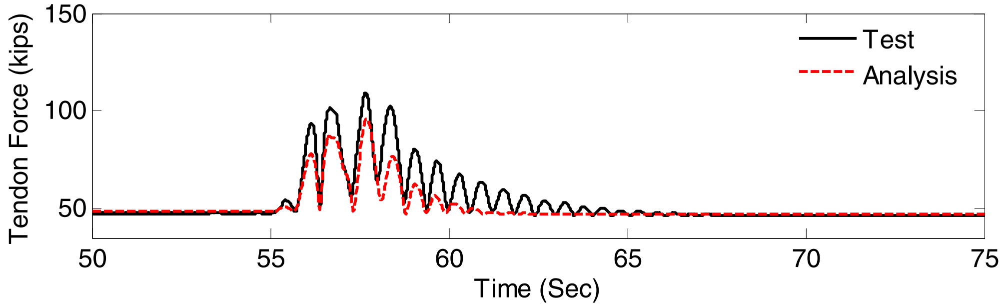

(a) Design level

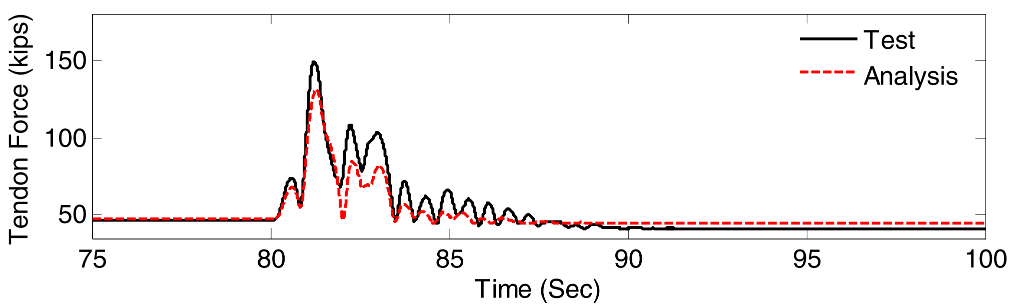

(b) Maximum level

Fig. 5.41 Prestressing force of PRC-UJ specimen based on recommended model

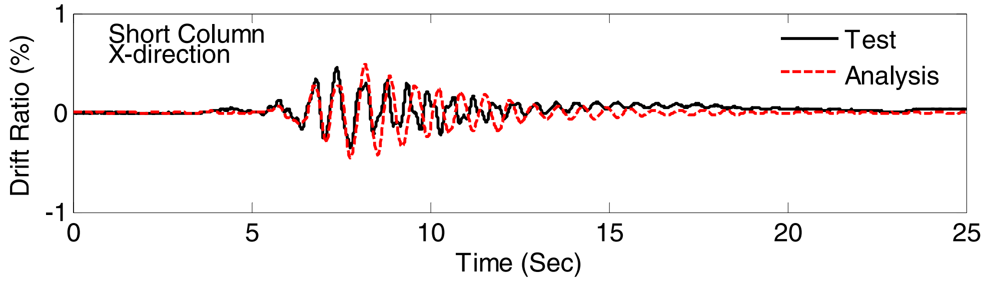

(a) Elastic level

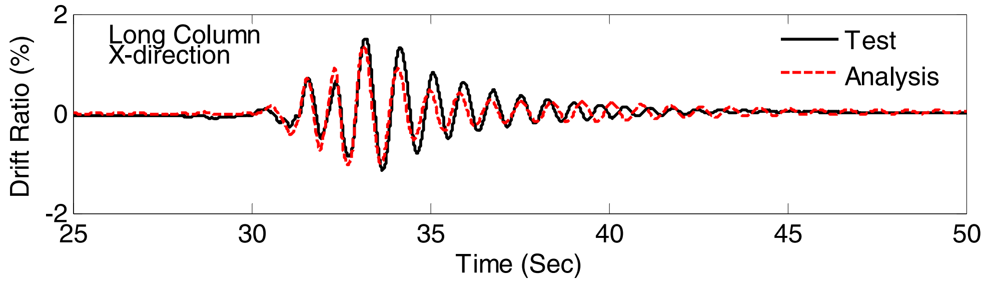

(b) Yield level

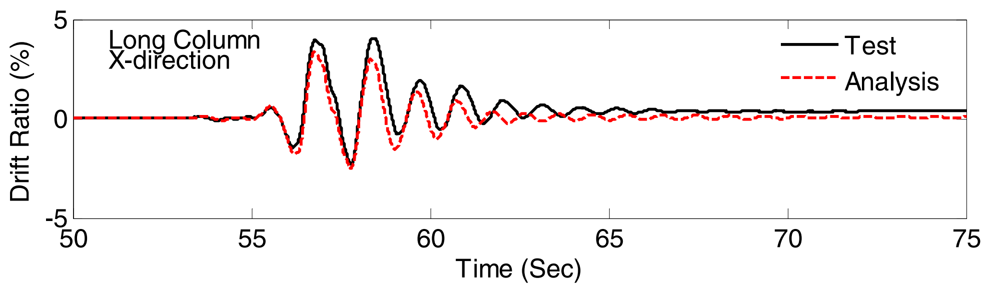

(c) Design level

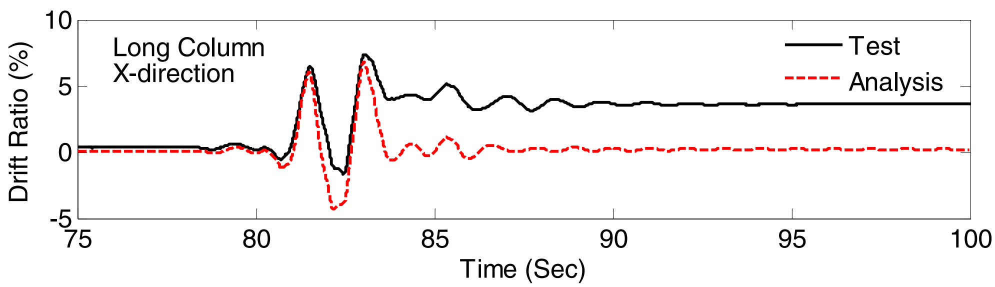

(d) Maximum level

Fig. 5.42 Displacement of PRC-system specimen based on recommended model (long column, *x* direction)

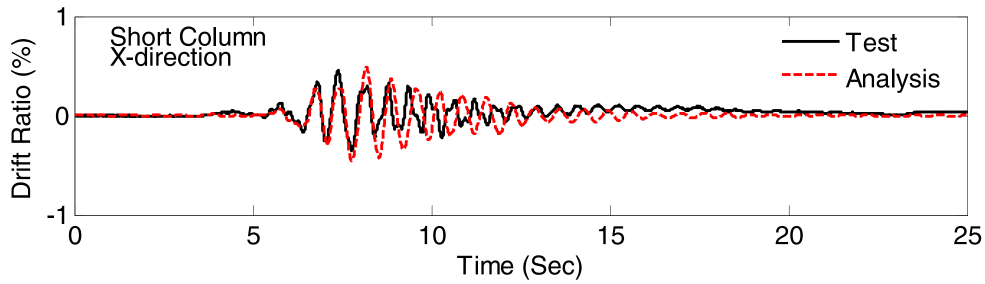

(a) Elastic level

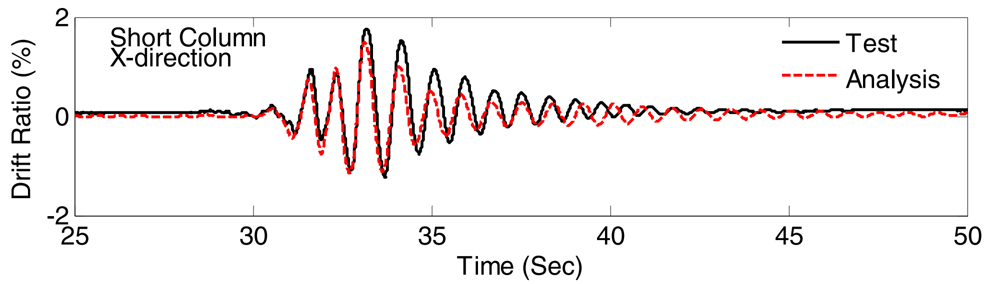

(b) Yield level

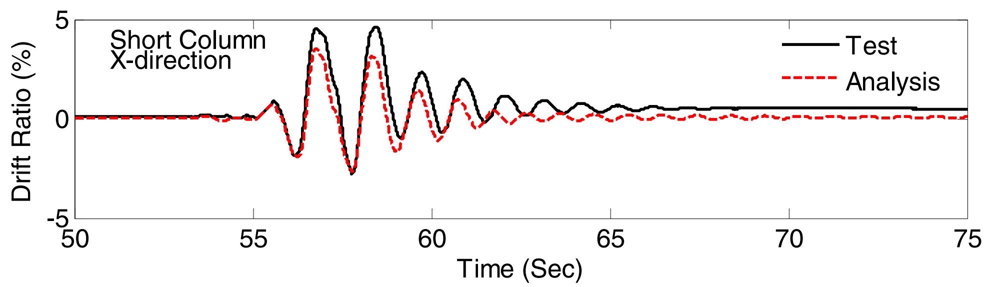

(c) Design level

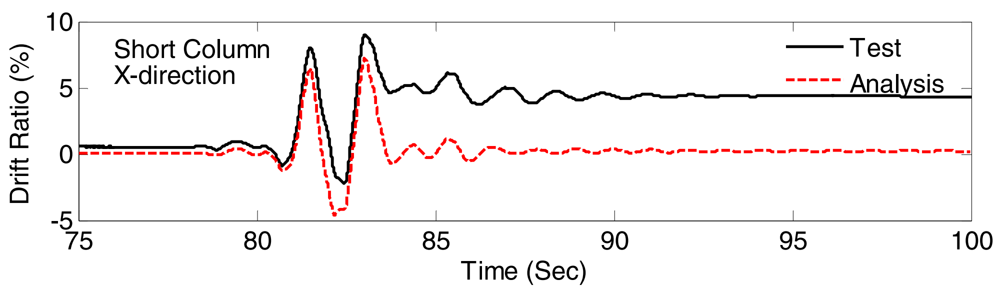

(d) Maximum level

Fig. 5.43 Displacement of PRC-system specimen based on recommended model (short column, *x* direction)

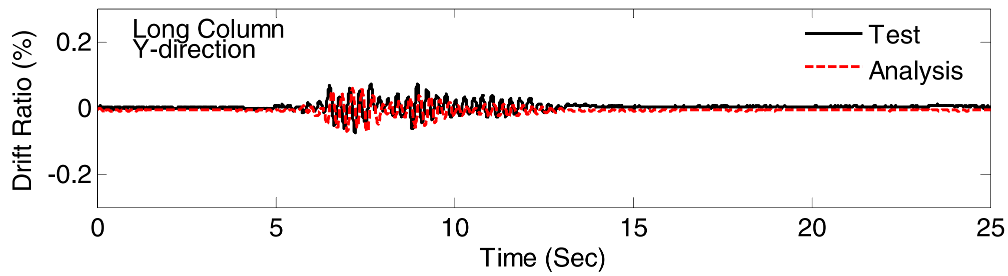

(a) Elastic level

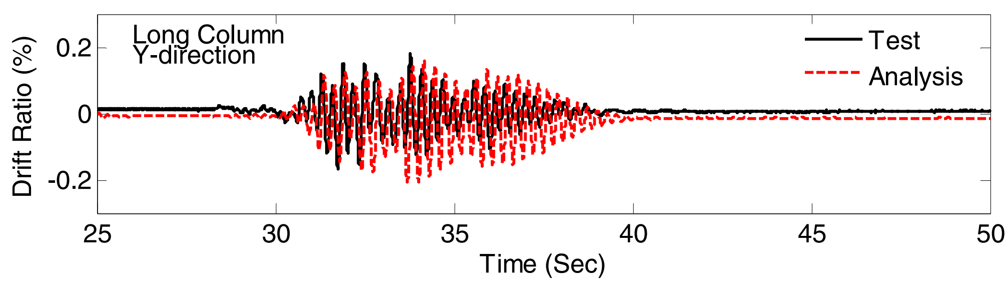

(b) Yield level

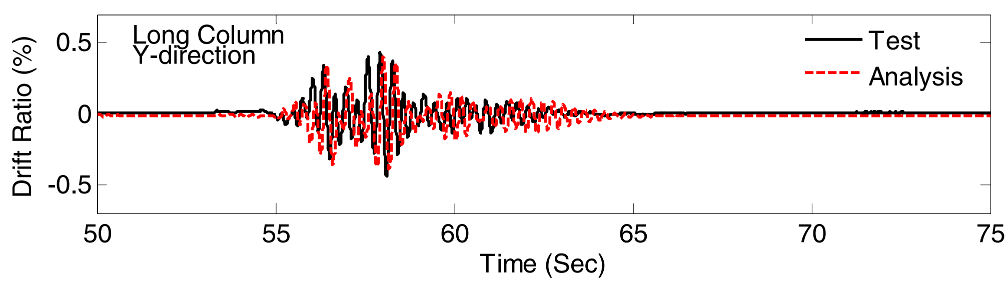

(c) Design level

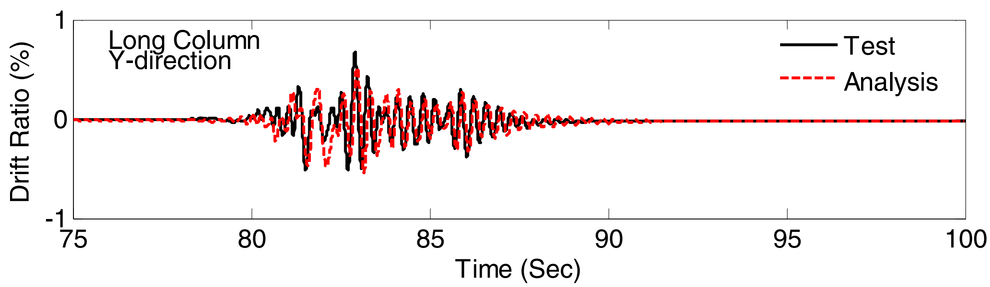

(d) Maximum level

Fig. 5.44 Displacement of PRC-system specimen based on recommended model (long column, *y* direction)

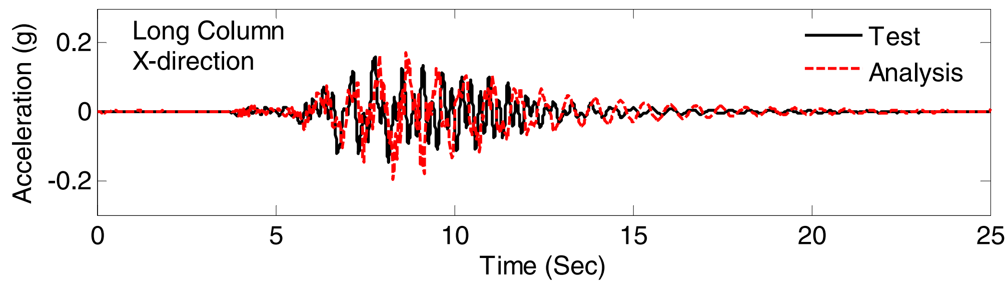

(a) Elastic level

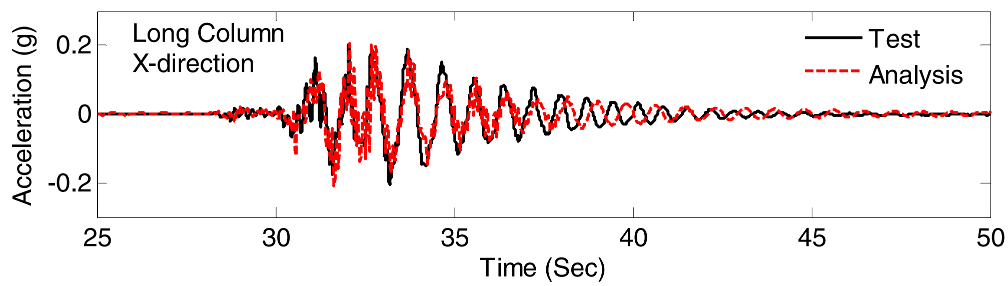

(b) Yield level

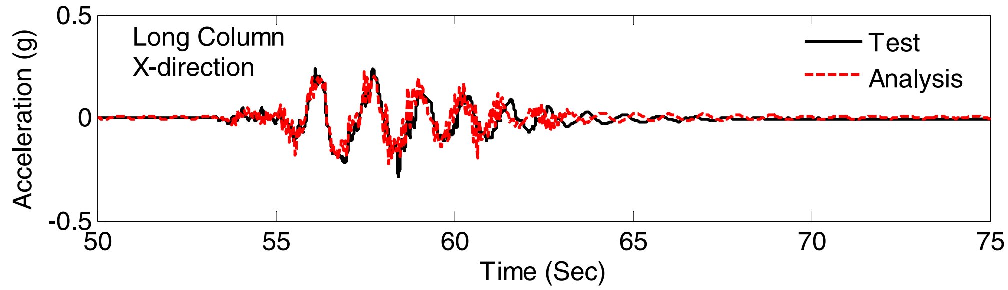

(c) Design level

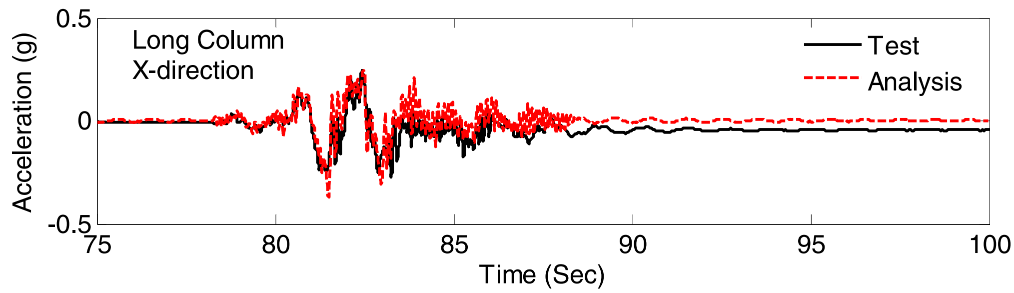

(d) Maximum level

Fig. 5.45 Acceleration of PRC-system specimen based on recommended model (long column, *x* direction)

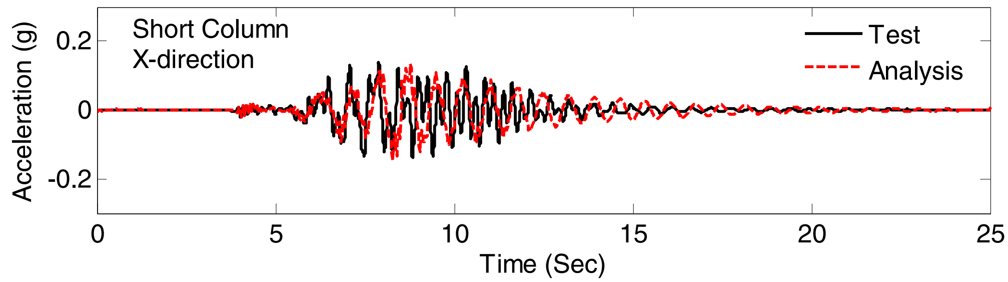

(a) Elastic level

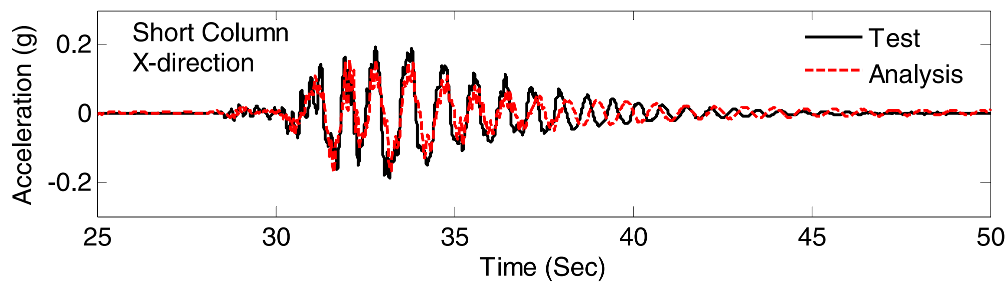

(b) Yield level

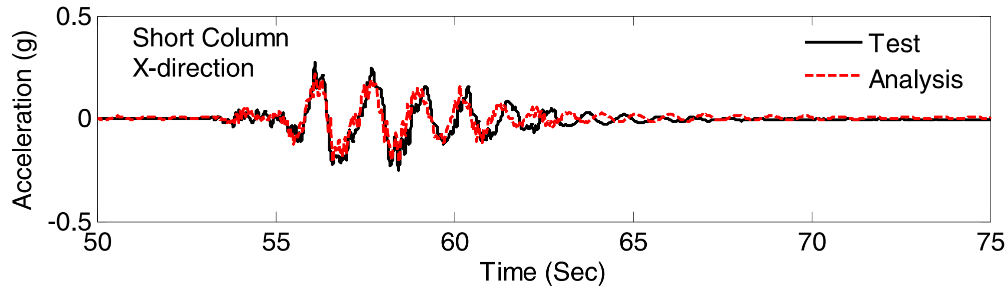

(c) Design level

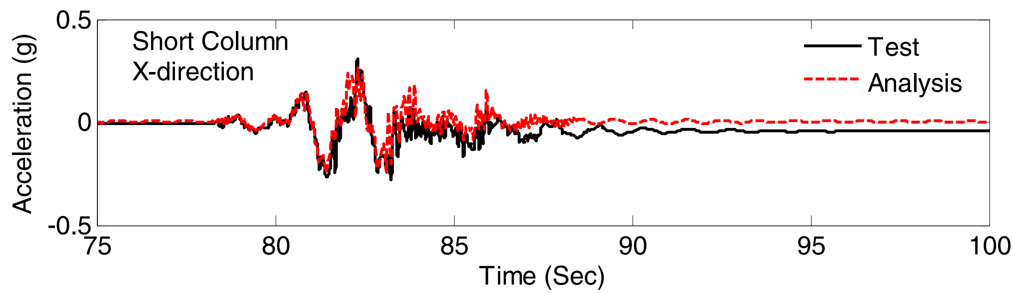

(d) Maximum level

Fig. 5.46 Acceleration of PRC-system specimen based on recommended model (short column, *x* direction)

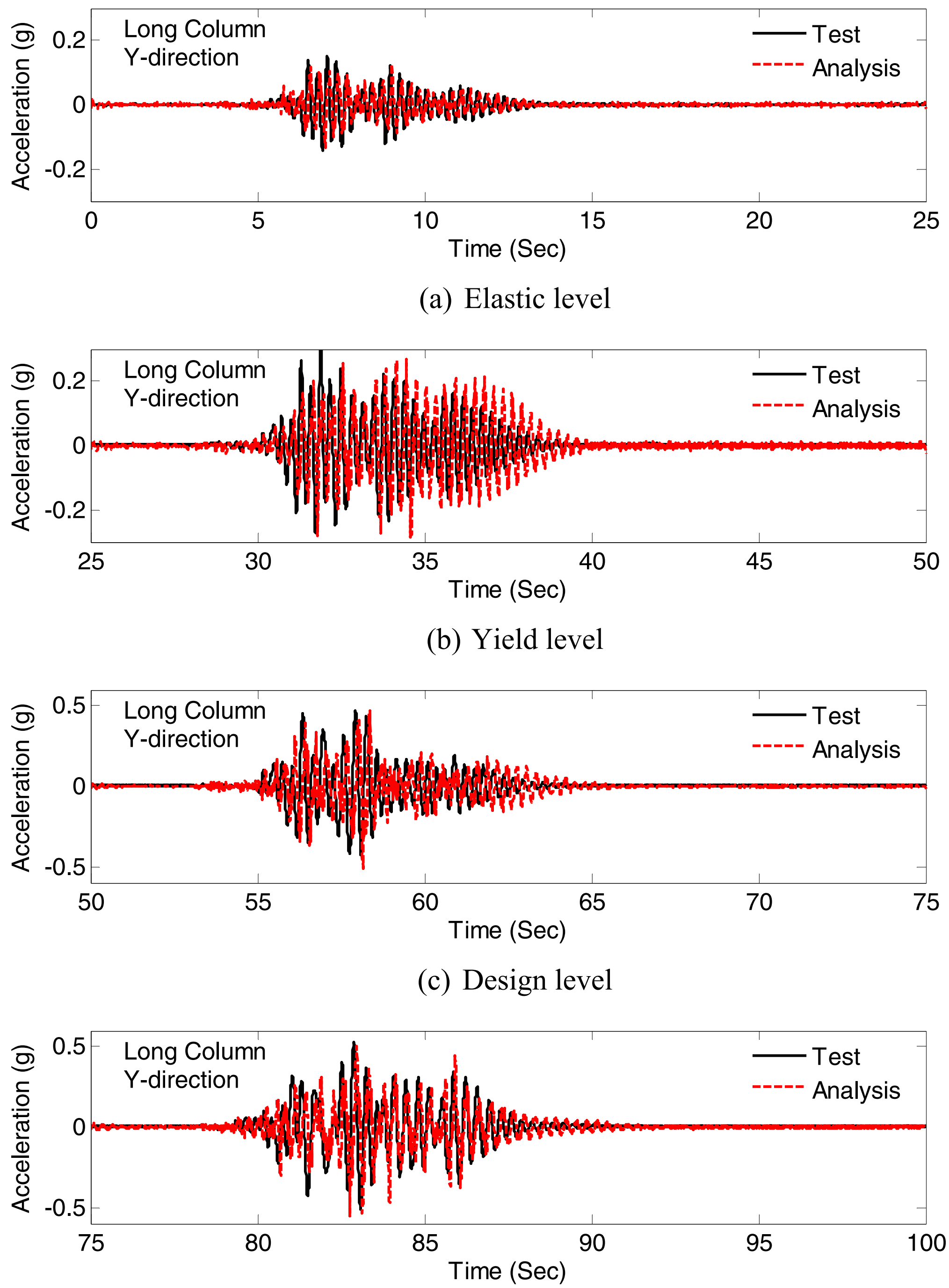

(a) Elastic level

(b) Yield level

(c) Design level

(d) Maximum level

Fig. 5.47 Acceleration of PRC-system specimen based on recommended model (long column, *y* direction)

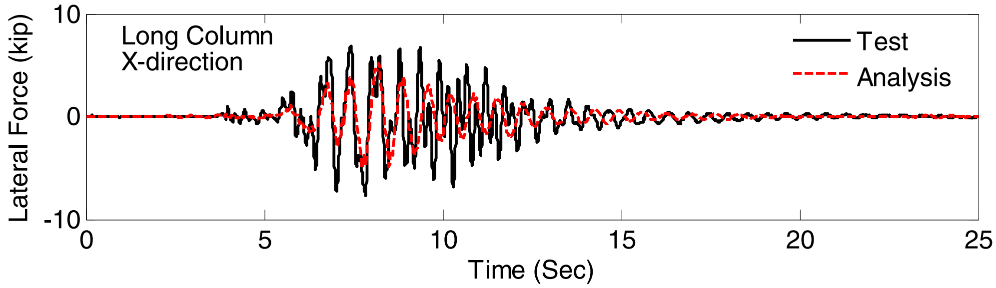

(a) Elastic level

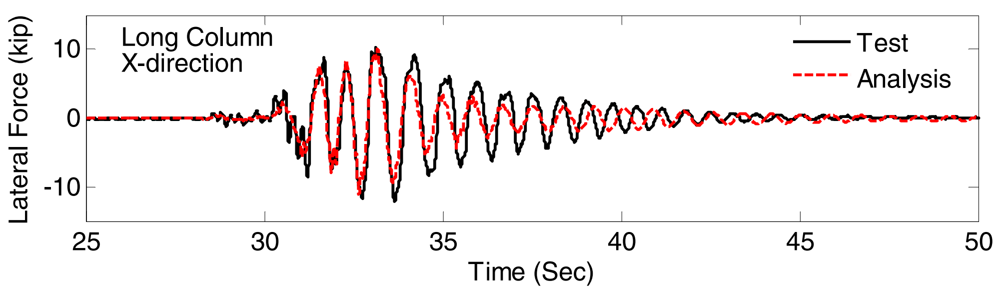

(b) Yield level

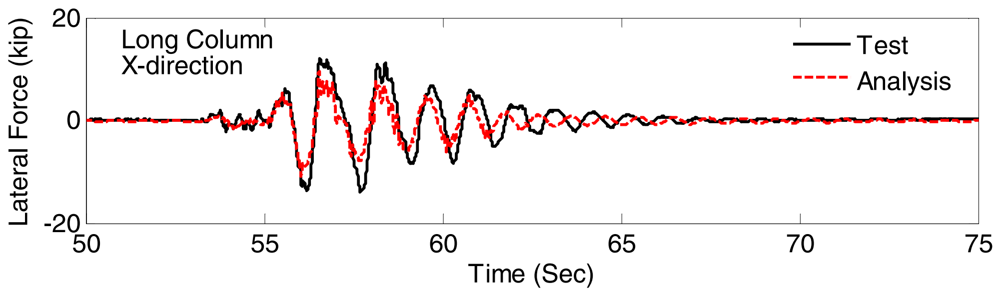

(c) Design level

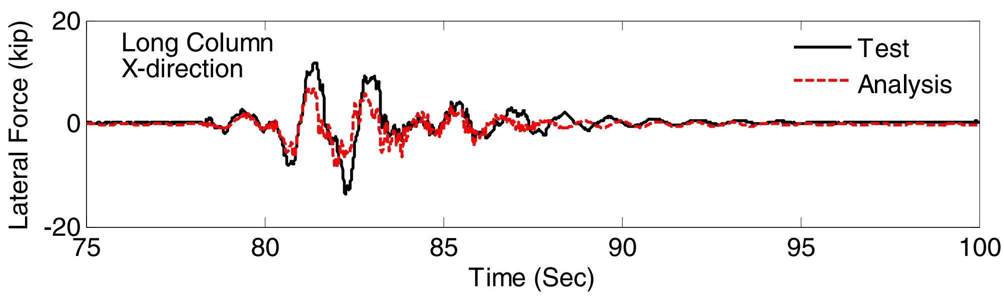

(d) Maximum level

Fig. 5.48 Shear force of PRC-system specimen based on recommended model (long column, *x* direction)

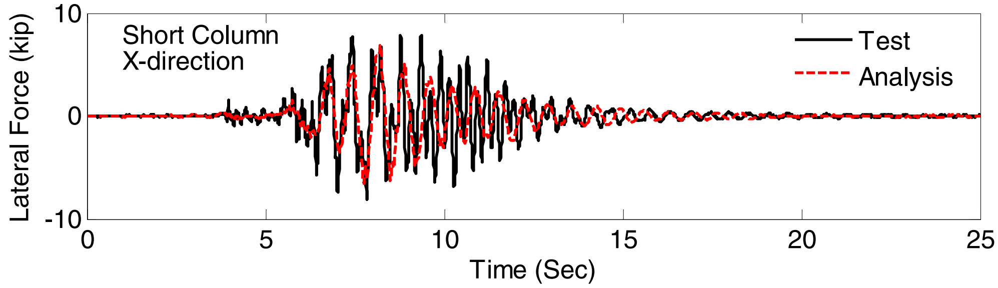

(e) Elastic level

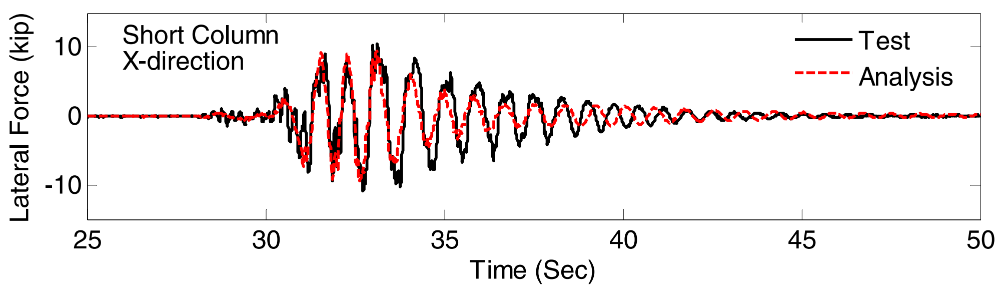

(f) Yield level

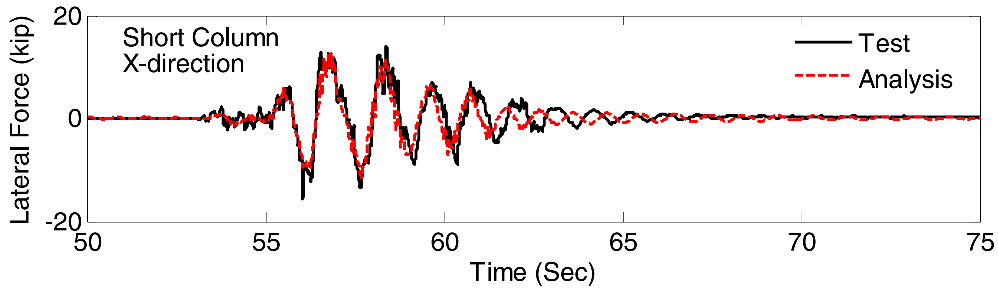

(g) Design level

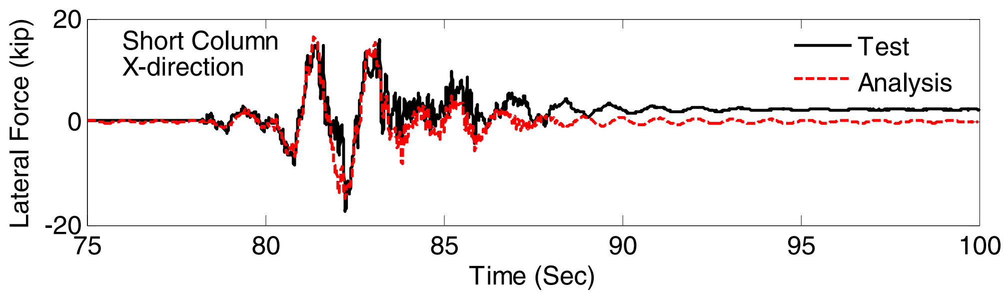

(h) Maximum level

Fig. 5.49 Shear force of PRC-system specimen based on recommended model (short column, *x* direction)

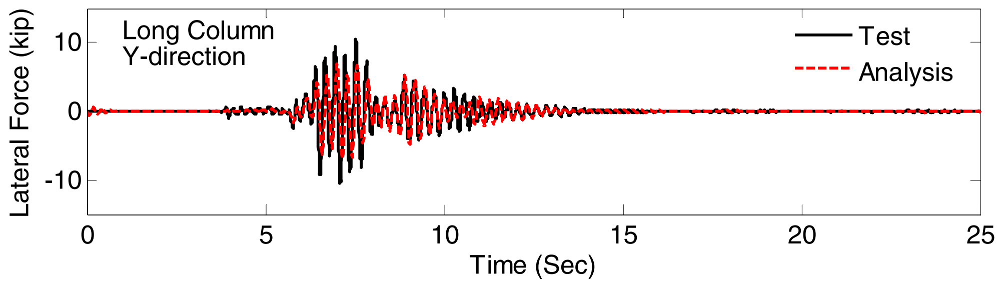

(a) Elastic level

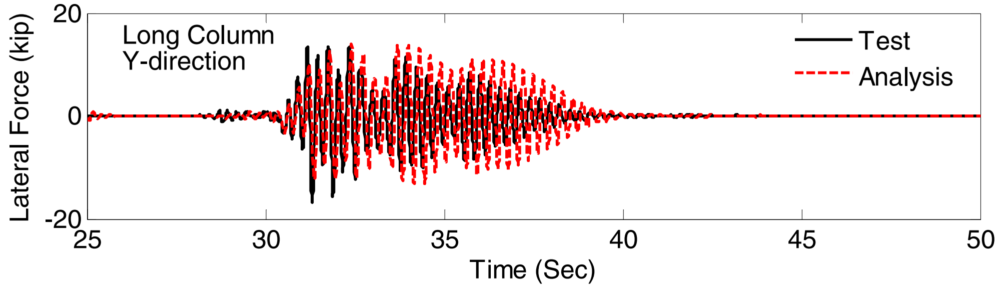

(b) Yield level

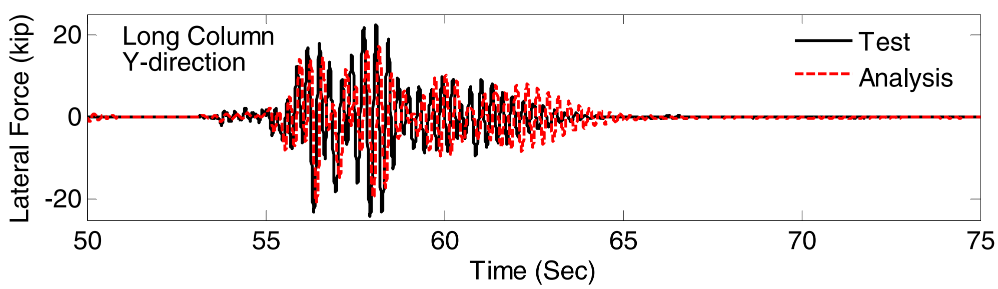

(c) Design level

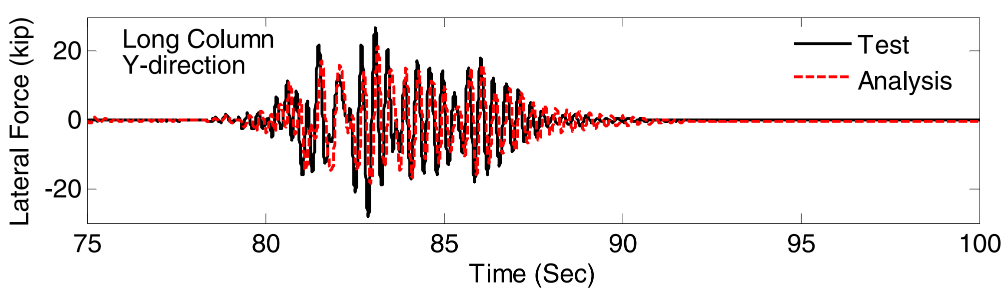

(d) Maximum level

Fig. 5.50 Shear force of PRC-system specimen based on recommended model (long column, *y* direction)

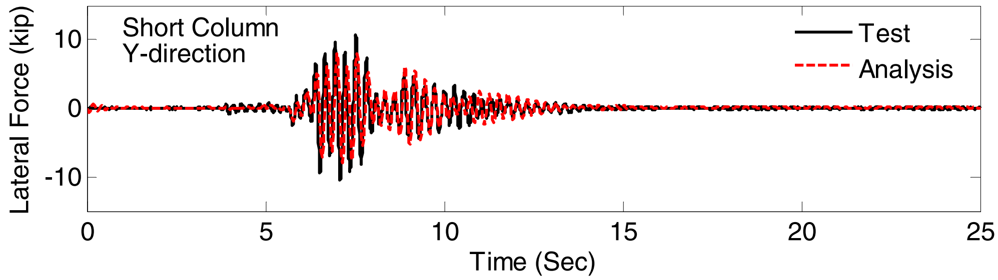

(i) Elastic level

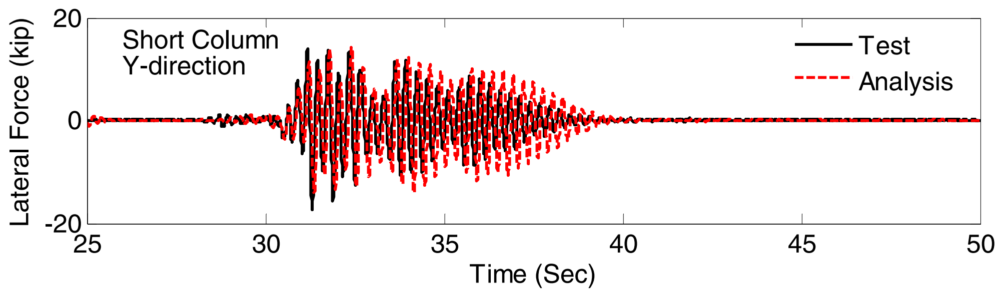

(j) Yield level

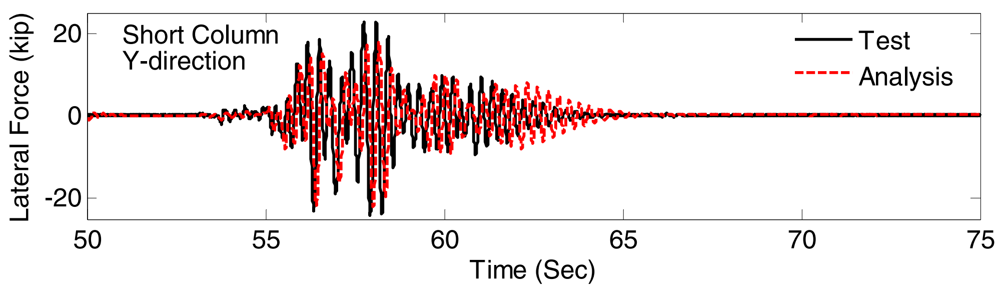

(k) Design level

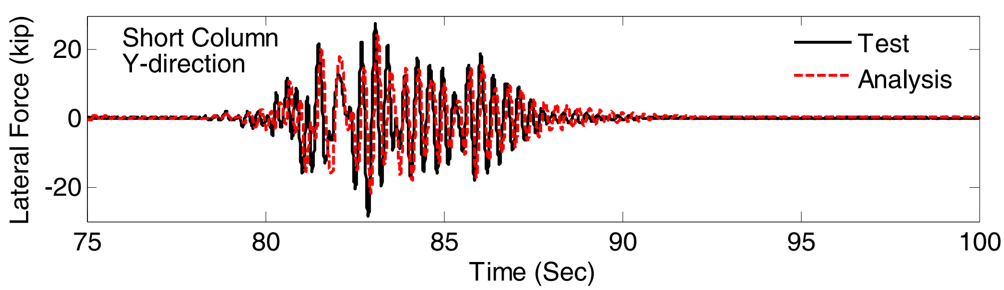

(l) Maximum level

Fig. 5.51 Shear force of PRC-system specimen based on recommended model (short column, *y* direction)

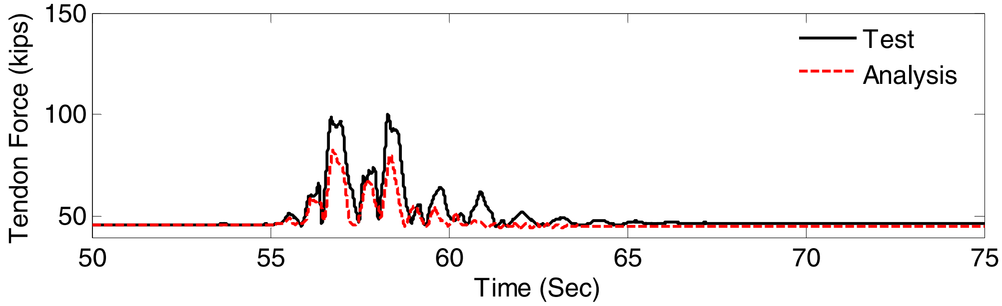

(a) Design level

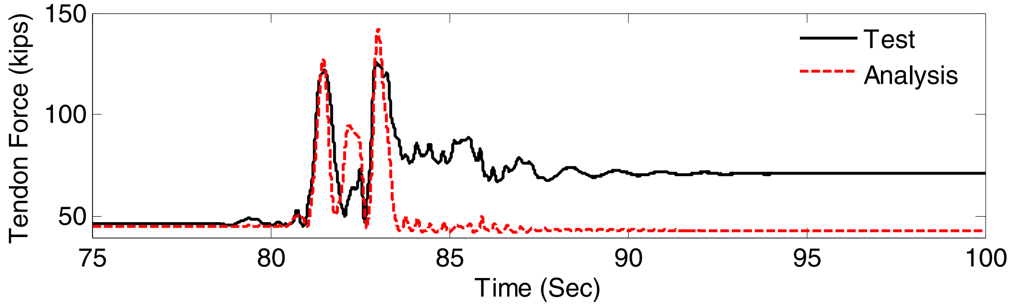

(b) Maximum level

Fig. 5.52 Prestressing force of PRC-system specimen (long column) based on recommended model

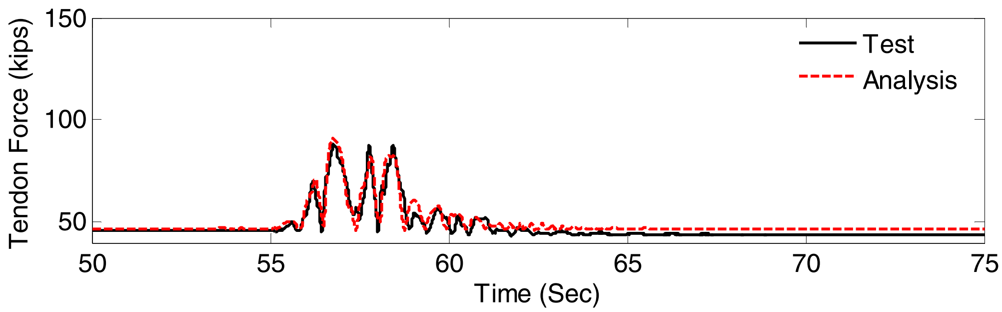

(a) Design level

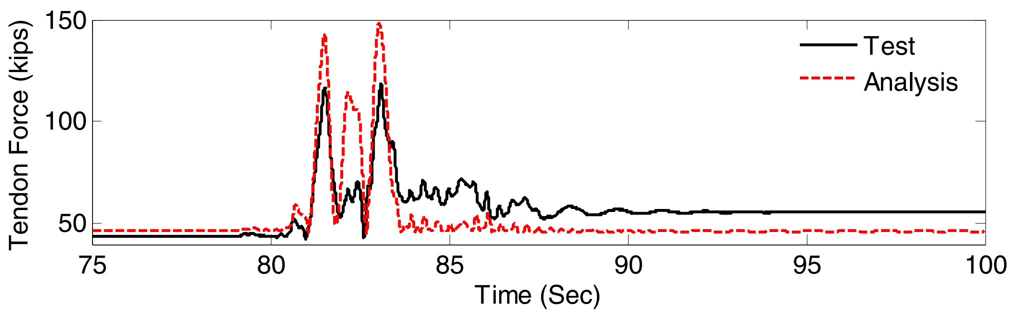

(b) Maximum level

Fig. 5.53 Prestressing force of PRC-system specimen (short column) based on recommended model

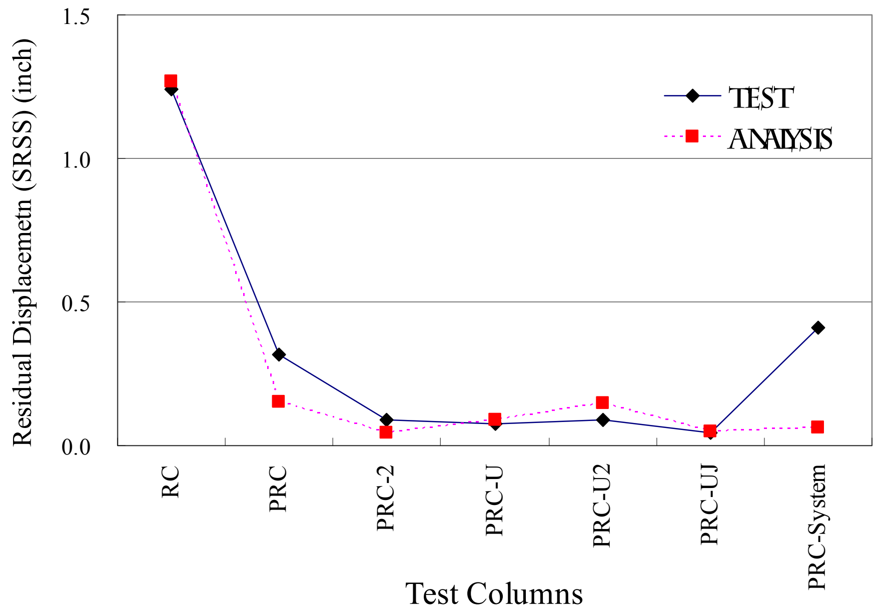

(a) Design level

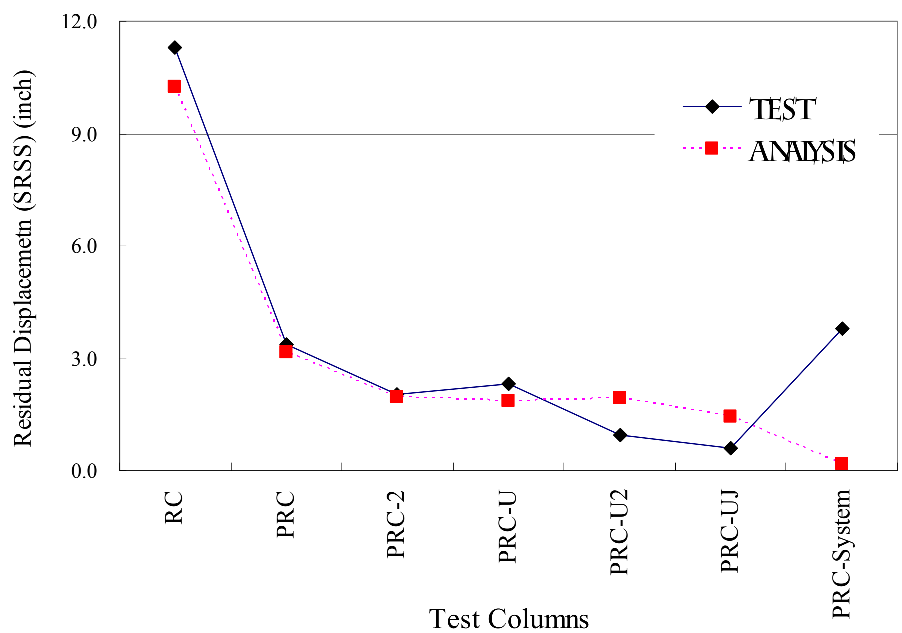

(b) Maximum level

Fig. 5.54 Comparison of analytical and test results for residual displacement (SRSS) of all specimens

6 Parametric Study

6.1 INTRODUCTION

While the experimental programs in Chapter 3 indicate substantial benefit of the new method for reduction of residual displacements, the investigations were based on a limited number of column designs and only one ground motion. In Chapter 5 analytical models for predicting the seismic performance, especially residual displacement, of reinforced concrete bridge columns were developed. Using those models, this chapter describes parametric studies conducted to investigate the effect of different ground motions and of different column configurations. Prior studies (Sakai and Mahin 2004) have examined the effect of various details, such as the amount of prestressing tendon and prestressing force, amount of mild longitudinal reinforcement, strength of concrete, etc., on the hysteretic shape and re-centering properties of partially prestressed concrete columns under quasi-static cycling loading. A series of dynamic analyses (Sakai and Mahin 2004) were also carried out using traditional, but uncalibrated, numerical models to assess the ability of these self-centering columns to reduce residual displacements compared to conventional reinforced concrete columns. The improved analytical models developed in Chapter 5 will allow more accurate and refined investigations of the effects of design variables on performance.

Two series of dynamic analysis were performed as described in this chapter. One focused on the response of conventional columns and re-centering columns under different earthquake inputs; the other focused on the effects of the aspect ratios (periods) of the column.

Presented first is the series of analysis examining the effects of a self-centering column with different earthquake inputs. The RC, PRC, and PRC-UJ type columns are compared. Each column was subjected to 10 ground motions scaled to match a specified intensity measure (IM). This series of analysis is described in Section 6.3.

The second set of analysis is the parametric study of different height-to-diameter (aspect) ratios of the column. Each column was subjected to the same earthquake inputs used in the first set of analysis. This configuration analysis is described in Section 6.4.

The summary of both sets of analysis is presented in Section 6.5.

6.2 DESIGN OF COLUMNS CONSIDERED IN PARAMETRIC INVESTIGATIONS

The baseline column was selected from the prototype column of the previous test program (see Section 3.2.1). The design of the column used in this study was performed according to the Caltrans Bridge Design Specification (BDS) (California Department of Transportation 2004) and the SDC. In this section, a brief outline of the column details is presented. The details of the design procedure of the column can be found in the previous research paper (Sakai and Mahin 2004). Based on the RC column, the designs of the PRC and PRC-UJ columns follow.

Figures 6.1(a–b) show the cross sections of the RC and various PRC baseline columns. The diameter of all the columns is fixed at 6 ft (1.83 m); the columns are reinforced with No. 9 (29-mm diameter) deformed bars and No. 5 (16-mm diameter) spirals at 3-in. (76-mm) pitch. The longitudinal reinforcement ratio (ρ_l) and the volumetric ratio of spiral reinforcement (ρ_s) are 1.18% and 0.61%, respectively. The longitudinal reinforcement of RC (48 bars) is reduced by half to 24 No. 9 (29-mm diameter) bars in the two PRC baseline columns (PRC and PRC-UJ). All other detailing-related properties of the PRC columns are the same as those of the RC column. Prestressing strand that has similar area to longitudinal reinforcement is used in the middle of the column for the PRC specimens.

The material properties of the concrete and steel are summarized in Tables 6.1(a–c). The expected unconfined concrete strength is set at 5 ksi (34.5 MPa), and Gr60 reinforcing bars with the expected yield strength of 68.8 ksi (475 MPa) are used for both longitudinal and spiral reinforcement. Gr250 (1,035 MPa) strand is used as prestressing steel. Column PRC-UJ's steel jacket thickness and properties are chosen in this study to have the same unconfined concrete strength as the RC specimen, but to have 10% positive post-yield stiffness after attaining the confined concrete strength. The aspect ratios of the baseline columns are selected to systematically range from 4 [h = 24 ft (7.32 m)] to 10 [h = 60 ft (18.29 m)] to give a fundamental period ranging from about 0.7 to 2.7 s. The dead load supported by the columns (P) is taken to be 1,020 kip (4.5 MN); therefore, the ratio of the axial load to the axial load capacity of the column ($P/f'_{co}A_g$) is 5%. The prestressing force (P_s) is taken to be 1,428 kip (6.3 MN); therefore, $P_s/f'_{co}A_g$ of the baseline PRC-type columns is 7%. Thus, the total prestressing force ratio of the PRC-type columns is 12% of the axial load capacity of the column; this is similar to the total prestressing force ratio of the PRC specimens (PRC-2, PRC-U, and PRC-UJ) in Chapter 3. The column is assumed fixed at the base and the flexibility of the foundation is not included.

Table 6.2 shows the basic seismic evaluation of each RC column with different aspect ratios based on the methods outlined in the SDC. The columns designed in this study have an ultimate ductility capacity in the range of 4.8 to 6.2. As expected, as the column height increases, the ultimate displacement capacity increases but ductility capacity decreases. The details of material properties and seismic evaluation can also be found in the previous analytical research paper (Sakai and Mahin 2004).

6.3 COMPARISON OF RC AND VARIOUS PRC MODELS

The conclusions drawn from the test results presented in Chapter 3 are based on input from only one earthquake (Loma Prieta, 1989) with increasing intensity levels; the results might change with different earthquake input. In this section, 20 different earthquake records cataloged by the I-880 Testbed Committee of the PEER research program (Kunnath 2007) are used for ground motions for the RC, PRC, and PRC-UJ columns with an aspect ratio of 6.

6.3.1 Hazard Analysis and Ground Motions

Hazard is specific to the site of the structure; the site of a testbed structure study of an I-880 bridge performed by PEER (Kunnath 2007) is chosen as the site of this study. This hazard is dominated by earthquakes on the Hayward fault, which is located about 4.4 mi (7 km) east of the site. The Hayward fault is a strike-slip fault that has the potential to generate earthquakes having magnitudes as large as 7.0. The site has geographic coordinates of lat 37.80 N, long 122.25 W.

In this study, IM is the elastic spectral acceleration (S_a) magnitude at the fundamental period of the structure with a 5% damping ratio ($S_a(T_1)$). The IMs are chosen from seismic hazard analysis. The seismic hazard curve is derived by plotting the return periods against the magnitude of the spectral accelerations at the characteristic structural period. Several studies have shown that for a relatively wide range of intensities, the seismic hazard curve can be approximated as a linear function on a log-log scale. In particular, Kennedy and Short (1994) and Cornell (1996) have proposed that the seismic hazard curve be approximated as

$$\lambda(IM) = k_0 (S_a)^{-k} \tag{6.1}$$

For the I-880 bridge site, it was determined that k_0 = 0.0011 and k = 2.875. The hazard curve is shown in Figure 6.2.

Two sets of 10 ground motions were assembled from a record set prepared by Somerville and Collins (2002) for the I-880 Testbed Committee of the PEER research program. One set of 10 ground motions was used for a 50% probability of being exceeded in 50 years (see Table 6.3). The other set of 10 ground motions was used for both a 10% and a 2% probability of being exceeded in 50 years (see Table 6.4). The sets consisted entirely of near-fault ground motions because the bridge site, along with the vast majority of bridges in California in general, are within 6.2 mi (10 km) of a major fault. Additional information on the selection of the ground motion histories is reported in the paper prepared for the testbed project by Somerville and Collins (2002).

The performance of each column is evaluated for three earthquake hazard levels. These hazard levels correspond to 50%, 10%, and 2% probability of being exceeded in 50 years. The mean return period for each of these hazard levels is 72, 474, and 2,475 years, respectively. The selected time histories have to be scaled in a manner that is consistent with the choice of IM. Using the response spectra of the strike-normal component, a scale factor is determined for each strike-normal record at each of the three hazard levels. This scale factor is applied to the strike-parallel component of the earthquake recording to preserve the relative scaling between the components. A scaled strike-normal record is used for the longitudinal (*x*) direction and a scaled strike-parallel record is used for the transverse (*y*) direction.

Figure 6.3 shows the scaled response spectrum of strike-normal records for an IM [$S_a(T_1)$ = 0.8g)] that corresponds to the 10%-in-50-years hazard level.

6.3.2 Analytical Procedure

The bridge column was modeled using the OpenSees platform. A schematic representation of the bridge model is shown in Figures 5.7–5.9 for the RC, PRC, and PRC-UJ columns. The model is three-dimensional, allowing two components of the ground motion to be evaluated in the analysis; although the third component (the vertical direction) was available, it was not used. Each column was modeled based on the analytical models developed in Chapter 5 for the RC, PRC, and PRC-UJ specimens.

The RC column is modeled with a single concentrated-plasticity fiber beam-column [beamWithHinges] element as shown in Figure 5.7. For all columns, the plastic hinge length is calculated with the Priestley equation. The cracked stiffness value for the elastic region of the beam for the RC column is 0.3 EI, as recommended in Chapter 5. The column is assumed fixed at the base. The Concrete02 model with suggested descending parameters in OpenSees is used for the cover and confined concrete. The ReinforcingSteel model in OpenSees is used for reinforcing steel modeling. The Rayleigh stiffness-only proportional damping matrix with a damping ratio of 3% is used for the damping modeling.

A co-rotational truss [OpenSees CorotTruss] element with initial strain is used to model the prestressing tendon in the PRC column as seen in Figure 5.8. The cracked stiffness value for the elastic region of the beam for the PRC column is 0.4 EI, as recommended in Chapter 5. To model unbonded mild rebar for the PRC-UJ column (Fig. 5.9), one integration point for the steel fiber is used as explained in Section 5.2.7. Steel jacketing is assumed as a continuous spiral to compute enhanced strength and strain capacity of concrete confined by the steel jacket.

An eigenvalue analysis of the baseline bridge model yielded a first mode period of approximately 1.2 s.

The models are considered fixed at the bottom of the footing. Geometric nonlinearity is included in all analyses by using the P-Δ option in OpenSees.

The dynamic analyses were performed using two components of motion for each ground motion record: the fault-normal and fault-parallel components. In the analyses, the fault-normal component and the fault-parallel component (the more severe of the two) were applied in the *x* and *y* directions of the column, respectively.

For lateral mass of the RC, PRC, and PRC-UJ columns, the axial loadratio ($P/f'_{co}A_g$) is 5%, corresponding to 1,020 kip (4.6×10^5 kg). The rotational moment of inertia of the superstructure for the three columns is assumed to be 1.27×10^6 kip·in^2 (3.74×10^6 kg·m^2). The prestressing force ratio of the PRC and PRC-UJ columns ($P_{ps} / f'_{co} A_g$) is 7%.

To perform the dynamic analysis at three different hazard levels for a specific IM, the ground motions had to be scaled to each intensity level. In this study, the motions were scaled based on the fault-normal component of motion, and the same scale factor was applied to the fault-parallel component. This procedure was recommended in Somerville and Collins (2002).

Dynamic analysis was performed at three different intensity levels. As noted above, these three levels corresponded to the hazard levels of 50%, 10%, and 2% in 50 years. The intensity levels chosen for the hazard levels are shown in Table 6.5.

6.3.3 Comparison

The time-history responses of one of the earthquakes cataloged by Somerville and Collins (2002) is presented in Figures 6.4 and 6.5. These figures compare the drift ratios of the PRC column and the reference reinforced concrete column (RC) subjected to the Los Gatos Presentation Center record obtained during the 1989 Loma Prieta earthquake (earthquake No. 1 in Table 6.4) for the 10%-in-50-years and 2%-in-50-years hazard levels.

The maximum response drift ratio of the x direction for the 10%-in-50-years hazard level of the RC column is 4.3%, while that of the re-centering column is 4.6%. The residual drift ratio of the x direction at the 10%-in-50-years hazard level is 0.75% for the RC column, while that of the re-centering column is 0.06%. At the 2%-in-50-years hazard level, the residual drift ratio in the x direction is 3.75% for the RC column and only 0.2% for the PRC column. Similar trends show in the y direction. The maximum drift ratios of the PRC column are slightly larger than those of the RC column, but the residual drift ratios are much smaller. The PRC column displays good re-centering characteristics as shown in the test results of the previous chapters.

To investigate general response characteristics of the PRC columns, the dynamic responses for the 10 ground motions listed in Table 6.4 at the 2%-in-50-years hazard level are presented. Figures 6.6(a–b) summarize the maximum and the residual displacements (SRSS) of the RC and PRC columns. As a whole, the maximum responses of the PRC column are slightly larger than those of the RC column. Especially large residual displacements are produced in the RC column for the earthquake No. 10 (Erzincan, Turkey) record. The residual displacements of the re-centering column (PRC) are significantly smaller than those of the reference column (RC) for all the ground motions. The use of prestressing strands in reinforced concrete columns is proved to be an effective method to reduce residual displacements after earthquake excitations for this baseline column.

To help assess the seismic performance of the PRC columns, the maximum and the residual distances (SRSS, the square root of sum of squares of *x*- and *y*-direction displacements) of the PRC column are normalized with the values obtained from the RC column. Thus, the normalized maximum distance (N_D) and the normalized residual distance (N_{RD}) are defined here as follows:

$$N_D = \left| \frac{d_{max \cdot ReC}}{d_{max \cdot rc}} \right| \tag{6.2}$$

$$N_{RD} = \left| \frac{d_{r \cdot ReC}}{d_{r \cdot rc}} \right| \tag{6.3}$$

where $d_{max \cdot rc}$ and $d_{r \cdot rc}$ are the maximum and residual distances of the RC column; and $d_{max \cdot ReC}$ and $d_{r \cdot ReC}$ are those of the re-centering PRC (PRC and PRC-UJ) columns.

Figures 6.7(a–b) show the normalized maximum distance (N_D) and the normalized residual displacement (N_{RD}) of the RC and PRC columns. The maximum distances of the PRC columns are approximately 10% larger on average than those of the RC column. The residual displacements of the re-centering columns are about 20% those of the reference column, except for earthquake No. 7, which produced relatively small residual displacement in the RC specimen (see Fig. 6.5).

The results obtained for the records scaled to three different hazard levels (50% in 50 years, 10% in 50 years, and 2% in 50 years) are presented in Figures 6.8–6.11. Table 6.7 lists mean values for the maximum and residual drifts and for the ratio of residual drift to peak drift at each intensity level for the RC, PRC, and PRC-UJ columns.

Figures 6.8(a–b) compare the peak drift ratios of the RC and PRC columns. In general, the peak drifts for the two systems are close for a given intensity level. The mean peak drift is about 10% larger at the 2%-in-50-years hazard level for the PRC design, but the coefficient of variation (C.V.) is about 24% less. The performance of the PRC columns with respect to peak drift response was as desired; in the design of the PRC columns, the goal was to proportion the columns such that the peak drift response would be similar (to within 15%).

A comparison between the residual drift ratios of the RC and the PRC columns is shown in Figures 6.9(a–b). Unlike with peak drift response, there is a clear difference in the residual response of the two systems. With increasing intensity, the bridge with RC columns begins to sustain significant residual displacements, with large variation in the magnitudes of the residual displacements for the different ground motions. In contrast, the bridge with PRC columns retains substantially lower residual displacements with increasing intensity, and the range of residual displacements is comparatively small.

At the 50%-in-50-years IM level [$S_a(T_1) = 0.36g$], the median residual drift ratio of the RC column is approximately 0.1%, whereas the median residual drift ratio of the PRC columns is approximately 0.04%. This magnitude of residual displacement for both column systems is low enough that both bridges would likely be considered usable following an earthquake. At the 2%-in-50-years hazard level, a weakness in the RC column system is exposed: five of the records lead to residual displacements in the columns greater than 1% and the mean residual drift is 2%. In cases where the residual drift ratio exceeds 1%, the post-earthquake functionality of the bridge in this state is questionable. For the PRC column system, the median residual drift ratio at the 2%-in-50-years hazard level is 0.16%; in no case do any of the records lead to a residual drift ratio greater than 1%, with a maximum value of 0.84%. These lower residual drift ratios sustained by the PRC column would likely leave the bridge in an operational state following an earthquake. Because the maximum displacements of the RC and PRC columns are similar, the PRC column would require local repair to remove and replace spalled concrete and correct any buckled bars. Similar results can be found in the recent research by Lee (2007). Lee (2007) performed incremental dynamic analysis for a bridge with conventional RC columns and with PRC columns, using a set of 17 near-fault ground motions; he found that the mean residual drift for the RC and PRC columns was 0.6% and 0.25%, respectively, at the 2%-in-50-years hazard level. The smaller mean residual drift ratio of the PRC column in his research (0.6% vs. 2% in this research) might arise from the analytical model difference; Lee (2007) calibrated his analytical model of the RC column only for the design level.

The C.V.'s of the maximum displacements of the RC and PRC columns are much lower than those of the residual displacements of both columns. The C.V.'s of the maximum displacement of columns RC and PRC at the 2%-in-50-years hazard level are 40.32% and

32.76%, respectively, while those of the residual displacement of RC and PRC are 139% and 151%, respectively.

A comparison between the ratios of residual drift to peak drift of the RC and the PRC columns is shown in Figures 6.10(a–b) and Table 6.7. As the hazard level increases, as reflected by increased values of $S_a(T_1)$, the ratio also increases in the RC column from 0.06 to 0.26, while the ratio remains quite stable around 0.03 in the PRC columns. In the RC specimen, damage increases with increasing intensity, so that the ratio of residual to peak drift increases as expected for the conventional column; in the re-centering column, the ratio does not change much with increasing intensity due to the re-centering characteristics of the PRC column.

A comparison between the peak and residual drift ratios of the PRC and PRC-UJ columns is shown in Figures 6.11(a–b) and Table 6.7. Only the mean values of each intensity level for each column are show in the figures for simplicity. The peak drift ratios of the two PRC columns are quite similar; this is as expected because the only analytical modeling difference between PRC and PRC-UJ is the confinement effects of the concrete at the plastic hinge region. At the lower level, the residual drifts also do not differ much between PRC columns, but differences are apparent at the 2%-in-50-years IM level. The enhancement of the confinement effect by using a steel jacket or other jacketing material reduces the residual displacement. As discussed in the experimental program of Chapter 3, the PRC-UJ or other jacketed designs can also prevent damage of the column, e.g., spalling of cover concrete and buckling of mild rebar, and demonstrates good sustainability post-earthquake.

A comparison between the residual-to-peak drift ratios of the PRC and PRC-UJ columns is shown in Figure 6.11(c). The mean values of the ratio for residual to peak are placed between 2% and 3% regardless of the intensity levels and column model. Based on these results, the residual displacement of the PRC columns might be expected as a function of peak displacements.

6.4 PARAMETRIC STUDY OF DIFFERENT ASPECT RATIOS

The results drawn from the analysis presented in the previous section are based on only one column configuration. In this section, to provide more insight into the re-centering column (PRC), the RC reference column and PRC columns assume different configurations for analysis with two sets of 10 different earthquake inputs from the I-880 Testbed Committee of the PEER research program (Kunnath 2007) at three different hazard levels. The parameter considered is the aspect ratio (fundamental period) as shown in Table 6.6.

6.4.1 Hazard Analysis and Ground Motions

Most aspects of the hazard analysis are the same as detailed in the previous Section 6.3.1. The same site of the structure is chosen in this chapter. The intensity measure selected for the previous section's analysis was $S_a(T_1)$, spectral acceleration of a specific period (namely, the fundamental period of the structure) — possibly due to the invariable structural configuration; but the IM selected for this section is peak ground acceleration (PGA) because the natural period changes with different configurations.

The same set of records presented in Table 6.3 is used as earthquake inputs; for the analyses performed in this study, all 20 ground motions are used. The performance of each column is evaluated at three earthquake hazard levels. These hazard levels correspond to 50%, 10%, and 2% probability of being exceeded in 50 years. The IM for each hazard level is presented in Table 6.5.

Figure 6.12 shows the scaled response spectrum of strike-normal records for an IM (PGA = 0.64*g*) that corresponds to the 10%-in-50-years hazard level. The vertical dotted lines in Figure 6.12 represent the fundamental periods of different aspect ratios.

6.4.2 Columns with Various Aspect Ratios

To investigate the sensitivity of the seismic response of the reference RC and re-centering PRC columns to the natural period, additional columns with various aspect ratios are analyzed (see Table 6.2). The columns have aspect ratios varying between 4–10, but to simplify comparisons herein have the same section geometry and reinforcement as that of the design baseline column with aspect ratio 6. Because the columns all have the same section, they have different ductility demands for each period, and therefore may not consistently represent performance expectations. The fundamental natural periods evaluated from eigenvalue analyses range from 0.69 to 2.49 s. Shorter periods were not examined, since the SDC recommends that columns have fundamental periods greater than 0.7 s.

To examine the effect of bidirectional loading, the PRC column is analyzed with unidirectional loading in addition to bidirectional loading. The scaled 10 fault-normal components are applied in the *x* direction of the column as unidirectional loading for each hazard level.

Figures 6.13 and 6.14 show RC and PRC maximum and residual drift ratio response (maximum or residual displacement (SRSS):column height) spectra for 10 different earthquakes, along with the mean value, at the 2%-in-50-years intensity level. The maximum drift ratios for the RC and PRC columns are quite similar, whereas the residual drift ratios for PRC are greatly reduced compared with the RC column. The maximum drift ratios for both the RC and PRC columns remain stable as the natural period increases in most earthquake cases, while the residual distance for the RC and PRC columns does not show any consistent trend for the set of earthquake inputs.

Figures 6.15(a–b) show the ratio of residual and peak drift response spectra for the 10 earthquakes, as well as the mean value, at the 2%-in-50-years intensity level. The ratios of the PRC column increase from 0.02 to 0.06 as the natural period increases for each earthquake, while the ratios of the RC column remain between 0.1 and 0.2. The ratios of the RC column of aspect ratio 6 in this section are lower than those of Section 6.3.3 due to the difference of the scaling of ground motions. The fixed value of the PGA used in this section is 25% less than the mean value of the variable PGAs of the scaled ground motions used in Section 6.3.3.

Figures 6.16(a–b) show the mean maximum and residual response spectra for all 10 records at the 2%-in-50-years hazard level. Figure 6.16(a) also shows the yield drift ratio with different aspect ratio. As mentioned earlier, while picking the same section used for all aspect ratios, it results in different ductility demands for the different aspect ratio. Table 6.8 lists mean values of the maximum and residual drift ratios and of the ratio of residual drift to peak drift at the 2%-in-50-years intensity level for RC and PRC columns with different aspect ratios. The maximum drift ratios of both columns remain between 3% and 4% as the natural period increases. The residual drift ratios of the RC column remain between 0.4%–0.8% while those of the PRC column remain between 0.1%–0.2% as the natural period increases.

Because the response of the columns is sensitive to ground motion characteristics, the normalized maximum distance (N_D) and the normalized residual distance (N_{RD}) are statically analyzed to investigate general trends. Figures 6.17(a–b) show mean normalized maximum and residual response spectra for all 10 records at the 2%-in-50-years hazard level. The mean maximum drift ratios are only 3–19% larger than those of the reference column, and the residual displacements are reduced about 80% compared to those of the reference column. Generally, the residual distances of the PRC column are significantly smaller than those of the conventional column regardless of period range.

Figures 6.18 and 6.19 show mean maximum and residual drift ratio response spectra of the PRC column with unidirectional and bidirectional loading in the *x* direction and for SRSS values for 10 different earthquakes at the 2%-in-50-years intensity level. Table 6.9 lists mean values of the maximum and residual drift ratios and of the ratio of residual drift to peak drift at the 2%-in-50-years intensity level for unidirectional and bidirectional loading of the PRC column with different aspect ratios.

The maximum drift ratios of the *x* direction for unidirectional and bidirectional loading are very close for all aspect ratios, while those of the SRSS values are increased for bidirectional loading. The residual drifts of the *x* direction for bidirectional loading are larger than those of unidirectional loading in most cases.

6.5 SUMMARY

Using the models developed in Chapter 5, parametric studies were performed to evaluate the effect of different ground motions and different column configurations. From the analyses presented herein, the following conclusions are determined:

- The residual displacements of the re-centering column (PRC) are significantly smaller than those of the reference column (RC) for all the ground motions over the period range considered. The use of prestressing strands in reinforced concrete columns is proved to be an effective method to reduce residual displacements after earthquake excitations.
- The coefficients of variance (C.V.) of the maximum displacements of the RC and PRC columns are much lower than those of the residual displacements of both columns.
- The enhancement of confinement effect by using steel jacketing in the PRC column reduces the residual displacement. It also reduces the need to repair local damage due to spalling of concrete, etc.
- For the PRC column, the ratios between residual and peak distance response spectra of mean value for the 2%-in-50-years intensity level increase from 0.02 to 0.06 as the

natural period increases for each earthquake, while the ratios in the RC column remain between 0.1 and 0.2.

- The maximum drift ratios of the *x* direction for unidirectional and bidirectional loading are very close for all aspect ratios, while those of the SRSS values increase for bidirectional loading. The *x*-direction residual drifts for bidirectional loading are larger than those of unidirectional loading in most cases.

Table 6.1 Material properties

(a) Concrete

Strength of unconfined concrete	5 ksi (34.5 MPa)
Young's modulus	4,000 ksi (27.6 GPa)
Unconfined concrete compressive strain at the peak stress	0.002
Spalling strain of unconfined concrete	0.005
Strength of confined concrete	6.14 ksi (42.4 MPa)

(b) Steel (Gr60)

Expected yield strength	68.8 ksi (475 MPa)
Expected yield strain	0.0024
Young's modulus	29,000 ksi (200 GPa)
Onset of strain hardening	0.0125
Ultimate tensile strain	0.12
Expected tensile strength	94.9 ksi (655 MPa)

(c) Prestressing Strand

Yield strength	250 ksi (1.73 GPa)
Young's modulus	29,000 ksi (200 GPa)

Table 6.2 Seismic evaluation of designed RC column by SDC

Aspect ratio	**Column height** H (ft)	**Effective period** T_1 (s)	**Yield displacement** ***dy*** (ft)	**Ultimate displacement** ***du*** (ft)	**Ultimate ductility** ***du/dy***	**Yield drift ratio (%)** $\mu_y = dy / H$	**Ultimate drift ratio (%)** $\mu_u = du / H$
4	24 (7.32 m)	0.68	0.164 (0.050 m)	0.93 (0.283 m)	5.69	0.68	3.88
5	30 (9.14 m)	0.96	0.256 (0.078 m)	1.37 (0.418 m)	5.40	0.85	4.57
6	36 (10.97 m)	1.26	0.367 (0.112 m)	1.90 (0.580 m)	5.19	1.02	5.28
7	42 (12.80 m)	1.58	0.499 (0.152 m)	2.52 (0.768 m)	5.05	1.19	6.00
8	48 (14.63 m)	1.94	0.390 (0.199 m)	3.22 (0.981 m)	4.94	0.81	6.71
9	54 (16.46 m)	2.31	0.823 (0.251 m)	4.00 (1.220 m)	4.86	1.52	7.41
10	60 (18.29 m)	2.71	1.017 (0.310 m)	4.87 (1.485 m)	4.79	1.70	8.12

Table 6.3 Ground motion set for 50%-in-50-yrs. hazard level

Number	Earthquake	Mw	Station	Distance (km)
1	Coyote Lake, 1979/6/8	5.7	Coyote Lake Dam abutment	4.0
2	Coyote Lake, 1979/6/8	5.7	Gilroy No. 6	1.2
3	Parkfield, 1966/6/27	6.0	Temblor	4.4
4	Parkfield, 1966/6/27	6.0	Array No. 5	3.7
5	Parkfield, 1966/6/27	6.0	Array No. 6	8.0
6	Livermore, 1980/1/27	5.5	Fagundes Ranch	4.1
7	Livermore, 1980/1/27	5.5	Morgan Territory Park	8.1
8	Morgan Hill, 1984/4/24	6.2	Coyote Lake Dam abutment	0.1
9	Morgan Hill, 1984/4/24	6.2	Anderson Dam downstream	4.5
10	Morgan Hill, 1984/4/24	6.2	Halls Valley	2.5

Table 6.4 Ground motion set for 10%-in-50-yrs. and 2%-in-50-yrs. hazard levels

Number	Earthquake	Mw	Station	Distance (km)
1	Loma Prieta, 1989/10/17	7.0	Los Gatos Presentation Center	3.5
2	Loma Prieta, 1989/10/17	7.0	Saratoga Aloha Ave.	8.3
3	Loma Prieta, 1989/10/17	7.0	Corralitos	3.4
4	Loma Prieta, 1989/10/17	7.0	Gavilan College	9.5
5	Loma Prieta, 1989/10/17	7.0	Gilroy historic	12.7
6	Loma Prieta, 1989/10/17	7.0	Lexington Dam abutment	6.3
7	Kobe, Japan, 1995/1/17	6.9	Kobe JMA	0.5
8	Tottori, Japan, 2000/10/6	6.6	Kofu	10.0
9	Tottori, Japan, 2000/10/6	6.6	Hino	1.0
10	Erzincan, Turkey, 1992/3/13	6.7	Erzincan	1.8

Table 6.5 Intensity measures

Hazard level	PGA	$S_a(T_1) = 1.2$ s
50% in 50 years	0.34	0.41
10% in 50 years	0.64	0.80
2% in 50 years	0.90	1.42

Table 6.6 Parametric values used for analysis

Parameter	Values	Number of values
Aspect ratio	3, 4, 5, (6), 7, 8, 9, 10	8

Table 6.7 Results for different column types at different hazard levels

		Column type		
		RC	PRC	PRC-UJ
IM (PGA) 50% in 50 years	Mean maximum drift ratio (%)	**1.47**	**1.60**	**1.60**
	Coefficient of variance (%)	**28.14**	**33.94**	**33.94**
	Mean residual drift ratio (%)	**0.09**	**0.04**	**0.04**
	Coefficient of variation (%)	**84**	**65**	**65**
	Residual/peak ratio	**0.06**	**0.03**	**0.03**
	Coefficient of variance (%)	**67**	**55**	**55**
IM (PGA) 10% in 50 years	Mean maximum drift ratio(%)	**3.21**	**3.55**	**3.54**
	Coefficient of variation (%)	**33.03**	**29.47**	**29.47**
	Mean residual drift ratio(%)	**0.43**	**0.08**	**0.07**
	Coefficient of variation (%)	**85**	**57**	**56**
	Residual/peak ratio	**0.14**	**0.02**	**0.02**
	Coefficient of variation (%)	**60**	**50**	**50**
IM (PGA) 2% in 50 years	Mean maximum drift ratio(%)	**5.83**	**6.44**	**6.40**
	Coefficient of variation (%)	**40.32**	**32.76**	**31.71**
	Mean residual drift ratio(%)	**2.01**	**0.16**	**0.11**
	Coefficient of variation (%)	**139**	**151**	**94**
	Residual/peak ratio	**0.26**	**0.03**	**0.02**
	Coefficient of variation (%)	**99**	**101**	**59**

Table 6.8 Analytical results of RC and PRC columns with different aspect ratios

		Aspect ratio						
		4	5	6	7	8	9	10
RC column	Mean maximum drift ratio(%)	3.08	3.42	3.13	3.25	3.38	3.31	3.10
	Coefficient of variation (%)	45.94	47.62	51.00	52.93	53.61	54.31	56.38
	Mean residual drift ratio(%)	0.49	0.63	0.52	0.54	0.74	0.76	0.69
	Coefficient of variation (%)	107	84	139	139	118	111	121
	Residual/peak ratio	0.16	0.19	0.17	0.17	0.22	0.23	0.22
	Coefficient of variation (%)	73	65	105	107	78	61	67
PRC column	Mean maximum drift ratio(%)	3.67	3.75	3.25	3.53	3.59	3.47	3.19
	Coefficient of variation (%)	50.49	47.56	52.03	53.05	53.58	54.74	57.44
	Mean residual drift ratio(%)	0.11	0.10	0.12	0.13	0.20	0.21	0.22
	Coefficient of variation (%)	113	96	107	130	69	80	71
	Residual/peak ratio	0.03	0.03	0.04	0.04	0.05	0.06	0.07
	Coefficient of variation (%)	70	63	77	82	44	54	48

Table 6.9 Analytical results of unidirectional and bidirectional loading of PRC column with different aspect ratios

		Aspect ratio						
		4	5	6	7	8	9	10
1-D loading	Mean maximum drift ratio (%)	**3.21**	**3.23**	**3.02**	**2.95**	**3.42**	**3.23**	**2.88**
	Coefficient of variation (%)	**62.31**	**45.62**	**51.42**	**57.64**	**59.57**	**61.95**	**66.35**
	Mean residual drift ratio(%)	**0.15**	**0.07**	**0.07**	**0.07**	**0.13**	**0.14**	**0.16**
	Coefficient of variation (%)	**203**	**65**	**91**	**120**	**113**	**78**	**99**
	Residual/peak ratio	**0.05**	**0.02**	**0.02**	**0.02**	**0.04**	**0.04**	**0.06**
	Coefficient of variation (%)	**128**	**44**	**75**	**85**	**78**	**56**	**74**
2-D loading	Mean maximum drift ratio (%)	**3.67**	**3.75**	**3.25**	**3.53**	**3.59**	**3.47**	**3.19**
	Coefficient of variation (%)	**50.49**	**47.56**	**52.03**	**53.05**	**53.58**	**54.74**	**57.44**
	Mean residual drift ratio(%)	**0.11**	**0.10**	**0.12**	**0.13**	**0.20**	**0.21**	**0.22**
	Coefficient of variation (%)	**113**	**96**	**107**	**130**	**69**	**80**	**71**
	Residual/peak ratio	**0.03**	**0.03**	**0.04**	**0.04**	**0.05**	**0.06**	**0.07**
	Coefficient of variation (%)	**70**	**63**	**77**	**82**	**44**	**54**	**48**

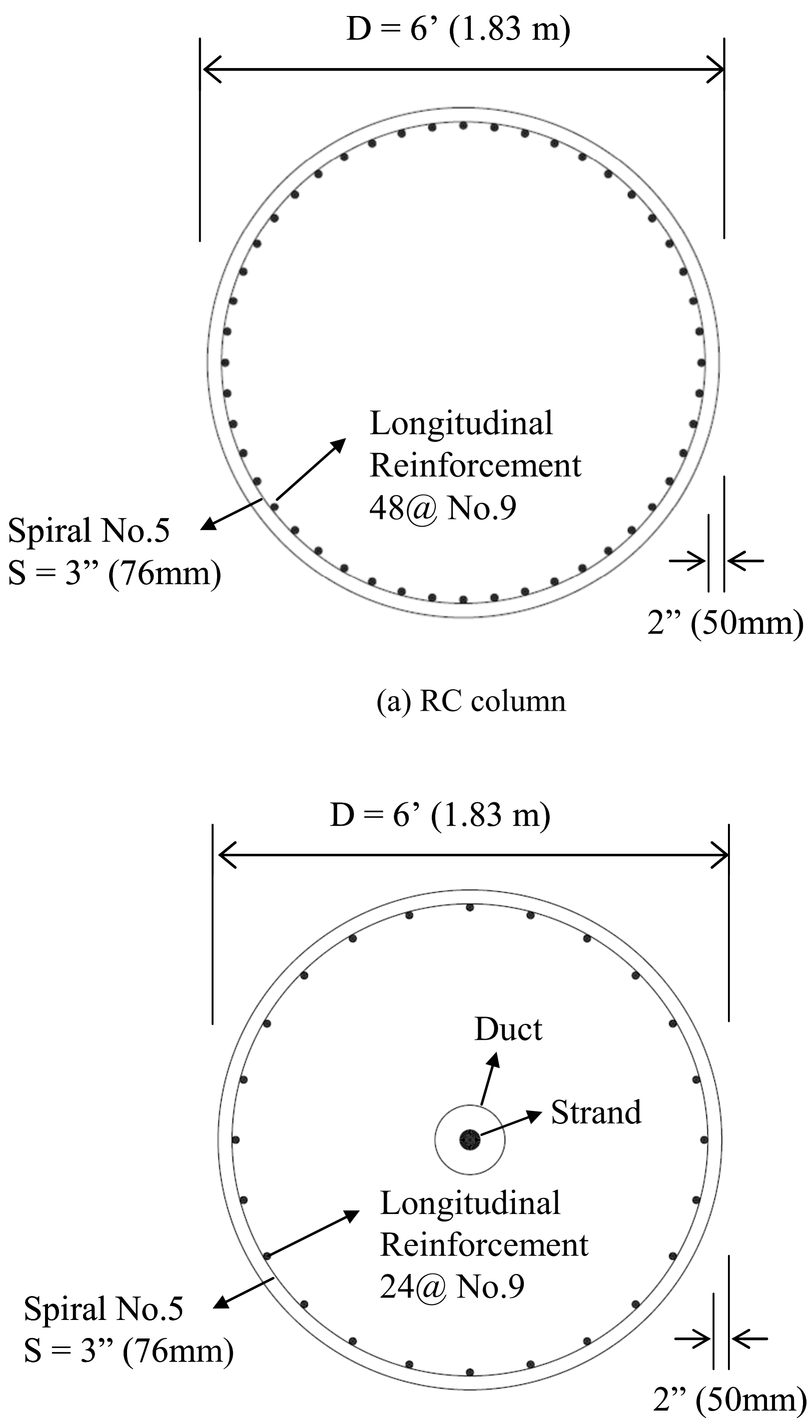

(a) RC column

(b) PRC columns

Fig. 6.1 Cross sections of columns analyzed

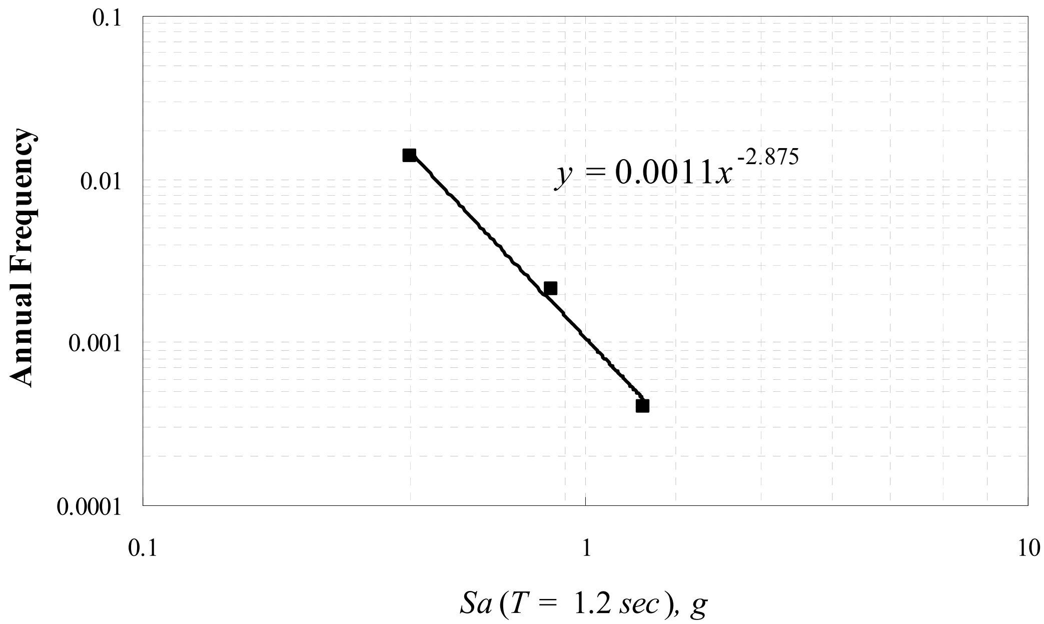

Fig. 6.2 Seismic hazard curve, I-880 bridge site

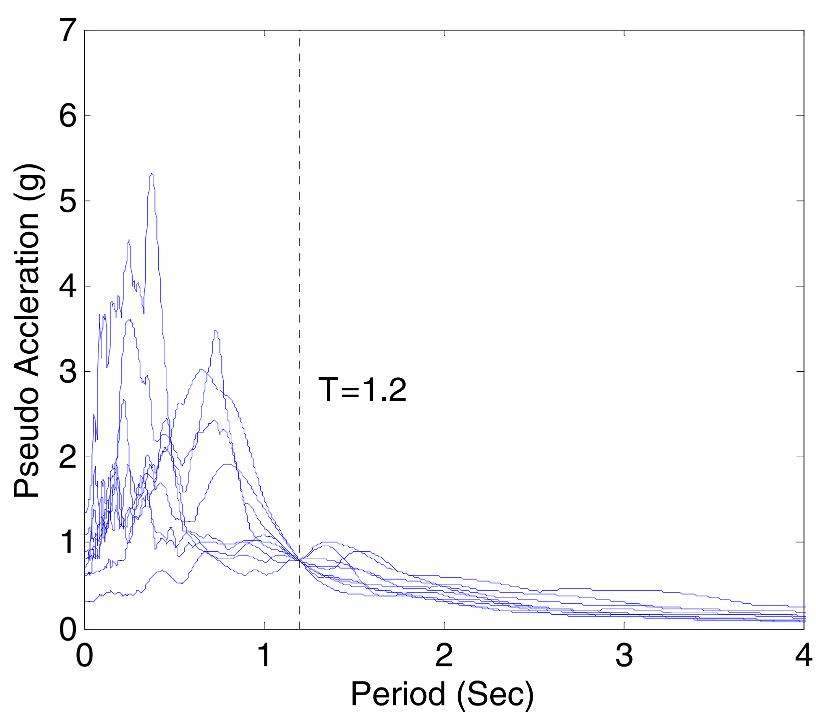

Fig. 6.3 Scaled response spectrum for an IM [$S_a(T_1) = 0.8g$]

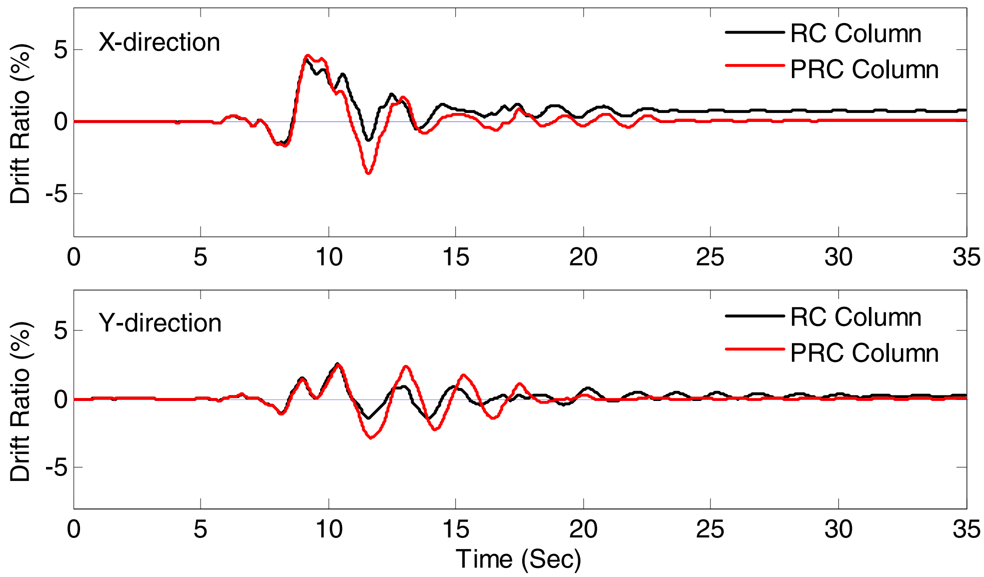

Fig. 6.4 Displacement response of 10%-in-50-yrs. earthquake (No. 1)

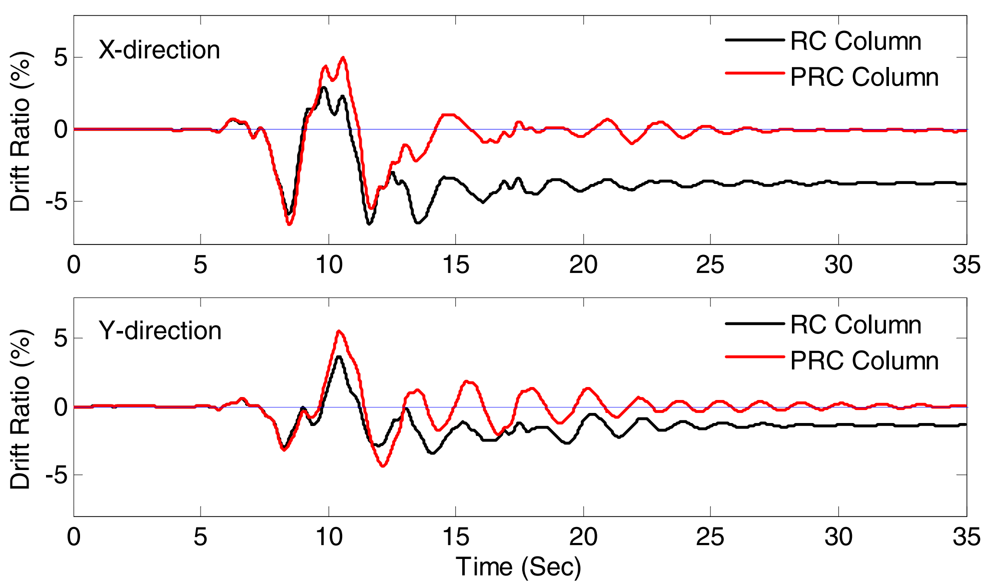

Fig. 6.5 Displacement response of 2%-in-50-yrs. earthquake (No. 1)

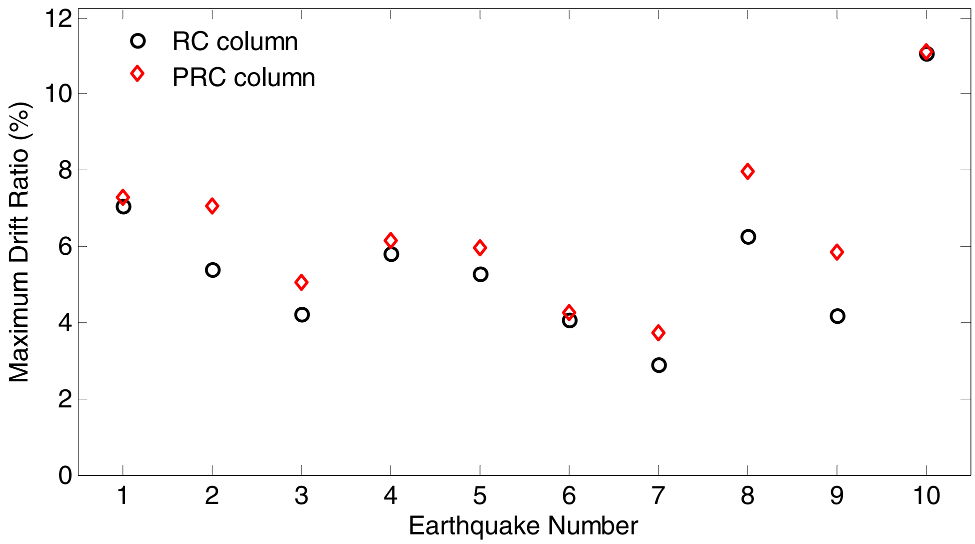

(a) Maximum displacement

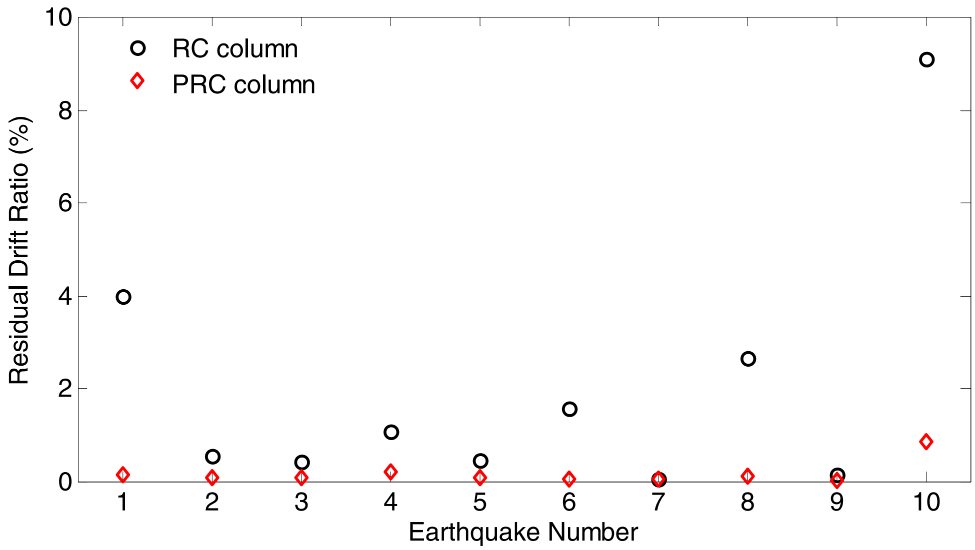

(b) Residual displacement

Fig. 6.6 Maximum and residual drift ratios of RC and PRC columns for 2%-in-50-yrs. hazard level

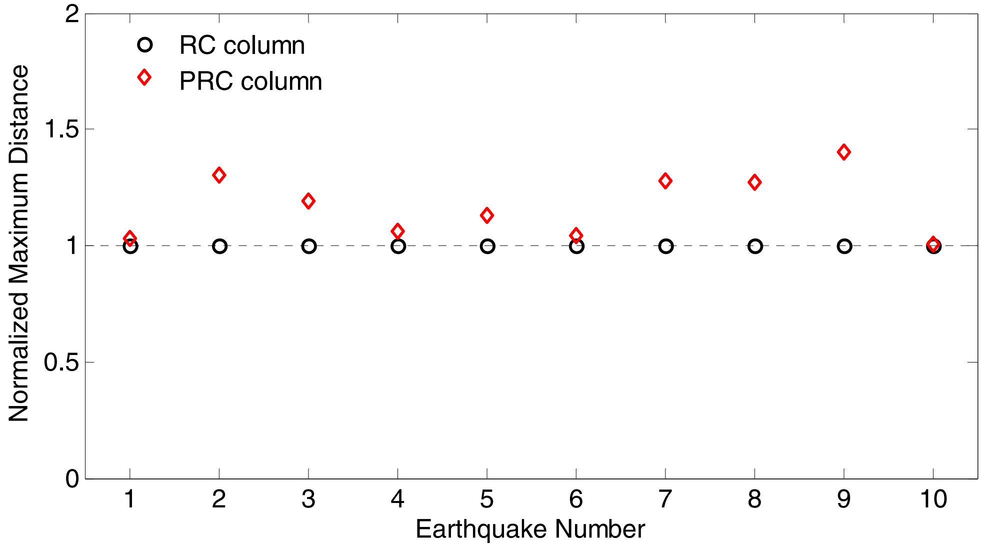

(a) Maximum displacement

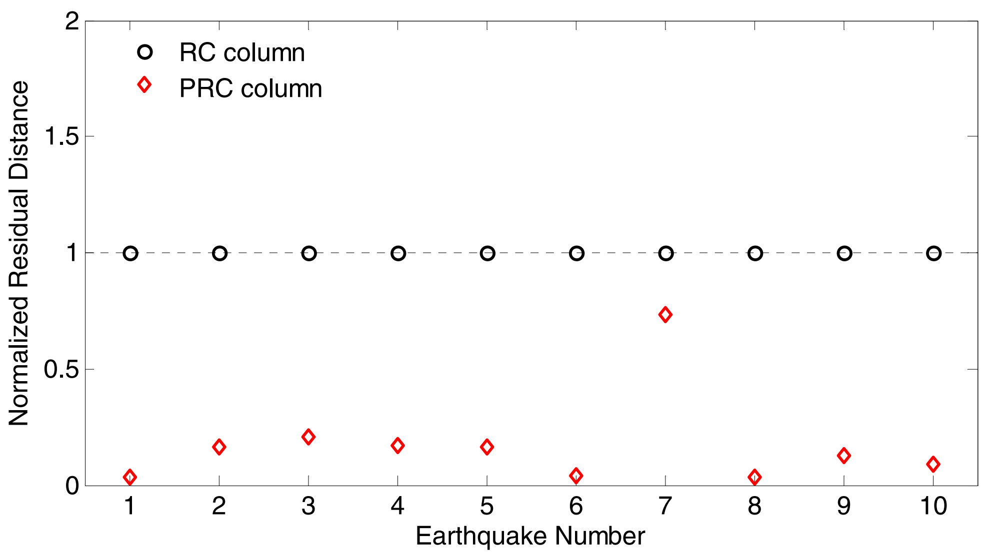

(b) Residual displacement

Fig. 6.7 Normalized maximum and residual displacement of RC and PRC columns for 2%-in-50-yrs. hazard level

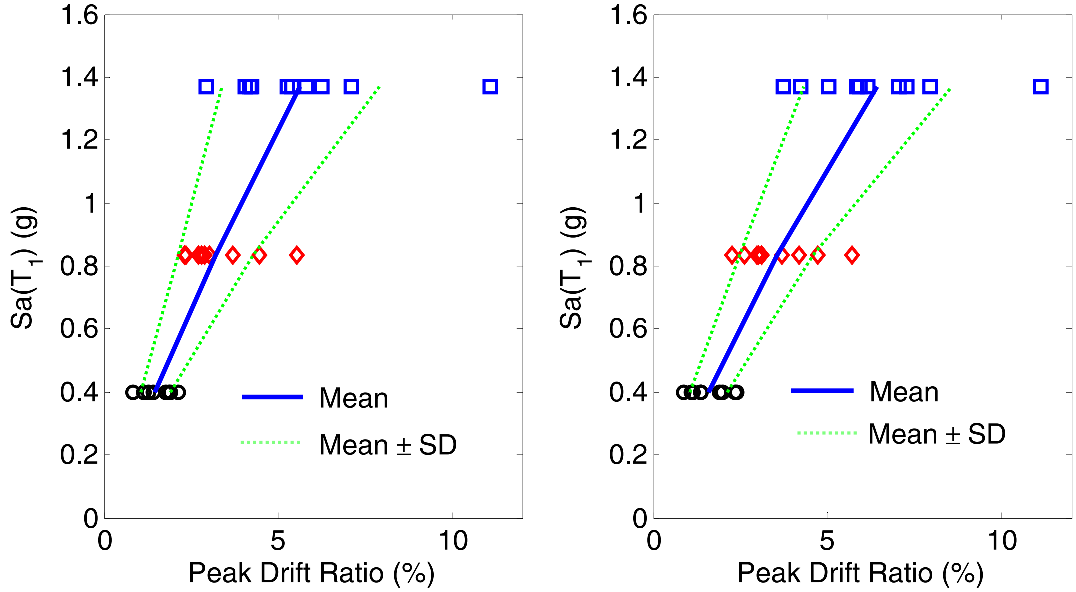

(a) RC column (b) PRC column

Fig. 6.8 Comparison of peak drift ratios at different hazard levels

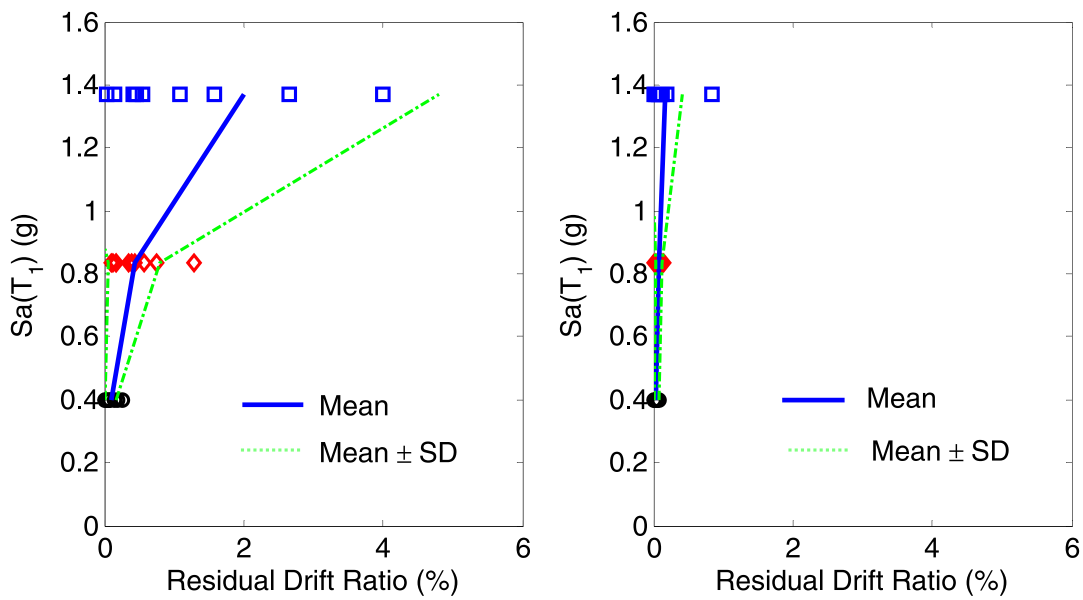

(a) RC column (b) PRC column

Fig. 6.9 Comparison of residual drift ratios at different hazard levels

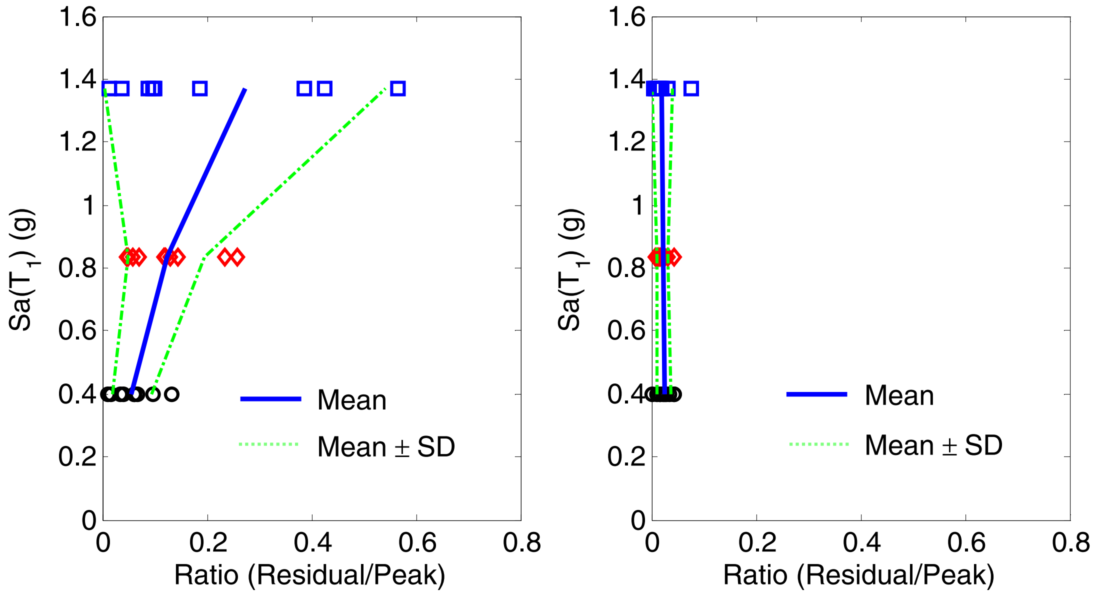

(a) RC column (b) PRC column

Fig. 6.10 Comparison of residual/peak ratios at different hazard levels

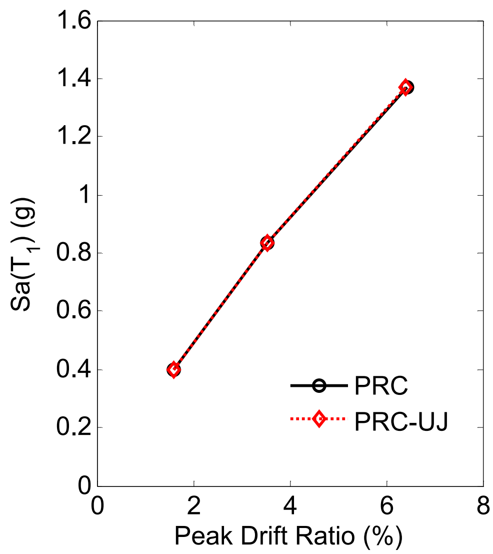

(a) Peak drift ratio

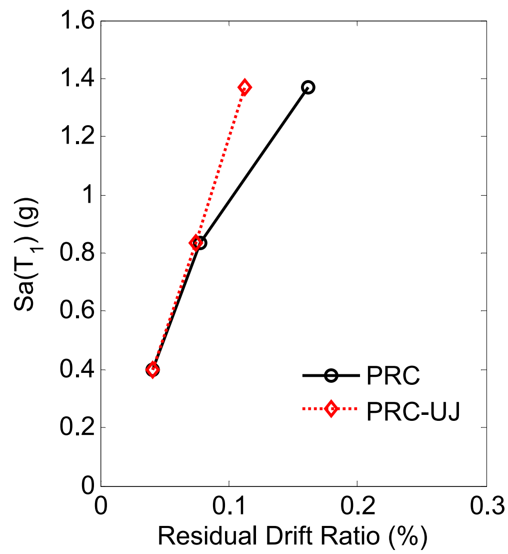

(b) Residual drift ratio

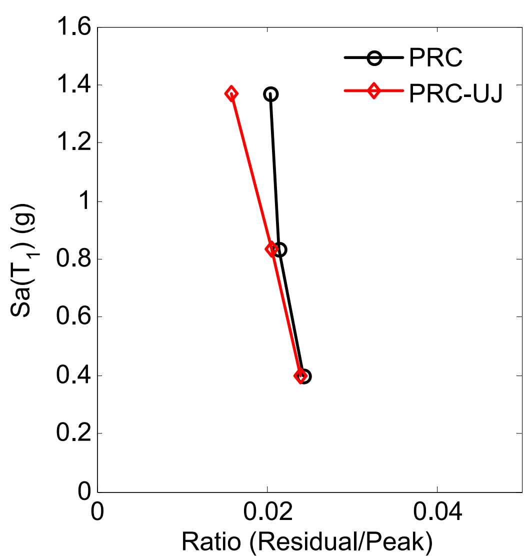

(c) Ratio (residual/peak)

Fig. 6.11 Comparison of concrete confinement effects

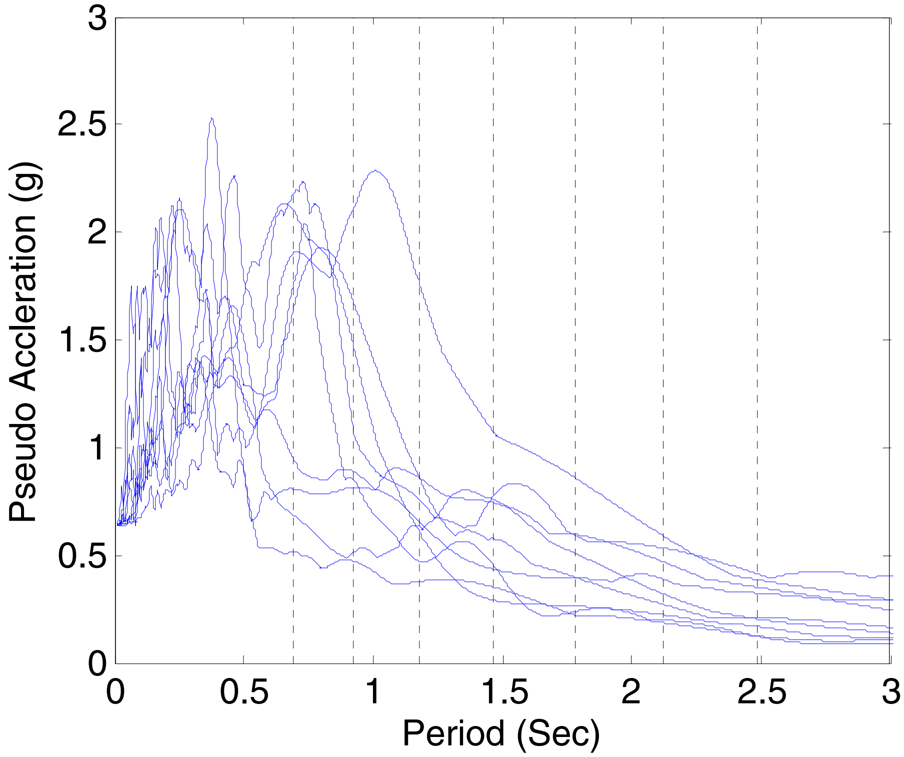

Fig. 6.12 Scaled response spectrum for an IM (PGA = 0.64*g*]

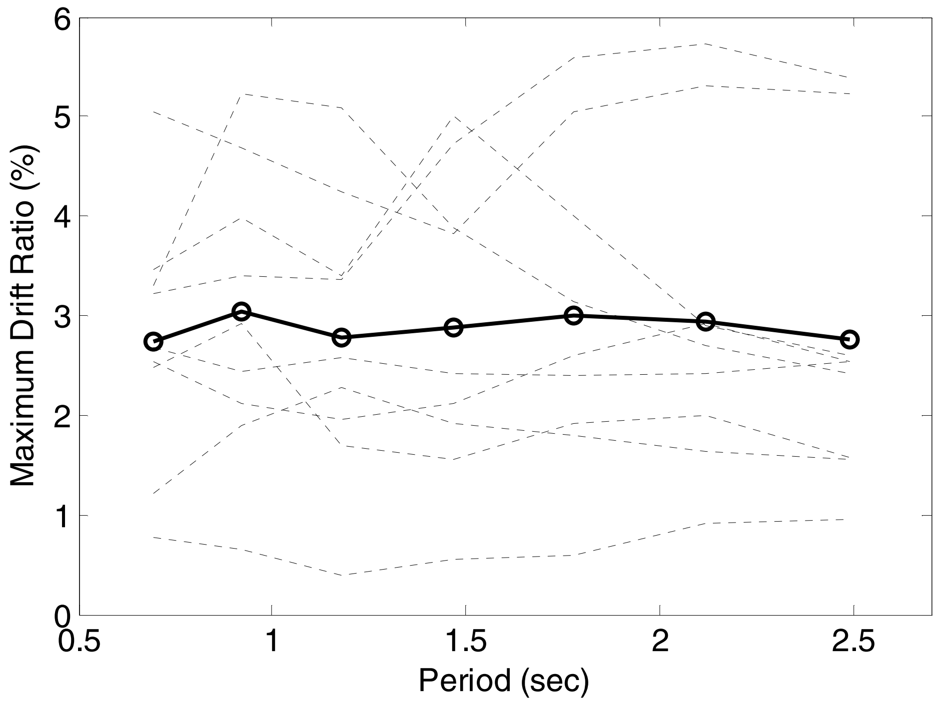

(a) RC column

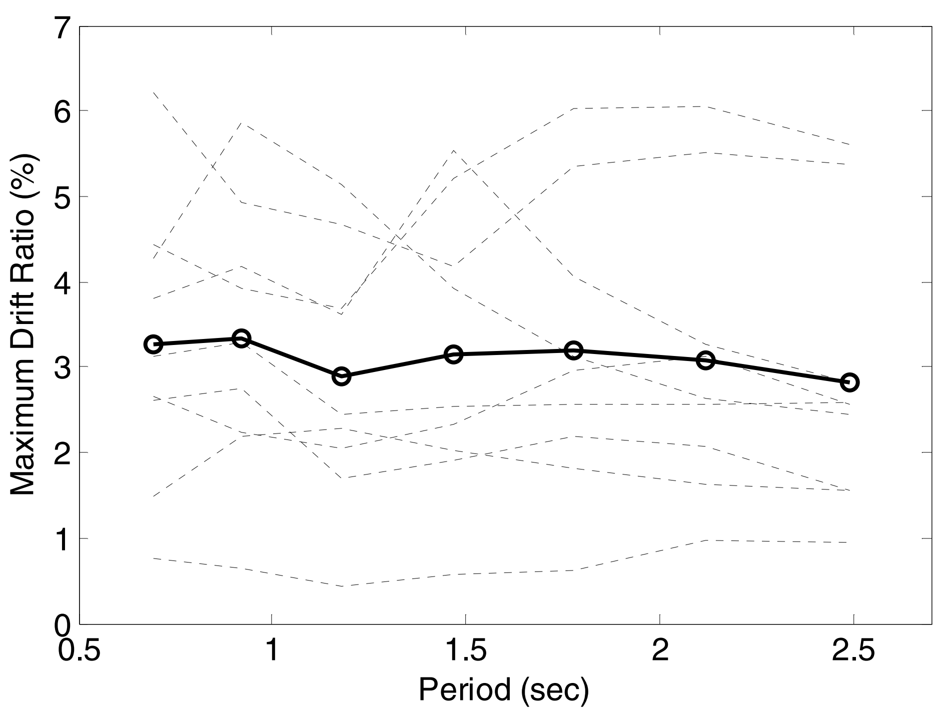

(b) PRC column

Fig. 6.13 Maximum drift ratio response spectra (2%-in-50 yrs.)

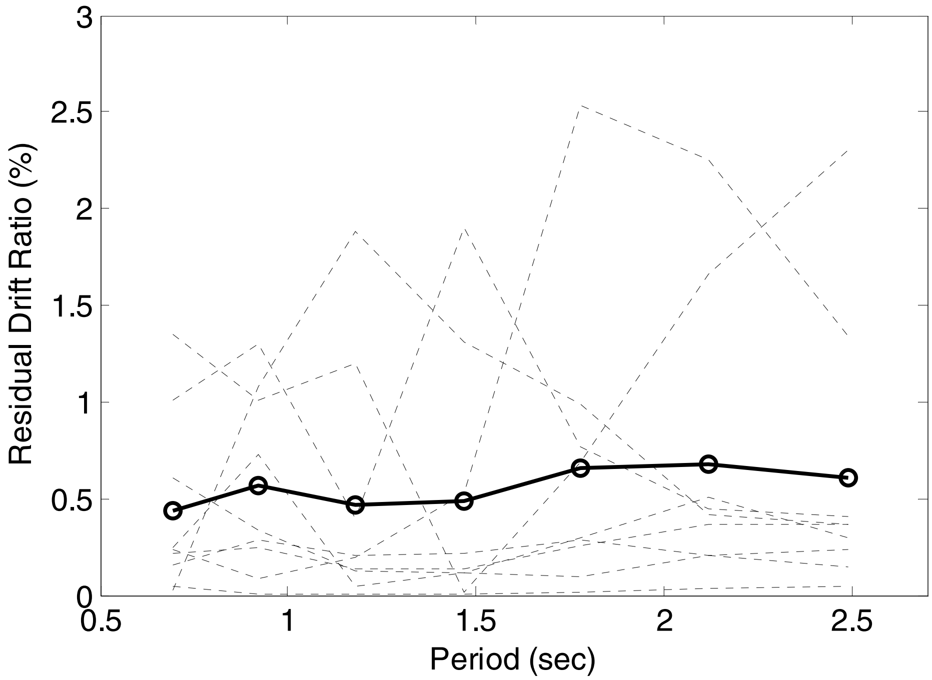

(a) RC column

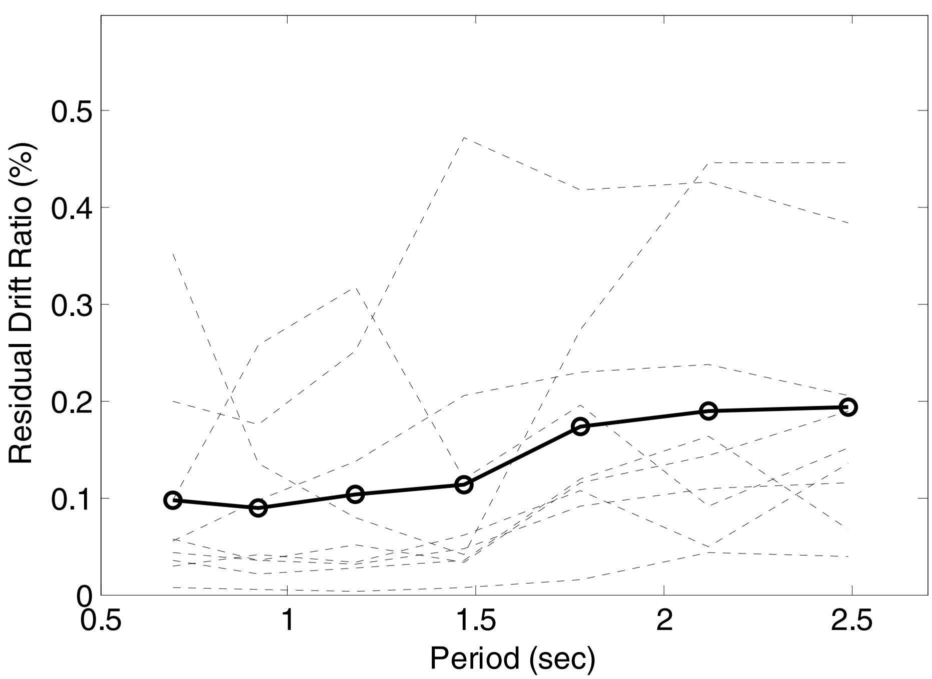

(b) PRC column (different scale shown for clarity)

Fig. 6.14 Residual drift ratio response spectra (2%-in-50 yrs.)

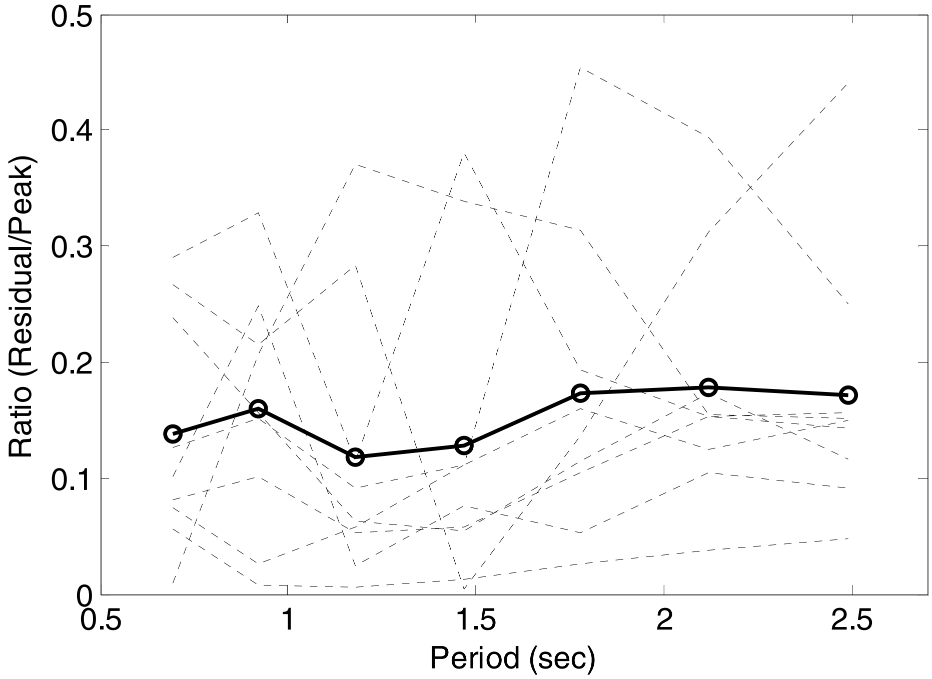

(a) RC column

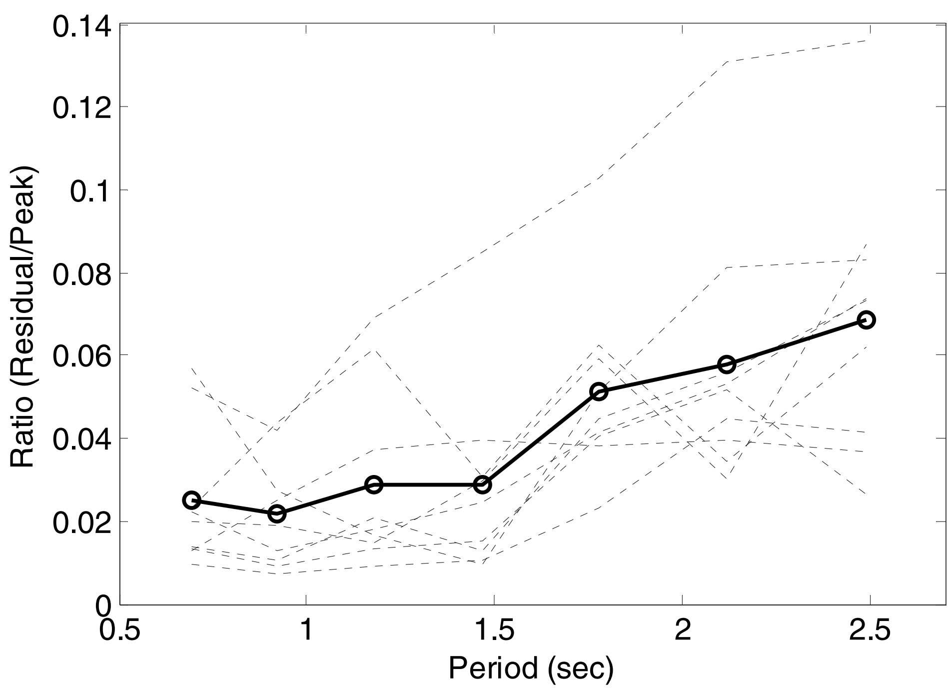

(b) PRC column

Fig. 6.15 Ratio (residual/peak) response spectra (2%-in-50 yrs.)

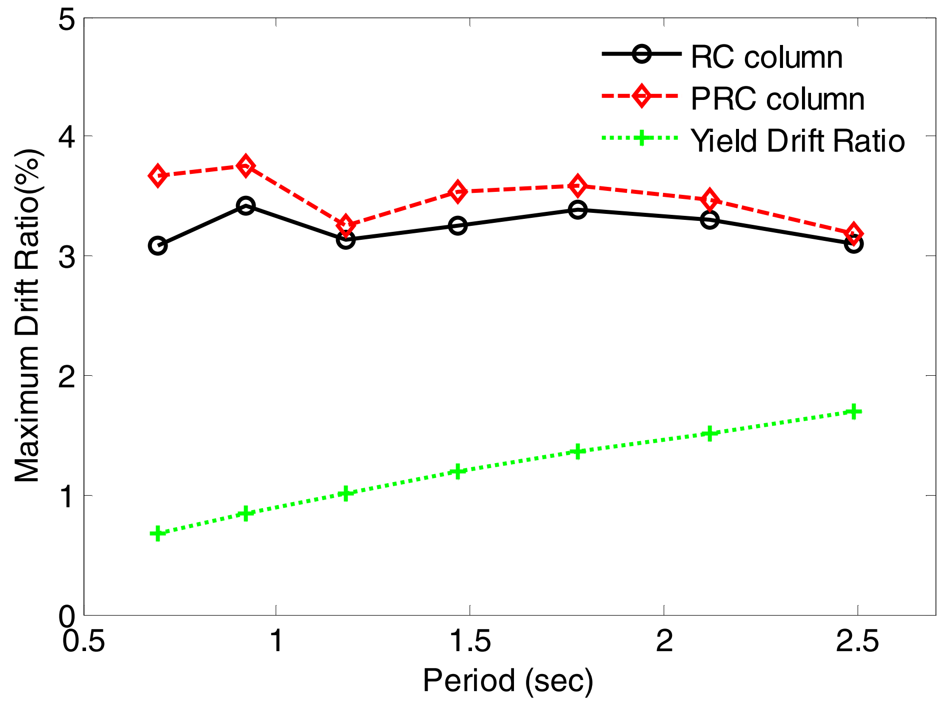

(a) Maximum distance

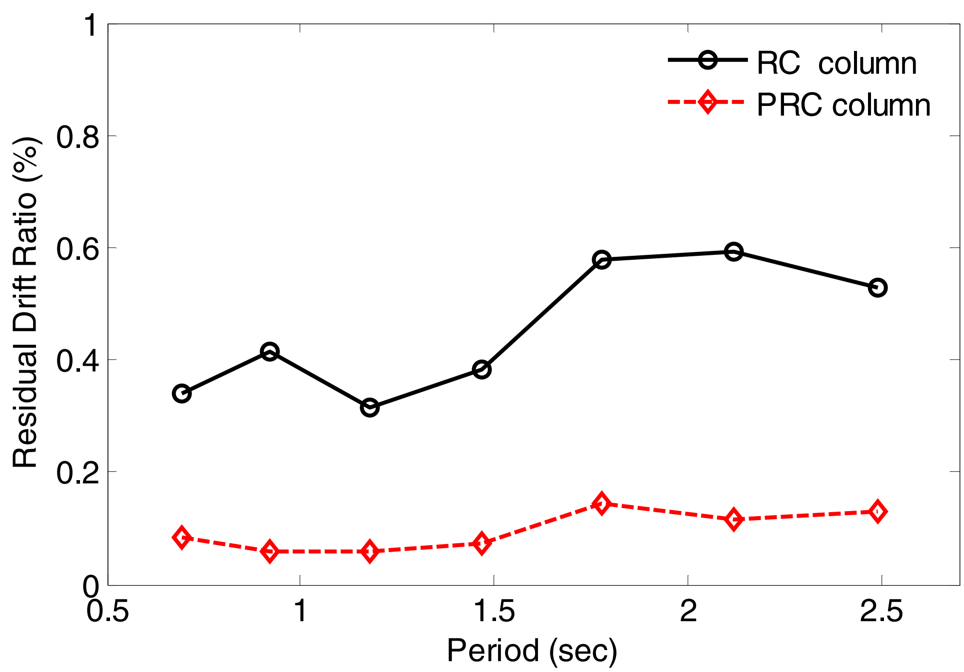

(b) Residual distance

Fig. 6.16 Mean maximum and residual response spectra (2%-in-50 yrs.)

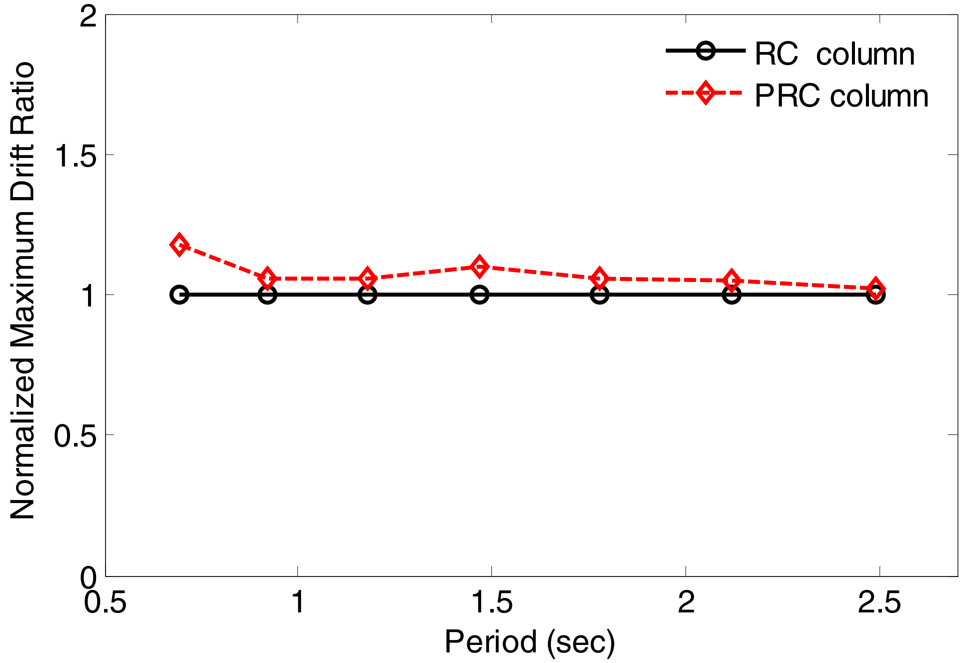

(a) Maximum distance

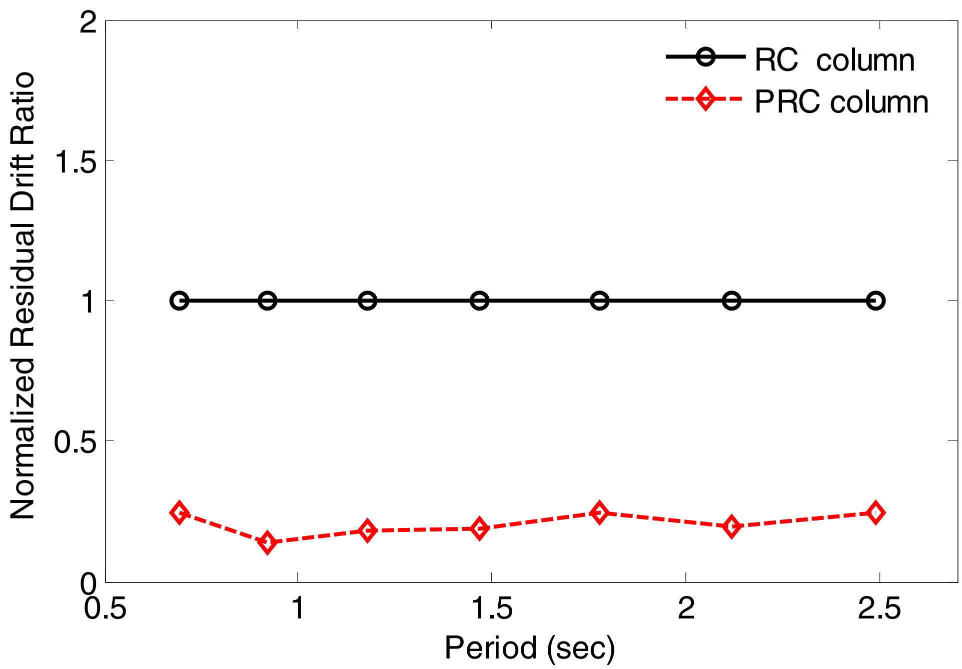

(b) Residual distance

Fig. 6.17 Mean normalized maximum and residual response spectra (2%-in-50 yrs.)

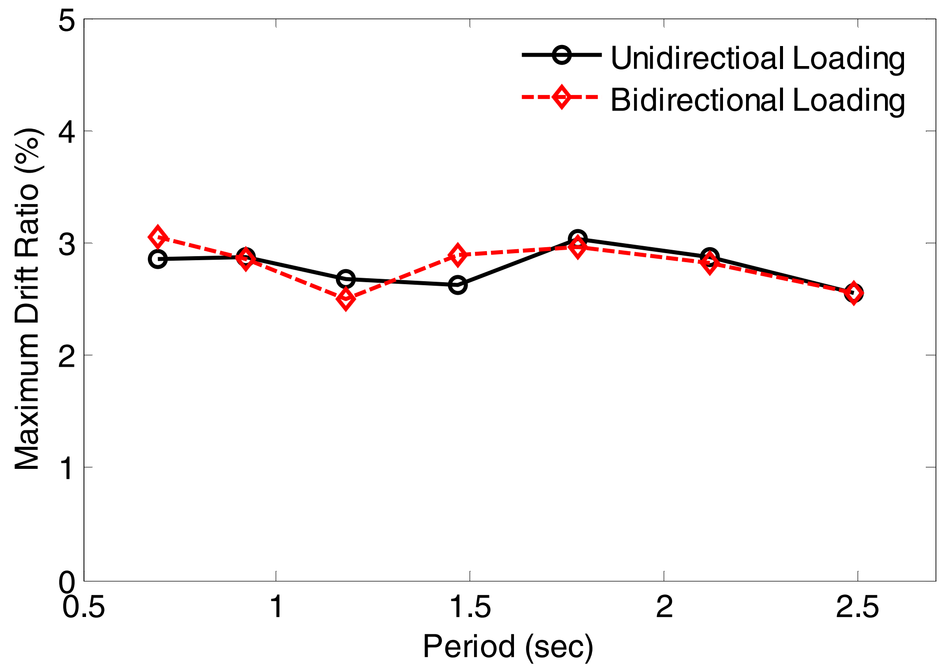

(a) *X* direction

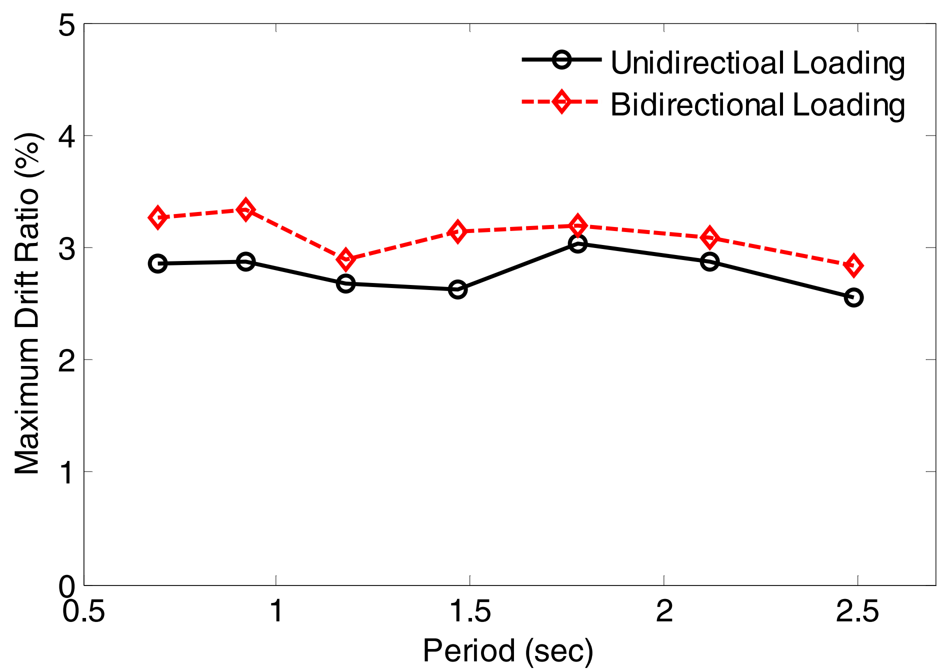

(b) SRSS value (square root sum of squares)

Fig. 6.18 Maximum distance response spectra (2% in-50 yr) of PRC column (bidirectional and unidirectional loading)

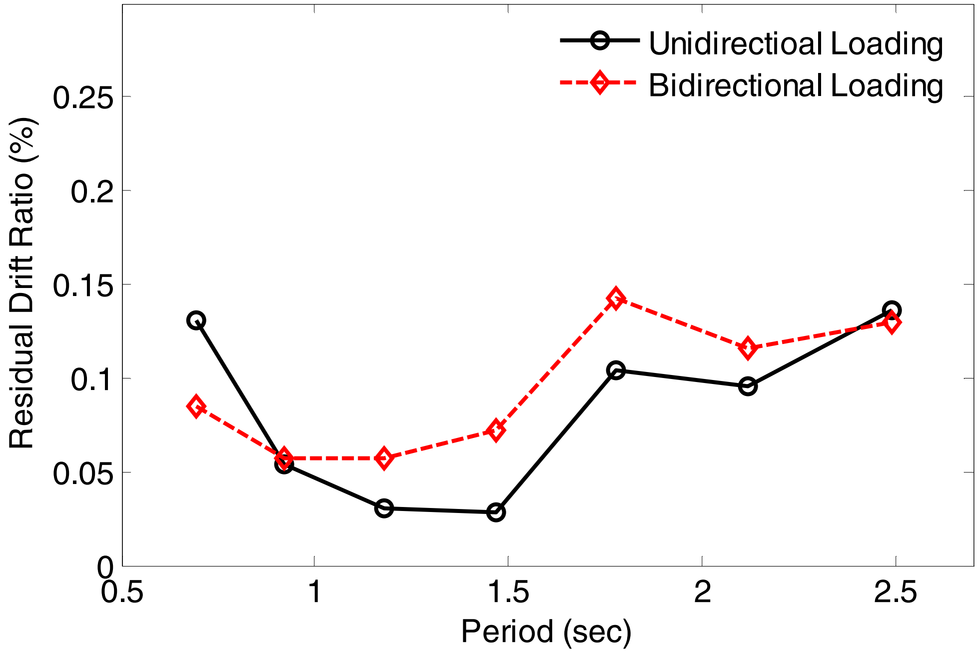

(a) *X* direction

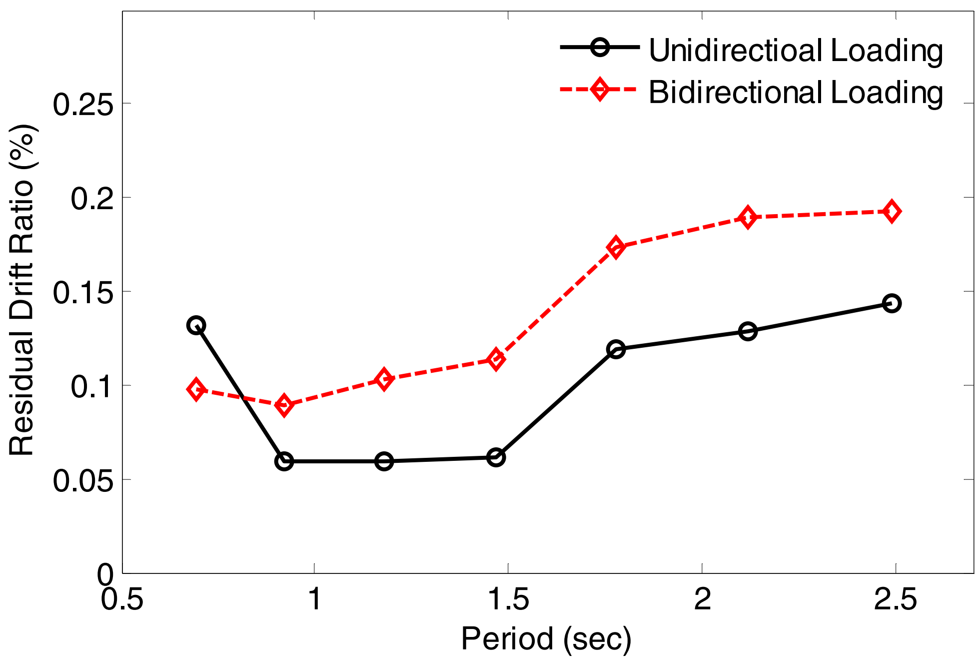

(b) SRSS value (square root sum of squares)

Fig. 6.19 Residual distance response spectra (2%-in-50 yrs.) of PRC column (bidirectional and unidirectional loading)

7 Conclusions

As part of a long-term research program to improve the post-earthquake functionality of conventional reinforced concrete bridges, a series of experimental and analytical investigations has been conducted to assess and improve the ability of partially prestressed reinforced concrete columns to reduce the residual displacements resulting from severe ground shaking. The research reported herein builds on earlier research on this topic by Sakai and Mahin (2004, 2006). The specific research objectives of the work reported herein were to develop and validate new refined design methods for bridge columns that inherently have relatively small residual displacements following severe earthquake shaking; to develop and validate analytical methods and models that can accurately capture key performance attributes of conventional concrete columns and unbonded post-tensioned concrete columns under earthquake excitation using the test data; and to evaluate the effect of different ground motions and different column configurations.

7.1 EXPERIMENTAL INVESTIGATION OF ONE-COLUMN SPECIMENS

A series of four 1/4.5 scale shaking table tests was conducted to assess the ability of partially prestressed reinforced concrete columns with unbonded post-tensioning tendons to reduce residual displacements resulting from strong earthquake ground motions. The specific objectives of this test were to examine the effect of debonding the mild reinforcing bars in the area of the expected plastic hinge, to study the effect of incorporating steel jacketing combined with local unbonding of the mild reinforcement, and to investigate the effects of magnitude on the prestressing force.

Below are the conclusions determined from the shaking table tests:

- All four specimens exhibited similar maximum cumulative response displacement (SRSS) of about 4.8 in. (122 mm) during the first design-level excitation, for a displacement ductility of 5. During the maximum-level test, the maximum cumulative response displacements (SRSS) increased up to about 10 in. (254 mm) for all four specimens. The higher prestressing force specimen PRC-U2 and steel jacket specimen PRC-UJ exhibited slightly lower responses, but the difference was modest.

- After the design-level test, all specimens demonstrated an impressive ability to re-center. The cumulative residual displacements (SRSS) for all these specimens were smaller than a drift of 0.1%, corresponding to about 10% of the yield displacement. The cumulative residual displacements (SRSS) increased during the maximum-level test and showed more variability from specimen to specimen, but all were less than 2.5 in. (63 mm) (< 2.5% drift). The cumulative residual displacements (SRSS) were 2.30 in. (58 mm) (2.3% drift), 0.61 in. (15 mm) (0.6% drift), 2.05 in. (52 mm) (2.1% drift), and 0.93 in. (24 mm) (0.9% drift) for specimens PRC-U, PRC-UJ, PRC-2, and PRC-U2, respectively, demonstrating that incorporating the steel jacket and higher prestressing force effectively reduces the residual displacement after strong ground excitation. Similarly, unbonding of the longitudinal mild reinforcement reduces steel strain somewhat, but results in much lower post-yield tangent stiffness and larger residual displacement.
- All four specimens showed similar lateral force versus lateral displacement hystereses until the design-level test. As noted previously (Sakai and Mahin 2006), upon unloading, the force-displacement relations projected onto the *x*- and *y*-axes did not show a characteristic origin-oriented hysteresis shape. During the maximum-level test, specimens PRC-U and PRC-U2 (with the unbonded mild reinforcing bars) exhibited slightly negative post-yield tangential lateral stiffness, corroborating the results of previous analysis. Incorporating the steel jacket in specimen PRC-UJ resulted in a modestly positive post-yield tangential lateral stiffness.
- Observed local damage of all specimens (except specimen PRC-UJ) after the design-level tests was very similar. After experiencing a response displacement ductility demand of 5, no core concrete crushing, no buckling of longitudinal reinforcement, and no fracture of longitudinal and spiral reinforcement was observed. After the maximum-level tests, however, some of longitudinal rebar of specimens PRC-U and PRC-U2 were buckled and one spiral bar of specimen PRC-2 was fractured. Specimen PRC-UJ showed moderate “elephant foot” buckling at the bottom of the steel jacket; in order to prevent this type of damage, Caltrans requirements stipulate that a gap be provided between the bottom of the jacket and the top of the footing.

- During the second design-level test following the maximum level excitation, all of the longitudinal rebar of specimen PRC-U2 buckled and two bars fractured; two of the longitudinal rebar of specimen PRC-2 fractured as well.
- For all four specimens, the tendon remained elastic during the tests.
- Comparing the responses of specimens PRC-U and PRC-2 showed that unbonding of the mild bar resulted in a shorter plastic hinge region and a slightly larger maximum displacement and residual displacement, most likely due to the lower flexibility and negative post-yield stiffness in the x and y directions.
- As might be expected, the use of a higher prestressing force decreased the maximum displacements and residual displacements when subjected to the design and maximum-level tests, but the damage to specimen PRC-U2 was more severe than to specimen PRC-U, due to the effect of the higher prestressing force.
- A confining steel jacket sheathing a partially prestressed reinforced concrete column with locally unbonded mild reinforcement prevented any significant observable damage throughout the entire test program. For the design-level excitation, the residual drift index of specimen PRC-UJ was less than 0.1%, and remained less than 0.6% even for the maximum-level test. This test program demonstrates the substantial benefits of partially prestressed reinforced concrete columns with locally unbonded mild reinforcement and surrounded by a steel jacket.

7.2 EXPERIMENTAL INVESTIGATION OF A TWO-COLUMN BENT SPECIMEN

To evaluate the practical application of the re-centering system to a more realistic bridge system, a series of shaking table tests was conducted on a two-column model of a single-column viaduct. The specific objective of this testing was to validate the beneficial effect of sheathing with a steel jacket and unbonding the mild reinforcing bars in the vicinity of the expected plastic hinge for a two-column bent system.

Below are the conclusions determined from the shaking table tests:

- The cumulative peak displacements were larger in the transverse (x) direction of the viaduct, equaling 4.23 in. (107.4 mm) and 4.44 in. (112.8 mm) for the long column and short column, respectively. During the maximum-level test, the cumulative maximum response displacements from the origin were 7.7 in. (196 mm) and 8.7 in. (221 mm) for the long column and short column, respectively, corresponding to a nominal displacement ductility of about 8.

- After the design-level test, the specimen demonstrated an ability to re-center. The cumulative residual displacements for the two columns were smaller than a drift of 0.1%, corresponding to about 10% of the yield displacement. But the cumulative residual displacements from the origin greatly increased during the maximum-level test; the cumulative residual displacements from the origin were 3.78 in. (96 mm) and 4.18 in. (106 mm) for the long column and short column, respectively.
- During the design-level test, both columns showed similar lateral force versus lateral displacement hystereses as they moved away from the origin in the *x* and *y* directions. The results do not show negative post-yield stiffness; however, the residual displacement was larger in the maximum-level test.
- The design-level test resulted in some additional cracks in the middle of the columns, but no spalling of the cover concrete was observed. For each column, a large crack was found at the joint of the column and footing in the gap between the steel jacket and footing. A small crack was also detected in this area at the joint of the column and top block for each column. The maximum-level earthquake caused an increase in displacement demand and resulted in the opening of a large crack and crushing at the bottom of the column between the steel jacket and the footing. The cracks enlarged in the middle of the column away from the jackets, but still no spalling of the cover concrete was observed. Until the maximum-level test, no damage was observed at the steel jacket.
- For both columns, the tendon remained elastic during the tests.

7.3 DEVELOPMENT AND VALIDATION OF ANALYTICAL MODELS

Based on the comparison of measured global responses and nonlinear analysis for different specimens, analytical models for predicting the seismic performance, especially residual displacement, of reinforced concrete bridge columns were devised from available material and element models in OpenSees.

The following are the general findings from the analysis of different parametric modelings:

- The analytical response is very sensitive to natural frequency in the elastic system. When the elastic response governs at lower-level excitations, it is important to match the natural frequency of the system in order to achieve good agreement between the measured and the calculated results. It is difficult to control natural frequency of the analytical model using a nonlinear beam-column element; the natural frequency can be controlled by changing the effective flexural stiffness with a beam with hinges element.
- In contrast, at the higher levels (design and maximum) the maximum responses are controlled by the material nonlinearity of the system. The analytical results are not so sensitive to the natural frequency.
- The maximum response quantities (displacement, shear, acceleration) at higher levels are not sensitive to different material hysteretic models; regardless of the different steel and concrete models considered, the maximum responses are similar.
- Residual displacements are very sensitive to modeling of material hysteretic relations and viscous damping. The following are parameters that affect residual displacement in column modeling:
    - Concrete descending branch and the character of the unloading and reloading region;
    - Steel hardening ratio (a lower value gives some residual);
    - Isotropic hardening in steel (using a small value for the isotropic hardening option in the compression region gives some residual displacement); and
    - Damping ratio (lower damping in higher level analysis gives more residual displacement).

The comparison of the dynamic analysis and the test results for each specimen suggests the following important observations:

- After studying different modeling parameters of the RC specimen, an analytical model that gives good agreement with the measured results is suggested for modeling a reinforced cantilever concrete bridge column.
- The analytical results using a co-rotational truss element with initial strain to represent the unbonded prestressing tendon for specimen PRC (which is otherwise identical to the RC specimen model) give good agreement with the measured results.
- The analytical results for the PRC-2 specimen closely match the test results for several global responses. The analysis of the PRC-2 specimen confirms that the analytical model for specimen PRC is appropriate with different material parameters.

- The analytical results for the PRC-U specimen provide a very good match with the test results for global responses at the design level. There are slightly greater differences at the maximum level, especially in residual displacement. The differences might come from the difficulty of modeling unbonded rebar at the plastic hinge region.
- The analytical results for the PRC-U2 specimen using a different initial strain for the co-rotational truss element to reproduce the higher post-tensioning force match well with the test results for global responses. There are some differences at the maximum level in the *y* direction, especially in residual displacement.
- The analytical results for specimen PRC-UJ using the constitutive model by Mander at al. (1988) for modeling the steel jacket by treating the steel jacket as a continuous spiral match well with the test results for global responses, except for small errors in residual displacement at the maximum level.
- The analytical results for maximum response of the PRC-system specimen model (based on the analytical model of the PRC-UJ specimen) are well matched through all the test levels with measured response, but the residual displacement responses reveal quite a difference between the analytical and test results at both the design and maximum levels. The analysis shows almost no residual displacement, as expected, but the test results show some residual displacement. This is apparently due to the severe localized damage in the gap between the steel jackets and the footing.

Based on the findings of the analysis, the following recommendations are made regarding the modeling of RC and PRC columns [indicates OpenSees object]:

- Column modeling:
  - Beam with hinge (BWH) model [beamWithHinges element];
  - Priestley plastic hinge length; and
  - Effective stiffness for the elastic region of the BWH model: 0.2–0.3 EI for RC column with a lower axial force, 0.4–0.6 EI for PRC column with a higher axial force;
- Concrete modeling:
  - [Concrete02] with the following suggested descending parameters for confined concrete:
    - Suggested residual stress (f_{cu}) is 50–70% of peak compressive stress (f'_c);

- Suggested strain at ultimate stress(ε_{cu}) is 2.5–3.0 times the strain at peak compressive stress (ε_{co});

- Steel modeling: [ReinforcingSteel];
- Damping: stiffness-only damping (2–3%); and
- Prestressing tendon: co-rotational truss element [CorotTruss] with initial strain.

7.4 PARAMETRIC STUDY

Using the model developed in this study, parametric studies were performed to evaluate the effect of different ground motions and different column configurations.

From the analyses presented herein, the following conclusions are determined:

- The residual displacements of the re-centering column (PRC) are significantly smaller than those of a comparable conventional reinforced concrete column (RC) for all the ground motions. The use of unbonded prestressing strands in reinforced concrete columns is demonstrated for a wide variety of column geometries and periods to be an effective method to reduce residual displacements after earthquake excitations.
- The coefficients of variance (C.V.) of the maximum displacements of the RC and PRC columns are much lower than those of the residual displacements of both columns.
- The enhancement of confinement effect by using steel jacketing or other jacketing material in the PRC column reduces the residual displacement.
- The residual distances of the PRC column are generally smaller than those of the conventional column regardless of period range.
- For the PRC column, the ratios between residual and peak distance response spectra of mean value for the 2%-in-50-years intensity level increase from 0.02 to 0.06 as the natural period increases for each earthquake, while the ratios in the RC column remain between 0.1 and 0.2.
- The maximum drift ratios of the *x* direction for unidirectional and bidirectional loading are very close for all aspect ratios, while those of the SRSS values increase for bidirectional loading. The *x*-direction residual drifts for bidirectional loading are larger than those of unidirectional loading in most cases.

7.5 RECOMMENDATIONS FOR FUTURE RESEARCH

This research has provided valuable information on developing a self-centering reinforced concrete column system and analytical models for RC and PRC columns. However, several issues are worth further investigation to apply this system to the real bridge structure. Some of them are briefly described below:

- From the results of experiments, several technical aspects of the details of re-centering column systems deserve further research: the gap at the jacket; the length or unbonding of the jacket; the need for shear reinforcement at the interface of the column and footing; the use of engineered cementitious composite (ECC) or fiber-reinforced concrete in the plastic hinge region compared to steel or composite jacketing; and unbonding methods and length of mild reinforcement could be considered.
- Additional large-scale experimental research is needed to refine and confirm design details, especially for actual detailing employed in the field, and to understand the seismic response of entire bridge systems incorporating these details.
- The prediction of residual displacements is generally difficult, and the results are very sensitive to the model parameters. In this research, some of the parameter values are suggested that match the test results, but an in-depth study to develop a refined analytical model is suggested. The following modeling parameters could be considered:
    - The descending branch and loading and unloading behavior of concrete modeling;
    - The hardening ratio and isotropic hardening aspect of steel modeling; and
    - Other factors such as bar slip and damping.
- A wide range of bridge structures with different design parameters for re-centering columns, including column diameter, height, span length, longitudinal bar ratio, prestressing force ratio, and prestressing tendon, need to be analyzed to give detailed design guidelines for self-centering bridge systems.
- Fundamental study to identify aspects of structure and ground motion that affect residual displacement deserves further investigation.

REFERENCES

Berry, M. P., and Eberhard, M. O. (2006). “Modeling of reinforced concrete bridge columns.” Presentation at the PEER annual meeting, San Francisco, California.

Billington, S. L., and Yoon, J. K. (2004). “Cyclic response of unbonded post-tensioned precast columns with ductile fiber-reinforced concrete.” *ASCE J. Bridge Engineering*, 9(4): 353–363.

Blakeley, R. W. G., and Park, R. (1971). “Seismic resistance of prestressed concrete beam-column assemblies.” *J. ACI*, 68(57): 677–692.

California Department of Transportation (2004). *Bridge design specifications*. Sacramento, CA.

California Department of Transportation (2001). *Seismic design criteria, ver. 1.2*. Sacramento, CA.

Chang, G., and Mander, J. (1994). *Seismic energy-based fatigue damage analysis of bridge columns: part I – evaluation of seismic capacity*. Report No. NCEER-94-0006, Department of Civil and Environmental Engineering, State University of New York at Buffalo, NY.

Cheng, C-T. (2007). “Energy dissipation in rocking bridge piers under free vibration tests.” *Earthquake Engineering and Structural Dynamics*, 36(4): 503–518.

Chou, C-C., and Chen, Y-C. (2006). “Cyclic tests of post-tensioned precast CFT segmental bridge columns with unbonded strands.” *Earthquake Engineering and Structural Dynamics*, 35(2): 159–175.

Christopoulos, C., Filiatrault, A., and Folz, B. (2002a). “Seismic response of self-centering hysteretic SDOF systems.” *Earthquake Engineering and Structural Dynamics*, 31(5): 1131-1150.

Christopoulos, C., Filiatrault, A., Uang, C-M., and Folz, B. (2002b), “Post-tensioned energy dissipating connections for moment-resisting steel frames.” *ASCE J. Structural Engineering*, 128(9): 1111–1120.

Cornell, C. A. (1996). “Calculating building seismic performance reliability: a basis for multi-level design norms.” *Proc. of 11th Conference on Earthquake Engineering*, Paper No. 2122, Acapulco, Mexico.

Dodd, L., and Restrepo-Posada, J. (1995). “Model for predicting cyclic behavior of reinforcing steel.” *ASCE J. Structural Engineering*, 121(3): 433–445.

El-Sheikh, M. T., Sause, R., Pessiki, S., and Lu, L-W. (1999). “Seismic behavior and design of unbonded post-tensioned precast concrete frames.” *PCI J.*, 44(3): 54–71.

Espinoza, A. and Mahin, S. (2006). "Rocking of bridge piers subjected to multi-directional earthquake loading." *Proc. of 8th National Conference on Earthquake Engineering,* Paper No. 965, EERI, San Francisco, CA.

Hachem, M. M., Mahin, S. A., and Moehle, J. P. (2003). *Performance of circular reinforced concrete bridge columns under bidirectional earthquake loading*. Report No. PEER-2003/06, Pacific Earthquake Engineering Research Center, University of California, Berkeley, CA.

Hewes, J. T., and Priestley, M. J. N. (2002). *Seismic design and performance of precast concrete segmental bridge columns*. Report No. SSRP-2001-25, University of California at San Diego, La Jolla, CA.

Holden, T. J., Restrepo, J. I., and Mander, J. B. (2003). "Seismic performance of precast reinforced and prestressed concrete walls." *ASCE J. of Structural Engineering*, 129(3): 286–296.

Iemura, H., and Takahashi, Y. (2000). "Development of high seismic performance RC piers with unbonded bars." *Proc. of 1st Symposium for the Enhancement of Earthquake Performance of Infrastructures Based on Investigation into Fracturing Process*, Japan.

Iemura, H., Takahashi, Y., and Sogabe, N. (2002). "Innovation of high-performance RC structure with unbonded bars for strong earthquakes." *JSCE J. Structural Mechanics and Earthquake Engineering*, 710(I-60): 283–296 (in Japanese).

Ikeda, S. (1998). "Seismic behavior of reinforced concrete columns and improvement by vertical prestressing." *Proc. of 13th FIP Congress: Challenges for Concrete in the Next Millennium*, Balkema, Rotterdam, The Netherlands, 1: 879–884.

Japan Road Association. (1996). *Design specification of highway bridges: part V – seismic design.* Japan (in Japanese).

Japan Road Association. (2002). *Design specification of highway bridges: part V – seismic design.* Japan (in Japanese).

Karsan, I. D., and Jirsa, J. O. (1969). "Behavior of concrete under compressive loading." *ASCE J. Structural Division*, 95(ST-12).

Kawashima, K., MacRae, G. A., Hoshikuma, J., and Nagaya, K. (1998). "Residual displacement response spectrum and its application." *ASCE J. Structural Engineering*, 124(5): 523–530.

Kawashima, K., Watanabe, G., Sakeraraki, D., and Nagai, T. (2005). "Rocking isolation of bridge foundations." *Proc. of 9th World Seminar on Seismic Isolation, Energy Dissipation and Active Vibration Control of Structures*, Kobe, Japan, 609-630.

Kennedy,R. P., Short, S. A. (1994). *Basis for seismic provisions of DOE-STD-1020.* UCRL-CR-111478, Technical report prepared for U.S. Department of Energy, Washington, D.C.

Kim, J., Stanton, J., MacRae, G., Day, S., and Sugata, M. (2004). “Cyclic load testing of precast hybrid frame connections.” *Proc. of 13th World Conference on Earthquake Engineering*, Paper No. 1671, Vancouver, Canada.

Krawinkler, H., and Moncarz, P. D. (1982). “Similitude requirements for dynamic models.” *Dynamic Modeling of Concrete Structures, ACI SP 73-1*, Detroit, MI, 1–22.

Kunnath, S. K. (2007). *Application of the PEER PBEE methodology to the I-880 viaduct*. Report No. PEER-2006/10, Pacific Earthquake Engineering Research Center, University of California, Berkeley, CA.

Kurama, Y. C. (2000). “Seismic design of unbonded post-tensioned precast concrete walls with supplemental viscous damping.” *ACI Structural J.*, 97(4): 648–658.

Kurama, Y. C., Sause, R., Pessiki, S., and Lu, L-W. (1999a). “Lateral load behavior and seismic design of unbonded post-tensioned precast concrete walls.” *ACI Structural J.*, 96(4): 622 – 632.

Kurama, Y. C., Pessiki, S., Sause, R., and Lu, L-W. (1999b). “Seismic behavior and design of unbonded post-tensioned precast concrete walls.” *PCI J.*, 44(3): 72–93.

Kurama, Y., Sause, R., Pessiki, S., and Lu, L-W. (2002). “Seismic response evaluation of unbonded post-tensioned precast walls.” *ACI Structural J.*, 99(5): 641–651.

Kurama, Y., Weldon, B., and Shen, Q. (2006). “Experimental evaluation of post-tensioned hybrid coupled wall subassemblages.” *ASCE J. Structural Engineering*, 132(7): 1017–1029.

Kwan, W. P., and Billington, S. L. (2003a). “Unbonded post-tensioned concrete bridge piers: part I – monotonic and cyclic analyses.” *ASCE J. Bridge Engineering*, 8(2): 92 –101.

Kwan, W. P., and Billington, S. L. (2003b). “Unbonded post-tensioned concrete bridge piers: part II – seismic analyses.” *ASCE J. Bridge Engineering*, 8(2): 102 –111.

Lee, W. K. (2007). “Simulation and performance-based earthquake engineering assessment of self-centering post-tensioned concrete bridge systems.” PhD dissertation, Department of Civil and Environmental Engineering, Stanford University, Stanford, CA.

Lee, W. K., and Billington, S. L. (2006). “Performance-based assessment of a self-centering bridge pier system for seismic regions.” *Proc. of 100th Anniversary Earthquake Conference*, San Francisco, CA.

Lee, W. K., Billington, S. L., and Rouse, J. M. (2004). "Damage estimation of a self-centering precast concrete bridge pier system using a performance-based assessment methodology." *Proc. of 13th World Conference on Earthquake Engineering*, Paper No. 1703, Vancouver, Canada.

Mackie, K., and Stojadinović, B. (2004). "Residual displacement and post earthquake capacity of highway bridges." *Proc. of 13th World Conference on Earthquake Engineering*, Paper No. 1550, Vancouver, Canada.

Mander, J. B., and Cheng, C. T. (1997). *Seismic resistance of bridge piers based on damage avoidance design*. Report No. NCEER-97-0014, Department of Civil and Environmental Engineering, State University of New York at Buffalo, NY.

Mander, J. B., Priestley, M. J. N., and Park, R. (1988). "Theoretical stress-strain model for confined concrete." *ASCE J. Structural Engineering*, 114(8): 1804 –1826.

McCormac, J. C. (2004). *Design of Reinforced Concrete*. 6th Ed., Wiley, NY.

The Open System for Earthquake Engineering Simulation. "OpenSees home page." http://opensees.berkeley.edu/index.php

Ou, Y., Wang, J., Chang, K., and Lee, G. C. (2006). "Experimental evaluation of precast prestressed segmental concrete bridge columns." *Proc. of 2006 Structures Congress: Structural Engineering and Public Safety*, Structural Engineering Institute, St. Louis, MO.

Phan, V., Saiidi, M. S., Anderson J., and Ghasemi, H. (2007). "Near-fault ground motion effects on reinforced concrete bridge columns." *ASCE J. Structural Engineering*, 133(7): 982–989.

Priestley, M. J. N., and MacRae, G. A. (1996). "Seismic tests of precast beam-to-column joint subassemblages with unbonded tendons." *PCI J.*, 41(1): 64 –81.

Priestley, M. J. N., and Tao, J. R. (1993). "Seismic response of precast prestressed concrete frames with partially debonded tendons." *PCI J.*, 38(1): 58 –69.

Priestley, M. J. N., Seible, F., and Calvi, G. M. (1996). *Seismic design and retrofit of bridges*. Wiley, NY.

Rahman, A., and Sritharan, S. (2006). "An evaluation of force-based design vs. direct displacement-based design of jointed precast post-tensioned wall systems." *Earthquake Engineering and Engineering Vibration*, 5(2): 285 –296.

Ricles, J. M., Sause, R., Garlock, M. M., and Zhao, C. (2001). "Post-tensioned seismic resistant connections for steel frames." *ASCE J. of Structural Engineering*, 127(2): 113–121.

Ricles, J., Sause, R., Peng, S. W., and Lu, L-W. (2002). "Experimental evaluation of earthquake resistant post-tensioned steel connections." *ASCE J. of Structural Engineering*, 128(7): 850–859.

Ruiz-García, J., and Miranda, E. (2006). "Residual displacement ratios for assessment of existing structures." *Earthquake Engineering and Structural Dynamics*, 35(3): 315 –336.

Sakai, J., and Mahin, S. A. (2004). *Analytical investigations of new methods for reducing residual displacements of reinforced concrete bridge columns*. Report No. PEER-2004/02, Pacific Earthquake Engineering Resource Center, University of California, Berkeley, CA.

Sakai, J., and Mahin, S. A. (2006). *Earthquake simulation tests on reducing residual displacements of reinforced concrete bridge columns*. PEER Report (in preparation), Pacific Earthquake Engineering Resource Center, University of California, Berkeley, CA.

Sakai, J., and Unjoh, S. (2006). "Earthquake simulation test of reinforced concrete bridge column under multidirectional loading." *Proc. of 4th International Workshop on Seismic Design and Retrofit of Transportation Facilities*, MCEER, San Francisco, CA.

Scott, M. H., and Fenves, G. L. (2006). "Plastic hinge integration methods for force-based beam-column elements." *ASCE J. of Structural Engineering*, 132(2): 244 –252.

Somerville, P., and Collins, N. (2002). *Ground motion time histories for the I-880 bridge, Oakland.* Technical report prepared for the PEER testbed project, URS Corporation, Pasadena, CA.

Somerville, P., Smith, N., Punyamurthula, S., and Sun, J. (1997). *Development of ground motion time histories for phase 2 of the FEMA/SAC steel project.* Report No. SAC/BD-97/04, SAC Joint Venture, Richmond, CA.

Stanton, J. F., and Nakaki, S. D. (2001). "Precast concrete frames designed for seismic conditions." *Proc. of 70th Annual Convention*, SEAOC, Sacramento, CA, 161–165.

Stone, W. C., Cheok, G. S., and Stanton, J. F. (1995). "Performance of hybrid moment-resisting precast beam-column concrete connections subjected to cyclic loading." *ACI Structural J.*, 92(2): 229–249.

Taucer, F. F., Spacone, E., and Filippou, F. C. (1991). *A fiber beam-column element for seismic response analysis of reinforced concrete structures*. Report No. UCB/EERC-91/17, Pacific Earthquake Engineering Research Center, University of California, Berkeley, CA.

Yamashita, R., and Sanders, D. (2006). “Seismic performance of unbonded prestressed concrete columns constructed with precast segments.” *Proc. of 100th Anniversary Earthquake Conference*, San Francisco, CA.

Zatar, W. A., and Mutsuyoshi, H. (2001). “Control of residual displacements of RC piers by prestressing.” Technical paper included in *Modeling of inelastic behavior of RC structures under seismic loads*, ASCE, 590–604.

PEER REPORTS

PEER reports are available from the National Information Service for Earthquake Engineering (NISEE). To order PEER reports, please contact the Pacific Earthquake Engineering Research Center, 1301 South 46th Street, Richmond, California 94804-4698. Tel.: (510) 665-3405; Fax: (510) 665-3420.

PEER 2008/06 *Shaking Table Tests and Numerical Investigation of Self-Centering Reinforced Concrete Bridge Columns.* Hyung IL Jeong, Junichi Sakai, and Stephen A. Mahin. September 2008.

PEER 2008/05 *Performance-Based Earthquake Engineering Design Evaluation Procedure for Bridge Foundations Undergoing Liquefaction-Induced Lateral Ground Displacement.* Christian A. Ledezma and Jonathan D. Bray. August 2008.

PEER 2008/04 *Benchmarking of Nonlinear Geotechnical Ground Response Analysis Procedures.* Jonathan P. Stewart, Annie On-Lei Kwok, Yousseff M. A. Hashash, Neven Matasovic, Robert Pyke, Zhiliang Wang, and Zhaohui Yang. August 2008.

PEER 2008/03 *Guidelines for Nonlinear Analysis of Bridge Structures in California.* Ady Aviram, Kevin R. Mackie, and Božidar Stojadinović. August 2008.

PEER 2008/02 *Treatment of Uncertainties in Seismic-Risk Analysis of Transportation Systems.* Evangelos Stergiou and Anne S. Kiremidjian. July 2008.

PEER 2008/01 *Seismic Performance Objectives for Tall Buildings.* William T. Holmes, Charles Kircher, William Petak, and Nabih Youssef. August 2008.

PEER 2007/12 *An Assessment to Benchmark the Seismic Performance of a Code-Conforming Reinforced Concrete Moment-Frame Building.* Curt Haselton, Christine A. Goulet, Judith Mitrani-Reiser, James L. Beck, Gregory G. Deierlein, Keith A. Porter, Jonathan P. Stewart, and Ertugrul Taciroglu. August 2008.

PEER 2007/11 *Bar Buckling in Reinforced Concrete Bridge Columns.* Wayne A. Brown, Dawn E. Lehman, and John F. Stanton. February 2008.

PEER 2007/10 *Computational Modeling of Progressive Collapse in Reinforced Concrete Frame Structures.* Mohamed M. Talaat and Khalid M. Mosalam. May 2008.

PEER 2007/09 *Integrated Probabilistic Performance-Based Evaluation of Benchmark Reinforced Concrete Bridges.* Kevin R. Mackie, John-Michael Wong, and Božidar Stojadinović. January 2008.

PEER 2007/08 *Assessing Seismic Collapse Safety of Modern Reinforced Concrete Moment-Frame Buildings.* Curt B. Haselton and Gregory G. Deierlein. February 2008.

PEER 2007/07 *Performance Modeling Strategies for Modern Reinforced Concrete Bridge Columns.* Michael P. Berry and Marc O. Eberhard. April 2008.

PEER 2007/06 *Development of Improved Procedures for Seismic Design of Buried and Partially Buried Structures.* Linda Al Atik and Nicholas Sitar. June 2007.

PEER 2007/05 *Uncertainty and Correlation in Seismic Risk Assessment of Transportation Systems.* Renee G. Lee and Anne S. Kiremidjian. July 2007.

PEER 2007/04 *Numerical Models for Analysis and Performance-Based Design of Shallow Foundations Subjected to Seismic Loading.* Sivapalan Gajan, Tara C. Hutchinson, Bruce L. Kutter, Prishati Raychowdhury, José A. Ugalde, and Jonathan P. Stewart. May 2008.

PEER 2007/03 *Beam-Column Element Model Calibrated for Predicting Flexural Response Leading to Global Collapse of RC Frame Buildings.* Curt B. Haselton, Abbie B. Liel, Sarah Taylor Lange, and Gregory g. Deierlein. May 2008.

PEER 2007/02 *Campbell-Bozorgnia NGA Ground Motion Relations for the Geometric Mean Horizontal Component of Peak and Spectral Ground Motion Parameters.* Kenneth W. Campbell and Yousef Bozorgnia. May 2007.

PEER 2007/01 *Boore-Atkinson NGA Ground Motion Relations for the Geometric Mean Horizontal Component of Peak and Spectral Ground Motion Parameters.* David M. Boore and Gail M. Atkinson. May. May 2007.

PEER 2006/12 *Societal Implications of Performance-Based Earthquake Engineering.* Peter J. May. May 2007.

PEER 2006/11 *Probabilistic Seismic Demand Analysis Using Advanced Ground Motion Intensity Measures, Attenuation Relationships, and Near-Fault Effects.* Polsak Tothong and C. Allin Cornell. March 2007.

PEER 2006/10 *Application of the PEER PBEE Methodology to the I-880 Viaduct.* Sashi Kunnath. February 2007.

PEER 2006/09 *Quantifying Economic Losses from Travel Forgone Following a Large Metropolitan Earthquake.* James Moore, Sungbin Cho, Yue Yue Fan, and Stuart Werner. November 2006.

PEER 2006/08 *Vector-Valued Ground Motion Intensity Measures for Probabilistic Seismic Demand Analysis.* Jack W. Baker and C. Allin Cornell. October 2006.

PEER 2006/07 *Analytical Modeling of Reinforced Concrete Walls for Predicting Flexural and Coupled–Shear-Flexural Responses.* Kutay Orakcal, Leonardo M. Massone, and John W. Wallace. October 2006.

PEER 2006/06 *Nonlinear Analysis of a Soil-Drilled Pier System under Static and Dynamic Axial Loading.* Gang Wang and Nicholas Sitar. November 2006.

PEER 2006/05 *Advanced Seismic Assessment Guidelines.* Paolo Bazzurro, C. Allin Cornell, Charles Menun, Maziar Motahari, and Nicolas Luco. September 2006.

PEER 2006/04 *Probabilistic Seismic Evaluation of Reinforced Concrete Structural Components and Systems.* Tae Hyung Lee and Khalid M. Mosalam. August 2006.

PEER 2006/03 *Performance of Lifelines Subjected to Lateral Spreading.* Scott A. Ashford and Teerawut Juirnarongrit. July 2006.

PEER 2006/02 *Pacific Earthquake Engineering Research Center Highway Demonstration Project.* Anne Kiremidjian, James Moore, Yue Yue Fan, Nesrin Basoz, Ozgur Yazali, and Meredith Williams. April 2006.

PEER 2006/01 *Bracing Berkeley. A Guide to Seismic Safety on the UC Berkeley Campus.* Mary C. Comerio, Stephen Tobriner, and Ariane Fehrenkamp. January 2006.

PEER 2005/16 *Seismic Response and Reliability of Electrical Substation Equipment and Systems.* Junho Song, Armen Der Kiureghian, and Jerome L. Sackman. April 2006.

PEER 2005/15 *CPT-Based Probabilistic Assessment of Seismic Soil Liquefaction Initiation.* R. E. S. Moss, R. B. Seed, R. E. Kayen, J. P. Stewart, and A. Der Kiureghian. April 2006.

PEER 2005/14 *Workshop on Modeling of Nonlinear Cyclic Load-Deformation Behavior of Shallow Foundations.* Bruce L. Kutter, Geoffrey Martin, Tara Hutchinson, Chad Harden, Sivapalan Gajan, and Justin Phalen. March 2006.

PEER 2005/13 *Stochastic Characterization and Decision Bases under Time-Dependent Aftershock Risk in Performance-Based Earthquake Engineering.* Gee Liek Yeo and C. Allin Cornell. July 2005.

PEER 2005/12 *PEER Testbed Study on a Laboratory Building: Exercising Seismic Performance Assessment.* Mary C. Comerio, editor. November 2005.

PEER 2005/11 *Van Nuys Hotel Building Testbed Report: Exercising Seismic Performance Assessment.* Helmut Krawinkler, editor. October 2005.

PEER 2005/10 *First NEES/E-Defense Workshop on Collapse Simulation of Reinforced Concrete Building Structures.* September 2005.

PEER 2005/09 *Test Applications of Advanced Seismic Assessment Guidelines.* Joe Maffei, Karl Telleen, Danya Mohr, William Holmes, and Yuki Nakayama. August 2006.

PEER 2005/08 *Damage Accumulation in Lightly Confined Reinforced Concrete Bridge Columns.* R. Tyler Ranf, Jared M. Nelson, Zach Price, Marc O. Eberhard, and John F. Stanton. April 2006.

PEER 2005/07 *Experimental and Analytical Studies on the Seismic Response of Freestanding and Anchored Laboratory Equipment.* Dimitrios Konstantinidis and Nicos Makris. January 2005.

PEER 2005/06 *Global Collapse of Frame Structures under Seismic Excitations*. Luis F. Ibarra and Helmut Krawinkler. September 2005.

PEER 2005//05 *Performance Characterization of Bench- and Shelf-Mounted Equipment.* Samit Ray Chaudhuri and Tara C. Hutchinson. May 2006.

PEER 2005/04 *Numerical Modeling of the Nonlinear Cyclic Response of Shallow Foundations.* Chad Harden, Tara Hutchinson, Geoffrey R. Martin, and Bruce L. Kutter. August 2005.

PEER 2005/03 *A Taxonomy of Building Components for Performance-Based Earthquake Engineering.* Keith A. Porter. September 2005.

PEER 2005/02 *Fragility Basis for California Highway Overpass Bridge Seismic Decision Making*. Kevin R. Mackie and Božidar Stojadinović. June 2005.

PEER 2005/01 *Empirical Characterization of Site Conditions on Strong Ground Motion.* Jonathan P. Stewart, Yoojoong Choi, and Robert W. Graves. June 2005.

PEER 2004/09 *Electrical Substation Equipment Interaction: Experimental Rigid Conductor Studies.* Christopher Stearns and André Filiatrault. February 2005.

PEER 2004/08 *Seismic Qualification and Fragility Testing of Line Break 550-kV Disconnect Switches.* Shakhzod M. Takhirov, Gregory L. Fenves, and Eric Fujisaki. January 2005.

PEER 2004/07 *Ground Motions for Earthquake Simulator Qualification of Electrical Substation Equipment.* Shakhzod M. Takhirov, Gregory L. Fenves, Eric Fujisaki, and Don Clyde. January 2005.

PEER 2004/06 *Performance-Based Regulation and Regulatory Regimes.* Peter J. May and Chris Koski. September 2004.

PEER 2004/05 *Performance-Based Seismic Design Concepts and Implementation: Proceedings of an International Workshop.* Peter Fajfar and Helmut Krawinkler, editors. September 2004.

PEER 2004/04 *Seismic Performance of an Instrumented Tilt-up Wall Building.* James C. Anderson and Vitelmo V. Bertero. July 2004.

PEER 2004/03 *Evaluation and Application of Concrete Tilt-up Assessment Methodologies.* Timothy Graf and James O. Malley. October 2004.

PEER 2004/02 *Analytical Investigations of New Methods for Reducing Residual Displacements of Reinforced Concrete Bridge Columns.* Junichi Sakai and Stephen A. Mahin. August 2004.

PEER 2004/01 *Seismic Performance of Masonry Buildings and Design Implications.* Kerri Anne Taeko Tokoro, James C. Anderson, and Vitelmo V. Bertero. February 2004.

PEER 2003/18 *Performance Models for Flexural Damage in Reinforced Concrete Columns.* Michael Berry and Marc Eberhard. August 2003.

PEER 2003/17 *Predicting Earthquake Damage in Older Reinforced Concrete Beam-Column Joints.* Catherine Pagni and Laura Lowes. October 2004.

PEER 2003/16 *Seismic Demands for Performance-Based Design of Bridges.* Kevin Mackie and Božidar Stojadinović. August 2003.

PEER 2003/15 *Seismic Demands for Nondeteriorating Frame Structures and Their Dependence on Ground Motions.* Ricardo Antonio Medina and Helmut Krawinkler. May 2004.

PEER 2003/14 *Finite Element Reliability and Sensitivity Methods for Performance-Based Earthquake Engineering.* Terje Haukaas and Armen Der Kiureghian. April 2004.

PEER 2003/13 *Effects of Connection Hysteretic Degradation on the Seismic Behavior of Steel Moment-Resisting Frames.* Janise E. Rodgers and Stephen A. Mahin. March 2004.

PEER 2003/12 *Implementation Manual for the Seismic Protection of Laboratory Contents: Format and Case Studies.* William T. Holmes and Mary C. Comerio. October 2003.

PEER 2003/11 *Fifth U.S.-Japan Workshop on Performance-Based Earthquake Engineering Methodology for Reinforced Concrete Building Structures.* February 2004.

PEER 2003/10 *A Beam-Column Joint Model for Simulating the Earthquake Response of Reinforced Concrete Frames.* Laura N. Lowes, Nilanjan Mitra, and Arash Altoontash. February 2004.

PEER 2003/09 *Sequencing Repairs after an Earthquake: An Economic Approach.* Marco Casari and Simon J. Wilkie. April 2004.

PEER 2003/08 *A Technical Framework for Probability-Based Demand and Capacity Factor Design (DCFD) Seismic Formats*. Fatemeh Jalayer and C. Allin Cornell. November 2003.

PEER 2003/07 *Uncertainty Specification and Propagation for Loss Estimation Using FOSM Methods.* Jack W. Baker and C. Allin Cornell. September 2003.

PEER 2003/06 *Performance of Circular Reinforced Concrete Bridge Columns under Bidirectional Earthquake Loading*. Mahmoud M. Hachem, Stephen A. Mahin, and Jack P. Moehle. February 2003.

PEER 2003/05 *Response Assessment for Building-Specific Loss Estimation.* Eduardo Miranda and Shahram Taghavi. September 2003.

PEER 2003/04 *Experimental Assessment of Columns with Short Lap Splices Subjected to Cyclic Loads*. Murat Melek, John W. Wallace, and Joel Conte. April 2003.

PEER 2003/03 *Probabilistic Response Assessment for Building-Specific Loss Estimation.* Eduardo Miranda and Hesameddin Aslani. September 2003.

PEER 2003/02 *Software Framework for Collaborative Development of Nonlinear Dynamic Analysis Program.* Jun Peng and Kincho H. Law. September 2003.

PEER 2003/01 *Shake Table Tests and Analytical Studies on the Gravity Load Collapse of Reinforced Concrete Frames.* Kenneth John Elwood and Jack P. Moehle. November 2003.

PEER 2002/24 *Performance of Beam to Column Bridge Joints Subjected to a Large Velocity Pulse.* Natalie Gibson, André Filiatrault, and Scott A. Ashford. April 2002.

PEER 2002/23 *Effects of Large Velocity Pulses on Reinforced Concrete Bridge Columns.* Greg L. Orozco and Scott A. Ashford. April 2002.

PEER 2002/22 *Characterization of Large Velocity Pulses for Laboratory Testing.* Kenneth E. Cox and Scott A. Ashford. April 2002.

PEER 2002/21 *Fourth U.S.-Japan Workshop on Performance-Based Earthquake Engineering Methodology for Reinforced Concrete Building Structures*. December 2002.

PEER 2002/20 *Barriers to Adoption and Implementation of PBEE Innovations.* Peter J. May. August 2002.

PEER 2002/19 *Economic-Engineered Integrated Models for Earthquakes: Socioeconomic Impacts.* Peter Gordon, James E. Moore II, and Harry W. Richardson. July 2002.

PEER 2002/18 *Assessment of Reinforced Concrete Building Exterior Joints with Substandard Details.* Chris P. Pantelides, Jon Hansen, Justin Nadauld, and Lawrence D. Reaveley. May 2002.

PEER 2002/17 *Structural Characterization and Seismic Response Analysis of a Highway Overcrossing Equipped with Elastomeric Bearings and Fluid Dampers: A Case Study.* Nicos Makris and Jian Zhang. November 2002.

PEER 2002/16 *Estimation of Uncertainty in Geotechnical Properties for Performance-Based Earthquake Engineering.* Allen L. Jones, Steven L. Kramer, and Pedro Arduino. December 2002.

PEER 2002/15 *Seismic Behavior of Bridge Columns Subjected to Various Loading Patterns.* Asadollah Esmaeily-Gh. and Yan Xiao. December 2002.

PEER 2002/14 *Inelastic Seismic Response of Extended Pile Shaft Supported Bridge Structures.* T.C. Hutchinson, R.W. Boulanger, Y.H. Chai, and I.M. Idriss. December 2002.

PEER 2002/13 *Probabilistic Models and Fragility Estimates for Bridge Components and Systems.* Paolo Gardoni, Armen Der Kiureghian, and Khalid M. Mosalam. June 2002.

PEER 2002/12 *Effects of Fault Dip and Slip Rake on Near-Source Ground Motions: Why Chi-Chi Was a Relatively Mild M7.6 Earthquake.* Brad T. Aagaard, John F. Hall, and Thomas H. Heaton. December 2002.

PEER 2002/11 *Analytical and Experimental Study of Fiber-Reinforced Strip Isolators*. James M. Kelly and Shakhzod M. Takhirov. September 2002.

PEER 2002/10 *Centrifuge Modeling of Settlement and Lateral Spreading with Comparisons to Numerical Analyses***.** Sivapalan Gajan and Bruce L. Kutter. January 2003.

PEER 2002/09 *Documentation and Analysis of Field Case Histories of Seismic Compression during the 1994 Northridge, California, Earthquake.* Jonathan P. Stewart, Patrick M. Smith, Daniel H. Whang, and Jonathan D. Bray. October 2002.

PEER 2002/08 *Component Testing, Stability Analysis and Characterization of Buckling-Restrained Unbonded Braces™.* Cameron Black, Nicos Makris, and Ian Aiken. September 2002.

PEER 2002/07 *Seismic Performance of Pile-Wharf Connections.* Charles W. Roeder, Robert Graff, Jennifer Soderstrom, and Jun Han Yoo. December 2001.

PEER 2002/06 *The Use of Benefit-Cost Analysis for Evaluation of Performance-Based Earthquake Engineering Decisions*. Richard O. Zerbe and Anthony Falit-Baiamonte. September 2001.

PEER 2002/05 *Guidelines, Specifications, and Seismic Performance Characterization of Nonstructural Building Components and Equipment*. André Filiatrault, Constantin Christopoulos, and Christopher Stearns. September 2001.

PEER 2002/04 *Consortium of Organizations for Strong-Motion Observation Systems and the Pacific Earthquake Engineering Research Center Lifelines Program: Invited Workshop on Archiving and Web Dissemination of Geotechnical Data, 4–5 October 2001*. September 2002.

PEER 2002/03 *Investigation of Sensitivity of Building Loss Estimates to Major Uncertain Variables for the Van Nuys Testbed.* Keith A. Porter, James L. Beck, and Rustem V. Shaikhutdinov. August 2002.

PEER 2002/02 *The Third U.S.-Japan Workshop on Performance-Based Earthquake Engineering Methodology for Reinforced Concrete Building Structures*. July 2002.

PEER 2002/01 *Nonstructural Loss Estimation: The UC Berkeley Case Study.* Mary C. Comerio and John C. Stallmeyer. December 2001.

PEER 2001/16 *Statistics of SDF-System Estimate of Roof Displacement for Pushover Analysis of Buildings.* Anil K. Chopra, Rakesh K. Goel, and Chatpan Chintanapakdee. December 2001.

PEER 2001/15 *Damage to Bridges during the 2001 Nisqually Earthquake.* R. Tyler Ranf, Marc O. Eberhard, and Michael P. Berry. November 2001.

PEER 2001/14 *Rocking Response of Equipment Anchored to a Base Foundation.* Nicos Makris and Cameron J. Black. September 2001.

PEER 2001/13 *Modeling Soil Liquefaction Hazards for Performance-Based Earthquake Engineering.* Steven L. Kramer and Ahmed-W. Elgamal. February 2001.

PEER 2001/12 *Development of Geotechnical Capabilities in OpenSees.* Boris Jeremi . September 2001.

PEER 2001/11 *Analytical and Experimental Study of Fiber-Reinforced Elastomeric Isolators*. James M. Kelly and Shakhzod M. Takhirov. September 2001.

PEER 2001/10 *Amplification Factors for Spectral Acceleration in Active Regions.* Jonathan P. Stewart, Andrew H. Liu, Yoojoong Choi, and Mehmet B. Baturay. December 2001.

PEER 2001/09 *Ground Motion Evaluation Procedures for Performance-Based Design.* Jonathan P. Stewart, Shyh-Jeng Chiou, Jonathan D. Bray, Robert W. Graves, Paul G. Somerville, and Norman A. Abrahamson. September 2001.

PEER 2001/08 *Experimental and Computational Evaluation of Reinforced Concrete Bridge Beam-Column Connections for Seismic Performance*. Clay J. Naito, Jack P. Moehle, and Khalid M. Mosalam. November 2001.

PEER 2001/07 *The Rocking Spectrum and the Shortcomings of Design Guidelines.* Nicos Makris and Dimitrios Konstantinidis. August 2001.

PEER 2001/06 *Development of an Electrical Substation Equipment Performance Database for Evaluation of Equipment Fragilities*. Thalia Agnanos. April 1999.

PEER 2001/05 *Stiffness Analysis of Fiber-Reinforced Elastomeric Isolators.* Hsiang-Chuan Tsai and James M. Kelly. May 2001.

PEER 2001/04 *Organizational and Societal Considerations for Performance-Based Earthquake Engineering.* Peter J. May. April 2001.

PEER 2001/03 *A Modal Pushover Analysis Procedure to Estimate Seismic Demands for Buildings: Theory and Preliminary Evaluation.* Anil K. Chopra and Rakesh K. Goel. January 2001.

PEER 2001/02 *Seismic Response Analysis of Highway Overcrossings Including Soil-Structure Interaction.* Jian Zhang and Nicos Makris. March 2001.

PEER 2001/01 *Experimental Study of Large Seismic Steel Beam-to-Column Connections.* Egor P. Popov and Shakhzod M. Takhirov. November 2000.

PEER 2000/10 *The Second U.S.-Japan Workshop on Performance-Based Earthquake Engineering Methodology for Reinforced Concrete Building Structures.* March 2000.

PEER 2000/09 *Structural Engineering Reconnaissance of the August 17, 1999 Earthquake: Kocaeli (Izmit), Turkey.* Halil Sezen, Kenneth J. Elwood, Andrew S. Whittaker, Khalid Mosalam, John J. Wallace, and John F. Stanton. December 2000.

PEER 2000/08 *Behavior of Reinforced Concrete Bridge Columns Having Varying Aspect Ratios and Varying Lengths of Confinement.* Anthony J. Calderone, Dawn E. Lehman, and Jack P. Moehle. January 2001.

PEER 2000/07 *Cover-Plate and Flange-Plate Reinforced Steel Moment-Resisting Connections.* Taejin Kim, Andrew S. Whittaker, Amir S. Gilani, Vitelmo V. Bertero, and Shakhzod M. Takhirov. September 2000.

PEER 2000/06 *Seismic Evaluation and Analysis of 230-kV Disconnect Switches.* Amir S. J. Gilani, Andrew S. Whittaker, Gregory L. Fenves, Chun-Hao Chen, Henry Ho, and Eric Fujisaki. July 2000.

PEER 2000/05 *Performance-Based Evaluation of Exterior Reinforced Concrete Building Joints for Seismic Excitation.* Chandra Clyde, Chris P. Pantelides, and Lawrence D. Reaveley. July 2000.

PEER 2000/04 *An Evaluation of Seismic Energy Demand: An Attenuation Approach.* Chung-Che Chou and Chia-Ming Uang. July 1999.

PEER 2000/03 *Framing Earthquake Retrofitting Decisions: The Case of Hillside Homes in Los Angeles.* Detlof von Winterfeldt, Nels Roselund, and Alicia Kitsuse. March 2000.

PEER 2000/02 *U.S.-Japan Workshop on the Effects of Near-Field Earthquake Shaking.* Andrew Whittaker, ed. July 2000.

PEER 2000/01 *Further Studies on Seismic Interaction in Interconnected Electrical Substation Equipment.* Armen Der Kiureghian, Kee-Jeung Hong, and Jerome L. Sackman. November 1999.

PEER 1999/14 *Seismic Evaluation and Retrofit of 230-kV Porcelain Transformer Bushings*. Amir S. Gilani, Andrew S. Whittaker, Gregory L. Fenves, and Eric Fujisaki. December 1999.

PEER 1999/13 *Building Vulnerability Studies: Modeling and Evaluation of Tilt-up and Steel Reinforced Concrete Buildings.* John W. Wallace, Jonathan P. Stewart, and Andrew S. Whittaker, editors. December 1999.

PEER 1999/12 *Rehabilitation of Nonductile RC Frame Building Using Encasement Plates and Energy-Dissipating Devices.* Mehrdad Sasani, Vitelmo V. Bertero, James C. Anderson. December 1999.

PEER 1999/11 *Performance Evaluation Database for Concrete Bridge Components and Systems under Simulated Seismic Loads.* Yael D. Hose and Frieder Seible. November 1999.

PEER 1999/10 *U.S.-Japan Workshop on Performance-Based Earthquake Engineering Methodology for Reinforced Concrete Building Structures.* December 1999.

PEER 1999/09 *Performance Improvement of Long Period Building Structures Subjected to Severe Pulse-Type Ground Motions.* James C. Anderson, Vitelmo V. Bertero, and Raul Bertero. October 1999.

PEER 1999/08 *Envelopes for Seismic Response Vectors.* Charles Menun and Armen Der Kiureghian. July 1999.

PEER 1999/07 *Documentation of Strengths and Weaknesses of Current Computer Analysis Methods for Seismic Performance of Reinforced Concrete Members.* William F. Cofer. November 1999.

PEER 1999/06 *Rocking Response and Overturning of Anchored Equipment under Seismic Excitations.* Nicos Makris and Jian Zhang. November 1999.

PEER 1999/05 *Seismic Evaluation of 550 kV Porcelain Transformer Bushings.* Amir S. Gilani, Andrew S. Whittaker, Gregory L. Fenves, and Eric Fujisaki. October 1999.

PEER 1999/04 *Adoption and Enforcement of Earthquake Risk-Reduction Measures.* Peter J. May, Raymond J. Burby, T. Jens Feeley, and Robert Wood.

PEER 1999/03 *Task 3 Characterization of Site Response General Site Categories.* Adrian Rodriguez-Marek, Jonathan D. Bray, and Norman Abrahamson. February 1999.

PEER 1999/02 *Capacity-Demand-Diagram Methods for Estimating Seismic Deformation of Inelastic Structures: SDF Systems.* Anil K. Chopra and Rakesh Goel. April 1999.

PEER 1999/01 *Interaction in Interconnected Electrical Substation Equipment Subjected to Earthquake Ground Motions.* Armen Der Kiureghian, Jerome L. Sackman, and Kee-Jeung Hong. February 1999.

PEER 1998/08 *Behavior and Failure Analysis of a Multiple-Frame Highway Bridge in the 1994 Northridge Earthquake.* Gregory L. Fenves and Michael Ellery. December 1998.

PEER 1998/07 *Empirical Evaluation of Inertial Soil-Structure Interaction Effects.* Jonathan P. Stewart, Raymond B. Seed, and Gregory L. Fenves. November 1998.

PEER 1998/06 *Effect of Damping Mechanisms on the Response of Seismic Isolated Structures.* Nicos Makris and Shih-Po Chang. November 1998.

PEER 1998/05 *Rocking Response and Overturning of Equipment under Horizontal Pulse-Type Motions.* Nicos Makris and Yiannis Roussos. October 1998.

PEER 1998/04 *Pacific Earthquake Engineering Research Invitational Workshop Proceedings, May 14–15, 1998: Defining the Links between Planning, Policy Analysis, Economics and Earthquake Engineering.* Mary Comerio and Peter Gordon. September 1998.

PEER 1998/03 *Repair/Upgrade Procedures for Welded Beam to Column Connections.* James C. Anderson and Xiaojing Duan. May 1998.

PEER 1998/02 *Seismic Evaluation of 196 kV Porcelain Transformer Bushings.* Amir S. Gilani, Juan W. Chavez, Gregory L. Fenves, and Andrew S. Whittaker. May 1998.

PEER 1998/01 *Seismic Performance of Well-Confined Concrete Bridge Columns.* Dawn E. Lehman and Jack P. Moehle. December 2000.

ONLINE REPORTS

The following PEER reports are available by Internet only at http://peer.berkeley.edu/publications/peer_reports.html

PEER 2008/101 *Seismic Performance Objectives for Tall Buildings.* William T. Holmes, Charles Kircher, William Petak, and Nabih Youssef. August 2008.

PEER 2007/101 *Generalized Hybrid Simulation Framework for Structural Systems Subjected to Seismic Loading.* Tarek Elkhoraibi and Khalid M. Mosalam. July 2007.

PEER 2007/100 *Seismic Evaluation of Reinforced Concrete Buildings Including Effects of Masonry Infill Walls.* Alidad Hashemi and Khalid M. Mosalam. July 2007.